Cryogenic Engineering

Fifty Years of Progress

Klaus D. Timmerhaus
Richard P. Reed (Eds.)

Springer

CRYOGENIC ENGINEERING

INTERNATIONAL CRYOGENICS MONOGRAPH SERIES

Current Volumes in this Series:

Klaus D. Timmerhaus and Richard P. Reed (Eds.)

CRYOGENIC ENGINEERING

Fifty Years of Progress

Springer

Klaus D. Timmerhaus
Department of Chemical and
    Biological Engineering
University of Colorado
Boulder, CO 80309
USA
Klaus.timmerhaus@colorado. edu

Richard P. Reed
Cryogenic Materials, Inc.
2625 Iliff
Boulder, CO 80305
USA
rpreed@comcast.net

9 8 7 6 5 4 3 2 1

springer.com

Preface

The Cryogenic Engineering Conference (CEC) marked its 50th anniversary this past year. To highlight the occasion the CEC Board, in conjunction with the International Cryogenic Materials Conference (ICMC) Board, proposed that a special 1-day anniversary program be scheduled prior to the CEC–ICMC joint meeting in Keystone, Colorado, that would review the advances in cryogenic engineering which had occurred in this distinct but relatively invisible field of engineering during the past 50 years. Accordingly, a program of 14 papers, covering both the interest of CEC attendees and ICMC attendees, was envisioned to cover the various aspects of cryogenic engineering. Authors were invited to prepare these review papers, but because of time restrictions the technical program was limited and not all papers were presented orally. As a result, the CEC and ICMC boards recommended that a separate monograph, in addition to the regularly published two volumes of *Advances in Cryogenic Engineering*, be prepared which would include all of the invited papers. This monograph is the result of that recommendation.

To provide an assessment of the status of cryogenic engineering 50 years ago, a historical summary of cryogenic activity is presented in the first chapter. The purpose is to review the events occurring during the 100-year period prior to 1950 as well as to provide a better understanding of the events that took place after 1950. With that historical background, the advances in establishing databases for cryogenic fluids and properties of materials, both metallic and nonmetallic, are discussed and their present status evaluated. The advances in cryogenic fundamentals are then covered, with reviews of cryogenic principles, progress in cryogenic insulation, development of low-loss storage systems for cryogenic fluids, establishment of modern liquefaction processes, modifications occurring in helium cryogenics, and improvements achieved in cryogenic thermometry.

The monograph then reviews several well-established applications resulting from the cryogenic advances noted above. The cryocoolers developed for aerospace missions are many in number and show a steady progress to achieve long-life coolers and cryostats. The actual application of superconductivity is noted in two chapters, one considering low-temperature superconductivity activities and the other considering high-temperature superconductivity activities. Both are contributing to modern concepts of power transmission and storage, high-power magnets, and

sophisticated medical equipment. Cryopreservation of tissues and organs is undergoing considerable change with a better understanding of the effects of cryoprotectants. Obviously, there are other applications that could have been included, but the value of the monograph would have been lost.

The preparation of even a monograph requires the assistance of many individuals. The editors thank the authors for their interest and time required to prepare a review, a process that normally necessitates considerable effort in literature review and evaluation. We also want to thank the many reviewers of the chapters and the constructive comments that were provided. Finally, we want to recognize the many contributions made by Cynthia Ocken, from the University of Colorado and assistant to one of the editors. Her daily updating of changes made in the chapters over many months and the overall control of the publication process are greatly appreciated and admired.

KLAUS D. TIMMERHAUS
RICHARD P. REED

Contents

About the Authors

R.F. Barron is Professor Emeritus of Mechanical Engineering at the Louisiana Tech University. He is the author of *Cryogenic Systems* (1st ed., 1965; 2nd ed., 1985; Russian translation, 1989) and *Cryogenic Heat Transfer* (1999). He is a past member of the Cryogenic Engineering Conference Board and a member of the Cryogenic Society of America, where he serves on the Editorial Board of *Cold Facts*. He is a fellow of ASME.

J.G. Baust is Lead Professor in the Biological Sciences and Bioengineering Department and Director of the Institute of Biomedical Technology at the State University of New York at Binghamton, New York. He has authored or coauthored hundreds of papers, reviews, and patents in cell-tissue cryopreservation, hypothermic organ preservation, tissue engineering, and cancer therapy. He has been heavily involved in numerous cryobiology companies and presently serves as President and CEO of BioLife Solutions, Inc.

J.M. Baust serves as President and CEO of Cell Preservation, Inc. and Professor in the Bioengineering and Biology Department at the State University of New York at Binghamton, New York. He has authored or coauthored many papers, reviews, and patents in the area of low-temperature biology and has been a leader in advancing this field into the molecular biological arena, focusing on the areas of transduction and apoptosis. He serves on several advisory and editorial boards of several biotech corporations and journals, respectively.

W.F. Castle is retired after working for BOC in the UK for 48 years, where he was Project and Technical Director as well as International Sales Project Director. He is the immediate Past President of Commission A2 of the International Institute of Refrigeration and has presented many papers at international meetings covering topics on cryogenic process design, selection of air separation plants for specific product demands, and review of advances in cryogenic technology.

H.C. Freyhardt is Director of the Zentrum für Funktionswerkstoffe in Goettingen, Germany, and a member of the University of Goettingen's Institute für Materialphysik. Most of his extensive publications relate to his studies on superconductors and semiconductors, including alloys, composites, thin film oxides, and thin film

high transition temperature alloys. He has been active in the International Cryogenic Materials Conference.

G. Hartwig is retired from the Forschungszentrum Karlsruhe, where he developed a strong program investigating the low-temperature behavior of both polymers and composites. In this area he has published extensively and directed numerous international conferences.

E.E. Hellstrom has devoted nearly 20 years to the study of high-temperature superconductors at the University of Wisconsin in Madison. His research interests involve the study of the underlying materials science applicable to the development of wire conductors for high-current and high-field use, focusing on the Bi-based high-temperature superconducting materials and recently on MgB_2.

W.L. Hufferd has 40 years of experience in structural design and analysis of solid-fuel rocket engines. He is the author of many technical reports in this area, with studies on stress and fracture analysis and materials aging and associated service life. He served as Director of the CPIA over the last 10 years on an extensive literature retrieval system while cooperatively reconstructing the former National Bureau of Standards (NBS) cryogenic database.

E.D. Marquardt has more than 17 years of cryogenic experience at the National Institute of Standards and Technology (NIST) and Ball Aerospace and Technologies, with major emphasis on pulse-tube, Stirling, and Joule–Thomson cryocoolers. He is actively involved in material properties and with development of cryogenic literature databases. Presently, he serves on the boards of the International Cryocooler Conference and the Cryogenic Engineering Conference.

R.A. Mohling has over 30 years of experience in cryogenic systems development while employed with AFRPL, Beech Aircraft/Cryogenic Division, Ball Aerospace, and Technology Applications, Inc. (TAI). He is currently President of TAI, a small business company specializing in technology development and fabricating prototypes of cryogenic and thermal management systems. He led a collaborative effort for NASA—Marshall Space Flight Center with the CPIA and NIST to reconstruct the former NBS cryogenic database.

F. Pavese is Principal Scientist at the National Institute for Research in Metrology, formerly the Istituto di Metrologia ("G. Collonetti") in Turin, Italy. He has over a 40 year record in cryogenic thermometry, resulting in many publications, including the text *Modern Gas-Based Temperature and Pressure Measurements*. He also is a recognized authority in the establishment of recent international low-temperature scales.

R. Radebaugh is Group Leader of the Cryogenic Technologies Center at the NIST in Boulder, Colorado. He has been a leader in cryocooler research and in the development of models for cryogenic properties and processes at temperatures ranging from 10 mK to room temperature. He has authored or coauthored over 120

papers and has received a number of awards, including the DOC Gold and Silver Medal, the R&D 100 Award, and the J&E Hall Gold Medal.

R.F. Ross, Jr. is Supervisor of Cryogenics and Advanced Thermal Technologies at NASA's Jet Propulsion Laboratory, having been with the latter since 1968. In his work on many space-science and space-cryogenics missions, he has published more than 160 papers, over 50 of which are in the field of cryocoolers and cryogenic instruments. He is a past chair of the International Cryocooler Conference and has been its Proceedings Editor for the past 12 years.

R.P. Reed has been heavily involved over the past 40 years in the study of low-temperature properties of materials, with an extensive publication record. He initially was with the NIST in Boulder, Colorado, and now serves as President of Cryogenic Materials, Inc., consulting in the fields of cryogenic materials, specializing in structural alloys and composites for superconducting applications.

R.G. Scurlock is Emeritus BOC Professor of Cryogenic Engineering and former Director of the Institute of Cryogenic and Engineering at the University of Southhampton in the UK. With over 40 years of experience in cryogenic fluid mechanism and heat transfer, he now consults with Kryos Technology. Results of his work are now standard worldwide in low-loss storage containers and are published in a text of that same title. He was awarded the CEC S.C. Collins award and is the first individual outside of the US to receive this honor.

M. Suenaga currently directs the Metallurgy and Materials Science Division at Brookhaven National Laboratories and serves as Adjunct Professor of Materials Science at the State University of New York at Stony Brook. He has continuously contributed over the past 30 years to the understanding of type A15 and cuprate superconductors and their use in many applications.

K.D. Timmerhaus is a President's Teaching Scholar at the University of Colorado in Boulder, Colorado, after 47 years of teaching, research, and administration at the institution. His 50-year association with the Cryogenic Engineering Conference has involved many offices, including editor of the *Advances in Cryogenic Engineering* for 25 years. He is the recipient of awards from the CEC, CSA, AIChE, ASEE, SAE, IIR, and NSF. He is Past President of the IIR, AIChE, Sigma Xi, and a member of the NAE.

S.W. Van Sciver is a Distinguished Research Professor in the Mechanical Engineering Department and Program Director with the National High Magnetic Field Laboratory (NHMFL) at Florida State University. He is the author of over 150 publications in low-temperature physics, liquid helium technology, cryogenic engineering, and magnet technology and is author of the textbook *Helium Cryogenics* (1986). He is a Fellow of ASME and American Editor for *Cryogenics*.

Part 1
Background Information

1
Historical Summary of Cryogenic Activity Prior to 1950[1]

R. RADEBAUGH

National Institute of Standards and Technology, Boulder, Colorado, 80305 USA

Abstract

Cryogenics is the science and technology dealing with temperatures less than about 120 K, although this historical summary does not adhere to a strict 120 K definition. The techniques used to produce cryogenic temperatures differ in several ways from those dealing with conventional refrigeration. In practice, these two areas often overlap and the boundary between conventional and cryogenic refrigeration is often indistinct. Significant reductions in temperature often have very pronounced effects on the properties of materials and the behavior of systems.

Many cryogenic applications have developed as the refrigeration techniques prior to 1950 have improved, although many applications still face stiff competition from ambient temperature phenomena because of the associated refrigeration problems. This review shows how the development of new applications over the past 50 years is closely tied to the advances in cryogenic refrigeration prior to 1950.

1.1 Introduction

Temperature affects processes and material properties more than any other variable, such as pressure, magnetic field, electric field, etc. The ability to harness and apply these temperature effects is a unique feature of mankind, and it has contributed to great advances in our civilization. Mankind has discovered abundant uses for high temperatures, beginning in prehistoric times with the use of fire for warmth, light, and cooking. Later, but still more than 20 centuries ago, mankind learned to forge tools and make crude pottery using heat from fires. As civilization advanced and higher temperatures could be achieved, stronger metals, such as iron, could be forged into tools, and much stronger pottery and china could be produced by the higher temperature firing (sintering) of clay. The industrial revolution ushered in

---

[1] Contribution of the National Institute of Standards and Technology, not subject to copyright.

the steam engine and the ability to generate tremendous power for efficient manufacturing and transportation. The enhancement of chemical reactions at higher temperatures has been exploited for the production of vast amounts of new and improved materials in the last century or so.

High-temperature applications began rather early in the history of civilization owing to the ease of producing increasingly hotter fires. In contrast, mankind's use of low temperatures has greatly lagged that of high temperatures because of the greater difficulty in producing low temperatures. Low-temperature applications were limited for many centuries to the use of naturally occurring ice. The practice of using natural ice to treat injuries and inflammation was carried out by Egyptians as early as 2500 BC [1], and the Chinese began to use crushed ice in food around 2000 BC. Although ice was first created artificially in the laboratory in 1755, it was not until near the mid 1800s with the development of the steam engine and practical compressors in the industrial revolution that artificial ice could be produced in sufficient quantities to replace natural ice cut from lakes. Until then the sole use of low temperatures was with natural ice for food preservation and a few medical procedures.

The science of thermodynamics was just beginning to develop around 1850, which related heat, work, and temperature. Though the concept of absolute zero at –273 °C was put forward in the mid 1700s, the means of reaching temperatures much below 0 °C were not known or possible until the development of thermodynamics and high-pressure reciprocating compressors around 1850. Thus, nearly all understanding and uses of low temperatures have occurred in the last 150 years. Prior to that time, laboratory techniques for reducing temperatures relied on the liquefaction of a small quantity of gas at high pressure in a thick-walled glass tube surrounded by ice, followed by a rapid expansion of the vapor phase to atmospheric pressure through a valve. The temperature of the remaining liquid phase then dropped to its normal boiling point. Faraday used this one-shot process on several gases, beginning in 1823 with chlorine (normal boiling point of 239 K) [2]. Over the next several decades nearly all of the gases were liquefied at the ice point under sufficient pressure. Ethylene, with a critical temperature of 282 K and a normal boiling point temperature of 169 K, yielded the lowest achievable temperature with this technique. Those known gases such as methane, carbon monoxide, oxygen, nitrogen, and hydrogen that could not be liquefied by this technique, even with pressures up to 40 MPa, were called "permanent" gases.

In an 1834 British patent, Perkins, an American who had moved to England, showed how to carry out the Faraday process of liquefaction and expansion continuously [3]. That was the beginning of today's vapor-compression refrigerators, shown schematically in Figure 1.1. The Perkins refrigerator was designed for use with ethyl ether, although the actual refrigerator built by John Hague and shown in Figure 1.2 used caoutchoucine, a distillate of India rubber readily available at that time, to produce small quantities of ice soon after 1834.

New applications of cryogenics are made possible whenever some lower temperature is achieved. The difficulties and problems associated with achieving a

FIGURE 1.1. Vapor compression cycle developed by Perkins [3].

VAPOR-COMPRESSION CYCLE
(Steady Flow)
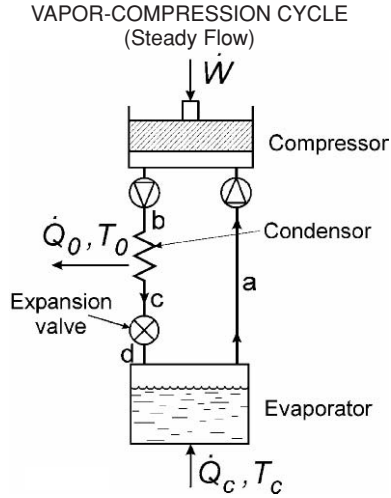
particular temperature greatly influence the development of applications of these temperatures. As a result, this review examines the development of refrigeration techniques and cryocoolers to show how cryogenic applications are strongly dependent on improvements in refrigeration techniques.
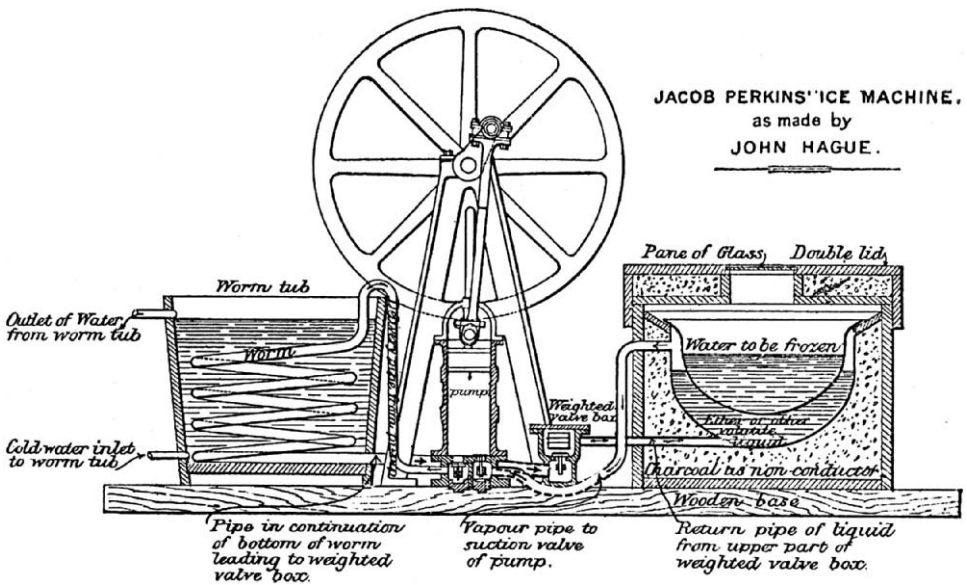
FIGURE 1.2. Perkin ice machine built by Hague.
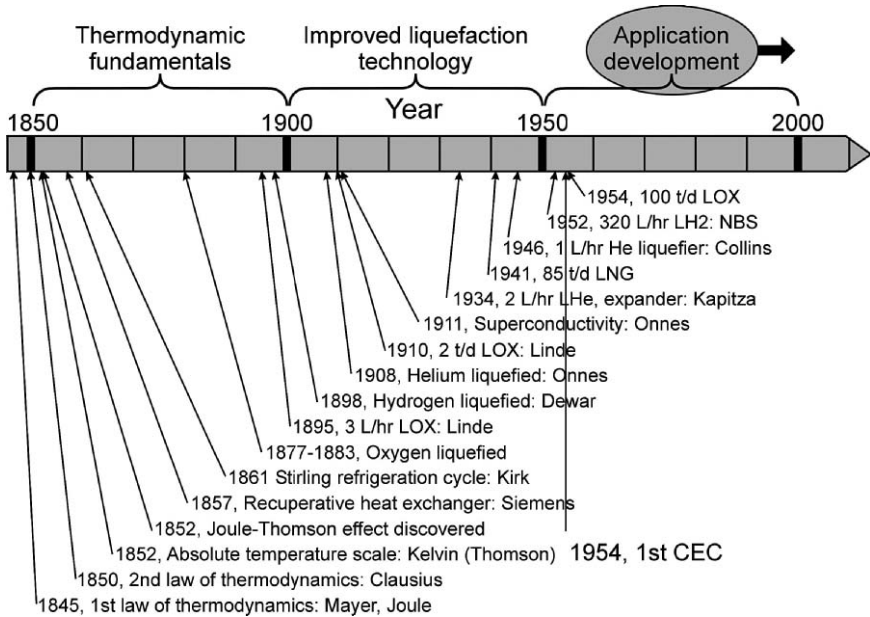
FIGURE 1.3. Cryogenic developments from 1850 to 1950.

1.2 The Beginning of Cryogenics

In examining low-temperature developments over the past 150 years, we note that there is a convenient and interesting division into three 50-year time segments, where the developments in each time segment have their unique characteristics. Figure 1.3 summarizes the important developments in each time segment. Though the papers in this monograph focus mostly on the last 50 years, it is instructive to examine briefly the developments in refrigeration and cryogenics that occurred in the two previous 50-year segments to understand how they contributed to the status of cryogenics at the time of the first Cryogenic Engineering Conference (CEC) in 1954. Also, by comparing developments in each 50-year segment, we may have a better idea how quickly future developments might progress in the first half of the 21st century.

Figure 1.3 shows that the development of thermodynamic fundamentals was the primary contributor to advances in cryogenics between about 1850 and 1900. The advances in that half century were primarily of interest only to scientists, and there were almost no applications for temperatures below the ice point. At the beginning of that time period the first and second laws of thermodynamics were just being proposed. As part of those developments the thermodynamic cycles required to liquefy the "permanent" gases like oxygen, nitrogen, hydrogen, and helium were being invented. The critical temperatures of these "permanent" gases are far below the ice point, and their very low normal boiling temperatures are now

referred to as cryogenic temperatures. Cryogenics is usually defined as the science and technology dealing with temperatures less than about 120 K [4,5], although this review does not adhere to a strict 120 K definition. Onnes first coined the adjective "cryogenic" in 1894 by using it in a paper entitled, "On the cryogenic laboratory at Leiden and on the production of very low temperatures" [6]. The techniques used to produce cryogenic temperatures differ significantly from those dealing with conventional refrigeration. One of the most important differences is the need to precool the compressed gas before it is expanded in order to reach cryogenic temperatures when starting from 0 °C or higher. Precooling can be accomplished with a cascade of refrigerant baths or with a heat exchanger. The concept for a recuperative counterflow heat exchanger was developed by Gorrie [7] in 1851 and refined by Siemens [8] in 1857. The Joule–Thomson (JT) effect discovered in 1852 [9] was not sufficiently large to produce cryogenic temperatures when starting from the ice point without the precooling afforded by such a heat exchanger.

Oxygen was first liquefied (in the form of a mist) in 1877 by using the older techniques of Faraday and Perkins, but with a cascade of precooling baths. Cailletet in Paris used a hand-operated screw jack with mercury to pressurize oxygen hydraulically (155 K critical temperature T_{cr}) to 20 MPa in a thick-walled glass tube cooled to 169 K by a surrounding bath of liquid ethylene. The liquid ethylene ($T_{cr} = 282$ K) had been produced earlier using the Faraday technique with an ice bath for precooling. When the pressure on the oxygen was released via the screw jack handwheel, a fog appeared in the glass tube, but it quickly disappeared because of the heat input from the glass tube [9,10]. On the same day, Pictet in Geneva produced a continuous mist of liquid oxygen from a JT valve by using a cascade of vapor-compression systems for precooling the oxygen. The cascade of precooling baths was operated continuously using piston compressors. The cascade consisted of sulfur dioxide ($T_{cr} = 431$ K, $T_{NBP} = 263$ K) and solid carbon dioxide ($T_{cr} = 304$ K, $T_s = 195$ K). The flowing high-pressure oxygen was cooled successively by the two baths before expanding through the JT valve to the atmosphere. A jet of liquid oxygen mist at 90 K sprayed out from the JT valve [9,10]. The first to produce enough liquid oxygen and liquid nitrogen to study their properties were Wroblewski and Olszewski of Poland in 1883. They used the same cascade method as Cailletet, but the final stage was a pumped liquid ethylene bath at a temperature of 137 K [11]. Because the temperature of that bath was less than the 155 K critical temperature of oxygen, liquid formed inside the glass tube under a pressure of about 2.5 MPa. Upon reducing the pressure to 1 atm, a small quantity of liquid boiling at 90 K remained in the tube for a short period of time. Figure 1.4 shows the path in a temperature entropy ($T–S$) diagram followed by the various methods for liquefying oxygen.

Though the recuperative heat exchanger had been invented in 1857 by Siemens, little use was made of it until 1895 when Hampson replaced the cascade baths used previously for precooling oxygen with the recuperative heat exchanger. A JT valve at the cold end of the heat exchanger provided the cooling during expansion. Figure 1.5 is a schematic of the cycle used by Hampson to liquefy air [12], which
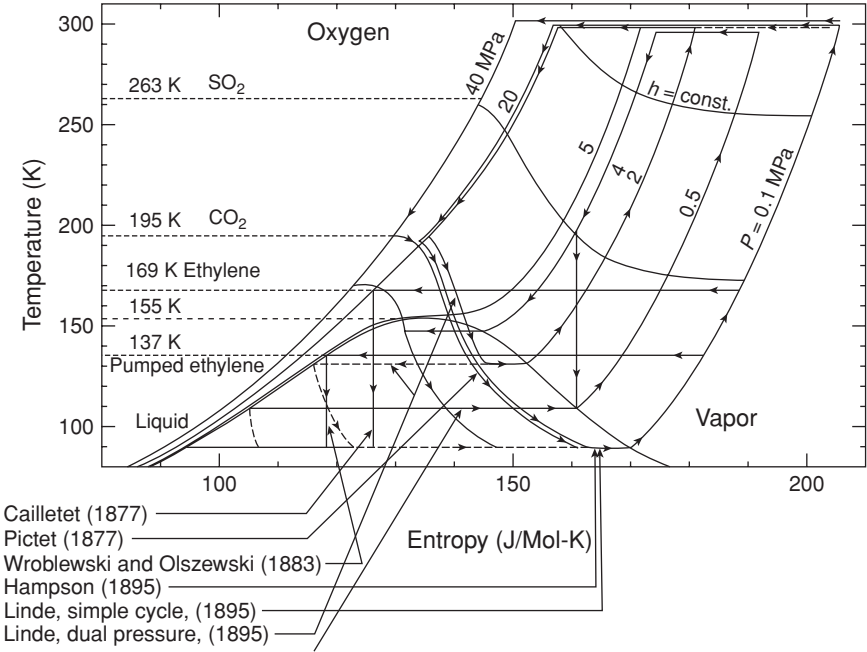
FIGURE 1.4. Cryogenic approaches taken to liquefy oxygen and shown on a $T-S$ diagram.
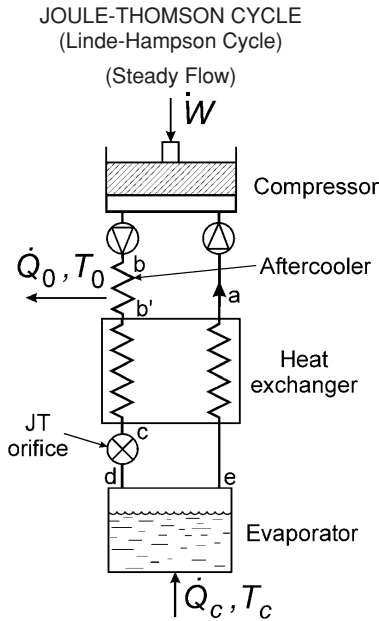
FIGURE 1.5. Schematic of the JT cycle used by Hampson to liquefy air.

FIGURE 1.6. Drawing of Hampson's air liquefier.
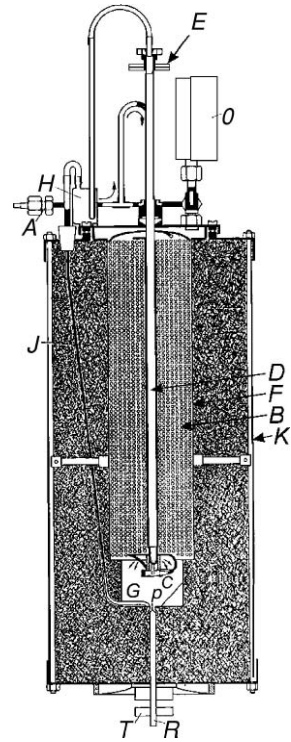
is usually referred to today as simply the JT cycle. Figure 1.6 is a drawing of Hampson's air liquefier showing the closely packed copper tubing heat exchanger in the annular space between tubes D and F. The JT valve C is controlled by the handle E. Glass wool surrounds the evaporator G and the heat exchanger. The liquefaction rate was 1 L/h [13]. A very effective heat exchanger is necessary to reach cryogenic temperatures with the warm end at 300 K. The requirement for such a heat exchanger is one feature that distinguishes cryogenic refrigeration from normal refrigeration. At the same time as Hampson's work, Linde in Germany also used the combination of a JT valve and a recuperative heat exchanger for the continuous liquefaction of air in 1895 [14]. The simple cycle first used by Linde is the same cycle Hampson used as depicted in Figure 1.5. Linde also developed a dual-pressure cycle, as sketched in Figure 1.7, which was more efficient than the simple cycle. About 80% of the gas was expanded from 20 MPa to 4 MPa and returned to the second-stage compressor. The remaining 20% (mostly liquid) was expanded from 4 MPa to 0.1 MPa, with the gas fraction being returned to the first-stage compressor [15]. Figure 1.4 shows the path of this cycle on a $T-S$ diagram. With this cycle Linde was able to produce about 10 L/h of liquid air. Linde quickly went on to commercialize the process and developed the technique of distilling liquid air into oxygen and nitrogen. By 1899 Linde was producing
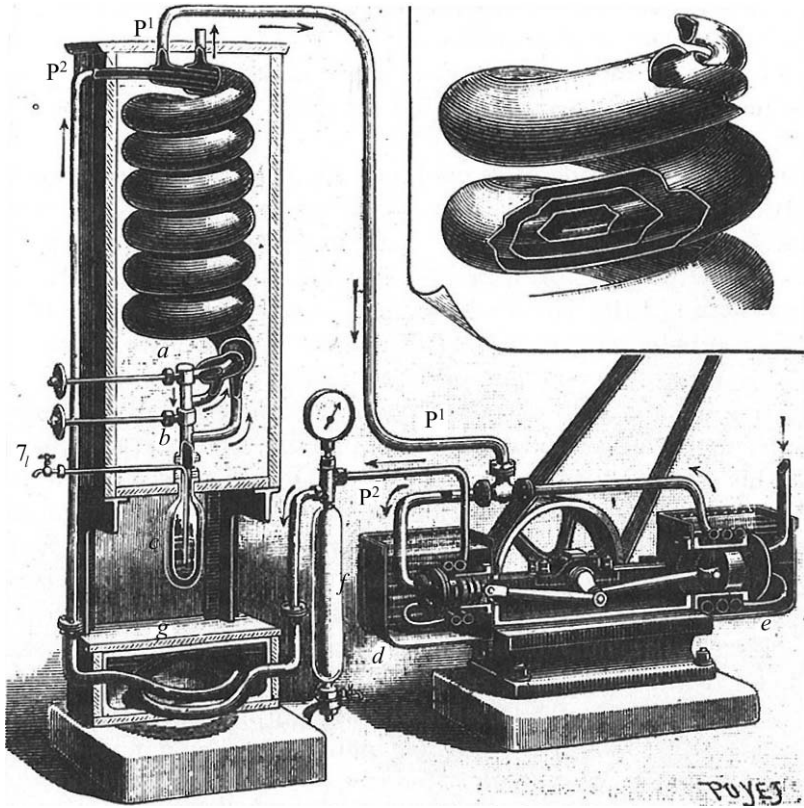
FIGURE 1.7. Drawing of Linde's dual-pressure JT air liquefier.

liquid air at the rate of 50 L/h [13]. The early liquefiers of Hampson and Linde used glass wool for insulation, even though Dewar had invented the use of vacuum for thermal insulation in 1873 and the silvered glass vacuum container in 1892 [9].

The regenerative heat exchanger (regenerator) was invented by Stirling in 1816 for use in an engine with oscillating flow. He called the device an economizer, in which heat is stored for a half cycle in the heat capacity of the regenerator matrix. The Stirling engine, as patented by Robert Stirling in 1817 [16], was first used to pump water from a quarry and had the advantage of being much safer than the steam engines of that time. The operating frequency was probably a few hertz. Stirling's patent drawing, given in Figure 1.8, shows the use of a displacer (#9 in the figure) to move the working gas between the hot and ambient temperature regions. However, the drawing does not show an ambient temperature heat sink or the specific regenerator arrangement. In 1834, Herschel proposed to reverse the cycle and use it as a refrigerator for producing ice [17]. However, it was not until about 1861 that Kirk [18] reduced the concept to practice. Figure 1.9 shows a drawing of the Kirk ice machine. The displacer filled with wire gauze O for the
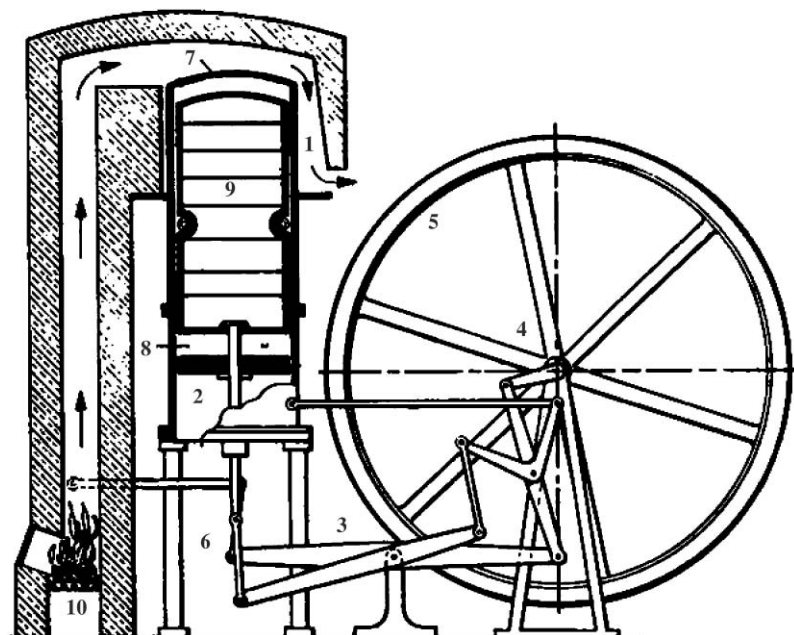
FIGURE 1.8. Stirling engine patented by Stirling.
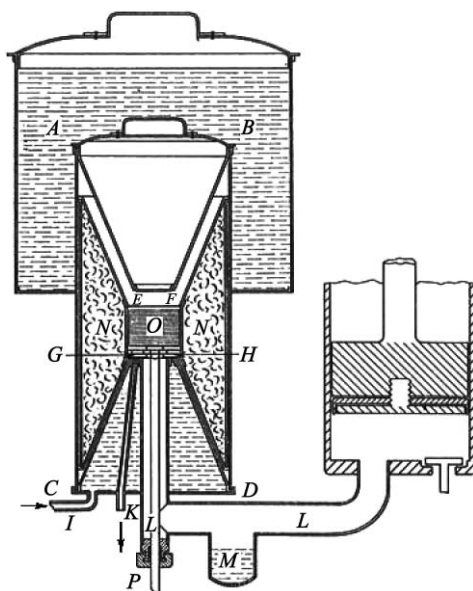
FIGURE 1.9. Kirk ice machine.
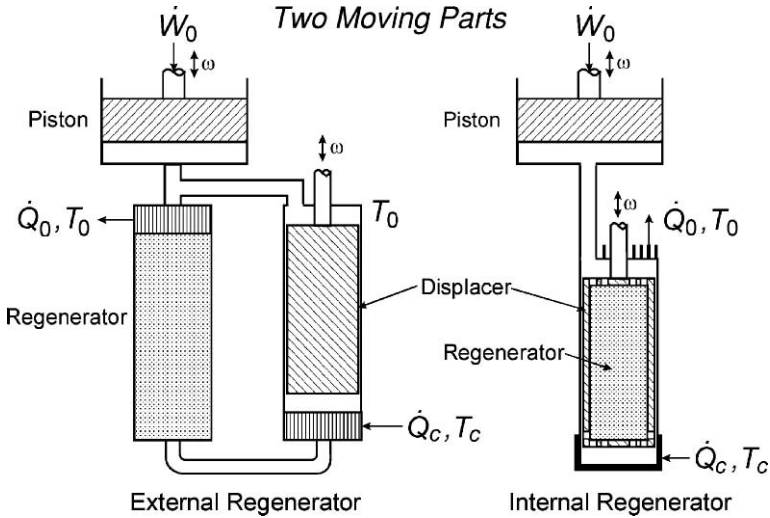
FIGURE 1.10. Two versions of the Stirling refrigerator.

regenerator has conical end pieces connected to it with insulation between them. Fresh water entering at C removes the heat of compression. Air was the working fluid in this early regenerative cooler. In spite of the high efficiency of the Stirling cooler, Kirk never made any attempt to reach temperatures below about $-40\,°C$. [19]. Schematics of two versions of the Stirling cooler are given in Figure 1.10. Kirk used the version with the internal regenerator. No further work was carried out on the Stirling cooler for about the next 80 years.

An air-expansion engine for steady flow, similar to steam engines of that period, was first used by Gorrie in 1851 for an ice-making machine [7,19]. Several other air expansion engines for use in producing ice were developed in the latter half of 1800 [19]. In 1896, Onnes discussed in detail his concept to liquefy hydrogen with the aid of an expansion engine, but the technical difficulties forced him to abandon the idea [20]. The first successful use of an expansion engine to produce cryogenic temperatures was by Claude. He liquefied air in 1902 by allowing a portion of the high-pressure air in a JT cycle to expand and cool in a reciprocating engine before returning it to the low-pressure side of the heat exchanger [19,21]. This combined cycle, now called the Claude cycle and shown in Figure 1.11, increased the efficiency of the liquefaction process and permitted the use of lower pressures. The arrangement used by Claude in 1902 did not have the third heat exchanger (HX3) shown in Figure 1.11. The path on a $T-S$ diagram is shown in Figure 1.4. Claude initially used a high pressure of 2.5 MPa (increased to 4 MPa by 1906), compared with the 20 MPa used by Hampson and Linde for a JT expansion [13]. Figure 1.12 is a photograph of the original expansion engine used by Claude. Its construction was very similar to the steam engines and compressors of that period. Claude found that a leather cup worked satisfactorily as a flexible and dry sealing mechanism

FIGURE 1.11. Schematic of the Claude air liquefier.
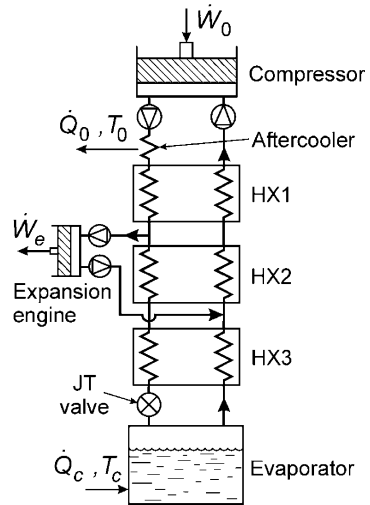
for the piston at low temperatures [19]. Within a few weeks of liquefying air, Claude formed the company L'Air Liquide to commercialize the production of oxygen using his air liquefaction technique and air separation through distillation. Oxygen could be produced by air separation much more cheaply than by chemical means. Both Claude and Linde were marketing the oxygen to the rapidly growing demands of the welding industry for use in oxyacetylene torches perfected by
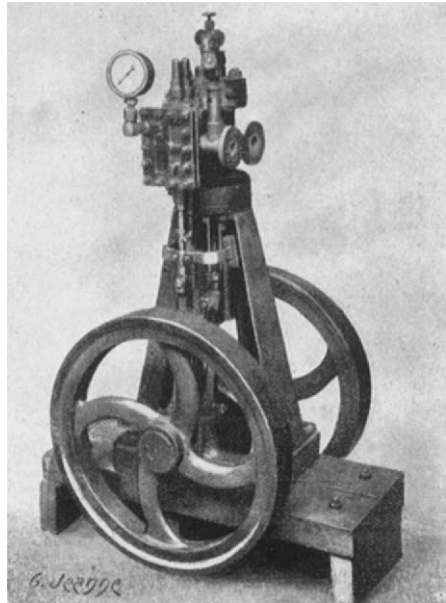
FIGURE 1.12. Expansion engine used in Claude liquefier.

Picard in 1900 [13]. Steel welding and cutting then became the first significant application of cryogenics, and continues on to the present day.

Hydrogen was first liquefied at a temperature of 20 K in 1898 by Dewar using the JT techniques of Linde and Hampson, but with a precooling bath of liquid air [22]. The liquefaction rate was about 0.25 L/h. Dewar made use of the silvered, vacuum-insulated glass dewars he had invented earlier to hold the liquid air and liquid hydrogen with low boiloff rates after successfully liquefying hydrogen.

Helium was first discovered in the sun in 1868 and then found on Earth in the mineral cleveite in 1895. After hydrogen was liquefied in 1898, the attention of the cryogenic scientific community then turned to helium because it was the only remaining "permanent" gas that had not been liquefied. Around 1900, both Dewar of the Royal Institution in England and Onnes of the University of Leiden in the Netherlands sought to obtain sufficient quantities of helium to liquefy it. Contrary to common belief, their competition to be the first to liquefy helium remained rather cordial and each provided the other helpful suggestions [23]. In order to liquefy helium with the JT cycle, Onnes needed a sufficient quantity of liquid hydrogen for precooling the helium. Previously, in 1894, Onnes had set up a cascade air liquefier using the vapor-compression cycle in four separate stages of methyl chloride (249 K), ethylene (169 K), oxygen (90 K), and air (82 K) [6]. No recuperative heat exchangers are required in this cycle. This liquefier produced 14 L/h of liquid air. To liquefy hydrogen, Onnes would first liquefy a sufficiently large quantity of air (about 75 L) in the cascade liquefier. This liquid air was then siphoned into the hydrogen liquefier through an expansion valve, where the liquid air at subatmospheric pressure would precool the high-pressure hydrogen. The hydrogen was pressurized up to 20 MPa by a compressor that utilized a column of mercury to eliminate leakage of hydrogen by the piston. This type of compressor was invented by Cailletet for his use in liquefying oxygen and nitrogen. Counterflow heat exchangers between the high-pressure hydrogen and the returning low-pressure air and hydrogen were also incorporated into the apparatus to reduce the boiloff rate of the liquid air. After being cooled to 64 K, the high-pressure hydrogen passed into the recuperative heat exchanger and then expanded through the JT valve to form liquid hydrogen. Onnes completed this liquefier in 1906, which produced 4 L/h of liquid hydrogen, much more than the 1 L/h hydrogen liquefier of Dewar [24].

Onnes then built a similar liquefier for helium, but with the liquid air being replaced by liquid hydrogen, which precooled the high-pressure helium to 15 K before entering the recuperative heat exchanger and expanding it in the JT valve to cool to the liquefaction point. The helium gas was pressurized to as high as 10 MPa by the same mercury-sealed compressor that had been used for the hydrogen liquefier. The unsilvered glass dewar for the liquid helium was surrounded by a liquid hydrogen bath and a liquid air bath, both of which were in silvered glass dewars with a slit in the silver to observe the liquid helium. Onnes succeeded in producing about 100 mL of liquid helium at a temperature of 4.2 K on July 10, 1908 [25], for which he received the Nobel Prize in 1913. With the capability to reach temperatures of 2 K, Onnes then discovered superconductivity in high-purity

mercury in 1911 at a temperature of 4.2 K [26]. No other laboratory was able to produce liquid helium until 1923, when McLennan at the University of Toronto built a helium liquefier similar to that of Onnes. [27]. The first helium liquefier in the US was constructed by Brickwedde at the US National Bureau of Standards (NBS) in 1931. It also used liquid air and liquid hydrogen baths for precooling a JT stage and produced 0.15 L/h of liquid helium [28].

As summarized in Figure 1.3, the years between 1900 and about 1950 saw significant improvements in liquefaction technology, in which efficiency and reliability were greatly improved and liquefaction rates were increased by orders of magnitude. In the case of liquid oxygen, the liquefaction rate for a typical plant was increased from about 3 L/h in 1895 to 2 t/day in 1910 and to 100 t/day in 1954 (1 t = 1000 kg). The fast growth in oxygen liquefaction capacity was driven by the first commercial application of cryogenics, which was the use of oxygen for oxygen–acetylene welding. Soon after Dewar liquefied hydrogen in 1898, he proposed an exhibit on liquid hydrogen for the British Pavilion at the 1904 St Louis World's Fair. The hydrogen liquefier built for the fair had a two-stage reciprocating hydrogen compressor capable of producing 20 MPa at the output with 0.6 MPa at the intermediate stage [29]. The flow rate was about 14 N m^3/h. The high-pressure hydrogen was precooled first to 203 K with liquid CO_2, then to 83 K with liquid air at atmospheric pressure, and then to 68 K with a pumped liquid air bath before expanding through a JT valve to form liquid at 20 K. The liquefaction rate was not given; but, if we assume a liquid yield of 7% (85% heat exchanger effectiveness), then about 1 L/h would have been produced. It performed well, but the leather piston rings had to be replaced during the night after each day's run. Thus, its mean time to failure was probably not much more than 1 day.

At the close of the 1904 World's Fair, the NBS, formed in 1901 (called the National Institute of Standards and Technology after 1988), purchased the hydrogen liquefier for research at low temperatures. It was not used for several years because of the daily maintenance required; but, in the early 1920s it was overhauled by the British Oxygen Company, with the compressor being replaced by one using steel piston rings. The overhauled liquefier produced 2 L/h of normal liquid hydrogen, which boiled rapidly because of the heat of conversion to parahydrogen [29]. Then, in 1950, the US Atomic Energy Commission funded the NBS to design and construct a much larger hydrogen liquefier for the development of the hydrogen bomb. In 1952, the equipment fabricated in Washington was shipped to the new NBS facility in Boulder [30]. The plant first liquefied hydrogen on March 23, 1952, and a short time later was able to produce 320 L/h of normal liquid hydrogen [4,31]. After installing an ortho–para converter in the liquefier in 1953, the plant could produce 240 L/h of liquid parahydrogen. The NBS liquefier used JT expansion of hydrogen compressed to 12 MPa and precooled with baths of liquid nitrogen at 77 K and 65 K. The liquid yield was 24.5%, compared with a theoretical value of 26.1% [4], which indicates a heat exchanger effectiveness of 98.4%.

In 1934, Kapitza, working at the Royal Society Mond Laboratory of Cambridge, described a helium liquefier based on the Claude cycle [32]. The reciprocating expansion engine replaced the liquid hydrogen precooling bath of Onnes's JT

process. A liquid nitrogen bath was still used. The lower operating pressure of 1.7 MPa also relaxed the requirements on the compressor. Kapitza developed a nonlubricated expansion engine using a clearance seal with labyrinth grooves on the piston. The expansion work was dissipated at room temperature in a hydraulic mechanism. The connecting rod, in the form of a thin-walled tube, had a room-temperature gland to prevent the leakage of helium. The liquefier produced about 1.7 L/h of liquid helium [33].

Kapitza visited Moscow on vacation in 1934 and was detained there by government authorities until his death in 1984. He eventually became the director of the Institute for Physical Sciences of the Academy of Sciences in Moscow. He built another helium liquefier in Moscow to study the properties of helium. In 1937, Kapitza [34] and Allen et al. [35] independently discovered superfluidity in liquid helium below 2.17 K. Kapitza received the Nobel Prize in 1978 for this work and for his work with helium liquefaction techniques.

The use of expansion turbines for gas liquefaction appears to have been first carried out in 1934 at the Linde facilities in Germany [19,36]. In 1939, Kapitza described the design and construction of an air liquefier with an 80 mm diameter expansion turbine supported by ball bearings at room temperature and rotating at a speed of 40,000 rpm [19,37]. The inlet pressure was 0.56 MPa, and the power output of the turbine was 4 kW. The turbine handled about 570 kg/h of air and achieved an isentropic efficiency of 79%.

In 1935, Collins also began work on a helium liquefier using the Claude cycle and reciprocating expansion engines. The work was interrupted by World War II, but the liquefier was completed in 1946 [38]. Collins used two reciprocating expansion engines to eliminate the need for both liquid nitrogen and liquid hydrogen precooling. He also used a clearance seal on the piston, as did Kapitza, but the expansion space was on top of the piston, so the connecting rod was always in tension. Thus, the connecting rod could be made with a thin flexible rod to minimize heat leaks. The liquefaction rate with no liquid nitrogen precooling was about 1 L/h using a commercial compressor providing a pressure of 1.5 MPa and driven with a 7.5 hp (about 10 kW) motor. This efficient helium liquefier has become known as the Collins helium cryostat or liquefier [19]. This liquefier was then commercialized and allowed laboratories all over the world to produce liquid helium for low-temperature research. The first commercial helium liquefier of about 1950, shown in Figure 1.13, produced about 4 L/h with liquid nitrogen precooling. Between 1947 and 1970, 365 units were marketed [39].

After the liquefaction of ^{4}He at 4.2 K by Onnes there was no other gas with a lower boiling point, except for the rare isotope ^{3}He with a boiling point of 3.2 K. Temperatures of about 0.7 K could be achieved by pumping on liquid ^{4}He. An entirely new refrigeration method using adiabatic demagnetization of electron paramagnetic salts was proposed independently by Debye [40] and by Giauque [41] in 1926 to reach temperatures much lower than 1 K. For this technique the salt is magnetized at a higher temperature around 1 K to align the magnetic spins with the field and reduce the entropy. The heat of magnetization is transferred to the surrounding bath. The salt is then thermally isolated from the bath and, as the

FIGURE 1.13. Collins helium liquefier.
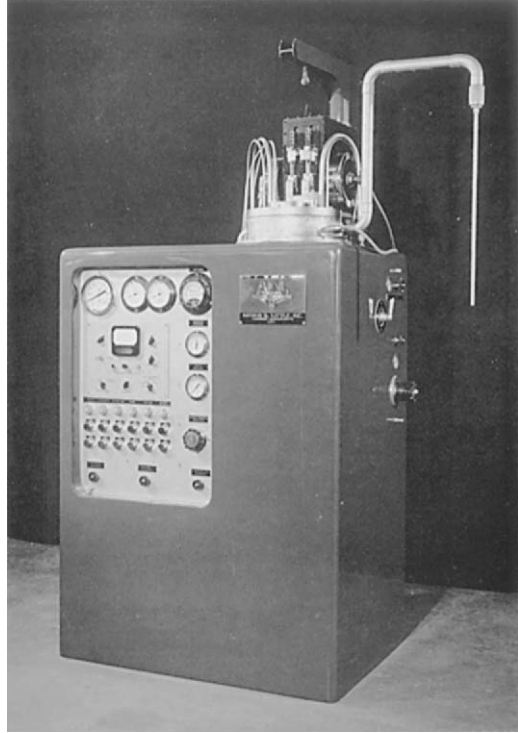
magnetic field is removed, the salt cools to some lower temperature. This is a one-shot process, and the salt warms up as it absorbs heat. The first successful experiment was carried out in Berkeley in 1933 by Giauque and MacDougall, in which a magnetic field of 0.8 T was applied to the $Gd_2(SO_4)_3 \cdot 8H_2O$ paramagnetic salt at 1.29 K and then demagnetized to a final temperature of 0.242 K [42]. Giauque received the Nobel Prize in 1949 for his work with adiabatic demagnetization and the third law of thermodynamics. Many researchers enter this field of adiabatic demagnetization of paramagnetic salts using higher magnetic fields and better salts to achieve lower temperatures. In 1950, de Klerk et al. [43] at Leiden reached a low temperature of 1.4 mK using a mixed salt of chromium alum and aluminum alum.

In 1938, the Philips Research Laboratories in the Netherlands began research on the Stirling engine to develop electric generators which were later used to power radios in remote areas during World War II [44]. The effort was carried out during the war and led to a rather efficient engine. When it was driven in reverse with an electric motor it acted as an effective refrigerator, like the machine developed by Kirk in 1862 for production of ice. In 1946, the temperature of liquid air was achieved when low-pressure hydrogen was used as the working fluid and loose cotton wool was used as the regenerator [45]. The refrigeration capacity was low, but the results were encouraging enough that a small group was set up at the Philips Laboratories and headed by Kohler to study the Stirling cycle for use in
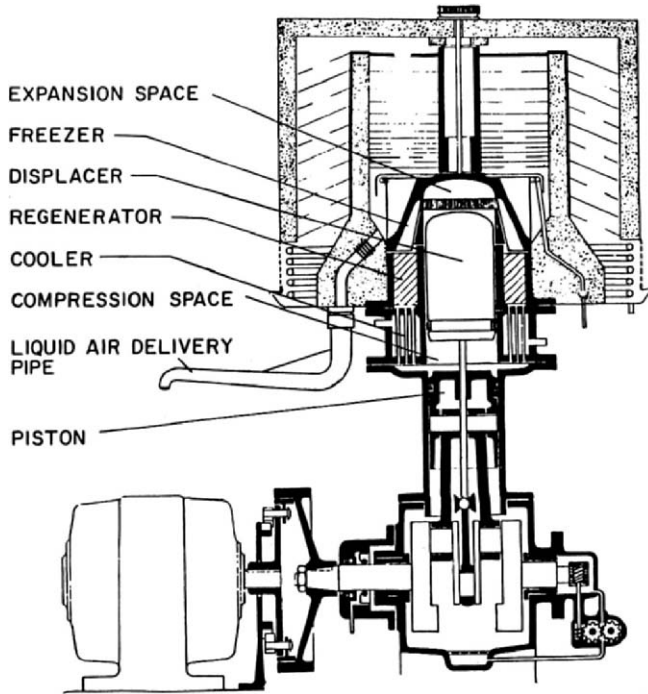
FIGURE 1.14. Cross-sectional drawing of the Philips air liquefier.

liquefying air. After increasing the pressure of the hydrogen and using a dense metal screen, liquid air condensed on the outside of the cylinder at a rapid rate. An engineering model was demonstrated for the first time in 1953 at Grenoble for the International Institute of Refrigeration [46] and the first commercial machine (called the A-machine) was on the market in 1955 [45]. The operating principles and construction details were given by Kohler and Jonkers [47]. A cross-sectional drawing of the machine is shown in Figure 1.14. It is an integral machine with the piston and displacer in the same cylinder. The regenerator of fine metal screen is in the annular space outside the displacer. The helium or hydrogen working fluid was at an average pressure between 1.6 and 3.5 MPa with an operating frequency of about 24 Hz. The high speed and the high pressure resulted in a small machine with high refrigeration capacity. It could produce 6.6 L/h of liquid air with a yield of 1.14 L/kWh. A photograph of the first commercial machine (A-machine) is shown in Figure 1.15.

1.3 Cryogenic Applications Around 1950

Around 1950 the only significant applications of cryogenics involved the use of cryogenic liquids. The liquefaction technology for these cryogens was developed primarily in the years between 1850 and 1900, and the transfer of the liquefaction

FIGURE 1.15. Photograph of the Philips A-machine liquefier.
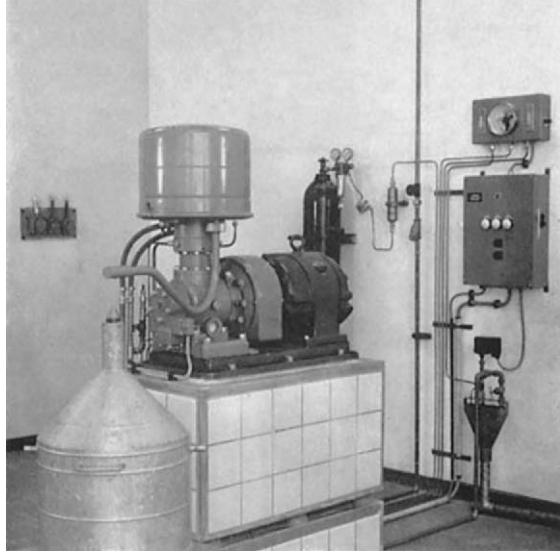
technology to industry and the rapid scale up of liquefaction rates occurred primarily in the years from 1900 to 1950. As mentioned previously, the first application of cryogenics was for the production of oxygen to meet the needs of the welding industry. That application continues through to today. The size of a typical oxygen production plant grew from about 2 t/day in 1910 to 35 t/day in 1925 to about 100 t/day in 1950. Figure 1.16 compares a 2 t/day plant from 1910 with a 100 t/day plant of the early 1950s. The largest plants in 1950 produced about 200 t/day of oxygen. In 1947, the US production for oxygen was 0.541×10^6 t (407×10^6 m^3 of gas). By 1954 the production had increased to 0.830×10^6 t. The nitrogen production in 1947 was 0.0167×10^6 t, which increased to 0.534×10^6 t in 1960 [48]. The delivery of oxygen or nitrogen from these plants to end users required the use of vacuum-insulated tank trucks and rail cars, a relatively large industry in itself at this time. Some of the nitrogen from these air separation plants was used for inert atmospheres in the steel and aluminum industries and was beginning to be used for the production of some chemicals, such as ammonia. Development of the basic oxygen furnace for the production of steel was initiated in Switzerland by Durrer in the late 1940s. The use of pure oxygen in these furnaces oxidizes impurities more efficiently, increases production rates and reduces the nitrogen content of the steel compared with the use of air. The first commercial 35-ton converter was set up in Austria in 1952. Similar furnaces were soon being used in the US to meet the rapidly growing steel demands of the automotive industry. This new application for oxygen was poised in the early 1950s to bring about a very rapid increase in the demand for oxygen. Other uses of oxygen in the 1950s were for medical and military breathing supplies.

The first use of liquid oxygen for rocket propulsion began with experiments by Goddard. On March 16, 1926, he achieved the first successful flight with a
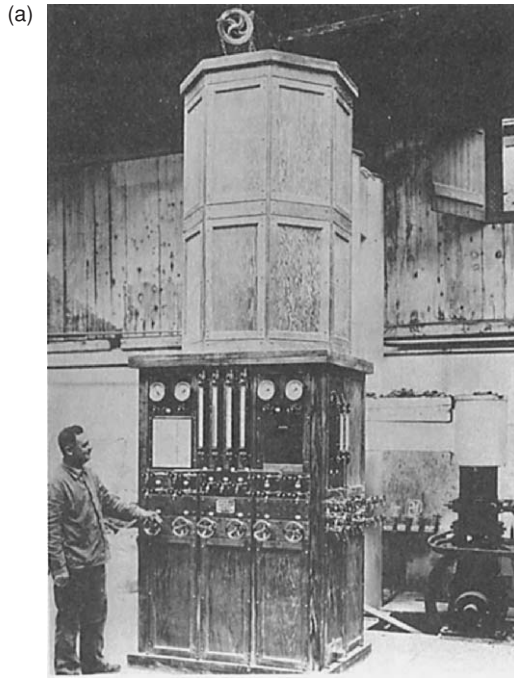
FIGURE 1.16. (a) 2 ton/day oxygen plant available around 1910. (b) 100 ton/day oxygen plant available in the early 1950s.

rocket fueled by gasoline and liquid oxygen. Though the 12.5 m high flight was unimpressive, it led to much more development in this field of rocket science. The V-2 rocket (in Germany called the A-4) developed by Germany during World War II used alcohol (3800 kg) and liquid oxygen (4967 kg) for thrust [49]. Though small (14 m long by 1.7 m diameter, 249 kN thrust) compared with today's rockets, it burned about 1 ton of the fuel–oxygen mixture every 7 s. After the war, further developments of the V-2 rocket were carried out in the US, which led to the second generation V-2, the Redstone rocket (21 m long by 1.8 m diameter, 333 kN thrust). It was first launched on August 20, 1953, from Cape Canaveral, Florida [50].

In about 1945 the US Air Force at Wright Field began to look for aviation fuels with higher energy content [51]. A 1945 Navy report showed that the hydrogen–oxygen combination offered the highest specific impulse [52]. Near to Wright field was the cryogenic laboratory at Ohio State University under the direction of Johnson, where a hydrogen liquefier of about 25 L/h capacity had been built using the JT cycle precooled with liquid air, like that of Dewar. The Air Force contracted with Johnson's laboratory to study hydrogen as a fuel and to study its properties. In 1948, some large-scale experiments were conducted to investigate hydrogen as a fuel for ramjets. From 1947 to 1951, experiments with hydrogen–oxygen and hydrogen–fluorine in small rockets were carried out, including investigations of liquid hydrogen pumps similar to the V-2 liquid oxygen pumps. Similar research was being carried out on the West Coast under Navy funding at the Jet Propulsion Laboratory and at Aerojet General. A hydrogen liquefier patterned after the Johnson liquefier was built there that produced 30 L/h in 1948. The capacity was increased to 80 L/h in 1949 by adding additional compressors. To produce enough liquid hydrogen, the liquefier was run nearly continuously for 3 months with 4 days of lost time due to repairs. The rocket tests were mostly successful, but a change in emphasis in the Air Force and Navy led to these programs fading away.

In January of 1950, President Truman of the US gave the directive to begin development of the thermonuclear (hydrogen) bomb and conduct some critical tests. The Los Alamos Laboratory then intensified their study of thermonuclear fusion and determined liquid deuterium would be required. Hydrogen liquefiers were critical for this development. Los Alamos recommended a national laboratory for cryogenic engineering be established. The Atomic Energy Commission selected the NBS to build such a laboratory because of its extensive experience with cryogenics originating with the purchase of the Dewar hydrogen liquefier from the St Louis World's Fair in 1904. A new site in Boulder, Colorado was selected, and in May 1951 construction of a research building and a liquefier building began. The buildings were completed in March 1952 and the hydrogen, helium, and nitrogen liquefiers were installed. As mentioned earlier, the hydrogen liquefier constructed at NBS in Washington was shipped to Boulder and installed there. This effort was described at the first Cryogenic Engineering Conference, held at NBS-Boulder in 1954 [53]. In March 1952 the hydrogen liquefier was operating and producing 320 L/h of normal liquid hydrogen or 240 L/h of liquid parahydrogen by 1953 [4]. Figure 1.17 shows this liquefier.
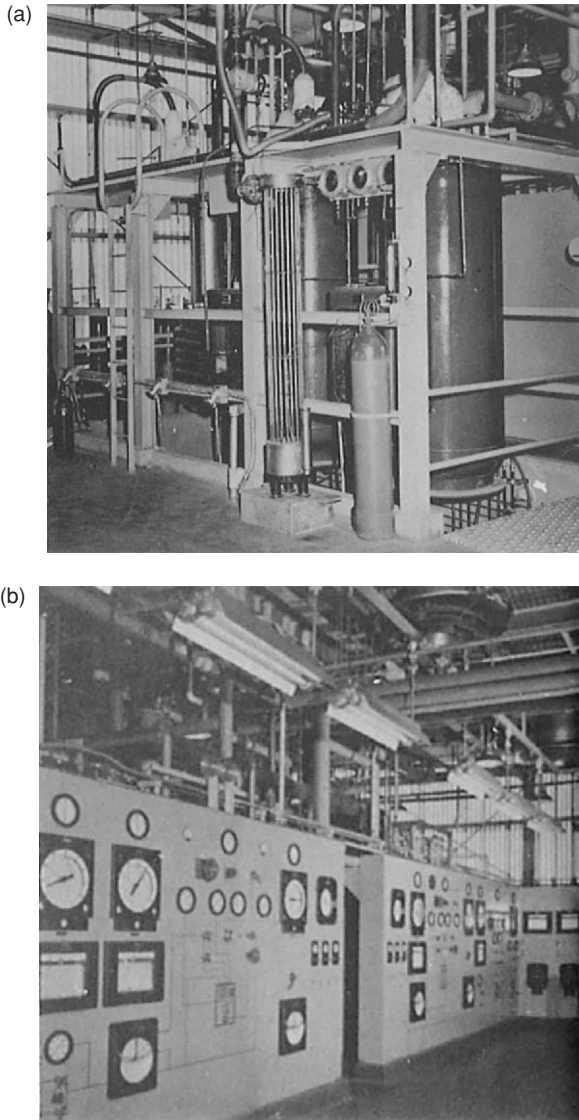
FIGURE 1.17. (a) Hydrogen liquefier installed at NBS in 1953. (b) Instrument panel for 1953 NBS hydrogen liquefier.

Large transportable dewars for liquid hydrogen were developed during that time, some of which included a small cryocooler to reliquefy the boiloff. A nonrefrigerated 750 L dewar had a boiloff rate of 1% per day and was designed for air transport [54]. A third hydrogen liquefier was shipped to the Eniwetok Atoll in the Pacific Ocean for the liquefaction of deuterium for the first hydrogen bomb
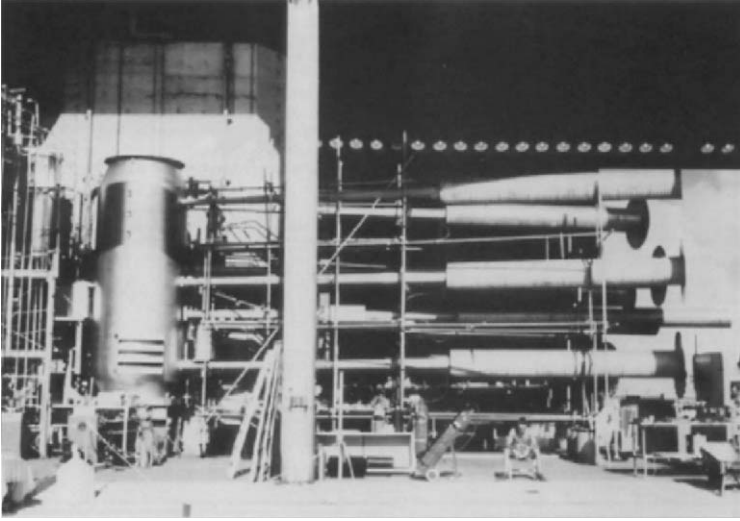
FIGURE 1.18. Hydrogen bomb setup on the island of Elugelab in the Pacific Ocean.

test on the nearby island of Elugelab. This first bomb was named Mike and was basically a large dewar of liquid deuterium 6 m high and about 2 m in diameter with a fission nuclear bomb at the top to trigger the system, as shown in Figure 1.18. Transportable dewars were used to bring liquid deuterium (23.3 K) from the liquefier to the Elugelab Island test site. On November 1, 1952, the bomb was detonated, as shown in Figure 1.19, with a yield of 10.4 megatons of TNT that vaporized the island and left a crater about 1.6 km wide. Subsequent H-bombs used the solid lithium deuteride instead of the liquid deuterium. The end of the

FIGURE 1.19. Hydrogen bomb detonation cloud.

"wet" bomb program reduced the need for liquid hydrogen after about 1954, but research on its properties continued at NBS-Boulder.

In about 1954 a super-secret program funded by the US Air Force returned to the study of liquid hydrogen for fuel, but this time for an air-breathing aircraft engine capable of flying at an altitude of about 30,000 m with a speed of Mach 2.5 [51]. The purpose was for very high-altitude reconnaissance to replace the U-2 spy plane. The plane to be built by Lockheed was designated the CL-400, but was better known as the Suntan. Large quantities of liquid parahydrogen would be needed, so a study and design of several sizes (up to 45,000 kg/day) of parahydrogen liquefiers were completed. A 0.68 t/day liquefier was built in Painsville, Ohio, near a plant producing excess gaseous hydrogen. This liquefier was named "Baby Bear" and became operational in May 1957. Another liquefier was built in Florida with a capacity of 4.5 t/day and was called "Mama Bear." A third liquefier for 27 t/day was installed near "Mama Bear" and was called "Papa Bear." It became operational in January 1959 and was the world's largest hydrogen liquefier. The last two liquefiers used expansion turbines and lower pressures and became the model for most subsequent hydrogen liquefiers [51]. However, before the CL-400 aircraft could be built and tested, various political and management problems led to the cancellation of the $100 million program in 1959. The liquefiers would not sit idle for very long, however, as the US space program was about to begin.

The reliability of liquefaction systems in the 1950s was much improved over that of 50 years earlier, but was much inferior to what is expected today. For example, compressors required constant maintenance [55]. Also, cryogenic containers and large cryogenic tanks experienced relatively large boiloff losses due to heat leaks through the insulation system and support structures.

Methane was first liquefied in small droplets by Cailletet in 1867 at a temperature of 112 K using his technique of compression and rapid expansion. The first large liquefaction plant for natural gas (mostly methane) was installed in Cleveland, Ohio, in 1941 with a capacity of 75 t/day (1.1×10^5 m^3/day gas, 177 m^3/day liquid). It used a cascade JT cycle with ammonia and ethylene stages for precooling. The total power input was 2.4 MW [56,57]. It was used for a peak shaving application with three spherical storage tanks of 2700 m^3 liquid volume each. After a new cylindrical storage tank was added in 1944 it failed, resulting in a fire and the loss of 200 lives. Interest in other liquefied natural gas (LNG) facilities was dampened at that time until 1952, when a barge-mounted liquefier was put into operation near Lake Charles, Louisiana, on the Mississippi River. It produced 114 t/day of LNG, which was intended to be shipped via barge to Chicago [57]. However, the transport of the LNG along the Mississippi River was never approved because of a poor design of the LNG containers on the barges. However, this concept was revived in the late 1950s when the British North Thames Board started shipping LNG from Lake Charles, Louisiana, across the Atlantic Ocean to Canvey Island in the UK. This success prompted an LNG transfer operation that is very much in effect today.

1.4 Summary

To provide a background as to why applications in cryogenics did not begin to evolve until the last 50 years, it is helpful to understand the basic advances that were required even to achieve these temperatures. This historical summary has provided a progress report dating back to 1850, when thermodynamic concepts were just being introduced and high-pressure equipment was being developed for steam power stations. Prior to that time, laboratory techniques for reducing the temperature of a gas, liquid, or solid only a few degrees below ambient temperature required considerable skill and only attempted by a few scientists around the world. As practical schemes were visualized to achieve lower temperatures and as supporting equipment was developed, the progress to achieving lower temperatures required between 50 to 100 years to obtain sufficient quantities of cryogenic fluids to provide the opportunities of using these fluids in applications that would benefit mankind. This opportunity has presented itself only over the past 50 years, and some of these applications are covered in this monograph.

References

1. Freiman, A., and Bouganim, N., *Dermatology Online Journal*, 11(2), Article #9, 2005.
2. Faraday, M., *Liquefaction of Gases: Papers*, University of Chicago Press, Chicago, 1906.
3. Perkins, J., Britain Patent No. 6662, 1834.
4. Scott, R.B., *Cryogenic Engineering*, D. Van Nostrand Company, Princeton, New Jersey, 1959.
5. Kurti, N., *Cryogenics* 10, 183, 1970.
6. Onnes, H.K., *Comm. Phys. Lab., Leiden*, No. 14, 1894.
7. Gorrie, J., *History and Origins of Cryogenics*, Scurlock, R.G., ed., Clarendon Press, Oxford, 1992.
8. Siemens, C.W., *History and Origins of Cryogenics*, Scurlock, R.G., ed., Clarendon Press, Oxford, 1992.
9. Scurlock, R.G., *History and Origins of Cryogenics*, Scurlock, R.G., ed., Clarendon Press, Oxford, 1992.
10. Flynn, T.M., *Cryogenic Engineering*, Marcel Dekker, New York, 1997.
11. Rafalowicz, J., *History and Origins of Cryogenics*, Scurlock, R.G., ed., Clarendon Press, Oxford, 1992, p. 101.
12. Hampson, W., and Claude, G., *Liquid Air, Oxygen, and Nitrogen*, Cotrell, H.E.P., trans., J & A Churchill, London, 1913, p. 88.
13. Dennery, F.M., *History and Origins of Cryogenics*, Scurlock, R.G., ed., Clarendon Press, Oxford, 1992, p. 141.
14. Linde, C., and Claude, G., *Liquid Air, Oxygen, and Nitrogen*, Cotrell, H.E.P., trans., J & A Churchill, London, 1913, p. 75.
15. Daunt, J.G., *Encyclopedia of Physics, Vol. XIV, Low Temperature Physics*, Flugge, S., ed., Springer Verlag, Berlin, 1956, p. 1.
16. Stirling, R., *History and Origin of Cryogenics*, Scurlock R.G., ed., Clarendon Press, Oxford, 1992.

17. Herschel, J., *The Athenaeum*, Jan. 5, 1850, p. 22.
18. "Alexander C. Kirk," *Min. Proc. Inst. Civ. Engrs*, 37, 244, 1974.
19. Collins, S.C. and Cannaday, R.L., *Expansion Machines for Low Temperature Processes*, Oxford University Press, London, 1958.
20. Onnes, H.K., *Comm. Phys. Lab.*, *Leiden*, No. 23, 1896.
21. Claude, G., *C. R. Acad. Sci. Paris*, 134, 1568, 1902.
22. Dewar, J., *Collected Papers of Sir James Dewar*, Lady Dewar, ed., Cambridge University Press, Cambridge, 1927, p. 678.
23. Gavroglu, K., *Eur. J. Phys.*, 15, 8, 1994.
24. Onnes, H.K., *Comm. Phys. Lab., Leiden*, No. 94, 1906.
25. Onnes, H.K., *Comm. Phys. Lab., Leiden*, No. 108 (1908).
26. Onnes, H.K., *Comm. Phys. Lab., Leiden*, No. 120b (1911).
27. McLennan, J.C., and Shrum, G.M., *Roy. Soc. Canada, Trans.*, 16(Sect. 3), 181, 1922.
28. Brickwedde, F.G., Hammel, E.F., and Keller, W.E., *History and Origins of Cryogenics*, Scurlock, R.G., ed., Clarendon Press, Oxford, 1992. Brickwedde, F.G., *Engineering Experiment Station News*, The Ohio State University, June 30, 1946.
29. Hands, B.A., *Advances in Cryogenic Engineering*, Vol. 49A, American Institute of Physics, New York, 2004, p. 3.
30. McIntosh, G.E., *Advances in Cryogenic Engineering*, Vol. 49A, American Institute of Physics, New York, 2004, p. 9.
31. Johnson, V.J., and Wilson, W.A., *Advances in Cryogenic Engineering*, Vol. 1, Plenum Press, New York, 1960, p. 329.
32. Kapitza, P., *Proc. Roy. Soc. London A*, 147, 189, 1934.
33. Shoenberg, D., *History and Origins of Cryogenics*, Scurlock, R.G., ed., Clarendon Press, Oxford, 1992.
34. Kapitza, P., *Nature*, 141, 74, 1938.
35. Allen, J.F., Peierls, R., and Uddin, M.Z., *Nature*, 140, 62, 1937. Allen, J.F., and Misener, A.D., *Nature*, 141, 75, 1938. Allen, J.F., and Jones, H., *Nature*, 141, 243, 1938.
36. Linde, R., *Z. ges. Kälteindustr.*, 41, 183, 1934.
37. Kapitza, P., *Russian J. Phys.* (English transl.) 1, 7, 1939.
38. Collins, S.C., *Review of Scientific Instruments*, 18, 157, 1947.
39. Collins, S.C., *Cryocoolers*, Plenum Press, New York, 1983, p. vii.
40. Debye, P., *Ann. Phys.*, 81, 1154, 1926.
41. Gianque, W.F., *J. Am. Chem. Soc.*, 49, 1864, 1927.
42. Giauque, W.F., and MacDougall, D.P., *J. Am. Chem. Soc.*, 57, 1175, 1935.
43. De Klerk, D., Steenland, M.J., and Gorter, C.J., *Physica*, 16, 571, 1950.
44. Walker, G., *Miniature Refrigerators for Cryogenic Sensors and Cold Electronics*, Clarendon Press, Oxford, 1989.
45. Staas, F.A., *History and Origins of Cryogenics*, Scurlock, R.G., ed., Clarendon Press, Oxford, 1992.
46. Kohler, J.W.L., *Suppl. Bull. Inst. Int. Froid*, Annex 2, 1955.
47. Kohler, J.W.L., and Jonkers, C.O., *Philips Tech. Rev.*, 16, 69, 1955. Kohler, J.W.L., and Jonkers, C.O., *Philips Tech. Rev.*, 16, 105, 1955.
48. Baker, C.R., and Fisher, T.F., *History and Origins of Cryogenics*, Scurlock, R.G., ed., Clarendon Press, Oxford, 1992, p. 217.
49. www.aeromuseum.org/Articles/Oct04/V2PartThree.htm.
50. www.thespaceplace.com/history/rocket2.html; www.solarviews.com/eng/rocket.htm.
51. www.hq.nasa.gov/office/pao/History/SP-4404/contents.htm.

52. Lemmon, A.W., *History and Origins of Cryogenics*, Scurlock, R.G., ed., Clarendon Press, Oxford, 1992.
53. Brickwedde, F.G., *Advances in Cryogenic Engineering*, Vol. 1, Plenum Press, New York, 1960, p. 1.
54. Birmingham, B.W., Brown, E.H., Class, C.R., et al., *Advances in Cryogenic Engineering*, Vol. 1, Plenum Press, New York, 1960, p. 49.
55. Croft, A.J., *Experimental Cryophysics*, Jackson, L.C., Hoare, F.E., and Kurti, N., eds, Butterworths, London, 1961, p. 105.
56. Clark, L.J., and Miller, P., *Oil Gas J.*, 39, 57, 1941.
57. Haselden, G.G., *History and Origins of Cryogenics*, Scurlock, R.G., ed., Clarendon Press, Oxford, 1992, p. 599.

Part 2

Advances in Cryogenic Data Development over the Past 50 Years

2
Sources of Cryogenic Data and Information

R.A. MOHLING[a], W.L. HUFFERD[b], AND E.D. MARQUARDT[c]

[a]*Technology Applications, Inc., Boulder, CO 80301, USA*
[b]*Chemical Propulsion Information Agency, Columbia, MD 21044, USA*
[c]*Ball Aerospace & Technologies, Boulder, CO 80301, USA*

Abstract

It is commonly known that cryogenic data, technology, and information are applied across many military, National Aeronautics and Space Administration (NASA), and civilian product lines. Before 1950, however, there was no centralized US source of cryogenic technology data. The Cryogenic Data Center of the National Bureau of Standards (NBS) maintained a database of cryogenic technical documents that served the national need well from the mid 1950s to the early 1980s. The database, maintained on a mainframe computer, was a highly specific bibliography of cryogenic literature and thermophysical properties that covered over 100 years of data. In 1983, however, the Cryogenic Data Center was discontinued when NBS's mission and scope were redefined. In 1998, NASA contracted with the Chemical Propulsion Information Agency (CPIA) and Technology Applications, Inc. (TAI) to reconstitute and update Cryogenic Data Center information and establish a self-sufficient entity to provide technical services for the cryogenic community. The Cryogenic Information Center (CIC) provided this service until 2004, when it was discontinued due to a lack of market interest. The CIC technical assets were distributed to NASA Marshall Space Flight Center and the National Institute of Standards and Technology. Plans are under way in 2006 for CPIA to launch an e-commerce cryogenic website to offer bibliography data with capability to download cryogenic documents.

2.1 Introduction

Prior to 1959 there were only two cryogenic engineering books: *Separation of Gases* by Ruhemann and *Cryogenic Engineering* by Scott [1]. For many years, this field of research was restricted to only a few laboratories. Many of the earlier books on low-temperature physics contained a great deal of material which is now considered to be cryogenic engineering. During these early years, several important applications of cryogenics were developed; as a result, a large number of engineers became engaged in efforts that required very low temperatures and

hardware to accomplish the delivery of the applications hardware. Very quickly, numerous papers were published and a few books on the subject appeared with these applications.

Much of this cryogenic research and development (R&D) activity came as a result of funding from the Department of Defense (DoD), the Department of Energy, and the National Aeronautics and Space Administration (NASA). This R&D activity provided a trained cadre of engineers and scientists working in cryogenics, providing cryogenic technical know-how, and building a technical base of cryogenic engineering information which helped make the US cryogenics industry what it is today. For the 30-year period starting in the mid 1950s, the National Bureau of Standards (NBS) Cryogenic Data Center captured much of this information in the form of a bibliography and many technical documents.

With the discontinuance of the Cryogenic Data Center in the early 1980s, there was a period of 15 years where there was no centralized US source of cryogenic technical data. In 1997, the Cryogenic Information Center (CIC), a not-for-profit corporation, was established to preserve and distribute cryogenic information to the government, industry, and academia. The CIC accessed the long history of information traceable back to the Cryogenic Data Center. The heart of the CIC was a uniform, consistent source of cryogenic data that comprised previous analyses, designs, materials and processes, and test information. The CIC's resources included the largest and most comprehensive collection of cryogenic-related articles, papers, and journals, with citations going back as far as 1829.

With the demise of the CIC at the end of 2004 due to lack of market interest, the technical assets have been distributed to NASA Marshall Space Flight Center (MSFC) and the National Institute of Standards and Technology (NIST). The Chemical Propulsion Information Agency (CPIA), one of the 11 Information Analysis Centers (IACs) of the Defense Technical Information Center (DTIC), has presented a plan to make the bibliography database and technical documents available to the cryogenics community at an e-commerce website. The CPIA plans to launch this website in 2006.

2.2 Early Sources of Data

Before the mid 1950s there was no single source of comprehensive fluid or material properties for low-temperature applications. Cryogenic data were hard to find and not always in a form convenient for use. To complete a cryogenic system design, engineers relied on multiple books, handbooks, and compendiums, each with a bit of information needed for material and fluid data. From the authors' experience, a few engineers in each organization seemed to collect this precious cryogenic data: fluids data usually in the hands of a thermal engineer and materials data with a structural engineer. The best engineers in the organization were those who had this information at their fingertips, and the young engineers naturally gravitated to these engineers as sources of data, relying on them for these data as well as design and analysis advice.

Some of the early handbooks commonly found in the engineering library were Eshbach's *Handbook of Engineering Fundamentals* and Baumeister and Marks's *Standard Handbook for Mechanical Engineers*. The handbooks contained a wealth of reference tables and charts. Extrapolations were often necessary to extract approximate information at the lower temperatures.

In the late 1950s the NBS produced *The Cryogenic Materials Data Handbook*, sponsored originally by the Air Force Ballistic Missile Division. This handbook contained mechanical and thermal property data on 66 different structural alloys and nonmetals. Data were primarily those measured at the NBS to 20 K during the 1950s, although over 1100 references were surveyed and about 300 were included. The first report was issued by the Superintendent of Documents, US Government Printing Office, Washington, DC, and later quarterly reports from the Office of Technical Services [2,3]. Later this effort was transferred to the Martin Company in Denver, under supervision of NBS personnel with funding of the Air Force Material Lab, Wright–Patterson Air Force Base (AFB).

In the early 1960s, the Wright Aeronautical Division, with the help of the NBS, published the three part-series entitled *A Compendium of the Properties of Materials at Low Temperature* [4]. The compendium covered 10 properties of 10 fluids (Part I), three properties of solids (Part II), and an extensive bibliography of references (Part III). Density, expansivity, thermal conductivity, specific heat and enthalpy, transition heats, phase equilibria, dielectric constants, adsorption, surface tension and viscosity for the solid, liquid, and gas phases of helium, hydrogen, neon, nitrogen, oxygen, air, carbon monoxide, fluorine, argon and methane were given wherever adequate data could be collected. Thermal expansion, thermal conductivity, specific heat, and enthalpy were given for a number of solids of interest. Data sheets, primarily in graphic form, were presented from "best values" of data collected. The source of the material used, other references, and tables of selected values with appropriate comments were furnished with each data sheet to document the data presented. Conversion tables and other helpful information were also included.

2.3 National Bureau of Standards Cryogenic Data Center

The former NBS maintained a database of cryogenic technical documents that served the national need well from the mid 1950s until the early 1980s. The electronic database was maintained by the Cryogenic Data Center of the Cryogenics Division of NBS, located in Boulder, CO. The database, maintained on a mainframe computer, was a highly specific bibliography of cryogenic literature and thermophysical properties that covered over 100 years of data [5,6].

In the early days of the Cryogenic Data Center, literature on cryogenics that was being generated by the NBS, along with a few other government agencies, universities, and companies, was being collected and cataloged by the Cryogenic Data Center. The 20-year period from 1950 to 1970 saw the peak of cryogenic R&D. The Cryogenic Data Center gathered all the technical papers generated at

this time, as well as historic documents on the early development of the field of cryogenics. By 1980, the Cryogenic Data Center had over 115,000 technical documents (hardcopy and microfiche) covering a period from 1829 to 1980.

The Cryogenic Data Center's responsibilities included data compilation, documentation, and technical services. A dedicated group of professionals supported these activities at the NBS for several decades. A brief description of the three major database activities at the Cryogenic Data Center, taken from a 1967 NBS reference, is included below to give a snapshot in time and describe the thoroughness and extent of NBS professional staff involvement in maintaining the electronic and hardcopy databases [7].

2.3.1 Data Compilation

Data compilation included the evaluation and compilation of data on the thermophysical properties (thermodynamic, transport, and other properties) for the principal fluids, and common mixtures of these fluids, used at low temperatures. These fluids were helium, hydrogen, neon, nitrogen, oxygen, air, carbon monoxide, fluorine, argon, methane, xenon, and krypton.

The literature for these fluids was monitored on a continuing basis. As specific tasks were undertaken, comprehensive bibliographies were prepared and sometimes published. Task notebooks were made for preliminary selection of data and, where feasible, preliminary data sheets were issued. The senior staff, consisting of two physicists, one thermodynamic engineer, one chemist, and one physical chemist, did critical evaluation.

2.3.2 Documentation

The documentation activities at the NBS Data Center are summarized in Table 2.1.

2.3.3 Technical Services

The technical-service activities of the Cryogenic Data Center are summarized in Table 2.2.

In the 1970s, the NBS published two useful handbooks containing materials and fluids data at low temperatures, namely the *Handbook on Materials for Superconducting Machinery* and *LNG Materials and Fluids* [8,9]. The latter handbook title is a misnomer, since it contains properties data on all of the common cryogens. Both are excellent resources for consistent data for materials and fluids used in the successful design of many cryogenic systems.

In the late 1970s, the NBS implemented a change in its charter. As a result, it not only took on a new name, the NIST, but also took on new research directions. The field of cryogenics was considered to be a mature discipline, one that no longer required research using NIST base funding. NIST management undertook a gradual reorganization of the Cryogenics Division staff. New divisions were formed with the former Cryogenics Division staff as leaders. The database of bibliographic references was transferred from magnetic tape to floppy disks, and many documents

TABLE 2.1. Summary of documentation activities

Activity	Description
Literature searching	Regular review of nearly 200 periodicals and some 15 abstract journals, and noting references in cryogenic documents; 150–200 items were noted weekly.
Literature procurement	Published literature was obtained from local, national, and foreign libraries; report literature was procured from the large national centers (NASA, DDC, and clearinghouse); many reports were obtained directly from corporate sources as part of an information exchange program.
Cataloging, coding and processing	Data were coded into nine main subject categories, such as properties of solids and fluids, cryogenic processes and equipment, instrumentation and laboratory apparatus, and cryogenic techniques; further characteristic coding was assigned to the type of document, temperature range, type, and range of data; comprehensive subject coding followed, based on a thesaurus of terms.
Bibliographic storage and retrieval	All cataloging and coding was converted to machine-readable form for automated processing on the NBS's Control Data Corporation 3600 computer; principal programs were used for searching, dictionary term identification, and for catalog tape output; custom bibliographies were prepared for specific subjects or for broad subject areas.
Distribution of literature and data	Announcements and abstract cards of new literature evolving from the laboratory's program were sent to more than 4000 persons and institutions periodically; nearly 500 separate items of literature were available; 15,000 to 20,000 documents a year were distributed in response to some 2000 orders.

TABLE 2.2. Description of technical services at the Cryogenic Data Center

Activity	Description
Current awareness	Weekly lists of new literature of cryogenic interest were prepared and distributed to subscribers; subscription price was $10 per year ($15 for foreign with airmail delivery).
Custom bibliographies	Over 42,000 accessions of cryogenic literature were entered into the Cryogenic Data Center's system; approximately 20,000 of these on properties of materials (for both fluids and solids) were processed for machine searching; detailed and/or extensive bibliographies could be prepared with computer facilities; likewise, some 2000 patents, 2000 articles on processes and equipment, and 1000 articles on instrumentation were processed for machine retrieval; cost of custom searches was based on rate of $12 per minute of computer time plus 15 cents per reference for listing and indexing.
Preliminary data and advice	Data and advice on the thermodynamic and transport properties of cryogenic fluids and selected solids could be obtained from the Project Leader for the Data Compilation Group.
Announcements of reports	Available to anyone wishing to be placed on the mailing list; requests could be made for inclusion on the mailing list by completing and returning a postal reply card.
Local use of Data Center	Visitors were invited to use the center's library, world literature file, catalog and abstract files, and microfilm facilities; the staff of both the Data Compilation and Documentation units helped with answers to questions, and with hard-to-find types of literature, or offered advice as to best sources of information.

related to superconductivity/solid material properties were transferred to the Naval Research Laboratory in Washington, DC, and eventually placed in storage at the National Archives. The fluid properties library, along with fluids research, was retained at NIST.

With this disbanding event, there was no centralized US source of cryogenic technical data. Existing data were fragmented and dispersed, and coverage was incomplete for engineers and scientists. In the years that followed the closure of the Cryogenic Data Center, there was a trend in which many experienced cryogenic engineers were either retiring or being relocated to other job specialties. In addition, the lack of a home for the data collected by the Cryogenic Data Center meant the eventuality of losing this valuable resource. There was an obvious need in government and industry for a highly specific database to provide a uniform, consistent source of cryogenic data and access to previous analyses, designs, materials and processes, and test data.

2.4 Period after National Bureau of Standards Data Center

2.4.1 Commercial Electronic Databases

In the 1980s, many commercial electronic databases were available with access to bibliographic citations including the field of cryogenics. The list of network vendors is long; several noteworthy databases having science and engineering backgrounds include Nerac, Inc. at http://asp.nerac.com and Dialog Corporation at www.dialog.com. These vendors will assist the user in locating information with extensive search engines and provide alerts on industry and patent developments as they occur. Once the citation of interest is located with author, title, and source information, in many cases it is up to the user to locate the document by using a nearby library or interlibrary loan service.

There are several shortcomings of these commercial electronic databases, in that they provide access to only the most recent citations (usually 7–10 years); i.e., they do not provide citation searches and/or document access in the 1950–1970 period—a period often referred to as the "Golden Age of Cryogenics," when a wealth of cryogenic R&D data was generated and published for NASA and DoD projects.

2.4.2 Book on Cryogenic Materials

In 1983, the NIST materials staff published a book, *Materials at Low Temperatures*, that includes discussion and review of mechanical, thermal, electrical, and magnetic properties of metals, alloys, superconductors, and composites at low temperatures [10]. It is the latest book now published on cryogenic materials.

2.4.3 Cryogenic Information Center

By 1997, several individuals within the government and aerospace industry recognized the difficulties in satisfying requests for cryogenic data research conducted

during the last generation. Technology Applications, Inc. (TAI), using its contacts within the aerospace industry, contacted the CPIA, a DTIC agency. With the help of CPIA, an industry/government survey was conducted that demonstrated a need to retrieve and update the information contained in the former NBS Cryogenic Data Center, as well as a willingness to support this effort.

CPIA, the IAC having the closest fit and significant overlap of cryogenic activity, is located at Johns Hopkins University at Columbia, MD. CPIA is the US national clearinghouse for worldwide information, data, and analysis on chemical, electrical, and nuclear propulsion. Many of the nation's chemical launch and upper-stage vehicles use cryogenic propellants, including oxygen, hydrogen, and methane. The Propulsion Information Retrieval System (PIRS), maintained by CPIA, is a combined database and retrieval system that consists of over 53,000 document citations that relate to missile, space, and gun technology.

A proposal was submitted to NASA-MSFC in 1997 by CPIA and TAI. This team, in collaboration with NIST, submitted a three-phase, 3-year program that would: (1) retrieve the information contained in the former Cryogenic Data Center maintained at the NBS until 1980 and transfer these data to PC-based technology; (2) update the library to include current literature back to those entries contained in 1980; and (3) become a self-sufficient entity providing technical services to the cryogenic community.

Funding and in-kind support were provided by a combination of NASA centers and DoD agencies given in the Acknowledgments section of this chapter. The first phases of the contract were completed with the release of two CD-ROM products containing updates to the NBS bibliography database along with a Windows-compatible search engine. The third phase was completed in 2001 with the formation of the not-for-profit CIC. The original contract concluded in the fall of 2001, meeting all the requirements of the contract deliverables, including CD-ROMs of the bibliography database now referred to as the Cryogenic Information Retrieval System (CIRS).

By the end of 2003, over 43,000 entries had been added from the original database, and over 40,000 abstracts had been added to the original database bibliographic entries. No other library or database has a more comprehensive collection of cryogenic-related articles, papers, and journals. Any researcher seeking technical information in the field of cryogenics will not find a more inclusive set of data to meet their needs.

Priorities were set for updating and adding bibliographic references to the CIRS database. The highest priority was given to several long-term series, such as *Advances in Cryogenic Engineering*, *Cryocooler*, *Thermophysical Properties Symposium*, *International Cryogenic Engineering Conference*, *Applied Superconductivity Conference*, and the periodical journal *Cryogenics.*

Within this priority area, every publication available to the CIC staff through personal collections and libraries was reviewed and added to the database. Abstracts were written or copied into the bibliographic references from the original NBS collection. Many meeting papers had been entered into the Cryogenic Data Center database from preprints collected at conferences and meetings, in the interests of

TABLE 2.3. Updates to the CIRS database

Date	No. of journals and proceedings	No. of bibliographic citations	No. of citations with abstracts
Sep 1998	1	110,000	0
Jul 1999	10	133,000	5,758
Jan 2000	10	137,680	10,438
Jun 2000	11	140,500	26,248
Jul 2001	16	146,021	33,130
Sep 2003	22	153,570	40,679

immediacy. The references to these papers have now been changed to reflect their appearance in published proceedings. In addition, references and abstracts were added from publications after 1980 to bring coverage of these first-priority series up to date.

Several other series have been added to the CIRS database, including the International Conference on Cryogenics and Refrigeration, the Cryogenic Optical Systems and Instruments Conference, and the periodical journals *IEEE Transactions on Applied Superconductivity*, *Superconductor Science and Technology*, *Cryogenic Engineering* (Japan), and *Journal of Low Temperature Physics*.

From 2001 to 2004, the products and services of the CIC were made available to those in the cryogenics community requiring such information. Subscriptions, per-use-fees, and product sales were the primary means of funding operations. The primary product was CIRS, a bibliography database, which was initially updated on a yearly basis by incorporating new reports and documents as they became available. CIRS now contains references to over 153,000 documents, dealing with cryogenic engineering, materials development and properties, and applications. Unlike other electronic databases, CIRS contains data from the period 1950 to 1970, the most intensive period of cryogenic R&D.

CIRS originally contained about 115,000 references (some were duplicates and/or corrupt) from the former NBS Cryogenic Data Center. A second release added references on fluid properties collected by NIST after the Cryogenic Data Center was disbanded, along with more recent references collected from CPIA's PIRS, NASA-RECON, and DTIC electronic databases. Table 2.3 provides a chart showing the progression and volumes added to the database.

CIRS is a helpful asset to locate specific articles within large-volume periodicals and journals such as *Advances in Cryogenic Engineering*. For example, by performing a keyword or author search, one is able to locate the article of interest by volume and page number.

Figure 2.1 highlights the collection and span times of the database. CIRS gives the user the capability of simple searches and advanced searches by title, author, corporate facility (of the first author), reference source, date, and subject matter as found in the abstract, alone or in any combination. It allows simple refinement or limiting of a search after review of an initial search. It provides means of printing formatted reports on the results of searches.
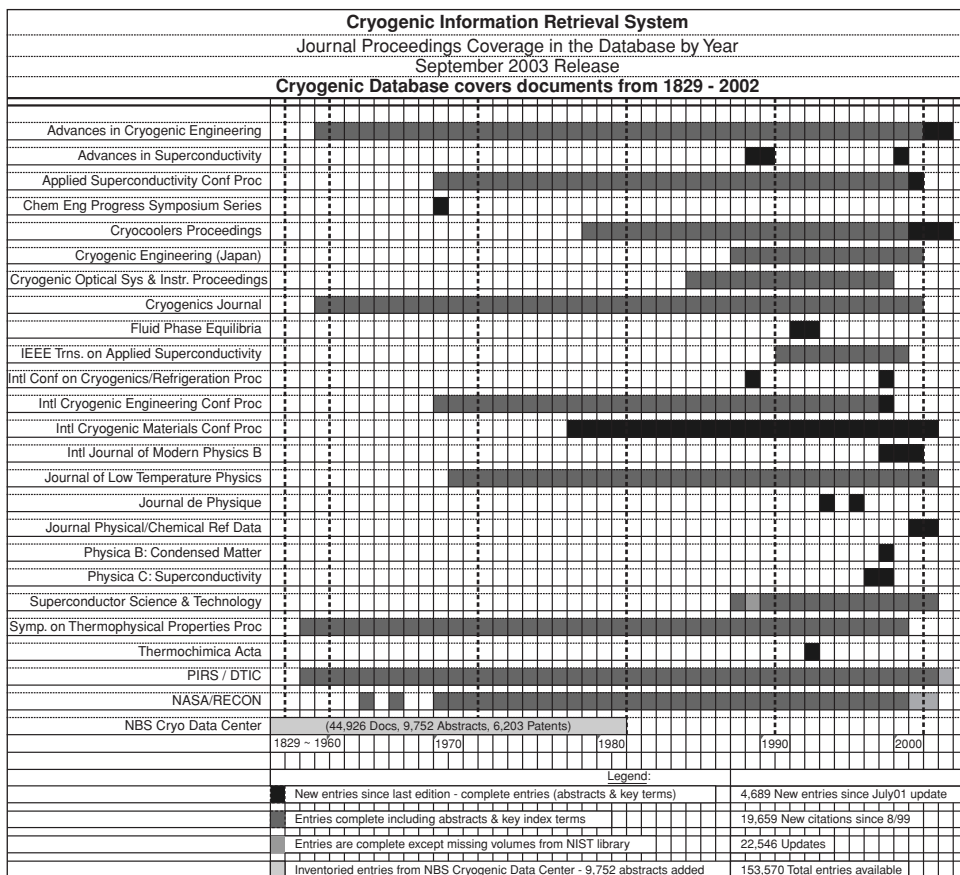
FIGURE 2.1. Journals and proceedings coverage in the database by year.

The CIC staff also provided an engineering design software program called the Cryogenics Material Properties (CMP) Program. The CMP Program is a "user-friendly" interface that provides access to various materials and properties at cryogenic temperatures. The data provided are directly traceable to NIST [11]. CMP makes available the material property data in a form convenient for engineers. CMP is currently only available for the Windows operating system.

The initial set of materials was selected for their common use in cryogenics. Currently, available properties include thermal conductivity, specific heat, and thermal expansion. Table 2.4 shows the material properties collected in CMP in 2003.

Graphs or tables may be created for any property. The table option works much like a spreadsheet, and data can be selected and copied to other programs as desired. The user can create a graph of any property and has complete control over the appearance. Figure 2.2 shows a publication-quality graph created by CMP and

TABLE 2.4. Material properties collected in CMP in 2003

| Material	Thermal conductivity	Linear thermal expansion	Specific heat	Thermal expansion coefficient	Yield strength	Young's modulus
1. Aluminum 3003-F	×	×	×			
2. Aluminum 5083-O	×	×	×			
3. Aluminum 6061-T6	×	×	×			
4. Balsa Wood	×					
5. Beechwood/Phenolic Composite	×					
6. Beryllium Copper	×	×				
7. Fiberglass/epoxy G-10CR	×	×				
8. Glass Fabric/Polyester Composite	×					
9. Inconel 718	×	×				
10. Invar 36	×	×	×			
11. Kevlar 49	×					
12. Nickel Steel (Fe2.25Ni)	×	×	×			
13. Nickel Steel (Fe3.5Ni)	×	×	×			
14. Nickel Steel (Fe5.0Ni)	×	×	×			
15. Nickel Steel (Fe9.0Ni)	×	×	×			
16. Oxygen-Free Copper (Avg)	×	×	×	×		
17. Oxygen-Free Copper (RRR)	×	×	×	×	×	×
18. Oxygen-Free Copper (Typical)	×	×	×	×	×	×
19. Phosphor Bronze				×		
20. Polyamide	×	×				
21. Polyimide	×					
22. Polystyrene Foam	×		×			
23. Polyurethane Foam	×		×			
24. Polyvinyl Chloride	×		×			
25. Stainless Steel 304	×	×	×			
26. Stainless Steel 304L	×	×	×			
27. Stainless Steel 310	×	×	×			
28. Stainless Steel 316	×	×	×			
29. Teflon	×	×	×			
30. Titanium 6Al4V	×	×				

imported directly into this document. Any number of graph or table windows can be open at one time, allowing easy comparisons.

Two sets of units are available, SI and English. References are provided so that the user can have confidence in the data. Limited room-temperature data are provided for each material and are based upon manufacturers' information.

The final accomplishment of the CIC was to collect the superconductivity/solid material properties documents (hardcopy and microfiche) from the National Archives in Washington, DC, in 2001. The documents were stored in 130 boxes for safe keeping. Upon inspecting the documents at arrival at TAI, all documents

FIGURE 2.2. Graph created in CMP and directly imported into document.
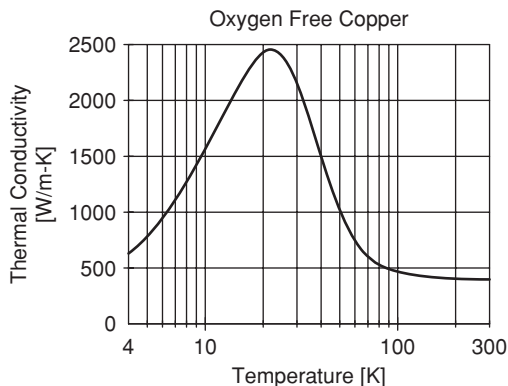
were in readable condition, although many of the older documents' paper showed signs of deterioration. Many of these older documents are difficult to find in libraries. The CIC staff was able to offer copies of these documents as a service to the cryogenic community for a small fee.

Owing to a lack of interest by the cryogenic community to use the services of the CIC, it was decided to discontinue the subsidiary in 2004. While in operation, the CIC staff accomplished three significant milestones for the cryogenics community. These are: (1) the CIRS bibliography database containing over 130,000 citations dating back to 1829; (2) the CMP Program with material properties of 30 different materials; and (3) the return and use of approximately 80,000 superconductivity/solid material property documents from the former NBS Cryogenic Data Center.

In early 2005, the CIC technical assets were distributed to two governmental organizations: NASA–Marshall Space Flight Center and NIST. MSFC has the hard-copy documents from the former NBS Cryogenic Data Center and is currently electronically scanning them for incorporation into their LaSSe program. LaSSe, which uses a full text search engine, is available to approved government contractors. At the conclusion of the scanning effort in early 2006, the hard-copy documents will be returned to NIST's Cryogenic Technologies Group in Boulder, CO.

TAI will continue to offer the CIRS bibliography database through the year 2006. The latest CD-ROM version, updated in 2003 and released in 2004, can be purchased by contacting TAI through their website (www.techapps.com) and completing the Information Request Form.

The CMP Program, a software package designed to provide thermophysical material properties for both metals and nonmetals, has been transferred to NIST's Cryogenic Technologies Group. For material properties information at cryogenic temperatures, please contact:

Peter Bradley   (303) 497-3465
NIST   Fax (303) 497-5044
325 Broadway, Boulder, CO 80303   pbradley@boulder.nist.gov

2.4.4 Information Resources: Defense Technical Information Center and the Information Analysis Centers

The DTIC (http://www.dtic.mil/dtic/index.html) is the repository for all DoD Science and Technology documents, and houses the program office for 11 DoD-sponsored IACs (http://iac.dtic.mil/). DTIC was established as a DoD Field Activity in 2004 under the Under Secretary of Defense for Acquisition, Technology, and Logistics and reporting to the Director, Defense Research & Engineering.

DTIC customers include the DoD, industry, and academia. It is responsible for the DoD IACs, supporting highly specialized technical areas. The scope of DTIC's collection includes areas normally associated with defense research, as well as information on biology, chemistry, energy, environmental sciences, oceanography, computer sciences, sociology, logistics, and human factors engineering.

DTIC serves as the central collection and dissemination point for DoD's scientific reports—over 2 million collected since DoD's inception in World War II, with an annual acquisition of 25,000–30,000 new reports. Ongoing and planned R&D project information is garnered from both the DoD community and industry. DTIC also provides web services to over 100 DoD websites, including the official DoD site (http://www.defenselink.mil/) and various DoD sites related to R&D.

IACs are research and analysis organizations chartered by the DoD and operated by DTIC to help researchers, engineers, scientists and program managers improve the productivity in the defense research, development, and acquisition communities by collecting, analyzing, synthesizing, and disseminating worldwide scientific and technical information in clearly defined, specialized fields or subject areas. The IACs are staffed by experienced technical area scientists, engineers, and information specialists. They establish and maintain comprehensive knowledge bases, which include historical, technical, scientific, and other information collected throughout the world and pertinent to their respective technical communities.

The IACs' secondary mission is to promote standardization within their respective fields. They accomplish these missions by providing in-depth analysis services and by creating products. IACs respond to technical inquiries; prepare state-of-the-art reports, handbooks, and databooks; perform technology assessments; and support exchanges of information among scientists, engineers, and practitioners of various disciplines within the scope of the IAC. IACs also collect, maintain, and develop analytical tools and techniques, including databases, models, and simulations. Eleven contractor-operated DoD IACs are administratively managed by the Office of the Program Manager, DoD IACs within the DTIC. Ten others are managed by other DoD activities. The IACs offer:

- Abstracts & Indexes: announcements of pertinent reports in the IAC's field of interest
- Bibliographic Inquiry Services: culled and authoritative bibliographic search reports

TABLE 2.5. History of DoD IACs

Current name	Previous names/collections
Advanced Materials and Processes Technology IAC (AMPTIAC) http://amptiac.alionscience.com	Metals and Ceramics Information Center, Metals IAC, Ceramics IAC, High-Temperature Materials IAC, Metal Matrix Composites, Plastics Technology Evaluation IAC
Chemical Warfare/Chemical Biological Defense IAC (CBIAC) www.cbiac.apgea.army.mil	
Chemical Propulsion Information Analysis Center (CPIAC) www.cpiac.jhu.edu	Chemical Propulsion Information Agency (CPIA)
Data and Analysis Center for Software (DACS) http://iac.dtic.mil/dacs	
Information Assurance Technology Analysis Center (IATAC)http://iac.dtic.mil/iatac	
Manufacturing Technology IAC (MTIAC) http://mtiac.alionscience.com	
Nondestructive Testing IAC (NTIAC) www.ntiac.com	
Reliability Information Analysis Center (RIAC) http://quanterion.com	Reliability Analysis Center (RAC), Supportability Investment Decision Analysis Center
Sensors Information Analysis Center (SENSIAC) www.sensiac.gatech.edu	Infrared Information Analysis Center (IRIA)
Survivability/Vulnerability IAC (SURVIAC) www.bahdayton.com/surviac	
Weapon Systems Technology IAC (WSTIAC) http://wstiac.alionscience.com	Guidance and Control Information Analysis Center (GACIAC), Defense Modeling & Simulation Tactical Technology, Tactical Warfare Simulation & Technology, Tactical Technology Center

- Critical Reviews & Technology Assessments: the latest scientific and engineering information on specific technical subjects
- Current Awareness: newsletters and literature to promote subject area awareness
- Referrals: consultation with or referral to world-recognized technical experts
- Scientific & Engineering Reference Works: useful and authoritative information in handbooks, data books, and databases
- State-of-the-Art Reports: summaries of the status of current technologies
- Technical Area Tasks: detailed expert assistance in a wide range of technical support services
- Technical Inquiry Services: expert and authoritative advice in response to technical questions.

The IAC areas of expertise cover the full spectrum of defense science and technology. The areas are shown in Table 2.5. The two IAC's that are information sources for cryogenic data are the Advanced Materials and Processes Technology IAC (AMPTIAC) and the Chemical Propulsion IAC (CPIAC). AMPTIAC is a focal point for data and information relating to advanced materials and processes.
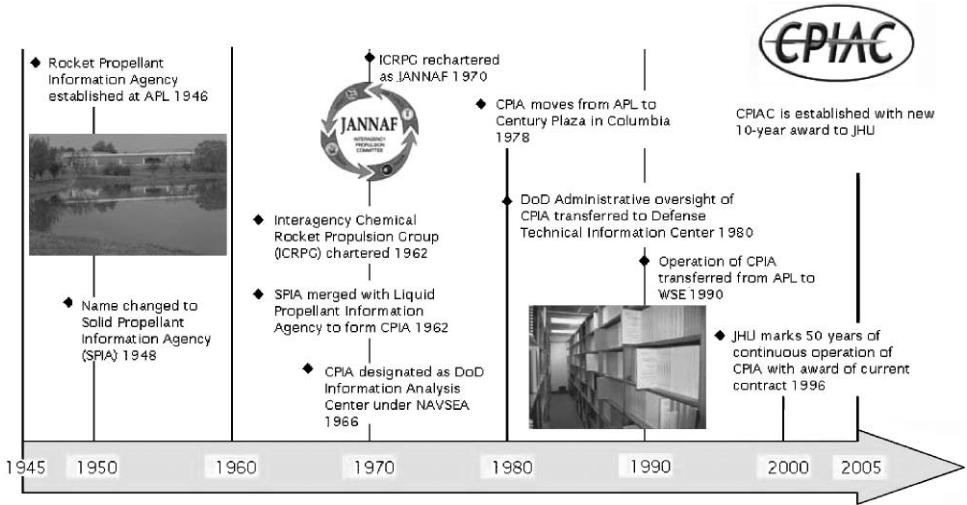
FIGURE 2.3. CPIAC has been continuously operated since 1946.

AMPTIAC's technical scope includes all scientific and technical information pertaining to:

- ceramics and ceramic matrix composites
- metals, alloys, and metal matrix composites
- electronic/optical and photonic materials
- environmental protection and special function materials
- organic structural materials and organic matrix composites.

The CPIAC, formerly the CPIA, is the oldest of the DTIC IAC's and has been continuously operated by The Johns Hopkins University since 1946; refer to Figure 2.3 for the CPIAC historic timeline.

The broad technical areas covered by CPIAC include chemical propulsion support to space, missiles, and guns and to the applications of cryogenics technologies within the DoD. More specifically, the areas of interest include: assisting in solutions to cryogenics and propulsion problems; standardizing tests and nomenclature; coordination of interagency technology programs; and promoting exchange of technical information in the fields of cryogenics and rocket, missile, space-vehicle, launch-vehicle, air-breathing, and gun propulsion based on chemical, electrical, and nuclear energy release. The scientific and engineering areas of interest of the Joint Army, Navy, NASA, Air Force (JANNAF) Interagency Propulsion Committee and CPIAC include: chemical synthesis; thermochemistry; kinetics; fluid dynamics; combustion; interior ballistics; and the physical chemical, mechanical, and engineering behavior and characterization of cryogens, propellants, grains, fuels, and inert propulsion materials and components; nondestructive evaluation;

theoretical and experimental performance; component and propulsion unit design; reliability; vulnerability; safety and environmental protection; exhaust plume flow fields; and operational life and serviceability.

CPIAC also provides technical and administrative support to JANNAF in accordance with the JANNAF Agreement and Charter. CPIAC provides long-term corporate memory for the DoD and the opportunity to avoid duplicate operations in various DoD components.

2.4.5 National Institute of Standards and Technology

The Cryogenic Technologies Group at NIST (http://cryogenics.nist.gov) is working to make available equation fits to the most common materials used in cryogenic systems.

NIST Pure Fluids is a widely used tool for providing data for the thermophysical properties of pure fluids. The standard property surfaces provided in the database are presented as thermodynamically consistent models which can be used for such applications as custody transfer, calibrations, and innovation, and design and optimization of processes involving pure fluids. Version 5.0 is a complete revision of the pure fluid database, and it is based on the most accurate pure-fluid equations currently available. For each fluid, the recommended thermodynamic surface is represented by an empirical multiparameter classical equation of state based either on a modified Benedict–Webb–Rubin equation of state or a more general type of Helmholtz energy equation of state. The viscosity and thermal conductivity are modeled with either fluid-specific correlations or a new variation of the extended corresponding states model. Other properties, such as the dielectric constant, surface tension, and melting line, are calculated with the fluid-specific correlations.

A graphical user interface, designed for Windows operating systems, generates tables and plots for any user-specified fluid. Online help is provided. Numerous options to customize the output are available as well. The fluids now available in this database are:

Ammonia	Hexane	Propane
Argon	Hydrogen	R-123
Butane	Isobutane	R-124
Carbon dioxide	Methane	R-125
Carbon monoxide	Neon	R-134a
Deuterium	Nitrogen	R-143a
Ethane	Nitrogen trifluoride	R-152a
Ethylene	Oxygen	R-22
Fluorine	Parahydrogen	R-32
Helium	Pentane	Xenon
Heptane	Krypton	

2.4.6 Vendor Data Packages

Cryodata (http://www.cryodata.com): Hepak, Gaspak, Cryocomp, and Metalpak. These are electronic material properties databases for a variety of common cryogenic materials.

CINDAS is an electronic version (http://cindasdata.com) of the venerable 'Thermophysical Properties of Matter Database' (i.e., Touloukian). This is an excellent source for a very large set of material properties and does contain some cryogenic properties.

While not directed at cryogenic materials, the Material Properties Database by JAHM Software (http://www.jahm.com) contains numerous useful materials in an easy-to-use format for finite element analyses or spreadsheet use.

2.4.7 NASA Centers

MAPTIS is a program at the NASA Marshall Space Flight Center (MSFC) with the goal of providing a single-point source for materials properties for NASA and NASA-associated contractors and organizations. The MAPTIS-II system contains physical, mechanical and environmental properties for metallic and nonmetallic materials. The MAPTIS homepage can be found at http://maptis.nasa.gov.

As mentioned previously, MSFC personnel maintain a program named LaSSe, which provides on-line access to historical propulsion documents for NASA and associated contractors and organizations. It uses a full text search engine for a large number of cryogenic documents, including the documents recovered and scanned from the NBS Cryogenics Data Center. The LaSSe homepage can be found at http://lasse.nasa.gov.

2.4.8 Universities

In a search of university websites for material and fluid properties data, no useful cryogenic information was found. Many universities are involved and use cryogenic information, but none is available on their websites for public use.

One website, however, has a paper with good data and references. Weisend et al. have a paper "A Reference Guide for Cryogenic Properties of Materials" of both solid and fluid properties which can be found at http://www.slac.stanford.edu/cgi-wrap/getdoc/slac-tn-03-023.pdf. This paper provides excellent references to most of the good literature sources for cryogenic data, as well as several electronic databases and programs.

2.4.9 New Book Releases

Several new books have been published that offer excellent handling, processes, and materials information. The first was released in early 2006 by Jack Ekin of NIST, Boulder, CO. It is titled *Experimental Techniques for Low Temperature Measurements* by Oxford University Press (www.oup.co.uk). This book presents

a highly integrated, step-by-step approach to the design and construction of low-temperature measurement apparatus. It is effectively two books in one: a text-book on cryostat design techniques and an appendix data handbook that provides materials-property data for carrying out that design. The main text encompasses a wide range of information written for specialists, without leaving less experienced students behind. After summarizing cooling methods, Part I provides core information in an accessible style on techniques for cryostat design, selection of materials, construction, wiring, and thermometry, accompanied by graphs, data, and clear examples. Part II gives a practical user's perspective of sample mounting techniques and contact technology. Part III applies the information from Parts I and II to the measurement and analysis of superconductor critical currents, including in-depth measurement techniques and the latest developments in data analysis and scaling theory. The appendix is a ready reference handbook for cryostat design, encompassing 70 tables compiled from the contributions of experts and over 50 years of literature.

The other books are described in *Cold Facts, The Magazine of the Cryogenic Society of America, Inc*. and repeated here for completeness [12]. *Low Loss Energy Storage and Handling of Cryogenic Liquids: The Application of Cryogenic Fluid Dynamics* is a new monograph by Ralph Scurlock, Emeritus Professor Cryogenic Engineering and former director of the Institute of Southampton. He brings 50 years of experience and research in the fundamentals of liquid behavior of cryogenic fluids, which supports the research and design of liquid storage systems. To order, contact Kryos Technology, 22 Brookvale Road, Southampton SO17 1QP, UK (scurlock@soton.ac.uk).

Cryogenics—Low Temperature Engineering and Applied Sciences by the late Traugott H.K. Frederking, Professor Emeritus, UCLA, and Sidney W.K. Yuan, Raytheon Space & Airborne Systems. This book is a complex discussion of cryogenic practices. Combining the authors' professional experience and research, the book reviews basic principles of cryogenic substances and cooling processes, superconducting and other magnets, safety issues of cryogenic systems, and future prospects. To order, go to www.yutopian.com/Yuan/Book.html.

Industrial Noise Control and Acoustics by Randall F. Barron, describes useful procedures in the design of industrial noise-abatement systems and equipment to reduce the generation and transmission of noise and to comply with Occupational Safety & Health Administration, US Environmental Protection Agency, and other standards. Cryogenic engineers can apply the information to design for noise reduction from compressors, pumps, fans, and other equipment used in gas liquefaction systems. It contains case studies and example problems illustrating the principles discussed in each chapter. To order, contact Taylor, Francis and Routledge, Inc., 800/272-7737, and provide the ISBN number: 0-8247-0701-X.

2.4.10 Monographs

Special cryogenic topics have been printed with the International Cryogenic Monograph Series since 1964. The publisher printed limited copies for sale;

TABLE 2.6. Cryogenic topics printed in monographs

Title	Author	Status
Thermoelectric Refrigeration	H.J. Goldsmid	Out of print
Electrical Resistance of Metals	G.T. Meaden	Out of print
Specific Heats at Low Temperatures	E.S.R. Gopal	Out of print
Safety with Cryogenic Fluids	M.G. Zabetakis	Out of print
Applied Superconductivity, Metallurgy and Physics of Titanium Alloys—Volume 1: Fundamentals and Volume 2: Applications	E.W. Collings	Out of print
Cryocoolers—Volume 1: Fundamentals and Volume 2: Applications	G. Walker	Out of print
Heat Transfer at Low Temperature	W. Frost	Out of print
Helium Cryogenics	S.W. VanSciver	In print
Modern Gas-Based Temperature and Pressure Measurements	F. Pavese and G. Moliner	Out of print
Polymer Properties at Room and Cryogenic Temperatures	G. Hartwig	In print
Stabilization of Superconducting Magnetic Systems	V.A. Altov, et al.	Out of print
Superconducting Electron – Optic Devices	I. Districh	Out of print
Superconducting Materials	E.M. Savitski, et al.	Out of print
Cryogenic Process Engineering	K.D. Timmerhaus and T.M. Flynn	Out of print
Safety in the Handling of Cryogenic Fluids	F.J. Edeskuty and W.F. Stewart	In print
The Hall Effect in Metals and Alloys	C.M. Hurd	Out of print
The Generation of High Magnetic Fields	D.H. Parkinson and B.E. Mulhall	Out of print
Helium-3 and Helium-4	W.E. Keller	Out of print
Cryogenic Laboratory Equipment	A.J. Croft	Out of print
Current Trends in Cryobiology	A.V. Smith	Out of print
Advanced Cryogenics	C.A. Bailey	Out of print
Mechanical Properties of Materials at Low Temperatures	D.A. Wigley	Out of print
Thermodynamic Properties of Cryogenic Fluids	R.T. Jacobsen, et al.	In print
Cryogenic Regenerative Heat Exchangers	R.A. Ackerman	In print
Heat Capacity and Thermal Expansion at Low Temperatures	T.H.K. Barron and G.K. White	In print
Joule–Thomson Miniature Cryocooler	B.-Z. Maytal	In preparation
Space Cryogenics	P. Mason and F. Scaramuzzi	In preparation
Cryogenic Mixed Refrigerant Cycles	G. Zenkatarathnam	In preparation

unfortunately, once they are gone, the publisher will not print more. The titles, authors, and status of each monograph are shown in Table 2.6.

Nancy J. Simon of NIST and several coauthors published a number of noteworthy references involving solid material properties. The references are listed below:

- Simon, N.J., Drexler, E.S., and Reed, R.P., *Properties of Copper and Copper Alloys at Cryogenic Temperatures*, NIST Monograph 177, National Institute of Standards and Technology, Boulder, CO (1992).
- Simon, N.J., Drexler, E.S., and Reed, R.P., *Review of Cryogenic Mechanical and Thermal Properties of Al-Li Alloys and Alloy 2219*, NISTIR 91-3971, National Institute of Standards and Technology, Boulder, CO (1991).

- Simon, N.J., *A Review of Irradiation Effects on Organic-Matrix Insulation*, NISTIR 93-3999, National Institute of Standards and Technology, Boulder, CO (1993).
- Simon, N.J., *Irradiation Damage in Inorganic Insulation Materials for ITER Magnets—A Review*, NISTIR 94-5025, National Institute of Standards and Technology, Boulder, CO (1994).
- Simon, N.J., *Cryogenic Properties of Inorganic Insulation Materials for ITER Magnets*, NISTIR 94-5030, National Institute of Standards and Technology, Boulder, CO (1994).
- Simon, N.J., Wong, F., and Reed, R.P., *Metallic Materials Mechanical and Thermal Property Database, Annex I, Metallic Material Specifications for ITER Magnets*, Superconducting Coils and Structures Division, ITER EDA, Naka Joint Work Site, Naka, Japan (1997).

2.5 Plans for Data Retrieval and Material Properties

2.5.1 Data Retrieval System

Approximately 130 boxes of reports and microfiche were transferred from the National Archives to TAI and NIST-Boulder, and subsequently shipped to NASA-MSFC where the documents have been electronically scanned. These scanned documents, linked to the CIRS, will be available for purchase in 2006 from an e-commerce website to be developed and maintained by CPIAC.

In addition to providing documents for purchase, CPIAC will provide a number of links on the site to other sites that the cryogenics community might find useful. In particular, there will be links to NIST for their fluid compatibility database, high-temperature material property data, and their CMP software (if it is made available on the web).

2.5.2 Material Properties

For future assembly and distribution of cryogenic materials references (including papers and reports and unpublished reports), the International Cryogenic Materials Conference (ICMC), the National High Magnetic Field Laboratory in Tallahassee, FL, and the National Institute for Materials Science in Tsukuba, Japan, are tentatively discussing the creation of a worldwide data network [13]. This network would have focused US and Japanese cryogenic data collection and dissemination activities in the US and Japan, respectively, and worldwide data gathering (and, possibly, dissemination) coordinated by the ICMC.

2.6 Conclusions

The former NBS Cryogenic Data Center served as a centralized US source of cryogenic technology data from the mid 1950s until the early 1980s. When the Cryogenic Data Center was discontinued in 1983, it created a cryogenics data

gap for engineers and scientists. The CIC was established in 1997 to preserve and distribute cryogenic information to government, industry, and academia users. The CIC captured the long history of information traceable back to the NBS Cryogenics Data Center. While in operation, the CIC was able to complete and deliver: (1) the CIRS bibliography database of over 130,000 citations dating back to 1829; (2) the CMP Program with material properties of 30 different materials; and (3) the return of approximately 80,000 superconductivity/solid material property documents from the former NBS Cryogenic Data Center.

Unfortunately, the CIC was discontinued in 2004 due to lack of market interest by the cryogenics community. Good stewardship demands that this situation be turned around before it is too late and the technical assets of the CIC are lost. These assets were distributed to NASA-MSFC and NIST. Plans are under way in 2006 for CPIAC to launch an e-commerce cryogenic website to offer bibliography data and downloading of cryogenic documents. NIST plans to continue the CMP Program at their Boulder Group.

In summary, there is now a wealth of data and information available to the cryogenics engineer and scientist. Unfortunately, it is sometimes difficult to locate. From only a couple of books in 1959 on cryogenic engineering, there is now available a multitude of data and information, numerous books, published papers, and websites.

References

1. McClintock, M., *Cryogenics*, Reinhold Publishing Corporation, New York, 1964, p. v.
2. McClintock, M., and Gibbons J., *Mechanical Properties of Structural Materials at Low Temperatures,* NBS Monograph 13, June 1, 1960.
3. *The Cryogenic Materials Data Handbook*, Cryogenic Engineering Laboratory, Air Force Ballistic Missile Division Contract No. AF 04(647)-59-3, Office of Technical Services, United States Department of Commerce, Washington, DC.
4. Johnson, V.J., *WADD Technical Report* 60–56, "Part I: Properties of Fluids, Part II: Properties of Solids and Part III: Bibliography of References (Cross-Indexed), A Compendium of the Properties of Materials at Low Temperature (Phase I)," National Bureau of Standards, Boulder, CO, 1960.
5. Mohling, R.A., Hufferd, W.L., and Marquardt, E.D., "Cryogenic Technology Information Database Program," *Advances in Cryogenic Engineering*, Vol. 45, Plenum Press, New York, 1999, pp. 1181–1188.

6. Mohling, R.A., Marquardt, E.D., Fusilier, F.C., and Fesmire, J.E., "Cryogenic Information Center," *International Congress of Refrigeration*, Washington, DC, 2003.
7. "Cryogenic Data Center—Resume of Activities and Services," NBS, Boulder, CO, 1967.
8. Mann, D.B., *LNG Materials and Fluids*, Cryogenics Division, National Bureau of Standards, Boulder, CO, 1977.
9. *Handbook on Materials for Superconducting Machinery, Mechanical, Thermal, Electrical and Magnetic Properties of Structural Materials*, Metals and Ceramics Information Center, Battelle, Columbus Laboratories, Columbus, OH, 1977.
10. Reed, R.P., and Clark, A.F., *Materials at Low Temperatures*, American Society for Metals, 1983.
11. Marquardt, E.D., Le, J.P., and Radebaugh, R., "Cryogenic Material Properties Database," *11th International Cryocooler Conference*, Kluwer Academic/Plenum, New York, June 20–22, 2000.
12. *Cold Facts*, Cryogenic Society of America, Inc., Fall 2005, Vol. 21, No. 4, p. 33.
13. Reed, R.P., Cryogenic Materials, Inc., Boulder, CO, personal communication, 2005.

3
Trends and Advances in Cryogenic Materials

R.P. REED

Cryogenic Materials, Inc., Boulder, CO, 80305 USA

Abstract

Increased emphasis has been placed on research and development of specialized materials for use in low-temperature applications. Most research has been driven by (1) the construction of large superconducting coils, (2) requirements for transport and storage of liquefied natural gas, and (3) the discovery of superconductors with critical temperatures T_c as high as 90 K. The integration between structural design and material properties for critical low-temperature applications has been facilitated by the incorporation of fracture mechanics concepts. This development has led to measurement of an entirely new set of mechanical properties at low temperatures, to increased nondestructive inspection to measure in-situ flaw sizes, and to the development of fracture control practices for a number of cryogenic applications.

3.1 Introduction

To provide focused dissemination of new low-temperature-materials property information, the International Cryogenic Materials Conference (ICMC) was formed in 1974. The conference provided the only means for presenting and discussing the research and development of low-temperature structural metals and alloys and their welds, structural composites, and electrical and thermal insulators, as well as the application of fracture mechanics to inspection, properties, and design for cryogenic structures. And, since it held its meetings in parallel with the Cryogenic Engineering Conference, it provided an opportunity for synergistic interactions between cryogenic engineers and cryogenic materials specialists.

For discussion of cryogenic materials research over the past several decades, this paper is divided into two parts, namely overall trends and more significant specific technological advances. In the discussion of overall trends, the papers published in the ICMC proceedings are used to provide quantitative comparisons of variables, such as the origins of the research from various laboratories and worldwide and US trends. The trends of the focus of research (such as on structural alloys, composites,

or superconductors) are categorized over this time period. The use of the ICMC proceedings is thought to be a representative source for quantitative estimates of the trends in low-temperature materials (other than superconductors) research since they represent the only source, worldwide, that is focused on this subject. On the other hand, the general trends of research presented on superconductors in the ICMC proceedings may be skewed, since there are other conferences, of equivalent or larger size, on applied superconductivity and specialized workshops on high-T_c superconductors.

The second part of this review covers the technological advances that are related to materials at low temperatures. Since other review papers in this book focus on achievements related to superconductors, and since the author's interests have been directed toward structural alloy and composite development and characterization, this part emphasizes advancements in nonsuperconducting materials.

3.2 Trends in Cryogenic Materials Research

To quantify the overall trends of cryogenic materials research related to origins of the research, both worldwide and locally in the US, and the types of material studied, the number of papers in each volume of the proceedings of the biannual ICMC conferences held in the US and Canada for the past 30 years are tabulated. Two factors affect the correlation between the number of papers published in each of the proceedings and the number of papers actually presented at each conference: (1) not all speakers chose to prepare papers and (2) a modest number ($\sim$5%) of submitted papers have been rejected. It is doubtful that these variables will result in skewed results of the trends presented in this section.

Over the past 30 years, the number of papers included in the ICMC proceedings in volumes 22 to 52 (even-numbered volumes only) from 1975 to the present [1] have increased from about 60 during the two early, formative conferences. The number peaked at nearly 190 papers in 1995, and currently it is about 150 papers. This trend is illustrated in Figure 3.1. The decline from the conference in 2003 is likely caused by the less accessible location of the conference, i.e. Alaska.

The contributions from the US and Canada, Europe including Russia (RF) and Ukraine (Ukr), and Asia plus Australia to each of these proceedings are shown in Figure 3.2. In some cases, the conference location or timing of the conference has affected attendance from particular parts of the world. But, if averaged over the last six conferences, the US and Canada have contributed about 40% of the papers, Asia and Australia about 38%, and Europe including RF and Ukr 22%. Thus, the contributions of the US and Canada and Asia and Australia are almost equivalent, despite the fact that all the conferences have been held in the US and Canada. Over the entire 30-year period, these data indicate a slight increase in low-temperature R&D from the US and Canada and Europe including RF and Ukr, but a much greater increase in Asia plus Australia. This large increase correlates well with the strong increases in technological growth and gross national product of many of the Asiatic countries during this time period.
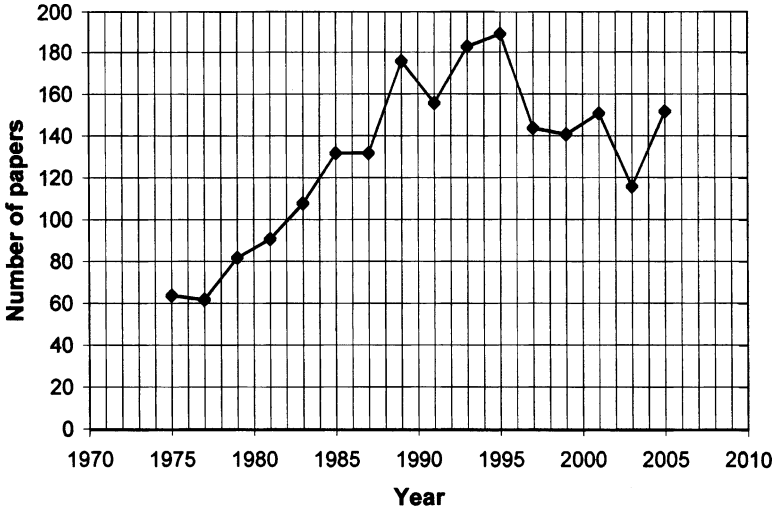
FIGURE 3.1. Total number of ICMC papers from 1975 through 2005.

Figure 3.3 presents the distribution of papers related to the types of material that were studied. The material classes used for this presentation include structural alloys (structural metals and alloys), composites/insulators (structural composites, thermal and electrical insulators, resins), functional (regenerator materials, normal-metal conductors, shape-memory alloys, others), and high- and low-T_c

FIGURE 3.2. Geographical distribution of first authors of all ICMC papers from 1975 to 2005.

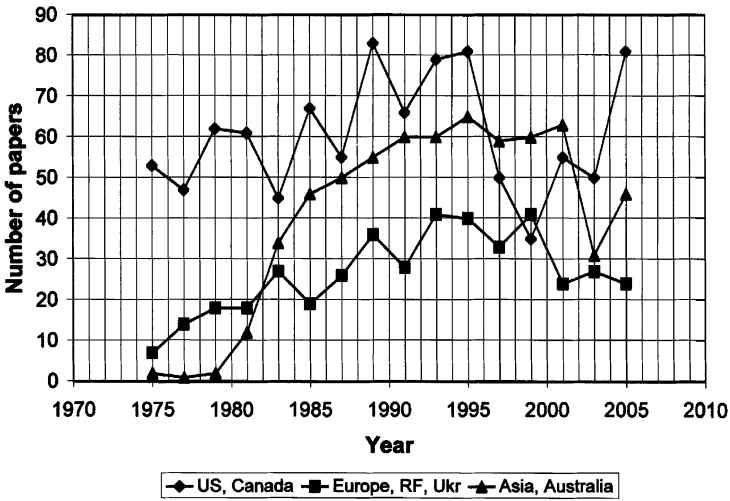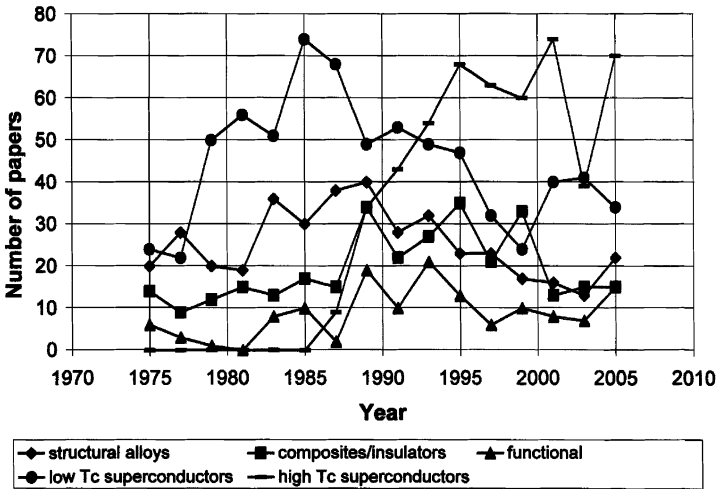FIGURE 3.3. Topical distribution of all ICMC papers from 1975 to 2005.

superconductors. Obviously, there was a sudden and large emphasis in the R&D related to high-T_c superconductors after their discovery in 1986. Research on other material classes has increased slightly or remained constant. However, since the 1985–1989 time period, emphasis on low-T_c superconductors, structural alloys, and composite/insulator materials has steadily declined.

When we consider only three material categories (superconductors, structural alloys/composites, functional), their relative trends are easily recognizable (Figure 3.4). Emphasis on superconductors has continued to increase, functional

FIGURE 3.4. Very general topical distribution of all ICMC papers from 1975 to 2005.

FIGURE 3.5. Geographical distribution of ICMC papers on structural alloys from 1975 to 2003.

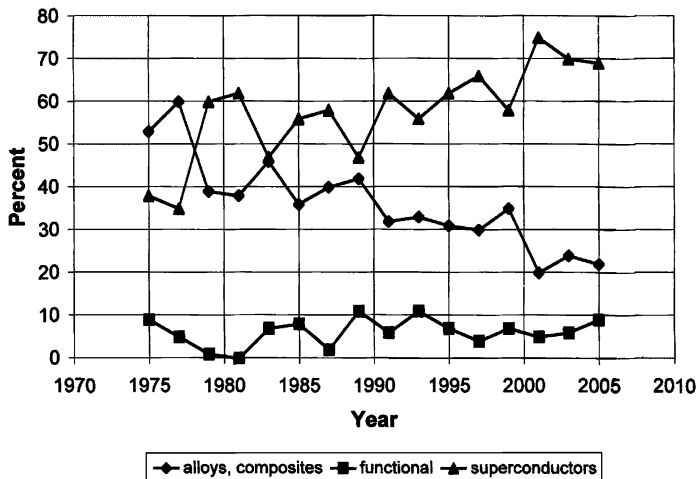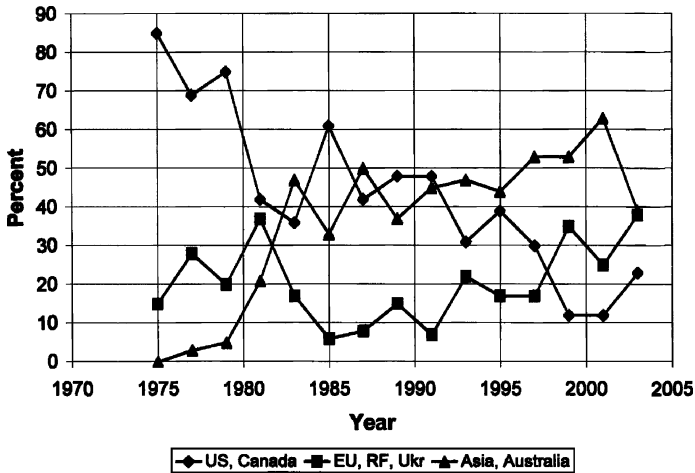material studies remain about constant, and emphasis on alloys and composites has declined. These trends represent the perception that additional studies related to superconductivity are likely to be more productive than gradual improvement of structural materials and insulation. The relative trends of the major continental areas for research on structural metals and alloys are shown in Figure 3.5. Note the ever-decreasing pattern of US contributions. Since about 1985, contributions from both Europe and Asia have gradually increased. Very similar 30-year trends are found in research contributions on composites (structural composites, electrical and thermal insulation and resins) shown in Figure 3.6. If we consider only the past 20 years, it is evident that all geographical sectors have contributed about equally and constantly over this period of time. Thus, since Europe and Asia have made equivalent contributions over the past 20 years, we may conclude that the US no longer dominates research on structural metals and alloys and composites. In fact, since all ICMC conferences have been held in the US or Canada, scientists from overseas are less likely to attend. This suggests that more R&D is currently being performed in Europe and Asia than in the US on these topics.

Figure 3.7 depicts the relative trends of US studies in alloys (structural metals and alloys), composites (structural composites, electrical and thermal insulation, resins) and superconductors (high and low T_c). The contributions on functional materials are omitted from this figure; these contributions have remained constant at about 10% over the time span considered. Quite clearly, as indicated in the overall projections, research has been increasing in superconductors and decreasing in alloys and composites. Now, over three times more research is presented on superconductors than on alloys and composites. Since ICMC is typically the only international conference used for the presentation of low-temperature alloy and composite information but is the smallest of several conferences for the
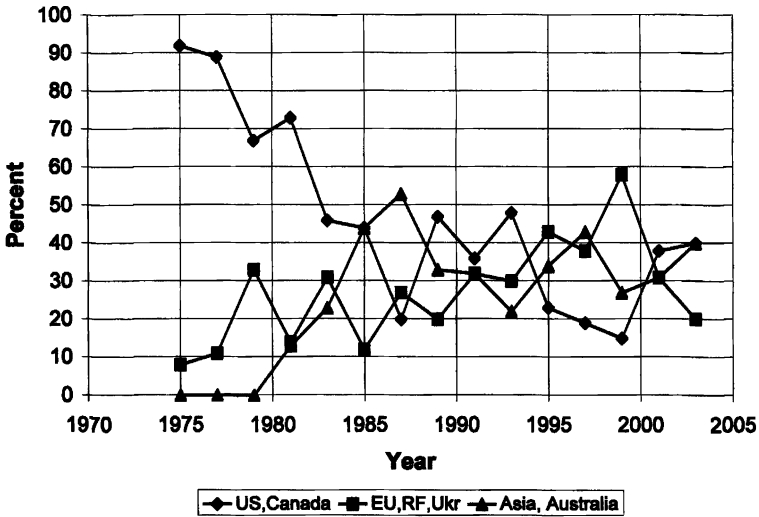
FIGURE 3.6. Geographical distribution of ICMC papers on composites from 1975 to 2003.

presentation of research on superconductors, the ratio of superconductor to al-
loys plus composite papers may be an order of magnitude greater, perhaps 35:1.
Figure 3.7 suggests that this ratio continues to increase.

The relative contributions of government laboratories, industry, and universities
to all cryogenic materials research are plotted in Figure 3.8. University contri-
butions are steadily increasing. The contributions from industry and government
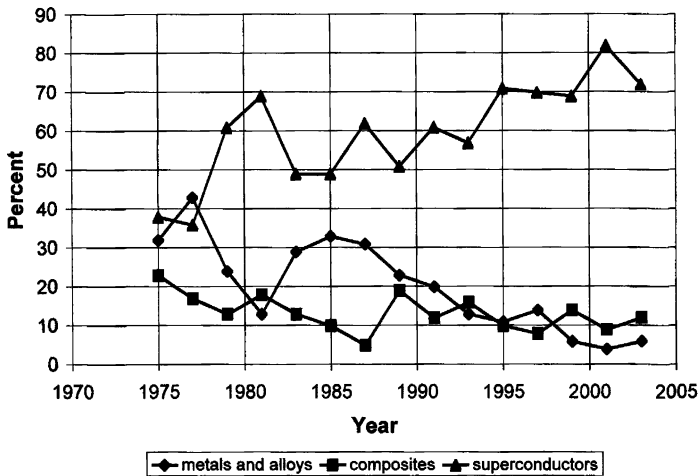
FIGURE 3.7. Topical distribution of US ICMC papers from 1975 to 2003.
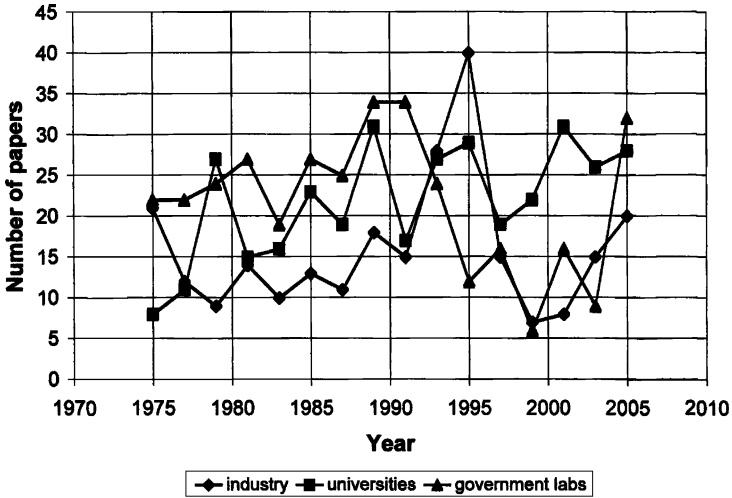
FIGURE 3.8. Distribution of US ICMC papers from companies, industry, and universities.

laboratories are irregular but approximately equivalent and tend to remain constant over time.

The contributions from various US government departments and agencies are plotted in Figure 3.9. The general decline in contributions from the Department of Commerce (exclusively, the National Institute of Standards and Technology
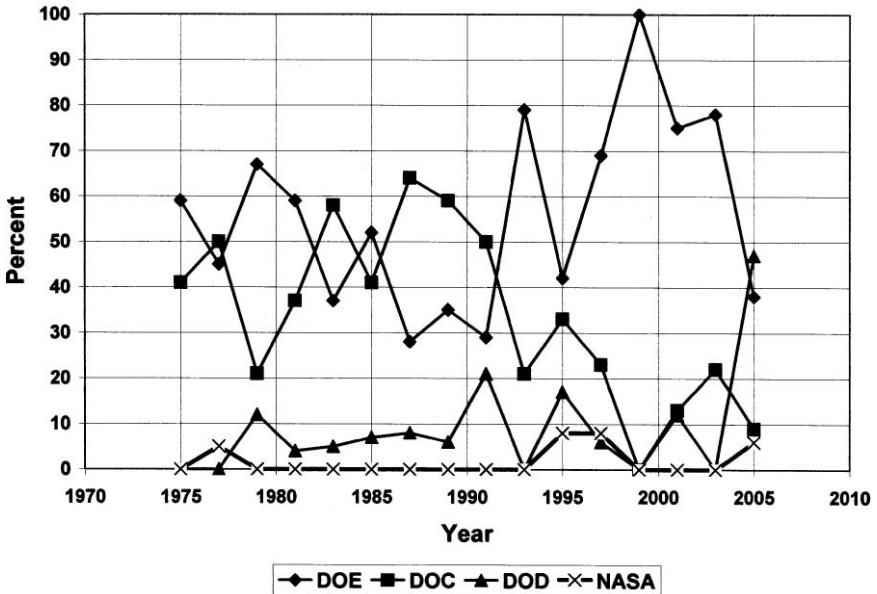
FIGURE 3.9. Percentage of US papers from various US government laboratories.

(NIST)) over the 30-year time frame is due to the gradual reallocation of internal resources to other R&D activities and to abatement of obligations to other agencies. The contributions from research at the Department of Energy (DOE) laboratories (Brookhaven, Argonne, Lawrence Livermore and Berkeley, Fermi, and Los Alamos) have remained at about a constant percentage over time and have usually exceeded those from other government laboratories. Contributions from Department of Defense (DOD) groups have been relatively low but constant until 2005, when a large increase occurred. One wonders whether this portends an adjustment towards low-temperature materials research in several DOD laboratories or whether it represents a reaction toward the first ICMC chairman from a DOD laboratory. Finally, one must be surprised at the very low, particularly in the 14-year time frame from 1979 to 1993, nonexistent contributions from NASA. At best, it contributed only two papers in 1997. The absence of NASA papers clearly suggests a divergent management philosophy, one that forsakes in-house expertise and, thus, sacrifices decision-making and corporate memory relative to materials design, properties, and processing for its emphasis on contracting to many and divergent companies. It is worth noting that very few NASA subcontract results have been reported at ICMC and that, typically, NASA has not sponsored alternative low-temperature material workshops.

In summary, the following trends on low-temperature materials R&D over the past 30 years can be discerned from the papers published in the ICMC proceedings:

- Overall, the total amount of research has increased.
- This increase has been confined to the study of superconductors, whereas R&D on structural metals and alloys, composites and insulators, and functional materials has remained approximately constant.
- Asia's R&D on low-temperature materials has increased notably; that of the US and Europe has increased very modestly.
  - Research on structural metals and alloys has increased in Asia and decreased in the US, relatively.
  - Research on composites (structural composites, resins, electrical and thermal insulation) has declined in the US, relatively.
  - Research on superconductors has significantly increased in all geographic sectors.
- US research on superconductors has increased, relatively, while research on structural metals and alloys and composites has declined.
- US research has been presented in nearly equal numbers by companies, universities, and government laboratories.
- The DOE, of all the US government departments and agencies, has tended to contribute the greatest number of papers, while NASA's contribution has been very low or nonexistent.

3.3 Advances in Cryogenic Materials R&D

This part focuses on advances in low-temperature materials research related to metals and alloys and composites. The application of fracture mechanics and

the related testing to establish sound fracture control for large-scale cryogenic applications are also included. Research on superconductors is not emphasized in this review; others are reporting on this topic.

3.3.1 Fracture Mechanics

During the past several decades, one of the major advances in materials research for cryogenic applications has been the introduction of fracture mechanics concepts, testing, and analysis. In particular, the testing laboratories at the NIST in Boulder, Colorado (Tobler, Read, Reed), at Forchungszentrum Karlsruhe in Karlsruhe, Germany (Nyilas), at the National Institute for Materials Science in Tsukuba, Japan (Ogata), and at the Japan Atomic Energy Research Institute in Naka, Japan (Nakajima, Yoshida, Shimamoto), have been leaders in providing properties and analyses related to fracture mechanics for the cryogenic community.

Fracture mechanics relates particular material properties to flaw size and operational stresses to produce quantitative predictions. Estimates of minimum flaw size that would result in structural failure, maximum allowable operating static and cyclic stress, and expected operational lifetime can be calculated. This section briefly describes the basis, testing and properties, and prediction techniques that are now used in fracture mechanics analysis for cryogenic structures. Good, generalized descriptions of fracture mechanics concepts and utility are found in presentations by Hertzberg [2] and Dieter [3].

The fracture mechanics approach assumes that flaws exist within the structural material. Regardless of their content or geometry, the flaws are assumed to be cracks. The stress distribution K around the crack can be described, in most cases, by the generalized form

$$K = Y\sigma\sqrt{\pi a}, \tag{3.1}$$

where σ is the applied stress and a is the crack (through-thickness) length or depth and Y is a parameter that depends on crack geometry and specimen type or loading parameters. Here, K is called the stress-intensity factor. Tabular lists of Y parameters for various crack locations and geometries have been developed [4–6]. When the stress intensity at the crack tip reaches a critical value, fracture occurs. This critical value is called the fracture toughness K_c. The fracture toughness is a material property, dependent on metallurgical variables, crack orientation, plastic deformation and temperature. When the plastic deformation at the crack tip is very limited, plain-strain loading conditions are prevalent, and the fracture toughness is a minimum value labeled K_{Ic}. When testing, specimen thickness is maximized in an attempt to achieve plain-strain loading conditions.

One can substitute the fracture toughness K_{Ic} for K, the maximum allowable applied stress; σ_{op} for σ; and the critical flaw size a_c for a in Equation (3.1) and use the equation for quantitative assessment of any of the three major design (σ_{op}), material (K_{Ic}), and inspection (a_c) parameters if the other two are known or assumed.

$$K_{Ic} = Y\sigma_{op}\sqrt{\pi a_c}. \tag{3.2}$$

For example, the critical flaw size a_c that will result in fracture can be calculated if one uses the maximum allowable operating stress and minimum value of fracture toughness. Or, if the minimum fracture toughness and minimum inspectable flaw size are known, the maximum allowable operating stress can be calculated. In some cryogenic applications, the calculated critical flaw size may exceed the wall thickness. In these cases, if the structure contains a cryogen, when the crack size exceeds the wall thickness under fatigue conditions, leakage before breakage will occur. In the transport of cryogens, such as liquefied natural gas (LNG), "leak before break" design criteria may be employed, and sensitive leak detection equipment must be demonstrated to preclude subsequent failure and/or dangerous buildup of inflammable gases. In other cases, such as superconducting conduits that contain liquid helium and are enclosed within a vacuum, conduit wall leakage will be evidenced by loss of vacuum.

Ultrasonic, nondestructive inspection (NDI) is usually used to detect small flaws in cases where their size is critical. Flaw sizes of about 5 to 10% of the plate or wall thickness are usually detectable with calibrated ultrasonic NDI techniques.

Maximum allowable stresses for cryogenic applications with ductile structural alloys are usually one-half to two-thirds of the minimum tensile yield strength or one-half of the tensile ultimate strength at the operating temperature, whichever is lower. In many cases, ASME Structural Codes, Section 8 for Pressure Vessel guidelines [7] are followed. Usually, for annealed alloys, such as 316 and 316LN, two-thirds of the tensile yield strength results in a lower allowable stress. When less ductile structural alloys are used, the design criteria are sometimes lowered from one-half to one-third of the tensile ultimate strength.

3.3.1.1 Fracture Toughness

The fracture toughness is usually measured by using compact tension specimens. This type of specimen contains a sharp, machined notch along one side (see Figure 3.10) that is oriented normal to the direction of the applied load. At the base of this notch, a crack is formed by cyclic loading of the specimen at 77 K for fracture toughness tests at 4 K. Guidelines for compact-tension specimen geometry and dimensional tolerances, precracking conditions, and performance of the test are
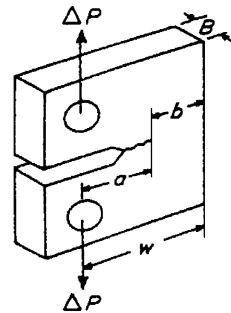

FIGURE 3.10. Compact-tension specimen that is commonly used to measure the fracture toughness and fatigue crack-growth rates, where P is the applied load.

TABLE 3.1. Typical fracture toughness, tensile yield strength,
and Young's modulus at 4 K for common structural alloys

Alloy	σ_y(MPa)	K_{Ic}(MPa m$^{1/2}$)	E(GPa)
AISI 304 (annealed)	500	330	209
AISI 316 (annealed)	800	260	207
AISI 316LN (annealed)	1000	215	207
JN-1 (Japan, austenitic)	1240	200	207
Inconel 718 (aged)	1400	110	211
	1200	165	211
Incoloy 908 (aged)	1250	265	175
	1280	155	175
Al 2090-T81	680	50	79
Al 2219-T87	530	45	78
Ti–5Al–2.5Sn (annealed)	1520	35	133
	1291	80	125
Fe–9Ni (quenched, tempered)	1340	70	205
4340 steel (ferritic)	1750	35	200

given in ASTM E-399 [8]. A minimum specimen thickness is always necessary
to achieve plane-strain loading conditions. A clip-on strain-gage extensometer
that senses crack-opening displacement is usually used to measure crack growth.
After precracking, the specimen is loaded at the test temperature to achieve stress
intensity levels at the crack tip that are sufficient to promote additional crack
growth or immediate fracture. If the specimen fails after limited crack growth and
plastic deformation at the crack tip, usually the ATSM guidelines for linear-elastic
fracture toughness can be used to calculate the fracture toughness K_{Ic} from the
load–crack-growth curve. If more extensive crack growth and associated plastic
deformation occur prior to fracture, elastic–plastic conditions are prevalent, and
the J-integral ASTM E-813 test guidelines [9] must be employed to measure
$K_{Ic}(J)$.

   Typical values of the fracture toughness at 4 K for common structural alloys are
listed in Table 3.1. The reader is cautioned, however, that for any particular alloy,
there can be large variabilities in the fracture toughness at 4 K that result from the
amount of cold work, heat treatment, impurity levels, grain size, amount and lo-
cation of precipitates, and specimen crack orientation relative to the orientation of
these metallurgical variables. Owing to this sensitivity of low-temperature fracture
toughness on metallurgical parameters, it is necessary to conduct fracture tough-
ness measurements at the lowest operating temperature and to use specimens with
cracks oriented in specific worst-case directions on heats of alloys selected for use.

   Also included in Table 3.1 are the tensile yield strength σ_y and Young's modulus
E for the same metallurgical condition corresponding to the fracture-toughness
condition. The tensile yield strength, like fracture toughness, is considerably more
sensitive to metallurgical and test variables at 4 K than at room temperature. (For
example, see the discussion of the temperature dependence of nitrogen addition
and grain size on yield strength of austenite in Section 3.3.2.1.) Therefore, tensile

FIGURE 3.11. Fracture
toughness of two ferritic
steels (Fe–5Ni, Fe–9Ni)
and one austenitic steel
(Fe–13Cr–19Mn–0.2N)
at low temperatures.
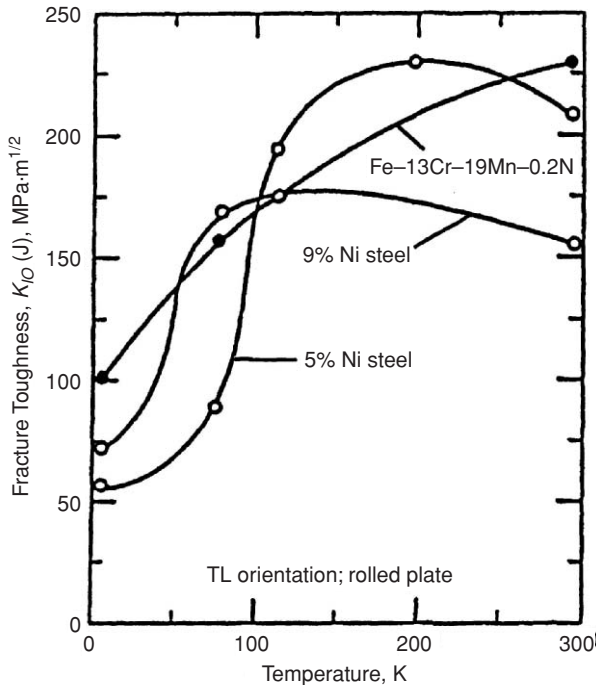
tests of actual alloy heats used for fabricating cryogenic devices are required when
the design stress levels and design yield strengths are close to each other.

The fracture toughness depends only mildly on temperature for most face-
centered cubic metals and alloys (e.g. aluminum and copper alloys, austenitic
steels). An example is the temperature dependence of the austenitic Fe–13Cr–
19Mn–0.2N steel shown in Figure 3.11. Most body-centered cubic (e.g. ferritic
and martensitic steels, refractory metals) and hexagonal close-packed alloys (e.g.
titanium and magnesium alloys) exhibit a *ductile-to-brittle transition* at lower tem-
peratures, as illustrated for two ferritic/martensitic Fe–Ni alloys in Figure 3.11.
The temperature range of the transition can be lowered by improving alloy purity
and, in the case of ferritic/martensitic steels, also by modifying the composition
and heat treatment.

3.3.1.2 Fatigue Crack-Growth Rate

By using identical or very similar compact-tension specimens and ASTM E-647
guidelines [10], fatigue crack-growth rates da/dN (where a represents crack
growth and N is the number of fatigue cycles) can be measured. In such tests,
crack extension is continuously monitored with strain-sensing equipment similar
to that used in fracture-toughness testing. Maximum and minimum stresses (ΔK
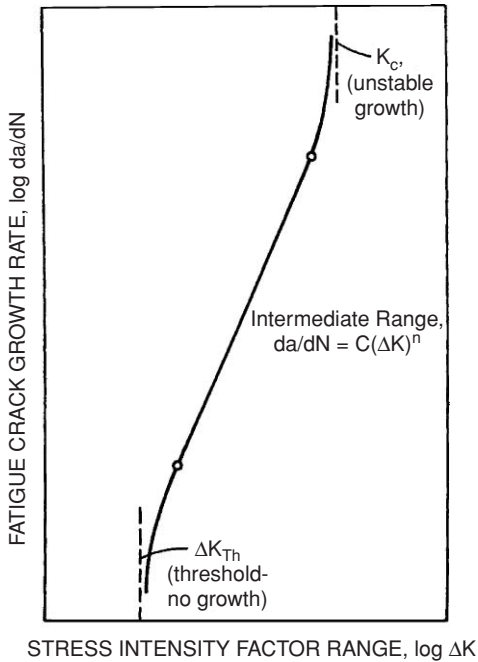values) are never negative during these tests ($R > 0$). During the test, increasing

FIGURE 3.12. Schematic curve of fatigue crack-growth rate versus applied K, illustrating the three stages of crack-growth rates.

crack extension results in ever-increasing stress intensity at the crack tip; thus, one obtains crack-growth rates as a function of ΔK during each test.

Plots of log da/dN versus log ΔK have three stages, as depicted in Figure 3.12. At low ΔK and da/dN levels, a ΔK threshold value is reached, below which there is no detectable crack growth during fatigue cycling. At intermediate values of each variable is the *Paris range*, where log da/dN is linear with log ΔK and

$$da/dN = C(\Delta K)^n. \tag{3.3}$$

Here, C and n are constants that vary with alloy and test parameters (such as R, the ratio of ΔK_{max} to ΔK_{min}). At higher ΔK values, crack growth is accelerated and ΔK approaches the fracture toughness K_c. These concepts are illustrated in Figure 3.12.

Fatigue crack-growth rates at 4 K of a number of structural alloys are presented in Figure 3.13. Note that the very brittle (at 4 K) Fe–9Ni alloy has much higher fatigue crack-growth rates than the other structural alloys. In Figure 3.13, the "normalized" values of $\Delta K/E$, plotted versus da/dN, are also included. Similar to the case of K_{Ic}/E versus σ, plotting 4 K data in this manner results in much smaller variability for a large range of different structural alloys. The da/dN is virtually independent of temperature (over the range 4 to 300 K) for austenitic steels (see Figure 3.14 for the temperature dependence of 316LN); this is likely true for most face-centered cubic metals and alloys.
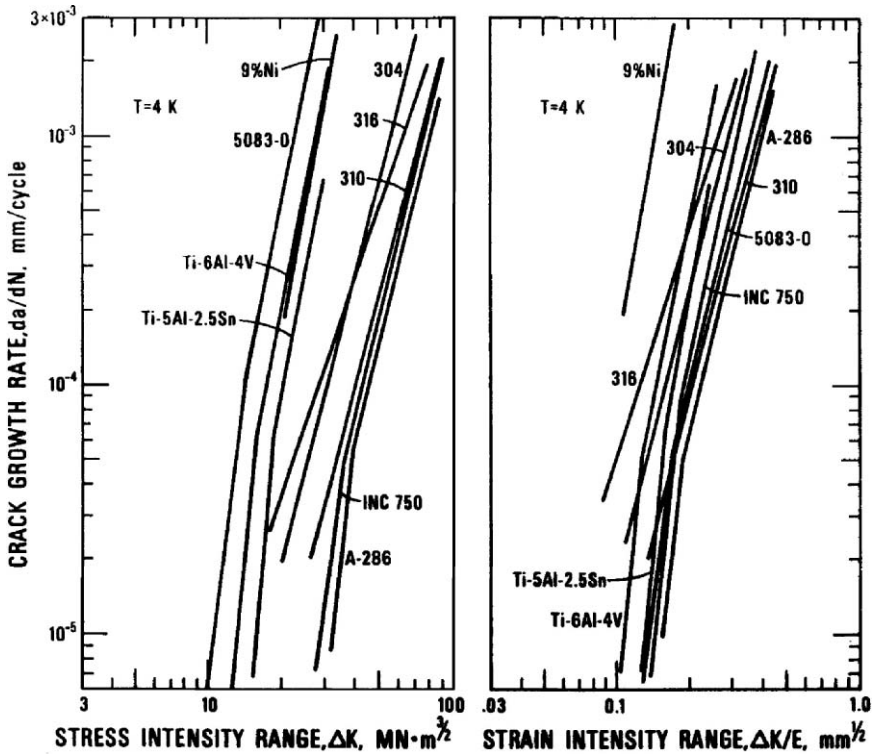
FIGURE 3.13. Fatigue crack-growth rates for austenitic steels (304, 316, 310, A-286), titanium alloys, an aluminum alloy (5083-0), an age-hardened nickel alloy (INC 750), and a ferritic steel (9% Ni) as a function of applied ΔK and "normalized" $\Delta K/E$.

Equation (3.3) is used to estimate the length of crack growth with prior knowledge of the initial stress intensity (from crack configuration and cyclic applied stress), initial flaw size (from NDI), and desired operating lifetime. Typically, estimates of the initial flaw size are derived from estimates of the minimum measurable size from ultrasonic inspection. Flaws may safely grow under fatigue conditions (subcritical crack growth) until the critical flaw size (determined from fracture toughness tests and described earlier) is reached; at that time catastrophic failure will occur. Safety factors of at least two are employed in the design criteria to account for measurement imprecision and material variability.

3.3.2 Austenitic Steel Advancements

Austenitic steels have been selected almost exclusively as the structural material for restraining the magnetic forces of superconducting magnets. Their excellent toughness and relatively high strength, combined with high elastic modulus, low

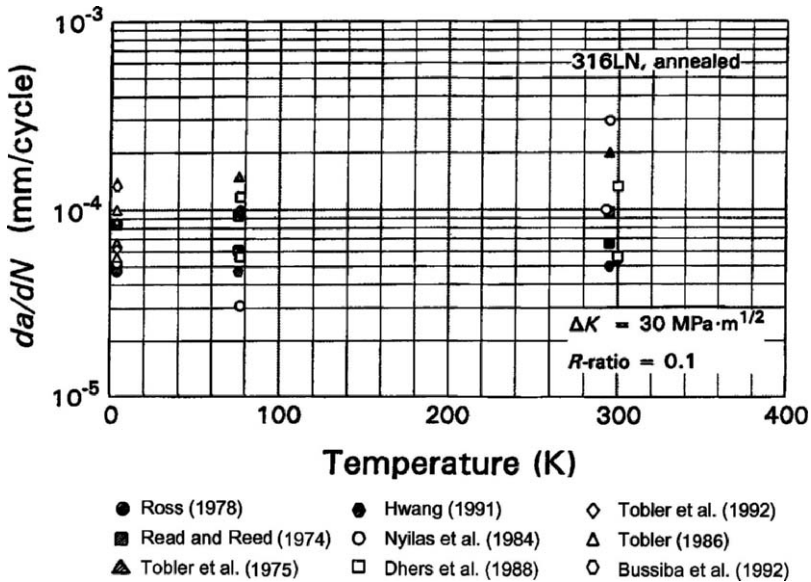FIGURE 3.14. A compilation of the measured temperature dependence of da/dN for austenitic steel AISI 316LN at a constant ΔK of 30 MPa m$^{1/2}$ and R ratio of 0.1.

magnetic permeability, low thermal and electrical conductivities, and relative ease of welding, have led to their selection for many cryogenic applications. On the basis of the emphasis placed on the use of austenitic steels for the principal structural alloy for the case and, perhaps conduit, for the International Thermonuclear Experimental Reactor (ITER), a tremendous amount of research on this alloy class has been conducted over the past 20 years. This effort includes development of an entirely new set of commercial-grade, high-nitrogen austenitic steels in Japan. Development of these steels followed realization, through research in the US (NIST: Tobler, Read, Reed, Simon, Walsh) and Japan (Japanese Atomic Energy Research Institute (JAERI): Shimamoto, Yoshida, Nakajima; Nippon; Kobe; Japanese Steel Works; and Kawasaki steel companies) that adding nitrogen, relatively inexpensively, to base-300-series stainless steels resulted in substantial increases of the tensile yield strength at 4 K. Primarily strength, toughness, and fatigue mechanical properties and contraction and conductivity thermal properties have been measured. The effects of thickness, orientation with respect to the rolling direction, metallurgical and processing variables, and test parameters have been studied on this alloy class for 4 K applications. This section briefly reviews selected advances from this research over a number of decades under the subsections of strength, toughness, and alloy development. Over this period of time, a number of reviews that include development, low-temperature properties, welding, and utilization of austenitic steels for cryogenic applications have been published [20–30].

3.3.2.1 Strength

Although it has been known for a long time that nitrogen additions to austenitic steels increases their strength, only in the past 20 years has nitrogen strengthening been used to develop alloys for use at cryogenic temperatures [20]. The addition of nitrogen to the melt of austenitic steels through alloying (such as adding chrome nitride) or through gas (bubbling under positive pressure) is relatively easy and not expensive. The addition of nitrogen increases austenite phase stability, corrosion resistance, and improves strength. Nitrogen occupies interstitial lattice sites in the austenite matrix, and it is especially effective in increasing strength at low temperatures. The temperature dependence of the nitrogen-strengthening effect is quite strong: The addition of 0.1 wt% nitrogen increases the σ_y at room temperature by about 50 MPa, but the same amount of added nitrogen results in an increase in σ_y of about 250 MPa at 4 K—a factor of five difference. Figure 3.15 depicts the dependence of σ_y on nitrogen as a function of temperature [20]. The
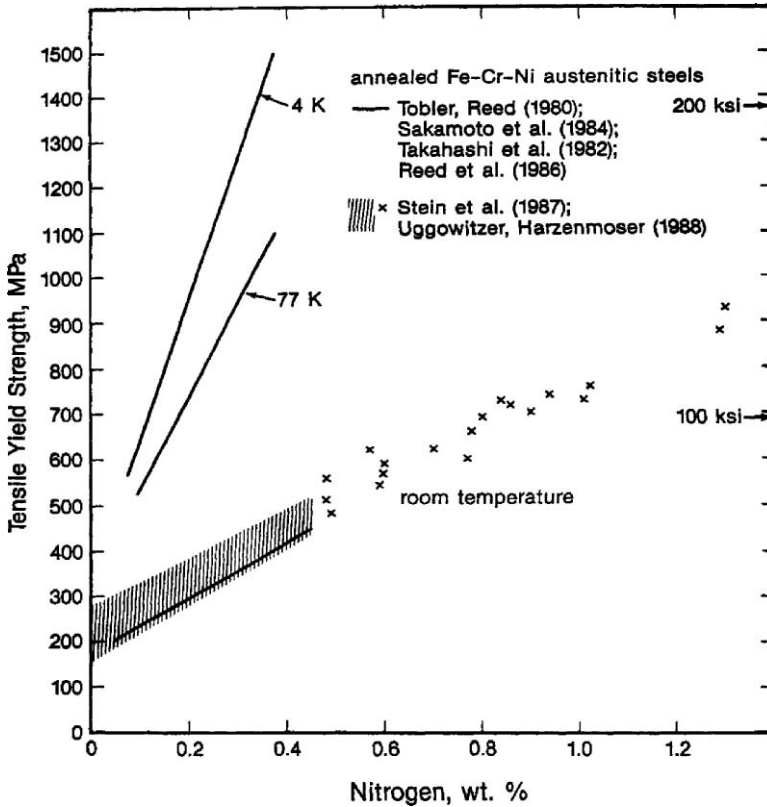

FIGURE 3.15. Dependence of the tensile yield strength on nitrogen content for Fe–Cr–Ni austenitic steels at 295 K, 77 K, and 4 K [31–36].
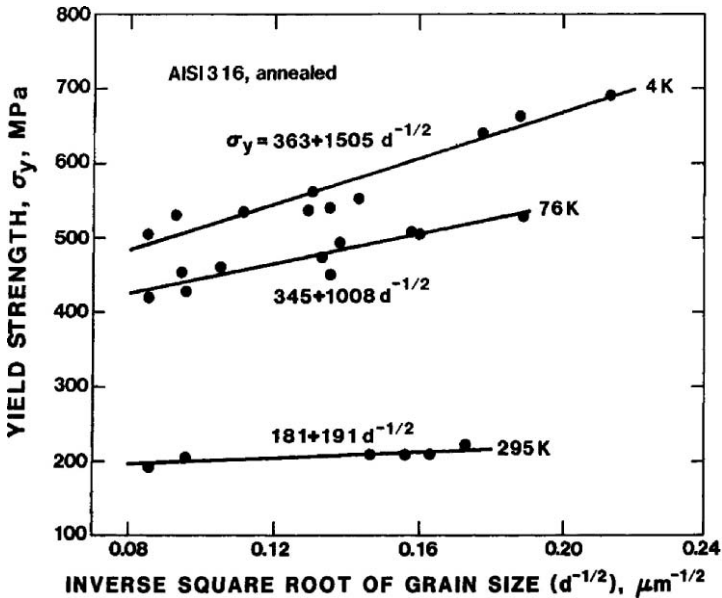
FIGURE 3.16. Dependence of tensile yield strength on grain size in annealed AISI 316 austenitic steel as a function of temperature.

alloys with nitrogen contents above about 0.5 wt% were produced by using special, noncommercial, pressurized nitrogen atmospheres with electroslag-remelting techniques.

The yield strength of an austenitic steel also depends on its grain size. Figure 3.16 illustrates that smaller grain sizes result in stronger alloys and also indicates that this strengthening effect is temperature dependent. At 4 K the dependence of σ_y on grain size is approximately twice that at room temperature. Indeed, grain size variability from 50 to 100 μm in an austenitic steel plate results in variations of σ_y of ±100 MPa. In Figure 3.16, a Hall–Petch relationship is assumed: $\sigma_y = kd^{-1/2}$, where d is the average grain diameter and k is a constant.

The yield strength at 4 K is predictable for AISI 316-type austenitic steels if one uses a linear fit for dependence on [N] content (weight percent) and a Hall–Petch fit ($d^{-1/2}$, where d is in micrometers) for the grain size dependence:

$$\sigma_y(\text{MPa}) = 430 + 2500[\text{N}] + 740\, d^{-1/2}. \tag{3.4}$$

This relationship was obtained from regression analysis of about 100 NIST tensile measurements at 4 K of AISI 316, 316LN, and 316LHN alloys produced in the US, Japan, and Europe [21]. The standard deviation of the fit to the data is 45 MPa, and the standard deviations of the three coefficients are 20 MPa, 90 MPa, and 116 MPa respectively. The use of Equation (3.4), or similar equations developed for other austenitic steels, enables alloy design to a preselected tensile yield

strength by either variation of the nitrogen content or thermomechanical processing to affect the grain size.

The addition of carbon is not as effective as the addition of nitrogen in increasing austenitic steel strength at 4 K. The contribution from carbon is about half that of nitrogen for equivalent weight percent additions. Additionally, carbon additions decrease the weldability of austenitic steels and increase the tendency toward sensitization (embrittling carbide forms at grain boundaries during cooling through the temperature range from about 300 to 600 °C after welding).

The additions of solid-solution alloying elements, such as molybdenum and manganese, contribute to strength increases at 4 K much less significantly, and properties resulting from these additions have not been clearly characterized. Cold work also increases low-temperature strength, but, again, data are insufficient to provide quantitative detail.

3.3.2.2 Toughness

At low temperatures, the toughness of austenitic steels depends strongly on their strength, nickel content, impurity level, and inclusion spacing.

At NIST, extensive testing of various commercial grades of austenitic steels at 4 K established a clearly linear relationship between decreasing fracture toughness and increasing tensile yield strength (see Figure 3.17). All the strengthening mechanisms described in the previous section contribute to reductions of austenitic steel toughness. Throughout the yield strength range of about 300 MPa to 1500 MPa, the fracture toughness (both linear elastic and J-integral) was found to decrease linearly in 4 K tests from about 350 MPam$^{1/2}$ to 50 MPa m$^{1/2}$ respectively.

The addition of nickel beyond the 8 wt% normally required for most specifications of austenitic steels increases the low-temperature toughness of these steels, as illustrated in Figure 3.18 for an Fe–20Cr–4Mn base alloy with sufficient nickel additions to ensure austenite stability. Nickel additions also increase the stacking-fault energy. Thus, in alloys of higher nickel content, one expects less deformation-induced martensitic transformation products (from increased nickel stability and stacking-fault energy) and less deformation twinning (from increased stacking-fault energy).

Cracks initiate primarily at inclusion sites in ductile austenitic alloys. Alloys that contain fewer or smaller inclusions, usually referred to as *cleaner steels*, exhibit higher toughness at low temperatures. The reduction of impurity content contributes to cleaner steels. A number of mills, at added cost, can process austenitic steels by using electroslag remelting (ESR); this process results in considerably cleaner steels. Current specialized melting practices, such as ESR, result in phosphorus and sulfur levels below about 0.015 wt% and 0.005 wt%, respectively, which is a significant improvement over conventional practices that result in weight % ranges of 0.020 to 0.045 for these impurities. Quantitative correlations between increasing inclusion content and decreasing fracture toughness have been
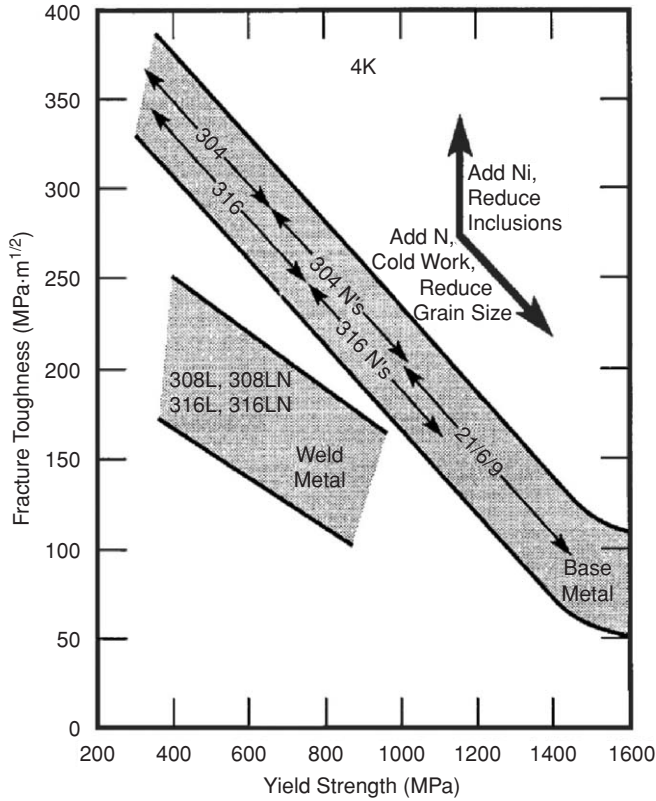
FIGURE 3.17. Trends of the dependence of fracture toughness on tensile yield strength at 4 K of austenitic steels as influenced by variations of cold work, grain size, nickel content, inclusions, and welding.

determined for austenitic steel welds. Estimates for 316LN base metals at 4 K were determined by the ITER project [29]:

$\sigma_y = 1080$ MPa   inclusion spacing $= 0.06$ mm $K_{Ic} = 160$ MPa m$^{1/2}$
$\sigma = 1080$ MPa   inclusion spacing $= 0.14$ mm $K_{Ic} = 350$ MPa m$^{1/2}$
$\sigma = 930$ MPa   inclusion spacing $= 0.06$ mm $K_{Ic} = 210$ MPa m$^{1/2}$
$\sigma_y = 930$ MPa   inclusion spacing $= 0.14$ mm $K_{Ic} = 400$ MPa m$^{1/2}$

Inclusion spacings larger than 0.14 mm are found in high-purity ESR-treated material. Weld-metal inclusion spacings are typically less than 0.10 mm.

In Figure 3.17, note that the fracture toughness of stainless steel welds is lower than that of the base metals at 4 K for equivalent yield strength. Usually this difference is due to the larger size and amount of inclusions within the welds, although, in some cases, ferrite is present, and premature cracking in this phase leads to degradation of weld toughness.

FIGURE 3.18. Dependence of fracture toughness at 4 K for two austenitic steels as a function of nickel content.
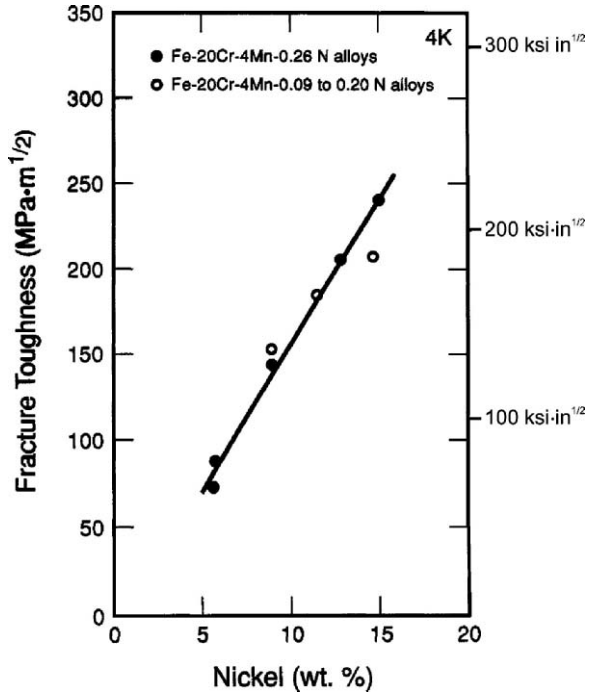
3.3.2.3 Alloy Development

A number of improved austenitic steel alloys were developed in Japan during the early 1980s. At that time, the JAERI encouraged the Japanese steel companies to develop extremely strong and tough austenitic steels by establishing design objectives for structural alloys to be used in high-field superconducting magnets of the ITER project [30]. After taking into consideration high magnetic forces and the ability to inspect austenitic steels and then adopting fracture mechanics principles to establish a sound fracture control plan, JAERI arrived at the alloy re-search objectives of 200 MPa m$^{1/2}$ fracture toughness and 1200 MPa tensile yield strength at 4 K. Since construction of these objectives produces two sides of a box on toughness–yield strength plots (see Figure 3.17), these guidelines were termed the *JAERI box*. As Figure 3.17 shows, these guidelines were considerably above the tensile and toughness properties of commercial-grade steels at the beginning of the 1980s. The Japanese steel industry (Nippon, Kobe, Kawasaki, Japanese Steel Works) chose to use both Fe–Cr–Ni and Fe–Cr–Mn alloys to develop six or seven new austenitic steels whose strength and toughness at 4 K were suffi-cient to be placed within the JAERI box. Better manufacturing practices (vacuum-induction melting, ESR, vacuum oxygen decarburization, submerged-arc refining, rapid cooling after hot rolling), use of higher purity alloying (e.g. electrolytic-grade manganese) and alloy additions (nickel and, in some cases, chromium) to improve

toughness; nitrogen to improve strength; and manganese and chromium to increase the nitrogen solubility range) were employed. Impurities were maintained at very low levels: less than 0.005 wt% sulfur, usually less than 0.015 wt% phosphorus, and minimal oxygen. Use of large-capacity hot-rolling mills led to smaller, more uniform grain sizes. This consistently small grain size, combined with hot work, also improved the yield strength of these alloys at 4 K.

3.3.3 Nonmetallic Composite Electrical Insulation

Considerable improvements and characterization of existing nonmetallic composites and development of new composites for use as electrical insulation at low temperatures have taken place over the last few decades. In particular, glass-fiber-reinforced epoxy-resin matrix composites have been rather thoroughly studied. Applications have focused primarily on turn, layer, and ground insulation and on matrix bonding of superconducting coils. Many have made strong contributions: Okada and Nishijima (Osaka University) in Japan; Evans (Rutherford Laboratories) and Broadbent (Oxford Instruments) in England; Rey (CEA/Saclay) in France; Weber (Atominstitut der Österreichischen Universitäten) in Austria; and Kasen, Schramm, and Simon (NIST), Fabian, Munshi, Rice, and Schutz (Composite Technology Development, Inc.), Benzinger (Spaulding Fiber, Inc.), and Reed (Cryogenic Materials, Inc.) in the US.

Other research on composites has been directed toward low-temperature, thermal–mechanical support structures, such as straps and struts (tubes, cylinders). Adequate reviews of developments and properties for thermal–mechanical supports have been presented previously [37,38]. This presentation is limited to applications for superconducting coils.

Three general types of composites are prepared by different fabrication schemes for use as electrical insulation of superconducting coils. The fabrication techniques are high-pressure lamination (HPL), resin preimpregnation (usually called *prepreg* (PP)), and resin-transfer molding (commonly called *vacuum-pressure impregnation* (VPI) by the superconducting-coil community). Properties and characteristics of composites fabricated by these three techniques are compared in Table 3.2. Recent advances in each of these areas are presented in the following subsections. Advances in the development of new resins, in new test techniques, and in radiation testing and analysis are also discussed.

3.3.3.1 High-Pressure Laminates

For many years, the composite laminates used in plate or block form in superconducting coils for fill within spaces, as buffer zones, to brace incoming or outward going leads, and for ground or layer insulation have been the National Electrical Manufacturers Association (NEMA) grades G-10 and G-11. These grades are composed of E-glass fibers and bonded within a matrix of epoxy resin. However, as the sophistication of superconducting coil design increased, so did the need to know more precise mechanical, thermal, and electrical properties at the operating

TABLE 3.2. Typical properties at 4 K and characteristics of glass–epoxy composites used in superconducting coils (50 vol.% glass content)

	Type of composite		
Property	HPL (G-10CR)	PP (TGDM–glass–Kapton)	VPI (epoxy–glass)
Density (g/cm^3)	1.8	1.8	1.8
Young's modulus (GPa)			
in plane	35	22	22
through thickness	22		
Shear modulus (GPa)			
interlaminar	9.0	4.4	7.6
Shear strength (MPa)			
interlaminar	80	40	70
Compressive strength (MPa)			
through thickness	800	800	800
Thermal contraction 295 K → 4 K (%)			
in plane	0.24	0.20	0.20
through thickness	0.72	0.70	0.73
Thermal conductivity [W/(m K)]			
through thickness (4 K/300 K)	0.030/0.55	0.064/0.47	0.062/0.50
Inspection	Complete visual Detailed electrical	Complete visual Detailed electrical	No visual General electrical
Repair	Complete exchange of parts	Defect cut/grind followed by replacement PP	Not possible
Manufacture	Independent of coil fabrication	Wrap around conduit/conductor	On line
	Industrial laminate	Off line Under pressure, cure at 150–300 °C	Final stage Complete coil resin cure at 110–150 °C

temperature of 4 K. It was discovered that the NEMA specifications for G-10 and G-11 were astoundingly broad. Various types of E-glass cloth weaves could be used; the volume fraction of glass varied more than 25%; many different resin systems could be used with or without fillers (SiO_2, Al_2O_3); the pressure and temperatures for the high-pressure laminate cure were not specified; and the maximum porosity was not specified. Whereas these broad specifications, primarily electrical, had been sufficient for most uses at room temperature, they resulted in very large property variations at cryogenic temperatures. With this incentive, Kasen (NIST), working primarily with Benzinger (Spaulding) and the NEMA committees, was successful in developing two specialized grades of high-pressure laminates that had much narrower specifications: NEMA grades G-10CR and G-11CR. They were developed in the late 1970s, and their low-temperature mechanical, thermal, and electrical properties were thoroughly characterized [39,40].

The NEMA grades G10-CR and G11-CR are produced under high pressure (about 7 MPa). Consequently, their void content is very low and their glass content is relatively high (55 to 65 vol.%). Thus, their mechanical and electrical properties tend to be quite good. The laminate grades can be procured in various shapes (plates and cylinders) and sizes (as thick as 10 cm), and other forms can be obtained by cutting and/or grinding. Recently, however, it has not been possible to obtain G11-CR in other than complete mill runs, owing to lack of demand for this grade.

3.3.3.2 Pre-impregnation

The use of pre-impregnation of glass cloth with resin that assumes a very viscous, sticky (B-stage) composure, called *prepreg*, had limited use for the insulation of superconducting coils. However, for the ITER central solenoid model coils (one each was constructed in the US and in Japan) in which the react, then wind coil-fabrication sequence was employed, the turn insulation around the conduit was fabricated by using composite prepreg technology [41]. With this procedure after the Nb_3Sn reaction, the pre-impregnated cloth in tape form is cowound with Kapton tape around the conduit. It is then cured and inspected prior to winding the insulated conduit onto the coil mandrel. The resin-cure cycle is performed under pressure (expandable silicone rubber sleeves may be used) at slightly elevated temperatures (about 150 to 300 °C). Advantages of this fabrication technique include: (1) use of Kapton film for an electrical barrier that does not impede the flow or placement of resin is an option; (2) complete visual and electrical inspection is possible; (3) repair procedures are relatively easy and not space restricted if local areas of the prepreg composite sheath do not meet the inspection criteria; (4) more radiation-resistant resin systems than the low-viscosity resins required for the VPI process can be used when needed; (5) the pressure cure ensures a better bond between the turn insulation and conduit; and (6) the pressure cure in combination with the independent strength and orientation of each turn of the precured prepreg composite (with or without Kapton) acts to preclude failure of the turn insulation system and to limit debonding from the conduit when tensile forces are generated between the turn insulation and conduit of the coil during cool-down or operation. Balanced against these many positive factors are the relative novelty of this process in the superconducting coil community, the costs that are added to procure special orders of prepreg tape, and the time and costs for setup and pressure-curing at elevated temperatures of the prepreg resin system after winding around the conduit. Also, the use of epoxy-based prepreg turn insulation precludes the wind-and-react fabrication coil procedure.

3.3.3.3 Resin-Transfer Molding (Vacuum-Pressure Impregnation)

The last step in the fabrication of superconducting coils is the transfer of resin into the coil form to bond all turns into a monolithic structure. The three, fundamentally different approaches to this resin-transfer process are (1) flood filling, (2) partially sealed tool, and (3) sealed tool. In the flood-filling technique, the coil is placed within a containment vessel, and this system is placed within a vacuum chamber. After evacuation, resin is pumped or poured into the containment vessel. This

most simple system has been used for some of the coils in the CERN Atlas program and in increasing applications of magnetic resonance imaging (MRI), where routine coil fabrication of many similar coils is required. In the partially sealed tool technique, the coil is placed within a resin-tight (but not vacuum-tight) tool assembly that is then positioned in a vacuum chamber. Resin is transferred into the tool assembly after evacuation. The sealed-tool technique consists of vacuum- and resin-tight tooling surrounding the coil. Resin is transferred into the tooling following evacuation. Traditionally, this technique has been used on one-of-a-kind coils and on most large-scale coils.

A detailed report [42] of the very large-scale VPI process for the US ITER central solenoid model coil (about 2.7 m in diameter and about 2.84 m high) includes resin data, laboratory resin-flow research and trial runs, resin-injection equipment, large-scale trial runs, model-coil tooling and temperature and pressure control, and input data during the transfer of 1400 L (370 gal) of resin into the coil. To assist resin flow for the VPI process and to provide strength, glass-cloth tape is wound around each conduit or conductor prior to assembly into coil form. The resin plus glass cloth form a glass–epoxy composite whose strength depends on the volume fraction of glass, the amount of porosity within the cured resin, temperature, radiation, and orientation of the applied stress relative to the orientation of the glass-cloth layers. Interlaminar shear strengths (with cracks running only through the matrix resin) are always lower than in-plane tensile or compressive strengths. During the past 20 years, the effects of many of the variables listed above on the orientation-dependent strengths of glass–epoxy composites have been investigated. The influence of radiation (so important for potential superconducting magnets for fusion and high-energy physics) on VPI composite mechanical properties at low temperatures has been examined. In most superconducting coils that are exposed to large radiation doses (especially neutron), the glass–epoxy composite formed by the VPI process has been considered the weak mechanical link in the complex superconducting coil structure.

Unfortunately, use of the VPI-produced composite structure as an integral electrical insulation system presents problems:

- The setup and process is time consuming, expensive, and very detailed to prevent vacuum and resin leaks and to ensure complete resin flow throughout the coil.
- The resulting glass–epoxy composite insulation cannot be inspected, and internal defects are not repairable.

During the resin impregnation process, the flow of the resin throughout the entire coil, usually from the resin inlet at the coil bottom to the outlet(s) at the top of the coil, may be irregular and follow the path of least resistance. This may result in areas void of resin within the coil. Sometimes, these voids cannot be seen from the surface of the coil. Even if they are observed, they are seen only after resin cure and removal of the coil tooling. Thus, the builder is faced with the dreaded decision of either accepting the flawed coil or starting the fabrication process all over again. Intuitively, design of one-of-a-kind, noncommercial coils should strive for the independent mechanical and electrical integrity of the turn, layer, and ground insulation through the use of high-pressure laminates and prepreg composites.

3.3.3.4 Test Techniques

Glass fibers act to both stiffen and strengthen glass–resin composites. They stiffen because their elastic moduli are considerably higher than the resin. They strengthen because the fibers act as crack arrestors: cracks prefer to grow through the resin matrix, not through layers of glass cloth. Thus, crack propagation under inter-laminar shear always is rather easy, as there are no glass layers along this path to impede crack growth. This results in relatively low values of the interlaminar shear strength. However, the interlaminar shear strength depends on the associated normal stress, whether that be in compression or tension. In superconducting coils, cool-down and magnetic forces produce both interlaminar shear and, usually, normal compressive forces on the glass plies of the turn insulation. A new test was developed to measure the "shear/compression" strength of composites [43]. This test enables variation of the ratio of applied interlaminar shear to normal compressive stresses on composite or bonded specimens at any desired temperature (see Figure 3.19 for specimen and loading details). A plot of shear/compression properties for a VPI E-glass cloth–epoxy composite is shown in Figure 3.20. Fatigue tests can also be conveniently conducted with this measurement procedure. In Figure 3.20 note that the fatigue strengths at 10^5 and 10^6 cycles at 76 K are included. From the figure, static and fatigue strengths can be easily compared and design envelopes with appropriate safety factors obtained.

This shear/compression test has been used during the past 15 years to quantify the applicable properties of various proposed insulation systems and to assess the radiation sensitivity of resin systems. They may also be used to provide quantitative design criteria to establish maximum allowable shear/compression operation stress levels.
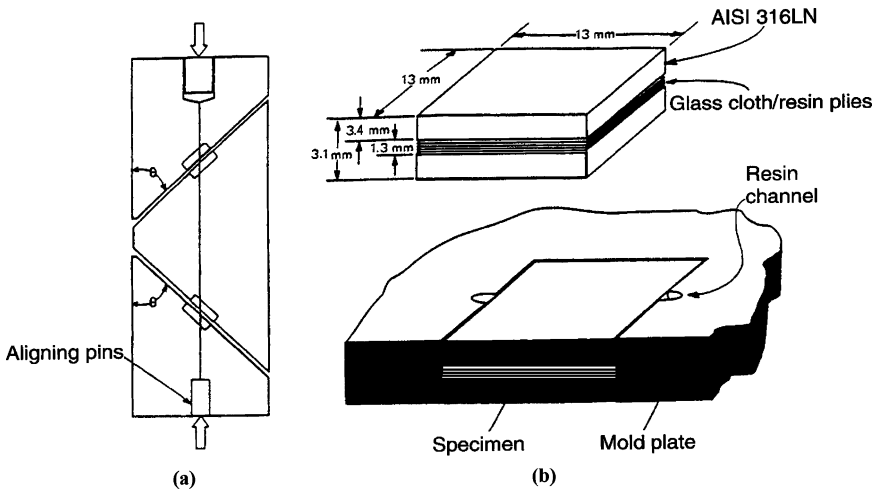

FIGURE 3.19. (a) Schematic of test fixture and specimens used to load two composite insulation specimens in shear and compression. (b) Specimen configuration (later specimens were circular in shape) and mold used to fabricate specimens using either the VPI or PP process.
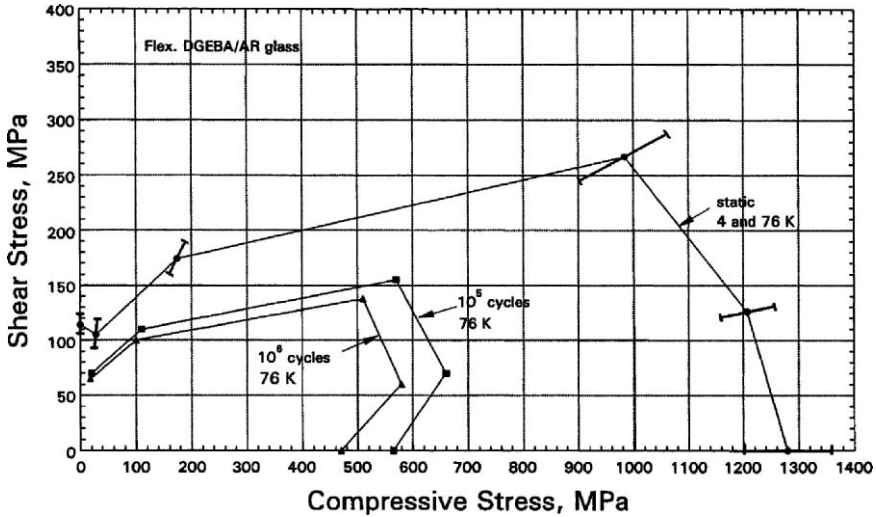
FIGURE 3.20. Combined shear and compressive stress to cause failure of VPI fabricated epoxy as-received (AR) S-glass specimens with about 50 vol.% glass under static loading (4 K and 76 K) and after 10^5 and 10^6 fatigue cycles at 76 K for various loading angles (ratio of shear to compressive stress).

During this time period, the dramatically increased computer capabilities have led to more precise and comprehensive finite-element stress analyses for super-conducting coil insulation systems. These analyses have been assisted by mea-surements of some of the nine elastic constants for the orthotropic fiber-reinforced composites. Unlike isotropic metals, along the three major axes of fiber-reinforced composites (warp, fill, through-thickness for glass-cloth reinforcement), both ten-sile/compression and shear elastic constants and the associated Poisson's ratio are all distinct. Even now, additional ultrasonic or resonance measurements at low tem-peratures could increase the accuracy of these constants and indicate their variabil-ity with glass content and processing pressure. However, the inclusion of detailed stress analyses combined with improved compression and shear-strength measure-ment techniques has led to the inclusion of mechanical properties in the design criteria for composite electrical insulation for large superconducting coil projects.

3.3.3.5 Radiation: Resins and Coatings

Most applications for superconducting coils in the recent past have been for MRI medical equipment; large, high-energy physics facilities; and fusion plasma con-tainment (ITER). In the latter two applications, coils must operate in a radiation environment. Nonmetallic composite matrix resins are usually the most radiation-sensitive component within these coils. Consequently, there have been a number of studies to characterize the more sensitive mechanical properties at 4 K to radiation dose or neutron fluence. Associated with these studies has been the introduction of new resin and insulation systems that are more radiation resistant. Leaders in

the development of these potentially better systems have been Evans, formerly of Rutherford–Appleton Laboratories in England, Composite Technology Development, Inc. in the US, and Nishijima and Okada of Osaka University in Japan (JA).

Some of the resin systems that have recently been used in large-scale magnets projects are[1]

DBEBA/anhydride epoxy	CERN Atlas	VPI
	JA (central solenoid coil)	VPI
	EU (toroidal field coil)	VPI
DGEBF–anhydride	US (central solenoid coil)	VPI
DGEBF–DETD–PPGDGE	CERN Atlas	VPI
TGDM–aromatic amine	US (central solenoid coil)	PP (turn insulation)

Other systems have been developed and proposed for use in superconducting coils that are exposed to very large radiation doses ($>5 \times 10^7$ Gy) [44–48]:

cyanate ester	VPI
cyanate ester–polyimide	VPI, HPL
cyanate ester–epoxy	VPI, HPL
ceramic	PP, coating
ceramic–epoxy	VPI

The cyanate ester systems are more radiation resistant than the epoxy systems listed earlier, but, unfortunately, they are quite a bit more expensive. Cyanate ester–epoxy or polyimide blends have been proposed to reduce the added costs somewhat. Utilization of ceramic prepreg or coating, wound around or applied to the conductor, enables the use of the wind, then react, coil-fabrication procedure. The ceramic prepreg, after curing to a green state at around 150 °C, will solidify and withstand the Nb_3Sn reaction heat treatment of 600 to 700 °C for about 240 h. Research has also been directed toward application of a ceramic coating directly on the conductor and to anodization, if the conductor is aluminum; both of these possibilities enable the use of the wind, then react, coil-fabrication sequence.

After radiation at low temperatures and warming to room temperature H_2, CO, and CO_2 gases are formed in epoxy resin systems. Some of the gas molecules diffuse and escape from the composite surface, especially the smaller H_2 molecules. Typical gas evolution rates of about $1.2 \, cm^3/g \cdot MGy$ have been measured for epoxy resin systems; the evolved gas is primarily hydrogen [49]. This evolved hydrogen gas must be considered a safety issue during coil warm-up.

Some of the gases, mostly the larger CO and CO_2 molecules that have more trouble diffusing through the matrix, remain trapped within the composite and contribute to internal swelling. Swelling as much as 5 to 6% in the through-thickness direction of glass–epoxy composites has been reported for dose levels of 5×10^7 Gy [50]. Similar measurements along in-plane directions revealed no

---

[1] DBEBA: diglycidyl ether of bisphenol-A; DGEBF: diglycidyl ether of bisphenol-F; DETD: diethyl toluene diamine; PPGDGE: polypropylene glycol diglycidyl ether; TGDM: tetraglycidyl diaminodiphenyl methane.

evidence of swelling. Quite obviously, the presence of swelling would contribute to increased compressive stress in the through-thickness direction of the insulation systems.

When conducting tests to assess the radiation sensitivity of various matrix resin systems within glass–resin composites, it is very important that the test be designed so that the crack path proceeds within the resin system and does not have to intersect layers of glass cloth, for it is the resin that is sensitive to radiation; glass remains insensitive at radiation levels normally contemplated for use in superconducting coils. Interlaminar shear testing results in crack initiation in the resin system and growth within the resin layers bounded by the laminar glass cloth. All other compression and shear tests result in crack-growth intersection with glass-cloth layers. Many such cryogenic tests have been reported in the literature.

3.3.4 Superconductors

Rapidly following the identification of the presence of high-temperature superconductivity in the Ba–La–Cu–O alloy system by Bednorz and Muller [51], reported in 1986, Y–Ba–C–O superconductors with T_c values slightly above 90 K were discovered. This stimulated research in four new areas: (1) the search for even higher T_c superconductors; (2) the characterization of these new high-T_c superconductors; (3) optimized processing and chemistry of the new superconductors; and (4) applications incorporating the use of these new superconductors.

The obvious potential for practical applications of high-T_c superconductivity has produced a rapid acceleration in research on this topic and, since at many agencies total research is a "zero-sum game," the new focus may have been responsible for corresponding decreases in research on other aspects of cryogenic materials (see Figure 3.4 for comparisons). The very significant advances from research on low- and high-T_c superconductors are not detailed here.

3.3.5 Other Advances

Other areas of cryogenic materials research over the same time period that, perhaps, should have been included in this review are listed here.

For ITER, the US conduit structural alloy Incoloy 908 (an age-hardened, nickel-based alloy) was developed at MIT and International Nickel Co. [52]. It has the desirable traits of matching thermal contraction to the conductor and excellent low-temperature strength, toughness, and stiffness. The alloy suffered from possible stress-accelerated oxide precipitation at the grain boundaries during the Nb_3Sn reaction treatment; considerable research was performed to minimize the effects of this trait.

The mechanical properties of the new Al–Li alloy series and its welds at low temperatures for aerospace use were extensively studied [53]. These alloys are stronger than the industry standard, i.e., 2219-T87, and their toughness is good in certain orientations. However, the grain structure of the commercial alloys is very laminated and, consequently, they tend to delaminate when tested in certain orientations.

Composites for use as structural reinforcement for cryogenic tankage or for thermal–mechanical strap or strut supports have also been studied at low temperatures [54]. For these applications, the composite-fabrication technique is usually filament winding. With filament winding, fiber tows can be oriented as desired under winding tension (to ensure straightness). Carbon, boron, S- and E-glass, and alumina fiber–epoxy matrix composites have been tested for their low-temperature properties.

3.4 General Discussion

Over the time frame considered, materials research at low temperatures has increased, but there are signs that the effort has leveled off during the past 10 years. Within this time span, superconductor R&D has steadily increased, but structural material and insulation-oriented R&D has correspondingly declined. The discovery of higher T_c superconductivity in 1986 provided the spark for increased interest in superconductors. During this time frame, the low-temperature strength and toughness of structural alloys have been improved sufficiently to meet the current needs for cryogenic applications. Research on electrical and thermal insulators has also achieved an adequate status quo, with available materials and properties to meet most application needs. There are many exceptions to these very general statements: electrical insulation materials for superconducting coils are very sensitive to radiation requirements and to coil fabrication conditions and sequence; conduit alloys for large-scale coils, such as ITER, require further R&D to justify their selection and use. Research related to space propulsion and vehicles has experienced a relative dearth of activity over the past 30 years, and R&D on thermal insulation, superconductivity, structural alloys and composites, as well as fracture control, would likely prove very productive for materials used in advanced space structures.

But, when one looks back, it is clear that the cryogenic materials community has come a long way. Reliable fracture control practices are usually in place for critical cryogenic structures. The structural alloys (austenitic steels, aluminum alloys, Fe–Ni alloys, age-hardened nickel-base alloys, and titanium alloys) are well characterized, and much experience has been gained in the joining of these alloys and in their use. We now know the important properties of most composites at cryogenic temperatures, and many glass fiber–epoxy and some carbon fiber–epoxy composites are now in use at low temperatures. Early work on thermal insulation and later R&D of electrical insulation has led to a large body of low-temperature data for these materials.

References

1. *Advances in Cryogenic Engineering (Materials)*, Vols. 22–46 (even numbers only), Plenum Press, New York, 1977–2000; vols. 48, 50, American Institute of Physics, New York, 2002, 2004.

2. Hertzberg, R.W., *Deformation and Fracture Mechanics of Engineering Materials*, John Wiley, New York, 1989.
3. Dieter, G.C., *Mechanical Metallurgy*, McGraw-Hill, New York, 1986.
4. Tada, H., Paris, P.C., and Irvin, G.R., *The Stress Analysis of Cracks Handbook*, Del Research, Hellertown, PA, 1973.
5. Shi, G.C.M., *Handbook of Stress Intensity Factors,* Lehigh University, Bethlehem, PA, 1973.
6. Murakami, Y., ed., *Stress Intensity Factors Handbook*, Pergamon Press, Oxford, 1987.
7. "Standard Test Method for Plain-Strain Fracture Toughness of Metallic Materials," Section 3, *Annual Book of ASTM Standards*, E399-90, American Society for Testing and Materials, Philadelphia, PA, 1993.
8. "Standard Test Method for $J_{Ic,}$ A Measure of Fracture Toughness," *Annual Book of ASTM Standards*, E813-89, American Society for Testing and Materials, Philadelphia, PA, 1993.
9. "Pressure Vessels," Section VIII *ASME Boiler and Pressure Vessel Code*, American Society of Mechanical Engineers, New York, 1998.
10. "Standard Test Method for Measurement of Fatigue Crack Growth Rates," *Annual Book of ASTM Standards*, American Society for Testing and Materials, Philadelphia, PA, 1993.
11. Ross, J., "Superconducting A.C. Generators Trial Rotor Forging Investigation," IRD/TM 78-47, EED/AP62/TM-174, International Research and Development Company, Ltd., Newcastle upon Tyne, England, 1978.
12. Hwang, I., "Mechanical Properties of Alcator C-MOD Superstructure Materials, Department of Materials Science and Engineering, Massachusetts Institute of Technology, Cambridge, Massachusetts, 1991.
13. Tobler, R., Berger, J., and Bussiba, A. "Long Crack Fatigue Thresholds and Short Crack Simulation at Liquid Helium Temperatures," *Advances in Cryogenic Engineering (Materials)*, Vol. 38, 1992, pp. 159–166.
14. Read, D., and Reed, R., "Fracture and Strength Properties of Selected Austenitic Stainless Steels at Cryogenic Temperatures," *Materials Studies for Magnetic Fusion Energy Applications at Low Temperatures—II*, NBSIR 79-1609, National Bureau of Standards, Boulder, Colorado, 1979, pp. 79–122.
15. Nyilas, A., Krauth, H., Metzner, M., and Munz, D., *Proc. Fatigue 84*, Second International Conference on Fatigue and Fatigue Thresholds (Birmingham, Alabama), Institut für Technische Physik, Kernforschungszentrum Karlsruhe, Germany, 1984, p. 1637.
16. Tobler, R., "Near-Threshold Fatigue Crack Growth Behavior of AISI 316 Stainless Steel," *Advances in Cryogenic Engineering (Materials)*, Vol. 32, 1986, pp. 321–328.
17. Tobler, R., and Reed, R., "Fatigue Crack Growth Rates of Structural Alloys at Four Kelvin," *NBS–ARPA Materials Research for Superconducting Machinery III*, Semi-Annual Technical Report September 1, 1974–March 1, 1975, National Bureau of Standards, Boulder, Colorado, 1975, pp. 87–104.
18. Dhers, J., Foct, J., and Vogt, J., "Influences of Nitrogen Content on Fatigue Crack Growth Rate at 77 K and 293 K of a 316L Steel," *Proc. HNS-88* (Lille, France), Institute of Metals, London, 1989, pp. 199–203.
19. Bussiba, A., Tobler, R., and Berger, J., "Superconductor Conduits, Fatigue Crack Growth Rate, and Near-Threshold Behavior of Three Alloys," *Advances in Cryogenic Engineering (Materials),* Vol. 38, 1992, pp. 167–174.
20. Reed, R., "Nitrogen in Austenitic Stainless Steels," *J. Met.* 41, 16–21, 1989.

21. Reed, R., and Simon, N., "Design of 316LN-Type Alloys," *Advances in Cryogenic Engineering (Materials)*, Vol. 34, Plenum Press, New York, 1988, pp. 165–173.
22. Reed, R., "Recent Advances in the Development of Cryogenic Steels," in *Supercollider 3*, Nonte, J., ed., Plenum Press, New York, 1991, pp. 91–106.
23. Reed, R., "Austenitic Stainless Steels with Emphasis on Strength at Low Temperatures," *Alloying*, ASM International, Materials Park, OH, 1988, pp. 225–256.
24. Reed, R., Purtscher, P., and Delgado, L., "Low-Temperature Properties of High-Manganese Steels," *High Manganese Austenitic Steels*, Lula, R., ed., ASM International, Materials Park, OH, 1988, pp. 13–21.
25. Morris, J., and Hwang, S., "Fe–Mn Alloys for Cryogenic Use: A Brief Survey of Current Research," *Advances in Cryogenic Engineering (Materials)*, Vol. 24, Plenum Press, New York, 1978, pp. 82–90.
26. Morris, J., "Structural Alloys for High Field Superconducting Magnets," *Advances in Cryogenic Engineering (Materials)*, Vol. 32, Plenum Press, New York, 1986, pp. 1–22.
27. Horiuchi, T., Ogawa, R., and Shimada, M., "Cryogenic Fe–Mn Austenitic Steels," *Advances in Cryogenic Engineering (Materials)*, Vol. 32, Plenum Press, New York, 1986, pp. 33–42.
28. Reed, R., and Horiuchi, T., eds., *Austenitic Steels at Low Temperatures,* Cryogenic Materials Series, Plenum Press, New York, 1983.
29. Simon, N., Wong, F., and Reed, R., "Metallic Material Mechanical and Thermal Property Database, Annex 1, Metallic Material Specifications for ITER Magnets," ITER EDA, Naka Joint Work Site, JAERI, Naka, Japan, 18 August 1997.
30. Shimamoto, M., Nakajima, N., Yoshida, K., and Tada, E., "Requirements for Structural Alloys for Superconducting Magnet Cases," *Advances in Cryogenic Engineering (Materials)*, Vol. 32, Plenum Press, New York, 1986, pp. 23–32.
31. Tobler, R., and Reed, R., "Interstitial Carbon and Nitrogen Effects on the Tensile and Fracture Parameters of AISI 304 Stainless Steels," *Materials Studies for Magnetic Fusion Energy Applications at Low Temperatures—III*, NBSIR 80-1627, National Bureau of Standards, Boulder, Colorado, 1980, pp. 15–48.
32. Sakamoto, T., Nakagawa, Y., Yamauchi, I., Zaizen, T., Nakajima, H., and Shimamoto, S., "Nitrogen-Containing 25Cr–13Ni Stainless Steel as a Cryogenic Structural Material," *Advances in Cryogenic Engineering (Materials)*, Vol. 30, Plenum Press, New York, 1984, pp. 137–144.
33. Takahashi, Y., Yoshida, K., Shimada, M., Tada, E. Miura, R., and Shimamoto, S., "Mechanical Evaluation of Nitrogen Strengthened Stainless Steels at 4 K," *Advances in Cryogenic Engineering (Materials)*, Vol. 28, Plenum Press, New York, 1982, pp. 73–81.
34. Reed, R., Simon, N., Purtscher, P., and Tobler, R., "Alloy 316LN for Low-Temperature Structures: A Summary of Tensile and Fracture Data," *Materials Studies for Magnetic Fusion Energy Applications at Low Temperatures—IX*, NBSIR 86-3050, National Bureau of Standards, Boulder, Colorado, 1986, pp. 15–26.
35. Stein, G., Menzel, J. and Dörr, H., "Möglichkeiten zur Herstellung von Schmiedestrücken mit hohen Stickstoffgehalten in der Desu-Anlage," *Moderne Stähle, Ergebnisse der Werkstoff-Forschung*, Vol. 1, Schweizerische Akademie der Werkstoffwissenschaften, Zurich, 1987, pp. 181–193.
36. Uggowitzer, P., and Harzenmoser, M., "Strengthening of Austenitic Stainless Steels by Nitrogen," *Proc. HNS–88* (Lille, France), Institute of Metals, London, 1989, pp. 175–179.
37. Reed, R., and Golda, M., "Properties of Cold-to-Warm Support Straps," *Cryogenics* 38, 39–42, 1998.

38. Reed, R., and Golda, M., "Cryogenic Composite Supports: A Review of Strap and Strut Properties," *Cryogenics* 37, 233–250, 1997.
39. Kasen, M., MacDonald, G., Beekman, D., and Schramm, R., "Mechanical, Electrical, and Thermal Characterization of G-10CR and G-11CR Glass-Cloth/Epoxy Laminates between Room Temperature and 4 K," *Advances in Cryogenic Engineering (Materials)*, Vol. 26, Plenum Press, New York, 1980, pp. 235–244.
40. Benzinger, J., "Manufacturing Capabilities of CR-grade Laminates," *Advances in Cryogenic Engineering (Materials)*, Vol. 36, Plenum Press, New York, 1980, pp. 252–258.
41. Reed, R., Fabian, P., and Schutz, J., "Turn Insulation for U.S. CS Model Coil," U.S. ITER Insulation Program for Plasma Science and Fusion Center, Massachusetts Institute of Technology, Cambridge, Massachusetts, 1 March 1998.
42. Reed, R., and Clark, P., "Vacuum Pressure Impregnation of U.S. CS Model Coil," US ITER Insulation Program for Plasma Science and Fusion Center, Massachusetts Institute of Technology, Cambridge, MA, 31 March 1999.
43. Simon, N., Reed, R., and Walsh, R., "Compression and Shear Tests of Vacuum-Impregnated Composites," *Advances in Cryogenic Engineering (Materials)*, Vol. 38A, Plenum Press, New York, 1992, pp. 363–370.
44. Fabian, P., Munshi, N., Feucht, S., Bittner, K., Rohrhofer, X., Huner, K., and Weber, H., "Low Temperature Mechanical Properties of Cyanate Ester Insulation Systems after Irradiation," *Advances in Cryogenic Engineering (Materials)*, Vol. 50A, American Institute of Physics, Mellville, NY, 2004, pp. 289–296.
45. Codell, D., and Fabian, P., "Development of Pre-preg Ceramic Insulation for Superconducting Magnets," *Advances in Cryogenic Engineering (Materials)*, Vol. 50A, American Institute of Physics, Mellville, NY, 2004, pp. 259–265.
46. Puigsegur, A., Rondeaux, F., Prouzet, E., and Samoogabalan, K., "Development of an Innovative Insulation for Nb_3Sn Wind and React Coils," *Advances in Cryogenic Engineering (Materials)*, Vol. 50A, American Institute of Physics, Mellville, NY, 2004, pp. 266–272.
47. Bata, F., Hascicek, Y., Sumption, M., Arda, L., Aslanoglu, Z., Akin, Y., and Collings, E., " A Sol–Gel Approach to the Insulation of Rutherford Cables," *Advances in Cryogenic Engineering (Materials)*, Vol. 50A, American Institute of Physics, Mellville, NY, 2004, pp. 273–280.
48. Zeller, A., "Anodized Insulation for CICC Coils," *Advances in Cryogenic Engineering (Materials)*, Vol. 48A, American Institute of Physics, Melville, NY, 2002, pp. 255–260.
49. Reed, R., Fabian, P., and Schutz, J., "U.S. ITER Insulation Irradiation Program," Final Report to Plasma Fusion Center, Massachusetts Institute of Technology, Cambridge, MA, 31 August 1995.
50. Reed, R., Fabian, P., and Schutz, J., "U.S. ITER Insulation Irradiation Program, Final Report to Plasma Fusion Center, Massachusetts Institute of Technology, Cambridge, Massachusetts, 31 August 1995.
51. Bednorz, J., and Muller, K., "Possible High-T_c Superconductivity in the Ba–La–Cu–O System," *Z. Phys. B*, 64, 189, 1986.
52. Hwang, I., Ballinger, R., Morra, M., and Steeves, M., "Mechanical Properties of Incoloy 908—An Update," *Advances in Cryogenic Engineering (Materials)*, Vol. 38, Plenum Press, New York, 1992, pp. 1–10.
53. Simon, N., Drexler, E., and Reed, R., *Review of Cryogenic Mechanical and Thermal Properties of Al–Li Alloys and Alloy 2219*, NISTIR 3971, National Institute of Standards and Technology, Boulder, Colorado, 1991.
54. Hartwig, G., "Status and Future of Fibre Composites," *Advances in Cryogenic Engineering (Materials)*, Vol. 40, Plenum Press, New York, 1994, pp. 961–975.

4
History and Applications of Nonmetallic Materials

G. Hartwig

Forschungszentrum Karlsruhe, 76133 Karlsruhe, Germany

Abstract

Nonmetallic materials are used for electrical and thermal insulation and structural elements. Ceramics are important for high-frequency insulation and support elements under compression. Polymers are applied for impregnation and as a matrix for fiber composites under compression. Fiber composites are used for lightweight construction and for fatigue-resistant and tensile structural elements.

The following properties will be considered:

- Modulus
- Strength
- Stress-concentration factor
- Fracture energy
- Mechanical damping
- Specific heat
- Thermal conductivity
- Thermal expansion
- Electrical resistivity
- Dielectric damping
- Electric strength

A brief treatment of functional nonmetallics is given in Section 4.3.4.

4.1 Introduction

Each period in the history of mankind is characterized by special materials: wood, stone and bones were the first nonmetallics used:

- The application of stone is older than the International Cryogenic Materials Conferences (ICMCs).
- The application of carbon fiber composites, however, is younger than the Cryogenic Engineering Conference.

Low-temperature technology has been triggered by superconductivity. However, superconducting applications include the use of nonmetallic insulators and structural elements. Polymers and composites, especially for cryogenic applications, were considered unimportant in the 1970s. In fact, the design study for the Large CERN-Collider was modified partly because of the lack of data on insulating and structural materials.

The organization of several ICMCs on nonmetallics in Munich and Heidelberg, Germany, in Geneva, Switzerland, and in Hawaii greatly assisted in the accumulation of low-temperature data. The need for cryogenic nonmetals was enhanced by new applications. In addition to superconductivity, hydrogen technology is now becoming important. Liquid hydrogen is under consideration as a fuel. Hydrogen motor cars work rather well; however, logistical problems arise from hydrogen distribution. Especially important for a clean environment is the introduction of hydrogen propulsion in airplanes. For all these developments, nonmetallic materials, especially fiber composites and ceramics, are necessary.

4.2 History and Materials Development

The oldest nonmetallic, structural materials are stone, wood and bones. Stone is a strong and cheap material, but is expensive to shape.

The application of clay offered much more flexibility in shaping earthenware, but it is brittle and weak. Probably in ancient times, when people heated their meals in clay pots they realized that clay became harder when exposed to fire. Thus, ceramics began to be produced about 6000 BC. Since 4000 BC, ceramic wares were produced in special stoves in factories.

Glass production started in Egypt at about the same time by mixing and heating of quartz, sodium, and lime. Then, glass was used for screening metallic parts, and later on for glassware. Strings of glass were used to reinforce bottles.

Roughly at the same time, metal production became important in the Far East. It is astonishing that gold was the first metal to be used by mankind. The reason for its early application comes from its easy production. Gold is an inert element and can be obtained directly in its pure state. Copper was the next metal worked by man, since 3500 BC. It is known that extensive copper mining started as early as 2500 BC. Reduction processes necessary for copper production had been well developed at that time. From 2000 BC, bronze alloys became a common material, initiating the Bronze Age. Iron production is more complicated, since several chemical processes and heat treatments are necessary. In antiquity, iron was more expensive than gold. Iron production started in the Far East in about 1800 BC; steel production began somewhat earlier in Armenia. After that time, there was a long time period without great material developments.

In 1870, the properties of liquid crystalline polymers were described (but never used until 1970). They consist of strong polymer segments that are able to align themselves. In the direction of alignment they are very strong and could be used as fibers.

Production of fiberglass started in 1930. At that time, the matrix of fiber composites was bakelite. It is important to note that geometric shape determines the strength of a material. Fiber geometry strongly influences fracture strength and elongation. Fibers are much stronger than bulk material. The modulus, however,

is unaffected by shape. After 1950, polymer production started on an industrial scale. Polymers were used also as a matrix for fiber composites. For fiberglass, the most important application worldwide, started in recent years, was optical data transmission and telecommunication. A pair of 0.1 mm thickness fibers can be used for a simultaneous optical transmission of nearly 2 million phone calls, both for terrestrial and transoceanic lines.

The invention of carbon fibers in 1970 increased the importance of fiber composites. Several types are produced: high-strength fibers, high-stiffness fibers, and intermediate grades. Common to all carbon fibers is their strong fatigue resistance. Their low-temperature thermal contraction is nearly zero; thermal conductivity is low only at low temperatures.

Kevlar fibers, produced since 1970, consist of aligned aramide molecules that are connected by hydrogen bridges and Van der Waals forces. They are strong in the fiber direction, but weak in the perpendicular direction. The thermal expansion coefficient is negative (they expand when cooled).

Superconductivity of niobium alloys at temperatures near 4 K was discovered in 1911, but real applications started much later. Superconducting magnets have been built on a technical scale since 1960. The problem is the very low temperature needed for their operation. Superconducting high-T_g ceramics, discovered in 1980, have the great advantage of working at much higher temperatures. Their disadvantage is brittleness.

The history of materials development is sketched in Figure 4.1.

4.3 Applications and Properties

4.3.1 Ceramics

The following applications are important for ceramics:

- Electrical resistivity
- Devices with low dielectric losses
- Dielectrics in condensers
- Devices for high voltage
- Thermal insulation
- Support elements under compression
- Fatigue-resistant elements

There are special types of high-T_g ceramics which become superconducting when cooled. The functional ceramics for piezo-, ferro-, or pyro-electrical applications are described Section 4.3.5. These types of ceramic contain dipoles, which can be oriented by electrical, thermal, or mechanical loads.

4.3.1.1 Properties of Ceramics

Vessels used by ancient mankind were made out of clay, which was transformed into ceramic by heat treatment. The basic process is dehydration of, e.g., aluminum silicate hydrate.

METAL. PERIODS			NONMETAL. PERIODS			
		100 000 BC	STONE AGE			
			material: not moldable, brittle			
GOLD AGE			CERAMIC PERIODS			
			material: hot moldable (melting), brittle			
COPPER AGE		3500 BC				
material: hot moldable (melting)						
BRONZE AGE		2500 BC				
material: hot moldable (melting)						
			GLASS			
STEEL IN ARMENIA		1900 BC	material: hot moldable (melting) brittle			
IRON AGE		700 BC				
material: hot moldable						
		1931 AD	FIBER GLASS			
SUPERCONDUCTING ALLOYS		1950 AD	PLASTIC AGE			
			material: cold moldable, little heat			
			treatment (cuting)			
			brittle at low temperatures			
			POLYMERS (Industrial scale production)			
		1950 AD	EPOXY RESINS			
			KEVLAR FIBERS			
		1970 AD	CARBON FIBERS			
			SiC			
SUPERCONDUCTING CERAMICS	1984					

FIGURE 4.1. History of material development.

The properties of ceramics are determined by

- Chemical composition
- Density and porosity
- Grain size
- Mixing of different ceramic types

Ceramics (e.g., Al_2O_3) are known to have a very high (probably the highest) compressive strength, which is rather independent of temperature. The ceramic compound Al_2O_3 has the highest compressive strength of ~4.5 GPa at room temperature.

The tensile strength of ceramics is much lower and also independent of temperature. The description of this property is difficult, since it is influenced by different stress concentrations at microcracks, voids, or dislocations.

The elastic modulus is rather high; tungsten carbide has the highest value of ~720 GPa at room temperature. Common ceramics exhibit values in the range ~200–400 GPa at this temperature.

The modulus is strongly dependent on grain size and density (porosity), which is determined by the production method. The strong influence is demonstrated for Al_2O_3 values at room temperature, where the elastic modulus is ~410 GPa for 100% density and ~250 GPa for 88% density.

Degradation by fatigue loading is rather low for tensile threshold cycling ($R = 0$), but higher for tension–compression loading ($R = -1$).

The critical stress concentration factor K_{IC} and the critical fracture energy G_{IC} for ceramics are rather low. Crack initiation is enhanced because of low K_I values, and during crack propagation little fracture energy G_I is consumed. This is the reason for the brittleness of ceramics. Most ceramics show values in the following ranges:

$$K_{IC} \approx 2\text{–}8 \text{ MPa m}^{1/2}$$
$$G_{IC} \approx 0.02\text{–}0.05 \text{ kJ/m}^2.$$

Glass shows values still lower by an order of magnitude. For comparison, steel has much higher values: $K_{IC} \approx 70\text{–}150 \text{ MPa m}^{1/2}$ and $G_{IC} \approx 6\text{–}12 \text{ kJ/m}^2$.

The thermal conductivity κ of most ceramics is low, and values range from 3 to 100 W/mK at room temperature. SiC has a higher value, similar to that of metals, namely 30–200 W/mK at this temperature. The large data spread is due to grain size and porosity.

The specific heat of ceramics is high relative to a volume or weight basis. Heat storage is achieved mainly by using ceramics. There are several ceramics which have the same molecular weight and, therefore, a similar specific heat. For example, the specific heat for AlN, Al_2O_3, and SiC at room temperature is ~0.7–1.0 J/(g K), but for ZrO_2 it is ~0.45 J/(g K). At low temperatures the specific heat decreases. At $-200°$C, the specific heat is lower by an order of magnitude. Above the Debye temperature, the specific heat is essentially constant.

Thermal expansion of ceramics and glass-ceramics is very low, being about $0\text{–}0.5 \times 10^{-6}$/K for glass-ceramics and $0\text{–}5 \times 10^{-6}$/K for glass at room temperature.

Electrical insulation is one of the main applications for several types of ceramics, both for dc and ac applications. Electrical insulation includes low electrical resistivity, low dielectric losses, and a high breakdown voltage. These requirements are realized by several ceramics.

The electrical resistivity of ceramics exhibits a wide band of values. The specific resistivity comprises at least 20 orders of magnitude. The highest specific resistivity at 300 K has been found for Al_2O_3, namely 10^{14} Ω cm. It increases at lower temperatures. As already mentioned, SiC has a low resistivity at room temperature of 0.1–100 Ω cm, similar to that of metals.

The dielectric loss factor is very low, e.g., for Al_2O_3 at 300 K it is approximated by $\tan \delta_e \approx 10^{-4}$ to 10^{-5}. At low temperatures the values are still lower.

The dielectric strength of ceramics is very high, comparable to that of fiberglass composites. For a gap of 1 mm it is 40–110 kV/mm. The breakdown voltage by no means is a linear function of the gap width. Dielectric properties are important for capacitors. There are special types of ceramics, such as barium titanate, with a dielectric permittivity as high as 10 000. The high value comes from a strong interaction of dipoles within the material. A disadvantage is the low breakdown voltage and the fact that this value is realized only at high temperatures. A compromise has been achieved by alloying with other materials (e.g., ZrO_2). Most ceramics have lower values because of lower dipole interactions ($\varepsilon_e \approx 3$–10 at room temperature). The permittivity decreases somewhat at low temperatures.

4.3.2 Polymers

Polymers have these main applications:

- impregnation (e.g., of superconducting coils)
- matrix of fiber composites
- high mechanical damping capability
- electrical insulation
- thermal insulation
- heat storage

The properties are somewhat influenced by the amorphous, semicrystalline, or cross-linked structures of polymer chains. Liquid crystalline polymers consist of rigid segments with self-orientation. Polymer properties are more difficult to describe, since two different binding potentials are involved:

- weak Van der Waals potential between chains
- strong covalent potential within chains

Special low-temperature properties and processes are discussed in the following subsections.

4.3.2.1 Low Temperature Asymptotic Behavior of Polymers

Many polymers show similar mechanical and thermal properties at very low temperatures whether they are amorphous, semicrystalline, or cross-linked polymers. The first example is given in Figure 4.2 for the elastic modulus E below 15 K (the results are analogous for the shear modulus) [1]. Polymers are very ductile at elevated temperatures, but they become brittle at low temperatures; for example, the fracture strain at 4 K is $\varepsilon \approx 2$ % for most polymers.

The specific heat is independent of chemical composition even up to temperatures of 100 K. This is shown for four different cross-linked polymers in Figure 4.3. The great similarity of values is surprising [2].
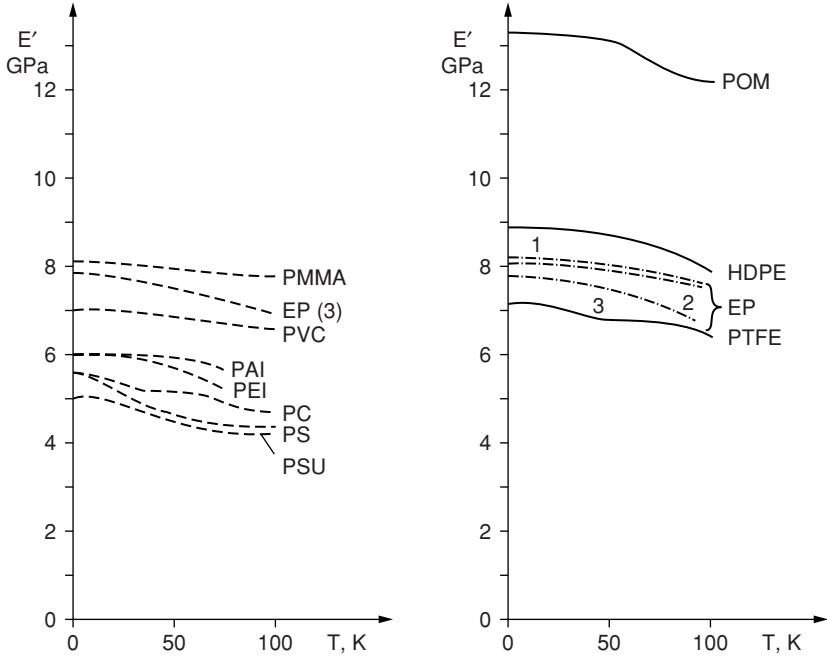
FIGURE 4.2. Elastic moduli at very low temperatures of different classes of polymers: – – – amorphous; —— semicrystalline; – · – · cross-linked [1]. EP: epoxy; PMMA: Plexiglas; PVC: polyvinylchloride; PAI: polyamide-imide; PEI: polyethylene-imide; PC: polycarbonate; PS: polystyrol; PSU: polysulfone; POM: polyoxymethylene; HDPE: high-density polyethylene; PTFE: Teflon.
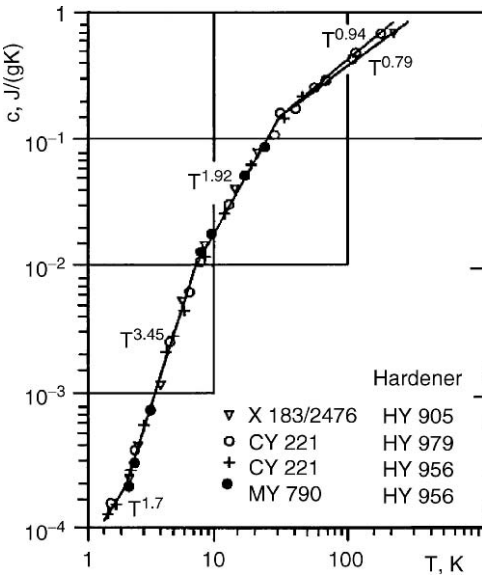

FIGURE 4.3. Specific heat of four different epoxy systems versus temperature.

For amorphous thermoplastics or semicrystalline polymers, the results are analogous; however, the range of values shifts somewhat. An interesting feature is the temperature dependence of the specific heat C. Several vibrating modes with different temperature dependencies are involved and overlap. At very low temperatures, tunneling vibration prevails:

$$C \propto T \text{ below } 1 \text{ K} \quad \text{(tunneling vibrations).}$$

At low temperatures, only long-wavelength chain vibrations of low energy (interchain vibrations) in the weak Van der Waals potential can be activated. Longitudinal standing phonon waves in three dimensions are possible, which lead to

$$C \propto T^3 \quad T \approx 2 \text{ K to } 10 \text{ K} \quad \text{(interchain vibrations).}$$

Because of intrinsic chain stiffness, three-dimensional transverse vibrations are also possible, which leads to

$$C \propto T^{1/2} \quad T \approx 10 \text{ K to } 50 \text{ K} \quad \text{(bending vibrations).}$$

At higher temperatures, short-wavelength, one-dimensional standing waves within the covalently bonded polymer chains become dominant. Here, the specific heat is proportional to the absolute temperature, or

$$C \propto T \quad \text{(one-dimensional intrachain vibrations).}$$

For the transverse component it is evident that

$$C \propto T^{-1/2} \quad \text{(one-dimensional bending vibrations).}$$

Each of these contributions becomes dominant in a certain temperature range, as shown in Figure 4.3.

The mechanical damping (loss factor) $\tan \delta$ of most amorphous polymers is similar at very low temperatures:

$$\tan \delta_m \approx 10^{-3} \text{ at } 4 \text{ K to } 15 \text{ K.}$$

Dielectric damping, however, is different within polymers, since dipole moments specific to the material are involved. But the ratio of mechanical to dielectric loss factors is a polymer-specific constant independent of temperature [3]:

$$\tan \delta_e / \tan \delta_m = f(\mu).$$

The ratio is a function of the mean dipole moment μ of the polymer considered. In Figure 4.4, the mechanical and dielectric loss factors are plotted versus temperature. On the semilogarithmic ordinate, both loss factors are shifted by a constant value, i.e., they differ by a constant factor.
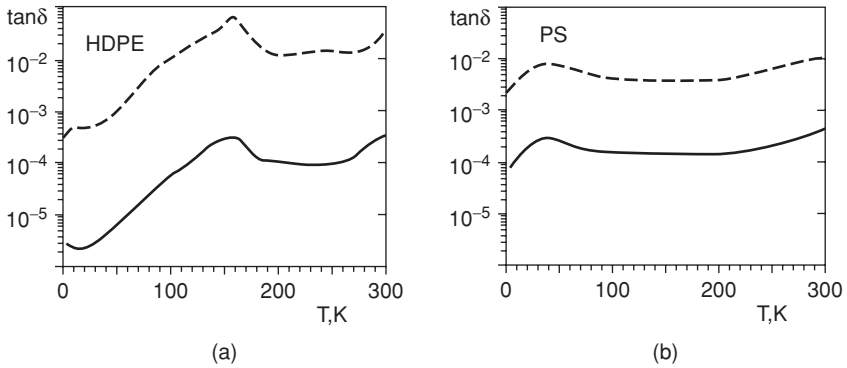
FIGURE 4.4. Mechanical (dashed line) and dielectric (solid line) loss-factors: (a) HDPE: high-density polyethylene; (b) PS polystyrene [3].

Fatigue behavior at 77 K is shown in Figure 4.5 for two polymers [4]. The fatigue endurance limit after 10^7 load cycles is rather low. It should be mentioned that moduli do not degrade remarkably in uniaxial fatigue cycling.

4.3.2.2 Electrical Properties

Dielectric damping was introduced in the preceding section. The topics of this section are electrical resistivity, permittivity, and breakthrough voltage (or dielectric strength).

Electrical resistivity is rather high for polymers. The specific resistance is on the order of

$$\rho \approx 10^{12} - 10^{13} \ \Omega \ cm \quad \text{at RT.}$$
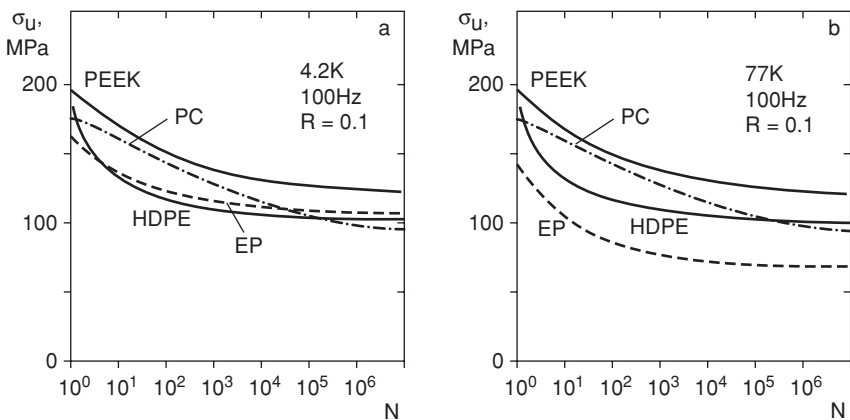
FIGURE 4.5. Wöhler curves of some polymers at 4 K and 77 K. EP: epoxy E 162/E 113, Shell [4]; PEEK: polyether ether ketone.
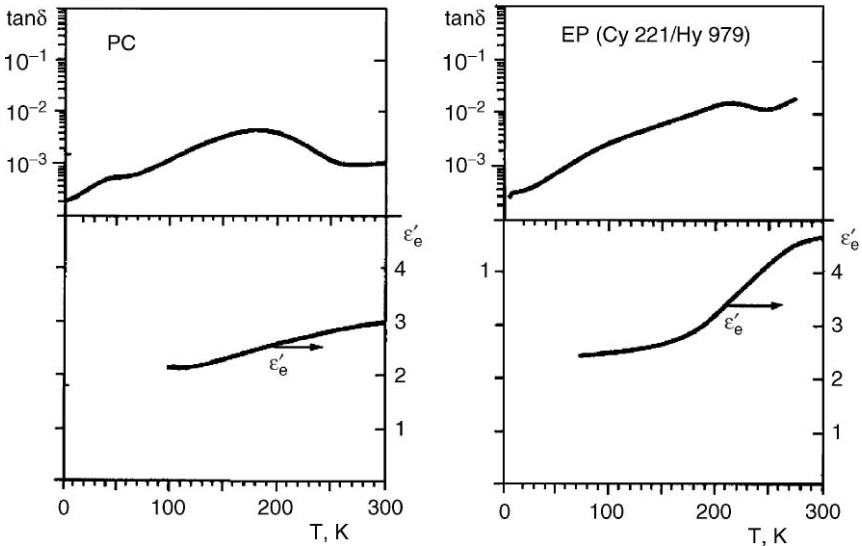
FIGURE 4.6. Dielectric permittivities and loss factors of polymers as a function of temperature.

The dielectric permittivity ε' of polymers is a strong function of the temperature, since dipole orientations by an external field are involved. At very low temperatures no orientation is possible and only a constant electron polarization remains. As is shown in Figure 4.6, the constant electron permittivity is about $\varepsilon' \approx 2$. The range of ε' for polymers is $\varepsilon' \approx 2-15$.

Dielectric strength is a function of temperature, since different modes of conductivity are activated at different temperatures (see Figure 4.7). It is also a strong, but not linear, function of the thickness of the insulator. A stack of many thin foils withstands a much higher voltage than a foil of the same total thickness. In a thick foil, a large electron avalanche develops. With many thin foils, these developments are stopped many times.

4.3.2.3 Boundary Scattering

Thermal conductivity of semicrystalline polymers at elevated temperatures is higher than that of amorphous polymers [5]. Below 30 K, however, they show lower values because of boundary scattering of the phonons at the crystallites. This effect becomes dominant only at very low temperatures and only for very small filler particles. Smaller filler particles have a larger total surface per filler content. The smaller the particle, the higher is the total boundary resistance and the lower is the thermal conductivity. Consider the following example. The thermal conductivity of polymers at 2 K can be reduced by a factor of 50 when filled with $\phi \approx 1$ μm glass particles to 30 vol.%. The thermal resistance of the filler is negligible compared with the boundary resistance.
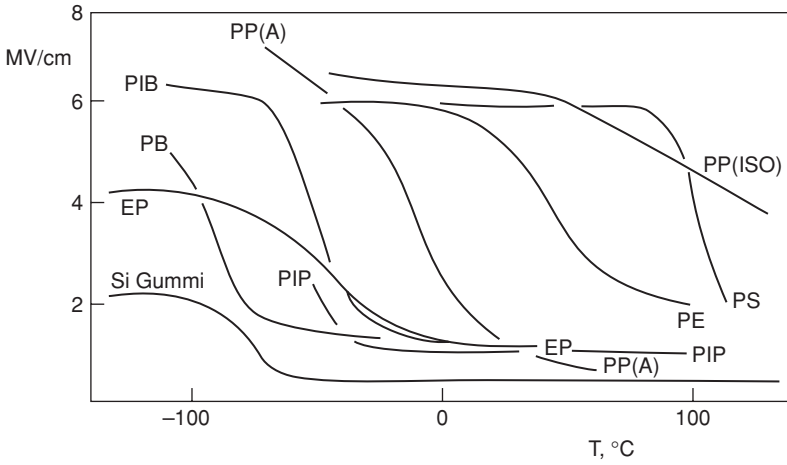
FIGURE 4.7. Dielectric strengths of different polymers as a function of temperature. PP: polypropylene; PB: polybutadiene; PIB: polyisobutylene.

Figure 4.8 shows the thermal conductivities of semicrystalline and amorphous polymers. At low temperatures the thermal conductivity of semicrystalline polyethylene (PE) becomes lower than that of amorphous polymers, e.g., PC or PVC. This is a consequence of boundary scattering at low temperatures.

4.3.2.4 Glass Transitions of Polymers

It has been shown in the last section that, at low temperatures, most properties are rather independent of chemical composition. This is true only below the glass transition temperature T_g. Most glass transitions start above 100 K. T_g marks the
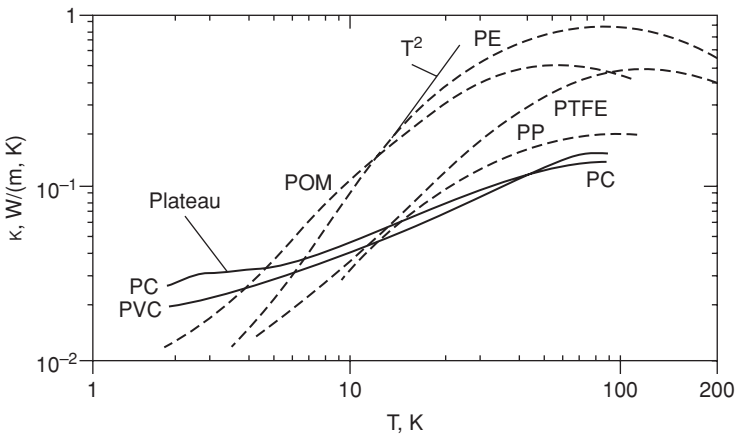

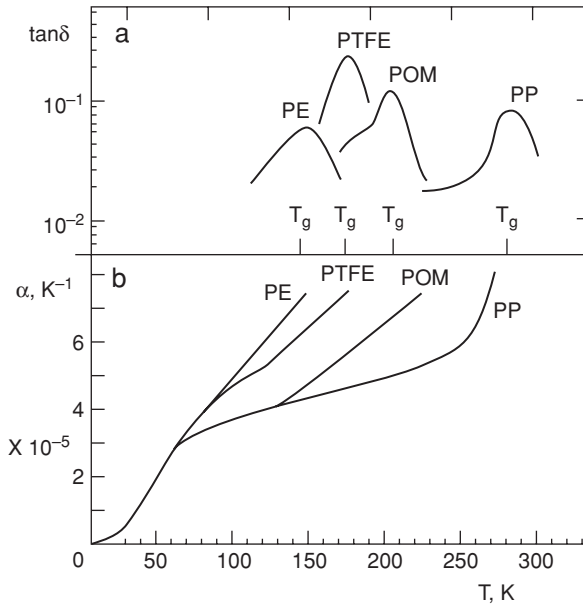FIGURE 4.8. Thermal conductivity of semicrystalline and amorphous polymers.

FIGURE 4.9. Thermal expansion of several semicrystalline polymers; T_g is glass-transition temperature.

unfreezing of a molecular group depending on its chemical composition. Several groups can be arranged in two (or more) positions. The transition between both positions is hindered by binding forces. They can be overcome by high thermal (vibrating) energy together with applied external energy. There is a time delay between load and reaction. This time shift causes damping, which is given by the loss factor tan δ. At T_g, the loss factor tan δ has a damping peak. Temperatures above T_g cause the expansion and chain segments gain more thermal mobility. The following changes occur above T_g:

• Modulus and strength decrease (larger chain distance, lower binding density)
• Thermal expansion increases (more volume involved)
• Mechanical and dielectric damping increase (damping peaks at T_g)

   In Figure 4.9 the rise of the thermal expansion coefficient at the glass transition temperature is shown for several semicrystalline polymers [6].

4.3.3 Fiber Composites

Fiber composites are used mainly for the following applications:

• Reduced-weight construction
• High-tensile or high-stiffness elements
• Fatigue-resistant elements for carbon-fiber composites

TABLE 4.1. Fiber properties at room temperature

Fiber	Modulus (GPa)	σ (GPa)		ε tensile (%)	Fatigue strength	Thermal expansion
		Tensile	Comp.			
Carbon high tensile	High	Very high	Medium	Medium	Very high	Very low and negative
	300–500	4–8	1–2	1.5–2		
high modulus	Very high 500–900	Medium 2–3	Medium 1–2	Low <1	Very high	Zero
Kevlar	Medium 130–180	High 3–4	Low	High 2–3	High	Negative
Glass	Low 70–90	Very high 3–6	High 2–3	Very high 3–5	Medium	Medium
Ceramic (SiC, Al$_2$O$_3$)	Medium 200–350	Medium 2–3	High 2–4	Low <1	Low	Medium

- Electrical insulation for glass-fiber composites
- Thermal insulation
- Compensation elements with negative thermal expansion
- Zero-expansion elements
- Cryostats for hydrogen tanks (motorcars and airplanes)

Composite properties depend on the following parameters:

- Fiber type. The specific merits or disadvantages of fiber types are summarized in Table 4.1.
- Fiber thickness. Thin fibers exhibit improved mechanical properties. The usual thickness is about 7 µm. Only ceramic fibers are produced with a large thickness of about 20 µm.
- Fiber volume. This property is especially important in the thickness direction for nondirectional properties.
- Matrix type (rigid epoxy matrix, flexible thermoplastic matrix, ceramic matrix). The matrix type is important for several properties. Astonishing is the fact that the matrix controls the fatigue endurace limit of Wöhler curves. We have verified this behavior on many carbon-fiber matrix systems. Figure 4.10 shows an example
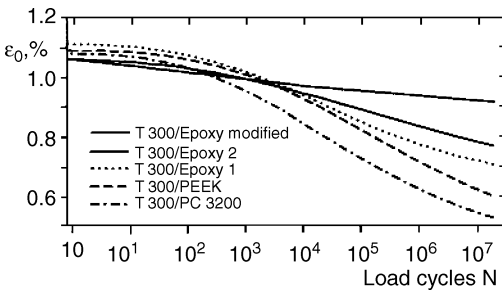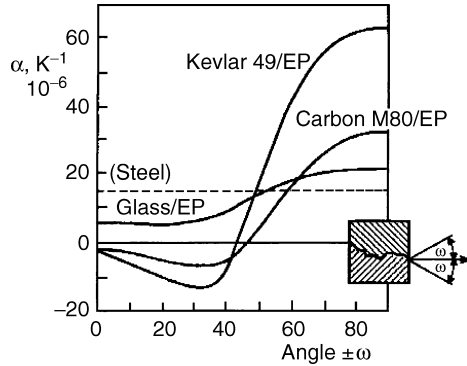

FIGURE 4.10. Strain life diagrams of UD–carbon-fiber composites with different matrices [7].

FIGURE 4.11. Thermal expansion coefficient α for several angle plies versus fiber angle [8].

for unidirectional composites with one fiber type but several matrices [7]. At high load cycles a lower fatigue degradation has been found for rigid epoxies than for different thermoplastic matrices. The reason is not very clear, but microscopic inspections suggested that different fracture mechanisms are developed during cycling. Transverse cracks are found in epoxy matrices and defibrilation occurs with thermoplastic matrices.

- Fiber–matrix interface.
- Fiber arrangement (unidirectional, cross-plies, and angle plies). Fiber arrangement at $\pm\omega$ angles allows for a great variation of properties. The following arrangements are important for applications of carbon and Kevlar composites:

$$\omega \approx 0°$$
$$\omega \approx \pm 30° \text{negative thermal expansion (the magnitude}$$
$$\text{is about that of steel, but with a negative sign)}$$
$$\omega \approx \pm 45° \text{zero-expansion composites.}$$

The thermal expansion coefficient is shown versus fiber angles $\pm\omega$ in Figure 4.11.

The thermal conductivity is also controlled by fiber orientation. As is seen from Figure 4.12, this is true at elevated temperatures. At decreasing temperatures, however, a small-value band is approached rather independent of fiber angles. The reason for isotropic behavior is the phonon wavelength, which becomes larger than the fiber distance at very low temperatures. The general results for unidirectional composites hold: static values are controlled by the fibers; the fatigue endurance limit, however, is strongly influenced by the matrix. A rigid epoxy matrix yields a higher value than a thermoplastic one [8].

4.3.3.1 Properties in the Thickness Direction

The following properties depend on the fiber volume, but not on the fiber direction. The specific heat is related to the mass of fiber composites. In addition, the specific
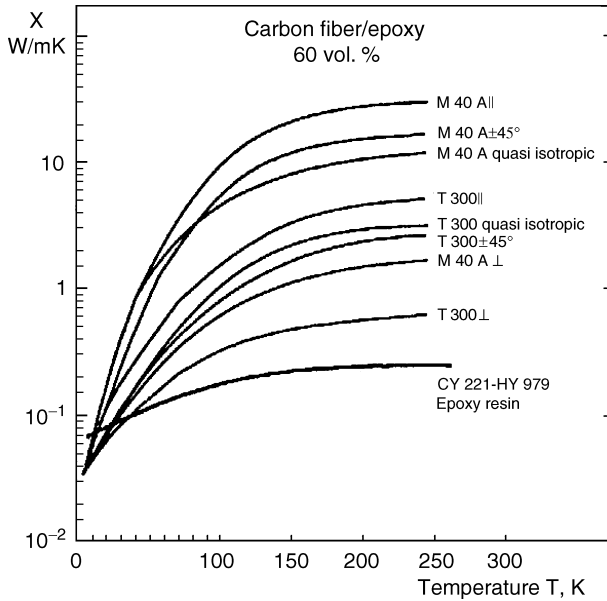
FIGURE 4.12. Thermal conductivities of differently arranged carbon fibers [9].

heat is rather independent of the fiber type, at least for fiber glass and carbon; this
is shown in Figure 4.13 [10].

Permittivity ε' and dielectric loss factor tan δ are shown in Figure 4.14 [2].

The dielectric strength is rather high, especially for fiber-glass compos-
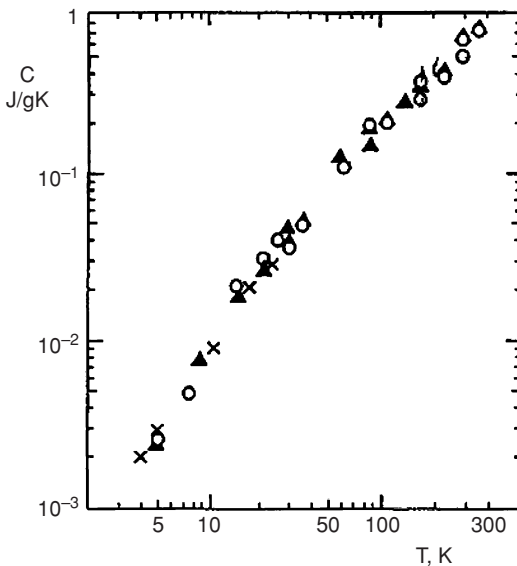ites. The highest values for materials at room temperature are probably about

FIGURE 4.13. Specific heats of
glass-fiber and carbon-fiber
composites versus temperature.
▲, ○: E-glass-fiber composites;
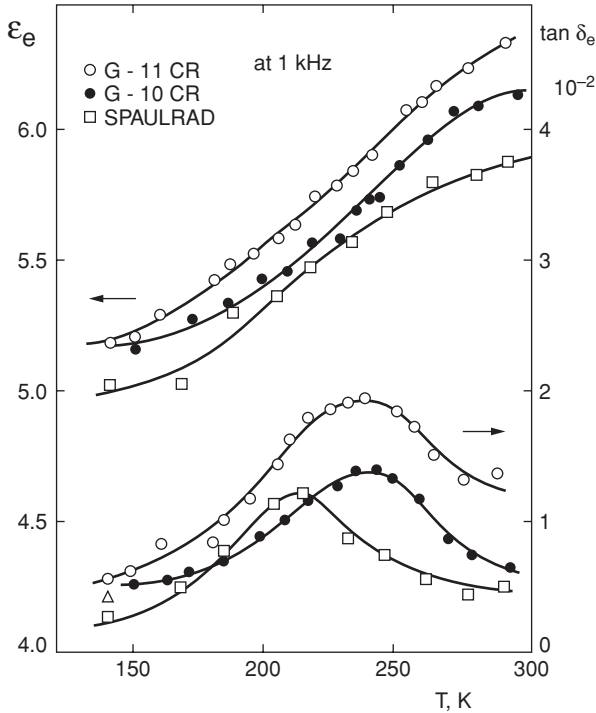×: carbon-fiber composites.

FIGURE 4.14. Permittivity ε' and dielectric loss factor for different fiber-glass composites.

50–100 kV/mm for a 1 mm gap. At low temperatures, the values are even higher because the dielectric strength of the polymers is increased.

The specific resistivity at room temperature is on the order of 10^{16} Ω cm for fiber-glass composites and 10^4 Ω cm for carbon-fiber composites.

4.3.4 Functional Nonmetallics

4.3.4.1 Superconducting Ceramics

Several high-T_g ceramics, e.g., yttrium ceramics, have been discovered that become superconducting by moderate cooling (about -180 °C). A rather high current density is maintained in high magnetic fields. The critical current density versus the magnetic field strength (induction) is shown in Figure 4.15 at constant temperatures for each material [11]. A current density of $\sim10^7$ A/cm^2 can be achieved at low fields and temperatures.

4.3.4.2 Conducting Polymers

Several polymers with alternating single and double bonds in the chain backbone, e.g., polyacetylenes, can be made conducting by doping with fluorine or bromine.
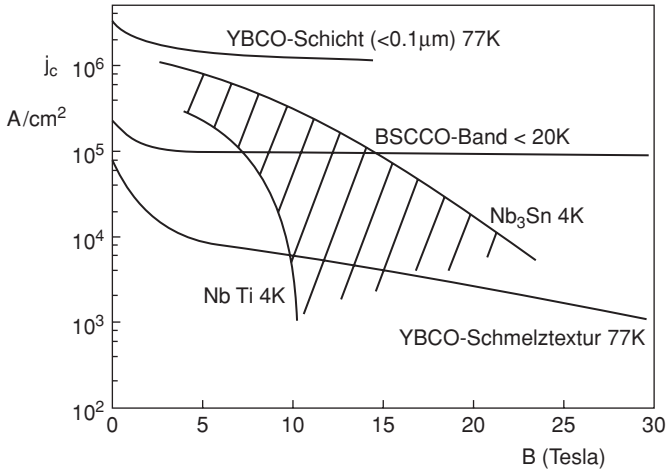
FIGURE 4.15. Critical current density of several superconducting ceramic materials versus magnetic field.

The double bonds are shifted by an external voltage and cause electron transport. The conductivity is rather high, on the order of $\sim 10^2 - 10^4/(\Omega$ cm) at room temperature for conducting polymers. The disadvantage is the soft consistency of that material. It would be a lightweight electric conductor.

4.3.4.3 Conducting Carbon Fibers

Carbon fibers can also be made more conductive than copper by doping them with fluorine or bromine.

4.3.5 Polarization Properties

Several ceramics or polymers contain dipoles which can be oriented by an electrical field, by stirring or by freezing under strain at decreasing temperatures.

Piezoelectric materials convert the field strength applied into strain, and vice versa. The most reactive ceramic is barium titanate. Its coefficients are $g = 400 \times 10^{-12}$ m/V and $d = 590$ pC/N. The reaction of the polymer is lower by a factor of 100; e.g., consider polyvinydilene difluoride and quartz. An electric signal can be induced by strain, and vice versa.

Ferroelectric materials convert an electrical field change into a temperature change.

Pyroelectric materials are able to freeze-in field-induced polarization by decreasing temperatures under the application of an electrical field. Such materials include polyvinydilene difluoride, polyvinyl chloride, and barium titanate. The pyroelectric constant b for PVC at room temperature is $4 \times 10^{-6}/(\text{cm}^2$ K).

References

1. Hartwig, G., *Polymer Properties at Room and Cryogenic Temperatures*, Plenum Press, 1994, p. 160.
2. Reference [1], p. 58.
3. Reference [1], p.179.
4. Reference. [1], p. 214.
5. Reference [1], p. 110.
6. Reference [1], p. 82.
7. Hartwig, G., in *Handbook of Applied Superconductivity*, Seeber, E., ed., Institute of Physics, 1998, p. 1032.
8. Reference [7], p. 1018.
9. Reference [7], p. 1049.
10. Reference [7], p. 1052.
11. Goldacker, K., Report, Institute for Technical Physics, Forschungszentrum Karlsruhe, Karlsruhe, Germany, 1994.

General Reading

Hertzberg; R.W., *Deformation and Fracture Mechanics of Engineering Materials*, John Wiley, 1976, pp. 369–372.

Kroschwitz, J.I., ed., *Concise Encyclopedia of Polymer Science and Engineering*, John Wiley, 1990, pp. 220, 300–305.

Kroschwitz, J.I., ed., *Concise Encyclopedia of Composite Material Science and Engineering*, John Wiley, 1990, pp. 46, 63.

Part 3

Improvement in Cryogenic Fundamentals over the Past 50 Years

5
Advances in Cryogenic Principles

R.F. BARRON

Louisiana Tech University, Ruston, LA 71272, USA

Abstract

During the past 50 years, the use of digital computers has significantly influenced the design and analysis of cryogenic systems. At the time when the first Cryogenic Engineering Conference was held, thermodynamic data were presented in graphical or tabular form (the "steam table" format), whereas thermodynamic data for cryogenic system design is computer generated today. The thermal analysis of cryogenic systems in the 1950s involved analytical solutions, graphical solutions, and relatively simple finite-difference approaches. These approaches have been supplanted by finite-element numerical programs which readily solve complicated thermal problems that could not be solved easily using the methods of the 1950s. In distillation column design, the use of the McCabe–Thiele graphical method for determination of the number of theoretical plates has been replaced by numerical methods that allow consideration of several different components in the feed and product streams.

5.1 Introduction

The first Cryogenic Engineering Conference was held at the National Bureau of Standards (now National Institute for Standards and Technology) Laboratories in Boulder, Colorado, on September 8, 9, and 10, 1954. During the 50 years following that initial conference, the use of digital computers has significantly influenced the principles and techniques used in the design and analysis of cryogenic systems.

In the 1950s, the primary computational tool used by cryogenic engineers and scientists was the slide rule. In fact, the ubiquitous slide rule attached to the student's belt was one of the identifying characteristics of university engineering and science students. In the 1970s, the hand-held electronic calculator replaced the slide rule as the technical computational tool. Today, engineers and scientists use the laptop computer for many of their design and analysis activities.

The computers of the early 1960s, such as the IBM 1620 mainframe, were room-sized systems that required an air-conditioned environment for survival. In 2005,

the mainframe computers used by engineering organizations are on the order of the size of a small household refrigerator. In fact, mainframe computers are being replaced in many areas by networked computer systems with terminals distributed throughout the plant or university.

The availability of the digital computer has enabled cryogenic engineers and scientists to solve problems that would have been intractable in the 1950s. For example, in analysis of transfer lines for cryogens, Jacobs [1] observed that:

The solution of Equation (14) for the investigation of any particular problem can become quite involved. If extensive analyses are to be undertaken, it is recommended that the equation be plotted for the range of variables which are of interest. Then, all results can be readily obtained by interpolation.

The equation mentioned is

$$p_0 = \frac{fL}{D}\frac{(m/A_c)^2}{2\rho} + \exp\left[\frac{\frac{\lambda}{RT_0}}{1 + \left(\frac{mc_pT_0}{\pi DL q''}\right)}\right]. \tag{5.1}$$

The friction factor f in turbulent flow was evaluated from the following correlation:

$$f = 0.00560 + \frac{1}{2}\mathrm{Re}^{-0.32}. \tag{5.2}$$

The pipe cross-sectional area $A_c = \frac{1}{4}\pi D^2$ and the Reynolds number $Re = D(m/A_c)/\mu$ both involve the inside pipe diameter D. The objective was to solve the equation for the inside pipe diameter, given the liquid inlet pressure and temperature (p_0 and T_0), the pipe length L, the liquid mass flow rate m, the heat transfer rate per unit surface area q'', and the fluid properties (density ρ, heat of vaporization λ, gas constant R, and specific heat c_p). This problem may be easily solved and the results graphically displayed by present-day standard computational tools, such as MathCAD® or TKSolver®.

Present-day commercial computational fluid dynamics (CFD) computer programs have the capability of solving much more complicated and extensive cryogenic fluid dynamics problems than were possible to solve using the computational tools available in the 1950s. For example, the laminar flow over a surface having a backward-facing step could not have been solved using computational techniques of the mid-1900s; however, this problem is frequently used as a standard test problem for numerical methods in use at present [2].

5.2 Thermodynamics

At the time of the first Cryogenic Engineering Conference in 1954, thermodynamic data were generally presented in graphical (analog) form or in tabular form (the "steam table" format). In one of the pioneering books of cryogenic engineering

prepared by Russell B. Scott, and published in 1959 [3], all of the thermodynamic data are presented in temperature–entropy or pressure–enthalpy diagrams. Thermodynamic data (density or specific volume, enthalpy, internal energy, and entropy) for several cryogens were available in tabular form for gases such as air [4], helium [5], normal hydrogen [6], and nitrogen [7] in the early 1960s. The tabulation of the data for helium and nitrogen required a digital computer, because the equation of state used to develop the data (a modified Benedict–Webb–Rubin equation) involved 16 or 17 constants and 16 or 17 terms.

Fifty years after the first Cryogenic Engineering Conference, thermodynamic data, including transport properties, needed for design of cryogenic liquefiers and cryocoolers may be generated directly from commercially available computer programs, including NIST-12®, GASPAK®, and HEPAK® (for helium) [8].

Although the first and second laws of thermodynamics have not changed during the past 50 years, the presentation in engineering publications has evolved somewhat. The explicit inclusion of the "mechanical equivalent of heat" ($J = 778$ ft-lb$_f$/Btu) and the "gravitational constant" ($g_c = 32.2$ ft-lb$_m$/(lb$_f$ s^2)) has been discontinued. For example, Hohmann and Patterson [9] presented the "general energy equation" or first law of thermodynamics for steady flow as follows.

$$h_1 + \frac{\mathbf{V}_1^2}{2g_c J} + \frac{g\,z_1}{g_c J} + q = h_2 + \frac{\mathbf{V}_2^2}{2g_c J} + \frac{g\,z_2}{g_c J} + \frac{w}{J}. \tag{5.3}$$

The constants J and g_c are actually conversion factors for units and are not necessary in the equations. The widespread use of the SI system for units has influenced the elimination of J and g_c, because work and heat are expressed in the same units in the SI system. The energy expression would be written as follows in present-day notation:

$$h_1 + \frac{1}{2}\mathbf{V}_1^2 + g\,z_1 + q = h_2 + \frac{1}{2}\mathbf{V}_2^2 + g\,z_2 + w. \tag{5.4}$$

5.3 Heat Transfer

In the widely used 1954 heat transfer textbook by McAdams [10], the techniques used in solution of conduction heat transfer problems included analytical (algebraic equations), graphical, analog, and relatively simple numerical methods. Many of the analytical solutions were presented in graphical form, such as the Heisler charts for transient heat transfer in a slab, cylinder, or sphere. Nomographs were used extensively as design tools to solve thermal problems.

Transient conduction problems, such as the determination of the temperature distribution in the evacuated powder insulation on a cryogenic fluid storage vessel, were often solved using a graphical technique, called the *Schmidt method* [11]. The first few steps in the graphical method applied in solving for the temperature distribution in the cryogenic vessel during cool-down are shown in Figure 5.1. T_n^{t+1}, the temperature at any point x_n and at the time t_{t+1}, is found graphically,
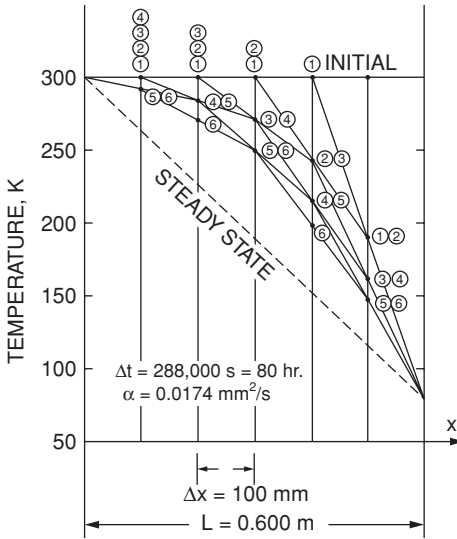
FIGURE 5.1. Schmidt graphical solution for the cool-down of a cryogenic vessel insulation layer. The initial wall temperature is uniform at 300 K and the cold surface temperature is suddenly reduced to 80 K. The insulation thickness is 0.600 m (23.6 in) and the insulation thermal diffusivity is $\alpha = 0.0174$ mm^2/s (6.74×10^{-4} ft^2/h).

based on the following expression:

$$T_n^{t+1} = \frac{1}{2} \left(T_{n+1}^t + T_{n-1}^t \right). \tag{5.5}$$

The space increment Δx and the time increment Δt are related by the following expression for the graphical Schmidt method:

$$\frac{(\Delta x)^2}{\alpha \, \Delta t} = 2, \tag{5.6}$$

where α is the thermal diffusivity of the material. For example, for an insulation thickness of $L = 600$ mm and $\Delta x = 100$ mm (six space increments) and an insulation thermal diffusivity $\alpha = 0.01736$ mm^2/s, the required time increment for the graphical method is

$$\Delta t = \frac{(0.100)^2}{(2) \left(0.0173636 \times 10^{-6} \right)} = 288,000 \text{ s} = 80 \text{ h} = 3\frac{1}{3} \text{ days.}$$

It may be noted that 16 pages were devoted to the graphical method in the first edition of Kreith's textbook on heat transfer (published in 1958), whereas the graphical method of solution was not mentioned in the fifth edition of *Principles of Heat Transfer* (published in 1993) [12].

The Schmidt graphical method involves the restriction on the time increment, given by Equation (5.6), in order that the method be numerically stable, because the method is an explicit method. In addition, the Schmidt method required that the thermal properties of the materials be treated as constants. This is a highly restrictive requirement for cryogenic heat transfer problems, because the thermal

properties of the materials generally vary considerably with temperature in the cryogenic range [13].

Cryogenic engineers often employ the finite-element method (FEM) in thermal analysis and design today [14]. The FEM is especially advantageous for solution of problems involving complicated shapes and boundary conditions. In addition, the FEM can easily include effects of variable material properties. Several commercial FEM packages, such as ANSYS®, are available for thermal analysis. These programs generally include preprocessing (grid generation) and postprocessing (color display of temperature distribution) features.

The FEM involves discretization of the temperature field equation for a finite element of material. The equations for the temperatures in the discrete elements are solved by matrix manipulations. For the transient thermal problem (cool-down of a cryogenic insulation layer) mentioned previously, the governing matrix equations are of the following form [15]:

$$[\mathbf{K}]\left\{\mathbf{T}^{t+1}\right\} + [\mathbf{M}]\left(\left\{\mathbf{T}^{t+1}\right\} - \left\{\mathbf{T}^{t}\right\}\right)/\Delta t = \left\{\mathbf{Q}_{\text{gen}}\right\} + \left\{\mathbf{q}_{\text{bnd}}\right\}. \qquad (5.7)$$

The quantity $[\mathbf{K}]$, called the *conductivity matrix*, involves the thermal conductivity of the material and may be a function of the temperature T at the various element nodes. The quantity $[\mathbf{M}]$, called the *thermal mass matrix*, involves the material density and specific heat and may also be a function of the element temperatures. The temperature vector $\left\{\mathbf{T}^{t+1}\right\}$ involves the element temperatures at the next (future) time step, and $\left\{\mathbf{T}^{t}\right\}$ involves the temperatures at the present time step. This is an implicit method of solution, because all of the "future" temperatures are unknown and must be computed by solving a set of simultaneous equations. The vectors $\left\{\mathbf{Q}_{\text{gen}}\right\}$ and $\left\{\mathbf{q}_{\text{bnd}}\right\}$ are the heat "generation" or heat "source" vectors (rate of energy dissipation per unit volume) and boundary heat flux vectors, respectively.

The solutions of the cool-down of a cryogenic insulation layer by the Schmidt method and by the FEM are compared in Table 5.1. In the Schmidt solution, the

TABLE 5.1. Temperature distribution obtained from Schmidt graphical solution compared with the finite element solution for the cool-down of a cryogenic vessel insulation layer

	T (K)			
	Schmidt graphical solution		Finite-element solution	
Location x (mm)	480 h	Steady state	480 h	Steady state
0	300	300	300	300
100	293	263	296	279
200	273	227	287	255
300	252	190	271	226
400	200	153	241	190
500	149	117	186	145
600	80	80	80	80
Heat flux at cold surface (W/m^2)	0.825	0.440	0.868	0.445

thermal conductivity and thermal diffusivity were taken as constant, $k = 1.20$ mW/(m K) and $\alpha = 0.0174$ mm^2/s.

In the FEM solution, the thermal conductivity and specific heat for an evacuated powder insulation were taken as the following functions of temperature [16]:

$$k = k_0 \exp\left(\frac{T}{T_r}\right),$$ (5.8)

where $k_0 = 0.335$ mW/(m K) and $T_r = 157.5$ K, and

$$c = a_0 + a_1\left(T/T^*\right) + a_2\left(T/T^*\right)^2,$$ (5.9)

where $a_0 = -0.088$ kJ/(kg K), $a_1 = 1$ kJ/(kg K), $a_2 = -0.25866$ kJ/(kg K), and $T^* = 250$ K.

The temperature distributions found by the two methods are significantly different because of the variation of the material properties. The values for the heat flux at the cold side of the insulation layer are not significantly different in the steady state, because the mean thermal conductivity corresponding to Equation (5.8) was used in the Schmidt method.

With little increase in complexity, the FEM may be applied to solve two-dimensional transient problems, such as cool-down of a cryogenic vessel insulation with pipe penetrations through the insulation layer. On the other hand, the Schmidt method is limited to one-dimensional transient analysis only.

Analog techniques were extensively used in solving cryogenic heat conduction problems in the 1950s [17]. The analog methods included electrical analogies, membrane or soap-film analogies, and hydrodynamic analogies. The principle of the various analogies is that the governing differential equations for conduction heat transfer (Fourier equation, etc.) are mathematically similar to the equations governing electrical current flow (Ohm's law, etc.) or deflection of a membrane or streamlines in inviscid fluid flow.

In 1957, Kayan and Gates [18] used the electrical analogy to study the performance of fins used in cryogenic equipment. The electrical circuit used to determine the temperature distribution and heat transfer in the fin is shown in Figure 5.2. The temperature difference along the length of the fin was proportional to the electric voltage change at the same point, and the heat transfer rate was proportional to the electrical current. Thermal conduction and convection resistances were proportional to the corresponding electrical resistances used in the analogy. The difference between the analytical solution and the solution by the electrical analogy was on the order of 1 to 2% for the cryogenic fin problem.

Analog techniques are seldom used in solving cryogenic heat transfer problems today. *Liquid crystal thermography* has been used in investigations of the temperature field around a cryosurgery probe tip [19]; however, thermography is not a true analog technique. Liquid crystals in the form of microcapsules (about 20 μm in diameter) or an unencapsulated grease are applied in a thin layer (approximately 10 to 20 μm thick) on another thin layer of chemically compatible black paint on the thermal model. Temperature changes of the liquid crystal layer produce changes in color of the material. For transient temperature measurements,
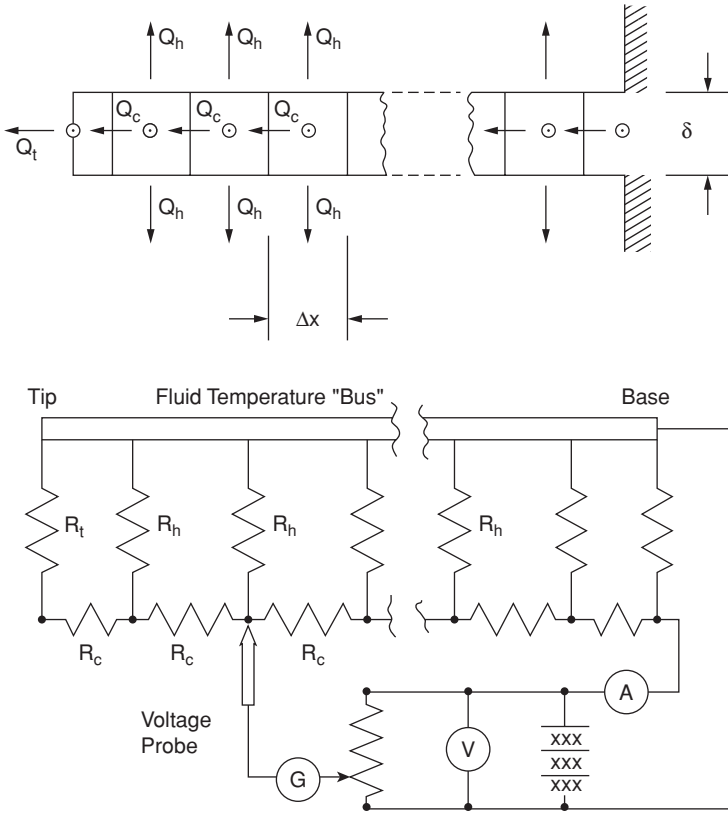
FIGURE 5.2. Electrical analogy for heat transfer in an air-cooled fin for cryogenic service [17]. The conduction thermal resistance is $R_C = 1/k_t P$, the convection thermal resistance is $R_h = 1/(2h_C P \Delta x)$, where P is the width of the fin, and $R_t = 1/h_C P(\Delta x + \delta p)$ is the convection resistance at the fin tip, where δ is the thickness of the fin.

the changes in color (or temperature) are recorded by a high-speed color video camera at approximately 200 frames/s. The system is calibrated by using a known temperature field, and then the model temperatures are determined by comparison of a particular combination of the red–green–blue hue ratios through a computer data-reduction program.

5.4 Gas Separation Systems

As was the case for thermal design, the principles of design of columns for gas sepa-ration were based on graphical techniques in the 1950s. The enthalpy–composition or $(h–x)$ diagram was used to determine the number of "theoretical plates" (plates on which the liquid and vapor are in thermodynamic equilibrium) for air separation
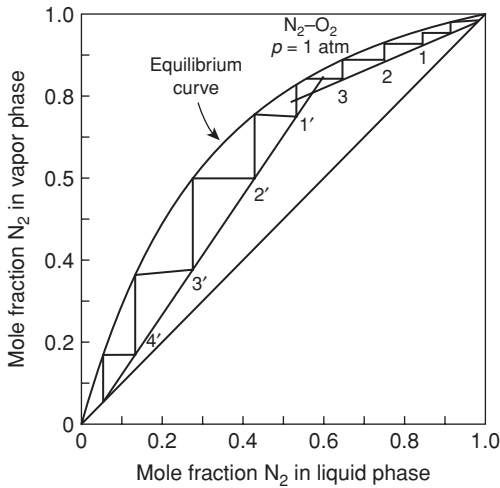
FIGURE 5.3. McCabe graphical method for determination of the number of theoretical plates in an air separation column. The equilibrium curve is given by Equation (5.18). The plot is for a liquid air distillation column (N_2 and O_2 only) operating at 101.3 kPa (1 atm).

systems [20]. An alternate graphical method, shown in Figure 5.3, called the *McCabe–Thiele method* [21], was also used to determine the number of theoretical plates; and with data on the plate efficiency, the number of actual plates could be found graphically.

The equilibrium curve shown in Figure 5.3 was obtained from the temperature–composition data at the column pressure. The vapor mole fraction y_1 of the lower boiling-point component (nitrogen in this example) was related to the liquid mole fraction of the same component x_1 by selecting the values from the dew-point curve and bubble-point curve at the same temperature for the N_2–O_2 mixture.

The "operating line" for the upper section (*enriching section*) above the feed plate was found from the following expression for the two-component mixture [22]:

$$(y_1)_n = \frac{L_{n+1}}{V_n}(x_1)_{n+1} + \frac{n_D x_{1,D}}{V_n}. \tag{5.10}$$

A similar expression may be written for the lower section (*stripping section*) of the column. The operating line relates the composition of the vapor leaving the nth plate to the composition of the liquid leaving the $(n + 1)$th plate.

The quantity (L_{n+1}/V_n) is called the *reflux ratio*, which is the ratio of liquid leaving the $(n + 1)$th plate (and entering the nth plate) to the vapor leaving the nth plate. The reflux ratio is related to the material enthalpies and heat transfer rate Q_D in the condenser.

$$\frac{L_{n+1}}{V_n} = \frac{(Q_D/n_D) + h_D - H_n}{(Q_D/n_D) + h_D - h_{n+1}}. \tag{5.11}$$

The quantity h_D is the enthalpy of the product material leaving the condenser, or the *top product*, which leaves the column at a molar flow rate of n_D. H and h are the vapor enthalpy and liquid enthalpy, respectively. The constant term in

Equation (5.10) is related to the reflux ratio:

$$\frac{n_D}{V_n} = 1 - \frac{L_{n+1}}{V_n}. \tag{5.12}$$

The vertical construction lines in Figure 5.3 correspond to the liquid on the corresponding plate or condenser surface. The example shown in Figure 5.3 is for an N_2–O_2 column operating at 101.3 kPa (1 atm) with a condenser heat transfer rate of 4745 J/mol and a top product leaving as a saturated vapor with a N_2 mole fraction of 0.95. The operating line equation for this example is as follows:

$$(y_1)_n = 0.426 \, (x_1)_{n+1} + (0.574)(0.95). \tag{5.13}$$

From the construction shown in Figure 5.3, the required number of theoretical plates for the enriching section is found to be four theoretical plates plus the condenser surface. If the plate efficiency is 80%, then the number of plates required in the enriching section would be $(4/0.80) = 5$ plates. Similarly, we find that four theoretical plates are required for the stripping section.

There are several restrictions that apply for the McCabe–Thiele graphical method. The method is limited to the analysis of columns with mixtures of only two components. Separation of multicomponent mixtures, such as N_2–O_2–Ar mixtures, could not be accommodated with the McCabe–Thiele method. In addition, the enthalpies of the liquid phase and vapor phase should not vary significantly with composition, or the accuracy of the method would be compromised.

Instead of using a graphical technique, air separation column design is carried out with the aid of a computer system today. The governing equations are solved directly for each plate in the column. For example, if the conservation of component mass is applied for the nth plate in the enriching section, then the following set of equations is obtained:

$$(y_i)_n - \frac{V_{n-1}}{V_n}(y_i)_{n-1} - \frac{L_{n+1}}{V_n}(x_i)_{n+1} + \frac{L_n}{V_n}(x_i)_n = 0. \tag{5.14}$$

The reflux ratio for the enriching section may be evaluated from Equation (5.11), and the other ratios may be found from the conservation of energy equation for the nth plate:

$$\frac{V_{n-1}}{V_n} = \frac{H_n - h_n}{H_{n-1} - h_n} - \frac{h_{n+1} - h_n}{H_{n-1} - h_n}\frac{L_{n+1}}{V_n}, \tag{5.15}$$

$$\frac{L_n}{V_n} = \frac{H_n - h_n}{H_{n-1} - h_n} + \frac{H_{n-1} - h_{n+1}}{H_{n-1} - h_n}\frac{L_{n+1}}{V_n}. \tag{5.16}$$

The Murphy plate efficiency for the ith component on the nth plate $(E_i)_n$ may be introduced to determine the number of "actual" plates:

$$(y_i)_n = (y_i)_{n-1} + (E_i)_n \left[(K_i)_n \, (x_i)_n - (y_i)_{n-1}\right]. \tag{5.17}$$

Curve-fit data are used for the relations between the liquid mole fraction of the ith component x_i and vapor mole fraction of the same component y_i on the nth

plate in thermal equilibrium:

$$(y_i)_n^{\text{eq}} = (K_i)_n (x_i)_n . \tag{5.18}$$

The distribution coefficient for the ith component K_i is a function of temperature. For example, the distribution coefficients for H_2, HD, and D_2 may be determined from an expression of the following form [23]:

$$\ln \left(\frac{K_i p}{p_{\text{ref}}} \right) = C_1 - \frac{C_2}{T} + C_3 T. \tag{5.19}$$

The quantity p is the mixture pressure, p_{ref} is a reference pressure (usually 101.325 kPa), and C_1, C_2, and C_3 are constants for a particular component of the mixture.

The set of simultaneous equations, Equations (5.14)–(5.19), may be solved by matrix techniques. The enthalpies are functions of composition and are obtained from real-gas equations of state, such as the modified Benedict–Webb–Rubin equation, and the generalized thermodynamic relations or from the commercially available thermodynamic property computer programs. The temperature of the fluid on each plate is found by iteration from the requirement that $\sum(y_i)_n = 1$ and $\sum(x_i)_n = 1$.

5.5 Fluid Flow and Convective Heat Transfer

The analysis and design of fluid flow systems and convection heat transfer problems in the 1950s involved empirical correlations based on experimental data, except for some special geometries, such as laminar flow through a tube and laminar flow over a flat plate. To generalize the relationships, dimensionless moduli, such as the Reynolds number and friction factor, were often used. For example, the experimental data for forced convection heat transfer and pressure drop for flow through woven-screen matrices used in cryogenic regenerators was correlated by an equation of the following form [24]:

$$f = \frac{C_1 \left(1 + C_2 \, \text{Re}^{0.88}\right)}{\text{Re}}, \tag{5.20}$$

$$j_{\text{H}} = \frac{Nu}{\text{Re} \, \text{Pr}^{2/3}} = C \, \text{Re}^{-n}. \tag{5.21}$$

The constants C_1, C_2, C, and n are functions of the void volume or porosity of the screen matrix and numerical values are found by least-squares curve-fitting techniques. For example, the constants C and n are given by the following empirical expressions:

$$C = 1.415 - 2.490 \, (1 - e_v), \tag{5.22}$$

$$n = 0.483 - 0.236 \, (1 - e_v). \tag{5.23}$$

The quantity e_v is the void volume or porosity of the screen. The range of validity of the empirical correlations was limited to the range of variables used in obtaining

the experimental data on which the correlation was based. For example, Equations (5.22) and (5.23) are valid for the range $0.55 < e_v < 0.85$.

With the development of complex CFD programs and computers with a large quantity of computing and storage capacity, it is possible to model a wide variety of components used in cryogenic fluid flow and convective heat transfer applications today. For example, a FLUENT® CFD software package was used to model and analyze the pressure drop and fluid flow through a screen regenerator under both steady unidirectional flow and oscillating flow conditions [25]. For one of the models, a total of 6.7 million elements were used, and the time for generation of the steady flow solution was 4 h with three parallel processors with 12 GB of memory. Both the pressure distribution and velocity distribution was obtained in the CFD solution. This amount of data was extremely difficult, if not impossible, to obtain experimentally in the 1950s.

The analysis and design of plate-fin heat exchangers represents another area in which CFD programs have allowed the solution of thermal and hydraulic problems that could be solved only by experimental methods in the 1950s. Plate-fin heat exchangers were introduced in gas turbine systems in the 1940s and were used in some cryogenic systems in the 1950s. Researchers at Stanford University initiated a program in 1947 to measure experimentally the friction factors and convective heat transfer coefficients for a variety of plate-fin geometries, including the offset strip-fin matrix [26]. The experimental data were presented in graphical and tabular forms in terms of dimensionless moduli (friction factor, Reynolds number, and Colburn J-factor). A multiple-regression power-law correlation was later developed to predict the values of the friction factor and Colburn J-factor for the offset strip-fin array [27].

In recent years, a general purpose CFD code called PHOENIX® has been used to solve the governing partial differential equations numerically to obtain the fluid velocity field and friction factor and to obtain the temperature field and heat transfer coefficient for forced convection heat transfer in an offset strip-fin array used in present-day cryogenic liquefaction and refrigeration systems [28]. Solutions for different fin spacing and fin dimensions were determined by the CFD code in a much shorter time and with a lower cost than that required for an experimental solution.

5.6 Technical Presentations

There has also been progress in the principles of presentation of papers at the Cryogenic Engineering Conference since the initial conference. The standard technique of presentation of data and results during the 1950s and 1960s involved the use of 35 mm slides and a carousel projector. Problems were often encountered with slides being loaded upside down or reversed in the carousel. During the 1970s, slides were used by many presenters; however, some presenters began using transparencies and an overhead projector for information presentation. The cost for preparation of the transparencies was much less than the cost for slides, because

the camera system needed for slide preparation was not required for transparencies. As computer tools improved, presenters began using computer-generated slides in their presentations. Graphs, pictures, etc. could be "scanned" by the computer and converted to files within the computer.

At the 2005 Cryogenic Engineering Conference, held in Keystone, CO, August 29–September 2, 2005, technical presenters utilized projectors driven by a laptop computer and a presentation program, such as PowerPoint®, which has become almost universally used in technical presentations today. The PowerPoint® presentations were transferred from the flash memory unit of the presenter to the laptop computer available in each room in which presentations were made. Both slides and short film clips could be presented through the same projection system, and the problem of the 1960s of changing back and forth from carousel projectors and movie projectors during a presentation was eliminated.

5.7 Conclusions

During the 50 years following the first Cryogenic Engineering Conference, much progress has been made in the design and analysis principles used in cryogenic systems, as is evident in the papers presented in the 50 volumes of *Advances in Cryogenic Engineering*, the collection of peer-reviewed papers from the conferences. Many of the advances were directly influenced by the use of the digital computer in design and analysis of thermal, thermodynamic, and mechanical systems.

Nomenclature

A_c	pipe cross-sectional area, m²
C, C_1, C_2, C_3	constants
c_p	fluid specific heat J/(kg K)
D	pipe inside diameter, m
e_v	void volume or porosity of wire matrix
$(E_i)_n$	Murphy efficiency for the ith component on the nth plate
f	friction factor
g	local acceleration due to gravity, m/s²
g_c	units conversion factor, 1 kg m/(N s²)
h_C	convective heat transfer coefficient, W/(m² K)
h_n	molar enthalpy of liquid on nth plate in a column, J/mol
h_1, h_2	enthalpy at the pipe inlet, outlet respectively, J/kg
H_n	molar enthalpy of vapor on nth plate in a column, J/mol
j_H	Colburn J-factor for heat transfer
J	"mechanical equivalent of heat"
k	thermal conductivity W/(m K)
K_i	distribution coefficient for the ith component
[K]	thermal conductivity matrix, W/(m³ K)
L	pipe length, m

L_{n+1}	molar liquid flow rate leaving the $(n + 1)$th plate, mol/s
m	mass flow rate, kg/s
[M]	thermal mass matrix, J/(m³ K)
n	constant
n_D	molar flow rate of the top product in a column, mol/s
Nu	Nusselt number, defined as equal to $h_C D/k$
p	pressure, Pa
p_0	pressure at the pipe inlet, Pa
p_{ref}	reference pressure, Pa
P	width of fin, m
Pr	Prandtl number, defined as equal to $\mu c_p/k$
q	heat transfer per unit mass, J/kg
q''	heat transfer rate per surface area of pipe, W/m²
Q_D	heat transfer rate from condenser in a column, W
$\{\mathbf{Q}_{gen}\}$	heat generation rate vector, W/m³
R	gas constant, J/(kg K)
Re	Reynolds number, defined as equal to $D(m/A_c)/\mu$
T	temperature, K
T_0	fluid absolute temperature at the pipe inlet, K
Δt	time increment, s
V_n	molar flow rate of vapor leaving the nth plate, mol/s
$\mathbf{V}_1, \mathbf{V}_2$	fluid velocity at the pipe inlet, outlet respectively, m/s
w	work per unit mass, J/kg
$(y_i)_n$	mole fraction of the ith component leaving the nth plate (vapor phase), mol
$(x_i)_n$	mole fraction of the ith component leaving the nth plate (liquid phase), mol
Δx	space increment, m
z_1, z_2	elevation of the pipe inlet and outlet, respectively, m

Greek symbols

α	thermal diffusivity, m²/s
δ	thickness of fin, m
λ	heat of vaporization, J/kg
μ	viscosity, Pa s
ρ	density, kg/m³

References

1. Jacobs, R.B., "Long Distance Transfer of Liquefied Gases," *Advances in Cryogenic Engineering*, Vol. 2, Plenum Press, New York, 1960, 303–317.
2. Gartling, D.K., "A Test Problem for Outflow Boundary Conditions–Flow Over a Backward-Facing Step," *International Journal for Numerical Methods in Fluids*, 11, 953–967, 1990.

3. Scott, R.B., *Cryogenic Engineering*, D. van Nostrand, Princeton, NJ, 1959, pp. 262–319.

4. Din, F., *Thermodynamic Functions of Gases*, Butterworth, London, 1956.

5. Mann, D.B., "The Thermodynamic Properties of Helium from 3 to 300 K Between 0.5 and 100 Atmospheres," *NBS Tech. Note 154*, US Government Printing Office, Washington, DC, 1962.

6. Dean, J.W., "A Tabulation of the Thermodynamic Properties of Normal Hydrogen from Low Temperatures to 300 K and from 1 to 100 Atmospheres," *NBS Tech. Note 120*, US Government Printing Office, Washington, DC, 1962.

7. Strobridge, T.R., "The Thermodynamic Properties of Nitrogen from 64 to 300 K Between 0.1 and 200 Atmospheres," *NBS Tech. Note 154*, US Government Printing Office, Washington, DC, 1962.

8. Weisend, J.G., *Handbook of Cryogenic Engineering*, Taylor and Francis, Philadelphia, PA, 1998, pp. 21–71.

9. Hohmann, C., and Patterson, W., "Cryogenic Systems as Auxiliary Power Sources for Aircraft and Missile Applications," *Advances in Cryogenic Engineering*, Vol. 4, Plenum Press, New York, 1960, pp. 184–195.

10. McAdams, W.H., *Heat Transfer*, 3rd ed., McGraw-Hill, New York, 1954, pp. 19–52.

11. Kreith, F., *Principles of Heat Transfer*, 1st ed., International Textbook Co., Scranton, PA, 1958, pp. 153–168. See also Schmidt, E., *Einführung in die technische Thermodynamik* (*Introduction to Engineering Thermodynamics*), Springer-Verlag, Berlin, 1936, p. 262. English translation, Keston, J., *Thermodynamics*, Oxford University Press, New York, 1949.

12. Kreith, F., and Bohn, M.S., *Principles of Heat Transfer*, 5th ed., West Publishing, St Paul, MN, 1993.

13. Barron, R.F., *Cryogenic Heat Transfer*, Taylor and Francis., Boca Raton, FL, 1999, p. 2.

14. Moaveni, S., *Finite Element Analysis*, Prentice-Hall, Upper Saddle River, NJ, 1999.

15. Reddy, J.N., and Gartling, D.K., *The Finite Element Method in Heat Transfer and Fluid Dynamics*, 2nd ed., CRC Press, Boca Raton, FL, 2000, pp. 45–48.

16. Kropschot, R.H., Knight, B.L., and Timmerhaus, K.D., "Thermal Diffusivity of Powder Insulation," *Advances in Cryogenic Engineering*, Vol. 14, Plenum Press, New York, 1969, pp. 224–229

17. Schneider, P.J., *Conduction Heat Transfer*, Addison-Wesley, Reading, MA, 1955, pp. 318–361.

18. Kayan, C.F., and Gates, R.G., "Performance Prediction of Low Temperature Air-Cooling Extended Surface by Several Comparative Methods," *Advances in Cryogenic Engineering*, Vol. 3, Plenum Press, New York, 1960, pp. 325–341.

19. Newton, P.J., Yan, Y., Stevens, N.E., Evatt, S.T., Lock, G.D., and Owen, J.M., "Transient Heat Transfer Measurements Using Thermochromic Liquid Crystal," *Int. J. Heat and Fluid Flow*, 24, 14–22, 1981.

20. Ruhemann, M., *The Separation of Gases*, 2nd ed., Oxford University Press, London, 1949, pp. 146-162.

21. McCabe, W.L., and Thiele, E.W., *Ind. Engr. Chem.*, 17, 605, 1925.

22. Barron, R.F., *Cryogenic Systems*, 2nd ed., Oxford University Press, New York, 1985, pp. 179–184.

23. Wooley, H.W., Scott, R.B., and Brickwedde, F.G., *J. Res. Nat. Bur. Standards*, 41, 379, 1948.

24. Tong, L.S., and London, A.L., "Heat Transfer and Flow Friction Characteristics of Woven-Screen and Crossed-Rod Matrices," *Transactions of ASME*, 79, 1558–1570, 1957.
25. Yarbrough, A.S., Flake, B.A., and Razani, A., "Computational Fluid Dynamic Modeling of Pressure Drop Through Wire Mesh Screen Regenerators," *Advances in Cryogenic Engineering*, Vol. 49, American Institute of Physics, Melville, NY, 2004, pp. 1138–1145.
26. Kays, W.M., and London, A.L., *Compact Heat Exchangers*, 2nd ed., McGraw-Hill, New York, 1964.
27. Joshi, H.M., and Webb, R.L., "Prediction of Heat Transfer and Friction in the Offset Strip Fin Array," *International Journal of Heat and Mass Transfer*, 30, 69–84, 1987.
28. Maiti, D., and Sarangi, S., "Fluid Flow and Heat Transfer in Offset Strip-Fin Heat Exchangers," *Proceedings of the 18th International Cryogenic Engineering Conference*, Narosa Publishing House, New Delhi, India, 2000, pp. 291–294.

6
Insulation Progress since the Mid-1950s

K.D. TIMMERHAUS

University of Colorado, Boulder, Colorado, CO 80309, USA

Abstract

Storage vessel and cryostat design for modern cryogenic systems has become rather routine as the result of the wide use of and application of cryogenic fluids. Such vessels for these fluids range in size from 1 L flasks used in the laboratory for liquid nitrogen to the more than 200,000 m^3 double-walled tanks used for temporary storage of liquefied natural gas before being transported overseas to their final destination. These storage vessels for cryogenic fluids range in type from low-performance containers insulated with rigid foam or fibrous insulation to high-performance containers insulated with evacuated multilayer insulations. The overriding factors in the type of container selected normally are of economics and safety. This paper will consider various insulation concepts used in such cryogenic storage systems and will review the progress that has been made over the past 50 years in these insulation systems.

6.1 Introduction

The major concern in the selection of the proper insulation for a cryogenic system is the reduction in the heat leak. The insulation strategy is to minimize the radiative heat transfer, minimize the convective heat transfer, and introduce a minimum of solid conductance media. Factors considered in the selection of the most suitable choice generally place thermal effectiveness and cost at the top of the list. However, other factors, such as convenience, ruggedness, volume required, mass involved, ease of fabrication, and handling, also need to be considered. Additionally, one must also consider the specific characteristics of the storage container or transfer line and what constraints they place on the insulation choice. These system characteristics include such items as type of liquid to be stored or transported, whether usage is intermittent or continuous, the environment surrounding the system, or the safety of the system. However, the choice of the insulation is governed by an attempt to balance the cost of the installed system with the savings anticipated from the lowered energy requirements.

The various types of insulation available to the designer of storage and transfer systems in the early 1950s included (1) vacuum insulation, (2) powder insulation, (3) foam and fiber insulation, and (4) some special purpose insulations. Multilayer insulation as an insulation concept was proposed by Peterson [1] in 1958. Once it became evident that this type of insulation could provide the possibility of an order of magnitude lower thermal conductivity for the insulation, many researchers turned their attention to improvements in the concept and established fabrication and operating guidelines. For example, from the more than 120 research papers covering some aspect of cryogenic insulation published in *Advances in Cryogenic Engineering* over the 20-year period beginning in 1960, more than 45% of the research activity was devoted to some aspect of multilayer insulation. Since 1980 this flurry of activity has decreased considerably as researchers have established the thermal effectiveness limits associated with multilayer insulation. Nevertheless, the more important advances associated with this high-effectiveness insulation that have occurred during the past 50 years will be noted in Section 6.5.

Heat transfer through these various insulations can occur by several different mechanisms, but generally involves solid conduction, gas convection and conduction, and radiation. The purpose of any insulation is to minimize the total transfer of heat by the various mechanisms. The apparent thermal conductivity of an insulation, measured experimentally to incorporate all of these heat transfer modes, still offers the best means by which to compare the effectiveness of any insulation that has undergone changes in materials used and modifications in operational procedures or process conditions.

6.2 Vacuum Insulation

The effectiveness of vacuum insulation in minimizing heat leak into cryogenic systems was recognized over 100 years ago by Sir James Dewar. Because of its simplicity in insulating cryogenic fluids, there has been little progress in trying to improve the performance associated with vacuum insulation over the past 50 years. The use of floating shields within the vacuum space between the warm and cold surfaces of a storage dewar or cryogenic engineering container involves one modification in this type of insulation system that has been considered. Another improvement in vacuum insulation has been the search for specialized polymers or paints that can be used to reduce the emissivity that exists between the warm and cold surfaces of these cryogenic systems. These concepts will be considered later in the discussion.

Of the several modes of heat transfer, vacuum insulation greatly minimizes gaseous convection. In addition, depending on the level of vacuum achieved, it can also significantly reduce the heat conduction through the residual gas. When the radiation from the warm surface to the cold surface is the dominating mode of heat transfer, the heat transferred can be approximated by a modified Stefan–Boltzmann equation as developed by Barron [2].

In order to reduce the emissivity factor and thereby decrease the heat transfer by radiation, floating shields with low emissivity surfaces can be inserted in the vacuum space between the warm and cold surfaces. The insertion of 10 floating low-emissivity shields in the vacuum space while avoiding thermal shorts between the floating shields can reduce the radiant heat transfer by as much as 300 times.

Even though radiation generally represents the key mechanism by which heat is transferred through a vacuum space and heat transfer by conduction through the supports is considered separately, gaseous conduction may also contribute to the total heat load [3]. At atmospheric pressure and above, the heat load is independent of pressure and a linear temperature gradient exists between the warm and cold surfaces. However, when high vacuum (1.3×10^{-10} MPa) conditions are established, free molecular conduction can exist, since the mean free path of the gas molecule is large relative to the distance between the two surfaces involved. When free molecular conduction exists, the heat flux per unit surface area varies linearly with changes in pressure. To determine, whether free molecular conduction is significant in the cryogenic system requires comparing the distances between the two surfaces that enclose the vacuum with the mean free path of the residual gas molecules in the vacuum space. Recognizing that the energy transferred per unit area of surface by free molecular conduction between these two surfaces is the product of the mass energy per unit mass, using the kinetic theory of gas and ideal gas law, and making some simplifying assumptions, permits evaluation of the free molecular gas conduction between the two surfaces. Computer programs are now available to perform these calculations.

6.3 Powder Insulation

The primary characterization of most powder insulations includes low thermal conductivity, low density, and particle size distribution to reduce shock and vibration effects. Powders have been used either in an evacuated or nonevacuated mode. One method of application is usually more suitable than the other for a given system. In most cases, the small particle size of the powder limits the gaseous heat transfer in evacuated powders to free molecular conduction. Often, the heat transfer by the residual gas is further reduced by the lower vapor pressure of the powder itself. The powders widely used at cryogenic temperatures include perlite, colloidal silica and silica aerogel. Other powders occasionally used are mica, diatomaceous earth, carbon, calcium, silicate, and plastic or glass microspheres. Recent interest has been generated in microspheres as a replacement for perlite [4].

6.3.1 Nonevacuated Powders

Insulation with specific nonevacuated powders is attributed to the reduction or minimization of convective heat transfer due to the small gas voids present within the powder. The presence of the fine powder also reduces radiation and inhibits gas

conduction. This leaves solid conduction and gas conduction as the predominant heat transfer mechanisms. Using the experience developed by Nusselt and Bayer [5] and making some simplifying assumptions justifiable at cryogenic temperatures reveals that the thermal conductivity of nonevacuated powders approaches the thermal conductivity of the residual gas. In the case of very fine powders, where the gas voids are smaller than the mean free path of the gas, nonevacuated powder insulation may even provide a lower conductivity than the residual gas by itself [6].

Like most insulation materials, nonevacuated powders have their limitations. For example, the fill-gas must be unreactive and compatible with the powder material. A vapor barrier is necessary around the powder to prevent diffusion of air or water into the insulation. These vapor barriers generally take the form of structural, membrane, or coating barriers.

Another limitation of most powder insulations, regardless of whether they are nonevacuated or evacuated powders, is their tendency to pack as a result of thermal contractions upon cooldown of a storage container and thermal expansion of the same container upon warmup. This action, as experienced in many liquid natural gas containers insulated with perlite powder, has created higher than anticipated solid conduction in one area of the container while leaving larger than expected insulation voids in another area [7]. This variation in packing density appears to have been lessened by the use of glass microspheres as the insulation material [8,9].

6.3.2 Evacuated Powders and Fibrous Insulations

To decrease the thermal conductivity of nonevacuated powders and fibrous insulations is to reduce the residual gas pressure in the insulation space. The effect of this reduction in gas pressure on the apparent thermal conductivity of several powder insulations is shown in Figure 6.1 [10]. Note that there are three distinct dependencies of thermal conductivity on residual gas pressure. Upon reducing the gas pressure from atmospheric to pressures around 1.3×10^{-3} MPa to about 1.3×10^{-6} MPa there is a linear log–log dependency of the thermal conductivity on gas pressure due to the existence of free molecular conduction. Upon further reducing the pressure below 1.3×10^{-6} MPa, the thermal conductivity again becomes independent of pressure and approaches a value that depends only on the heat transfer mechanisms of radiation and solid conduction.

For highly evacuated powders operating between room temperature and liquid nitrogen temperatures, calculations show that the heat transfer by radiation is normally larger than that by solid conduction. Thus, within this temperature range, evacuated powders can exhibit lower thermal conductivities than by vacuum alone, since the powders limit the radiative heat transfer. However, heat transfer by solid conduction with evacuated powder insulations becomes larger than that for radiation below liquid nitrogen temperatures. Therefore, vacuum insulation alone is frequently better than the highly evacuated powder.

The apparent thermal conductivity of a powder insulation is a function of the thermal conductivities of the powder and interstitial gas and the ratio of solid volume to total volume at cryogenic temperatures. The Fourier rate equation for
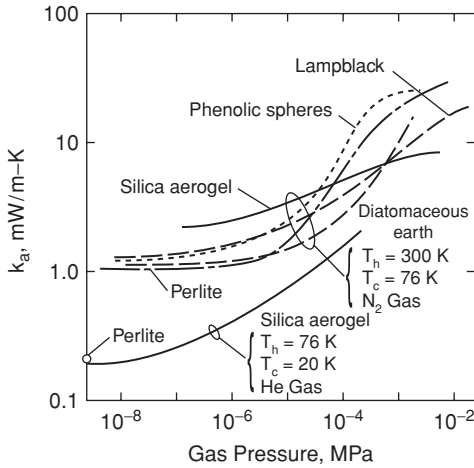
FIGURE 6.1. Apparent thermal conductivity of several powder insulations as a function of residual gas pressure.

conductive heat transfer is generally used to calculate the heat transfer rate per unit area through the evacuated powder insulations.

6.3.3 Opacified-Powder Insulations

The radiant heat transfer rate in powders can be significantly reduced by the addition of copper or aluminum flakes [11]. The insulating ability of these opacified-powder insulations approaches an optimum when the powder contains between 35 and 50 wt% of the metal flakes. Since aluminum has a large heat of combustion with oxygen, copper flakes are generally preferred. Even though thermal conductivity of the evacuated powder may be reduced significantly by using these metal opacifiers, there is a tendency for these flakes to settle with time and greatly increase the solid conduction mode of heat transfer in the lower section of the storage container. Work by Xu et al. [12] indicates that there is an optimum size of the metal flakes that will minimize its settling with time.

6.3.4 Microsphere Insulation

As noted earlier, microsphere insulation is considered a special type of evacuated powder insulation. Good thermal insulation performance has been achieved using packed, hollow glass spheres, typically of a size ranging from 15 to 150 μm in diameter and sometimes coated on the exterior of the glass spheres with a low-emittance film. These hollow spheres, with a wall thickness of 0.5 to 2.0 μm, substantially increase the conduction thermal resistance but significantly reduce the heat capacity and mass relative to the normal powder insulation. Hollow glass microspheres offer a lightweight and low heat capacity alternative to multilayer

insulation. Even though heat transfer rates for glass microsphere insulation are as much as seven times greater than installed multilayer insulation, their thermal isotropy and ease of use make them a potential choice for a variety of applications.

6.4 Foam and Fiber Insulations

Cryogenic foam insulations, such as polystyrene and polyurethane, are produced by gaseous expansion of organic and inorganic solids. The solid–gas mixture creates a low-density solid with many voids. This relatively lower density, an order of magnitude less than that for powder insulations, results in a smaller heat transfer by solid conduction. On the other hand, the cellular structure of the foam provides continuous paths by which more heat is conducted through the foam than in the powder insulations, where the interparticle contact areas are very small. The dominant heat transfer mechanism is conduction through the interstitial gas and there is a small contribution from radiation. Obviously, if the volume of the voids in the foam is decreased to permit free molecular gas conduction, then the overall performance of the insulation could be improved. However, since the thermal conductivity of these foams is also dependent upon the bulk density and mean temperature of the insulation, such attempts may provide only minimal improvement.

The major advantages of foam insulations are their ease of fabrication, relatively low cost, and self-supporting structure. However, one of the major disadvantages of foams, besides their higher thermal conductivity, is their large thermal expansion. In general, the thermal expansion coefficient of the foams considered is two to five times that of aluminum and four to ten times that of steel. Because of this large thermal expansion, it is necessary that the foam be designed and applied to accommodate this difference. The foam shrinks more than the metal when the foam is in contact with the cold surface, creating cracks that open passageways for the admission of both water vapor and air, which significantly increases the thermal conductivity of the insulation [13,14]. Several solutions to this problem of thermal expansion have been investigated, including the addition of glass fibers, reinforcing threads, expansion joints and the development of vacuum-panel insulation.

Another problem of concern with foams is the removal of the expansion gas from the interstices of the cellular foam. This gas removal is quite difficult and time consuming, because the gas-filled cells are closed. However, since the cells are semipermeable, atmospheric gases can slowly diffuse into the cellular foam and noticeably increase the apparent thermal conductivity. If the gases are helium or hydrogen diffusing into the cellular structure, then there can be a significant increase in the thermal conductivity of the foam.

Fiber insulations are generally preferred in insulation applications where vibration and shock to the cryogenic system are anticipated. For such applications, submicrometer-diameter glass fibers have been used [15]. Care must be exercised in the packing of the fiber insulation to eliminate gaps in the insulation resulting from the movement of components located in the insulation space during cooldown.

6.5 Multilayer Insulation

The most important advancement in cryogenic insulation over the past 50 years has been the development of multilayer insulation, also known as MLI. The concept of multilayer insulation was motivated by an attempt to minimize all possible modes of heat transfer. Multilayer insulation generally involves 30 to 80 layers of low-emittance radiation shields separated either by low-conductivity spacers or by crinkling or embossing the shields so that, when placed next to each other in the vacuum space, the shields only touch each other at a few discrete locations. For low-temperature applications the radiation-reflecting shield is many times a 6 μm aluminum sheet. However, for greater strength and ease in application, the shield is often a thin (5–76 μm) plastic material, such as polyethylene terepthalate (Mylar®), coated on one or both sides by a thin vapor-deposited layer ($\sim 10^{-8}$ m) of high-reflectance metal such as aluminum. Spacer materials range from very coarse nylon or silk net to more continuous substances such as low-density foam or glass-fiber mat. Most common among these are glass-fiber spacers such as Dexiglas® (71 μm nominal thickness) and Tissuglas® (15 μm nominal thickness). For example, Ohmori et al. [16] reported on the thermal performance of a number of multilayer insulation systems using different materials for the shields and spacers. They noted that a system using double aluminized Mylar® film with a fiberglass mat spacer combination provided better results than a system using dimpled and perforated double-aluminized Mylar® film without spacers. A search of the literature provides results for many different combinations of shields and spacers [17–26].

The multilayer assembly is placed perpendicular to the flow of heat in the insulation space for the cryogenic system. The space containing the multilayer assembly is evacuated and baked-out at an elevated, but safe, temperature for an extended period of time to remove as much of the adsorbed residual gases as possible [27]. Since a high vacuum in the insulation space is required to attain low apparent thermal conductivity values for the cryogenic system, a getter material such as activated charcoal or molecular sieve (cooled by thermal contact with the inner cold surface) is normally used to adsorb gases that desorb from the various surfaces in the evacuated insulation space. When the optimum density of multilayer insulation is properly applied, an apparent thermal conductivity as low as 1×10^{-3} W/mK can be achieved between temperature boundaries of 20 and 300 K [28].

Radiant heat transfer is directly proportional to the emissivity between the warm and cold surfaces and inversely proportional to the number of shields. By using many overlapping layers of low-emissivity material, radiation is significantly reduced as long as there is no compression load placed on the layers because of the space limitations in the evacuated insulation space [29]. The low conductivity of the fiberglass used as spacer material, the irregular size and geometry of the fibers, and the numerous discontinuities of the fibers all tend to reduce the solid conduction. Finally, by evacuating the gas from between the many shields, gas convection can be minimized and only free molecular conduction persists. Figure 6.2 shows
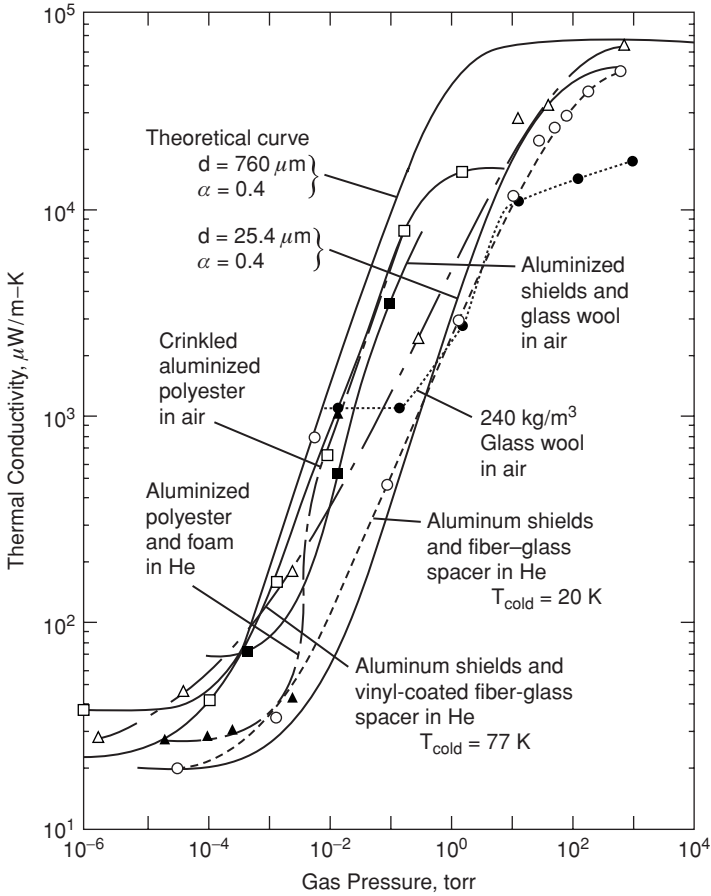
FIGURE 6.2. Effect of residual gas on the thermal conductivity of selected multilayer insulations.

the variation in apparent thermal conductivity of multilayer insulation as a function of residual gas pressure for several insulating material combinations [30].

For highly evacuated multilayer insulation, on the order of 1.3×10^{-10} MPa, heat is transferred through the insulation primarily by radiation and solid conduction and minimally by gas conduction. McIntosh [31] has presented a computational program that evaluates the heat contribution for each of these heat transfer modes for each layer of the multilayer insulation. In this calculation, one layer is defined as the combination of a reflecting shield and associated spacer, whereas the bulk density of the multilayer insulation is a combination of the spacer material per unit area and the number of layers per unit thickness. The resulting equation and calculation procedure provide the tools necessary to optimize the insulation with respect to number of layers, layer density, insulation mass, and separator configuration. Use of different thicknesses of spacer material (in strips) makes it

TABLE 6.1. MLI design guidelines

1	Floating shields, providing no thermal shorts are present, are superior to practical multilayer insulation with separators.
2	Heat transfer per unit area is continuously reduced with an increasing number of reflectors if the layer density does not increase.
3	There is an optimum layer density for each material combination and temperature range.
4	Optimum layer density decreases for lower temperature ranges.
5	For warm temperatures below 150 K, the outer multilayer insulation layer should be a reflector that does not touch the warm surface.

possible to determine variable-density multilayer insulation in which the colder layers have a lower layer density than those close to the warm surface, where thermal radiation has a greater impact [32].

By using the relationship described above, Stochl et al. [33] have established several guidelines useful in multilayer insulation design; these are listed in Table 6.1. Several experimental studies reinforce these conclusions [34,35].

The layer-to-layer calculation, however, does not take into account the effects of penetrations through the multilayer insulation [36], the effects of compressive loads, nor the method of attachment and how these effects may alter the apparent thermal conductivity. For example, Lindquist and Niendorf [37] found that the compression of multilayer insulation by the application of external forces resulted in an appreciable increase in heat flux best described with a linear relationship on a log–log scale. Black and Glaser [38] noted that between compressive loads of 6.9×10^{-5} and 0.10 MPa the heat flux through the multilayer insulation is proportional to the 1/2 to 2/3 power of the externally applied load. However, it has been shown that, once the compressive load is released, the multilayer insulation regains up to 90% of its original thickness and returns to near its original thermal conductivity.

Methods of attachment for multilayer insulation can also alter the apparent thermal conductivity of the insulation. Three basic techniques, developed in the space program, have been used to attach multilayer insulation to a cryogenic container. (Other techniques are also available.) The button type (see Figure 6.3) was developed to support fragile fiberglass spacers with either aluminized Mylar® or aluminum foil radiation shields. The buttons, fabricated of very low-conductivity material, add both a solid heat transfer element and a compressive load factor to the overall insulation conductivity. On the other hand, the shingle and tape methods require adequate strength in the multilayers to permit attachment along one side. Even though the solid heat conduction associated with the button attachments is eliminated, radiation tunneling between the shingles can increase the heat leak.

Another characteristic of multilayer insulation is that the overall thermal conductivities parallel to the radiation shields can be between three and six orders of magnitude greater than those normal to the layers [39,40]. Such a large disparity in the directional thermal resistance can cause problems in thermal insulation design for systems where structural supports and feedlines penetrate the insulation

FIGURE 6.3. Multilayer insulation attachment techniques developed in the US space program.
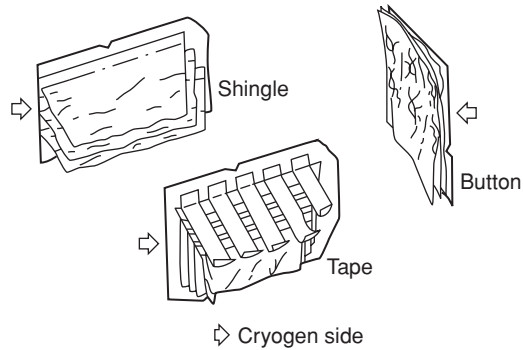
and provide lateral heat leaks at the junctions. An advantage of the aluminized Mylar® over the aluminum–glass fiber combination is that it reduces this lateral heat conduction.

Simply because of the variety of degrading effects on multilayer insulation, the laboratory experimentally determined thermal conductivity values obtained with careful attention to every design and fabrication detail are generally considerably lower than those actually observed in practice. Solutions to these problems generally take the form of improved reflecting shields with lower lateral thermal conductivity and efficient isotropic intermediary insulation systems around the external penetrations. Multilayer insulation, because of its complicated structure, not only is more difficult to apply, but is considerably more expensive than other insulation materials. The use of multilayer insulation is normally reserved for those applications requiring high thermal efficiency. To simplify the installation process and to reduce the material and installation costs, new insulation materials, such as aluminized polyester nonwoven fabric and aluminized carbon-loaded paper, have been developed and show considerable promise in certain applications.

6.6 Summary

As noted in prior sections, cryogenic insulations come in a variety of forms, with each having its own characteristic properties. Some of these properties are qualitative, such as ruggedness, convenience, and ease of fabrication. Other properties are very quantitative, including bulk density, emissivity, moisture content, evacuability, and porosity. The objective in selecting an insulation is to obtain greater savings in reduced cryogenic boiloff than are experienced in the purchase, installation, and maintenance of the insulation material.

It is evident that the most thermally resistant material is quite often not the most adequate insulation for a given application. Cryogenic systems generally have constraints, such as the desire for a low-density material for insulating a component scheduled for space flight. Table 6.2 presents a qualitative analysis of the cryogenic insulations used over the past 50 years.

TABLE 6.2. Advantages and disadvantages of cryogenic insulations used over the past 50 years

Advantages	Disadvantages
Fiberglass paper–aluminum foil combination	
Very low thermal conductivity	Needs high vacuum for best performance
Easily applied to cylindrical shapes	Paper relatively weak and easily torn
Thermal conductivity increases with compression, but less than for other layered insulants	Will not resist appreciable vibration
Can be heated sufficiently for outgassing	Difficult to apply to complex configurations
Not flammable in oxygen	Difficult to evacuate
Synthetic fiber net–aluminum foil combination	
Very low thermal conductivity	Needs high vacuum for best performance
Organic fiber strong and easily handled	Difficult to apply to complex geometries
Dimensionally stable	Upper temperature limit of 425–475 K
Resists vibration	Application skill required for best performance
Can be heated sufficiently for outgassing	Flammable
Organic nets give comparable performance to fiberglass but require fewer reflecting layers	Restricted to nonoxidizing materials
Readily obtained from many suppliers	Difficult to evacuate
Crinkled aluminized Mylar®	
Only single layer for shield and spacer	Does not resist compression
Very low thermal conductivity	Has greatest increase of conductivity with compression for layered insulation
Installation easier than for combination layered insulation	
Easily handled	Needs high vacuum for best performance
Low lateral heat flow	Flammable
Easily evacuated, outgassing completed during aluminizing step	Restricted to non oxidizing materials
Expensive	Nonflammable material is available but more expensive
Fiberglass	
Acceptable thermal conductivity	Requires careful packing for best performance
Fine fibers comparatively easy to handle	Difficult to install in vacuum-insulated vessels
Dimensionally stable	Needs protection from atmosphere
Elastic in compression; allows for contraction and expansion	
Not hygroscopic	
Recoverable after water contact	
Readily available	
Expanded perlite	
Acceptable thermal conductivity	Easily damaged during handling with increase in bulk density
Low density and low cost	Dusty and abrasive
Readily available	Cannot be used to insulate moving parts
Noninflammable	Maintenance may require complete removal of insulant
Non toxic or hygroscopic	Limited transformability
Easy to install in insulation space	Nonelastic in compression and may have insulation gap after pressure release
Flows readily when new	
Easily conveyed pneumatically	
Recoverable even after water contact	

TABLE 6.2. (*Continued*)

Advantages	Disadvantages
Does not cake in use	
Can be produced on site	
Useful in vacuum insulation	
Easy to evacuate	
Silica aerogel	
Acceptable thermal conductivity	Price is about 10 times that of expanded perlite
Lightweight and easy flowing	After water contact forms silica gel on drying
Dimensionally stable when dry	with an increase in bulk density by a factor of
Does not shrink when larger particles are broken	10 and decreased insulation properties
Slight elastic compressibility	
Will not settle due to vibration after initial compaction	Needs protection from atmosphere
Not hygroscopic	
Easy to evacuate	
Foamglass	
Strong structure	Expensive
Readily available	Needs skilled labor for proper installation
Closed pores, not permeable to water	Needs vapor barrier between insulation blocks
Useful as a support for inner vessel	Rather high thermal conductivity
Dimensionally stable	
Not hygroscopic	
Noninflammable	
Foamed plastics	
Lightweight	Needs skilled labor for proper installation
Acceptable thermal conductivity	Has large contraction and expansion
Relatively available in many grades	Upper temperature limit can be as low as 350 K
Useful as support for inner vessel	Foaming materials generally flammable
Available with closed pores, not permeable to water	Unusable in an oxygen-enriched atmosphere
Can be foamed in situ, simplifying installation	Requires nitrogen purge if used below 90 K

References

1. Peterson, P., "Some Means To Improve the Vacuum Insulation of the Dewar Flask," *Sartryck ur TVF*, 1958, p. 157.
2. Barron, R.F., *Cryogenic Systems*, 2nd ed., Oxford University Press, New York, 1985.
3. Scott, R.B., *Cryogenic Engineering*, D. Van Nostrand, Princeton, NJ, 1959, pp. 143-206.
4. Allen, M.S., et al., "Advances in Microsphere Insulation Systems," *Advances in Cryogenic Engineering*, Vol. 49A, American Institute of Physics, New York, 2004, pp. 619–626.
5. Nusselt, W., and Bayer, Z., *Revisions-ver*, Nos. 13 and 14, 1913.
6. Johnson, C.L., and Hollweger, D.J., "Some Heat Transfer Considerations in Nonevacuated Cryogenic Powder Insulation," *Advances in Cryogenic Engineering*, Vol. 11, Plenum Press, New York, 1966, pp. 77–88.

7. Leonhardt, E.H., "Pressure Characteristics of Perlite Insulation in Double-Wall Tanks Under Repeated Thermal Cycling," *Advances in Cryogenic Engineering*, Vol. 15, Plenum Press, New York, 1990, pp. 343–345.

8. Cunnington, G.R., and Tien, C.L., "Apparent Thermal Conductivity of Uncoated Microsphere Cryogenic Insulation," *Advances in Cryogenic Engineering*, Vol. 22, Plenum Press, New York, 1977, pp. 263–270.

9. Fesmire, J.E., and Augustynowicz, S.D., "Thermal Performance Testing of Glass Microspheres Under Cryogenic Vacuum Conditions," *Advances in Cryogenic Engineering*, Vol. 49A, American Institute of Physics, New York, 2004, pp. 612–618.

10. Fulk, M.M., Devereax, R.J., and Schrodt, J.E., "Heat Transfer Through Powders," *Advances in Cryogenic Engineering*, Vol. 4, Plenum Press, New York, 1957, pp. 163-165.

11. Hunter, B.J., et al., "Metal Powder Additives in Evacuated-Powder Insulation," *Advances in Cryogenic Engineering*, Vol. 5, Plenum Press, New York, 1960, pp. 146–156.

12. Xu, L., Gu, A.Z., Wang, R.S., and Li, S.M., "The Effects of Vibration on the Performance of Perlite Vacuum Insulation," *Advances in Cryogenic Engineering*, Vol. 41A, Plenum Press, New York, 1996, pp. 109–116.

13. Gruszcznski, M.J., et al., "Development and Test of a Liquid Hydrogen Propellant Tank Foam Insulation," *Advances in Cryogenic Engineering*, Plenum Press, New York, 1992, pp. 293–298.

14. Yamaguchi, M., Takahashi, K., and Ohmori, T., "Thermal Conductivty of Polyurethane Foam at Liquid Hydrogen Temperature Region," *Advances in Cryogenic Engineering*, Vol. 41A, Plenum Press, New York, 1996, pp. 117–122.

15. Christiansen, R.M., Hollingsworth, M., and Marsh, H.N., "Low-Temperature Insulation Systems," *Advances in Cryogenic Engineering*, Vol. 5, Plenum Press, New York, 1960, pp. 171–178.

16. Ohmori, T., et al., "Thermal Performance of Candidate SSC Magnet Thermal Insulation Systems," *Advances in Cryogenic Engineering*, Vol. 33, Plenum Press, New York, 1988, pp. 323–331.

17. Cunnington, G.R., Keller, C.W., and Bell, G.A., "Thermal Performance of Multilayer Insulations," NASA-CR 72605, 1971.

18. Cunnington, R., "Reducing Boiloff Losses in Cryogenic Storage Systems to the Minimum," *Advances in Cryogenic Engineering*, Vol. 29, Plenum Press, New York, 1984, pp. 767–776.

19. Jacob, S., "Multilayer Insulation in Cryoequipment—A Study of Reference Literature," KfK 5165, 1993-3.

20. Bell, G.A., Nast, T.C., and Wedel, R.K., "Thermal Performance of Multilayer Insulation Applied to Small Cryogenic Tankage," *Advances in Cryogenic Engineering*, Vol. 22, Plenum Press, New York, 1977, pp. 272–282.

21. Boroski, W.N., et al., "Thermal Performance of Various Multilayer Insulation Systems Below 80K," *Supercollider 4*, Plenum Press, New York, 1991.

22. Shu, Q.S., Fast, R.W., and Hart, H.L., "An Experimental Study of Heat Transfer in Multilayer Insulation System from Room Temperature to 77K," *Advances in Cryogenic Engineering*, Vol. 31, Plenum Press, New York, 1986, pp. 455–463.

23. Gonczy, J.D., Boroski, W.M., and Nieman, R.C., "Thermal Performance Measurements of a 100 Percent Polyester MLI System For the Superconducting Super Collider: Part II: Laboratory Results (30K–80K)," *Advances in Cryogenic Engineering*, Vol. 35A, Plenum Press, New York, 1990, pp. 497–506.

24. Getmanets, V.F., et al., "Cryogenic Superinsulations with Increased Efficiency," *Advances in Cryogenic Engineering*, Vol. 43B, Plenum Press, New York, 1998, pp. 1319–1325.
25. Mikhalchenko, R.S., et al., "New Efficient Composite Superinsulations," *Cryogenics*, 32(ICMC Supplement) 60, 1992.
26. Mikhalchenko, R.S., et al., "Study of Heat Transfer in Multilayer Insulations Based on Composite Space Materials," *Cryogenics*, 23, 309, 1983.
27. Glassford, A.P.M., and Lin, C.K., "Outgassing Rate of Multilayer Insulation Materials at Ambient Temperature," *J. Vac. Sci Technol.*, 17(3) 696, 1980.
28. Scurlock, R.G., and Sault, B., "Development of Multilayer Insulations with Thermal Conductivities Below 0.1 μW/cm K," *Cryogenics*, 16, 303, 1976.
29. Ohmori, T., Nakajama, M., Yamomoto, A., and Takahashi, K., "Lightweight Multilayer Insulation to Reduce the Self-Compression of Insulation Films," *Advances in Cryogenic Engineering*, Vol. 47B, American Institute of Physics, New York, 2002, pp. 1565–1572.
30. Green, M.A., "Heat Transfer Through a Multilayer Insulation System as a Function of Pressure in the Cryostat Vacuum Space," *Advances in Cryogenic Engineering*, Vol. 43B, Plenum Press, New York, 1998, pp. 1313–1318.
31. McIntosh, G.E., "Layer by Layer MLI Calculations Using a Separated Mode Equation," *Advances in Cryogenic Engineering*, Vol. 39B, Plenum Press, New York, 1994, pp. 1683–1690.
32. Nedayat, A., Hastings, L.J., and Brown, T., "Analytical Modeling of Variable Density Multilayer Insulation for Cryogenic Storage," *Advances in Cryogenic Engineering*, Vol. 47B, American Institute of Physics, New York, 2002, pp. 1557–1564.
33. Stochl, R.J., et al., "Variable Density MLI Test Results," *Advances in Cryogenic Engineering*, Vol. 41A, Plenum Press, New York, 1996, pp. 101–107.
34. Leung, E.M.W., et al., "Techniques for Reducing Radiation Heat Transfer Between 77 and 4.2 K," *Advances in Cryogenic Engineering*, Vol. 25, Plenum Press, New York, 1980, pp. 489–499.
35. Spradley, I.E., Nast, T.C., and Frank, D.J., "Experimental Studies of MLI Systems at Very Low Boundary Temperature," *Advances in Cryogenic Engineering*, Vol. 35A, Plenum Press, New York, 1990, pp. 477–486.
36. Shu, Q.S., Fast, R.W., and Hart, H.L., "Theory and Technique For Reducing the Effect of Cracks in Multilayer Insulation from Room Temperature to 77 K," *Advances in Cryogenic Engineering*, Vol. 33, Plenum Press, New York, 1988, pp. 291–298.
37. Lindquist, C.R., and Niendorf, L.R., "Experimental Performance of Model Liquid-Hydrogen Space Tankage with a Compressible Superinsulation," *Advances in Cryogenic Engineering*, Vol. 8, Plenum Press, New York, 1963, pp. 398–403.
38. Black, I.A., and Glaser, P.E., "Effects of Compressive Loads on the Heat Flux Through Multilayer Insulation," *Advances in Cryogenic Engineering*, Vol. 11, Plenum Press, New York, 1966, pp. 26–34.
39. Vliet, G.C., and Coston, R.M., "Thermal Energy Transport Parallel to the Laminations in Multilayer Insulation," *Advances in Cryogenic Engineering*, Vol. 13, Plenum Press, New York, 1968, pp. 671–679.
40. Tien, C.L., Jagannathau, P.S., and Chan, C.K., "Lateral Heat Transfer in Cryogenic Multilayer Insulation," *Advances in Cryogenic Engineering*, Vol. 18, Plenum Press, New York, 1973, pp. 118–123.

7

Development of Low-Loss Storage of Cryogenic Liquids over the Past 50 Years

R.G. SCURLOCK

Kryos Technology, 22 Brookvale Rd, Southampton SO17 1QP, UK

Abstract

Since 1954, the extraordinary growth in the use and application of cryogenic liquids has followed very significant improvements in cryogenic insulation. Today, for example, hold-times of 1000 days for liquid helium and liquid hydrogen systems can easily be achieved, in comparison with hold-times measured in hours some 50 years ago. These improvements have also been applicable to the low-loss transport and handling of liquid air gases for an ever-widening range of industrial uses.

Since 1960, the cryogenic liquid hydrocarbon business, including liquefied petroleum gas mixtures of liquid propane and butane, and liquefied natural gas mixtures of liquid methane with ethane and higher hydrocarbons, has expanded rapidly to become a major part of the global energy markets. The use of storage tanks with capacities up to and over $300,000 \, \text{m}^3$, and with hold-times well in excess of 1000 days, has become standard practice.

This review will discuss how applications have become practicable since 1954 through (1) the systematic development of insulations and structural materials and (2) studies on the convective behavior of cryogenic vapor and liquid columns, which have led to design criteria for minimizing heat leaks.

7.1 Introduction

The development of practicable applications of cryogenics over the past 50 years has taken place in parallel with the development of improved storage of cryogenic liquids (i.e. all liquids with normal boiling points below the ice-point at 273 K [1]). What is remarkable is that, before 1954, the low-loss storage of cryogenic liquids had progressed very little for over 60 years, following the pioneering work of Sir James Dewar at the Royal Institution in London, with his invention of the vacuum-insulated, double-walled, silvered-glass dewar vessel in 1892.

The change to higher efficiency cryogenic storage vessels began in 1952, when the National Bureau of Standards built the Cryogenic Engineering Laboratories (CEL) at Boulder, Colorado, to support the US hydrogen bomb (Super) program and, later, the NASA space program. Research and development effort was focused on the storage, transport and handling of large quantities of liquid hydrogen on a scale which was, at that time, at least an order of magnitude greater than any previous operation. It was based around the construction and operation of a "giant" hydrogen liquefier with a nominal output of 350 L/h.

In parallel with CEL starting work on hydrogen, the petroleum industry, in the USA but particularly in Europe, was becoming interested in liquefying natural gas at 112 K and shipping it across oceans in purpose-built seagoing tankers. In 1952, trial shipments in storage tanks mounted on barges were taking place up the Mississippi River from Lake Charles, Louisiana, to Chicago, Illinois, but without much commercial success. The first trans-oceanic shipments began in 1959 in a British-built liquefied natural gas (LNG) tanker, the Methane Pioneer, carrying 5000 m^3 of LNG from Lake Charles, Louisiana, across the Atlantic to Canvey Island, UK, under the auspices of the British North Thames Board (which became part of the British Gas organization). The success of these trials was followed in 1964 by the construction of two further British LNG tankers, the Methane Princess and Methane Progress of 27,000 m^3 capacity, together with land-based storage tanks, liquefiers and evaporators, to pioneer the first LNG supply chain between Algeria and the UK. Thereafter, from 1969 to the present time, many other shipyards in Europe, the US, Japan, and more recently in South Korea have been building larger and faster LNG tankers to meet the growing importance of natural gas as a global energy source.

The scale of LNG operations, with 50,000 tons of cryogenic liquid at one time, is some 25 times larger in scale than the 2000 tons of liquid oxygen (LOX) and liquid hydrogen required to propel the Space Shuttle into orbit. That both technologies developed in parallel during the late 1950s and 1960s was no coincidence: it was the period when cryogenics grew up from a laboratory tool into a global industry.

Returning to CEL catalyzing the growth of cryogenics in the US, the first of the series of US Cryogenic Engineering Conferences was held in Boulder in 1954. This was partly as a publicity exercise, to introduce US organizations to the CEL resources and expertise, which were suddenly no longer required by the Super program, following the introduction of noncryogenic deuterium. The concurrent declassification of CEL activities enabled universities and industrial organizations to join in the development of cryogenic engineering. It stimulated an explosion of research and commercial interest, contributing to improved cryogenic storage in particular, not only for liquid hydrogen and helium, but also for liquid air gases and the liquefied hydrocarbons.

This chapter discusses the various developments in low-loss storage, which are incorporated into the design and operation of all types and sizes of cryogenic systems today, and indeed into the many small cryogen-free systems coming into use in the last 10 years.

7.2 Heat Flows into a Cryogenic System

It is now well known that, for any reasonably well-insulated vessel or tank, the major heat flows entering the liquid are through the wetted area of the inner containing wall and are typically less than 100 W/m^2 for liquid nitrogen (LIN), LOX, and LNG, and 100 mW/m^2 for liquid helium. These heat flows include conduction through the insulation space, convection within the insulation space and in the ullage space above the liquid, and radiation from warmer parts of the container, the roof, neck, unwetted walls, and through the pipework.

The levels of heat flux are much too small for nucleate boiling to occur. For example, in LIN, a local heat flux of about 10,000 W/m^2 is required to initiate nucleate boiling, when there is a wall–liquid temperature difference of about 0.5 K. For liquid helium, a local heat flux of about 10 W/m^2 will initiate nucleate boiling, with a wall–liquid temperature difference of about 0.05 K. Studies at Southampton in the 1980s showed that heat entering the liquid is absorbed by primary convection currents which carry the heated liquid up to the surface, where surface evaporation takes place [2]. At the vertical walls of the container, a high-velocity boundary-layer flow develops and carries heated liquid into the surface layers. Heated liquid in contact with the container floor is swept across to join the vertical boundary-layer flow at the walls.

At the surface, the heated boundary-layer flow turns through 90° and moves radially inwards. During this inward radial flow, evaporation from this heated (superheated above the boiling temperature) liquid flow takes place. The studies showed that the evaporation mass flux is almost linearly dependent on the liquid superheat. At the center, the liquid motion becomes focused into a strong downward jet to complete the convection loop. This central jet carries excess heat (which has not been released by surface evaporation) into the liquid core, where secondary convective processes produce mixing and superheating. The mass flow in the primary convection loop is measured to be many times greater than the total evaporative mass flow. At no stage is there any nucleate boiling or bubbling; the commonly used term "boil-off" mass flow is a misleading description of the liquid evaporation, but we all use it.

7.3 Vapor Cooling to Reduce Heat In-Leaks

The principle of vapor cooling to reduce heat in-leaks did not become standard practice for cryogenic storage until the late 1960s. Basically, vapor cooling makes use of the fact that the sensible heat of the vapor, i.e. the total heat required to raise its temperature from the liquid boiling point up to ambient temperature, is available as a very significant quantity for absorbing heat in-leaks, as well as the latent heat of vaporization of the liquid. The sensible heat is 75 times the latent heat for liquid helium and is 10 times the latent heat for hydrogen, whereas for LOX and LIN the sensible heat is about equal to the latent heat. Good design should,

therefore, aim to use the sensible heat of the vapor from the evaporated liquid as well as the latent heat of the liquid.

Now, liquid boil-off is generated by heat in-leaks reaching the liquid and being absorbed by the latent heat of evaporation of the liquid. If the cold vapor is used to absorb much of the heat, then the residual heat in-leak reaching the liquid can be greatly reduced. The criterion for the design of low boil-off cryogenic liquid containers is, therefore, to divert the heat in-leaks so that they are absorbed by the sensible heat of the vapor, i.e. by vapor cooling.

A simple example, demonstrating the effectiveness of this criterion, is the vapor-cooled vent tube of a liquid helium dewar. It is obvious that the heat flow by conduction down the vent tube from ambient temperature can be partially absorbed by the mass of cold vapor flowing in the opposite direction up the vent tube. As the cold vapor mass flow increases, so the heat flow can be expected to reduce. In fact, for any geometry of the vent tube, there is a minimum vapor mass flow for *totally absorbing* the conduction heat flow, i.e. when the net conduction heat flow down the vent tube into the liquid is *zero*. Above this minimum mass flow, the vent tube is overcooled and is unnecessarily long.

An alternative interpretation is that there is a one-to-one correspondence between geometry and vapor mass flow for zero conductance at the bottom of the vent tube. Use of this phenomenon will take care of one major source of heat in-leak and is applicable to any cryogenic liquid container, whether for liquid helium, hydrogen, nitrogen, oxygen or LNG.

7.4 Vapor-Cooled Radiation Shields

The first improvement in the boil-off performance of liquid helium dewars was achieved by the discovery at Southampton University, in 1965, of the vapor-cooled radiation shield [3]. This simple device, consisting of one or more horizontal shields of copper, aluminum, or even plastic, placed in the cold vapor in the upper neck, enables all the ambient temperature radiation heat flow funnelling down the neck to be intercepted and absorbed by heating the shields and, hence, the cold vapor. Liquid helium cryostats were the first to benefit from the introduction of vapor-cooled radiation shields, with spectacular reductions in boil-off by a factor of three or more. Today, this device is in standard use for all helium cryostats. Vapor-cooled shields are also used in the largest scale storage of cryogenic liquids. For example, LNG storage tanks of more than 70 m diameter use a suspended deck version, in the cold natural gas vapor between the liquid surface and the tank roof, as standard practice to reduce boil-off and to simplify construction of these giant tanks.

7.5 Gas-Purged Insulations

A number of types of gas-purged insulation are available, including powders such as perlite and silica aerogel, fibers such as glass fiber or mineral wool, and foam

structures such as polyurethane foam, foam glass and balsa wood. In all these materials, gas convection is reduced by the creation of small gas cells within the matrix of low-conductivity solid fibers or foam walls. The lower limit of heat flow is determined by the thermal conductivity of the purge gas.

Continuous gas purging is necessary (1) to avoid the ingress of moisture and the formation of ice bridges as thermal shunts and (2) to prevent the condensation of oxygen-rich liquid through contact between atmospheric air and surfaces below the condensation temperature for air at 83 K, particularly those cooled by LIN at 77 K.

Nitrogen gas-purged insulations are used in cold boxes on air separation units, large static storage tanks and cluster tanks for LOX, LIN and liquid air, and in seagoing LNG tankers. Boil-off gas is commonly used as purge gas for the insulation of land-based storage tanks for LNG, liquid ethylene and liquefied petroleum gas (LPG).

7.6 Evacuated Powder Insulations

By reducing the gas pressure to 0.1 Torr, using mechanical rotary vacuum pumps only, the thermal conductivity of powder insulation is reduced by a factor of 10 or more. The gas conduction component has been largely removed. However, a penalty must be paid, since the outer casing must now be vacuum tight and strong enough to withstand a collapsing pressure differential of 1 atm.

With vacuum insulation, the geometry is limited to cylinders, spheres and their combinations for mechanical strength, and the size is limited to about 5 m in diameter. Such tanks are used as customers' storage tanks and on road and rail tankers.

7.7 Evacuated Multilayer Insulations

The major heat flow through multilayer insulation (MLI) is by thermal radiation, and this can be reduced by using multiple layers of reflecting material. For n thermally floating reflective layers with emissivity e, the radiation heat transfer is reduced by e/n. Thus, by using reflective sheets of aluminum foil or aluminized Mylar plastic, separated by insulating sheets of fiber-glass paper (with no filler) or nylon net, the MLI (or so called superinsulation) yields at least a 30-fold reduction in thermal conductivity below that of evacuated powder.

Development of MLI, by Linde and others, took place in the late 1950s. Once the techniques for wrapping some 50–100 layers of MLI around three-dimensional geometries had evolved, the use of MLI expanded rapidly to include all portable liquid helium, hydrogen and nitrogen containers, as well as low-loss liquid transfer lines. Today, MLI has largely taken over from evacuated powder insulations in vessels up to 5 m diameter, such as road and rail tankers. In general, the lowest thermal conductivities can be obtained by paying attention to residual conduction arising from molecular desorption in MLI. By using high-temperature vacuum bakeout,

with aluminum foil and carbon-getter-loaded glass-paper spacer, and by totally avoiding the use of plastics with their molecular adsorption/desorption properties, a further fourfold reduction in thermal conductivity, close to the theoretical minimum value for MLI, has been regularly achieved in tests at Southampton.

7.8 Multi-Shielding

A further improvement in insulation can be achieved by using the cold boil-off vapor to absorb some of the radiation heat flow into the overall liquid wetted surface, not just the neck. This cooling can be achieved by terminating every tenth layer, say, at successively higher temperature levels on the container neck wall during the wrapping of the MLI. Multi-shielding is widely used today in liquid helium storage dewars without the need for LIN cooling of intermediate shields.

7.9 Materials of Construction

Understanding the nature and dependence on plate thickness of the ductile–brittle transformation at low temperatures in b.c.c. materials (such as carbon steel) and its absence in f.c.c. materials (such as nickel and copper and austenitic-stabilized stainless steels) came about in the 1940s and 1950s. This understanding now provides a choice of metallic materials with adequate strength at low temperatures, to meet both the slow loading and impact loading conditions associated with the storage and handling of cryogenic liquids.

Since most plastic materials become brittle at low temperatures, the use of composites, such as glass-fiber- or carbon-fiber-reinforced epoxy composites, for low thermal conductivity dewar necks and supporting straps, has been an important development.

For the largest LNG and LPG tanks up to 100 m diameter, prestressed, frost-proof concrete has become an important, low cost, structural and load-bearing material. However, cryogenic concrete is not accepted as being liquid tight; therefore, an inner metal membrane is usually employed.

7.10 Evaporation Instabilities

A combination of (1) the increase in number of cryogenic liquid storage systems, (2) the scale of the storage tanks, and (3) the improvement in insulation techniques resulting in lower evaporation rates has led to an increase in the number of unstable evaporation events.

Rollovers and vapor explosions are examples of these, in which large amounts of vapor are suddenly produced. Variations in evaporation rates are commonly observed in laboratory-sized containers: LIN in a well-insulated dewar will produce puffs of vapor which are in fact miniature vapor explosions. These variations cannot

be tolerated in large-scale liquid storage tanks; hence steps must obviously be taken, say in handling 150,000 tons of LNG, to prevent associated rapid pressure rises causing tank failure and catastrophic leakage.

A number of studies of evaporation instabilities have been carried out at Southampton. These indicated how the heat flows entering the stored liquid are released solely by surface vaporization, as the heated liquid elements reach the liquid–vapor interface. Microthermometer and optical Schlieren studies show a complex and delicate micro-convective transport of heat to the surface where molecular evaporation takes place.

A major thermal impedance is provided by conductive heat transfer across a 100–500 μm thick conduction layer adjacent to the surface, via a thermal gradient on the order of 7500 K/m. In other words, the liquid must be superheated in order to drive the evaporation process. This conduction layer is easily disturbed and any physical disturbance of the surface, whether transient or continuous, leading to bulk superheated liquid penetrating this conduction layer, will lead to a large (10–100-fold) increase in local evaporation rate.

Many simulations of rollover reveal that stratification is the precursor. When two liquid layers with densities differing by 1% occur (from differences in composition or temperature) then the convection arising from heat flows entering the lower layer cannot penetrate through the upper layer to the surface. The heat flow is trapped in the lower layer, causing its temperature to rise and its density to fall. As the densities of the two layers become equal, they spontaneously mix, described as a rollover, accompanied by a large increase in boil-off. Simulation studies show that the spontaneous mixing occurs via vertical penetrative oscillations which intensify until they destroy the surface conduction layer. The evaporation rate rises 10–100-fold to the molecular evaporation limit until the excess energy in the unmixed layers is released.

Other studies on vapor explosions suggest that the delicate surface evaporation mechanism can be suppressed or enhanced by transitory rafts of a monomolecular impurity layer, such as water or carbon dioxide. A whole spectrum of evaporation spikes, varying in magnitude and length, has been observed.

Clearly, these evaporative instabilities must be avoided; the present method is to avoid stratification and to keep the contents of a container constantly but gently in a vertical mixing motion.

7.11 Particular Storage and Containment Developments

7.11.1 Liquid Helium Usage and Nuclear Magnetic Resonance, Magnetic Resonance Imaging and Magneto-Encephalograph Systems

In 1955, liquid helium usage was confined to low-temperature laboratory research cryostats, with an average liquid helium holding time of a few hours. Applications outside the research laboratory were not even on the horizon. By 1965,

improvements in design were beginning to allow 100 h holding times to be realized, so that a single filling of liquid helium on Monday morning would last throughout the week until Friday afternoon, or later. The lives of research students were no longer controlled by the irregular availability of short-lasting liquid helium fills, at antisocial hours of the day or night. Instead, they could work at regular hours for experimental runs at socially acceptable times of every day.

By 1975, 100-day hold times had become the norm, and the next 10 years saw the development of large nuclear magnetic resonance spectroscopy cryostats, followed by the even larger magnetic resonance imaging (MRI) body scanning systems, and more recently the combination of MRI with magneto-encephalographic systems for functional MRI, all depending on liquid helium refills at 100-day, or 3-monthly, intervals. By 1995, 1000-day, or 3 year, hold-times were being achieved on deep-space probes. By 2005, the advent of reliable, efficient, relatively low cost cryocoolers is making cryogen-free operation both practicable and attractive [4].

7.11.2 Superfluid Helium Usage in the Large Hadron Collider, CERN

The 26 km circular track of the Large Hadron Collider (LHC) at CERN, Switzerland, requires superconducting magnets along the entire length of the particle accelerator. The very highest fields possible with liquid-helium-cooled superconductors are required, and these can only be achieved by cooling to 2.0 K with superfluid helium. The LHC, therefore, contains a great deal of technology for producing and handling superfluid helium on a scale which has never been met before. The avoidance of superleaks into the vacuum insulation will be paramount along the 26 km of pipelines and cryostats.

7.11.3 Liquid Hydrogen for Fuel Cells

There is much talk today about fuel cells for motor vehicles, since the product of electrochemical combination of hydrogen and oxygen is water, the most environmentally attractive combustion product on our planet. Hydrogen has to be carried in portable containers, either as a cryogenic liquid at 1 bar, or under pressure of hundreds of bar in contact with suitable adsorber/desorber media.

The cryogenic liquid hydrogen route is being actively developed today by Linde and others. For example, around Munich, in southern Germany, liquid-hydrogen-fuelled internal-combustion-engined BMW motor cars are being designed in anticipation of fuel cells becoming available at commercially competitive costs in the near future. Development work includes the provision of a network of automated liquid hydrogen fuel stations, and the construction of ultra low-loss, vacuum insulated, trapezoidal tanks to fit within the boot, or trunk, of road vehicles.

Since hydrogen is flammable in air over a wide composition range, safe operation of such systems is paramount, and cryogenic storage tanks that can be sealed off for 10 days without venting are required. Fortunately, liquid hydrogen has a high

compressibility and heat capacity, which are considerable aids to achieving this zero-venting requirement. The use of hydrogen in fuel cells could eventually far exceed the quantities used by space rockets.

7.11.4 Liquid Neon and Liquid Air Coolants for Ceramic Superconductors at High Field

Ceramic superconductors with critical temperatures of 100 K, and higher, require to be operated at temperatures below one-half of their critical temperatures, i.e. 40–60 K, to realize their full potential as high-field, high current-density superconductors. This temperature range of 40–60 K represents a gap in the normal boiling points of cryogens, and requires some ingenuity in the use of refrigerants. Solid refrigerants, like solid nitrogen, have very poor thermal contact properties, so we are restricted to fluids such as neon, with a normal boiling point (NBP) of 27 K and a critical point at 44 K and 25 bar, or subcooled oxygen–nitrogen mixtures such as the liquid–solid eutectic down to 50.5 K, the 50:50 liquid mixture with a freezing temperature of 52 K, and liquid air with a freezing temperature of 63 K. The use of cryogens as refrigerants at elevated pressures, such as liquid neon at 40 K and 20 bar, or as subcooled liquids, such as the 50:50 oxygen–nitrogen liquid mixture down to 52 K under a helium atmosphere at a total pressure of 1 bar, are totally practicable, but are rarely employed by conservatively minded cryogenists.

Think how we use water in our everyday lives, as both a subcooled liquid and as a superheated one, with no problem!

7.11.5 Liquid Nitrogen as Standard Refrigerant for Food Freezing, Cryopreservation, Cryosurgery, etc.

LIN has become the standard refrigerant, because it can be made on a large scale in air separation plants and can easily be stored and transported at low cost. Atmospheric air is 79% nitrogen, so the use of LIN is nonpolluting and contributes zero global warming. Therefore, LIN is very environmentally attractive as a refrigerant in comparison with the Freons, although its use represents a costly waste of energy thermodynamically.

The use of LIN as a convenient source of cold has, therefore, grown enormously in many areas of application, including food freezing, cryopreservation of biological material, blood, semen and embryos, stem cells, tissues, etc., and in cryosurgery.

7.11.6 Liquid-Gas Cylinders

Gases are generally some 700 times less dense than the liquid at 1 bar pressure. When supplied at 200 bar pressure, the gases are still significantly less dense than the liquid, while the compressed gas cylinder weighs perhaps as much as five times the contained gas. Therefore, it makes economic sense to supply the gas in

liquid form as a superheated liquid under a suitable elevated pressure to match the application. The weight of the liquid container is now a fraction, perhaps 10%, of the contained gas in liquid form. A good example is propane, one of the LPG's, with an NBP of 231 K (–42 ˚C) and a critical point at 370 K (97 ˚C) and 42 bar.

The liquid air gases nitrogen, oxygen and argon are widely used as industrial gases at moderate pressures and lend themselves to being supplied in liquid form in so-called liquid cylinders. The vacuum insulation of the cylinder includes a vaporizing and pressure-raising coil so that the liquid can be vaporized automatically on demand and the gas supplied at pressures up to about 20 bar.

7.11.7 Liquefied Natural Gas and Liquefied Petroleum Gas in the Future

The global market for hydrocarbon energy products has changed very considerably since the first trial shipments of LNG were made in the early 1960s.

1. The rise in crude oil prices to $40 in the 1980s, and to over $60 a barrel in 2005, has helped to make LNG, with its expensive cryogenic chain of giant liquefaction plants, storage tanks, seagoing tankers and regasifiers, a much more competitive energy source today.
2. At the same time, the end of the Cold War has enabled the Russian states to enter the global market place with enormous reserves of natural gas and crude oil.
3. The rapidly advancing economies of India, China and South America are generating their own very large energy requirements, in competition with established energy users in the US, Europe and Japan, tied to energy sources in North and Central Africa, the Middle East, Australia, Alaska and South America.
4. Entrepreneurial countries like South Korea are taking over as the major constructors of LNG tankers from the European and US shipyards (the UK shipyards dropped out a long time ago).
5. The thinning of Arctic ice as global warming progresses is opening up the whole of the Arctic region for exploration and the development of new sources of natural gas and oil, and new global transport routes across the top of the world.

The net result of these changes is a tremendous upward surge in cryogenic technology of LNG refrigeration chains measured in billions of dollars of capital every year. In parallel is the upsurge in LPG usage at $-40°C$ as the flare gases from oil wells are captured to make another valuable energy source.

7.11.8 Cryogen-Free Operation

At the small end of the market, the advent of reliable cryocoolers with cooling capacities of 1 W at 4 K, 10 W at 20 K, or 100 to 1000 W at 80 K has opened up two types of application:

1. zero boil-off systems
2. cryogen-free systems.

From the storage and handling point of view, while both types are revolutionary, they rely heavily on all the improvements in insulation achieved over the past 50 years.

With zero boil-off systems, the cryocooler is used mainly as a cryogen recondenser, but also to absorb some of the heat in-leaks, while the liquid cryogen is used to provide thermal stability and security of operation. With cryogen-free systems, the low-temperature environment is entirely dependent on the reliability of the cryocooler in absorbing all the heat in-leaks. There is no liquid refrigerant to provide a back-up, just like the domestic freezer! In these days of computer control, the reliability is enhanced by the convenience of being able to dial up a required low temperature, but perhaps diminished by having to wait overnight for the necessary cooldown to thermal equilibrium.

7.12 Conclusions

Looking back over 50 years, the improvements achieved in insulation have been extraordinarily significant, with present-day insulations being at least 1000 times better than in 1950! At the same time, the confidence level with which cryogenic storage is viewed today (and the scale of the storage operations undertaken) has increased enormously. The driving force for these improvements came about in the late 1950s from the need to develop (1) liquid hydrogen as a fuel for space rockets and (2) the trans-ocean shipment of LNG. Nowadays, cryogenic liquids are in standard use for space rockets, but this represents only a small percentage of the total use of cryogenic liquids around the world today, including a major section of the energy business, the provision of oxygen for steelmaking and synthetic fuel-gas manufacture, argon for shielded arc-welding, high-purity nitrogen for silicon chip manufacture, helium for deep-sea diving, LIN for a host of medical and biological applications, and so on.

Looking into the future, the use of cryocoolers for cryogen-free operation can be expected to become the norm in many applications. While the Mark 1 versions of MRI body scanners are now used as a major medical diagnostic tool in most hospitals, the Mark 2 and 3 versions presently being developed will have far greater potential in the future, e.g. by enabling real-time studies of physiological and neurological processes in the body, the heart and the brain, to become normal practice.

The future of liquid hydrogen as a nonpolluting fuel for fuel cells and internal combustion engines is assured, but there needs to be considerable development effort before hydrogen can become effective as a real contributor to reducing global warming.

The attractiveness of LNG as an energy fuel, with its relatively small global warming potential, will continue to expand. As global warming causes the Arctic

and Antarctic ice to retreat, so new areas of exploration for, and exploitation of, natural gas will appear. The cryogenic technology of LNG refrigeration chains can then be expected to operate in colder and colder climes, among the ice fields.

References

1. Haynes, W.M., Kidnay, A.J., Olien, N.A., and Hiza, M.J., "States of Thermophysical Data for Pure Liquids and Mixtures of Cryogenic Interest, " *Advances in Cryogenic Engineering*, Vol. 29, Plenum Press, New York, 1983, pp. 919–942.
2. Scurlock, R.G., *Low Loss Storage and Handling of Cryogenic Liquids: The Application of Cryogenic Fluid Dynamics*, British Cryogenics Council, 2005.
3. Lynam, P., Proctor, W., and Scurlock, R.G., "Reduction of the Evaporation Rate of Liquid Helium in Wide-Necked Dewars, " *Bulletin of IIR*, Commission 1, Grenoble, Annexe 1965-2, 1965, p. 351.
4. Scurlock, R.G., "Low Loss Dewars and Tanks", *Cold Facts*, Cryogenic Society of America, 2004.

8
Fifty-Years' Development of Cryogenic Liquefaction Processes

W.F. CASTLE

The Meadow, Ystradowen, Cowbridge, Vale of Glamorgan CF71 7TR, UK

Abstract

In the 50th year of the Cryogenic Engineering Conference, the present review covers the development of cryogenic processes for oxygen, nitrogen, liquid hydrogen, and liquefied natural gas over that past period. It is confined to those processes of commercial interest, as applied to large-scale production. In all three sectors included in the present review, very significant advances have been made as the result of market forces. The developments that have contributed to the improvement in efficiency, scale of application, and economics are described.

8.1 Introduction

The three areas for review are dealt with sequentially. Although they have in common the employment of cryogenic technology, they are essentially separate developments. The last 50 years has seen large-scale applications of cryogenic processes in these fields.

Air separation to produce oxygen and nitrogen as major products is employed to supply steelmaking, petrochemicals and gasification projects.

Hydrogen liquefaction resources were needed to service the space program as a rocket fuel; subsequently, usage developed for bulk transport of hydrogen from production to user sites. Now, liquid hydrogen is being considered and used for automotive fuel in specific schemes.

Liquefied natural gas (LNG) complexes are amongst the largest installations of any cryogenic project. LNG is produced in fields rich with the gas or present in association with petroleum products; it is then shipped to countries that are poor in fuel supplies, or which do not possess clean fuel resources.

Each of these development sectors has something in common, although the detailed technology base is different. Around 1950–1955 seems to have been the start of significant expansion in the three sectors now reviewed. The process plants in each sector have developed to reduce product costs by designs for larger, more efficient plants. It is hoped that this chapter will illustrate the main techniques

adopted to achieve that result. A significant amount of cryogenic technology has been applied on the distribution, storage and revaporization of liquid products. However, the limitation on space for this chapter and on time for presentation means that the review has to be limited to the separation or liquefaction process.

8.2 Cryogenic Air Separation: Oxygen and Nitrogen

Briefly, the air separation process comprises the following typical steps:

1. air compression;
2. air purification, to remove mainly water and carbon dioxide;
3. heat exchange, in which air is cooled by outgoing cold products;
4. distillation, to separate oxygen, nitrogen and argon;
5. refrigeration (by work obtained from expanding some air from the heat exchanger into the low-pressure column);
6. the products, warmed by heat exchange with the air feed, are compressed externally with product compressors or can be pumped as liquid and vaporized to a desired pressure.

In the 1960s the cryogenic air separation process was regarded as a "mature" technology, but a significant amount of development has been applied to commercial applications and installations in all the above stages.

In 1950, the largest cryogenic oxygen plant had an oxygen output of about 500 tons/day (1 ton = 2000 lbs). By 1965–1970, the capacity had more than doubled to about 1200 tons/day. Currently, some plants under construction will have a single stream output of 4300 tons/day [1,2]. This increase in capacity was driven by the need to supply steelmaking, petrochemicals and gasification projects, which themselves have been enlarged to meet demand, and the reduction in costs obtained with greater scale. Apart from greater capacity, the drive has incorporated technological advances to improve overall efficiency as another way to improve costs.

Technological developments have been applied in all areas enumerated above, but probably the most significant have been in purification, heat exchange and distillation.

8.2.1 Purification and Heat Exchanges

Fifty-five years ago it was quite common for large, so-called tonnage plants to use regenerators for main heat exchange and air purification [3,4]. Regenerators usually operated in pairs and comprised vessels packed with granite chips. Process air passed through the packed bed, which had been cooled in a previous cycle with cold product gas. Water and carbon dioxide deposit on the packing as the air is cooled. At a certain point the flow is reversed, air switching to the other vessel while cold product gas flows through the first vessel to recool the packing. The process has to be controlled to ensure that pressures, temperatures and flows allow

the resublimation of water and carbon dioxide in the cold gas to be carried out with the product. A disadvantage with this is that the product gases are contaminated with air on changeover of each cycle, and process air losses are incurred. The exit gases contain water and carbon dioxide, which can be undesirable in some processes. By providing tube bundles within the packing of the regenerator, gases could be produced which would not be contaminated at changeover or because they had to carry away the impurities deposited from the air.

A later, more elegant solution was the use of reversing heat exchangers. These were multipass brazed aluminum units that were manifolded in parallel to provide for high capacity. Air and cold gas waste product alternated in specific passes, providing air clean up, as with regenerators, while product required to be uncontaminated was in a separate nonreversing pass or passes. Although these had the capability to produce more pure, uncontaminated product than the regenerators, the maximum that could be produced was about 55% of the process air. The limitation is imposed by the need to ensure cleaning of water and carbon dioxide in the air by control of the temperature differences and flow rates.

In the period 1970–1980 the demand for nitrogen (and argon) grew faster than that for oxygen, leading to a requirement for greater proportions of pure product. During the latter part of this period, molecular sieve adsorbents were increasingly used to remove water and carbon dioxide at near-ambient temperature [2]. The system initially had some penalties compared with reversing heat exchangers, in terms of power consumption and capital cost. But development of the process and equipment reduced cycle times for the adsorbers, and regeneration temperatures, so significantly reducing the penalties. In addition, the proportion of pure product rose, because only about 10–12% of the process air is used in regeneration of the adsorbent; the rest could be pure oxygen or pure nitrogen, with the latter potentially being two and a half times the oxygen product. The brazed aluminum heat exchangers following the purification were continuous in operation and flow, providing greater reliability [5, 6].

The developments in molecular sieve adsorption that greatly improved the systems application included higher capacity adsorbents, lower regeneration temperatures, shorter adsorption cycle times, and improved engineering design of molecular sieve adsorber systems. This system was then able to better the reversing heat exchanger system in product recovery and at least equal it on power consumption and on capital costs.

8.2.2 Distillation

Distillation for cryogenic air separation plants provides an equally significant advance. Most plants used the double-column system involving two columns, so-called HP (high pressure) and LP (low pressure) columns, mounted one above the other, being connected by the main condenser/reboiler. A detailed description will not be given here, but is given in [1].

In 1955 the distillation columns used sieve trays, vapor flowing vertically through the holes, while liquid passed over the tray. Successive trays effected
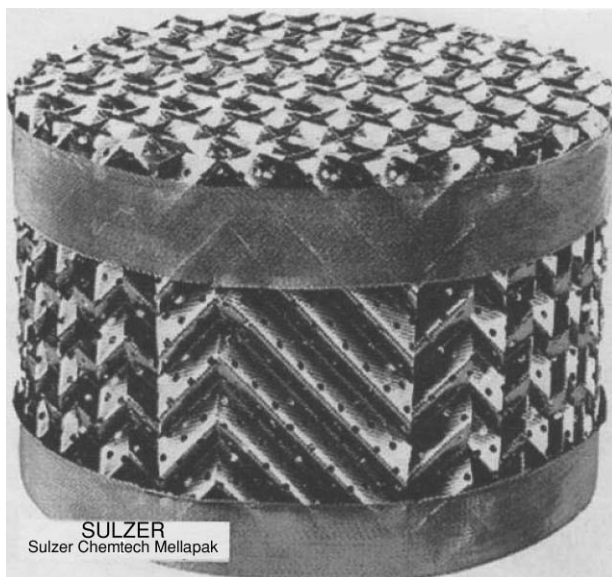
FIGURE 8.1. Mellapak® structured packing section (courtesy of Sulzer Chemtek).

separation of air, with the more volatile component, nitrogen, concentrating up the column in shorter cycle times, and oxygen below [7, 8]. Argon concentrated at an intermediate point in the LP column and was separately purified in a side column.

The biggest change in air separation distillation was the use of structured packing [9, 10]. This takes the form of corrugated and perforated metal sheets coiled so that adjacent corrugations are at 90° to each other, creating open channels and providing a means of efficient liquid–vapor contact with low pressure drop. The advantage of its use, especially in the low-pressure column of an air separation plant, is that the overall power consumption and separation efficiency are improved. The use of structured packing also permits the production of pure argon from the side column directly, since the low pressure drop and high efficiency provide between 150 and 220 theoretical separation stages within the allowable pressure differential [11, 12].

Figure 8.1 shows a portion of structured packing, and Figure 8.2 illustrates a chordal weir perforated tray configuration. Both provide for efficient contact between vapor and liquid, but the structured packing does so with lower pressure drop and often at higher efficiencies.

8.2.3 Other Technical Developments

Additional developments, which have contributed to lower costs and/or lower power consumption of cryogenic air separation, are summarized in Table 8.1, so as to keep within the constraints of space for this chapter.
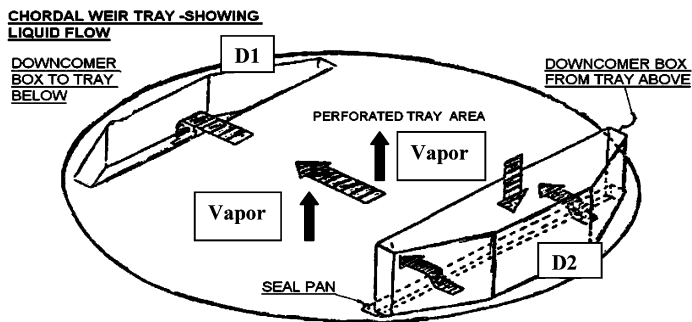
FIGURE 8.2. Chordal weir tray.

An important factor in air separation is that of the process cycle design. In the 1950s–1960s several different process types were built as an approach to achieve higher efficiencies and lower costs. A detailed description of each of these would not be appropriate here but brief reference can be made to those applied in commercial operations.

The processes involved are:

Linde–Frankl—regenerators with double-column distillation, with air in "balancing" stream [16];

TABLE 8.1. Other contributions to improved performance and costs of cryogenic air separation plants

Item	Initial practice (ca 1950)	Later development	Effect
Vessels within cold box	Copper fabrication	Aluminum fabrication	Lower costs, fewer leakage problems, better reliability
Cold box insulation	Mineral wool	Perlite	Lower heat losses, lower power consumption
Compressors	Design of compressor blades, wheels and internals	Three-dimensional machining of blades, computational fluid dynamics design and analysis [13]	Improved efficiency and flexibility
Expansion turbines	Blower- or generator-loaded	Turbo-expander and integral high-speed generator with active magnetic bearings [14]	Lower bearing losses, higher power recovery
Control systems	Analog pneumatic systems	Computer/electronic systems [15]	More precise control, improved purity
Process cycle development and optimization strategies	Calculation of specific cycles	Computer simulation and thermodynamic analysis	Improved efficiency, integrated control

Kellogg—low-pressure air, reversing heat exchangers, double distillation column [17];

Elliott—dryers, switch exchangers, single distillation column with nitrogen reflux system [18];

Oxyton—regenerators with three-column distillation [19];

Rescol—regenerators with single-column distillation [20];

and later:

low-pressure plant with adsorption air purification, double column [21].

The process cycles were developed to achieve advantages in lower power consumption, for either lower capital cost or higher recovery of products for certain demand patterns. The Rescol plant, as an example, in its later version was designed to produce up to 7% liquid oxygen, with some loss of gaseous product, to allow for an expected variation in gaseous oxygen demand for steelmaking. The Rescol plants provided the first tonnage oxygen supplies for steelmaking in the UK.

The low-pressure plant with feed air purification gave maximum product recovery and, with development of molecular sieve purification, little or no penalty in cost or power compared with reversing heat exchanger plants, together with increased reliability from heat exchanger leakages.

Product purities have increased over the period, gaseous oxygen improving from 99.5% to 99.8%, pure nitrogen from 20 vppm (gaseous volume parts per million) to 2 vppm—and in some cases even to 2 vppb (gaseous volume parts per billion).

8.2.4 Liquid Pump Plants

The conventional low-pressure gaseous oxygen plant employed an oxygen compressor to boost the oxygen product from the plant to user pressure of 450–600 psig. Today, the specific power consumption (kW/(tons/day)) for low-pressure tonnage gas plants, producing oxygen at about 1.5 psig, has been reduced to 45% of the figure achieved in 1955–1965 [1]. This has been brought about by a number of developments listed above, and the increase in capacity of individual units provides for use of larger, more efficient components and machinery.

The liquid pump cycle has been adopted for many large projects and product demands. The substitution of the liquid pump cycle enabled supply pressure to be attained without the somewhat critical design of the oxygen compressor. Liquid oxygen pumped from the condenser of the double column is vaporized by heat exchange with compressed air feed or, in some cases, a compressed nitrogen recycle stream.

The liquid pump plant is generally favored for gasification projects and similar large-scale applications. This application provides for simplification of control systems. The replacement of the oxygen compressor by an air or nitrogen compressor provides an advantage in overall capital costs and ease of maintenance. A liquid pump plant consumes a few percent more power than a gas compression cycle, but has some advantage in reduced capital costs [22–24].

8.2.5 Enhanced Oil Recovery

High-pressure nitrogen injected into oil wells is used to enhance oil recovery as the oil in fields is depleted. Air separation cycles have been devised to produce the required nitrogen product, where oxygen is not a prime product [25,26]. At Cantarell, in Mexico, four air separation units produce a total of 47,000,000 ft^3/h supplied at a pressure of 1750 psi [27]. Each separation unit processes air equivalent to a plant producing 3750 tons/day oxygen.

8.2.6 Summary: Air Separation

In summary, air separation development in 50 years has achieved an eightfold increase in single stream capacity, specific power consumption less than half, and product recovery increased by about two-and-half times, with increased purity of products.

8.3 Hydrogen Liquefaction

Liquid hydrogen demand increased dramatically with the US space program. Several liquefiers were built, increasing in capacity from 0.5 tons/day at Boulder in Colorado to 62 tons/day in California in 1965.

Different liquefaction cycles are appropriate depending on the size of the liquefier. A simple Joule–Thomson cycle with vacuum-boiling nitrogen precooling was used for 2 tons/day, whereas a more complex Joule–Thomson cycle with atmospheric- and vacuum-boiling liquid nitrogen precooling is favored for up to 5 tons/day. For even larger liquefiers, the staged nitrogen precooling of hydrogen is used in conjunction with refrigeration from a turbo-expander.

Gas feeds to the liquefier are pre-purified so as to contain less than 1 vppm impurities, since all the impurities will have a freezing point above the temperature of, and are not soluble in, liquid hydrogen.

The nitrogen refrigeration cycle provides cooling at normal liquid nitrogen temperature and also uses cooling by liquid nitrogen at subatmospheric pressure.

8.3.1 Ortho- to Para-Hydrogen Conversion

Hydrogen exists in two forms, i.e. ortho- and para-hydrogen. In ortho-hydrogen the two electrons in the molecule rotate in the same direction, whereas in para-hydrogen they rotate in opposite directions. Room-temperature hydrogen comprises 25% para content, whereas at its boiling point the equilibrium para content is 99.8%. The conversion of ortho to para is exothermic and, hence, can give rise to liquid evaporation losses, so a catalyst is provided to convert the hydrogen to the para form. The conversion should be carried out at warmer temperatures so as to reduce the power for heat pumping.
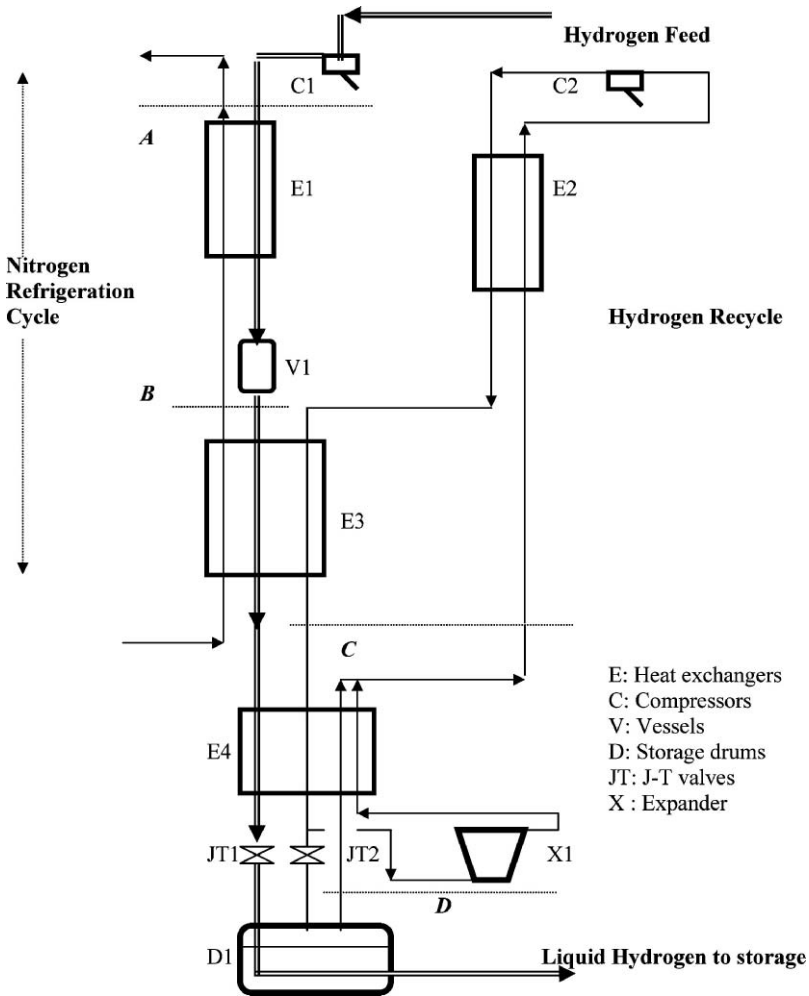
FIGURE 8.3. Hydrogen liquefier.

The catalyst used initially by the National Bureau of Standards was 20% chromic oxide on alumina. Later, hydrous ferric oxide was employed, having been found to be 6.6 times more effective. Subsequent catalysts have been nickel silicate (eight times more active than the chromic oxide) and 30% ruthenium on silica and alumina, this being in turn twice as active as nickel silicate [28].

In practice, the larger liquefiers employ staged conversion. This can be done in successive vessels at successively lower temperatures [29–31]. The schematic flowsheet in Figure 8.3 shows where these steps can be fitted in, at *A*−*B*, so the flowsheet element between these two dotted lines may be duplicated or tripled.

Similarly the circuit between *C* and *D* can be duplicated or even tripled so as to increase efficiency of the liquefier.

8.3.2 Hydrogen Liquefier Cycles

Choice of hydrogen liquefier cycles is generally between medium pressure (3 MPa) and high pressure (about 100 MPa). The recycle stream (Figure 8.3) is separate from the feed stream and can operate at a higher pressure. The feed stream has to undergo ortho–para conversion, but the recycle stream will have been converted.

The medium-pressure recycle stream will employ different equipment from the high-pressure system, this generally consisting of less costly compressors, heat exchangers, and turbo-expanders [32], but it will have a somewhat higher power consumption. With high pressure, the compressors used are reciprocating type, expensive wound tubular heat exchangers are employed, and expanders are reciprocating units, but power consumption will be lower.

As indicated in the previous section, hydrogen liquefier cycles can be adopted which feature multiple ortho–para and expander stages; this would be relevant to larger liquefiers. The added complexity is aimed at increased efficiency, i.e. reduction in power consumption, albeit at increased capital cost. Nevertheless studies have shown that the prime factor in production cost in large-scale liquefiers is power consumption [33].

8.3.3 Summary: Hydrogen Liquefiers

Although the initial impetus in the 1950s for building hydrogen liquefiers was from the space program in the US,, increasingly since then commercial applications exceed that. The aerospace program accounted for 20% of total demand in North America in 1991 [34]. The purity of liquid hydrogen created a demand for applications such as metalworking, float glass, etc.

The total capacity for hydrogen liquefaction in North America in 1991 was 190 tons/day [34]. With the potential commercial demand it can be expected that the overall capacity will increase and that larger production units will also be employed. The technology for liquefiers will be ready for such expansion.

More active and more efficient ortho–para catalysts have been developed. More efficient hydrogen liquefier cycles with multiple expanders have also emerged, and can be even better employed on larger units. As the cost of product is lowered, increases in total production and delivery should arise.

8.4 Liquefied Natural Gas

Large-scale liquefied natural gas (LNG) plants ship the LNG to a remote customer. The scale of such plants has greatly increased over about the last 40 years.

TABLE 8.2. Maximum base-load LNG plant capacity versus year

Year	Plant capacity (10^6 tons/year)
1964	0.45
1970	1.0
1980	1.5
1990	2.2
2000	3.5
2006	5.0[1]
2008 (?)	8.0–10.0[2]

[1] Under construction.
[2] Potential capacity.

LNG was delivered from a plant in Louisiana to the UK in 1959 [35]. Subsequent developments greatly increased the capacity of what are termed "base-load" plants for international delivery of LNG and shipment to many different countries.

The CAMEL plant located at Arzew, Algeria, was the first base-load LNG facility [36], being built in 1962–1964. The increase in maximum capacity of base-load plants over time is shown in Table 8.2.

The designs for such liquefiers have included a number of cycle developments. Some have used the classic cascade cycle. This uses a succession of separate refrigeration modules to achieve liquefaction, in which methane feedstock is cooled stepwise by propane, ethane and methane.

Others have used a mixed refrigerant cycle, using a single refrigerant with a mixture of components (Figure 8.4). Kleemenko [37] proposed this type of cycle. A mixed refrigerant can comprise, for example, butane, propane, ethane, methane and nitrogen.

The cycles applied to natural gas liquefaction are listed in Table 8.3 and also show how many trains of LNG for each cycle have been installed, including those under construction, as of 2004 [38].

Linde AG has recently announced "an almost complete natural gas liquefaction plant will complete a 2,700 nautical mile journey from Spain to northern Norway and is to be docked and connected to existing facilities." Capacity will be nearly 5 million tons LNG per annum.

8.4.1 Feed Pre-Purification

With many different feedstocks, pre-purification has to be considered for each installation. Impurities can include acid gases, carbon dioxide, hydrogen sulfide, water, mercury, carbonyl sulfide, mercaptans, etc. Processes to resolve this can be a promoted carbonate or other solvents followed by an adsorption process.

Mercury removal is essential where the downstream equipment is fabricated in aluminum, since this forms an amalgam with the mercury. Adsorption on carbon beds, impregnated with some sulfur or iodine, on active carbon itself, or molecular sieves have been employed [39].
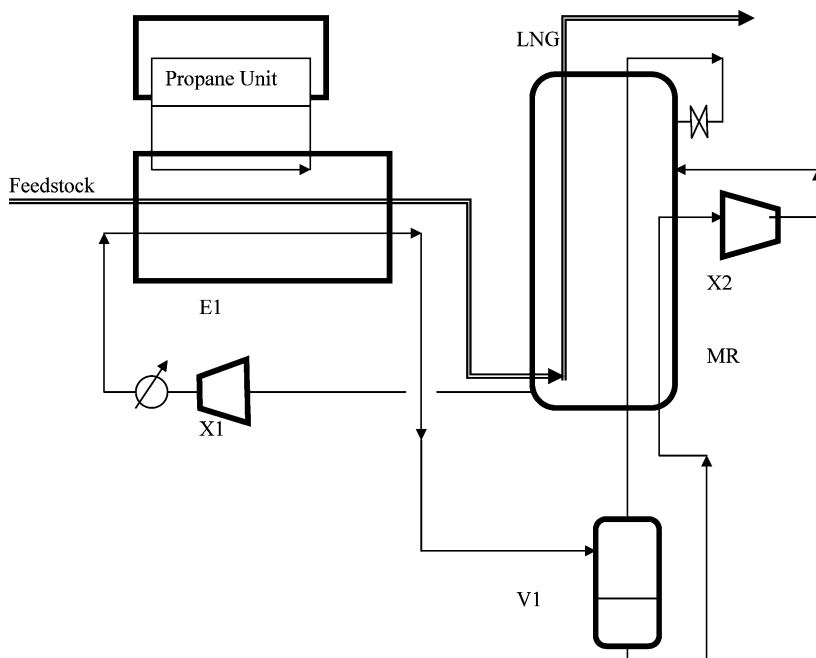
FIGURE 8.4. Propane precooled mixed refrigerant cycle schematic: APCI C3MR.

The gas treatment generally incurs a small proportion of the total plant cost (around 5%), but it can be a high-energy user [40]. Thus, the treatment process should be carefully optimized, and integration with the liquefier should also be considered.

8.4.2 Heat Exchangers

Main heat exchangers are usually a choice between spiral-wound tubing and brazed aluminum types. The many units designed for the C3MR cycle use spiral-wound

TABLE 8.3. Number of LNG trains installed or under construction

	LNG trains installed and under construction 2004
Cascade	4
Phillips optimized cascade	7
Propane precooled mixed refrigerant (APCI–C3MR)	64
Single mixed refrigerant (PRICO)	3
Dual mixed refrigerant	6(?)
TEAL dual-pressure mixed refrigerant (Technip–Air Liquide)	3
Multi-fluid cascade (Linde–Statoil)	1
AP-X cycle (proposed for 2008 and further units for 2009 and 2010 start-up)	

heat exchangers. Recent cascade cycle liquefiers employ brazed aluminum heat exchangers, with multi-core arrangements. These cores may number 40 for each LNG train, the cores being installed in eight cold boxes [41]. Problems of even distribution of vapor and liquid have to be resolved, and filtration utilized to prevent plugging is used extensively.

Spiral-wound heat exchangers measure up to 4.2 m in diameter, 54 m in height, and weigh up to 240 tons [41]. Transport to site needs a careful survey!

8.4.3 Compressors and Drivers, etc.

Compressors and drivers are a major feature of base-load plants. Gas turbines, steam turbines, and, in some instances, large electric motors have been employed. These dictate support complexes for energy supplies.

They are also a major consideration when deciding how many trains of LNG will be adopted for a given installation and capacity. Apart from cost of increasing/reducing the number of trains, reliability has to be considered and the ability of the complex to meet projected demands, while experiencing turndown and also maintenance and inspection schedules [41].

Overall capital costs of the LNG facility are large. For a 5 million tons/year facility, reported costs are said to be $300–500/ton per year [42]. Still larger facilities have a future target of $200/ton per year.

Projects recently completed have taken 4.5 years to completion from concept, and this is said to be 30% less than current utility benchmarks. Thus, it seems the drive to still greater cost reduction continues, so that product costs should follow the same trend.

8.4.4 Expanders

A recent development has been to employ liquid expanders, which generally replace one or more of the Joule–Thomson valves. An improvement in power consumption of about 2–3% is achieved, although 5–6% might be expected theoretically [42].

8.4.5 Plant Efficiency and Specific Powers

It becomes difficult to compare liquefiers precisely based on efficiency and specific power, since in different papers not all conditions are standardized. One paper [43] includes a comparison of the specific powers of the C3MR (12.2 kW/(tons/day)), the DMR cycle (12.5 kW/(tons/day)) and the Cascade (14.1 kW/(tons/day)).

8.4.6 Summary: Liquefied Natural Gas

Cycle designs are available to select the appropriate liquefier plant for a given project. The engineering of these large projects continues to pursue efficient performance and cost reductions, both in terms of equipment and construction. A

large effort is being made to design and specify increases in the size of liquefiers to produce LNG. The increased demand for LNG provides an incentive for this program of improvement.

Estimates [44] indicate that global liquefaction capacity in 2004 is 158.5 million tons/year; by 2014 the expected liquefaction capacity is 240 million tons/year, so a strong growth is indicated.

8.5 Overall Review

In each of the areas reviewed, the separation units or liquefiers have been the focus of attention, since to cover the whole of the complexes would involve a much larger discussion. While being the central part of each of the technologies, cryogenic concepts, technology, and engineering are applied to the other facilities, namely storage, vaporizers, transport tankers, and liquid transfer pipe work, and considerable effort is applied to these sectors.

Growth in total demand and for larger units in oxygen/nitrogen, liquid hydrogen, and LNG will mean challenges for cryogenic engineering and technology.

References

1. Castle, W.F., "Air Separation and Liquefaction: Recent Developments and Prospects for the Beginning of the New Millennium," *International Journal of Refrigeration*, 25, 158–172, 2002.
2. Petit, P., and Widawski, S., "Air Separation: Evolution over the Last Twenty Years," *Second International Conference Kryogenika '92*, Brno, Czechoslovakia, 1992, pp. 12–15.
3. Ward, D.E., "Some Aspects of the Design and Operation of Low Temperature Regenerators," *Advances in Cryogenic Engineering*, Vol. 6, Plenum Press, New York, 1961, pp. 525–536.
4. Bartsh, A., *Regeneratoren der Tieftemperaturtechnik*, VEB Verlag Technik, Berlin, 1961.
5. Lungsford, K.M., "Advantages of Brazed Heat Exchangers in the Gas Processing Industry," *Proceedings of 75th GPA Annual Convention*, Tulsa, OK, 1996, pp. 218–226.
6. Petit, P., "Air Purification: Water and CO_2 Removal by Adsorbents," *Coal, Gas and Air Conference*, Beijing, China, 1985.
7. Latimer, R.E., "Distillation of Air," *Chemical Engineering Progress*, 63(2), 35–59, 1967.
8. Lockett, M.J., *Distillation Tray Fundamentals*, Cambridge University Press, 1986.
9. Hug. A., "Structured Packings in Air Separation Plants,"*Proceedings Energy Week Conference, Book VI, Intersociety Cryogenics*, ASME, AIChE, IIR, PennWell Conference & Exhibition, Houston, TX, 1997, pp. 115–119.

10. Lockett, M.J., Larson, K.F., and Ricotta, J.P., "Recent Developments in Air Distillation," *International Congress of Refrigeration*, Washington, DC, 2003.
11. Thorogood, R.M., et al., European Patent Specification 0 341 854 B1, APCI, April 1989.
12. Rohde, W.J., et al, European Patent Specification No. 0 377 117 B1, Linde AG, 1992.
13. Dalbert, P., "Benefits of Using CFD in Compressor Design and Analysis," *7th European Congress on Fluid Machinery for the Oil, Petrochemical and Related Industries*, I.Mech.E Conference Transactions, 1990-2, 1999.
14. Keenan B., and Reuter, K., "The Design, Experience and Economic Advantage of Cryogenic Turbo-Expanders with Active Magnetic Bearings," *3rd International Conference Kryogenica '94*, Czech Society of Mechanical Engineers, 1994.
15. Espie, D.M., and Papageorski, S.C., "Validation of Dynamic Simulation Models of Cryogenic Air Separation Processes," *Proceedings of 11th Intersociety Symposium,* Houston, TX, January 1998, pp. 91–98.
16. Ruhemann, M., *The Separation of Gases*, 2nd ed., Oxford University Press, 1949, pp. 174–182.
17. Reference [16], pp. 182–184.
18. Duus, H.C., and Dodge, B.F., *Chemical Engineering Handbook*, 3rd ed, Perry, J.H., ed., 1950, pp. 1711–1172.
19. Grunberg, J.F., "The Oxyton Cycle in the Production of Tonnage Oxygen," *The Industrial Chemist*, February, 1950.
20. Schuftan, P.M., and Mackie, A.G., "The Rescol Process," *Transactions Institution of Chemical Engineers*, 36, 137–144, 1958.
21. Schmucker, B., "Optimizing Plant Concepts for Specific Projects in Air Separation," *Reports on Science and Technology*, Linde A.G. (62/2000), p. 27.
22. De Percin, G., "The Production of Oxygen Under Pressure," *Supplement to the Bulletin of the International Institute of Refrigeration*, Appendix 1955-2, pp. 27–37.
23. Petit, P., "Comparison between Oxygen and Nitrogen Production at Low Pressure and High Pressure and Special Issue of Argon Recovery," *Coal, Gas and Air Conference*, Beijing, China, 1985.
24. Castle, W.F., "Modern Liquid Pump Oxygen Plants: Equipment and Performance," *Cryogenic Processes and Machinery, A.I.Ch.E. Symposium Series. No. 294.* 89,*9th Intersociety Cryogenic Symposium*, Houston, TX, April 1991, pp. 14–17.
25. Nikitvin, V.D., et al., "Air Rectification Plant for the Production of Pure Nitrogen," GB Patent No. 1,215,377, 1970.
26. Agrawal, R., and Woodward, D.W., "Efficient Process to Produce Tonnage Nitrogen," *Proceedings of the 19th International Congress of Refrigeration,* 1995, The Hague, The Netherlands, Vol. IIIb, pp. 1011–1017.
27. Reference [21], pp. 30–31.
28. Kinard, G.E., "The Commercial Use of Liquid Hydrogen Over the Last 40 Years," *Proceedings of the 17th International Cryogenic Engineering Conference*, Bournemouth, UK, Institute of Physics, 1998.
29. Newton, C.L., "Hydrogen Production and Liquefaction," *Chemical and Process Engineering*, Dec. 1967, 51–58.
30. Isalski, W.H., *Separation of Gases*, Clarendon Press, Oxford, 1989, p. 182.
31. McIntosh, G.E., "Hydrogen Liquefiers Since 1950," *CEC–ICMC Conference*, September 2003.
32. Vander Arend, P.C., "Large-Scale Liquid Hydrogen Production," *Chem. Eng. Prog.* ,57, 62–67, 1961.

33. Quack, H., "Conceptual Design of a High Efficiency Large Capacity Hydrogen Liquefier," *Advances in Cryogenic Engineering*, Vol. 47, American Institute of Physics, Melville, NY, 2002, p. 255.
34. Nahmias, D., "Large-Scale Commercial Liquid Hydrogen Plants," *Proceedings XVIIIth International Congress of Refrigeration,* Montreal, Canada, Int. Inst. Refrigeration, 1991, Vol. 1, pp. 322–330.
35. Baker, C.R., and Fisher, T.F., "Industrial Cryogenic Engineering in the USA," *History and Origins of Cryogenics*, Scurlock, R.G., ed., Clarendon Press, Oxford, 1992.
36. Bourget, J., Garnaud, R., and Grenier, M., "Engineering Large-Capacity LNG Installations," *The Oil and Gas Journal*, August 30, 71–75, 1971.
37. Kleemenko, A.P., "One-Flow Cascade Cycle," *Proceedings of the Xth International Congress of Refrigeration*, Int. Inst. Refrigeration, 1960, Vol. 1, pp. 34–39.
38. "LNG: Is it as Good as the Real Thing?" *M.W. Kellogg*, 2004.
39. Reference [30], pp. 211–235.
40. Durr, C., and de la Vega, F., "Cost Reduction in Major LNG Facilities," *World Gas Conference*, Washington, DC, 1988, *Hydrocarbon Tech. Int'l*, 1993, pp. 81–86.
41. Collins, C., Durr, C.A., de la Vega, F.F., and Hill, D.K., "Liquefaction Plant Design in the 1990s," *Hydrocarbon Processing*, April 1995, pp. 67–76.
42. Collins, C., personal communication, August 2005.
43. Shell Paper, PS3.6, *12th International Conference & Exhibition on Liquefied Natural Gas*, Perth, Australia, May 1998.
44. TCC Progress Report, No. 6, March 31, 2003, http://www.igu.org /tcc.

9
Advances in Helium Cryogenics

S.W. Van Sciver

National High Magnetic Field Laboratory, Florida State University, Tallahassee, FL 32310, USA

Abstract

This review provides a survey of major advances that have occurred in recent years in the area of helium cryogenics. Helium-temperature cryogenics is the enabling technology for a substantial and growing number of low-temperature systems from superconducting magnets to space-based experimental facilities. In recent years there have been many advances in the technology of low-temperature helium, driven mostly by new applications. However, to keep the review from being too broad, this presentation focuses mainly on three of the most significant advances. These are: (1) the development of large-scale recuperative refrigeration systems mainly for superconducting magnet applications in accelerators and other research facilities; (2) the use of stored superfluid helium (He II) as a coolant for space-based astrophysics experiments; and (3) the application of regenerative cryocoolers operating at liquid helium temperatures primarily for cooling superconducting devices. In each case, the reader should observe that critical technologies were developed to facilitate these applications. In addition to these three primary advances, other significant helium cryogenic technologies are briefly reviewed at the end of this chapter, along with some vision for future developments in these areas.

9.1 Introduction

The field of cryogenics is generally referred to as those processes that occur in the temperature range roughly $T < 120$ K, where the permanent gases (nitrogen and oxygen) are condensed. This is an arbitrary but useful definition that makes cryogenics a unique field of thermal engineering. The subject cuts across many disciplines, including refrigeration, fluid mechanics and heat transfer, material science, and instrumentation. The field has wide-ranging applications in energy, materials processing, medicine, and basic science. Helium cryogenics is a sub-field of cryogenics that primarily focuses on even lower temperatures. As suggested

about 20 years ago in *Helium Cryogenics* [1]: "...helium cryogenics as described here emphasizes the range of temperature where the fluid has large scale potential applications as a coolant, $1 < T < 10$ K."

Helium is a unique enough fluid to garner special attention in science and engineering. The most abundant form of helium (^{4}He) becomes a liquid at its normal boiling point of 4.2 K, which is the lowest of common cryogenic fluids. Even more special is that helium will not solidify even at absolute zero unless an external pressure of greater than 2.5 MPa is applied. Thus, it has no triple point. ^{4}He can also exist in either of two liquid phases: He I and He II. He I is the normal liquid, existing between the critical point ($T_c = 5.2$ K; $p_c = 0.227$ MPa) and the lambda transition ($T_\lambda = 2.176$ K at saturated vapor pressure). He II, also sometimes referred to as superfluid helium, exists between T_λ and absolute zero and possesses exceptional transport properties which are of basic as well as applied technical interest. The present review will concentrate on ^{4}He technology; however, helium also has a rare isotope, ^{3}He, which is of particular importance to very low-temperature refrigeration ($T \ll 1$ K). ^{3}He also displays a superfluid transition, but at approximately 0.002 K.

The very low normal boiling point of helium is one of the reasons why it took until 1908 for it to be first liquefied by H. Kamerlingh Onnes in Leiden. In the early days, the other main impediment to production of liquid helium was its relative low abundance in nature [2]. With such small quantities of helium available and the required specialized equipment, the field of helium cryogenics was originally restricted to a very few research laboratories primarily involved in basic physics research at low temperatures. Fortunately, that has all changed.

In spite of these early beginnings, the rapid growth of helium cryogenics really got underway about a half century ago with the start of three major development activities:

1. The development and eventual commercial availability of the Collins helium liquefier/refrigerator.
2. The rapid expansion of the space exploration program led mostly by the Apollo mission to the moon.
3. The discovery and production into conductor form of the high-field superconducting materials Nb$_3$Sn and NbTi.

The Collins liquefier [3] for the first time allowed the production of liquid helium to move out of the physics research laboratories of a few experts and into facility-based operations, such as national laboratories and industrial concerns. It also permitted large quantities of helium to be separated from its main source, natural gas. The Collins liquefier is based on a thermodynamic cycle consisting of room-temperature compression, five counterflow heat exchangers, two expansion engines and a final Joule–Thomson expansion stage to produce liquid. Once developed, the Collins liquefier/refrigerator and its subsequent commercial production models permitted laboratories to produce their own liquid helium and cool a wide variety of experimental systems to $T < 4$ K. Larger versions of this

machine became part of a growing liquid helium production capability [4]. This capability, combined with the development of high-efficiency helium storage and transport vessels, allowed helium to be separated from its source in natural gas wells, liquefied at central locations, and delivered to users worldwide. Also, larger quantities of liquid helium could be provided in "closed-cycle" mode to cool major physics research facilities. This last application is best exemplified by the large particle-accelerator facilities in operation today.

The initiation of the manned space program, best exemplified by the US Apollo mission to land a man on the moon, rapidly developed a high demand for cryogenic fluids, although mostly for liquid propellants (liquid hydrogen and liquid oxygen). However, liquid helium was also extensively used in propulsion systems for cryopumping, purging, and leak testing, resulting in a demand for liquid helium that grew rapidly during this period, with annual consumption increasing by over a factor of 10 between 1950 and 1968 [5].

Finally, the discovery and production of high-field superconductors for magnets, which began in the 1960s [6], had a strong impact on helium cryogenics through demand for a coolant. Many of the superconducting magnet applications of today were conceived shortly after the successful production of the first Nb_3Sn and NbTi conductors. Today, there are a wide range of superconducting applications with literally thousands of superconducting magnet systems in operation, ranging from magnetic resonance imaging (MRI) systems in hospitals to the largest scale efforts at the particle physics and nuclear fusion facilities around the world.

In an effort to limit the scope and length of the present chapter, the focus of this review of recent developments in helium cryogenics is on three major technologies. The selection of these three technologies for the discussion is to a large extent arbitrary and based on the author's own experience and knowledge. However, the three technologies selected clearly represent major developments that have occurred over recent years. In addition, there are many other important helium cryogenics technologies worth mentioning, and some of these developments have synergy with the three that have been chosen for this review. Thus, following the main discussion, other helium cryogenics technologies of note are discussed, along with their prospects for the future.

9.2 Three Major Developments in Helium Cryogenics

The three helium cryogenics technologies that have been chosen for this review include the development of:

- large, efficient recuperative helium refrigerator/liquefier systems mostly for high-energy physics laboratories;
- large, efficient He II cryostats for space-based astrophysics experiments;
- small ($Q \approx 1$ W at 4 K) regenerative cryocoolers for cooling of superconducting devices.

9.2.1 Large Refrigerator/Liquefiers for Particle Accelerators

The development of the Collins liquefier and the high-field superconducting magnet both had an early and major impact on magnet applications, with the dominant being large physics facilities for accelerating of particles. Perhaps the first notable example of such an application was the superconducting bubble chamber magnet as exemplified by the 12 ft (3.7 m) bubble chamber magnet at Argonne, Illinois, [7] and the 4.7 m bubble chamber at CERN in Switzerland [8]. These systems required both specially constructed cryostats and closed-cycle helium refrigerators so that they could provide steady operation as particle detectors. Although bubble chamber magnets are no longer in use today, it is worth noting that today almost all major particle physics experiments use large superconducting magnets in their detectors and these magnets are cooled by modern versions of the Collins liquefier.

Subsequently, superconducting magnets were adopted for high-energy particle physics beam lines, with the first being the Energy Doubler at Fermi Lab initiated in the 1970s and continuing to operate as the highest energy particle accelerator today. The Large Hadron Collider (LHC) at CERN is expected to come on line later this decade and will result in a major advance in achievable particle energy. The cryogenics requirements for these accelerators are somewhat unique, as the superconducting dipole and quadrupole magnets are distributed over the circumference of the accelerator ring. Thus, in addition to the requirements for large refrigerators, these accelerators also have placed stringent requirements on magnet cryostat design and cryogenic helium distribution equipment.

In recent years, the impetus for developing helium refrigerators and cryogenic systems for particle accelerators has shifted somewhat. The first such shift is toward improved overall thermal efficiency, with a variety of refrigeration requirements at different temperatures. The cooling requirements for modern accelerators are in the range of tens of kilowatts at 4.5 K and thousands of liquid liters per hour. Thus, the thermodynamic efficiency of the refrigeration equipment has significantly impacted the operations budget of the facility. For example, the LHC main ring will be supplied by eight 18 kW refrigerators [9] at 4.5 K. The detailed design of these machines was up to the two vendors [10–12], with the requirement being a minimum combined cost of capital and operation over the 10-year period. Cycle optimization has led to high overall efficiency, with the projected value in the range of 27% of Carnot. Each 18 kW machine supplies several levels of cooling to the LHC. For example, under normal operating conditions, the machine supplies 2.6 kW of refrigeration at 4.5 K, 12.4 kW of nonisothermal refrigeration between 4.5 and 20 K for the beam screen, 22 kW of nonisothermal radiation-shield cooling between 50 and 75 K and 27 g/s of cooling to the magnet current leads. All these requirements demand a much more complex cycle than the original Collins liquefier. Figure 9.1 is a side-by-side comparison of the original Collins cycle to the Air Liquide 18 kW LHC refrigerator.

The other recent shift in helium refrigerator technology has been the growing number of particle accelerator refrigeration systems that operate around 2 K in the He II region. Again, perhaps the most notable of these systems is the LHC main

ring refrigeration system, with 2.5 kW of cooling at 1.8 K [13]. Other significant 2 K refrigeration systems have been developed for radio-frequency (RF) cavity accelerators, as exemplified by the CEBAF at the Thomas Jefferson Laboratory in Virginia or the Spallation Neutron Source currently under construction at Oak Ridge, Tennessee. All of these systems use multistage cold compressors to achieve the reduced temperature operation. Successful development of the cold compressor was an important technical achievement that enabled large kilowatt level He II refrigerators to be developed.

In addition, the operation of superconducting magnets at reduced temperatures was significantly improved by the development of the pressurized He II cryostat. This cryostat concept was originally conceived by G. Claudet and Aymar in connection with the Torus–Supra Tokamak project in France [14]. The essential advantage of such a design is that it maintains the magnet in a bath of He II nominally at 1.8 K, but pressurized to $p > 0.1$ MPa so that vapor cannot be generated in the magnet cryostat unless the local temperature exceeds 4.2 K. This approach provides excellent thermal stability for the magnet, while steady-state heat removal is
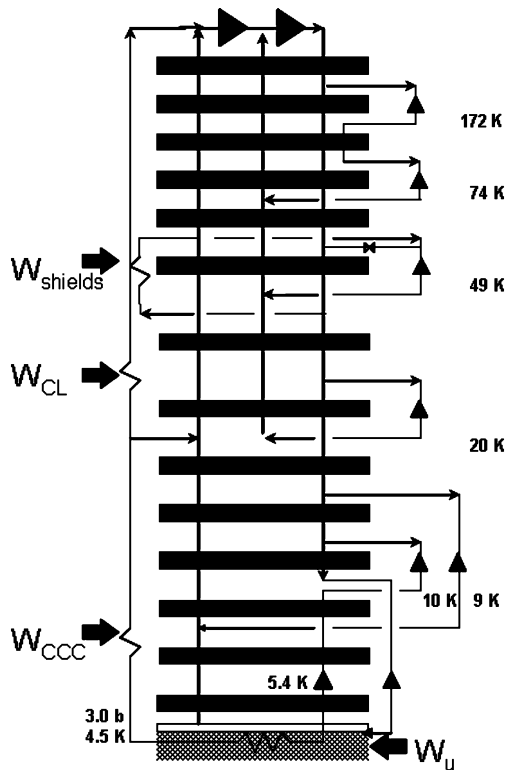
FIGURE 9.1. Comparison of the Air Liquide LHC 18 kW refrigerator cycle [12] with a standard Collins cycle.
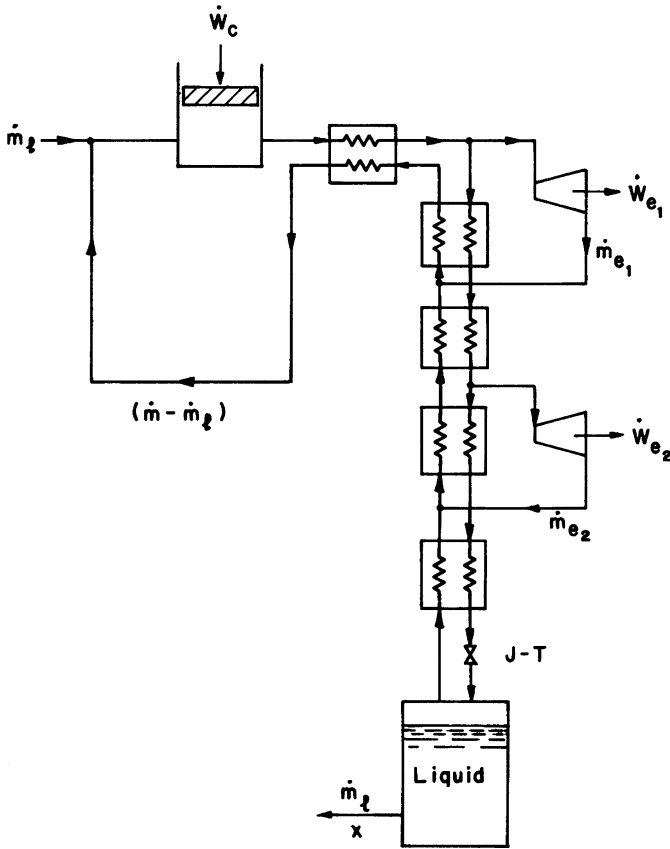
FIGURE 9.1. (*Continued*)

achieved by an immersed saturated He II heat exchanger that limits the volume of the low-pressure He II in the refrigerator. The "Claudet" cryostat has subsequently been used in almost all He II magnet systems, including the accelerator magnets for the LHC.

As with most developments in helium cryogenics, the future of large recuperative refrigerator systems will be dictated mostly by the demands of the applications, with the most dominant being particle physics experimental facilities. The future of high-energy physics particle accelerators (post-LHC) appears to be looking to the International Linear Collider, which is just beginning the design effort. However, current plans for this machine call for an RF cavity electron accelerator probably operating near 2 K and cooled with He II. Should this project go forward to construction, then it will most certainly place stringent demands on the efficiency of the helium cryogenic system for 2 K use, including the refrigerator and the associated cryostats for housing the RF cavities.

9.2.2 *Space-Based He II Cryogenic Systems*

The second significant topic in helium cryogenics to be reviewed here is the development of the technology to put large quantities (volume ∼1000 L) of He II in space and have it there for extended periods of time, up to years, for a variety of astrophysics experiments. This technology was pioneered with the Infrared Astronomical Satellite (IRAS) which performed an infrared survey above the Earth's atmosphere [15]. IRAS was launched in 1983 and was so successful that it spawned a series of infrared telescope launches, culminating most recently in the Spitzer Space telescope launched in polar orbit in 2003, see Figure 9.2 [16]. In addition, other space-based astrophysics experiments are also using stored He II cryogenic systems, including the 2004 launch of the Gravity Probe B experimental test of general relativity [17].

The cryogenic systems associated with space-based He II storage have several common features. First, the storage vessels are designed for extremely high thermal efficiency. For example, the projected hold time for the Spitzer telescope, which contains 49 kg of He II at launch, is between 4.2 and 5 years. To achieve the long hold times necessary for successful missions, great care combined with advanced cryogenics technology are required. Structural supports that can withstand the launch environment and disconnect in microgravity have been developed and applied in the Gravity Probe B experiment [18]. Other systems have used additional higher temperature stored cryogens on board for intermediate heat stationing. These efforts are essential to the mission success, as it is next to impossible to replenish the onboard cryogens and active refrigeration has insufficient capacity.

The other important enabling technology for space-based He II systems is the porous plug phase separator [19]. This device, originally proposed for the GPB cryostat and pioneered for the IRAS project, uses a unique property of He II called the fountain effect to maintain the liquid helium within the vessel while venting the vapor generated by the absorption of heat in the He II reservoir. A photograph of the porous plug phase separator developed for the IRAS He II tank is shown in Figure 9.3 [20]. This device consists of a sintered stainless steel plug approximately 50 mm in diameter, with a pore size in the range of 1 to 10 μm.

In operation, the outer surface of the porous plug in the vent line is exposed to space and pumped by the ambient vacuum. The inner, tank side of the plug is in contact with the He II reservoir and the contained liquid. Such a device achieves helium phase separation by the following method. As helium flows through the plug, its pressure and temperature drop. However, unique to He II contained to narrow channels and flowing at velocities less than the superfluid critical velocity v_{sc} is that a temperature difference across the plug produces a pressure difference according to London's equation:

$$\Delta p = \rho s \Delta T \qquad (9.1)$$

where ρs is the volumetric entropy of the He II. At 1.8 K ρs is equal to about 80 Pa/mK, which corresponds to about 60 mm of He II hydrostatic head. Since this so called "fountain pressure" is greater than the slope of the vapor pressure

FIGURE 9.2. Spitzer space telescope cryogenic tank assembly being prepared for vibration testing (tank volume: 363 L) [16].

curve for He II, the liquid is prevented from flowing through the plug and stays in the tank.

In steady operation, helium flows through the plug, exiting in the vapor phase so that the heat of vaporization is available to extract the cryostat heat load. Since the total mass flow is determined by the rate of heat extraction from the dewar, it can be shown that for ideal conditions [21]

$$\dot{m} = \frac{\rho d^2}{\beta \mu_n} \left(\frac{sT}{sT + \lambda} \right) \frac{\Delta p}{L} \tag{9.2}$$

FIGURE 9.3. He II Phase separator for the IRAS SFHE tank. The plug is approximately 50 mm in diameter and manufactured by Mott Corporation (formerly Mott Metallurgical Corp.) from sintered nickel. The attached germanium thermometer is for determining the downstream helium temperature (from Ref. [20]).

where β is a shape factor, μ_n is the viscosity of the normal fluid component of the He II, λ is the latent heat and d is the pore diameter within the plug. Equation (9.2) is identical to that which describes classical laminar flow through porous media with the additional term $[sT/(sT + \lambda) \approx 0.05]$. This expression effectively describes

the flow through the phase separator up to the critical velocity. Above that value, the pressure drop versus flow rate becomes nonlinear due to turbulence in the two fluid components.

As an example, the recently launched Spitzer infrared telescope cryostat is currently operating at 1.2 K with a ΔT of only 3 mK across the plug [16]. This ΔT corresponds to a fountain pressure of $\Delta p = 22$ Pa, which appears sufficient to contain the liquid in the dewar. Virtually all He II space-based systems now employ porous plug phase separators.

Although the technology of He II stored cryogens has proven to be successful in a large number of space-based experiments, the problems associated with launching a large dewar of He II into space have resulted in a number of challenges to the safe and reliable operation of such systems. As a result, it is unclear to what extent future space-based experiments will utilize this technology. As is discussed in the next section, great strides have recently been achieved with the development of long-life, reliable regenerative cryocoolers for $T < 4$ K operation. The future helium cryogenic systems for space-based experiments may, therefore, entail using active cryogenic equipment with the possibility of launching the experiment at ambient temperature followed by cooldown and operation in space.

9.2.3 4 K Regenerative Cryocoolers

In recent years, a number of technologies have arrived on the scene that operate around 4 K and below, but which only require a small amount of cooling power (typically $Q < 1$ W). One such technology is the conduction-cooled low-temperature superconductor (Nb_3Sn or NbTi)-based magnet system. Conduction-cooled superconducting magnets are now available in a variety of sizes and magnetic fields for DC magnetic field applications often at remote locations where access to liquid helium is restricted. Examples include magnets for physics and materials research, ore separation and MRI. This technology is quite advanced, and the magnetic fields achieved are comparable to those of magnets that are bath cooled by liquid helium [22]. The only disadvantage of these systems appears to be increased complexity and capital cost with longer cooldown times.

Conduction-cooled low-temperature superconducting systems have been enabled by the development of two necessary support technologies. The first technology is the cryocooler with cooling capacity of around 1 W at 4 K. Regenerative cryocoolers have been under development with steadily improving performance since their introduction as an alternative to the Collins cycle machine. For low-temperature operation, the Gifford–McMahon (GM) cycle, Figure 9.4, has advantages over other common cycles largely because its low-frequency operation enhances heat exchange with the regenerator [23]. The first GM refrigerator achieved a minimum temperature of 35 K in one stage [24], and within several years of that time one could acquire a multistage GM machine with useful cooling power at temperatures approaching 10 K. However, achievement of 4 K with a GM cryocooler depended on the introduction of new materials into the lower end of the regenerator.
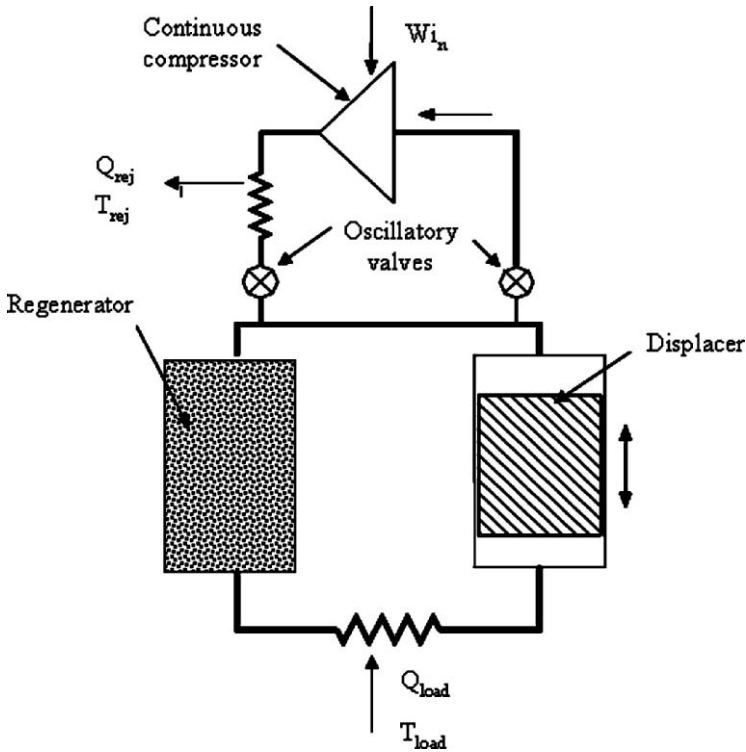
FIGURE 9.4. The GM cycle.

Regenerative cryocoolers differ from recuperative cycle machines (like the Collins cycle machine) in that the fluid flows in a periodic cycle within the machine, extracting heat from the lower end of the regenerator. The regenerator is similar to a heat exchanger, except that it needs to have a large volumetric heat capacity to allow significant heat removal per cycle. Early GM cryocoolers used copper and lead for the regenerator, with lead at the low-temperature region because of the larger heat capacity (compared with copper). These systems could reach 10 K in two stages. However, to achieve useful cooling at 4 K, the volumetric heat capacity of lead is insufficient. This required the introduction of new materials with large heat capacities at low temperature. Figure 9.5 is a plot from Nagao et al. [25] of the measured specific heat of several candidate regenerator materials for low-temperature application. Note that the volumetric specific heat of the rare earth materials at 4 K is much larger than that of lead. With the introduction of these high specific-heat materials into GM cryocooler regenerators, minimum temperatures in multistage GM cryocoolers were soon able to drop below 4 K, making their application in low-temperature superconducting devices a possibility. However, a noted disadvantage of GM cycle cryocoolers is their relative low efficiency and the active displacer that moves at low temperature. These
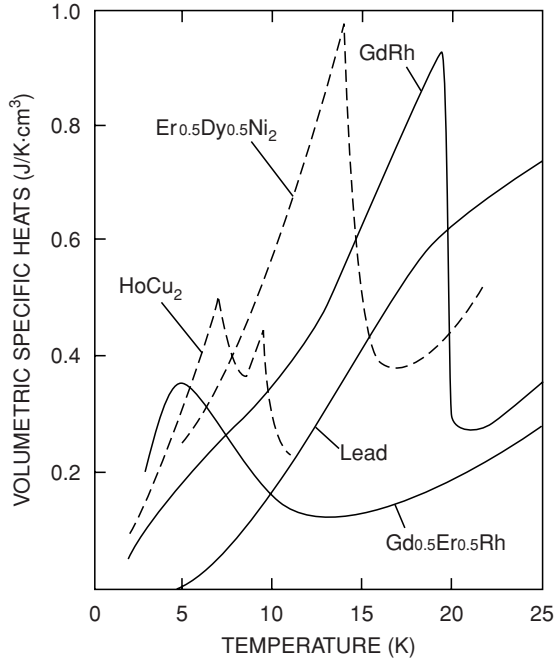
FIGURE 9.5. The volumetric specific heat of various rare earth compounds in comparison with that of lead (from Nagao et al. [25]).

limitations of GM cryocoolers have since encouraged their replacement with newer pulse tube cryocoolers. Pulse tube cryocoolers are now available with a range of cooling capacities down to temperatures below 4 K.

Pulse tube cryocoolers were invented in the 1960s by Gifford and Longsworth [26]; however, for a variety of reasons, the pulse tube was not a promising technology for low-temperature operation and, thus, most of the effort has been focused on higher temperature ($T \approx 80$ K) single-stage coolers [27]. The principal difference between a pulse tube cryocooler and other conventional cryocooler configurations is the replacement of the mechanical displacer with an acoustic wave. There are a number of different pulse tube configurations, with the two basic types being Stirling and GM. Figure 9.6 compares these two pulse tube configurations. The GM type has the same advantages over the Stirling type for low-temperature operation as the conventional machines. As a result, most 4 K pulse tubes are of the GM type, although 4 K Stirling-type pulse tubes are under development [28]. Currently, a number of commercial vendors supply two-stage GM pulse tube cryocoolers with about 1 W of cooling power at 4 K. The current record low temperature for a GM pulse tube cryocooler is 1.27 K, achieved in two stages with ^{3}He replacing ^{4}He in the second stage [29].

By combining careful thermal and structural design of the cryostat, it is possible to keep the steady heat load of a conduction-cooled DC superconducting magnet
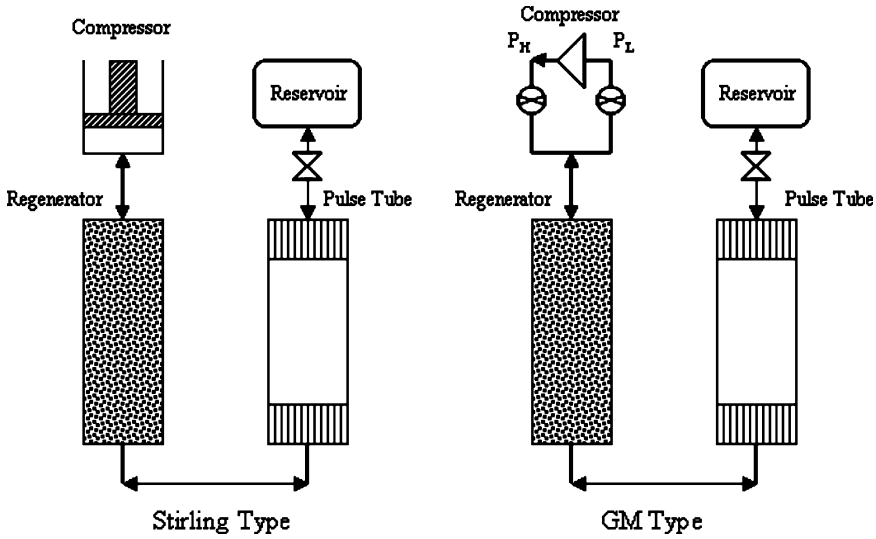
FIGURE 9.6. Comparison of the Stirling-type and GM-type pulse tube cryocoolers.

system sufficiently low to stay under the cooling power limits of modern 4 K cryocoolers. One important enabling technology is the high-temperature super-conductor current lead [30], which has allowed reasonable currents on the order of 100 A to be supplied to the magnet with minimal thermal impact on the 4 K cooling load. If the magnet is cooled with a two-stage cryocooler, then the upper cooling stage is used as a heat intercept for the normal metal section of the current lead. The high-temperature superconducting (HTS) portion can then link to the 4 K magnet, essentially eliminating joule heat absorption at 4 K. At present, conduction-cooled HTS current leads are readily available up to current capacities on the order of 1 kA. For higher current applications, vapor cooling is often utilized, particularly for the normal resistive section, where the heat load can be substantial.

There appears to be a growing need for small-scale refrigeration at temperatures near 4 K. In addition to conduction-cooled low-temperature superconducting magnets, other superconducting devices also utilize 4 K cryocoolers. For example, helium-bath-cooled superconducting magnets for a variety of applications use a 4 K cryocooler as a recondenser of the evolved vapor, thus reducing the liquid helium inventory and eliminating the need to refill [31,32]. This application will increase as the reliability of cryocoolers improves, with a corresponding reduction in the need for technician service to superconducting-magnet-based instruments.

The other area where 4 K cryocoolers may have a significant future impact is in space-based low-temperature astrophysics experiments that currently use stored He II cryogen to supply the required cooling capacity. As indicated above, technical problems with managing the stored He II reservoir, plus the limited experiment duration due to the finite volume, has encouraged consideration of alternate

approaches for future systems. One option is to use an entirely conduction-cooled system based on pulse tube cryocoolers [33]. Provided that the coolers can be made sufficiently reliable and that adequate thermal contact can be achieved, then space-based low-temperature experiments can have a much longer useful lifetime.

9.3 Other Significant Developments in Helium Cryogenics

In addition to the three major helium cryogenics technologies discussed above, there are a number of other significant technologies worth at least mentioning in the present review. This list may be incomplete, but clearly represents some very important advances in the field.

9.3.1 Small Cryocoolers for Intermediate Temperature Applications

There are many cryogenic applications that require a modest amount of cooling capacity at intermediate temperatures ($20 < T < 80$ K). These applications include most of the HTS devices being developed for power systems, as well as small-scale HTS devices used for sensitive magnetometers and cellular communications. In addition, there is a large effort in cold semiconductor device applications that require cooling. This latter group includes infrared sensors, cold electronics, and a variety of specialized instrumentation for research.

The vast majority of these small, intermediate temperature cryocoolers are either of the pulse tube variety if continuous cooling is required or Joule–Thomson expansion coolers for transient cooling. Sorption coolers are also developed particularly for specialized aerospace applications. Many of the details on specialized cryocooler technologies are described in Chapter 11.

9.3.2 Improvements in Rotating Machinery for Low-Temperature Helium Service

Advances in large-scale refrigeration for applications such as high-energy physics accelerators has benefited from steady improvements in the rotating machinery that supports the operation. Already discussed above is the noted development of the cold compressor for sub-4.2 K refrigeration and its associated impact on high-field superconducting magnet operation near 1.8 K. Low-temperature expansion engines have also advanced from the original reciprocating machines of the Collins refrigerator/liquefier to the use of high-speed turbine expanders, thus increasing reliability and efficiency. Finally, there has been a substantial development effort in cryogenic centrifugal pump technology for liquid helium distribution systems, such as the cooling circuit for large detector magnets in high-energy physics accelerator facilities [34].

9.3.3 Production of Standardized Liquid Helium Cryostats

One of the truly commercial activities in helium cryogenics has been the development of standardized cryostats for a wide variety of applications. Mobile liquid helium storage tanks are now manufactured in a range of standard sizes with volumes ranging from 25 L to in excess of 1000 L. Fixed liquid helium storage tanks can be even larger. For liquid helium transport, trailer trucks with capacities in the range of 40,000 L commonly deliver liquid from centralized liquefaction facilities to distribution centers around the country.

Superconducting magnet technology has also benefited from the availability of standard cryostat designs. Depending on the application and number of units required, their designs can take advantage of modern mass production techniques to reduce cost and increase thermal efficiency. For example, MRI and nuclear magnetic resonance magnets use highly efficient liquid helium cryostats to achieve very low rates of helium consumption, thus minimizing the disturbances to the use of the magnet by the helium refill process. In high-energy physics accelerators like the LHC, the dipole and quadrupole magnets are housed within cryostats that have many standard and common components.

Finally, the low-temperature research community has significantly benefited from the development of highly efficient, usually stainless steel liquid helium cryostat technology. No longer do we rely on skilled glass blowers to manufacture these experimental systems. Readily available are a number of vendors that can build fully welded metallic cryostats that have long life and require minimum maintenance.

9.3.4 ^{3}He–^{4}He Dilution Refrigeration

Although not in the nominally defined temperature range of helium cryogenics ($1 < T < 10$ K), dilution refrigeration certainly represents a very significant advance that has had enormous impact on very low-temperature research ($T < 100$ mK) [35]. The dilution refrigerator, which uses the unique properties of phase-separated ^{3}He–^{4}He mixtures at low temperature, now forms the basis for most of the very low-temperature research facilities. Prior to the development of the first dilution refrigerator in 1967 by Vilches and Wheatley [36], millikelvin temperatures were only achievable by adiabatic demagnetization of paramagnetic materials (see Section 9.3.5).

Dilution refrigerators, which are commercially available today from several vendors, can now provide continuous cooling power on the order of 1 to 10 μW at 10 mK. This temperature range is primarily of interest to low-temperature physics research laboratories, where the dilution refrigerator can be used as the heat sink temperature for even lower temperature experiments ($T < 1$ mK) mostly cooled by nuclear demagnetization refrigeration. This technology supports a range of physics research topics, including, in particular, the study of the superfluid phase of ^{3}He below 2 mK.

9.3.5 Magnetic Refrigeration

Low-temperature refrigeration using demagnetization of paramagnetic salts was first suggested by Debye and Giauque in 1925. Refrigeration in this system is achieved by ordering the electron spins in a paramagnetic material using an external magnetic field. Subsequently, the spins are allowed to disorder adiabatically, thus absorbing thermal energy from the material lattice [37]. Until the development of the dilution refrigerator, the adiabatic demagnetization refrigerator based on the above principle was the primary method for reaching the millikelvin temperature range. This technology continues to be attractive for certain specialized applications such as for space-based instruments, where dilution refrigerators are not suitable because of their large size and dependence on gravity to assist with the phase separation process [38].

Adiabatic demagnetization has also more recently gained acceptance as the most effective method for achieving sub-micro-kelvin temperatures. In this case, the demagnetization occurs within the nuclear spins (rather than the electron spins in a paramagnetic material). The record low lattice temperature of below 1 nK was achieved using a two-stage nuclear demagnetization refrigerator consisting of a high-purity copper first stage and a rhodium metal second stage [39].

References

1. Van Sciver, S.W., *Helium Cryogenics*, Plenum Press, New York, 1986.
2. Longsworth, R., "100th Anniversary of the Discovery of Helium in Natural Gas," *Advances in Cryogenic Engineering*, Vol. 51A, American Institute of Physics, New York, 2006, pp. 863–870.
3. Collins, S.C., "Helium Refrigerator and Liquefier," *Advances in Cryogenic Engineering*, Vol. 11, Plenum Press, New York, 1966, pp. 11–15.
4. Quack, H., "Large Scale Refrigeration," *Proc. ICEC 11*, Butterworths, Surrey, UK, 1986, pp. 21–26.
5. Brickwedde, F.G, Hammel, E.F., and Keller, W.F., "History of Cryogenics in the USA,"*History and Origins of Cryogenics*, Scurlock, R.G., ed., Clarendon Press, Oxford, 1992, pp. 383–384.
6. Hulm, J.K., Chandrasekhar, B.S., and Riemersma, H., "High Field Superconducting Magnets," *Advances in Cryogenic Engineering*, Vol. 8, Plenum Press, New York, 1963, pp. 19–29.

7. Jones, R.E., et al., "Construction of the 12-foot Bubble Chamber Superconducting Magnet Cryostat," *Advances in Cryogenic Engineering*, Vol. 15, Plenum Press, NY, 1970, pp. 141–149.

8. Wilson, M.N., *Superconducting Magnets*, Clarendon Press, Oxford, 1983, Ch. 2.

9. Claudet, S., Gayet, P., and Wagner, U., "Specification of Four New Large 4.5 K Helium Refrigerators for the LHC," *Advances in Cryogenic Engineering*, Vol. 45, Kluwer Academic/Plenum Publishers, New York, 2000, pp. 1269–1276.

10. Dauguet, P., Gistau, G.M., and Briend, P., "Two Large 18 kW Helium Refrigerators for CERN's LHC Project, Supplied by Air Liquide," *Advances in Cryogenic Engineering*, Vol. 45, Kluwer Academic/Plenum Publishers, New York, 2000, pp. 1277–1284.

11. Bosel, J., Chromec, B., and Meier, A., "Two Large 18 kW Helium Refrigerators for CERN's LHC Project, Supplied by Linde Kryotechnik AG," *Advances in Cryogenic Engineering*, Vol. 45, Kluwer Academic/Plenum Publishers, New York, 2000, pp. 1285–1292.

12. Dauquet, P., et al., "Design, Construction and Startup by Air Liquide of Two 18 kW at 4.5 K Helium Refrigerators for the New CERN Accelerator, LHC," *Advances in Cryogenic Engineering*, Vol. 49, American Institute of Physics, New York, 2004, pp. 147–153.

13. Claudet, S., et al., "Specification of Eight 2400 W @ 1.8 K Refrigeration Units for the LHC,"*Proc. 18th ICEC*, Mumbai, India, 2000, Narosa Publishing, New Delhi, 2000, pp. 207–210.

14. Claudet, G., and Aymar, R., "Tore Supra and He II Cooling of Large High Field Magnets," *Advances in Cryogenic Engineering*, Vol. 35, Plenum Press, New York, 1990, pp. 55–68.

15. Urbach, A.R., and Mason, P.V., "IRAS Cryogenic System Flight Performance Report," *Advances in Cryogenic Engineering*, Vol. 29, Plenum Press, New York, 1984, pp. 651–660.

16. Finley, P.T., and Schweickart, R.B., "Mid-Mission Update of Spitzer Space Telescope Cryogenic Performance," *Advances in Cryogenic Engineering*, Vol. 51B, American Institute of Physics, New York, 2006, 1295–1302.

17. Murray, D.O., Taber, M.A., and Burns, K.M., "Flight Performance of Gravity Probe B Cryogenic System," *Advances in Cryogenic Engineering*, Vol. 51B, American Institute of Physics, New York, 2006, 1303–1314.

18. Spradley, I.E., and Parmley, R.T., "Design and Test of a Modified Passive Orbital Disconnect Strut (PODS-IV)," *Advances in Cryogenic Engineering*, Vol. 33, Plenum Press, New York, 1988, pp. 935–942.

19. Petrac, D., and Mason, P.V., "Evaluation of Porous Plug Liquid Separators for Space Superfluid Helium System," *Proc. ICEC 7*, IPC Science & Technology Press, Surrey, England, 1978, pp. 120–123.

20. Van Sciver, S.W., "He II (Superfluid Helium)," *Handbook of Cryogenic Engineering*, Weisend II, J.G., ed., Taylor Francis, Philadelphia, 1998, p. 474.

21. Schotte, U., "He II Phase Separation with Slits and Porous Plugs for Space Cryogenics," *Cryogenics* 24, 536, 1984.

22. Sato, A., "17.3 T Achieved with Conduction-Cooled Magnet using 2 K Refrigerator," http://www.nims.go.jp/eng/news/nimsnow/Vol1/No5/p6.html.

23. McMahon, H.O., and Gifford, W.E., "A New Low-Temperature Gas Expansion Cycle," *Advances in Cryogenic Engineering*, Vol. 5, Plenum Press, New York, 1960, pp. 354–367.

24. Gifford, W.E., and Hoffman, T.E., "A New Refrigeration System for 4.2 K," *Advances in Cryogenic Engineering*, Vol. 6, Plenum Press, New York, 1961, pp. 82–94.

25. Nagao, M., Inaguchi, T., Yoshimura, H., Yamada, T., and Iwamoto, M., "Helium Liquefaction by a Gifford–McMahon Cycle Cryocooler," *Advances in Cryogenic Engineering*, Vol. 35, Plenum Press, New York, 1990, pp. 1251–1260.

26. Gifford, W.E., and Longsworth, R.C., "Pulse Tube Refrigeration Progress," *Advances in Cryogenic Engineering*, Vol. 10, Plenum Press, New York, 1965, pp. 69–79.

27. Radebaugh, R., "A Review of Pulse Tube Refrigeration," *Advances in Cryogenic Engineering*, Vol. 35, Plenum Press, New York, 1990, pp. 1191–1206.

28. Nast, T., Lockheed Martin Aerospace, personal communication.

29. Jiang, N., Lindemann, U., Giebler, F., and Thummes, G., "A ^{3}He Pulse Tube Cooler Operating Down to 1.3 K," *Cryogenics*, 44, 809, 2004.

30. Hull, J.R., "High Temperature Superconductor Current Leads," *IEEE Trans. Appl. Supercond.*, 3, 869, 1993.

31. Burgoyne, J.W., Danials, P., Timms, K., and Vale, S., "Advances in Superconducting Magnets for Commercial and Industrial Applications," *IEEE Trans. Appl. Supercond.*, 10, 703, 2000.

32. Van Sciver, S. W. "Cryogenic Systems for Superconducting Devices," *Physica C*, 354, 129, 2001.

33. Sugita, H., et al., "Cryogenic Infrared Mission 'JAXA/SPICA' with Advanced Cryocoolers," 2005 Space Cryogenics Workshop, *Cryogenics*, in press.

34. Delruelle, N., Haug, F., Junker, S., Passardi, G., Pengo, R., and Pirotte, O., "The Common Cryogenic Test Facility for the Atlas Barrel and End Cap Toroid Magnets," *Advances in Cryogenic Engineering*, Vol. 49A, American Institute of Physics, New York, 2004, pp. 249–256.

35. White, G.K., and Meeson, P.J., *Experimental Techniques in Low Temperature Physics*, 4th ed., Oxford Science, 2002, pp. 151–165.

36. Wheatley, J.C., "Experimental Properties of Pure ^{3}He and Dilute Solutions of ^{3}He in Superfluid ^{4}He at Very Low Temperatures: Application to Dilution Refrigeration," *Progress in Low Temperature Physics VI*, Gorter, C.J., ed., North Holland, Amsterdam, 1970, pp. 142–147.

37. Van Sciver, S.W., *Helium Cryogenics*, Plenum Press, New York, 1986, p. 362.

38. Shirron, P., et al., "A Compact High Performance Continuous Magnetic Refrigerator for Space Missions," *Cryogenics*, 41, 789, 2002.

39. Knuuttila, T., "Nuclear Magnetism and Superconductivity in Rhodium," PhD dissertation, Helsinki University of Technology, 2000, http://lib.tkk.fi/Diss/2000/isbn9512252147/.

10
Lessons Learned in 50 Years of Cryogenic Thermometry

F. Pavese

National Institute for Research in Metrology (INRiM),[1] *Turin 10135, Italy*

Abstract

This chapter reviews the basics of cryogenic thermometry in the past 50 years and its updated state of the art. First, it answers the question of why a temperature scale is needed and its meaning. Next, the basics of a scale definition and a short history of the temperature scales from 1955 are outlined, together with lessons learned in temperature calibration and international standards. Finally, the characteristics of the main types of thermometer developed in the past 50 years and used in cryogenics are summarized.

10.1 Introduction

The range of temperatures considered in cryogenics appears to be quite small, i.e. a few hundred kelvin, when compared with the millions of degrees encountered, for example, in the plasma region. However, much fundamental work in physics has been performed at temperatures well below 1 K. In fact, a logarithmic scale (Figure 10.1) for the temperature values is a more realistic way to portray the temperature scale than a linear one. Since absolute zero is approached logarithmically, it becomes equivalent to the upper boundary of the temperature scale, $+\infty$. In the very low temperature range, conditions occur that are quite different from human experience. Temperatures are commonly attained in laboratories where equilibrium temperature values may be different for different components of the solid substance and substantial temperature gradients may occur during nonequilibrium conditions; these conditions directly affect the capability of measuring very low temperatures.

The past 50 years cover a substantial part of the cryogenic history, at least of that part of the history following the pioneering work and when it became a technological field with important practical applications.

---

[1] Formerly Instituto di Metrologia "G.Colonnetti" (IMGC).
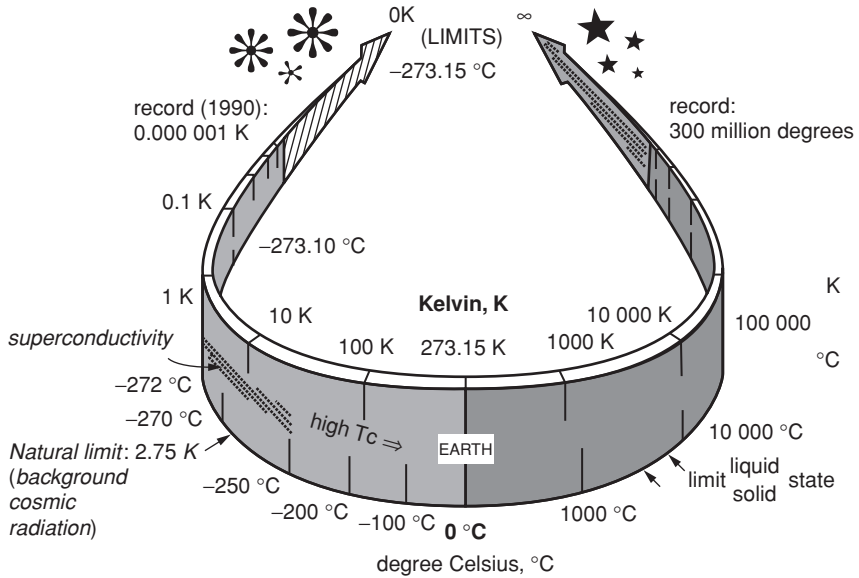
FIGURE 10.1. The logarithmic scaling of natural phenomena (from Pavese and Molinar 2002).

Thermometry was obviously an essential tool to measure the temperatures achieved and to describe temperature-dependent phenomena with the required accuracy. This dependence is particularly remarkable at very low temperatures. On the other hand, temperature is an intensive quantity, needing a "scale" for describing the "degree of warmth and of cold" and cannot be measured without using a "transducer," i.e. by measuring another temperature-dependent quantity. This makes its accurate measurement much less trivial than is commonly understood. The consequence of this quest for accuracy measurement has generated a relatively complicated history of its international standards and the need of the development of many types of those transducers in the time span considered.

It would be impossible to summarize in a clear way the many changes, improvements, and developments that have occurred in the past 50 years, and the mere history would be of little interest. Accordingly, this chapter will instead try to give an overview of the basics of cryogenic thermometry and of the updated state of the art.

This chapter presents an overview of why a temperature scale is needed and its meaning for thermometry. Then the basics of a scale definition and a short history from 1955 of the temperature scales will be summarized, together with a summary of the lessons learned in temperature calibration and international standards and of the future perspectives. The characteristics of the main types of thermometer developed over the past 50 years and used in cryogenics complete the presentation.

10.2 Temperature Scales

10.2.1 Thermodynamic Temperature

In principle, any thermodynamic law of physics or chemistry can be used to obtain a thermodynamic temperature. One such law governs the behavior of the ideal gas:

$$pV = nRT \tag{10.1}$$

where p is the pressure, T the temperature, V the volume, n the amount of substance, and R the gas constant.

In 1889, a thermodynamic scale, i.e. the normal hydrogen scale, was adopted by the Conférence Générale des Poids et Mesures, based on the work of Chappuis at the Bureau International des Poids et Mesures, using a calibration at the ice and steam point of water. The unit of temperatuare used was the "degree centigrade" (°C).

In 1927, an International Temperature Scale (ITS-27) was developed, whose definition is purely empirical, with the same unit. From 1927 to 2005 the international standard has always been distinct from the thermodynamic scale.

10.2.2 Empirical Temperature

Determination of the thermodynamic temperature from first principles is, in general, a difficult experiment. Every measurement is only an approximation, because of imperfections in the model used for describing the basic thermodynamic law, because of insufficient control of the secondary experimental parameters that are included in the model (the so-called "corrections"), or because of experimental random errors.

However, in nature, a temperature-independent phenomenon is rather the exception than the rule. Any temperature-dependent physical quantity can, in principle, be used to measure temperature: thermometers were invented long before principles of heat were understood. Whether a physical quantity is suitable or not as a thermometer is a matter of convenience; a choice may also depend on the required precision of the resulting temperature scale.

An important element to consider for the evaluation of a candidate empirical scale, apart from the trivial necessity for the physical quantity to behave monotonically with temperature (e.g. water density is not), is whether or not it is a linear transformation of the absolute temperature, to which it must always be referred to. If it is not linear, then the relationship between the physical quantity and the thermodynamic temperature must be carefully specified; this specification is often difficult to find, especially over long periods of time.

Most empirical temperature scales are defined in terms of the temperature dependence of a different quantity, e.g. electrical resistance, thermal expansion, vapor pressure, etc. The definition of the empirical scale will include the value of the measured parameter at various specified reference temperatures.

At least two defining points are used in an empirical scale definition. They are called the "*fixed points*" of that scale. None needs to be the defining point of the kelvin scale. The scale definition assigns them conventional temperature values. Though these values typically have been assumed to be exact thermodynamic temperature values, they are, at best, up-to-date approximations. The empirical temperature θ defined by these scales has been considered to be satisfactory as an approximation of the thermodynamic temperature T.

This point will be made clearer by the example of the platinum resistance thermometer. Note that the experimental data pertain exclusively to a specific substance such as platinum and cannot be extended, by means of a theory, to represent other metals. Other restrictions must be considered as well; for instance, the bulk material must be in well-defined chemical (oxidized, etc.) and physical (strain-free, etc.) states, and the results are valid only for a given range of chemical purity.

When some of the characteristics of the interpolating instrument can be specifically quantified, the range of the accepted values for these parameters must also be defined in the scale, to enable one following this prescription to be able to reproduce the results, viz. the scale. If this is not possible, as with diode thermometers or thermistors, then the results and the scale developed will be valid only for the specific production-lot of devices from which results were obtained.

The thermometer used in a scale of these types is known as an "interpolating instrument," because it is not itself required to reproduce a thermodynamic property, but only precisely the smooth selected function of the empirical temperature θ, $y = f(\theta)$. The latter is used to interpolate temperature values between the values assigned to the fixed points.

To summarize, there are three constitutive elements associated with an empirical scale:

1. an interpolating instrument;
2. a mathematical definition;
3. a set of definitions, or fixed points.

The interpolating instrument has already been discussed.

The mathematical definition should be the simplest mathematical function (or set of functions) representing, within the stated accuracy, the relationship between the measured quantity and the thermodynamic temperature; it has a number of free parameters (this is characteristic of an empirical scale) whose numerical values must be obtained from a "calibration" of the interpolation instrument at a number of reference points. The number of these defining fixed points must be equal to the number of free parameters, and their position must be such so as to permit the best compromise between the mathematical requirements and what is available in nature. The temperature value of the reference point is defined, i.e. fixed, by the scale definition.

A scale of this type, which is the most common, is affected by a specific shortcoming, which must be kept in mind, called nonuniqueness. This term expresses the concept that, in each particular unit implementing the interpolating instrument

(i.e. the thermometer), the relationship between the measured quantity and temperature is slightly different. Therefore, the mathematical interpolating procedure defined by the scale cannot adequately represent the measurements performed with each individual unit of the thermometer, but can only approximate the physical behavior of these units. In other words, if the scale definition is applied to two specific units of the thermometer placed in an isothermal enclosure, then there will be a measurable difference between the temperature values supplied by their calibration tables and the temperatures actually measured. This is true at every temperature except at the fixed points at which the units have originally been calibrated. Calibration at the fixed points means, by definition, to associate the measured numerical value of the property (e.g. of electrical resistance) to each temperature value of the calibration table (expressed in the scale, e.g. $\theta = T_{90}$). Note that for an empirical temperature θ a subscript should always be associated with T, since T only implies thermodynamic temperature.

The nonuniqueness effect cannot be reduced, since it is a systematic error intrinsic to thermometer fabrication. Consequently, it must not be included with errors in the scale realization, nor must it be ascribed to the limited ability of the mathematical definition to match the physical behavior of the thermometer; it is due, instead, to technical limits of the interpolating instrument itself.

10.2.3 International Temperature Scales

Since the measurement of temperature is a necessity in many laboratories, "laboratory scales," more or less based on thermodynamic determinations, have always proliferated. As a consequence of accurate requirements, an early International Temperature Scale was accepted. A historical review of the process of establishing a scale and periodic revisions can be found in many texts (e.g. Ref. [2]). The last version of the International Temperature Scale, ITS-90, was adopted in 1990 and is still in use. However, a basic change in scale definitions occurred in October 2005, and the next major revision is anticipated in 2011.

The meaning of an "official" scale is not bureaucratic, but scientific and technical. As in all types of measurement, to improve accuracy, not only must random errors (type A) be reduced, but also the largest possible number of causes of systematic deviations (type B errors) must be eliminated. This requires an international body, where the recognized specialists in the temperature measurements field meet and discuss their experiences and those of their colleagues in order to reduce the error limits. Another equally important role of this body is to assess the traceability of lower level approximations of the thermodynamic scale to the ITS, and to fill the gap in information between the ITS definition and the international codes developed for industry, e.g. by the Organisation International de Métrologie Légale (www.oiml.org) and the International Electrotechnical Commission (www.ietc.ch), or prepared by other international bodies, e.g. the International Union of Pure and Applied Chemistry (IUPAC: www.iupac.org) and the International Union of Pure and Applied Physics (www.iupap.org)

An outline of the basic definitions of the scales below 273.16 K since 1932 is given in Table 10.1. However, all the temperature values in this chapter are given on the ITS-90 scale (T_{90}) unless specified otherwise.

10.2.4 The 2005 Redefinition of the International Scale

The basics of the ITS-90 below 273.16 K and of the Provisional Low-Temperature Scale of 2000 (PLTS-2000) definitions are reported in Table 10.1, and the basic advancements in the realization of the fixed points necessary to calibrate the interpolating instruments are detailed in the following sections. The scales are updated on a regular basis (every 20 years on average) to take into account the advancement in the state of the art and to correct recognized discrepancies that may occur.

There are two main issues that prompted the 2005 revision, with a basic change in the principles, while the 2011 revision is supposed to be a real update of the ITS including the incorporation of the PLTS.

Relative to the 2005 revision, work is progressing toward a basic change of the definition of the unit for kelvin, which is supposed to be defined in the future in terms of a fundamental constant, as is the case for most of the fundamental SI units, namely the Boltzmann constant k.

Additionally, knowledge about the specific issues of the ITS-90 realization is progressing so quickly that the usual 20-year revision can become unacceptable. In this respect, the main issue has been the understanding that the isotopic composition variability in the substances used as fixed points was a reason for the relevant ambiguity in the definition of some basic substances, namely hydrogen, neon and water. More details are given in [3]. This prompted the Comité Consultatif de Thermométrie (CCT) to realize that it was not possible to wait until 2011 to fix this problem, and others that could arise, nor to make multiple and frequent corrections of the scale definition to update it to the new knowledge.

Consequently, and in view of the kelvin definition revision foreseen in 2011, it was recommended by the CCT in June and approved by the Comité International des Poids et Mesures (CIPM) in October 2005 [4] that a change be made in the philosophy underlying the scale definitions, adopted since 1927, by eliminating the conceptual separation between the thermodynamic scale and the "practical" scales:

The Comité Consultatif de Thermométrie is considering

- that the International Temperature Scale of 1990 (ITS-90) and the Provisional Low-Temperature Scale of 2000 (PLTS-2000) are internationally accepted practical temperature scales defining temperatures T_{90} and T_{2000} that are good approximations to thermodynamic temperature, T,
- that the uncertainty of realization of certain thermometric fixed points is limited by ambiguities in the defined isotopic composition of the materials for these fixed-points,

TABLE 10.1. The international temperature standards from 1927 to 2011

	ITS-27	IPTS-48 (from 1960)		IPTS-68		ITS-90	PLTS-2000	Mise en pratique	Future (foreseen)
	1927	ITS 1948	1954[a]	1968	1976	1990	2000	2005	2011
Unit	Degree centigrade, °C	Degree Celsius, °C	Degree kelvin, K; degree Celsius, °C	Kelvin, K; degree Celsius, °C	Kelvin, K; degree Celsius, °C	Kelvin, K; degree Celsius, °C	Kelvin, K; degree Celsius, °C	Kelvin, K; degree Celsius, °C	Kelvin, K; degree Celsius, °C
Reference T	0.000 °C and 100.000 °C	0 °C and 100 °C	273.16 K	273.16 K	273.16 K	273.16 K	273.16 K	273.16 K	none
Range	0.000 °C up	90.2 K up	90.2 K up	13.8 K up	13.8 K up	0.65 K up	0.9 mK–1 K		0.9 mK up
Interpolating instrument (cryogenic range, K)	None	SPRT	SPRT	SPRT; T_{58} (^{4}He VP), T_{62} (^{3}He VP) recommended	SPRT; T_{58} (^{4}He VP), T_{62} (^{3}He VP) recommended	0.65–3.2 ^{3}He VP 1.25–5 ^{3}He VP 3.0–24.6 ICVGT 13.8 up SPRT	0.9 mK–1 K melting curve ^{3}He	ITS-90, PLTS-2000, thermodynamic scale realizations; Technical Annex with changes of the above included. (see text)	Redefinition of kelvin in terms of Boltzmann constant k Scale major revisions of: ITS-xx, other *mises en pratique*, Technical Annex
Definition fixed points (cryogenic range)	None	NBP O_2	NBP O_2	TP H$_2$, VP H$_2$, NBP H$_2$, NBP Ne, TP O$_2$, NBP O$_2$	TP H$_2$, VP H$_2$, NBP Ne, TP O$_2$, NBP O$_2$	ICVGT: 3–5 K ^{3}He or ^{3}He VP, TP H$_2$, VP H$_2$, NBP H$_2$, TP Ne, TP O$_2$, TP Ar, TP Hg	None		
Mathematical definition (cryogenic range)	None	Single interpolation polynomial	Single interpolation polynomial	Reference function + correction polynomial for subranges	Same, but new reference function	VP: polynomials. ICVGT: quadratic polynomial SPRT: New ref. function and corr. polynomials; multiple definitions in some subranges	Polynomial	Technical Annex	
Thermodynamic scale	Excluded from definition[b]	Excluded from definition	Excluded from definition	Excluded from definition	Excluded from definition	Excluded from definition	Excluded from definition	Included	Included

[a] In 1964 a provisional definition between 13 and 90 K was adopted, CCT-64.

[b] Before 1927, the thermodynamic hydrogen "normal scale"(CVGT) was the standard; until 2005 the international scales were only empirical and an approximation of the thermodynamic T. SPRT: standard platinum resistance thermometer; VP: vapor pressure scale; NBP: normal boiling point; TP: triple point.

- that clear definitions of isotopic reference compositions will assist in the establishment of internationally compatible Calibration and Measurement Capabilities,
- that recent thermodynamic temperature measurements have refined the best estimates of the differences $T - T_{90}$ together with their uncertainties,
- that the creation of a formal *mise en pratique* of the definition of the kelvin would considerably simplify and clarify statements and recommendations of the CCT concerning the realization of the definition of the kelvin and the implementation of practical temperature scales,

recommends

- the creation of a *mise en pratique* of the definition of the kelvin containing, in due course, recommendations concerning the direct determination of thermodynamic temperature, the text of the ITS-90, the text of the PLTS-2000, a Technical Annex of material deemed essential for the unambiguous realization of both the ITS-90 and the PLTS-2000, and a section discussing the differences $T - T_{90}$ and $T - T_{2000}$ together with their uncertainties,
- approval by the CIPM of the text entitled "Technical annex for the *mise en pratique* of the definition of the kelvin", adopted by the CCT at its 23rd meeting, as initial entry to the Technical Annex.

The initial Technical Annex is reporting the definitions and the corrections concerning the isotopic composition of water [5] and of hydrogen [6]. In addition, in the definition of the kelvin, an isotopic composition of water is defined, corresponding to the Standard Mean Ocean Water [7].

The ITS-90 in particular is retained, but as one of the *mises en pratique*, and with the above corrections. However, realizations of the thermodynamic scale will possibly be endorsed in the future as *mises en pratique*. Obviously, the degree of consistency of all *mises en pratique* must be studied and established by the CCT.

10.2.5 Reference Points for Thermometry

First of all, the term "reference point" should be given a meaning that is more restrictive than which it is often associated with:

A thermometric reference point is an equilibrium state of a specified substance, the realization of which is necessary to the calibration of the interpolating instrument.

Accordingly, the "boiling points" mentioned in Table 10.1 should be termed reference points, whereas the vapor-pressure functions should not.

For a pure substance, this definition also applies to "triple points," a thermodynamic state in which three phases coexist: from Gibbs' rule, $F = c - \phi + 2$, where F are the degrees of freedom, c is the number of chemical substances and ϕ is the number of phases involved. It follows that both the temperature and pressure value at a triple point are unique. Only the solid–liquid–vapor type is the triple

point of a gas. Solid-to-solid (-vapor) and liquid-to-liquid (-vapor) transitions are also used as reference points, though of lesser quality.

Reference points are of great importance in thermometry, not only because they allow empirical scales (where they become "fixed points") to be defined, but also because each of them provides a reference temperature available, at which the calibrationof a thermometer of any type can be checked in any laboratory without resorting to the help of another.

10.2.6 Ideal Substances versus Standard Reference Materials

A reference temperature can be obtained by simple reference to the ideal substance or, instead, by specifying a sufficient number of relevant physical properties of it to define a single temperature-dependent state of the substance. The difference between the two alternative definitions is equivalent to that existing between a thermodynamic and an empirical temperature scale.

In the first case, the substance is defined only by means of its basic physical parameters so that anyone can reproduce the thermodynamic state in an independent way. Such parameters need to be listed and defined. These parameters can be the maximum level of impurities (or of a single impurity), the physical state (annealed, etc.), the composition (including the isotopic one, when relevant), and its tolerance in the case of mixtures.

Each experiment aimed at reproducing the real thermodynamic state and complying with the above specifications is expected to reproduce the same physical state, i.e. the same temperature value within a given uncertainty. Each such experiment is independent of other experiments and no specific procedures need be defined. In this respect, the exercises usually performed by major laboratories, especially metrological, such as intercomparisons of results, are normally to be considered as checks of their ability to perform the experiment correctly, not as checks of the quality of the substance employed. They are not aimed either at "calibrating" the fixed points.

In the second case, a certain amount of a substance is prepared to have uniform characteristics and is stored and made available by an organization. The physical–chemical characteristics of the substance, and its temperature value (besides its reproducibility between samples), are determined by measuring samples taken from the batch and are assigned to the whole batch of material considered. Subsequently, samples of that batch are made available to other laboratories together with a certificate of compliance with the characteristics of the batch. The materials used for this purpose are called "reference materials" (RMs), and the word "standard" (SRMs) is added when an official body certifies them. In principle, they need not comply with any of the specifications that an "absolute" reference point has to meet. The batch of material needs only to be uniform enough and stable with time to allow the desired reproducibility of certain property characteristics to be obtained between samples, in order to achieve the required accuracy of the temperature value. The users of these materials must rely on the certificate issued by the supplier, as well as the temperature scale based on these reference materials.

Sometimes, when it is not even possible to establish a certified value of the property for a whole batch of a material, each sample is certified individually. An example is provided by the realization of the fixed points based on superconducting transitions. The transition temperature value cannot be guaranteed to represent the value of a physical state. Therefore, it is usually certified as the transition value that is realized by the individual device and is said to be a "device temperature" value. Such a type of SRM relies only on the stability in time of the property certified.

10.2.7 Types of Cryogenic Reference Points

In the region of interest for cryogenics and superconductivity, the reference points mainly belong to three groups: one is based on the triple points and is discussed below, a second is based on superconducting transitions, and a third includes the superfluid transition of ^{4}He and solid-to-solid transitions. In the first case, several reference temperatures are available above 13.8 K. Superconducting transitions are useful for reference point realizations below 9.3 K, but they have lost any practical significance in the last 20 years. The ^{4}He superfluid transition occurs near 2.2 K. Solid-to-solid transitions are available above about 20 K and in the sub-millikelvin temperture range.

10.2.7.1 Realization of the Triple Point of Gases as Thermometric Fixed Points (>13 K)

A comprehensive discussion on a correct realization of fixed points based on the triple point of gases is given in [1]. For their further improvements in the last decade, see [8, 9].

During a traditional realization of a triple point, after the desired amount of gas has been condensed in a container fitted into the cryostat, the sample of gas is sealed into the apparatus by closing the valve connecting the cryostat to the gas filling system. This sample can be further manipulated in different ways by evaporating it back to the filling system, but at the end of the experiment the cryostat is warmed up to room temperature and the whole sample is usually discarded. If, at a subsequent time, from a few days to many years, another measurement has to be carried out, then another sample of gas will be used, generally taken from another storage bottle. In the meantime, the results of the previous measurements remain "stored" and available only by means of thermometers used during the measurements with the reference point assumed to remain stable in time.

This procedure was used until the mid 1970s and has many disadvantages. First, the fixed point is not readily available at all times for a new realization, except during the short period when the measurements are carried out. The storage of results in thermometers has proved to be unreliable, since they often do not show sufficient stability with time. In addition, the old procedures are not routine measurements, but each time they are actually new experiments, as a new sample of gas is generally used and, consequently, the degree of its purity has to be ascertained anew, which is not a trivial task. As noted earlier, because of the necessary new

handling of the gas, it is again possible that the sample will become more contaminated than certified by the supplier. It is not surprising that the measurements at the fixed points in the past were not made routinely; consequently, only calibrated thermometers were used until the technique of permanently sealing the sample in a cell was perfected.

This new method for gases has been developed only since the beginning of the 1970s, even though there were a few examples of earlier attempts, since it was used for a long time with liquids and solids in calorimetry. With gaseous substances, purity preservation, made possible by permanent sealing and the consequent elimination of further gas manipulation, had to be verified. For example, the container must not contaminate the sample; this is relatively simple with most solid or liquid samples, but not generally speaking easy to achieve with gases. Thirty years of experience has shown, however, that the method can be used with most gases, and the values of T_{tp} obtained with sealed cells have remained constant within a few tenths of a millikelvin over several decades [8, 10].

The design of a permanently sealed cell, in comparison with a traditional experiment, differs in one substantial feature: the realization of an accurate and stable fixed point is permanent. A sealed cell can be made small and fully self-contained, so that it can be mounted in the working chamber of most types of commercial cryostat (Figure 10.2).

The cryostat itself is greatly simplified; and since the cells are independent of the cryostat, they can be interchanged in a single cryostat, or more than one can be mounted at the same time (Figure 10.3).

The three constitutive elements of a sealed cell are:

1. *Container*. Any material can be used for its fabrication, provided it withstands the high internal room-temperature pressure (up to 200 bar). This accounts for most of the cell mass. The use of materials having high thermal conductivity
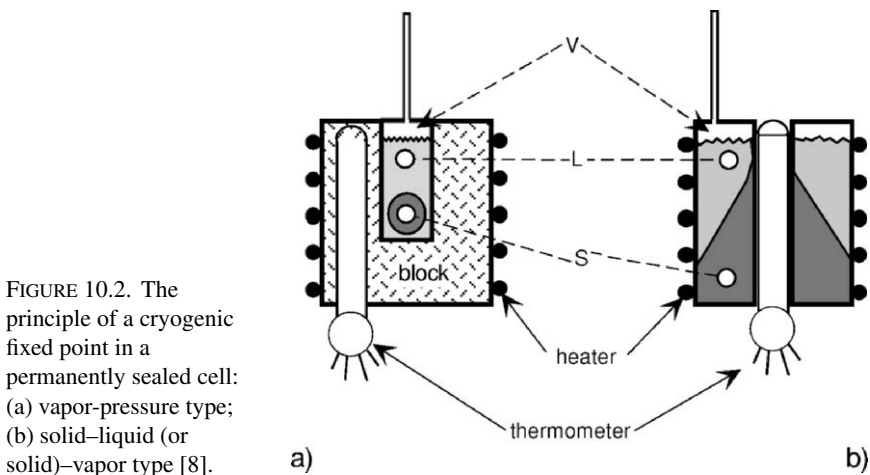
FIGURE 10.2. The principle of a cryogenic fixed point in a permanently sealed cell: (a) vapor-pressure type; (b) solid–liquid (or solid)–vapor type [8].
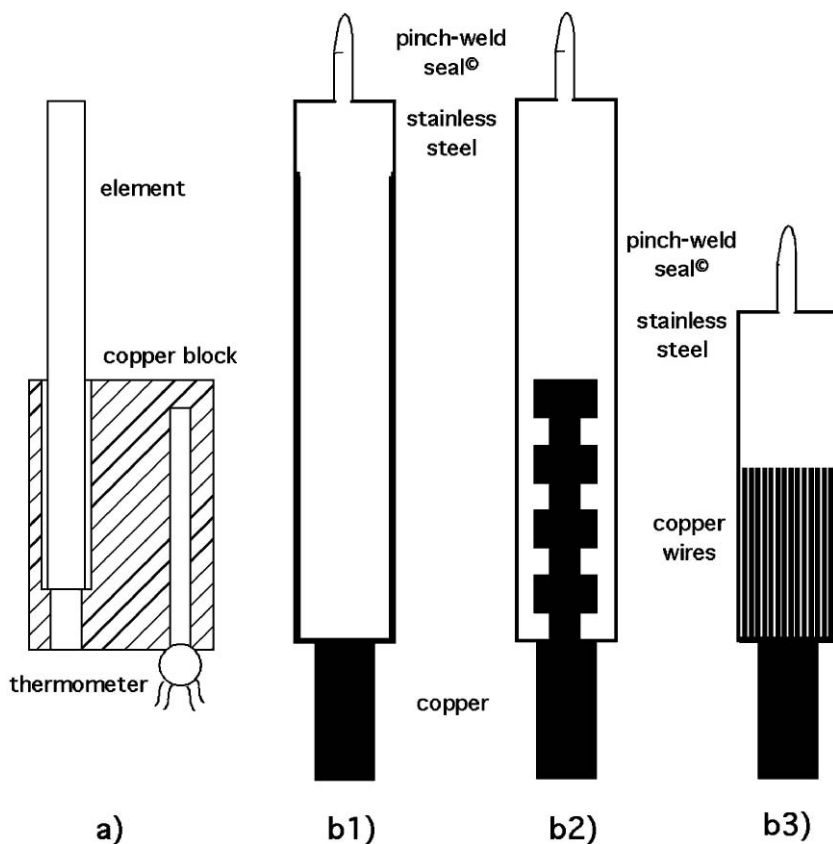
FIGURE 10.3. Modular sealed-cell models (not to scale): $D = 23$ mm (one element) to 50 mm (six elements), $L_{max} = 100$ mm and total mass $m = 170$ g (one element) to 400 g (six elements). (a) Copper block for up to six thermometers and six elements. (b) Cell elements (ø 12 mm), each sealed with a single substance: (b1) model with copper internal wall ($m = 56$ g); (b2) model with internal solid-copper body ($m = 53$ g); (b3) model with internal wireframe-copper body ($m = 47$ g) [3,10].

promotes a uniform temperature throughout the entire sample, but increases the thermal coupling between the heater and the thermometers.

2. *Inner body*. This element may contain the thermometers, as in Figure 10.2, or it may be used only to transfer the interface temperature to an external thermometer block, as in Figure 10.3. It is usually made of oxygen-free high-conductivity (OFHC) copper or stainless steel and needs fins or baffles to ensure a good thermal contact with the solid phase for as large a melted fraction as possible; however, the larger the inner cell surface, the more critical the problem of sample contamination may become.

3. *Sealing device*. The seal must remain leakproof for a very long time, under thermal cycling from room temperature to that of the cryogenic environment during each cool down. Patented pinch-weld seals have been used successfully [11].

The equilibrium technique is used for performing the fixed point and requires the use of an adiabatic calorimeter. It involves intermittent exchanges of energy with the sample. During each energy-exchange cycle, the thermal flow produces temperature gradients in the sample and which produce an increase of the melted fraction F. The sample is then left undisturbed under adiabatic conditions to reattain thermal equilibration. The temperature versus $1/F$ plot should be used to define the reference temperature as follows:

The temperature value T_{tp} of a triple point realization, when used as a reference fixed point, is defined by the equilibrium value obtained in melting a sample with the adiabatic calorimetric technique at the liquidus point, defined as $1/F = 1$ and obtained by extrapolation from the melting plateau, by means of the T versus $1/F$ plot.

With the modular design finalized during a European project in 2003 [12], it is possible to simultaneously obtain in the cryostat all the cryogenic fixed points needed for the calibration of SPRTs according to the ITS-90 definition for temperatures above 24.6 K. In fact, the mercury triple point [13] and the water triple point can be established using miniature sealed cells.

The improvement in the error budget in the last 50 years is shown in Table 10.2, and is thanks to the use of sealed cells for realizing the triple point (and the

TABLE 10.2. Typical and aimed uncertainty budget for cryogenic triple point measurements

#	Item[a]	Before 1975 (μK)	1975–2000 (μK)	After 2000 (μK)	Future aim (μK)
1	Nonisotopic impurities	100 2000[b]	50 → 2000[b]	40	10
2	Isotopic composition	up to 700[c]	up to 700[c]	30[d]	20
3	Induced by R^e_{cs}	200–500	50–200	30	10
4	Induced by τ^e	100–300	<100	20	10
5	Cryostat other effects[f]	100–300	20–300	10	10
6	Resistance measurement[g]	100–200	30–200	30	10[h]
7	T_{tp} definition[i]	100–300	20–300	20	0
Total		300–>2000	150–1000	70	30

[a] R_{cs}: static thermal resistance; τ: cell dynamic time constant; T_{tp}: triple point temperature.
[b] For Ar in O_2 or HD in D_2.
[c] For D in H.
[d] For the best certification uncertainty only.
[e] See [8].
[f] For meltings lasting less than ~12 h.
[g] Except with e-H_2 when measuring a CSPRT.
[h] Means equivalent to ≈1 μΩ for an SPRT above 40 K.
[i] For $\Delta T_{melt(20–80\%)} < {\sim}0.1$ mK.

solid-to-solid transitions) of pure substances such as hydrogen, deuterium, neon, nitrogen, oxygen, argon, and carbon dioxide. The cells are commercially available.

10.2.7.2 Reference Points Based on Superconducting Transitions (<9.3 K)

Superconductive transitions are solid-state phase changes of second order (no enthalpy change), in contrast to most fixed points used in thermometry. Essential peculiarities of the superconductive transitions are the larger effects of impurities, crystal defects, and physical strain that affect both the transition widths and temperatures T_{sc}. For application as thermometric fixed points, therefore, special sample preparation techniques and special methods for the detection of the superconductive transitions must be used. Superconductive temperatures, as realized, for example, by the National Institute of Standards and Technology (NIST) devices SRM 767 and SRM 768 [14, 15], were only used in the sense of a reference material (see above). None of these reference points is included in the definition of the ITS-90.

Modern sample preparation and handling techniques [16], in conjunction with convenient material characterization methods, are sufficient to guarantee an accuracy and stability of T_{sc} values of these reference points within about ± 1 mK if definite specifications concerning sample preparation are fulfilled. Further improvement is possible only by carefully annealing the samples and by selecting them on the basis of maximum allowed transition width, since the main difficulty is the influence of impurities and crystal defects. The influence of impurities is typically 1 mK ppma^{-1}. The residual electrical resistance is an excellent indicator of this influence, except in the few cases where localized moments exist; in this case, the influence can be much larger, so the concentration of the magnetic impurities must be specifically determined. The effect of crystal defects can be reduced to a few tenths of a millikelvin by using suitable preparation techniques, which may differ for different elements. For checking the magnitude of this effect it is important that the transition width always be smaller than the change in T_{sc} due to the defects. Hence, for the realization of superconductive reference points, detailed information concerning both the physical properties of the materials and the preparation and characterization methods is necessary. A simple and effective method for avoiding the summing up with time of strain in the samples is that of sealing each of them in small, thin glass ampoules together with some helium exchange gas [13].

Table 10.3a presents the 1987 T_{sc} best estimates of superconductive transitions with the total estimate of their uncertainty. The dependence of the T_{sc} value on the method used for its detection has been included. The mutual inductance technique is most effective because of its relative ease of application, the minimum stress transmitted to the sample, and the negligible sample contamination. Thermal anchoring of the samples and of the electrical leads is critical for the observation of nonhysteretic and reproducible transitions. Because of the absence of enthalpy change in transition, a high-quality adiabatic cryostat is necessary for accurate T_{sc} measurements. To check that the thermal conditions are adequate, the difference between the values obtained by increasing and decreasing the sample temperature

TABLE 10.3. Superconductive transition temperatures[a]

Substance	T_{sc} (K)	Reproducibility (mK)	Transition width (mK)
(a) *Best estimates of superconductive transition temperatures*			
Cadmium	0.5200	3.0	
Zinc	0.8500	3.0	
Aluminum	1.1810	2.5	
Indium	3.4145	2.5	
Lead	7.1997	2.5	
Niobium	9.2880	2.5	
(b) *Temperatures assigned to NIST superconductive fixed-point devices*			
Tungsten[b]	0.0160	0.2	0.7
Beryllium[b]	0.0230	0.1	0.2
Iridium[b]	0.0990	0.1	0.8
$AuAl_2$[b]	0.1605	0.1	0.3
$AuIn_2$[b]	0.2065	0.15	0.4
Cadmium[c]	0.5190	0.3	0.5–8.0
Zinc[c]	0.8510	0.4	2.5–10
Aluminum[c]	1.1796	0.4	1.5–4.0
Indium[c]	3.4145	0.2	0.5–2.5
Lead[c]	7.1996	0.2	0.6–2.0

[a] Note: T_{90} above 0.65 K.
[b] SRM 768.
[c] SRM 767.

through the transition range needs to be measured. The temperature should then be stabilized at the midpoint of the transition before the thermometer calibrations are carried out. Furthermore, external magnetic fields (Earth field and measuring field) can have an influence of a few millikelvin on T_{sc}; these effects can be negated by the use of magnetic shields or Helmholtz coils [17].

Table 10.3b reports the temperature values assigned to NIST devices SRM 767 and SRM 768. The values are assigned, since they are reference materials only; for the same reasons, the values can be slightly different from those of Table 10.3a. Other SRM devices were available from Physikalisch- Technische Bundesanstalt (PTB; niobium [16]) and INTiBS (indium in glass ampoules [18]).

10.2.7.3 The ^{4}He Liquid-to-Superfluid Liquid Transition (2.2 K)

Among liquid-to-liquid transitions, it is only worthwhile considering the ^{4}He λ-transition from normal to superfluid liquid, at 2.1768 K. It is easily achieved to very high accuracy, in a temperature region where no other references of comparable quality are available. Its temperature value occurs halfway between that of the superconducting transitions of aluminum and of indium. Further details are available in texts on helium properties, e.g. [19].

The λ-transition in the *p–T* plane is actually a line, as the two liquid phases exist in the pressure range below the solid phase boundary. The state being discussed is the lower endpoint of this line, where it joins the saturated vapor-pressure line. The transition is a second-order one, since entropy shows only a slope

discontinuity and no enthalpy of transition is involved. The specific heat value shows a logarithmic infinity at T_λ. Thermal conductivity varies from moderate values in normal liquid (0.02 W K^{-1} m^{-1} in ^{4}He I, but 0.5 W K^{-1} m^{-1} just below T_λ), to extremely high values in the superfluid phase (>1000 W K^{-1} m^{-1}), much higher than those exhibited by the best conducting metals.

In bulk liquid, the transition takes some time to involve all the liquid, as normal liquid helium (liquid ^{4}He I) shows thermal layering, and the superfluid liquid (liquid ^{4}He II) has its maximum density near T_λ. Therefore, liquid-II tends to leave the surface, where refrigeration takes place, and be replaced by liquid-I. Since no thermal gradients can exist in liquid-II, all liquid-II will remain at exactly T_λ until some liquid-I is present. For this reason, a flat temperature (and pressure) plateau is observed, even lasting for hours and appearing like that of a first-order transition. A thermometer immersed in liquid-II will accurately measure T_λ (with account being taken of the Kapitza effect). Care must also be taken to limit the hydrostatic temperature gradient in the liquid-II (about 100 mK MPa^{-1}, equivalent to about 1.5 mK per meter of liquid) if the bath is deep. The effect of impurities is not critical, equivalent only to –1.4 μK ppm^{-1} with ^{3}He, which is the only likely impurity (at a level of 0.5–2 ppm in ^{4}He).

This reference point can also be easily realized using a sealed device [20, 21]. For more detail, see also [1].

Further studies developed during this European project [12] in 2000–2003 using the cell of Figure 10.4 permitted the consolidation of the very simple procedure needed to obtain reproducibilities of the order of microkelvins and an accuracy much better than 0.1 mK (Figure 10.5) [22,23].

10.2.7.4 The Solid-to-Solid Transitions (from <1 mK to 90 K)

In solid-to-solid transitions, only the solid and vapor phases are present; only those occurring along the saturated solid–vapor line are suitable as reference points.
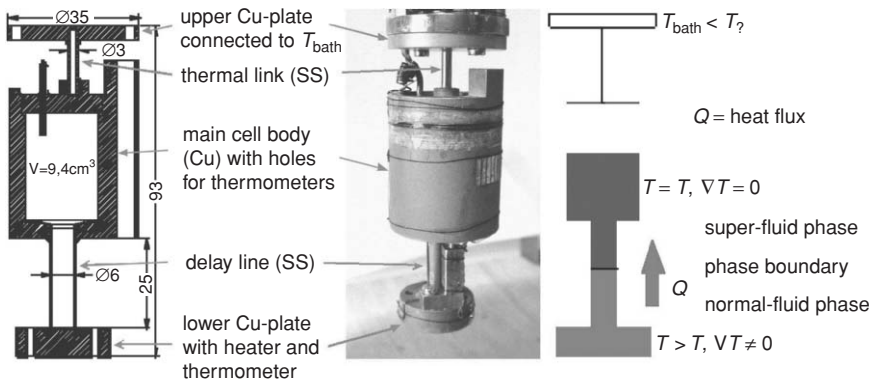
FIGURE 10.4. State of the art of the λ-point transition of ^{4}He.
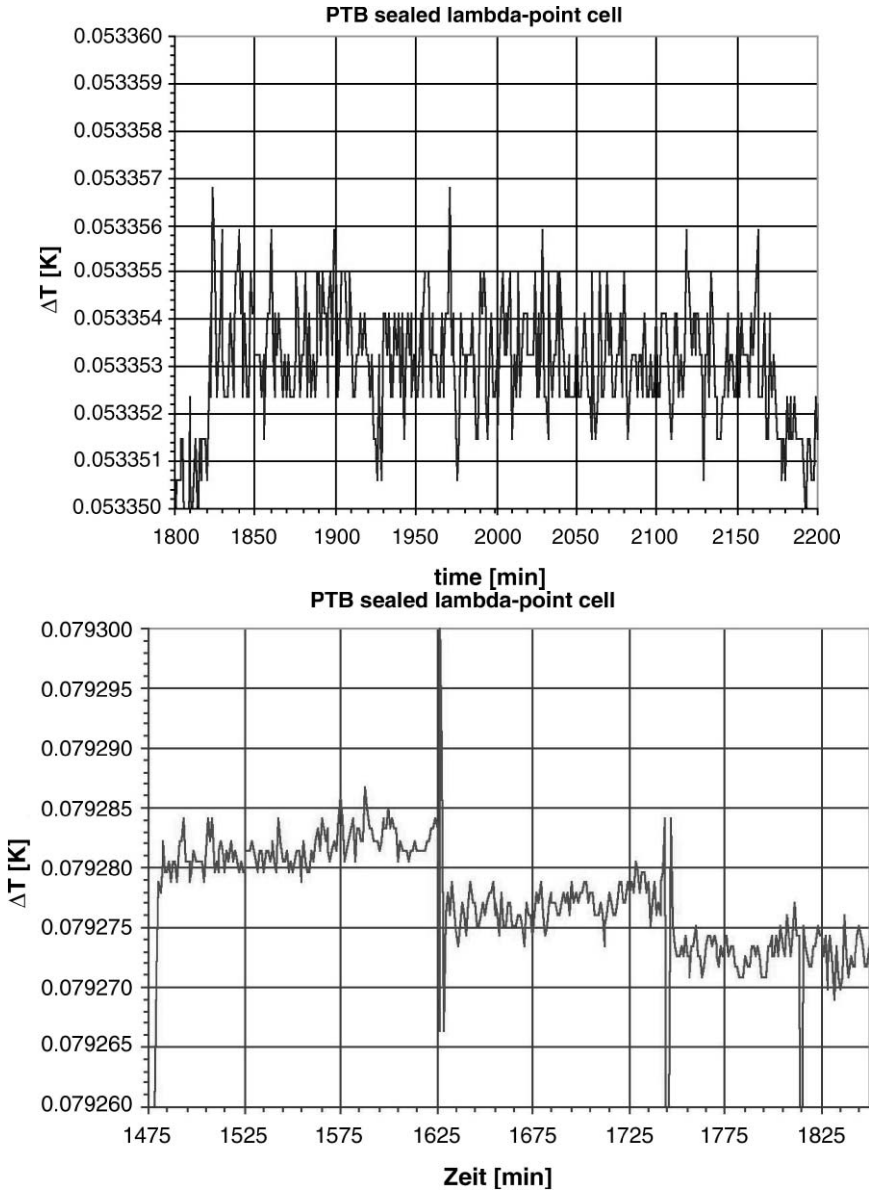
FIGURE 10.5. Errors in the λ-transition realization.

First-order transitions, such as the β–γ in oxygen, which exhibits an enthalpy of transition, behave like and, in principle, are obtained in the same way as the triple points. However, the quality required for the calorimeter is much higher, and the equilibration time much longer [24].
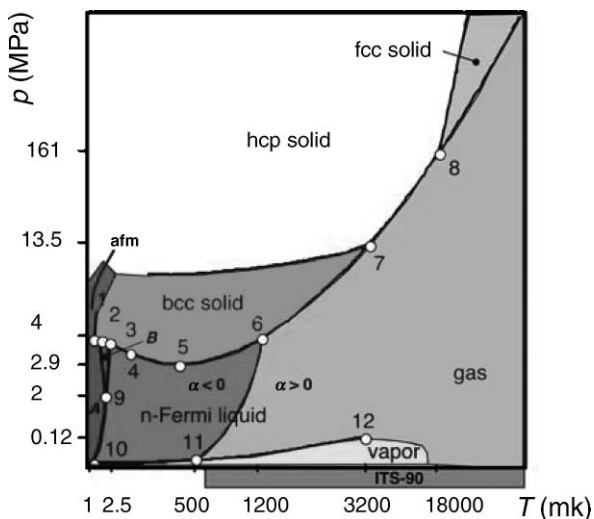
FIGURE 10.6.
Thermodynamic
properties of ^{3}He below
1 K. (after [25]). Not to
scale. See Table 10.5 for
caption of the specific
points. afm:
antiferromagnetic
ordering transition; A,B:
superfluid phases. (From
[1].)

Second-order transitions, such as those of nitrogen and methane, have no en-thalpy of transition and only show a heat capacity peak. Therefore, the transition in the T versus time representation does not show a flat plateau, but an S-shaped behavior, with a derivative value at the inflection point, $(dT/dt)_I \neq 0$, $c_{p,I} \neq \infty$. A transition width can be defined from the transition duration at T_{tr} obtained from the extrapolated lines for constant heat capacity before and after the transition, or between the first derivative maximums.

Though not of the same quality as obtained with triple points, these transitions can be used as reference points. For gases exhibiting such transitions (e.g. O$_2$, N$_2$, CH$_4$), they are an additional "bonus" in the use of sealed cells. ^{3}He exhibits solid-to-solid transitions at a temperature that can be useful in thermometry, as summarized in Figure 10.6 and Table 10.4. See [1] for more detail.

10.3 Thermometry

10.3.1 Gas Thermometry Below 273.16 K

Traditionally, gas thermometry is considered an issue reserved for specialists. Its foundations are briefly reported here mainly because it is part of the ITS-90 definition.

Until recently all research work on gas thermometry below 273.16 K was based only on ^{4}He. However, with the use of ^{3}He, gas thermometry can be carried out at temperatures lower than 2.5 K, thereby fully covering the range of ^{4}He vapor-pressure thermometry and overlapping also most of that of ^{3}He.

The use of ^{3}He in thermometry has become practical since the lighter isotope has become available with sufficient purity at a reasonable price and because its

TABLE 10.4. Key thermodynamic features of condensed ^{3}He

Point[a]	Type	T (mK)	p (MPa)	Reference
On the melting line				
1	Antiferromagnetic transition	0.902	3.43934	[3]
2	Superfluid A–superfuid B	1.896	3.43609	[3]
3	Normal liquid–superfluid A	2.444	3.43407	[3]
4	Inflection point $(\mathrm{d}p/\mathrm{d}T)_{max} = 4.08$ MPa K^{-1}	~8	~3.457	
5	Minimum pressure	315,24	2.93113	[3]
6	Change from negative to positive thermal expansion in liquid	1260	4.76	[4]
7	Solid b.c.c.–solid h.c.p. transition	3138	13.724	[4]
8	Solid h.c.p.–solid f.c.c. transition	17,780	162.9	[4]
In the liquid				
9	p_{min} for superfluid B	2.273	2.150	[1]
10	T_{min} for superfluid	0.929	~0	[1]
11	Joining-point of zero thermal-expansion line with vapor-pressure line	502	0.00002	[4]
12	Critical point	3316.2	0.11466	[5]

^{a} With reference to Figure 10.6.

virial (nonideality) corrections are now known to a high accuracy down to 1.5 K. Both isotopes are considered in the ITS-90 definition for use in gas thermometry between 3 and 24.6 K.

The basic equation of an ideal-gas thermometer is given in Equation (10.1). A full discussion on gas thermometry is given in [1]. The uncertainty of the value of R presently limits the accuracy of a temperature measurement to ± 3 mK at 300 K and to ± 0.3 mK at 30 K, but this uncertainty is suppressed by measuring temperature ratios with respect to a reference condition.

When, most commonly, the volume V and the molar amount of gas n are assumed to remain rigorously constant, the thermometer is designed as a "constant-volume gas thermometer" (CVGT): $T = T_{ref}(p/p_0)$. The constant-volume assumption concerns the requirements of the gas container, which are relevant only from the standpoint of the technical realization. On the contrary, the requirement for the amount n of gas to remain constant (as implied in Equation (10.1)) involves physical properties of the thermometric substance itself.

The grouping into "physical" and "technical" involves all the "corrections", i.e. the parameters which contribute to the overall uncertainty. Figure 10.7 gives an indication of the number and size of these influential parameters. Only the uncertainties in these parameters, not their values, are obviously relevant to the overall uncertainty.

10.3.1.1 Gas Thermometer Realizations

The general layout of gas thermometer designs is shown in Figure 10.8, which includes all possible options to be discussed below. Type (a) is the traditional one.
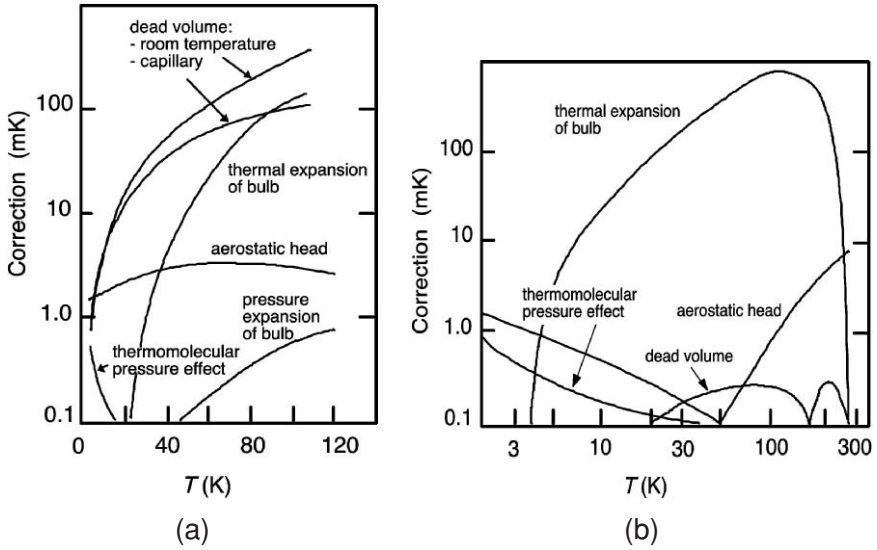
FIGURE 10.7. Typical size of the influence of technical parameters in CVGT, for reference temperature: (a) 27 K; (b) 273 K. (From [1].)
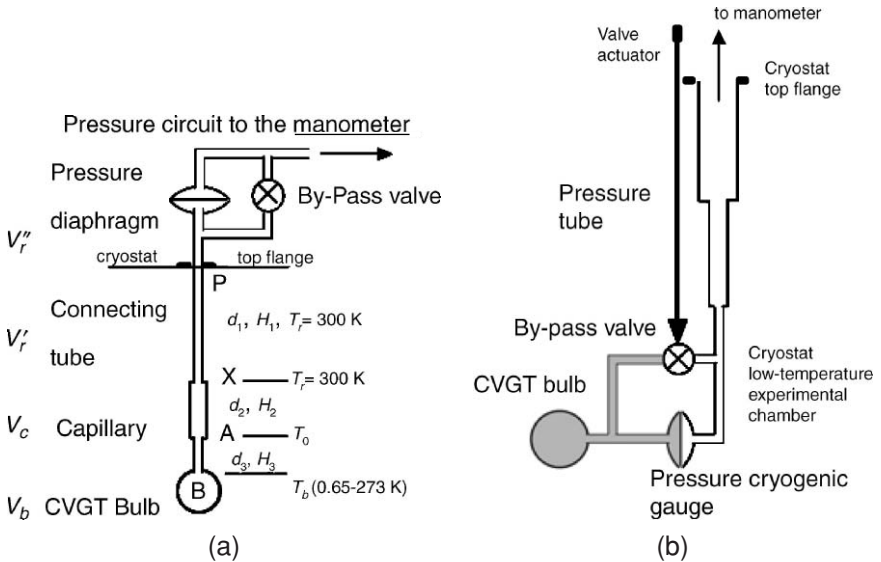
FIGURE 10.8. Scheme of a CVGT: (a) with room-temperature pressure measurement; (b) with cryogenic pressure transducer (from [1]).

Type (b) is not often used. It has been implemented for ^{4}He gas thermometers by Orlova and coworkers [29] in the 4–20 K range, by Astrov [29] in the 12–300 K range and by Van Degrift [30] for measurements below 10 K; and as an interpolated CVGT (ICVGT; see below) it has only been used by the IMGC [31].

A CVGT is fabricated by combining three parts (see Figure 10.8): (a) the measuring bulb, whose temperature defines the thermodynamic temperature; (b) the pressure capillary, connecting the bulb to the pressure measuring system, when it is placed at room temperature; and (c) the pressure measuring system. When the manometer is at room temperature, a 1 L OFHC copper-bulb volume is typical for top-accuracy devices, but volumes smaller by a factor of two or three have been used yielding nearly the same accuracy. A larger bulb volume makes the effect of the dead-volume less critical, but the temperature uniformity is more difficult to achieve. The surface that adsorbs the thermometric gas becomes larger, and so does the size of the entire experimental apparatus.

A capillary tube is unnecessary only for the case of the CVGT design equipped with a cryogenic pressure transducer, like shown in Figure 10.8. In all other cases, including the ICVGTs, its design involves many of the most difficult compromises between conflicting requirements and carries the main sources of uncertainty.

In the use of the ICVGT where no capillary parameter needs to be measured, the capillary must be designed to operate under stable and controlled thermal conditions, in order to have a stable and reproducible temperature distribution. This goal may be achieved by building an isothermal calorimetric environment around this tube. However, this is not the usual practice: several thermometers (generally thermocouples) are generally placed on the capillary in order to map its temperature distribution, a method that is not very satisfactory. Another rule is to keep the capillary as short as practicable, since there is never an advantage in a long capillary. For details on the high-accuracy realizations, see [1].

Other types of gas thermometry use an intensive property instead of an extensive property, e.g. dielectric constant, refractive index, or sound velocity. It has not been proved that an instrument based on these properties has superseded the CVGT. They are presently not used by the ITS-90, and for details see [1].

10.3.1.2 Gas Thermometers with a Built-in Cryogenic Pressure Measuring Device (as a Constant-Volume Gas Thermometer)

All major corrections in a traditional design (the one with the manometer at room temperature), except the virial and adsorption correction, are avoided with this design, because they are due to the capillary connecting the bulb to the manometer. The required pressure transducer must be of a special cryogenic type [1].

The use of a differential-pressure transducer for use at cryogenic temperatures generally entails a simpler design for a CVGT of this type, but still requires a pressure measuring line from the differential transducer to room temperature. Only the zero stability of the transducer is relevant, and it must be of the same order of magnitude as that required for the room-temperature types. Design options depend on the actual characteristics of the transducer employed. If the transducer has a

small and reproducible temperature coefficient, then it can be mounted directly as part of the gas bulb, thus eliminating the dead-volume completely. If this is not the case, then the transducer can be attached to the bulb by means of a short tube (which constitutes a small dead-volume), and maintained at a constant temperature. Thermal cycling to 300 K is unavoidable. If the transducer zero is insufficiently stable on thermal cycling, then an in-situ check is necessary.

A differential transducer must be connected to the standard pressure-measuring apparatus at room temperature by means of a tube, which can only be filled with helium gas. Therefore, if the manometer uses a working gas different from helium, then a second diaphragm transducer of suitable precision is necessary in the room-temperature manometric circuit. The pressure tube, however, is less critical than in the case of a traditional CVGT, since its design is the same that is used for vapor-pressure measurements, where large bores can be used, to minimize the thermo-molecular pressure effect.

The use of an absolute cryogenic pressure transducer is much more demanding and has never been attempted, except as an ICVGT (see Section 10.3.1.3). The measurement uncertainty of this transducer must range from $\pm 0.005\%$ to $\pm 0.02\%$ over a pressure interval from about 0.1 MPa to less than 1 kPa respectively. Its sensitivity must be better by about one order of magnitude. A transducer having a good zero reproducibility in thermal cycling is also likely to be a good one when pressure is cycled. Linearity is not strictly a requirement, as nonlinearity only slightly complicates the transducer calibration. In any case, in-situ calibration against an absolute pressure standard is required. With the use of an absolute-pressure transducer, a tube connecting the gas thermometer to room temperature is no longer necessary.

The use of a pressure transducer built into the gas thermometer bulb allows a complete change in the bulb design. The most outstanding modification is the bulb size, which can be very small, since the dead-volume effect is zero, or greatly reduced. The volume of the gas bulb might reduce to that of the pressure transducer itself. However, a question arises as to whether there is a minimum usable volume, a question that is essentially equivalent to asking whether there is a minimum amount of gas sufficient to keep the uncertainty due to unwanted changes in the active amount of gas n in a CVGT within a stated limit. See [1] for a discussion on this issue.

Obviously, even with a self-contained small gas thermometer, one cannot avoid corrections for the virials, gas purity, and the deformation of the bulb volume. In addition, the volume variation due to the diaphragm deflection of the pressure transducer, which usually can be neglected, should be carefully corrected when the bulb volume reduces and the deflection itself must be minimized.

10.3.1.3 Interpolating Constant-Volume Gas Thermometers

In Section 10.2.2, the meaning of "interpolating instrument" was introduced as one of the three elements necessary to define an empirical temperature scale. The decision to use a CVGT for defining an empirical scale instead of directly

measuring the thermodynamic temperature is prompted by different consider-
ations. One is the interest to improve measurement reproducibility beyond the
thermodynamic accuracy limit. Another is the simplification when the gas ther-
mometer is used as an interpolating instrument. It is part of the ITS-90 definition
in the 3–24.6 K range.

In general terms, an ICVGT differs from a CVGT in that it is calibrated at
more than one fixed point (i.e. the pressure is measured at temperatures whose
values are determined by independent means, e.g. by a CVGT). Then, a functional
relationship is used for interpolating between these fixed points, or for limited
extrapolation. There is a substantial difference and simplification with respect to
using a gas thermometer for thermodynamic measurements, since the corrections
for the technical parameters or for the measured pressure values no longer need
to be calculated or measured. In fact, all corrections are taken into account in the
"calibration" of the ICVGT at the fixed points, except for the corrections related
to the whole manometric system, including the separation diaphragm pressure
transducer which must still be applied. At the same time, one has to assume
that the physical conditions of the experiments and the thermal conditions of the
apparatus are reproduced in subsequent measurements and maintained perfectly
the same as they were at the moment of the calibration. This basic assumption
involves, for example, the temperature distribution in the capillary, which is not
necessarily measured with an ICVGT. Most of the ICVGTs developed to date are
of the type (a) in Figure 10.8 [32–34]. Only the design used by Steur et al. [31],
Figure 10.9, is of type (b). There is still design advantage in using a cryogenic
pressure transducer because of the large reduction in the bulb size and general
simplification of the experimental setup. It has been used in both the differential
[35] and in the absolute mode [36].

The reproducibility of an empirical ICVGT-defined scale depends both on
the selection and reproducibility of the technical parameters, and on the repro-
ducibility of the fixed points. It also depends on the capability of the stipulated
interpolating functional relationship to approximate the thermodynamic (T,p) re-
lationship in different experiments (the so-called nonuniqueness discussed above).
The accuracy of the scale depends on the accuracy of the thermodynamic tem-
perature values assigned to the fixed points. For a full treatment of the ICVGT,
see [1].

10.3.2 Vapor-Pressure Thermometry

Vapor pressures have often been used for temperature measurements or for calibrat-
ing thermometers against a physical property and they are still very popular, since
the saturated vapor pressure of a pure substance above its liquid phase depends only
on temperature and the measurements are relatively easy. Vapor pressures are also
very commonly used for the realization of the fixed points called "boiling points."
These points are simply specific points on the vapor pressure line, generally those
at 101,325 Pa (the normal boiling point).
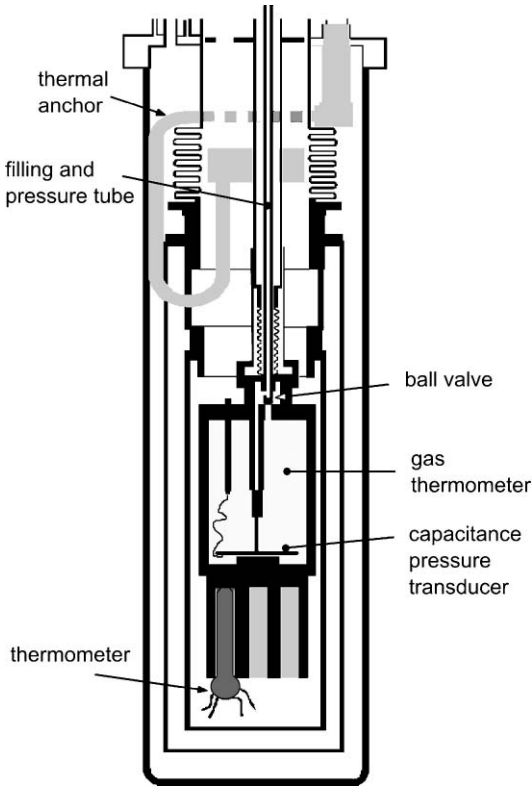
Present knowledge of the physics is adequate to provide an accurate analytical description of the relationship existing between pressure p and the thermodynamic temperature T. The following equation was established in the 1950s and can be found in many textbooks (e.g. Keller [25]):

$$\ln p = i_o - \frac{\Delta_{vap} H_{m,0\,K}}{RT} + \frac{5}{2} \ln T - \frac{1}{RT} \int_0^T S^L(T)\, dT$$

$$+ \frac{1}{RT} \int_0^p V^L(p)\, dp + \varepsilon(T) \tag{10.2}$$

where $\Delta_{vap} H_{m,0\,K}$ is the molar enthalpy of vaporization at 0 K; i_o is the chemical constant, defined by $\ln[g_\sigma (2\pi m_a)^{3/2} k^{5/2} h^{-3}]$, with m_a being the mass of a single atom and g_σ is the degeneracy due to nuclear spin; $\varepsilon(T)$ is the vapor virial correction, defined by

$$\ln \frac{pV^V}{nRT} - 2B(T)\frac{n}{V^V} - \frac{3}{2}C(T)\left(\frac{n}{V^V}\right)^2$$

with $B(T)$ and $C(T)$ being the virial coefficients; $S^{\mathrm{L}}(T)$ is the molar entropy of the liquid along the saturation line, and $V^{\mathrm{V}}(p)$ and $V^{\mathrm{L}}(p)$ are the volumes of the vapor and the liquid along the saturation line. However, not all the parameters involved in Equation (10.2) can be calculated from first principles with the accuracy desired for high-precision thermometry.

Below the λ-point with ^{4}He and below about 1 K with ^{3}He, calculations of a vapor-pressure scale allow an accuracy to within ± 0.5 mK, with only one unknown parameter, $\Delta_{\mathrm{vap}}H_{\mathrm{m,0\,K}}$. Only the first three terms are significant contributors. However, for higher temperatures, the other three terms must be considered as well, especially the contribution of entropy. With ^{4}He, a 1% uncertainty in these three terms contributes to the uncertainty in the vapor-pressure scale by about 3 mK at 3 K and by about 9 mK at 4 K.

For most substances, the uncertainty is much higher than with helium. Therefore, vapor-pressure scales cannot be used, at present, as top-accuracy thermodynamic thermometers. On the other hand, in the implementation of such a thermometer, the choice of the technical parameters is not as critical as for gas thermometry. Therefore, the exact relationship of Equation (10.2) is replaced by a semi-empirical, or even empirical, equation. The following is often used when only low accuracy is required:

$$\ln p = \alpha + \beta/T + \gamma \ln T \tag{10.3}$$

This relation is based on the Clapeyron equation and assumes that the heat of vaporization is a linear function of temperature and that $V^{\mathrm{L}} \ll V^{\mathrm{V}}$ and the vapor is an ideal gas. The parameters α, β and γ are found experimentally for each substance.

Vapor-pressure equations are expected to be valid for a broad variety of experimental conditions, and, in general, no calibration is necessary at any fixed point, as the values of all coefficients are specified (and tabulated as defining values). In fact, the p–T relationship of a specific pure substance, after being determined experimentally and being compared with a thermodynamic thermometer (such as a gas thermometer), is assumed to be valid, within the stated accuracy, irrespective of any specific implementation. At present, the definitions of ^{3}He and ^{4}He vapor-pressure scales are part of the ITS-90.

A scale of this type differs from an empirical scale, in that the realization of the latter requires a specific interpolating instrument. With the vapor-pressure scale definition, no fixed points are needed, as all the values of the parameters of the defining equation are defined.

The basic criteria of the vapor-pressure scale also differ from those of gas thermometry, in which the technical design may seriously affect the accuracy obtainable with individual apparatuses. For this reason, when a gas thermometer is used as an interpolating instrument, the value of a certain number of parameters of the defining equation must be obtained from calibration. No such requirement exists with vapor-pressure thermometry, since only the physical properties of a substance are significant.
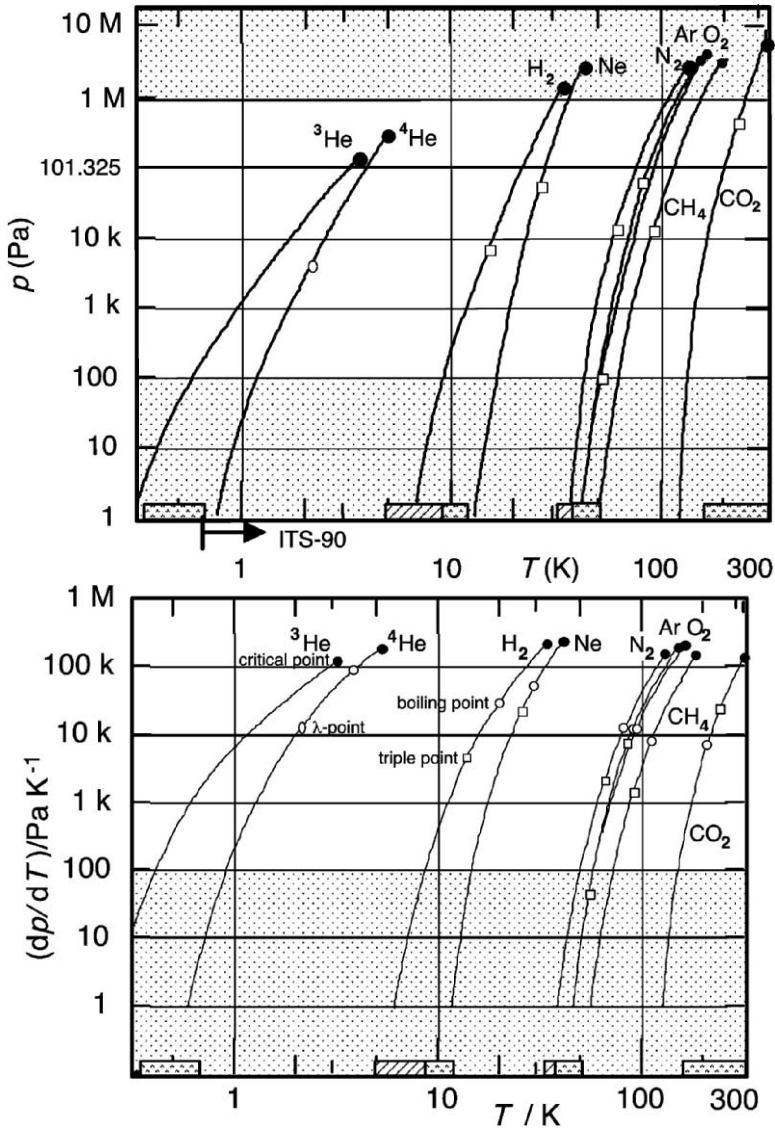
FIGURE 10.10. Vapor-pressure scales: ranges $p(T)$ and sensitivity dp/dT (from [1]).

On the other hand, each substance allows a scale of this type to be realized only over a very narrow temperature interval, as shown in Figure 10.10; unfortunately, over certain temperature intervals, vapor-pressure scale realization is not even possible or, at least, not to a high accuracy.

Both liquid–vapor and solid–vapor equilibriums have to be considered, though greater thermal problems are involved with solid–vapor equilibriums, which may limit the accuracy of the realization.

10.3.2.1 Influence of Physical Parameters

With an ideally pure gas, after some liquid has been condensed at the bottom of the bulb, after crossing the dew-point line, the pressure remains constant if the temperature is maintained at a fixed value during removal of the heat of condensation, providing further condensation of gas in the bulb from an external cylinder.

Temperature may become unstable only if so much liquid is condensed that it overflows the bulb displacing the vapor that was in equilibrium with the liquid at the temperature of the bulb. When this condition is avoided, the vapor pressure in the bulb realizes the same and unique vapor-pressure scale of a given pure real gas. Virial corrections are always the same on the saturated line, and saturation always occurs, at equilibrium, when some liquid is present.

However, no substance is perfectly pure; instead, a mixture forms with other substances that have, at each temperature, different vapor pressures. Impurities are a major source of uncertainty in vapor-pressure thermometry [1]. The effect of most nonvolatile impurities on $p = f(T)$, as observed in specific experiments (e.g. [37]), thus involves a change in all equation coefficients. The effect of impurities provides a possible explanation for discrepancies (as high as hundredths of a kelvin) that have often been observed between the temperature scales based on vapor pressures realized in different laboratories. Additionally, discrepancies may be due to different isotopic and isomeric composition. The pressure dependence on the vapor/liquid ratio, which is null for an ideally pure substance, can be used as a check to determine whether the effect of impurities is small enough for the required accuracy. On the other hand, for different isotopic compositions, the differences in the p–T relationship must be taken into account [4,38].

Vapor-pressure thermometry (like gas thermometry) is well suited and advisable for use in high magnetic fields—considering the persistent difficulties of employing electrical thermometers for this purpose—since they are not affected by magnetic fields, with the exception of a few substances like O_2 and ^3He.

10.3.2.2 Influence of Technical Parameters

A vapor-pressure thermometer is fabricated of a bulb, where the temperature is measured, and a manometer, connected to the bulb with a tube. In most cases, when the manometric gas is different from the thermometric substance, and when the high purity of the latter must be preserved, a differential diaphragm pressure transducer is used to separate the two gas circuits.

The design of a vapor-pressure thermometer appears to be similar to that of a gas thermometer (Figure 10.8a), but the design parameters are substantially different, since they play a very different role in the accuracy of the thermometer.

The thermometer volume is of very little relevance within a wide range of values with respect to both the bulb volume and the total volume, i.e. the bulb plus all its connections to the pressure-measuring system.

The amount of liquid that avoids bulb overfilling must be carefully computed [1]. It is necessary that all of the liquid phase remains in the thermometer bulb where

the temperature T is to be measured; otherwise, pressure values will be altered. The most critical effect is the so-called "cold spot", a zone of the thermometer wall outside the bulb where the temperature is lower than that of the bulb. This cold surface exerts an extremely effective pumping action on the liquid in the bulb, since pressure always tends to equilibrate at a value corresponding to the lowest (wall) temperature. A large change in volume due to condensation at the cold spot brings about a steady vapor flow. The mass flow, i.e. the mass of liquid transported, is very large, when compared with that obtained by a pumping action from room temperature, since the low-temperature density is much higher and the vapor flow takes place inside a much shorter tube. Even when mass transfer is very small, pressure alteration due to "cold spots" has very serious consequences in the measurement accuracy.

In vapor-pressure thermometry, the bulb, which must be massive to ensure temperature uniformity, does not require a large volume, as is necessary in gas thermometry if a dead-volume must be minimized. The typical size for the bulb is a few cubic centimeters. Accordingly, the volume of the connecting tube is insignificant to a large extent, and the tube need not be a capillary, as in gas thermometry. The diameter can then be several millimeters and, if necessary, be widened in steps up to several centimeters, according to the density decrease, in order to limit the effect of thermo-molecular pressure differences. An upper value for this volume is mostly a matter of convenience, or can be determined by the need to limit thermal exchange by convection or by the response time.

Pressure-measurement accuracy requirements increase with decreasing temperature, because the thermometer sensitivity decreases quickly. Figure 10.10 shows the dependence of sensitivity dp/dT on temperature. The upper limit of the thermometer range is set by the maximum pressure that the manometer can measure, or by the value of the critical pressure (always less than 10 MPa). The lower limit, on the contrary, is set by the absolute measurement uncertainty of the manometer, since sensitivity decreases with pressure (though relative sensitivity may increase). Of course, a lower range manometer could be used for this purpose, but a lower limit for absolute uncertainty is generally set at about 0.1 Pa, at best, by other unavoidable factors, such as the static vacuum limit attainable value. The sensitivity of a vapor-pressure thermometer at any temperature is about twice that of a gas thermometer.

The temperature value is obtained from a $p(T)$ relationship, where p is the pressure value at the liquid–vapor interface. The pressure value measured with the room-temperature manometer is different from p, because of the aerostatic and thermo-molecular effects. With respect to gas thermometry, the connecting-tube design can be optimized more satisfactorily and more easily, since there are no trade-off problems.

Thermal problems are much more critical with the solid phase because of its very poor thermal characteristics. Therefore, it is relatively much more difficult to obtain true thermal equilibrium, and, consequently, to obtain accurate values for vapor pressures of the solid–vapor interface. However, this is not impossible. With some substances, the extension of vapor-pressure measurements down to solid–vapor

equilibrium appreciably extends the range, and enhances the usefulness, of a vapor-pressure thermometer. See [1] for details.

10.3.2.3 Realization of Vapor-Pressure Temperature Scales

Since vapor-pressure thermometry is semi-empirical, an interpolating instrument is not defined and only an equation is specified. Should some of its coefficients be unknown, then their values are to be determined at an equal number of fixed points, thus "calibrating" the specific apparatus used. If all of the coefficients are defined, then fixed points are no longer necessary. International bodies generally take the latter solution when they officially endorse a vapor-pressure scale. When such an endorsement does not exist for a given substance (actually for any substances except helium isotopes), the first concern for a user must be to select an equation suitable to represent the $p = f(T)$ relationship, whose traceability to the thermodynamic temperature is reliably established to sufficient accuracy.

The next concern for a laboratory (or an industry) that wants to use a vapor-pressure thermometer is how to design an apparatus that is convenient to use while providing the required accuracy level. The aim is not to realize an empirical scale, but to reproduce thermodynamic equilibrium states; therefore, nonequilibrium conditions or experimental artifacts must not be allowed to affect the measurements within the stated uncertainty. The criteria and precautions discussed previously are the basis for such a design, irrespective of accuracy level. Design can be less careful (e.g. lower substance purity) when lower accuracy is sufficient.

For liquid–vapor equilibrium, the semi-empirical Equation (10.3) has been modified in several ways, by adding or suppressing terms. These changes cause the model to switch from a semi-empirical to a purely empirical model, a field where a wide set of mathematical tools is available for experimental data fitting. Actually, the literature abounds with far more papers on data fitting than on new experimental data.

Very few of the experimental papers specify the temperature scale. The lack of such an indication does not mean, in general, that the temperature values are obtained directly on the thermodynamic scale. Most often, practical thermometers calibrated on an empirical scale are used for measurements. Very seldom is there an explicit reference to any version of the International Scale, so that traceability to thermodynamic values is questionable. The equations derived from such papers are themselves affected by the same lack of traceability.

Therefore, when vapor-pressure measurements are used in thermometry, it is advisable to use those equations that have been subjected to international peer review, even in the absence of a formal endorsement. Specifically, IUPAC and the CCT [39] have performed this type of review for several gases. These international bodies do not endorse the equations, but they are, indeed, "recommended." They concern liquid–vapor pressures of e-H_2, Ne, N_2, Ar, O_2 and solid–vapor pressures of Ne, N_2 and Ar. At present, these equations and other selected equations from [1] are also available recalculated in the ITS-90 [40, 41].

A special case is helium vapor-pressure thermometry, because it has officially been endorsed by international bodies since the turn of the 1950s (T_{58} and T_{62} scales [1]). In the ITS-90, ^{3}He and ^{4}He vapor pressures constitute the only definition below 3 K and must also be used for the determination of the lower fixed point of an ICVGT.

An accurate measurement of helium vapor pressure involves specific precautions, especially when superfluid ^{4}He is measured below 2.1768 K and when ^{3}He is measured below about 1 K. Further details are given in the *Supplementary Information for the ITS-90* [2], in the *Techniques for Approximating the International Temperature Scale* [39], and in the relevant literature [1].

10.3.3 ^{3}He Melting Curve Thermometry

The ^{3}He $p–T$ phase transition (see Figure 10.6) was adopted as the basis from 0.9 mK to 1 K for the PLTS-2000 by the CIPM. The derivation of the scale is summarized as follows [26]:

1. The pressure scales of NIST and PTB were normalized so that they agree at the pressure minimum p_{min}, taken to be 2.93113 MPa. There being no reason to prefer one over the other, they were averaged, an amount $(p/p_{min})\Delta p$ being added to all PTB pressure values and subtracted from all NIST pressure values, where $\Delta p = 55$ Pa.
2. In addition to the adjustment of the pressures, the NIST-98 temperatures were reduced by 0.15% (see above).
3. In the temperature range 1 K > T_{2000} > 315.24 mK (the temperature at the pressure minimum), the PTB-96 equation is used (pressures adjusted as in 1).
4. In the temperature range 315.24 > T_{2000} > 25 mK, the PTB-96 equation is used (pressures adjusted as in 1), and with the first derivative decreased (absolute value increased) by a small amount (<2 Pa/mK), so that the PLTS-2000 coincides with the revised NIST-98 temperatures at 25 mK.
5. In the temperature range 25 > T_{2000} > 0.902 mK the PLTS-2000 is based on an interpolation between adopted (p, T_{2000}) values at 25 mK, 6 mK and at the transitions point 1, 2 and 3 in ^{3}He (see Table 10.4). At 25 mK and at 6 mK, the revised NIST-98 values are adopted. To obtain values at the transitions 1, 2 and 3, the PTB and University of Florida (UF) scales were normalized to the revised NIST scale by adding the amount $(T/6 \text{ mK})\Delta T$, where ΔT is 0.066 mK for PTB-96 and 0.136 mK for UF-95, which are the differences from the revised NIST-98 scale at 6 mK. Physically, this corresponds to changing the Curie constant in the Pt-NMR thermometry below 6 mK by +1.1% for PTB-96 and –2.3% for UF-95. These changes are close to the estimated uncertainties in the scales. The remaining differences were then sufficiently small that the average temperatures could be adopted in the PLTS-2000. The pressure values for the transitions 1, 2 and 3 are those of PTB (after adjustment as in 1 above), as these carry lower uncertainties.

6. Pairs of (p, T_{2000}) values were generated and fitted over the complete range by an equation expressing p as a power series in T_{2000}, as was used in PTB-96. The coefficients and the values of pressure and temperature at the feature values are as given in the scale definition.

In conclusion, at the lowest temperatures the PLTS-2000 is close to a thermodynamic extrapolation of the revised NIST-98 scale, passing between the UF and PTB feature values with differences of about $\pm 3\%$ at T_N.

The differences between the various laboratory scales and the PLTS-2000 are shown in Figure 10.11a and b. Figure 10.11b includes a thermodynamically-calculated scale chosen to be an overall best fit which deviates from the PLTS-2000 by no more than 0.02 mK. Similar calculations have been used to investigate the self-consistency of some other scales shown in the figure (Reesink and coworkers [48, 49]).

At 1 K the PLTS-2000 is expected to be in agreement with the International Temperature Scale of 1990, ITS-90, within 0.3 mK.

The standard uncertainty of the PLTS-2000 in thermodynamic terms is estimated from an assumed rectangular probability distribution overlapping the scale differences and uncertainties, and is 0.5 mK down to 500 mK, decreasing linearly to 0.2 mK at 100 mK. It decreases further as the temperature decreases, but in percentage terms it increases to about 0.3% of T at 25 mK and about 2% of T at 0.9 mK. The standard uncertainty in the absolute pressures is estimated to be about 60 Pa (in about 3 MPa).

10.4 Electric Thermometers for Cryogenics

Nearly all types of cryogenic thermometry are accomplished using electrical thermometers. The types of thermometer used at low temperatures show extreme variety (Table 10.5) [50, 51]. This variety reflects the difficulty of finding a single type with a broad range of applications. Figure 10.12 shows the change in sensitivity with temperature for the different types.

The characteristics of the thermometers listed in Table 10.5 will be reviewed with the aim of providing a guide to their selection relative to the particular application and desired accuracy level (Tables 10.6 and 10.7). This will be done while accounting for the parameters generally used for the characterization of sensors and with particular consideration to the typical problems in cryogenic applications.

A discussion of the calibration methods and of the accuracy that can be obtained with each type, with respect to the International Temperature Scale, has been prepared by the CCT [39].

10.4.1 The Choice of Cryogenic Thermometers

The temperature-dependent electrical parameter that is measured is different for different types: resistance, capacitance, voltage, e.m.f. It is related to temperature
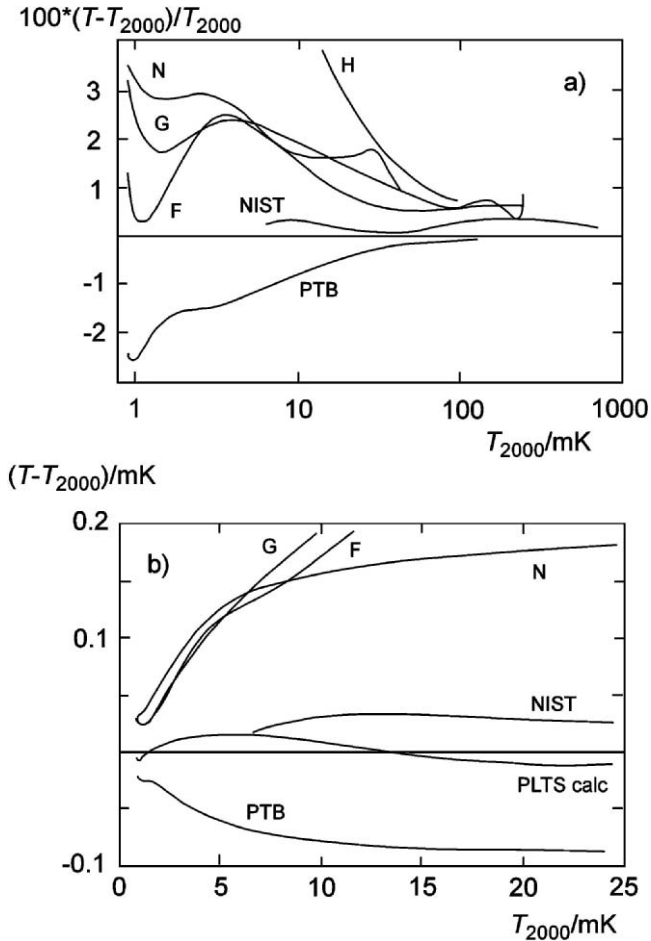
FIGURE 10.11. (a) Relative differences between laboratory scales and the PLTS-2000 as a function of temperature. H: Halperin, 1978; G: Greywall, 1986; F: Fukuyama et al., 1987; NIST: NIST-98, 1992, before and after reduction by 0.15% of T (see text); N: UF-95, 1995; PTB: PTB-96, 1999; all scales being defined by melting pressure equations. (b) Absolute differences below 25 mK, including a comparison with a thermodynamic calculation, "PLTS calc."

by a functional relationship, which may itself affect the overall precision in the use of the sensor. In the worst case, a nonmonotonic behavior, as with some capacitance thermometers, produces a gap in the useful temperature range, which must be spliced in two separate subranges. A similar case is when a monotonic behavior shows a sudden change in slope, due to a change of the underlying physical law, as with the silicon diode thermometers (Figure 10.12g): here, the characteristics must be spliced in two separate subranges In the narrow region where the slope shows the sharp change, the accuracy will be adversely affected.

TABLE 10.5. Types of cryogenic thermometer

Type	Typical temperature range (K)	Typical reproducibility (mK)
1. Thermocouples[a] (Figure 10.12a)		
1.1 Type T	77–>30	10[b]
1.2 Au + 0.07 at.% Fe-KP	<4–100	10[b]
1.3 Au + 2.10 at.% Co-KP	<4–300	10[b]
2. Resistance		
2.1 Platinum (Figure 10.12b)		
standard	14–>300	Better than 0.5
industrial	20–>300	50[c]
2.2 Rhodium–iron (Figure 10.12c)		
standard	0.5–>30	better than 0.3
industrial	<4–>300	10
2.3 Platinum–cobalt (Figure 10.12d)		
industrial	2–>300	10
2.4 CLTS	4–300	100
2.5 Germanium (Figure 10.12e)	1–100	$\Delta T/T = 0.00024$
2.6 Carbon (Figure 10.12e)	0.5–100	200
2.7 Carbon-glass (Figure 10.12e)	0.5–100	$\Delta T/T = 0.002$[d]
2.8 Thermistor	77–>300	100[e]
2.9 Cernox® (Figure 10.12h)	0.1–325	25[f]
2.10 Ge on GaAs (Figure 10.12i)	0.2–300[g]	10
3. Capacitance	2–300	100[h]
4. Diode		
4.1 Gallium arsenide (Figure 10.12f)	4–>300	50
4.2 Silicon (Figure 10.12g)	4–300	50[i]
5. Gas		
5.1 Vapor pressure	0.5–100	1–100
5.2 Gas	2–>300	1–100
6. Mechanical (bimetal)		1000

[a] Other types available; suitable only for industrial use: types E and K down to 77 K; types S and R down to 220 K. KP: chromel P.

[b] Best precision for laboratory use in the differential mode and with offset for parasitic e.m.f.s (up to several microvolts) corrected. Typical precision in the absolute mode (reference junction at refrigerant temperature): 100 mK.

[c] Can improve to 10 mK for selected units above 50 K.

[d] The relative precision in mK/K is preferred for this stable thermometer because of its $R \log(T)$ characteristics. Each unit does not cover the whole temperature range. The same applies for the carbon type.

[e] Can improve to a few millikelvin in narrow ranges above 200 K.

[f] Up to 77 K, 153 mK at 300 K.

[g] Also dual-range or T and B measurements in the same device.

[h] Not usable between 40 and 70 K, because of a slope inversion.

[i] Not usable between 20 and 50 K, because of a sharp change in slope.

The change in the underlying physical law is a very frequent case for thermometers to be used in both the liquid nitrogen and the liquid helium temperature ranges. Therefore, the difficulty in fitting with a single equation the whole working range is quite a common case.
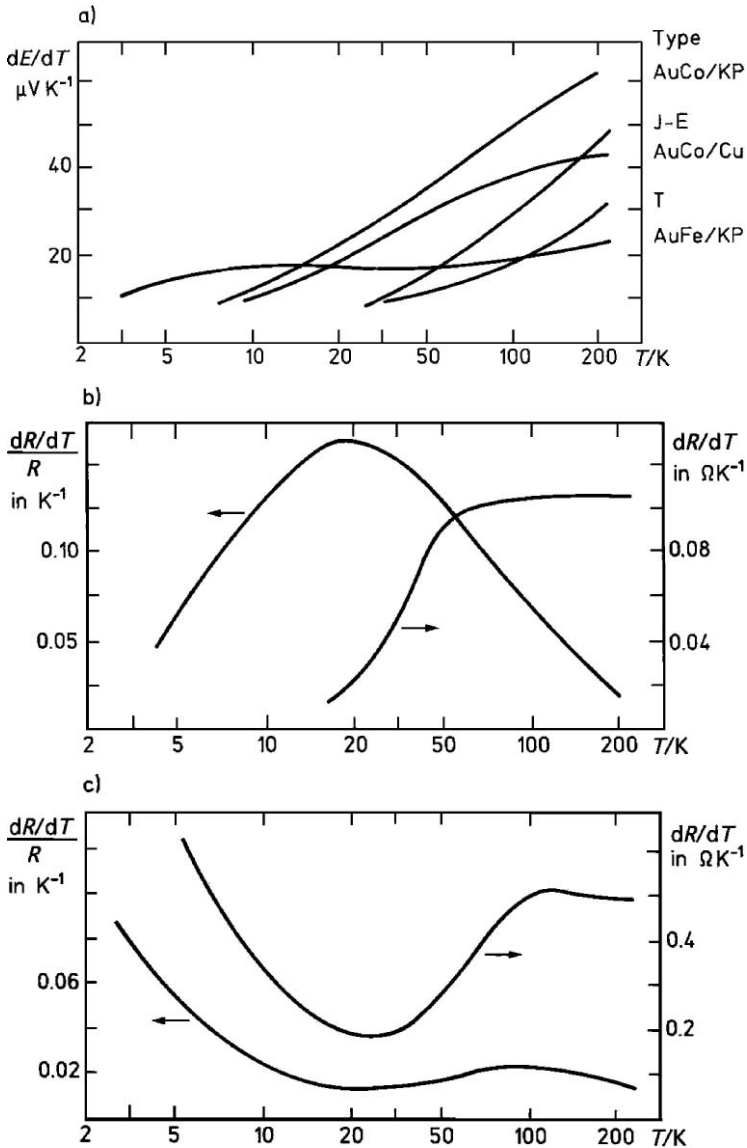
FIGURE 10.12. Typical characteristics of the main cryogenic thermometer types. The behavior with temperature of the sensitivity and of the relative sensitivity is indicated. (a) Thermocouples: refer to Table 10.5 for the types; KP: Chromel P. (b) Platinum resistor. (c) Rhodium–iron resistor. (d) Platinum–cobalt resistor. (e) Germanium (G) and carbon glass (CG) resistors. Carbon resistors show a behavior similar to CG. (f) Gallium arsenide diode. (g) Silicon diode (from [51]). (h) Cernox®resistance thermometer (mod. 1050) (from manufacturer's data sheet). (i) Kiev Ge on GaAs resistance thermometer (mod. TTR-D) (from [53]).
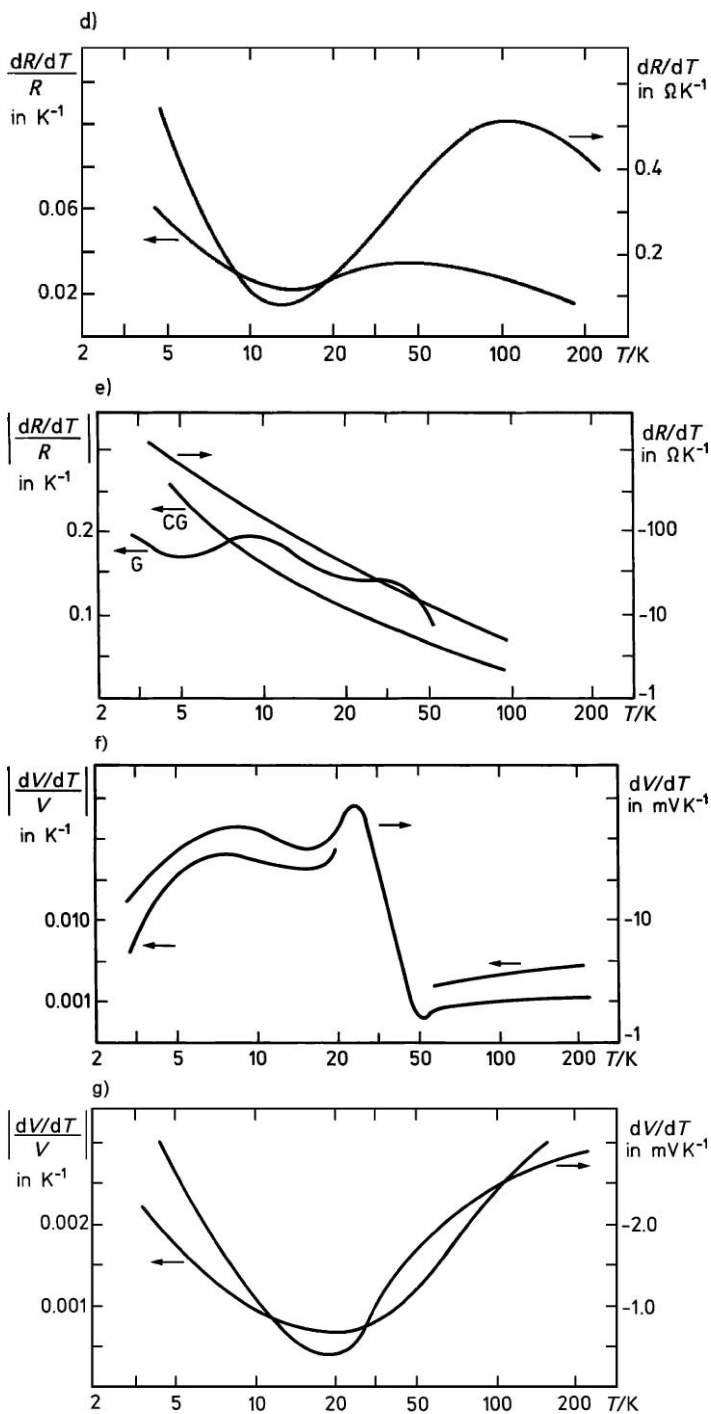
FIGURE 10.12. (*Continued*)
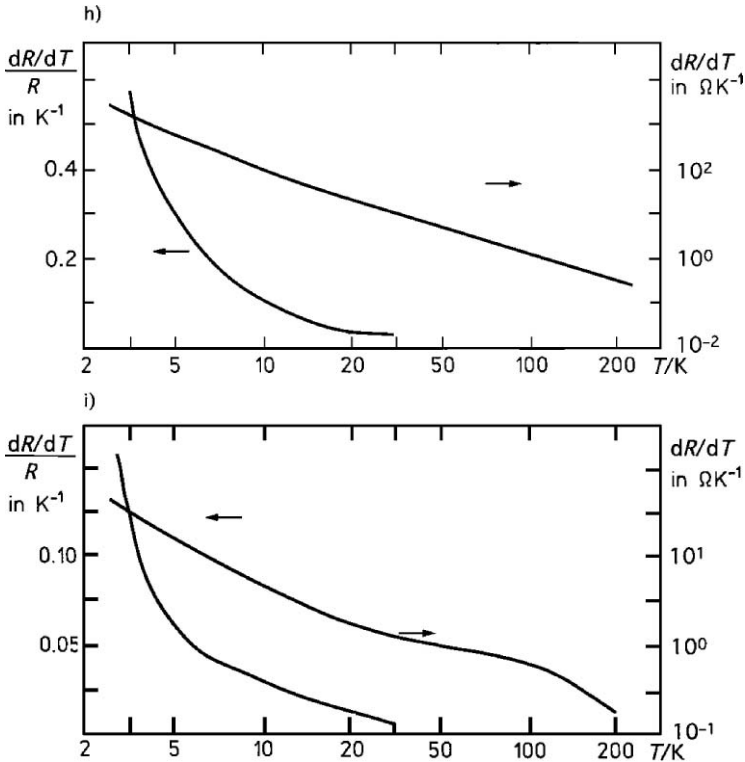
FIGURE 10.12. (*Continued*)

It is well known that high-order polynomials are needed to represent the characteristics of germanium thermometers accurately (Figure 10.12e) [39]. With the gallium arsenide diode thermometers (Figure 10.12f), the accuracy of fitting with a single equation from 4 to 300 K is even lower than the reproducibility.

Studies specific to CERNOX® thermometers can be found by Ichim et al. [52] and for the Kiev germanium on gallium arsenide thermometers by Mitin et al. [53].

The usual temperature range of use of each thermometer, taking into account these difficulties, is shown in Table 10.5 and the achievable accuracy levels are in Tables 10.6 and 10.7. The functional relationship relating the thermometric parameter to temperature is valid only for each well-defined thermometric substance. Therefore, the purity in case of pure elements (e.g. platinum), or the composition in case of alloys (e.g. rhodium–iron, gold–cobalt, etc.), must be specified precisely for the interchangeability of sensors nominally of the same type to be preserved or else each unit must be calibrated.

This interchangeability is an important parameter in industrial applications and is a weak point for most of the cryogenic thermometers, including the platinum type, which is one of the best in this respect above room temperature. For the

TABLE 10.6. Accuracy required in applied cryogenics and superconductivity

Better than 0.005 K	Measurement of reference properties; CERN LHC <2.2 K
From 0.005 to 0.02 K	Most laboratory measurements
	Testing of industrial prototypes
	Measurement of temperature differences
	Monitoring on running apparatus (especially below 10 K)
	High reliability requirements
	Quality level for transducers permanently mounted in industrial equipment
From 0.02 to 0.1 K	Most industrial monitoring applications
Above 0.1 K	Cooldown and generic monitoring; alarms

solid-state thermometers, interchangeability is even more difficult to achieve, as it depends on the uniformity and reproducibility of the doping. An insufficient degree of interchangeability can indirectly limit the overall accuracy of the measurements due to an insufficient flexibility of the measuring instrument in accounting for the spread of the sensor characteristics.

TABLE 10.7. Accuracy requirements for the measuring instrument

Sensor	Thermal parameter (max)	Sensitivity[a]	Max. accuracy (absolute and relative) required for:			
			1 K	0.1 K	0.01 K	0.001 K
Thermocouple	$e.m.f./mV$	$(\mu V\ K^{-1})$	(μV and (% or ppm))			
Type T	6	10–40	10 (0.6)	1 (0.06)	0.1 (60 ppm)	–
Au + 0.07 at.% Fe-KP	5	12–22	12 (0.4)	1 (0.04)	0.1 (40 ppm)	–
Au + 2.1 at.% Co-KP	14	5–70	5 (0.5)	0.5 (0.05)	0.05 (50 ppm)	–
Resistance	R_0/Ω	$(\Omega\ K^{-1})$	($m\Omega$ and (% or ppm))			
Platinum	25	0.004–0.1	4 (0.4)	0.4 (0.04)	0.04 (40 ppm)	4 $\mu\Omega$ (4 ppm)
Platinum (indust.)[b]	100	0.08–0.8	80 (8)	8 (0.8)	–	–
Rhodium–0.5% iron	100	0.15–0.6	150 (0.4)	15 (0.04)	1.5 (40 ppm)	0.15 (4 ppm)
CLTS	290	0.23	230 (0.1)	23 (0.01)	2.3 (10 ppm)	–
	$R_{4.2\ K}\ (\Omega)$					
Germanium	1000	0.1–1000	100 (10)	10 (1)	1 (0.1)	0.1 (0.01)
Carbon glass	1000	0.1–1000	100 (10)	10 (1)	1 (0.1)	–
Diodes	$V_{4.2\ K}/V$	$(mV\ K^{-1})$	(mV and (% or ppm))			
Gallium arsenide	1.5	0.6–3	0.6 (0.05)	0.06 (50 ppm)	6 μV (5 ppm)	–
Silicon	2	2–60	2 (0.2)	0.2 (0.02)	0.02 (20 ppm)	–
Capacitance	$C_{4.2\ K}/pF$	$(pF\ K^{-1})$	(pF and %)			
	15,000	(0)–300	150 (1)	15 (0.1)	1.5 (0.01)	–

[a] Absolute value in the temperature range indicated.
[b] $T > 20$ K. KP : chromel P.

Today, a sensor cannot simply be evaluated for its use in manual measurements. When selecting a type it is also important to consider the requirements set by it to the associated electronic instrumentation. In this respect, measuring a resistance or a voltage is considerably simpler than measuring a capacitance. Electronic or resonant thermometers (noise, quartz, quadrupole) require specialized and costly equipment; for this reason they are not considered here.

In Table 10.6, the requirements for relative and absolute accuracy of the measuring instrument are reported for each type of sensor; some of the best accuracy levels cannot actually be obtained due to other reasons, as indicated in Table 10.5.

The relationship between the thermometric parameter and temperature may also depend on other physical parameters, which are to be considered as spurious. The thermometers must be as insensitive to them as possible. However, some of these effects are intrinsic to the thermometric material and cannot be avoided or minimized, unless another material is used. This is the case of the effect of magnetic fields, which is a situation very specific to cryogenics, because most of the high-field magnets are of the superconducting type. In addition, the thermometers cannot generally be considered as isotropic in this respect.

Therefore, the direction of the field lines with respect to the axis of the element should be known to correct for its effect on most thermometers. The interesting solution of a dual sensor, measuring not only T but also B and allowing an in-situ field measurement, is now available [53]. In Table 10.8, the change relative to the calibration in zero field is reported as an equivalent temperature change. This way of indicating the effect, while common, is not entirely correct when the effect of the magnetic field on the thermometer is very large, because in this case it is also nonlinear, as the thermometer sensitivity is changed by both temperature and magnetic field.

This effect has been observed, for example, with the platinum–cobalt thermometers. Here, the magnetic field affects sensitivity so much that below 4 K and above 5 T it goes to zero. The change in the thermometer sensitivity, due to the effect of the magnetic field, is more or less present in all cases, but is generally not reported in the literature. Some cryogenic thermometers have been specifically developed for minimizing the calibration change in high magnetic fields. The thermometric material must be mounted in a device to form a sensor. This fabrication process often determines most of the overall quality of the sensor, especially its reproducibility on thermal cycling. In cryogenic sensors, the main source of instability arises from the mechanical effects induced by the different thermal expansion coefficients of different parts which produce a change each time the sensor is cooled down. Strain is introduced in the wire-wound or film types of resistance thermometer and in thermocouples. In the compound types (carbon or cermet thermometers), the grains of conductive material tend to move relative to each other; in the solid-state types, problems with the connecting leads are considered the main single source of instability.

The reproducibility levels for the different commercial types are given in Table 10.5; they are realistic figures, even if some better levels can often be suggested by the manufacturers.

TABLE 10.8. Magnetic field-dependent temperature errors (from [51,53])

Type	T (K)	Magnitude of relative temperature error $\Delta T/T$ (%) for values of B: magnetic flux density B (T)					Note
		1	2.5	8	14	19	
Carbon radio resistor (typ.)	0.5		2–4	5–13	7–20		1
	1.0		2–4	6–15	9–25		
	2.5		1–5	6–18	10–30		
	4.2		1–5	5–20	10–35		
KVM carbon composite res.	2.4		3	(at 5 T) 8			2
	4.2		1.5	5			
	10		0.4	1.4			
	20		0.1	0.4			
	80		<0.01	<0.01			
Carbon glass resistor	2.2		0.1	1.5	3	4	3
	4.2		0.5	2	5	7	
	10		0.2	1.1	3	7	
	20		<0.01	0.02	0.03	0.13	
	45		0.07	0.5	1.3	2	
	190		0.04	0.3	1	1.7	
Germanium resistor	2.0		8–10	60			4
	4.2		5–20	30–55	60–70		
	10		4–15	25–60	60–75		
	20		3–20	15–35	50–80		
	70		3–10	15–30	25–50		
Cernox®	2.0		1.3	3.1	3.9	5	5
	4.2		0.1	0.15	0.85	0.8	
	10		0.04	0.4	1.1	1.5	
	30		0.01	0.04	0.06	0.11	
	77		0.002	0.022	0.062	0.11	
Ge on AsGa	0.5		0.43	(at 6 T) 3.7			6
	1.0		0	0.8			
	2.0		0.82	6.8	24.1		
	4.2		0.4	2.7	12.5		
	77		0.13	0.3	2.0		
Platinum res. (industrial)	10		100				7
	20		2–8	25			
	40		0.5	3	6	9	
	87		0.04	0.4	1	2	
	190		<0.01	0.06	0.2	0.3	
Platinum res. (standard)	20		20	100			
	40		>1	5	10		
	87		<0.5	1	2		
Rh–Fe resistor	2.0		22				8
	4.2	2	11	(at 6 T) 40			
	20	0.8	4	(at 5 T) 10			
	40		1.5	12	30	40	
	87		0.2	1.5	4	6	
	190		0.03	0.3	0.9	0.9	

(*Cont.*)

TABLE 10.8. (continued)

Type	T (K)	1	2.5	8	14	19	Note
		— Magnitude of relative temperature error $\Delta T/T$ (%) for values of B: magnetic flux density B (T)					
Pt–Co resistor	2.0	25	30				9
	4.2	8	3	(at 5 T) 40			
	10	1	<0.1	12			
	20	0.2	1	3.5			
	30	0.2	0.3	3.5			
CLTS linear resistor	4.2	20					10
	10	17	100				
	30	5	30				
SrTiO$_3$ capacitor	2.2		<0.02	<0.02	0.02		11
	4.2		<0.01	<0.01	0.01		
	20		<0.05	<0.05	<0.05		
	50		<0.05	<0.05	<0.05		
	87		<0.01	<0.01	<0.01	<0.01	
	190		<0.01	<0.01	<0.01	<0.01	
Silicon diode	4.2	75					12
	10	20	30	50			
	20	4	7	10			
	30	3	4	5			
	77	0.2	0.5	0.5			
GaAs diode	4.2	2–3	30–50				12
	10	1.5–2	25–40	75–200			
	20	0.5–2	20–30	60–150			
	40	0.2–0.3	4-6	15–30			
	80	0.1–0.2	0.5–1	2–5			
Au + 0.07Fe –KP thermoc.	4.2	2	10	15			13
	10	3	20	30			
	20	2	15	20			
	45	1	5	7			
	100	0.1	0.8				
KP–Const thermocouple	10	1	3	7			13
	20	<1	2	4			
	45	<1	<1	2			
Cu + 0.01Fe–Cu thermoc.	4.2	2	(at 5 T) 3.5				13
	10	0.8	2				
	20	0.6	1.5				
	50	0.3	0.6				

Notes: 1. Relative temperature error monotonic in B and T and always positive. Higher nominal resistance units have smaller error. Radio resistors. 2. Resistor specifically developed as a thermometer. 3. Behavior similar to radio resistors, with improved stability to thermal cycling. Negative error below about 20 K. 4. Not recommended except in very low fields. Strong orientation dependance. 6. Mod. 1050, zirconium oxynitride. Negative error in some field/temperature regions. 6. Specially developed in Kiev for high magnetic fields. Orientation dependence <10%. Negative error in some field/temperature regions. 7. Small orientation dependence. Useful only for T > 30 K. 8. Little orientation dependence. Useful only in low fields. 9. Little orientation dependence. Negative error below 12 K and 2.5 T. 10. Extremely high error. Useful only in very low magnetic fields, or as a magnetometer. 11. Not useful between about 60 and 80 K because of a nonmonotonic behavior. 12. Orientation dependent. Smaller values for junction parallel to B. 13. Gradients in the magnetic field crossed by the wires can cause higher errors. KP: Chromel P.

References

1. Pavese, F., and Molinar, G.F., *Modern Gas-Based Temperature and Pressure Measurements*, The International Cryogenic Monograph Series, Plenum Press, New York, 1992.

2. BIPM, *Supplementary Information for the ITS-90* (Sévres, Bureau International des Poids et Mesures), 1990.

3. Pavese, F., *Metrologia*, 42, 194–200, 2005. Pagvese, F., Fellmuth, B., Head, D., Hermier, Y., Hill, K.D., and Valkiers, S., *Analytical Chemistry*, 77(15), 5076–5080, 2005.

4. BIPM, *Comptes Rendus Comité Consultatif de Thermométrie*, 23, (Sévres,Bureau International des Poids et Mesures), 2005.

5. White, D.R., Dransfield, T., Strouse, G.F., Tew, W.L., Rusby, R.L., and Gray, J., *Temperature, its Measurement and Control in Science and Industry*, Vol. 8, Ripple, D.C., ed., American Institute of Physics, New York, 2003, pp. 221–229.

6. Fellmuth, B., Wolber, L., Hermier, Y., Pavese, F., Steur, P.P.M., Peroni, I., Szmyrka-Grzebyk, A., Lipinski, L., Tew, W.L., Nakano, T., Sakurai, H., Tamura, O., Head, D., Hill, K.D., and Steele, A.G., *Metrologia*, 42, 171–193, 2005.

7. deLaeter, J.R., Vohlker, J.K., De Bievre, P., Hidoka, H., Peiser, H.S., Rosman, K.J.R., and Taylor, P.D.P., "IUPAC Technical Report," *Pure Appl. Chem.*, 75, 683–800, 2003.

8. Pavese, F., *Temperature, its Measurement and Control in Science and Industry*, Vol. 8, Ripple, D.C., ed., American Institute of Physics, New York, 2003, pp. 167–172.

9. Pavese, F., Ferri, D., Peroni, I., Pugliese, A., Steur, P.P.M., Fellmuth, B., Head, D., Lipinski, L., Peruzzi, A., Szmyrka-Grzebyk, A., and Wolber, L., *Temperature, its Measurement and Control in Science and Industry, Industry*, Vol. 8, Ripple, D.C., ed., American Institute of Physics, New York, 2003, pp. 173–178.

10. Pavese, F., Ancsin, J., Astrov, D.M., Bonhoure, J., Bonnier, G., Furukawa, G.T., Kemp, R.C., Maas, H., Rusby, R.L., Sakurai, H., and Ling Shankang, *Metrologia*, 20, 127–144, 1984. Pavese, F., Ferri, D., Giraudi, D., and Steur, P.P.M., *Temperature, its Measurement and Control in Science and Industry*, Vol. 6, Schooley, J.F., ed., American Institute of Physics, New York, 1992, pp. 251–256.

11. Pavese, F., and Ferri, D., *Advances in Cryogenic Engineering*, Vol. 35, Plenum Press, New York, 1990, pp. 1835–1837.

12. Pavese, F., Fellmuth, B., Head, D., Hermier, Y., Peruzzi, A., Szmyrka-Grzebyk, A., and Zanin, L., *Temperature, its Measurement and Control in Science and Industry,* Ripple, D.C., ed., American Institute of Physics, New York, 2003, pp. 161–166.

13. Lipinski, L., Szmyrka-Grzebyk, A., and Manuszkiewicz, H., *Meas. Sci. Technol.*, 11, 738–742, 2000.

14. Schooley, J.F., Evans, Jr., G.A., and Soulen, Jr., R.J., *Cryogenics*, 20, 193–199, 1980.

15. Schooley, J.F., and Soulen, Jr., R.J., *Temperature, its Measurement and Control in Science and Industry*, Vol. 5, Schooley, J.F., ed., American Institute of Physics, New York, 1982, pp. 251–260.

16. Fellmuth, B., Maas, H., and Elefant, D., *Metrologia*, 21, 169–180, 1985.

17. Pavese, F., "*Magnetic Shielding*," Chapter G10, *COMETT Encyclopedia of Applied Superconductivity*, IOP, London, 1998, pp. 1462–1483.

18. Lipinsky, L., Manuszckiewicz, H., and Szmyrka-Grzebyk, A., *Proc. IV Symp. on Temperature and Thermal Measurements in Industry and Science*, TEMPMEKO 90, 1990, pp. 126–130.

19. Van Sciver, S.W., *Helium Cryogenics*, Plenum Press, New York, 1986.

220   F. Pavese

20. Lin Peng, Mao Yuzhu, Hong Chaosheng, Yue Yi and Zhang Qinggeng, "Proc. ICEC 13," *Cryogenics*, Special Issue, 1990.
21. Song Naihao, Hong, C.S., Mao Yuzhu, Ling Peng, Zhang Qinggeng, and Zhang Liang, "Proc. ICEC 13," *Cryogenics*, 31, 87–93, 1991.
22. Maidanov, V.A., Engert, J., and Fellmuth, B., BIPM *Comptes Rendus Comité Consultif de Thermométrie* 21 (Sévres, Bureau des Poids et Mesures), 2001, Document CCT/-01-01.
23. Ling Peng, Mao Yuzhu, Hong Chaosheng, Pavese, F., Peroni, I., Head, D., and Rusby, R.L., *Temperature, its Measurement and Control in Science and Industry*, Vol. 8, Ripple, D.C, ed., American Institute of Physics, New York, 2003, pp. 191–195.
24. Lipinsky, L., Szmyrka-Grzebyk, A., Manuszkiewicz, H., Steur, P.P.M., and Pavese, F., Proc. *TEMPMEKO 97*, 1997, pp. 105–109.
25. Keller, W.E., *Helium-3 and Helium-4*, Plenum Press, New York, 1969.
26. BIPM, *Comptes Rendus Comité Consultatif de Thermométrie* 21 (Sévres, Bureau International des Poids et Mesures), 2001, Document CCT/01-40.
27. Greywall, D.S., *Phys. Rev. B*, 33, 7520–7538, 1986.
28. Durieux, M., and Rusby, R.L., *Metrologia*, 19, 67–72, 1983.
29. Astrov, D.N., Orlova, M.P., and Kytin, G.A., *Metrologia*, 5, 111–118, 1969.
30. Astrov, D.N., Belyanski, L.B., Dedikov Yu, A., Polunin, S.P., and Zakharov, A.A., *Metrologia*, 26, 151–166, 1989.
31. Steur, P.P.M., Pavese, F., and Peroni, I., *Temperature, its Measuremem and Control in Science and Industry*, Vol. 8, Ripple, D.C., ed., American Institute of Physics, New York, 2003, pp. 125–130.
32. Meyer, C.W., and Reilly, M.L., *Proc. TEMPMEKO 1996*, Marcarino, P., ed., Levrotto & Bella, Torino, Italy, 1997, pp. 39–44.
33. Sakurai, H., *TEMPMEKO*, Fellmuth, B., et al., eds, VDE Verlag, Berlin, Germany, 2002, pp. 537–542.
34. Hill, K.D., *TEMPMEKO*, Fellmuth, B., et al., eds, VDE Verlag, Berlin, Germany, 2002, pp. 543–548.
35. Pavese, F., Steur, P.P.M., Ferri, D., and Astrov, D.M., *Advances in Cryogenic Engineering*, Vol. 43, Plenum Press, New York, 1998, pp. 789–794.
36. Steur, P.P.M., Peroni, I., Ferri, D., and Pavese, F., *Proc. TEMPMEKO*, 2004, pp. 141–146.
37. Ancsin, J., *Metrologia*, 14, 1–7, 1978.
38. Pavese, F., Tew, W.L., and Steele, A.G., *Proc. TEMPMEKO*, Fellmuth, B., et al., eds, VDE Verlag, Berlin, Germany, 2002, pp. 429–434.
39. Bedford, R.E., Bonnier, G., Maas, H., and Pavese, F., *Techniques for Approximating the International Temperature Scale* (Sévres, Bureau International des Poids et Mesures), 1990, Monograph No. 1.
40. Pavese, F., *J. Chem. Thermodynamics*, 25, 1351–1361, 1993.
41. Bedford, R.E., Bonnier, G., Maas, H., and Pavese, F., *Metrologia*, 33, 133–154, 1996.
42. Halperin, W.P., Rasmussen, F.B., Archie, C.N., and Richardson, R.C., *J. Low Temp Phys.*, 31, 617–620, 1978.
43. Greywall, D.S., *Phys. Rev. B*, 33, 7520–7527, 1986.
44. Fukuyama, H., Ishimoto, H., Tazaki, T., and Ogawa, S., *Phys. Rev. B*, 36, 8921–8925, 1987.
45. Fogle, W.E., Soulen, R.J., and Colwell, J.H., *Temperature, its Measurement and Control in Science and Industry*, Vol. 6, Schooley, J.F., ed., American Institute of Physics, New York, 1992, pp. 91–99.

46. Ni, W., Xia, J.S., Adams, E.D., Haskins, P.S., and McKisson, J.E., *J. Low Temp. Phys.*, 99, 167–173, 1995. *Ibid.*, 101, 305–310, 1995.
47. Schuster, G., Homann, A., Hechtscher, D., and Kühne, M., *7th International Symposium in Temperature and Thermal Measurements in Industry and Science*, Dubbeldam, J., and de Groot, M., eds, 1999, pp. 129–138.
48. Reesink, A.L., and Durieux, M., *7th International Symposium on Temperature and Thermal Measurements in Industry and Science*, Dubbeldam, J., and deGroot, M., eds, 1999, pp. 50–55.
49. Reesink, A.L., PhD thesis, Leiden University, 2001.
50. Rubin, L.G., and Brandt., B.L., *Advances in Cryogenic Engineering*, Vol. 31, Plenum Press, New York, 1986, pp. 1221–130.
51. Pavese, F., *Fields of Application: Cryogenics*, *Thermal Sensors*, Vol. 4., *Sensors*, Ricolfi, T., and Scholz, H., eds., VCH, Weinheim, 1990, Ch. 10.
52. Ichim, D., Pavese, F., Balle, C., and Casas-Cubillos, J., *Advanced Mathematical and Computational Tools in Metrology V*, Vol. 57, World Scientific, Singapore, 2001, pp. 208–212.
53. Mitin, V.F., Boltovet, N.S., Basanets, V.V., Kholevchuk, V.V., Nemish, I.Yu., Mitin, E.V., McDonald, P.C., and Pavese, F., *Advances in Cryogenic Engineering*, Vol. 51B, American Institute of Physics, New York, 2006, pp. 1234–1250.

Part 4
Cryogenic Applications Development Over the Past 50 Years

11
Aerospace Coolers: A 50-Year Quest for Long-Life Cryogenic Cooling in Space

R.G. ROSS, JR.

Jet Propulsion Laboratory, California Institute of Technology, Pasadena, CA 91109, USA

Abstract

Cryogenic temperatures are critical to allow infrared, gamma-ray and X-ray detectors to operate with low background noise and high sensitivity. As a result, the world's aerospace industry has long dreamed of having the means for multiyear cryogenic cooling in space to enable long-life sensors of various forms for scientific, missile defense, and reconnaissance observations. Not long after the first Sputnik was launched into space in October 1957, engineers and scientists were actively seeking means of providing cryogenic cooling for evermore sophisticated and sensitive detectors in a variety of spectral regions. Although both passive cryoradiators and stored cryogens have provided a source of cryogenic cooling for many missions, the consistent dream of scientists and mission planners was always for a mechanical refrigerator that could achieve the temperatures of the coldest cryogens (vastly colder than possible with passive radiators) and have multiyear life without the finite life limitations of stored cryogens. The first cryocoolers in space were short-life Joule–Thomson and Stirling cryocoolers flown on both US and USSR missions around 1970. Since that time, extensive research and development of evermore sophisticated cryocoolers (Stirling, Vuilleumier, Brayton, magnetic, sorption, and pulse tube) has taken place in the world's aerospace industry. This chapter examines the enormous progress made by the aerospace industry over the past 50 years in developing both cryostats and cryocoolers to enable the widespread use of cryogenic temperatures in space.

11.1 Introduction

The quest for cryogenics in space has long been a worldwide endeavor by two main communities, i.e. the civilian space and Earth science communities and the military defense communities. The overlap between the communities' needs has been fortuitous, for this has allowed the combined funding of many of the cryogenic technology developments over the years. And although many of the military reconnaissance missions are themselves classified, the military contributions to

225

the cooler developments by themselves have generally not been. This provides relatively good visibility into the total scope of accomplishment.

In contrast to other cryogenic communities, the civilian and defense space communities share a fairly common set of constraints, the most common ones being the huge expense of getting a payload into orbit, the strong leverage that cryogenics has in terms of enabling improved science and reconnaissance measurements, and the small number of cooling units of a particular type that are ever needed. The result is a demand for high efficiency, very high reliability and long life, the ability to justify large levels of funding to achieve the desired performance, and the typical purchase of only one or two units of a particular design. Thus, space coolers (radiators, cryostats or cryocoolers) are distinct from typical commercial or tactical (ground-based military) products by their high level of sophistication, hand-built nature with few, if any, mass-produced components, and correspondingly high price (generally in the millions of dollars per unit).

In the bigger picture, the world's space community can be almost thought of as two communities: the Western world, which includes the US, Canada, Europe and most of Asia (Japan, China, Korea and India), and the Russian countries (Russia, Ukraine, etc). Since the days of the Cold War and the beginning of the space race, there has been only minimal interchange between these two politically separated communities, and each has developed more or less separately using its own set of cryogenic technologies, nomenclature, and jargon. As a result, Western conferences and journals contain only periodic references to the Russian accomplishments, which have been extensive. As a result, this review is mostly a record of the space cryogenics accomplishments of the Western world with only passing reference to some of the Russian accomplishments.

11.1.1 Cryogenic Applications in Space

Before reviewing the accomplishments over the past 50 years it is useful first to summarize briefly the space applications that are enabled by space cryogenics and their needs as they have evolved over time. From a broad perspective there are two classes of space applications: cryogenic-liquid rocket propellants (such as liquid hydrogen and liquid oxygen) and science applications (such as fundamental physics experiments and infrared, gamma-ray and X-ray instruments with cryogenically cooled detectors). This chapter focuses only on the latter applications, which are typically "operated in space," as opposed to being used to "get to space."

11.1.1.1 Infrared Sensors

As a result of the mutual benefit across the Earth, space-science, and reconnaissance communities, cryogenic infrared instruments are by far the largest application of space cryogenics. Viewing scenes in the infrared provides unique abilities in a number of fields: from measuring chemical constituents in the atmosphere, to viewing distant galaxies and stars, to identifying and tracking targets within a missile-defense system. Table 11.1 highlights the various wavelengths of the

TABLE 11.1. Types and wavelengths of electromagnetic radiation, the blackbody temperature that emits such radiation, and applicable detector types and their required operating temperature

Radiation Type	Wavelength (microns)	Blackbody Temp. (K)	Detector Technology	Detector Temp. (K)
γ-rays	10^{-5}	3×10^8 K	Ge Diodes	80 K
γ-rays	10^{-4}	3×10^7 K	Ge Diodes	80 K
x-rays	10^{-3}	3×10^6 K	micro calorimeters	0.05 K
x-rays	10^{-2}	3×10^5 K	micro calorimeters	0.05 K
UV	0.1	30,000 K	CCD/CMOS	200-300 K
visible	1	3000 K	CCD/CMOS	200-300 K
IR	2	1500 K	HgCdTe	80-130 K
IR	5	600 K	HgCdTe	80-120 K
LWIR	10	300 K	HgCdTe	35-80 K
LWIR	15	200 K	HgCdTe	35-60 K
LWIR	20	150 K	Si:As	7-10 K
LWIR	50	60 K	Ge:Ga	2 K
LWIR/μwaves	100	30 K	Ge:Ga	1.5 K
microwaves	200	15 K	Bolometers	0.1 K
microwaves	500	6 K	Bolometers	0.1 K
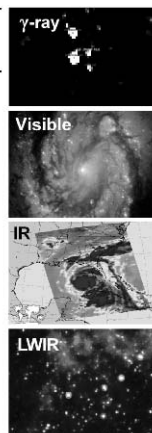
electromagnetic spectrum, the blackbody temperatures that emit such wavelengths, the applicable detector technologies used to see such wavelengths, and the temperatures to which such detectors must be cooled to achieve their required performance. Important regions for infrared observations include room-temperature (300 K) objects that emit in the 10–15 microns region and very cold celestial objects that emit in the 20–500 microns region. In these infrared wavelengths, it is not only necessary to cool the detector to cryogenic temperatures, but also to cool the optical system that illuminates the detector. As a result, infrared applications generally involve multistage cooling over a range of temperatures from 150 K down to near absolute zero.

11.1.1.2 Gamma-Ray Detectors

The second most popular subject for cryogenic space instruments is gamma-rays. As shown in Table 11.1, gamma-rays are extremely short-wavelength photons emitted from substances involved in very high-energy reactions (equivalent to temperatures of 100,000,000 K). The remote detection of gamma-rays emitted from planetary surfaces allows the spatial mapping of the abundances of surface elements such as O, Mg, Fe, Al, Si, Ti, K, Ca, Th, and U. Knowing the elemental composition on the surface of a planet is very important to understanding the origin and the evolution of the planet and also for understanding the origin and the evolution of the solar system.

Unlike optical or even X-ray photons, gamma-rays simply pass through most materials and thus cannot be reflected by a mirror. The most common detectors are room-temperature sodium iodide scintillation crystals that emit a burst of light when struck by a gamma-ray, and cryogenically cooled germanium-crystal diodes

that release an electrical charge when struck by a gamma-ray. Germanium detectors, each the size of a tea cup, offer better energy resolution, less noise, and better spatial resolution than room-temperature scintillators. However, they must be cooled to around 80 K to achieve their performance advantage.

11.1.1.3 X-Ray Detectors

X-rays are very short-wavelength photons, much shorter than ultraviolet light, but not as short as gamma-rays. Many celestial objects, such as stars and black holes, generate X-rays in extremely violent processes, such as when stars are born or explode. However, because Earth's atmosphere blocks out X-rays, celestial X-ray research must rely heavily on high-altitude balloon and space observations. The most common detectors are room-temperature gas scintillators that emit a burst of light when struck by an X-ray, and cryogenically cooled microcalorimeters that heat microscopically due to the absorbed energy of the incoming X-ray photons. To achieve useful performance, X-ray microcalorimeters must be cooled to around 50 mK,i.e. just one-twentieth of a degree above absolute zero.

11.1.2 Chapter Organization

The next five sections of this chapter review the history of space cryogenics over the past 50 years, with primary emphasis on the accomplishments in the Western countries. The work is organized by decade, starting 50 years ago in 1955, which also corresponds, more or less, with the beginning of the space program. Each decadal section describes the major space milestones of that decade, the key cryogenic missions carried out, and the research focus of the development work of that decade.

11.2 1955 to 1965: The Birth of the Space Program

The space age began to be considered as early as 1946, as scientists started using captured German V-2 rockets, and later Aerobee rockets, to make measurements in the upper atmosphere after the end of World War II. The US considered launching orbital satellites as early as 1945 under the Bureau of Aeronautics of the US Navy. A 1946 Rand report to the Air Force further blessed the idea.

By 1955 the Air Force and Navy were working on Project Orbiter, which involved using a Jupiter C rocket to launch a small satellite into orbit. With growing interest in the International Geophysical Year, which was to last from July 1957 to December 1958, the White House, on July 29, 1955, reported that the US intended to launch satellites into orbit by the spring of 1958. To the great surprise of the Western world, Russia successfully launched their first satellite, Sputnik I (Figure 11.1a), into Earth orbit in October 1957, and followed it soon after with Sputnik II carrying a much heavier payload, including a dog named Laika. Four months later, in January 1958, the US successfully placed Explorer I into orbit (Figure 11.1b).

FIGURE 11.1. The successful launch of Russia's Sputnik I and the US's Explorer satellites into orbit in the 1957–1958 time frame represented the start of the space program.

Building on these first successes, the space race was off and running, and grew to over 50 satellite launches per year over the next few years. By 1962 the US had a first flyby to Venus, Mariner 2, and discussions were ongoing in many circles on the scientific advances that could be made from satellite-based instruments. In 1964, Mariner 4 made the first close-up photographs of Mars, and Nimbus 1 was launched to carry out the first Earth-science observations.

Though the first cryogenic applications in space were still a few years away, development work was initiated on the first space cryocoolers for military applications [1]. Work on Brayton-cycle refrigerators started at Arthur D. Little in Cambridge, MA, in 1962 based on the rotary-reciprocating refrigerator (R³) concept [2]. The R³ design incorporated gas bearings, with the promise of reducing wear and extending refrigerator lifetime. Work on Vuilleumier (VM) cryocoolers was also started in the 1960s at Hughes Aircraft in California and at Philips Laboratories in Briarcliff Manor, New York [1].

Work on future space-science cryogenic missions also began, including initial funding of Gravity Probe B (GPB) in 1963. In the late 1950s, astronomers were using lead sulfide (PbS) detectors to study infrared radiation. To increase the sensitivity, the PbS cell was cooled to 77 K. This allowed infrared observations out to wavelengths of about 3 μm. In 1961, the first germanium bolometer was developed by Frank Low, and was hundreds of times more sensitive than previous detectors. It was capable of detecting far-infrared radiation when cooled to 4 K. In 1963, a germanium bolometer was attached to a balloon to make infrared observations of Mars.

11.3 1965 to 1975: Race to the Moon, First Cryogenics in Space

This was the decade of the great race to the Moon and the first cryogenics in space. The year 1966 brought the landing of the Surveyor spacecraft on the surface of the Moon and the launch of Nimbus 2 for a next level of Earth-science observations.

Also in 1966, the Goddard Institute of Space Sciences used balloons to conduct infrared surveys at 100 μm and discovered about 120 bright infrared sources. In 1967, cooled infrared telescopes were placed on rockets that could observe the sky for several minutes before reentry. The first infrared all-sky map resulted from a series of rocket flights by the Air Force Cambridge Research Laboratory. Although the total observation time accumulated by these Hi Star flights was only about 30 min, they successfully detected 2363 reliable infrared sources.

In 1968, Apollo orbited the moon and Nimbus B was launched for more Earth observations. Apollo 11 landed on the moon in 1969, followed by Apollo 12, and the Apollo 13 mishap occurred in 1970. While the follow-on Apollo missions were frequenting the moon, the first cryogenics missions to space were being launched.

11.3.1 1965–1975 Cryogenic Missions

11.3.1.1 1968: Apollo Fuel Cell Liquid Hydrogen and Liquid Oxygen Dewars

The first space dewars were probably those built by Beech Aircraft to hold supercritical liquid hydrogen and liquid oxygen for use in the Apollo Service Module fuel cells and breathing oxygen supply. It was one of these that was involved in the historic Apollo 13 mishap of 1970, though the problem was unrelated to the performance of the dewar. A total of 145 units were built in support of the Apollo program.

11.3.1.2 1969: Mariners 6 and 7 Nitrogen–Hydrogen Joule–Thomson Cooler

July–August 1969 brought the first cryocooler missions in space; these were two-stage nitrogen–hydrogen open-cycle Joule–Thomson (J–T) cryocoolers designed to cool the Mars infrared spectrometers on Mariners 6 and 7 to 22 K during the spacecrafts' flyby encounters with Mars [3]. Developed by the University of California, Berkeley, the spectrometers incorporated Ge:Hg detectors to allow infrared spectral surveys of Mars to be taken over the wavelength range from 6 to 14.3 μm. The Mariner 7 flight was totally successful, with the detector remaining below 22 K for about an hour; however, the nitrogen J–T stage of the Mariner 6 system failed to operate.

11.3.1.3 1971: RM-19 Malaker Stirling

July 1971 brought the first closed-cycle mechanical cryocooler in orbit: a Malaker Stirling cooler that cooled an Earth-background infrared radiometer built by Lockheed Missile and Space Co. (LMSC) in Palo Alto for the Department of Defense (DoD) [1]. The RM-19 radiometer and the Malaker Stirling are shown in Figure 11.2. Three detector assemblies were thermally connected to the two Stirling refrigerators by means of a flexible thermal strap, while each of the temperature-compensated infrared telescopes was passively cooled to 240 K. During the several-month mission, the refrigerators, operating in tandem, periodically cooled the

FIGURE 11.2. Malaker Stirling coolers flown on RM-19 in July 1971.
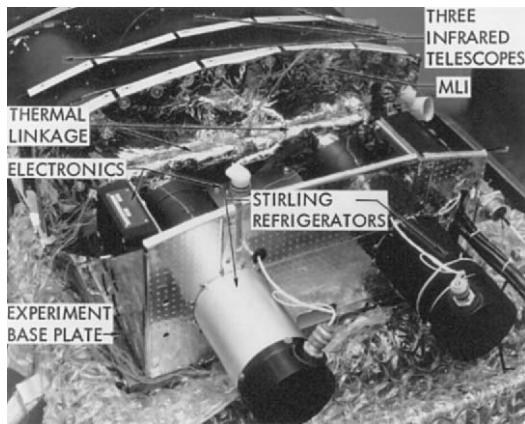
detectors to approximately 105 K in 3 to 4 h periods preceding radiometer operation. The cooling capacity of each cooler was 2 W at 100 K with a 40 W input. This first mission of a closed-cycle cryocooler was an important milestone; however, the total accumulated run time on the coolers during the mission was less than 1000 h.

11.3.1.4 1971: SESP 71-2 Hughes Vuilleumier Cryocooler

In October 1971, only a few months after the RM-19 flight, the first advanced technology cryocooler, a two-stage Hughes Aircraft VM cooler (Figure 11.3) was flown as part of the DoD's SESP 71-2 technology demonstration mission in conjunction with the Celestial Mapping Program [1]. The cooler provided 3.5 W at 60 K plus 0.15 W at 13 K for 427 W of input power. The system accumulated 1179 h of operation, which included 689 h of prelaunch checkout and 490 h of orbital operation. The system was operating at approximately nominal conditions

FIGURE 11.3. Hughes Aircraft two-stage VM cooler flown on SESP 71-2 in October 1971.

FIGURE 11.4. Lockheed solid carbon dioxide cryostat flown on SESP 72-2 in October 1972.

when the heat-rejection coolant loop failed, thus causing system shutdown. During most of the orbital operation, the unit maintained the specified temperatures.

11.3.1.5 1972: SESP 72-2 Lockheed Solid Carbon Dioxide Cryostat

Shortly after the first Stirling and VM cryocoolers were launched to support infrared missions in 1971, the first cryostats flew on SESP 72-2 in October 1972 to support a DoD gamma-ray mission. The mission consisted of two single-stage solid carbon dioxide cryostats, each providing cooling of a separate gamma-ray detector at 126 K; the cryostats were 40.6 cm in diameter by 35.6 cm long and lasted for 7 and 8 months [4,5]. Development of cryostats with both liquid and solid cryogens had been underway for nearly 10 years, and this first cryostat in orbit was built by Lockheed Palo Alto. A photograph of one of the cryostats is shown in Figure 11.4.

This first flight cryostat established Lockheed's cryostat design philosophy for many years [6]. Design elements include a folded cylinder support for the cryogen tank and a modular approach in which the detector and cooler could be separately developed and tested, and then integrated via a simple shrink-fit attachment that allowed a "drop in" mating of the two. To allow the detector to be maintained in a clean vacuum environment, the detector module was a sealed unit with its own vacuum system that consisted of a vac-ion pump. During ground operations and spacecraft integration, the cryogen was maintained in a nonvented condition by periodic circulation of liquid nitrogen (LN_2) through the cooling coils at approximately 1-week intervals.

With an orbital lifetime goal for the system of 1 year, the shorter 7–8 month lifetime achieved was attributed in part to contamination of the low-emissivity surfaces of the detector resulting from ice accumulation, and to initial heat rate predictions based on erroneous conductivity data for the support tube and the

FIGURE 11.5. Skylab was launched in 1973 and hosted two more cryogenic applications that used the Malaker Stirling coolers in space.

multilayer insulation (MLI) materials. Achieving longer life cryostats with better life prediction was a key technology focus for the next few years.

11.3.1.6 1973: Malaker Stirlings on Skylab

From May 1973 to February 1974, Malaker Stirling cryocoolers were used again in two Earth resources infrared experiments on Skylab (Figure 11.5) to evaluate the applicability and usefulness of sensing Earth resources from orbital altitudes in the visible through to the far-infrared spectral regions [7]. The two complementary units were the S-191 Visible-Infrared Spectrometer, built by Block Engineering of Cambridge, MA, and the S-192 13-band Multispectral Optomechanical Scanner built by Honeywell Research Center of Lexington, MA [8]. Both used HgCdTe photoconductive detectors cooled to ~100 K by Malaker Stirling cryocoolers to acquire data in their 6.2–15.5 μm and 10.2–12.5 μm far-infrared bands respectively. The S-191 experiment was basically a two-channel visible and infrared spectro-radiometer (manually pointed device), whereas the S-192 instrument utilized a 30 cm reflecting telescope with a rotating scan mirror.

11.3.1.7 1975: Nimbus 6 Limb Radiance Inversion Radiometer Cryostat

In June 1975, building on the success of their earlier solid CO_2 cryostat, Lockheed flew a dual-stage solid methane–solid ammonia cryostat on Nimbus 6 as part of the Limb Radiance Inversion Radiometer (LRIR) instrument. This cryostat, shown in Figure 11.6, provided cooling for a tri-metal detector array and the associated focusing optics and filters to 63 to 67 K (methane stage) and also provided cooling of other optical elements at 152 K (ammonia stage). Though the mission goal was 1 year, the detector remained within specified limits for approximately 7 months, while the lifetime of the ammonia was 12 months [6,9]. The design philosophy for this cryostat was similar to that of Lockheed's single-stage cooler, in which the
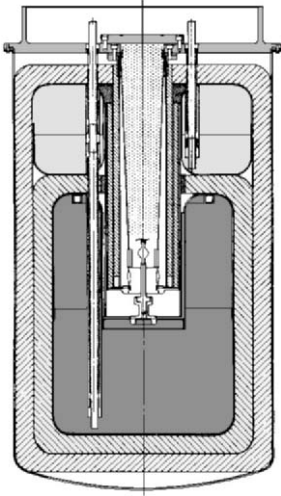
FIGURE 11.6. Lockheed solid methane–ammonia cryostat flown on Nimbus 6.

detector and secondary optics were housed in a separate capsule and interfaced with the cooler through shrink-fit elements. The cryogens were maintained in a nonvented mode by circulation of LN_2 at 10-day intervals. Once in orbit, explosive valves vented the cryogens and insulation vacuums to space.

11.3.1.8 Mid-1970s Liquid Helium Application

Although not in space, a far-infrared balloon-borne spectrometer was used for three flights in the mid-1970s to test the Big Bang theory. To increase its sensitivity, the instrument utilized germanium bolometers immersed in a cryostat cooled with superfluid helium. This is the first time that such a low temperature was used for infrared observations. The observations provided the most widely accepted support for the Big Bang theory until the launch of the Cosmic Background Explorer (COBE) satellite in 1989. The first superfluid helium cryostat in space would be on the Infrared Astronomical Satellite (IRAS) in 1983.

11.3.2 1965–1975 R&D Emphasis

During the late 1960s and early 1970s the focus of aerospace cryogenic research was on achieving long-life cryostats and cryocoolers for space use.

11.3.2.1 Cryostat Research

The major difficulty with the early solid cryogen coolers was the unpredictability of their lifetime, which was driven by the poorly quantified parasitic heat leaks associated with MLI and support materials. Given the shortfalls in operational life, extensive research (illustrated in Figure 11.7) was conducted to improve the

FIGURE 11.7. Early testing by Lockheed of candidate constructions of MLI.

characterization and fabrication processes of MLI and support materials [10–12]. This work was supported jointly with the launch-vehicle community, which also needed low thermal parasitics in cryogenic propellant tanks. Also, in support of GPB, the porous plug was invented in 1970 for retention of superfluid helium in zero gravity [13].

11.3.2.2 Cryocooler Research

The major difficulty with the early cryocoolers was also their short unpredictable lifetime. The DoD's primary desire was to achieve long-life cooling at 10–12 K for the latest longwave infrared (LWIR) focal-plane detector technologies, whereas the National Aeronautics and Space Administration (NASA) was concentrating on higher temperatures, around 65–80 K.

11.3.2.2.1 Vuilleumier Coolers

The work on VM cryocoolers that was started by the Air Force in the 1960s at Hughes and Philips Laboratories was now focused on three-stage machines capable of 0.3 W at 11.5 K, plus 10 W at 33 K, plus 12 W at 75 K, for an input power of 2700 W [14, 15]. The Philips unit had dual rotating shafts in a vibration-reducing rhombic configuration, and the Hughes unit, shown in Figure 11.8, used vibrationally balanced opposed pistons. Because the VM cycle is thermally powered, operation of the cycle directly with radioisotopes or solar heat sources was considered feasible, and various studies of systems of this type were performed. In parallel, NASA–Goddard Space Flight Center (GSFC) started supporting single-stage VM technology for higher temperature NASA applications in 1969, resulting in a 7 W at 75 K for 300 W input cryocooler built by Garrett AiResearch and tested for 6000 h [5].

FIGURE 11.8. Hughes three-stage 12 K VM cooler used dual opposed pistons.

11.3.2.2.2 10 K Rotary-Reciprocating Refrigerator

The work at A.D. Little initiated by the Air Force in 1962 on the R^{3}s led to the single-stage 77 K machine shown in Figure 11.9a. It utilized self-actuating, rotary gas bearings in both the compressor and expander sections, and linear motion to achieve the refrigeration. Thus, each moving member was both rotated and reciprocated. The machine also utilized clearance seals; thus, after startup, there were no rubbing surfaces in the machine.

In 1966, A.D. Little was sponsored by the Air Force to extend the 77 K R^3 machine to achieve 1 W at 3.6 K. A preliminary design of a complete refrigeration system suitable for spaceborne application was developed, and the expanders and associated drive system were tested. Shown in Figure 11.9b, this machine utilized a hybrid cycle coupling a Brayton upper stage with a 3.6 K J–T bottom stage [2, 16].

11.3.2.2.3 Sorption Coolers

Initial studies of the feasibility of hydride sorption coolers also started during this decade with the work of Van Mal and Maynheer [17]. This work was primarily directed at conceptual design studies and quantification of the sorption isotherms of candidate hydride materials.

11.4 1975 to 1985: The Struggle for Long-Life Coolers

By the mid-1970s the space age was maturing, and work on the Space Shuttle was actively underway. Military personnel were busy designing large missile de-
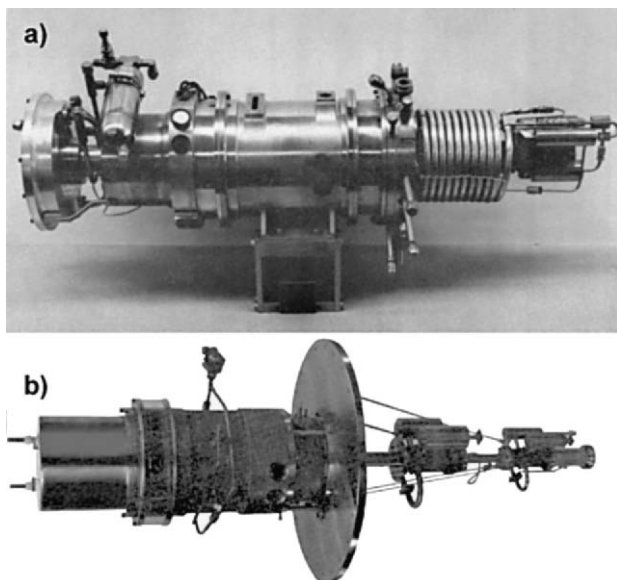
FIGURE 11.9. A.D. Little R^3s: (a) single-stage 77 K system; (b) 3.6 K hybrid Brayton/J–T system.

fense and reconnaissance satellite systems, and Earth and space scientists were planning various missions that could use the extensive access to space that would be provided by the Shuttle. Some of the proposed space-science studies focused on understanding the properties of superfluid helium in space and building on the early work to explore the cosmic microwave background (CMB) of the universe.

Also, during this decade, the development of infrared array detectors (as opposed to single pixels) caused another giant leap in observational capability. This development greatly increased the efficiency of infrared observations and led to the development of infrared cameras that could produce images much more quickly than with a single-element detector.

After several years of development, the first Shuttle launched in 1981 (Figure 11.10).

11.4.1 1975–1985 Flight Applications

11.4.1.1 1978: Nimbus 7 Limb Infrared Monitor of the Stratosphere Cryostat

The Limb Infrared Monitor of the Stratosphere (LIMS) instrument was flown aboard Nimbus 7 in October 1978 as a follow-on to the LRIR instrument that was flown in 1975 aboard Nimbus 6. Built by Honeywell, the instrument used an infrared detector and the same 65 K Lockheed methane–ammonia cryostat (shown in Figure 11.6) used on LRIR [6,9]. The objective of the LIMS experiment was

FIGURE 11.10. This was the decade of Shuttle development, leading to the first Shuttle launch in 1981.

to map the vertical profiles of temperature and the concentration of ozone, water vapor, nitrogen dioxide, and nitric acid in the lower to middle stratosphere range, with extension to the stratopause for water vapor and into the lower mesosphere for temperature and ozone.

11.4.1.2 1978: High Energy Astronomical Observatories Methane–Ammonia Cryostat

About the same time that Lockheed flew their second methane–ammonia cryostat on Nimbus 7, Ball Aerospace flew their version of a methane–ammonia cryostat [5] on the High Energy Astronomical Observatories (HEAO-B and HEAO-C). The Ball cryostat, shown in Figure 11.11, had a loaded weight of 75 kg and measured 76 cm long by 56 cm in diameter. Cooling coils with LN_2 were used to freeze the
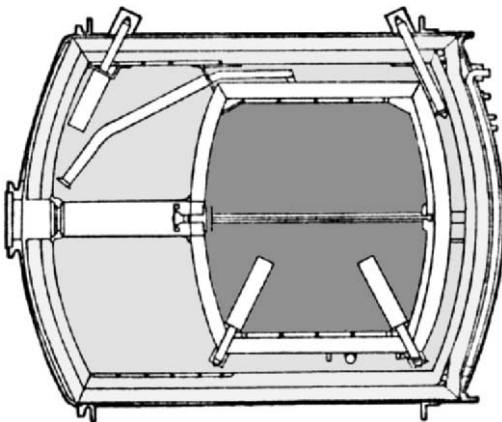
FIGURE 11.11. Ball methane–ammonia cryostat flown in 1978 on the High Energy Astronomical Observatories (HEAO-B and HEAO-C).

FIGURE 11.12. Philips rhombic-drive Stirling cooler launched on the STP 78-1 gamma-ray mission in 1979.
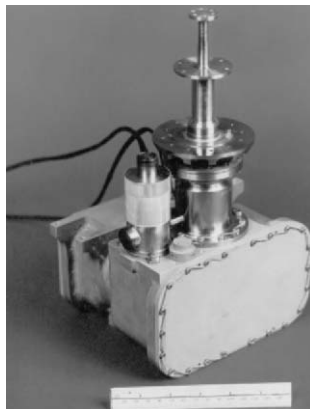
cryogen during the fill operation and to maintain it during ground storage. After the final servicing before flight, the cryogens gradually warm up until the vent seal is opened in orbit. Heat-exchange surfaces were located in both the primary and secondary tanks to promote even heat absorption by the cryogen.

11.4.1.3 1979: STP 78-1 Rhombic-Drive Stirling

Launched as part of a DoD gamma-ray mission in 1979, this new two-stage Stirling cooler (Figure 11.12) was developed specifically for long-term orbital operation by Philips Laboratories, with the Johns Hopkins Applied Physics Laboratory providing the electronic controls and space-qualification program. The overall gamma-ray system was developed by LMSC, and included two gamma-ray detectors, each with fully redundant cryocoolers, for a total of four coolers in the mission [18].

Each 7.2 kg cooler employed a grease-lubricated rhombic drive that utilized counter rotating weights to minimize generated vibration. Piston and displacer seals were glass-filled Teflon and Roulon. The cooling capacity of each cooler was 0.3 W at 77 K plus 1.5 W at 160 K, with an input power of 30 W. To support the redundancy approach, Lockheed developed self-actuating coefficient of thermal expansion-based thermal switches that disconnected the thermal link to the detector when a refrigerator was off (hot). However, the switches were not flown in the final configuration.

In total, the instrument was in orbit for 860 days, with cumulative operating times for the four individual coolers of 4700, 7200, 13,000 and 16,020 h [19]. Although this total run time was impressive, significant degradation in performance occurred. Consequently, after 130 days into the flight, both refrigerators were operated simultaneously in each instrument to provide the required cooling [19]. Not withstanding the performance degradation of the coolers, the utilization of the Stirling machines to provide instrument cooling over a continuous multiyear

FIGURE 11.13. Over 60 of these PRSA dewars were built by Beech Aircraft and Ball Aerospace to supply the Shuttle's fuel cells with hydrogen and oxygen.

period was, indeed, a significant accomplishment. Up until this time, no mechanical cooler had operated in space for more than 1000 h.

11.4.1.4 1981: Shuttle Power Reactant Storage Assembly Dewars

Originally developed by Beech Aircraft as a larger version of similar dewars first developed for the Apollo program (see Section 11.3.1.1) the power reactant storage assembly (PRSA) dewars (Figure 11.13) were developed to store supercritical liquid hydrogen and oxygen for use in the Shuttle's fuel cells to create electrical power and breathable oxygen. The LOX tank holds 317 L with an operating pressure of 900 psia, while the liquid hydrogen tank holds 606 L at an operating pressure of 250 psia [20]. Over 60 PRSA dewars were delivered over the years, 28 by Beech Aircraft and 32 by Ball Aerospace following their acquisition of Beech in 1986.

11.4.1.5 1983: Infrared Astronomical Satellite Helium Dewar

Shown in Figure 11.14, the Infrared Astronomical Satellite (IRAS) was launched in January 1983 with the first use of a superfluid helium dewar in space [21]. The 0.57 m infrared telescope contained 62 detectors and was a joint project of the US, the UK, and the Netherlands. The American team built the telescope, detectors and cooling system, the UK built the satellite ground station and control center, and the Dutch team built the spacecraft, which included the on-board computers and pointing system.

The cryostat, which was filled with 480 L of helium, was built by Ball Aerospace and involved the first space application of the porous plug that was invented at Stanford University in 1970 [13]. The infrared telescope was mounted in the center of the toroidal-shaped main cryogen tank, which was structurally supported through
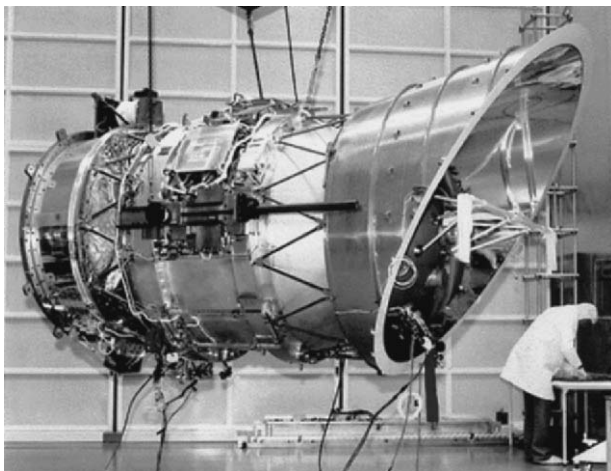
FIGURE 11.14. Launched in January 1983, the Ball Aerospace IRAS dewar was the first superfluid helium dewar in space.

nine fiberglass–epoxy bands that attached to the outer vacuum shell. Additional thermal protection was provided by three vapor-cooled shields and MLI in the dewar's vacuum space. The outer shell operated at 170 K via radiant cooling to reduce further the parasitic heat load into the main cryogen tank.

During its 290-day life, IRAS scanned more than 96% of the sky four times, providing the first high-sensitivity all-sky map at wavelengths of 12, 25, 60 and 100 μm. IRAS increased the number of cataloged astronomical sources by about 70%, detecting about 350,000 infrared sources. Discoveries included a disk of dust grains around the star Vega, six new comets, and very strong infrared emission from interacting galaxies. IRAS also revealed, for the first time, the core of the Milky Way.

11.4.1.6 1985: Atmospheric Trace Molecule Spectroscopy Stirling Cooler

The next mechanical cryocooler to fly was a CTI tactical Stirling cooler (Figure 11.15) that was part of the Atmospheric Trace Molecule Spectroscopy (ATMOS) instrument on the 7-day Spacelab 3 flight in April 1985. The split Stirling coldtip cooled an HgCdTe infrared detector within the ATMOS interferometer built by Honeywell of Lexington, MA. During three more Space Shuttle missions in 1992, 1993, and 1994, the instrument went on to measure solar absorption spectra from over 350 occultations from the upper troposphere to the lower mesosphere [22].

11.4.1.7 1985: Spacelab 2, Superfluid Helium Experiment

The Superfluid Helium Experiment (SFHE) was launched on Spacelab 2 in July 1985 to investigate the properties of superfluid helium in a microgravity environment [23]. An additional accomplishment was the qualification and
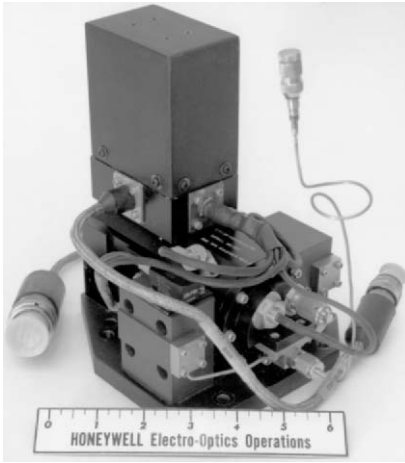
FIGURE 11.15. CTI Stirling cooler flown on the ATMOS instrument in 1985, 1992, and 1994.

characterization of the 120 L space-compatible cryostat developed by Ball Aerospace as a reflyable dewar for liquid helium microgravity experiments such as SFHE. In the future, the same dewar would be used for the Lambda Point Experiment (LPE) and the Confined Helium Experiment (CHeX), in 1992 and 1997 respectively.

11.4.1.8 1985: Spacelab 2, Infrared Telescope

A second superfluid helium dewar on the July 1985 Spacelab 2 mission supported the Infrared Telescope (IRT) experiment. The IRT system was comprised of a 250 L dewar, a helium transfer assembly, and a cryostat surrounding the infrared telescope [24]. By utilizing a vacuum-sealed rotary joint, the telescope could scan in one axis while the dewar remained stationary. A porous-plug phase separator was located in the transfer assembly so that only gas was delivered to the cryostat assembly. The helium in the dewar was maintained at 1.6 K, while temperature requirements for the cryostat varied from 2.5 K at the detectors to 60 K at the upper telescope sections. The dewar and cryostat for the IRT system were manufactured by Cryogenics Associates, while NASA–Marshall Space Flight Center and the University of Alabama were responsible for the helium transfer assembly and subsequent integration.

11.4.2 1975–1985 R&D Emphasis

A major factor in this decade was the DoD initiatives to develop a strategic missile defense system based on satellites using infrared tracking of intercontinental ballistic missiles. Having baselined the use of silicon LWIR detector arrays that required significant 10–12 K cooling, major efforts were expended to bring large long-life 10–12 K cryocoolers into flight readiness [25]. In parallel, the civilian

space agencies in the US and Europe supported the development of long-life cry-ocoolers for higher temperature (60–80 K) Earth-science applications.

11.4.2.1 Large Long-Life Missile Defense Coolers for 10 K

Building on their ongoing space cooler development efforts and their strong need for long-life 10–12 K coolers, the DoD adopted a strategy of multiple parallel cooler development efforts:

11.4.2.1.1 Vuilleumier

The DoD's VM cooler development program started back in the 1960s and led to a first flight cooler in 1971. By the 1980s the effort was focused on the development of the Hughes Aircraft "Hi Cap" machine (Figure 11.16) [5, 25]. Design requirements for this three-stage cooler were 0.3 W at 11.5 K plus 10 W at 33 K and 12 W at 75 K. Long-life operation was required with a maximum input power of 2700 W. The Hughes approach used dry lubricated ball bearings (MoS_2) with a bearing retainer made of Roulon A (filled Teflon) with 5% MoS_2. The machine employed rubbing seals on both the hot and cold displacers and flexure pivots at the displacer drive-rod interfaces. Past problems included metal fatigue, internal contamination, and seal wear. A major renewed effort to improve the reliability of the "Hi Cap" machine was undertaken in the mid-1980s [26]. This effort consisted of extensive testing of existing coolers to evaluate seals, regenerators, and other components.

11.4.2.1.2 10 K Rotary-Reciprocating Refrigerator

The goal for the 1980s two-stage R^3 cooler shown in Figure 11.17 was a cooling capacity of 1.5 W at 12 K plus 40 W at 60 K for an input power of less than 2600 W [27]. This development was an extension of the Air Force's longstanding program developing rotary reciprocating Brayton coolers at A.D. Little dating

FIGURE 11.16. Hughes Aircraft three-stage "Hi Cap" VM cooler.
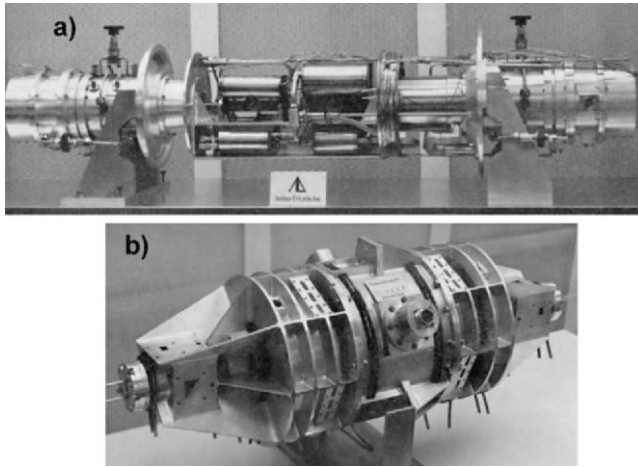
FIGURE 11.17. A.D. Little two-stage R^3: (a) the expander assembly; (b) one of two compressor modules.

from the 1960s [2]. Two of the first-generation machines were shown in Figure 11.9. As with the earlier machines, this cooler also utilized self-actuating, rotary gas bearings in both the compressors and the expanders to eliminate piston contact during the linear motion required to achieve refrigeration. By the mid-1980s the effort had been long and arduous, with a never-ending series of sophisticated problems requiring more advanced development [5].

11.4.2.1.3 10 K Turbo Brayton

Because turbomachinery employing rotary gas bearings offered a high potential for long lifetime, a reverse-Brayton turbo-refrigerator for space was initiated in the early 1970s under DoD sponsorship as an alternative to the ADL R^3 concept. The system goals were cooling loads of 1.5 W at 12 K and 30 W at 60 K, with a 30,000 h lifetime and a maximum power consumption of 4 kW [5]. The program resulted in a design of a four-stage turbo-refrigerator with gas bearings and included some component fabrication and testing. The contractor for the work was General Electric.

The Defense Advanced Research Project Agency (DARPA) initiated a follow-on turbo Brayton program in 1978 with Garrett AiResearch [28]. This system (Figure 11.18) was designed, fabricated and performance tested in the early 1980s. Although, it exhibited satisfactory operation, contamination and other issues prevented performance goals from being fully reached.

11.4.2.1.4 Large Rotary Magnetic Refrigerators

Given the difficulty of regenerative cryocoolers (such as Stirling coolers) achieving high efficiencies below 20 K, work was also initiated in the mid-1980s exploring

FIGURE 11.18. Garrett AiResearch turbo Brayton cooler.

the use of large magnetic coolers to bridge between 10 and 20 K [26,29,30]. The coolers, such as the one in Figure 11.19, targeted the use of a new paramagnetic material, $Gd_3Ga_5O_{12}$ (gadolinium gallium garnet) and higher temperature super-conducting magnet technology. All were rotary designs with a rotational rate of around 6–10 rpm. However, the development efforts faced extreme difficulties, as internal losses and high forces from the magnets made it very difficult to achieve the promised efficiencies [31].

11.4.2.2 Long-Life Stirling Coolers for 60–80 K

Building on the general success of the Philips Laboratories' rhombic-drive Stirling that flew in 1979 and on long-life pressure modulators developed at Oxford University, the Earth-science instrument community initiated development of 60–80 K long-life coolers focused at their higher temperature needs.

FIGURE 11.19. Hughes rotary magnetic cooler for cooling between 10 and 20 K.
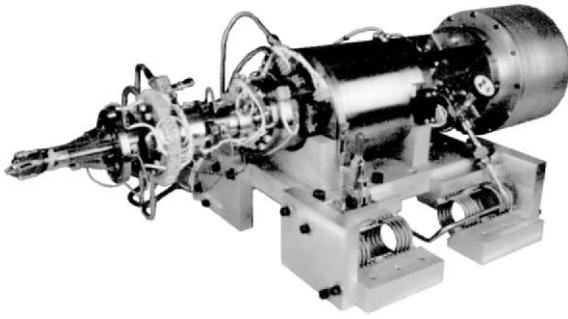
FIGURE 11.20. Magnetic bearing Stirling cooler built for NASA–GSFC by Philips in 1979.

11.4.2.2.1 Philips Magnet Bearing Stirling Cooler

In 1979, NASA–GSFC initiated funding of Philips Laboratories for a next-generation Stirling cooler capable of producing 5 W at 65 K for 180 W of input power and with a lifetime of 3–5 years [5]. The basic design philosophy of the cooler was (1) to have no rubbing surfaces in the machine, (2) to control axial position and piston/displacer phase angles electronically, (3) to utilize a linear drive system, and thus eliminate mechanical linkages, (4) to reduce the potential for internal contamination by eliminating all organics inside the working gas, and (5) to provide an essentially dynamically balanced machine.

Shown in Figure 11.20, an engineering model single-stage device was developed using magnetic bearings and 25 μm clearance seals in the compressor and expander to eliminate all possible wear [32]. Although several hundred hours of operation were achieved, the resulting hardware was large and complex in comparison with the competing technology developed at the same time in England at Oxford University and Rutherford Appleton Laboratory (RAL).

11.4.2.2.2 Flexure Stirling Coolers at Oxford University and Rutherford Appleton Laboratory

In 1980, Oxford University began work on a long-life Stirling cryocooler concept [33] that built on the flexure-bearing linear drive with clearance seals that was used for the pressure modulators that Oxford flew on PMR on Nimbus 6, SAMS on Nimbus 7, and VORTEX on Pioneer Venus [34–36]. The basic design philosophy of the so-called Oxford cooler was essentially the same as that enumerated above for the Philips Stirling. However, the implementation was much simpler, with passive flexure springs providing the piston support, as opposed to complex magnetic bearings. The Oxford cooler, shown in Figure 11.21, was also smaller, with a back-to-back pair targeted at 1.0 W of cooling at 80 K, a mass of 10 kg, and an input power of 80 W [37]. During the early 1980s, in conjunction with RAL, this concept was developed into two slightly different flight coolers: one for use on the ALONG Track Scanning Radiometer (ATSR) instrument on ERS-1, and the other for the Improved Stratospheric and Mesospheric Sounder (ISAMS) instrument on NASA's Upper Atmospheric Research Satellite (UARS) spacecraft [38–40]. A

FIGURE 11.21. Original Oxford Stirling cooler built by Oxford University in the early 1980s.
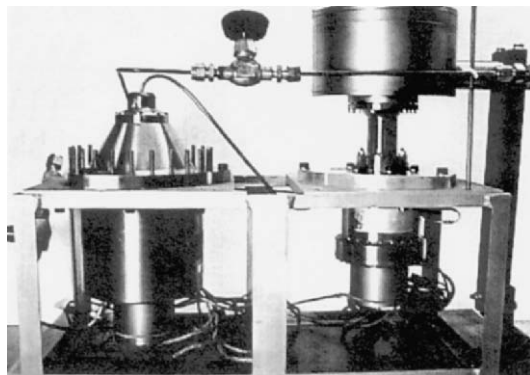
cross-section showing the Oxford cooler internal construction features is shown in Figure 11.22.

11.4.2.3 Long-life Sorption Coolers

Sorption technologies also started receiving modest recognition in the early 1980s as an alternative to the mechanical cooler concepts that were experiencing increasing difficulties in achieving long life. Work at the Jet Propulsion Laboratory (JPL) and Aerojet Corp. of Azusa, CA, centered on both helium–charcoal physical sorption concepts, as shown in Figure 11.23, and on hydride chem-sorption concepts, as shown in Figure 11.24 [41, 42].
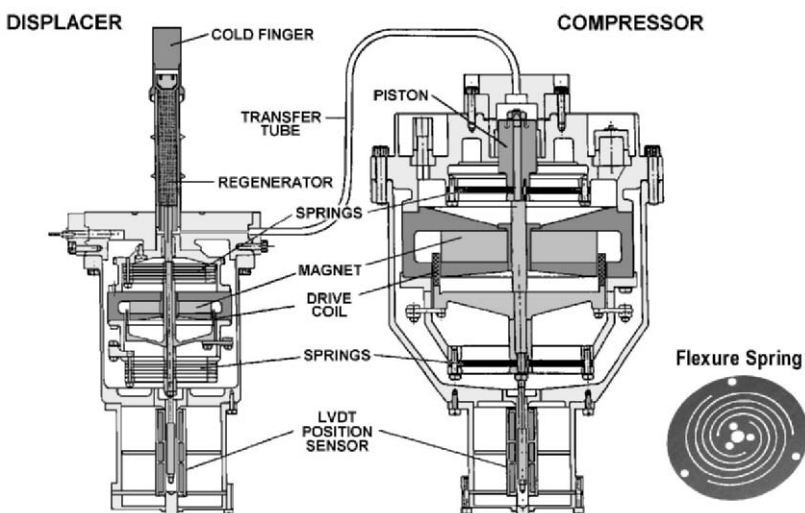
FIGURE 11.22. Cross-section of the Oxford Stirling cooler concept developed for ISAMS.
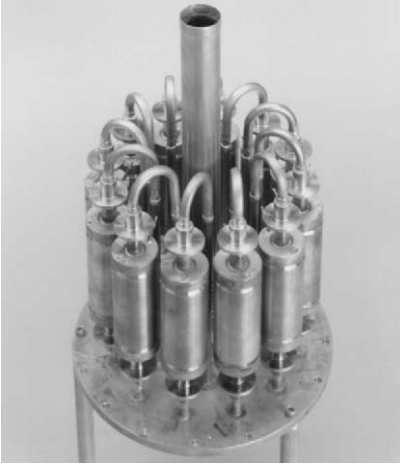
FIGURE 11.23. JPL 20 K charcoal–hydrogen sorption compressor of 1983.

11.4.2.4 Long-Life Cryostats

Cryostat technology had substantially matured by the 1980s, based on the extensive research conducted in the 1970's on MLI and conductive material properties. Based on these advances, new long-life ammonia–methane cryostats were developed by Lockheed and referred to as the Extended Life Cooler or Long-Life Cooler, and the Advanced Long-Life Cooler [6, 43, 44]. These cryostats used solid methane as the primary cryogen, solid ammonia as the secondary, and could use passive radiators as a low-temperature guard for the ammonia. One system had a total

FIGURE 11.24. 1982 JPL breadboard hydride– hydrogen cryocooler (650 mW at 29 K).

weight of around 245 kg and cooling capacities of 1.36 W-year at the 60 K methane temperature and 1.18 W-year at the 145 K ammonia temperature [6].

Another important area of cryostat research was the use of solid hydrogen [6]. In these studies, the fill and vent of a solid hydrogen cooler was demonstrated and detailed safety analyses were performed. As an add-on to this effort, a para-to-ortho hydrogen catalytic converter to greatly improve effluent gas cooling was developed [45].

At this point, solid hydrogen was being proposed as the cooling system for two instruments for the UARS originally scheduled to launch in 1988. The Challenger accident in 1986 would delay the UARS launch and rule out the use of hydrogen dewars on future Shuttle flights. However, a few years later, the solid hydrogen cryostat technology would be flown on the DoD's SPIRIT III mission in 1996.

11.5 1985–1995: Long-Life Cryocoolers Become a Reality

By the late 1980s the aggressive spending on defense technology during the Cold-War period was rapidly subsiding and the focus was beginning to shift toward smaller, more cost-effective approaches to missile defense. By the early 1990s the large DoD programs would be focused toward Brilliant Pebbles and Brilliant Eyes. However, the civilian space program, slower to feel the downsizing, was focused on great observatories like the Hubble Space Telescope (HST) launched in 1990, the Shuttle Infrared Telescope Facility (SIRTF), the Advanced X-ray Astrophysics Facility (AXAF), and the Gamma Ray Observatory (GRO). In this decade, the Earth scientists thoroughly embraced long-life cryocoolers and proposed dozens of instruments, many using cryocoolers, for NASA's huge Earth Observing System (EOS) platforms proposed for their Mission to Planet Earth.

A sobering event at the beginning of this period was the explosion of the Challenger Shuttle in 1986. This led to a careful reexamination of mission safety and put a halt to the possibility of liquid-fueled rockets being carried aloft in the Shuttle for use in missions beyond low-Earth orbit. A return to a greater reliance on unmanned launch vehicles was the trend of the future.

11.5.1 1985–1995: Cryogenic Missions

11.5.1.1 1989: Cosmic Background Explorer

The COBE mission launched in November 1989 using a dewar (Figure 11.25) that was based on the IRAS dewar with some small modifications [46]. COBE's objective was to map the infrared and microwave characteristics of the cosmic background radiation, i.e. the remains of the extreme heat that was created by the Big Bang. A team of American scientists announced, on April 23, 1992, that they had found the primordial "seeds" (CMB anisotropy) in data from COBE. The announcement was reported worldwide as a fundamental scientific discovery and ran on the front page of the New York Times.

FIGURE 11.25. Ball Aerospace superfluid helium dewar used for COBE was derived from the IRAS dewar flown in 1983.

11.5.1.2 1991: Upper Atmospheric Research Satellite Cryogenic Limb Array Etalon Spectrometer Instrument

NASA's UARS was launched in September 1991 with the Cryogenic Limb Array Etalon Spectrometer (CLAES) instrument that, before the Challenger accident, was scheduled to be cooled by a Lockheed cryostat with 944 L (78 kg) of solid hydrogen [5]. After Challenger, the solid hydrogen cryostat was changed into a 15 K solid neon–carbon dioxide cryostat (Figure 11.26) that weighed 1035 kg, with 152 L (436 kg) of solid neon and 326 L (220 kg) of solid carbon dioxide [47,48]. Part of NASA's Earth-sciences program, CLAES measured temperature profiles and concentrations of ozone, methane, water vapor, nitrogen oxides, and other important species, including chlorofluorocarbons, in the stratosphere using measurements of limb emission spectra in the 3.5 to 12 μm infrared wavelength range. These measurements were analyzed to understand better the photochemical, radiative, and dynamical processes taking place in the ozone layer. The dewar operated for 19 months in orbit, exceeding its 18 month design life.

FIGURE 11.26. Two-stage solid neon–carbon dioxide dewar built by Lockheed for the CLAES instrument launched in 1991 on UARS.
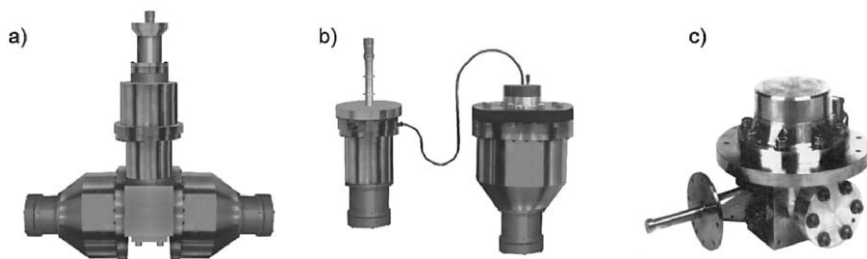
FIGURE 11.27. Space Stirling cryocoolers developed in the late 1980s: (a) RAL 80 K integral "Oxford" cooler flown on ATSR-1 and ATSR-2; (b) Oxford University 80 K ISAMS cooler flown on UARS; (c) Fujitsu 80 K Stirling cooler flown on JERS-1.

11.5.1.3 1991: The First Oxford-Style Coolers Reach Space

In July 1991 the Europeans launched their Earth Resources Satellite (ERS-1) with the ATSR-1 instrument that was cooled to 80 K via the RAL version (Figure 11.27a) of the Oxford flexure-bearing Stirling cooler [40]. Two months later, in September, the Oxford University version of the 80 K Stirling cooler (Figure 11.27b) was launched as part of their ISAMS instrument on NASA's UARS [38,39]. The success of these first long-life flexure-bearing Stirling coolers with clearance-type piston seals would lead to a dramatic change in the cryocooler world.

11.5.1.4 1992: First Japanese Stirling in Space

In February 1992, the Japanese company Fujitsu launched their first space Stirling cooler on the Japanese Earth Resources Satellite (JERS-1). Used to cool the Short-wave Infrared Radiometer, the cooler had a cooling capacity of 1 W at 80 K and was used to support 4000 short-period intermittent operations over a 2 year mission in space. The cryocooler design (Figure 11.27c) used an integral construction with rotary crank and had a measured mean lifetime of 3500 h [49].

11.5.1.5 1992: Lambda Point Experiment

The LPE was a Shuttle payload dedicated to the study of the properties of superfluid helium in zero gravity. LPE flew on STS-52 as part of the US Microgravity Payload (USMP-1) in October 1992 and used the same dewar as used by SFHE in 1985 [50].

11.5.1.6 1993: HTTSE I

The first High Temperature Superconductivity Space Experiment (HTSSE I) was designed as a technology demonstration experiment to validate HTS components in a space-based system. It was developed by the US Naval Research Laboratory (NRL) and launched in 1993 using a British Aerospace 80 K cryocooler to cool its

payload of superconducting devices. Unfortunately, the mission was lost before on-orbit startup when the host spacecraft failed [51].

11.5.1.7 1993: SHOOT

The Superfluid Helium On-Orbit Transfer (SHOOT) experiment successfully flew on STS-57 in 1993 and demonstrated using the fountain effect as the basis of a thermal mechanical pump for transferring superfluid helium between two tanks in a microgravity environment [52].

11.5.1.8 1994: Clementine

Launched in January 1994, the Clementine spacecraft was built by the US NRL as a joint DoD–NASA technology demonstration flight focused at gathering data on the Moon and the near-Earth asteroid Geographos. Its sensor payload included a near-infrared camera cooled to 70 K and an LWIR camera cooled to 65 K. Both were cooled by small Ricor K506B tactical cryocoolers [53].

11.5.1.9 1994: STRV-1b

Launched in June 1994, the STRV-1b spacecraft was developed by the Defence Evaluation Research Agency (DERA) of the UK Ministry of Defence as a small space technology test bed. The spacecraft carried a JPL-built cryocooler vibration-suppression experiment that demonstrated three-axis closed-loop control of the coldtip motion of a small 0.2 W at 80 K TI tactical Stirling cooler [54]. The cooler achieved over 3000 operational cycles, and was still functional when the mission was terminated after 4.5 years.

11.5.1.10 1995: ATSR-2

Launched on board the European Research Satellite (ERS-2) in April 1995, the second Along Track Scanning Radiometer (ATSR-2) was a follow-on instrument to ATSR-1, which was launched in 1991 to conduct sea-surface temperature measurements with the accuracy required for climate research [55]. ATSR-2 used the flight spare of the RAL-built Oxford-style Stirling cryocooler that flew on ATSR-1 in 1991 (Figure 11.27a).

11.5.1.11 1995: Cryo System Experiment

The Cryo System Experiment (CSE) was launched on STS-77 in February 1995 as part of NASA's InSpace Technology Experiments Program (IN-STEP). CSE demonstrated the successful operation in space of a Hughes 2 W at 60 K Standard Space Cryocooler (SSC) Stirling cooler and an experimental diode oxygen heat pipe also made by Hughes [56]. Such a heat pipe provides a means of conducting heat from a remote cryogenic load and thermally disconnecting the load when the cooler is off.

FIGURE 11.28. Japanese IRTS launched in 1995.
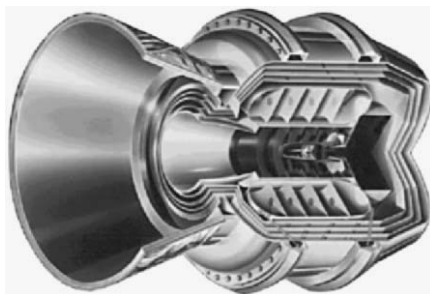
11.5.1.12 1995: Infrared Telescope in Space

The Infrared Telescope in Space (IRTS) was the first Japanese orbiting telescope dedicated to infrared astronomy. The 0.15 m telescope, shown in Figure 11.28, was cooled to 1.8 K in a superfluid helium cryostat. It was launched aboard a Japanese multipurpose space platform Space Flyer Unit spacecraft in March 1995 [57, 58] and surveyed approximately 7% of the sky with a relatively wide beam during its 28-day mission.

11.5.1.13 1995: European Space Agency's Infrared Space Observatory

Shown in Figure 11.29, the ESA's ISO was launched in November 1995 and operated for 2.5 years. At the time it was the most sensitive infrared satellite ever launched, 1000 times more sensitive than IRAS, and observed over a wide range of infrared wavelengths (2.5 to 240 μm). The 0.6 m diameter cryogenic telescope was mounted within a large dewar containing 2200 L of superfluid helium. The telescope held four instruments: an infrared camera, a photometer and two spectrometers working in different wavelength ranges. The instruments made use of different photoconductors based on InSb, Si and Ge that operated between 1.8 and 10 K [59].
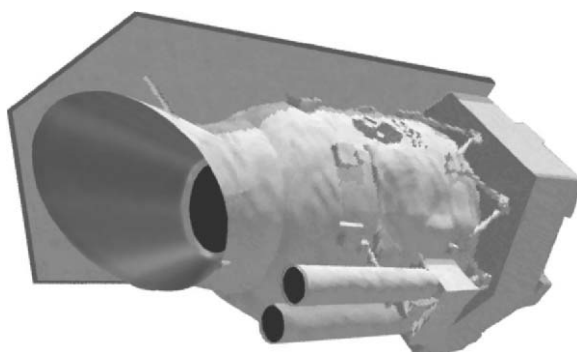
FIGURE 11.29. The European Space Agency's (ESA's) Infrared Space Observatory (ISO) launched in 1995.

11.5.2 1985–1995 R&D Emphasis

During this decade, the aggressive spending on missile-defense cryocooler technology made a major shift toward smaller more cost-effective approaches. By 1992 the large DoD programs on the VM, 12 K Braytons, and 10–20 K magnetic refrigerators all ended, and none were ever used in space. Instead, the focus shifted toward smaller, higher temperature (50–80 K) cryocoolers that were also in demand by the civilian space community to support their desire for increasingly sophisticated Earth-science instruments. As part of its Mission to Planet Earth, the civilian space program was planning an extensive EOS involving up to nine space platforms, each involving several large instruments (many with cryocoolers). At one point it was estimated that as many as 75 cryocoolers could be needed to support the full suite of nine EOS platforms. Cryostats, at this point, were considered fairly mature technology, and what little development was carried out was focused on specific missions like CLAES and ISO, which were building flight hardware.

11.5.2.1 Long-Life 60–80 K Stirling Coolers

Building on the success of the Oxford linear flexure-bearing Stirling coolers shown in Figures 11.22 and 11.27, a number of development contracts were awarded to expand this technology to the larger 2 W at 60–80 K heat loads estimated for the new DoD and NASA EOS applications. The Air Force, through their SSC initiative [60], and NASA through the JPL Atmospheric Infrared Sounder (AIRS) [61] and GSFC development [62] efforts, funded new cooler designs at Hughes, Lockheed/Lucas, British Aerospace, and Ball Aerospace. The coolers, shown in Figure 11.30, all

a) BAe 50-80K   b) Hughes SSC 2W 60K   c) Ball 2W 60K

d) Lockheed 1710   e) Lockheed SCRS   f) TRW mini Stirling
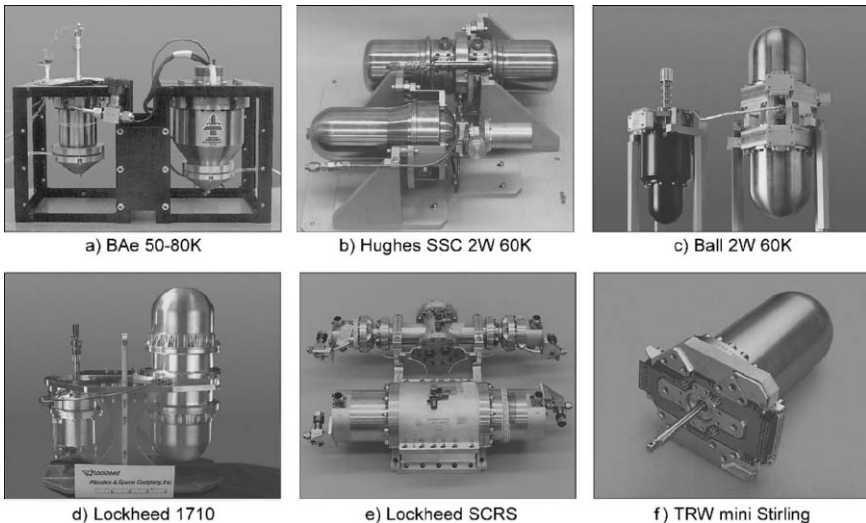
FIGURE 11.30. Oxford-heritage Stirling cryocooler developments in the 1985–1995 time frame.

FIGURE 11.31. Creare 65 K diaphragm Stirling cooler.
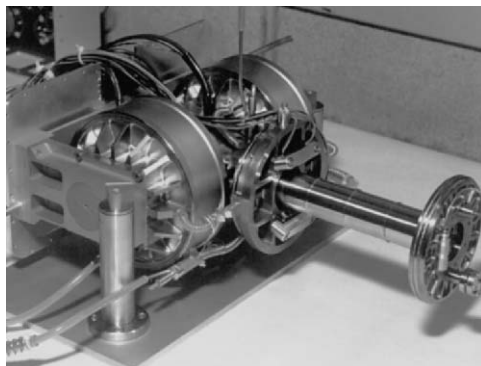
used variants of the Oxford flexure-spring supported linear drive with clearance seals. In Japan, Fujitsu and Mitsubishi also developed their versions of the Oxford cooler for the Advanced Spaceborne Thermal Emission and Reflection Radiometer (ASTER) instrument [63]. For smaller applications, TRW developed a miniature 1.4 kg Oxford-style Stirling cooler (Figure 11.30f) capable of 0.25 W at 65 K [64]. As an alternative to the Oxford design, the Air Force funded work on a diaphragm Stirling [65] at Creare (Figure 11.31) and work on a diaphragm compressor at Mechanical Technology, Inc. [60].

11.5.2.2 4 K Hybrid Oxford Stirling/Joule–Thomson at Rutherford Appleton Laboratory

In the late 1980s, the RAL in England began work on a two-stage Oxford-style Stirling cooler [66] for cooling in the 20–50 K range, and then mated it with a 4 K J–T bottom stage based on a two-stage Oxford-style compressor that used reed valves to achieve the required 9:1 compression-ratio DC gas flow [67]. Shown in Figure 11.32, the resulting 10 mW at 4 K cooler was targeted at the needs of
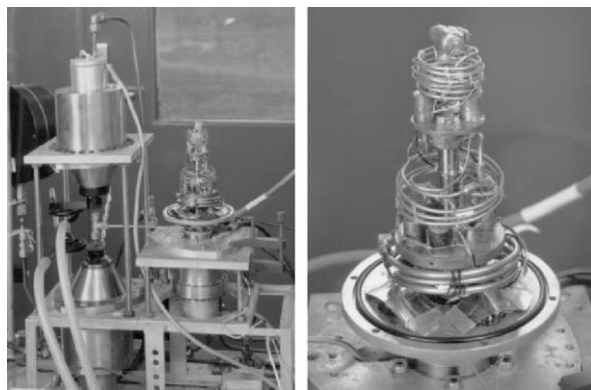
FIGURE 11.32. RAL 4 K brassboard cooler.

a) TRW mini pulse tube   b) TRW 1W 35K pulse tube   c) TRW 3503 and 6020 pulse tubes
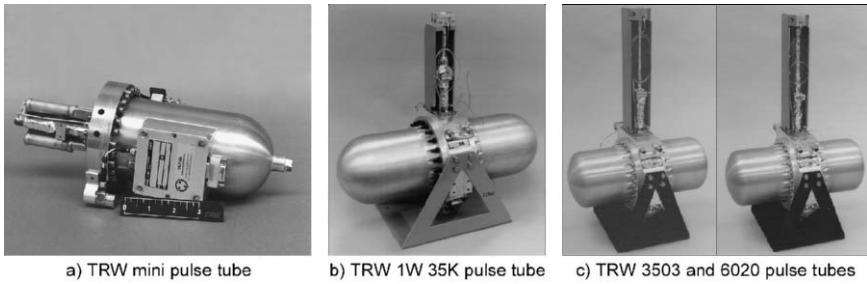
FIGURE 11.33. TRW pulse-tube cryocoolers using Oxford-heritage linear compressors.

future ESA space-science missions, such as the Far Infrared and Submillimetre Telescope (FIRST), Herschel, and Planck. Although the Russians flew a hybrid 4 K J–T/Stirling in 1981 [68], the unique aspect of the RAL design was the expected long life derived from using Oxford-style flexure-springs and clearance seals in both the J–T and Stirling compressors. This cooler served as the inspiration for future hybrid J–T/Stirling and pulse-tube coolers developed by Ball Aerospace and Northrop Grumman Space Technology (NGST) many years later for the NASA 6 K Advanced Cryocooler Technology Development Program (ACTDP) [69].

11.5.2.3 Long-Life Pulse Tubes at TRW

Under Air Force sponsorship, TRW (now NGST) began work around 1989 to mate emerging pulse-tube expander technology to Oxford-style linear compressors. In 1992 they developed a mini-pulse-tube cooler [70] capable of 0.3 W at 73 K (Figure 11.33a), and in 1993 achieved the first really high-efficiency pulse-tube cooler with the introduction of an inertance tube into their 20 cm^3 1 W at 35 K cryocooler [71] (Figure 11.33b). This and follow-on high-efficiency pulse-tube coolers such as the 3503 and 6020 [72,73] (Figure 11.33c) awakened the world to the merits of pulse-tube coolers and led to a whole series of follow-on cooler designs that were flown in space over the next several years. Other work at TRW in the early 1990s examined multistage pulse tubes for use at temperatures as low as 10 K.

11.5.2.4 Long-Life Brayton Coolers

Although all the large 10 K Brayton cooler development work at Garrett AiResearch and A.D. Little was stopped in 1991, interest continued in a smaller, single-stage version of a turbo-Brayton cooler for providing around 5 W at 65 K. Starting with a series of Small Business Innovative Research contracts for component development, Creare, Inc. of Hanover, NH, developed and delivered a complete Engineering Model cooler (Figure 11.34) in the 1993 time frame under contract with NASA–GSFC and the Air Force [74, 75]. An upgraded version of this cooler eventually flew as the Near-Infrared Camera and Multiple-Object Spectrometer (NICMOS) cooler on the HST in 2002 [76].

FIGURE 11.34. Creare 5 W at 65 K Turbo Brayton cryocooler.
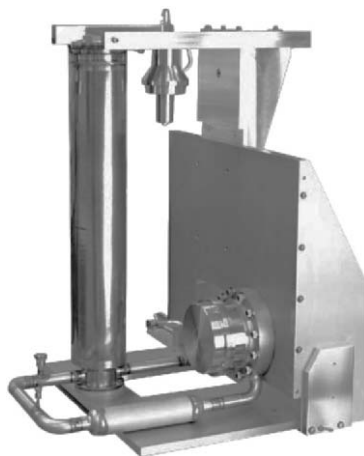
11.5.2.5 Long-Life Sorption Coolers

Sorption cooler technologies received increasing interest during the 1985–1995 time frame for two applications: periodic 10 K cooling for missile defense, and for zero-vibration cooling for precision telescopes, such as the HST; the HST was launched in 1990 without an infrared imaging capability.

11.5.2.5.1 Praseodymium Cerium Oxide O_2 Sorption Cooler for the Hubble Imaging Michelson Spectrometer

Within NASA–JPL, development work was carried out on a two-stage sorption cooler for the Hubble Imaging Michelson Spectrometer (HIMS) instrument that was proposed as an infrared replacement instrument for the HST. The cooler utilized an oxygen J–T to provide vibration-free cooling at 70 K based on a praseodymium cerium oxide (PCO) chem-sorbent compressor, teamed with a krypton–charcoal third stage at 140 K and thermoelectric cooler upper stages at 200 and 225 K [77]. Work continued through life testing of the brassboard unit shown in Figure 11.35, but was stopped when the competing NICMOS instrument, which used a solid nitrogen dewar, was selected for the HST.

11.5.2.5.2 10 K Hydride Sorption Cooler for the Department of Defense

In a combined program, JPL and Aerojet developed a hydride sorption cooler for periodic cooling to 10 K for the Strategic Defense Initiative Organization (SDIO) Brilliant Eyes mission. Following a successful breadboard test in 1991 [61], the Brilliant Eyes Ten-Kelvin Sorption Cryocooler Experiment (BETSCE) cooler, shown in Figure 11.36, was developed and flown on STS-77 as an in-space cryocooler demonstration in 1996 [78].
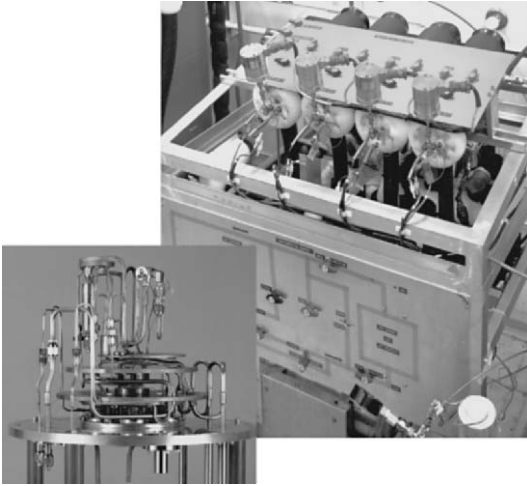
FIGURE 11.35. JPL's 70 K HIMS PCO–O_2 life-test sorption cooler.

11.5.2.5.3 Regenerative Sorption Concepts

Prior to the work on PCO and hydride compressors, a variety of regenerative physical-sorption compressors were studied and tested at JPL and Aerojet using methane (65 K) and krypton (140 K) together with charcoal as the sorbent material. Despite the use of regeneration, the low efficiency of the physical sorption process eventually led to these technologies being passed over [79].
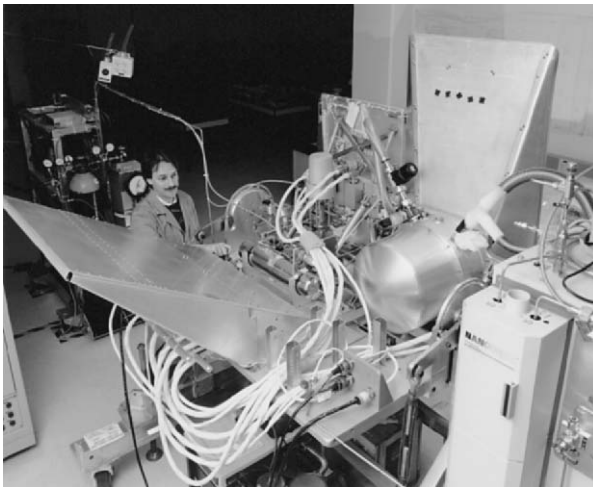
FIGURE 11.36. JPL's 10 K BETSCE solid hydrogen sorption cooler flown on STS-77 in 1996.

TABLE 11.2. Recent space cryocooler flight operating experience as of December 2005

Cooler / Mission	Running Hours	Comments	
Ball Aerospace 60K Stirling (HIRDLS)	12,000	Turnon: 8/04; ongoing no degrad.	
Creare Turbo Brayton (NICMOS)	34,000	Turnon: 3/02; ongoing no degrad.	
Fujitsu and Mitsubishi Stirling			
ASTER (2 units)	51,000	Turnon: 3/00; ongoing no degrad.	
NGST (TRW) Cryocoolers			
CX (Mini PT (2 units))	69,000	Turnon: 2/98; ongoing no degrad.	
HTSSE-2 (80K mini Stirling)	24,000	3/99 thru 3/02, miss'n end, no degr.	
MTI (6020 10cc PT)	51,000	Turnon: 3/00; ongoing no degrad.	
Hyperion (Mini PT)	44,000	Turnon: 12/00; ongoing no degrad.	
SABER (Mini PT)	35,000	Turnon: 1/02; ongoing no degrad.	
AIRS (10cc PT (2 units))	31,000	Turnon: 6/02; ongoing no degrad.	
TES (10cc PT (2 units))	12,000	Turnon: 8/04; ongoing no degrad.	
JAMI (6cc HEC PT)	6,000	Turnon: 4/05; ongoing no degrad.	
Oxford/BAe/MMS/Astrium Stirling			
ISAMS (80 K Oxford)	15,800	Turnon:10/91; instrument failed 7/92†	
HTSSE-2 (80K BAe)	24,000	3/99 thru 3/02, miss'n end, no degr.	
MOPITT (50-80K BAe (2 units))	47,000	Turnon: 3/00; one displacer failed at 10,300 hours; other still running†	
ODIN (50-80K Astrium (2))	42,000	Turnon: 3/01; ongoing no degrad.	
AATSR (50-80K Astrium (2))	33,000	Turnon: 4/02; ongoing no degrad.	
MIPAS (50-80K Astrium (2))	23,000	Turnon: 4/02; ongoing† no degrad.	
INTEGRAL (50-80K Astrium (4))	28,000	Turnon: 11/02; ongoing no degrad.	
Rutherford Appleton Laboratory			
ATSR 1 (80K Integral Stirling)	44,000	7/91 thru 6/96, mission end, no degr.	
ATSR 2 (80K Integral Stirling)	93,000	Turnon: 5/95; ongoing no degrad.	
Sunpower RHESSI Stirling	34,000	Turnon: 2/02; ongoing no degrad.	

† Cooler operating hours less than calendar hours due to instrument downtime

11.6 1995–2005: Long-Life Cryocoolers and Large Cryostats Become Mature Space Technologies

By the late 1990s, 5-year-life space cryocoolers built on the Oxford-cooler compressor concept were considered a reality, and pulse-tube cryocoolers became a focus of cryogenic research worldwide. Starting in December 1999, the three large NASA EOS platforms (Terra, Aqua and Aura) were launched, as was the large European Environmental Satellite (Envisat) platform. Together, they included over 10 long-life cryocoolers in seven separate instruments. As shown in Table 11.2, by 2005 over 25 Oxford-style coolers were in orbit on multiyear missions—the majority were Stirling, but nine were pulse tubes. Also, a first turbo-Brayton cooler was launched for a vibration-sensitive application on the HST.

Complementing the excellent progress of long-life cryocoolers at temperatures above 20 K, dewars provided the foundation for low-temperature missions requiring temperatures of 10 K and below during this time frame. Cryostats were also used in missions like the HST that require near-zero vibration. However, the cryostats, unlike the cryocoolers, suffered a mixed history of reliability, with over a third of the civilian cryostat missions suffering critical mishaps.

During this decade, cooler research and development was generally associated with building and qualifying the many coolers that were used in the missions. Thus, the majority of the funding for cooler research transferred away from pure R&D budgets, and was carried as part of flight-project funding for the specific space missions. This was largely true for both the civilian space-cooler development efforts and the military efforts [80].

11.6.1 1995–2005 Flight Applications

11.6.1.1 Long-Life Cryocoolers for 50–80 K

Building on the success of the Oxford flexure-bearing linear-drive Stirling that first flew in 1991 and the high-efficiency pulse-tube coolers demonstrated at TRW in 1993, a large number of 50–80 K cryocooler missions were flown between 1998 and 2005. Nearly all of the coolers achieved multiyear lives in space, as noted in Table 11.2.

11.6.1.1.1 1997: Lewis

The first two pulse-tube cryocoolers launched into space were on this NASA spacecraft that failed prior to turn-on of the payloads. The spacecraft contained a TRW mini pulse-tube cooler (shown earlier in Figure 11.33a) for TRW's HSI hyperspectral imager and a second TRW mini pulse-tube cooler for the NASA Goddard LEISA instrument.

11.6.1.1.2 1998: CX

Launched in January 1998, this Sandia-developed DoD payload was cooled by a pair of the same TRW mini pulse-tube cryocoolers (Figure 11.33a) that were used on the above Lewis mission. These were the first pulse-tube cryocoolers to operate in space [81].

11.6.1.1.3 1999: HTSSE II

The High Temperature Superconductivity Space Experiment (HTSSE II) was launched on the US Air Force's Advanced Research and Global Observation Satellite (ARGOS) in February 1999 as a second technology demonstrator to validate high-temperature superconductor (HTS) components in space-based systems. The experiment, managed by the US NRL, used a British Aerospace 80 K cryocooler (Figure 11.37) to cool a number of HTS-based devices in the main experiment, and included a second experiment cooled by a TRW mini Stirling cooler (see Figure 11.30f) [82].

11.6.1.1.4 1999: MOPITT

The Measurements Of Pollution In The Troposphere (MOPITT) instrument was launched on NASA's EOS Terra space platform in December 1999. It contains a pair of back-to-back British Aerospace 50–80 K cryocoolers (see Figure 11.30a)

FIGURE 11.37. BAe 80 K Stirling cooler.

that cool two separate sensors to 80 K [83]. Although one displacer failed after 11,000 h of operation, the compressors and second displacer remain running, as indicated in Table 11.2.

11.6.1.1.5 1999: Advanced Spaceborne Thermal Emission and Reflection Radiometer

The ASTER instrument was also launched on NASA's EOS Terra space platform in December 1999. It contains a pair of sensors each cooled by a Japanese 80 K Oxford-style Stirling cooler; one cryocooler was made by Fujitsu and the other was made by Mitsubishi [84].

11.6.1.1.6 2000: Multi-Spectral Thermal Imager

Launched in March 2000, the Sandia developed Multi-Spectral Thermal Imager (MTI) instrument is cooled by a 2 W at 60 K TRW pulse-tube cryocooler, referred to as the TRW 6020 (shown in Figure 11.33c) [85].

11.6.1.1.7 2000: STRV-2

The Space Technology Research Vehicle (STRV-2) was launched in June 2000 as the primary payload of the USAF TSX-5 spacecraft. The instrument was designed to detect aircraft from space and to collect imagery enabling the characterization of various infrared background types. The instrument's infrared focal plane was cooled to 80 K using an off-the-shelf DRS 1 W at 80 K Stirling cycle tactical cryocooler (Figure 11.38). The instrument also incorporated the test of a novel six degrees of freedom active vibration isolation and suppression system that could be used to isolate a precision payload from spacecraft-borne disturbances [86].

11.6.1.1.8 2000: Hyperion

Launched on NASA's New Millennium EO-1 spacecraft in November 2000, the Hyperion instrument was a technology demonstrator to support evaluation of
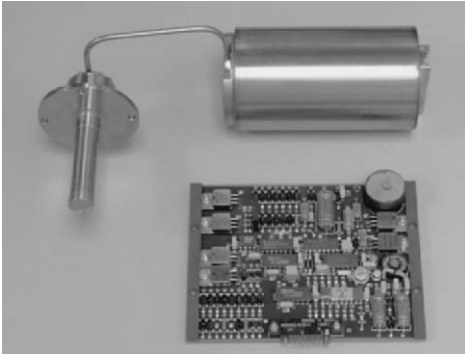
FIGURE 11.38. DRS 1 W at 80 K tactical cooler.

hyperspectral technology for future Earth observing missions. It has a single telescope and two spectrometers, one of which covers from 0.9 to 2.5 μm and is cooled to 110 K by a TRW mini pulse-tube cryocooler (shown in Figure 11.33a) [81, 87].

11.6.1.1.9 2001: Odin

Launched in February 2001, Sweden's 250 kg science satellite, Odin, carries both radiometers and spectrometers for investigations of celestial objects as well as the Earth's atmosphere. Its submillimeter radiometer consists of four submillimeter channels and a 1 mm wave channel. The mixers and intermediate frequency amplifiers are inside a cryostat and are cooled to approximately 130 K by a British Aerospace 80 K Stirling cooler (Figure 11.37) [88].

11.6.1.1.10 2001: SABER

Launched in December 2001 on the TIMED spacecraft, SABER uses a 10-channel infrared radiometer operating from 1.27 to 17 μm to investigate the relative importance of radiative, chemical, and dynamical sources and sinks of energy in Earth's atmosphere. Its focal plane is cooled to 75 K by a TRW mini pulse-tube cryocooler (Figure 11.33a).

11.6.1.1.11 2002: Ramaty High-Energy Solar Spectroscopic Imager

Launched in February 2002, the Ramaty High-Energy Solar Spectroscopic Imager (RHESSI) uses an array of nine large germanium gamma-ray detectors to observe solar flares from 3 keV to 25 GeV [89]. The detector array is cooled to 75 K by a Sunpower M77B Stirling cooler (Figure 11.39) operating at 65 K. This mission represents the first application of a low-cost commercial cooler to achieve multiyear operation in space [90]. Additionally, the cooler uses a heat intercept strap clamped to the Stirling coldfinger to provide simultaneous cooling to the instrument's higher temperature radiation shields at 155 K.

FIGURE 11.39. Sunpower M77B Stirling cooler flown on RHESSI in 2002.

11.6.1.1.12 2002: Near-Infrared Camera and Multiple-Object Spectrometer Turbo-Brayton Cryocooler

After the damaged solid-nitrogen dewar of the NICMOS instrument ran out of cryogen in January 1999, there was interest in restoring the instrument to life using a cryocooler. The 5 W at 65 K turbo-Brayton cooler developed by Creare in the early 1990s was the only cooler candidate with the cooling power and near-zero vibration required for use on the HST. By adding a turbine-pumped fluid loop to the turbo-Brayton cooler (Figure 11.40), a system was devised to cool the instrument to 77 K via its cooling coils originally used to freeze the cryogen in the dewar [76]. Astronauts installed the cooler, fluid loops, and a capillary-pumped-loop heat rejection system in February 2002. Prior to installation on the HST, the cooler was flown in 1998 on STS-95 as part of the Hubble Orbital Systems Test. The cooler retrofit was a resounding success, and NICMOS is now expected to continue to operate throughout the remainder of the HST's life [91].

11.6.1.1.13 2002: Advanced Along Track Scanning Radiometer

The Advanced Along Track Scanning Radiometer (AATSR) instrument continues the ATSR-1 and ATSR-2 observations of precise sea-surface temperature providing a 10-year near-continuous data set at the levels of accuracy required for climate research. Launched in March 2002 on the ESA Envisat spacecraft, AATSR is an imaging radiometer, sensing at thermal infrared, reflected infrared, and visible wavelengths. The focal plane for the thermal infrared wavelength region is cooled
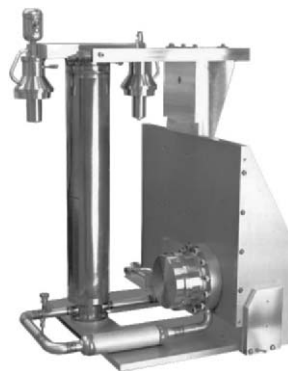
FIGURE 11.40. Creare NICMOS turbo-Brayton cryocooler flown on the HST in 2002.
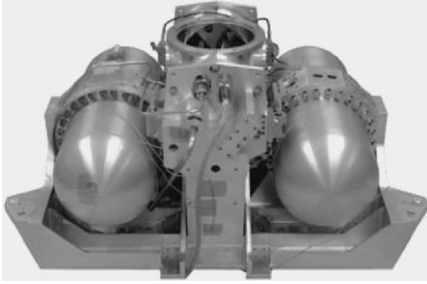
FIGURE 11.41. TRW 1.5 W at 55 K pulse tube coolers flown on AIRS in 2002.

to about 80 K by a pair of Astrium 50–80 K cryocoolers similar to those shown in Figure 11.30a [92].

11.6.1.1.14 2002: Michelson Interferometer for Passive Atmosphere Sounding

The Michelson Interferometer for Passive Atmosphere Sounding is a Fourier transform spectrometer for the measurement of high-resolution gaseous emission spectra at the Earth's limb. Launched in March 2002 on the European Envisat spacecraft, it operates in the near- to mid-infrared, where many trace gases that play a major role in atmospheric chemistry have important emission features. The infrared focal planes are cooled to 70 K by a back-to-back pair of Astrium 50–80 K cryocoolers [93].

11.6.1.1.15 2002: Atmospheric Infrared Sounder

JPL's AIRS instrument was launched on NASA's EOS Aqua space platform in May 2002 [94–96] to make precision global measurements of Earth's air temperature. It contains a redundant pair of TRW 1.5 W at 55 K pulse-tube cryocoolers (Figure 11.41) and was designed and built under JPL contract by Lockheed Martin Infrared Imaging Systems, Inc. (LMIRIS) of Lexington, MA (now BAE Systems IR Imaging Systems). AIRS was the first flight instrument to commit to a pulse-tube cryocooler, and in so doing it ushered this important new technology into space cryogenics.

11.6.1.1.16 2002: International Gamma-Ray Astrophysics Laboratory

The International Gamma-Ray Astrophysics Laboratory (INTEGRAL) is a medium-sized ESA science mission launched in October 2002 and dedicated to gamma-ray spectroscopy and imaging between 15 keV and 10 MeV. The gamma-ray spectrometer on the spacecraft uses a 30 kg array of germanium detectors maintained at 85 K by the suite of four Astrium 50–80 K Stirling cryocoolers shown in Figure 11.42 [97].

11.6.1.1.17 2004: Visible and Infrared Thermal Imaging Spectrometer

Launched on board the ESA's Rosetta spacecraft in March 2004, the Visible and Infrared Thermal Imaging Spectrometer (VIRTIS) instrument [98] contains two

FIGURE 11.42. Suite of four Astrium 50–80 K coolers used to cool the INTEGRAL instrument.
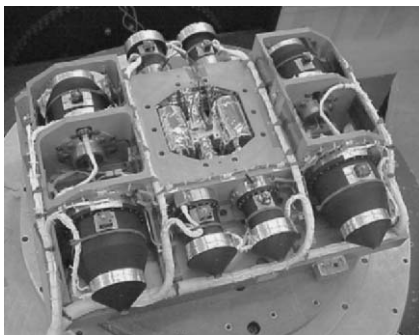
infrared spectrometers, each cooled to around 70 K by a miniature Ricor K508 tactical Stirling cryocooler (Figure 11.43). Rosetta is the first mission designed both to orbit and to land on a comet; its target is a rendezvous with the comet Churyumov–Gerasimenko in 2014.

11.6.1.1.18 2004: Tropospheric Emission Spectrometer

JPL's Tropospheric Emission Spectrometer (TES) instrument was launched on NASA's EOS Aura space platform in July 2004 to measure the chemical processes in the Earth's troposphere. It uses two identical TRW pulse-tube coolers (Figure 11.44) to cool two separate infrared focal planes to 62 K [99]. The coolers are a variant of the TRW 1.5 W at 55 K AIRS pulse-tube cooler, but with the pulse tube hard mounted to the compressor [100].

11.6.1.1.19 2004: High Resolution Dynamics Limb Sounder

The High Resolution Dynamics Limb Sounder (HIRDLS) instrument is an international joint development between the USA and UK and was launched on NASA's EOS Aura spacecraft in July 2004. Though, during launch, the instrument suffered an optical blockage that has severely restricted the acquisition of science data, its infrared detectors continue to be cooled to 65 K by an integral back-to-back Ball

FIGURE 11.43. Tiny Ricor K508 tactical cooler flown on VIRTIS in 2004.
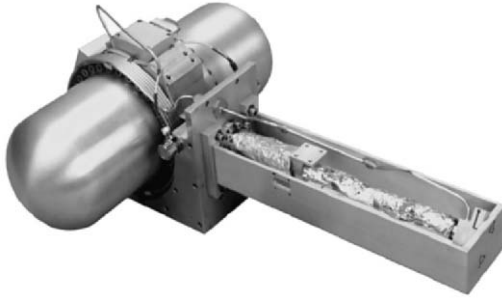
FIGURE 11.44. TRW 1.5 W at 55 K pulse-tube cooler flown on TES in 2004.

Aerospace Oxford-style Stirling cooler with single dynamically balanced displacer (Figure 11.45) [101].

11.6.1.1.20 2004: Messenger

NASA's first trip to Mercury in 30 years was launched in August 2004 with a small Ricor K508 (see Figure 11.43) tactical cryocooler that will cool a germanium gamma-ray detector to 90 K to conduct a study of gamma-ray emissions from the Mercurian crust, as well as solar winds and cosmic rays, as it flies by the planet in 2008 and 2009, and eventually orbits around Mercury in 2011.

11.6.1.1.21 2005: Japanese Advanced Meteorological Imager

The Japanese Advanced Meteorological Imager (JAMI) instrument was launched on the Japanese MTSAT spacecraft in March 2005 and was developed by Raytheon Santa Barbara Remote Sensing under contract to Space Systems/Loral. The overall objective of the mission is to provide meteorological data for operational weather needs for Japan, East Asia, and Australia. The instrument focal plane views the 0.55 to 12.5 μm spectral region and is cooled to 67 K using two TRW HEC pulse-tube coolers (Figure 11.46) [102].

FIGURE   11.45. Ball   Aerospace HIRDLS cryocooler.

FIGURE 11.46. TRW HEC pulse-tube cooler flown on JAMI in 2005.

11.6.1.1.22 2005: Compact Reconnaissance Imaging Spectrometer for Mars

Launched on NASA's Mars Reconnaissance Orbiter spacecraft in August 2005, the Compact Reconnaissance Imaging Spectrometer for Mars (CRISM) instrument uses a set of three parallel Ricor K508 tactical cryocoolers, similar to the one shown in Figure 11.43, to cool the instrument's 105 K focal plane; operation of the coolers will occur upon arrival at the planet in 2006. To provide for switching between the three cryocoolers, each cryocooler is connected to the focal plane using a methane diode heat pipe.

11.6.1.2 Cryostat Missions

Complementing the excellent progress of long-life cryocoolers at temperatures above 20 K, dewars provided the foundation for low-temperature missions requiring temperatures of 10 K and below during this time frame. Cryostats were also used in missions like the HST, which require near-zero vibration. Table 11.3 summarizes the key flight cryostat missions.

11.6.1.2.1 1996: Spatial Infrared Imaging Telescope III Solid Hydrogen Cryostat

In April 1996 the DoD Ballistic Missile Defense Organization conducted a Midcourse Space Experiment mission that included the Spatial Infrared Imaging Telescope III (SPIRIT III) cooled by a Lockheed 10 K solid-hydrogen cryostat (Figure 11.47) [103]. In addition to testing technologies to identify and track ballistic missiles during flight, the mission also performed many scientific investigations of the Earth's atmosphere and outer space. SPIRIT III contained an LWIR telescope with a high off-axis-rejection, a five-color radiometer, and a six-channel interferometer. It studied the infrared emission from the gas and dust that permeates the universe, and surveyed areas of the sky that were missed by IRAS. In November 1994, just prior to launch, the cryostat suffered a loss of vacuum in the insulation space; this resulted in extensive damage to it and the instrument. Although it was repaired prior to launch, some possible remaining damage to the MLI, not filling the dewar the entire way and a higher shell temperature than planned in orbit were felt to have

TABLE 11.3. Recent space cryostat flight operating experience

Mission	Cryogen	Launch Date	Operate Hours	Comments	
Ball Aerospace					
COBE (650 ℓ)	Sf He	1989	7,300	Similar to IRAS 1983 dewar	
PRSA (on Shuttle)	ScH_2, ScO_2	1991-04	500	60 dewars for Shuttle fuel cells	
BBXRT (shuttle)	solid Ar	1991-98	200	Multiple Shuttle experiments	
NICMOS (on HST)	solid N_2	1998	12,000	Damaged during launch	
Spitzer (360 ℓ)	Sf He	2003	17,500	As of 8/05, projected life 5 years	
Lockheed Martin					
CLAES (on UARS)	Ne-CO_2	1991	13,900	Was solid H_2 before Challenger	
MSX (Spirit III)	solid H_2	1996	7,300	DoD mission, lasted 10 mths	
WIRE	solid H_2	1999	15	Failed on deployment in orbit	
GPB (2400 ℓ)	Sf He	2004	12,600	As of 10/05 at end of mission	
GSFC					
XRS (25 ℓ)	Sf He	2005	750	Design life 3 years; lasted 30 days	
ESA					
ISO (2200 ℓ)	Sf He	1995	22,000	Operational 30 mths	

been responsible for the mission life of 10 months compared with the 18-month design life.

11.6.1.2.2 1997: Near-Infrared Camera and Multiple-Object Spectrometer Solid Nitrogen Cryostat

In February 1997, the NICMOS instrument was installed on the HST during its second servicing mission to provide an infrared imaging capability from 0.8 to 2.5 µm. Its HgCdTe photoconductive detectors were cooled to 65 K by a Ball Aerospace cryostat (Figure 11.48) using 120 kg of solid nitrogen [104]. Unfortunately, during repeated warming cycles prior to and during launch, the expanding nitrogen warped the dewar and led to a thermal short to one of the vapor-cooled shields [105]. As

FIGURE 11.47. SPIRIT III solid hydrogen cryostat.

FIGURE 11.48. NICMOS solid nitrogen cryostat.

a result of the increased heat leak, the mission lasted 23 months, far short of its 5-year design life. Five years later, the NICMOS instrument was brought back to life through the installation of the low-vibration Creare turbo-Brayton cryocooler installed during HST servicing mission 3B [76].

11.6.1.2.3 1999: Wide-Field Infrared Explorer 7.5 K Solid Hydrogen Cryostat

Launched in March 1999, the Wide-Field Infrared Explorer (WIRE) was one of NASA's small explorer series, a "faster, better, cheaper" mission designed to spend 4 months surveying the sky at mid-infrared wavelengths between 12 and 25 μm with a sensitivity 1000 times better than IRAS. The Lockheed-built cryostat, shown in Figure 11.49, consisted of two solid-hydrogen stages, one at 13 K to cool the telescope and serve as a thermal guard for the lower stage, and one at 7.5 K to cool the 128 $\times$ 128 Si:Ga detector array [106]. Unfortunately, an electronic glitch in the spacecraft resulted in the dewar lid getting ejected prematurely, prior to the telescope being stably pointed toward dark space. With sun shining into the telescope, in just 15 h the entire 4-month supply of hydrogen was vaporized, and the mission was lost.

FIGURE 11.49. WIRE 7 K solid hydrogen dewar.

FIGURE 11.50. SIRTF superfluid helium dewar.

11.6.1.2.4 2003: SIRTF 1.4 K Superfluid Helium Cryostat

One of NASA's great observatories, SIRTF began its development in 1983 as the Shuttle Infrared Telescope Facility, and over the years became the Space Infrared Telescope Facility when it was separated from the shuttle; it was renamed *Spitzer* after it was successfully launched in August 2003. Over its 20 years of development, SIRTF survived several changes in design philosophy, including the "cheaper, faster, better" paradigm of the early 1990s. The final cryogenic design of the 0.85 m infrared telescope (Figure 11.50) is remarkably well optimized and promises over 5 years of operation on 360 L of superfluid helium; this contrasts with the ISO's 2200 L used for a 0.6 m infrared telescope with a 30-month life [107]. Spitzer is much more sensitive than prior infrared missions and is studying the Universe over a range of wavelengths from 3 to 180 μm. Its three instruments together contain 11 detector arrays, operating from 1.4 to about 10 K, along with the attendant optics for imaging and spectroscopy. The detectors and instruments are cooled directly by the liquid helium cryostat, while the effluent gas is used to cool the telescope down to 6 K. Its key objectives are the study of brown dwarfs, superplanets, planetary systems revealed by protoplanetary and debris disks, and surveys of galaxy activity and the distant Universe.

11.6.1.2.5 2004: Gravity Probe B 1.8 K Superfluid Helium Cryostat

GPB began its life in 1963, even earlier than SIRTF, and was finally launched into orbit in April 2004 to test two unverified predictions of Einstein's general theory of relativity. Over its 40 years of development by Stanford University, GPB developed a wide array of cutting-edge technologies, one of which is the world's most precision gyroscopes. Two others are the 9 ft tall Lockheed-built dewar [108]

FIGURE 11.51. GPB superfluid helium dewar.

(Figure 11.51), which contains 2440 L of superfluid helium, and its porous-plug liquid–vapor phase separator [13]. The helium dewar provides the 1.8 K required for the instrument's superconducting quantum interference device magnetometers that measure the drift of the gyroscope's spin axis, and for other superconducting elements used in the instrument to monitor and shield-out external magnetic fields. The liquid helium lasted until September 30, 2005 (17 months from launch), providing 12 months of science data to test Einstein's theory.

11.6.1.2.6 2005: X-Ray Spectrometer

The X-Ray Spectrometer (XRS) instrument was originally slated for NASA's X-ray observatory (AXAF) back in 1985. When AXAF was replanned, XRS became a part of the joint Japanese–US Astro-E mission, which failed to achieve orbit in February 2000. Unfortunately, the third time was not a success either, as XRS consumed its 3-year supply of helium within a month after being successfully launched as the prime instrument of the Japanese Suzaku (formerly Astro-E2) spacecraft in July 2005. XRS was designed to measure the spectrum of celestial objects in the "soft" X-ray range (200 to 10,000 eV) to much higher resolution than had been previously possible. The X-ray detectors were cooled to 65 mK using a GSFC adiabatic demagnetization refrigerator (ADR) cooled by a superfluid helium dewar [109]. The 25 L, 1.3 K superfluid helium dewar was in turn cooled by a 17 K solid neon dewar provided by the Japanese, which in turn was cooled by a Sumitomo Stirling cryocooler to achieve a design life in orbit of 2.5 to 3 years. Although the excessive heat load ended the mission in just 29 days, XRS achieved 58 mK steady state, a new record low temperature for space.

11.6.1.3 Technology Demonstration Cryocooler Missions

In addition to the prime missions described above, the 1995–2005 period also had some important technology demonstration missions to test out new technologies or
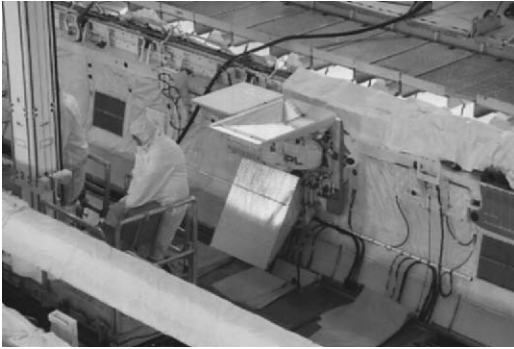
Figure 11.52. 10 K BETSCE cryocooler integrated onto Space Shuttle STS-77.

to run cryogenic experiments in space. These included both cryostat and cryocooler missions.

11.6.1.3.1 1996: Materials in Devices as Superconductors

The Materials in Devices as Superconductors (MIDAS) was a NASA cryogenic facility for the characterization of HTSs during extended flights. It was based on a Stirling cooler capable of 1 W cooling at 80 K, with a maximum power consumption of 60 W [110]. Launched on STS-79, it was installed on board the Russian space station Mir, where it operated for about 3 months before returning.

11.6.1.3.2 1996: Brilliant Eyes Ten-Kelvin Sorption Cryocooler Experiment

In May 1996, the BETSCE flew on board STS-77 (Figure 11.52) and demonstrated the capability to cool a 100 mW load to <11 K in less than 2 min, and then to continue to maintain the load at temperature for 10–20 min [111]. After this period, the closed-cycle JT sorption cryocooler recycled in preparation for another cooling cycle. The periodic nature of the cooler allowed the required input power to be averaged over the 4 h recycle time, thus providing a fast-cooldown 150 mW at 10 K cooler for a relatively low average power. The cooler, shown in Figure 11.36, was built for the SDIO by JPL and Aerojet and was based on metal hydride sorption compressors combined with three Hughes 7044H tactical Stirling cryocoolers to precool the hydrogen J–T gas stream to 65 K before making solid hydrogen at 10 K in the system's coldtip reservoir.

11.6.1.3.3 1997: Cryogenic On-Orbit Long-Life Active Refrigerator

In August 1997, the Cryogenic On-Orbit Long-Life Active Refrigerator (COOL-LAR) flew on board STS-85 and demonstrated a cooling capacity of 3.5 W at 65 K together with 5 W at 120 K. COOLLAR (Figure 11.53) is an oil-lubricated multipiston closed-cycle nitrogen J–T developed by Ball Aerospace for the DoD [112]. It was an important pathfinder for long-life space J–T cryocoolers.

FIGURE 11.53. Ball Aerospace COOLLAR closed-cycle 77 K J–T cryocooler.
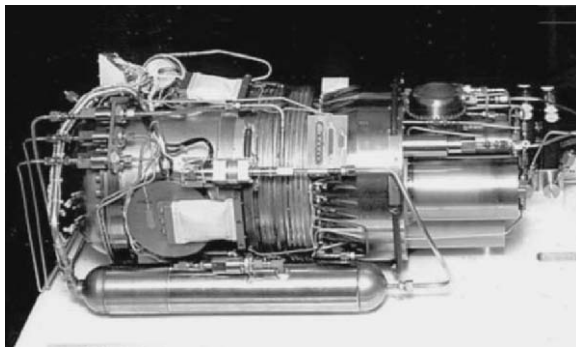
11.6.1.3.4 1997: Confined Helium Experiment

Flown on STS-87 in November 1997 as part of USMP-4, the CHeX was a follow-on experiment that used, for the last time, the same superfluid helium dewar as LPE in 1991. The experiment investigated the behavior of helium at the transition between superfluid and liquid state [113].

11.6.1.3.5 2000: STRV-1d

Launched in November 2000, the STRV1d spacecraft was developed by the DERA of the UK Ministry of Defence as a small space-technology test bed. The spacecraft carried a JPL-built quantum-well infrared photodetector focal-plane validation flight experiment cooled by a DRS 1 W at 80K tactical Stirling cryocooler (Figure 11.38) that cooled the detector to 50 K [114].

11.6.2 1995–2005 R&D Emphasis

During this decade of over 25 successful long-life space cooler missions, cooler research and development was principally associated with building and qualifying the many coolers that were used in the missions. Thus, the majority of the funding for cooler research transferred away from pure R&D budgets, and was carried as part of flight project funding for the specific space missions. This was largely true for both the civilian space cooler development efforts and the military efforts.

Following this trend, most of the development efforts for future space cooler missions was funded by approved future flight missions. These are described below:

11.6.2.1 Long-Life 35–80 K Stirling and Pulse Tube Coolers

Building on the work in the early 1990s, extensive development of third- and fourth-generation Oxford-style linear flexure-bearing coolers and drive electronics took place at NGST (formerly TRW), Ball Aerospace, Lockheed Martin, and Raytheon (formerly Hughes) between 1995 and 2005. Included in this work was the incorporation of active vibration cancellation [115], closed-loop control of
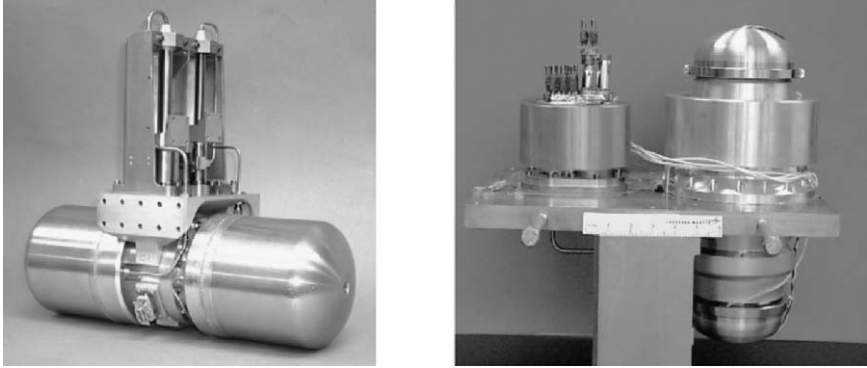
FIGURE 11.54. NGST (left) and Lockheed (right) two-stage HCC pulse-tube cryocoolers are designed for power levels up to 600 W.

coldtip temperature [116], and active suppression of current ripple fed back onto the spacecraft power bus. The TRW 1.5 W at 55 K AIRS [95] and 0.5 W at 55 K Integrated Multispectral Atmospheric Sounder [117] pulse-tube coolers served as pathfinders for many of these new performance-enhancement technologies incorporated into the cryocooler drive electronics.

Military applications, such as SBIRS-Low, also sponsored extensive development of single- and multi-stage coolers for a variety of applications, all building on the general designs of the earlier Oxford coolers. This included designs such as the NGST and Lockheed pulse-tube cryocoolers shown in Figure 11.54; these have input power ratings as high as 600 W with cooling capacities up to 2 W at 35 K plus 20 W at 85 K [118,119]. The primary focus of Raytheon and Ball Aerospace was on high-efficiency single- and multi-stage Stirling coolers targeted at the 35 K temperature range [120, 121].

11.6.2.2 Hybrid Joule–Thomson Sorption Cooling for Temperatures Down to 4 K

The European Planck mission, scheduled for launch in the 2007 time frame, sponsored the flight development of JPL hydride sorption coolers building on the work started by Jones [42] as early as 1982. The main objective of Planck is to map the temperature anisotropies of the CMB over the whole sky with high sensitivity. Achieving this goal requires bolometers operating at 100 mK, high electron mobility transistor devices operating at 20 K, and a low-emissivity cooled telescope at 60 K. The cryogenic system being developed for Planck is based on precooling to 60 K by passive radiators, cooling to 20 K with the JPL hydride sorption cooler [122, 123] (Figure 11.55), cooling to 4 K with an RAL helium J–T cooler based on Oxford mechanical compressors, and final cooling to 100 mK using an open-loop dilution refrigerator (discussed in Section 11.6.2.3). The RAL 4 K cooler

FIGURE 11.55. Planck sorption cryocooler compressor assembly as delivered for spacecraft integration.
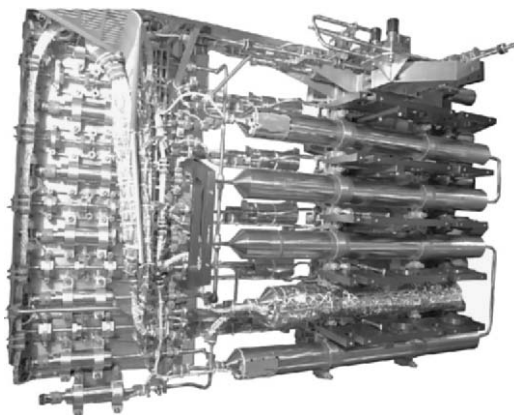
is a derivative of the developments started in the 1980s, shown in Figure 11.32 [124,125]. The planned mission lifetime for Planck is 15 months.

11.6.2.3 Sub-Kelvin Cryocoolers for Cooling Down to 50 mK

To enable sub-kelvin detectors on XRS, Herschel, Planck, and future space-science missions, a variety of sub-kelvin refrigerators were developed for flight between 1995 and 2005. This includes the 1999 launch of the NASA–Goddard single-stage ADR used to provide 65 mK cooling from a 1.3 K helium bath for the X-ray detectors on XRS. After the failure of the 1999 XRS launch, a second XRS ADR cooler was built for the reflight in 2005. This XRS single-stage ADR cooler had been under development since the early 1980s [109].

Additional sub-kelvin refrigerator development included an open-cycle ^{3}He sorption cooler to provide the 0.3 K cooling required by FIRST/Herschel [126], and the open-loop dilution refrigerator [127,128] designed by CRTBT in Grenoble and manufactured by Air Liquide to provide 100 mK cooling for Planck. Building on the concepts developed for XRS, NASA–Goddard also began development of a prototype four-stage ADR (Figure 11.56) for cooling X-ray microcalorimeters to 50 mK for the future NASA Constellation-X mission [129].

11.6.2.4 Hybrid Joule–Thomson Stirling and Pulse-Tube Cooling for Temperatures Down to 4 K

To enable a suite of evermore capable science observatories, NASA initiated funding in 2001 for long-life coolers in the 4–20 K temperature range. With three future missions as its focus, the Advanced Cryocooler Technology Development Program (ACTDP) was funded under the Terrestrial Planet Finder project to develop long-life mechanical cryocoolers with the necessary cooling power and integration features to accommodate the 6 K/18 K cooling of its target missions [130]. Three alternative concepts, shown in Figure 11.57, were selected for devel-

FIGURE 11.56. Sub-kelvin ADR for Constellation-X.

opment: two hybrid systems using Stirling/J–T and pulse-tube/J-T combinations, and a four-stage pulse tube with an optional integral flow loop. In 2005, based on the excellent progress made during breadboard fabrication and development testing, the ACTDP coolers were selected to cool the Mid Infrared Instrument on the James Webb Space Telescope (JWST), scheduled for launch in the 2013 time frame. At this time, in 2005, the ACTDP program has been transferred to the JWST to be managed as a flight cryocooler development program.

11.7 Summary

Since the beginning of the space program, in 1957, the world's aerospace industry has utilized cryogenic temperatures to enable infrared, gamma-ray and X-ray detectors to gather vast amounts of data for scientific, missile defense, and recon-
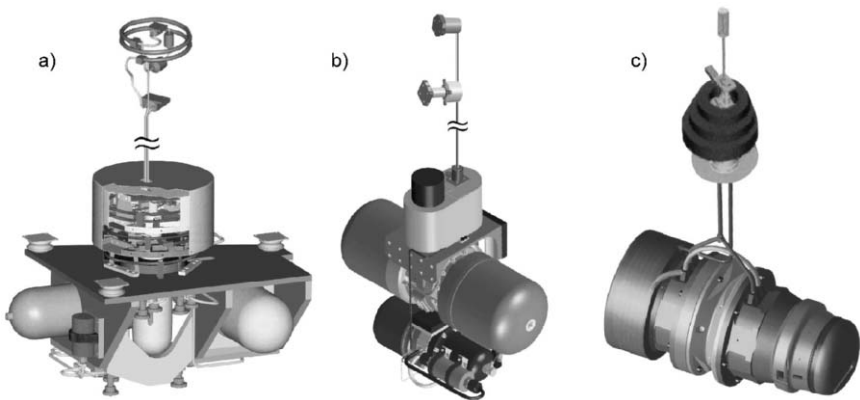
FIGURE 11.57. ACTDP coolers: (a) Ball 6 K J–T with 18 K Stirling precooler; (b) NGST 6 K J–T with 18 K pulse-tube precooler; (c) Lockheed Martin four-stage 6 K pulse tube.

naissance observations. Soon after the first satellites were in orbit, engineers and scientists began seeking means of providing multiyear cryogenic cooling for evermore sophisticated and sensitive detectors. Although passive cryoradiators were useful for temperatures above 150 K, stored cryogens and mechanical cryocoolers soon became the mainstay for extended low-temperature (0.1 to 80 K) observation from space. Through the years, cryostat and cryocooler technology has advanced to a tremendous degree, providing a source of cryogenic cooling for a great many missions.

However, the path to reliable, multiyear cooling from space has been long and difficult. Over the years, perhaps hundreds of millions of dollars has been expended examining every conceivable technology capable of providing long-life cooling. Stirling, VM, Brayton, magnetic, sorption, and pulse tube, all have been researched in great depth. But, at the end of the 50 years, not only do we have over two dozen long-life cryogenic missions currently circling the globe, we have enormous improvements in our understanding of the universe and Earth, including, from the DoD's perspective, vastly superior missile defense and reconnaissance observations. One can only conclude that, over the past 50 years, the quest for long-life cryogenic cooling in space has been a great success.

References

1. Nast, T.C., and Murray, D.O., "Orbital Cryogenic Cooling of Sensor Systems," AIAA paper No. 76-979, presented at the *System Designs Driven by Sensors AIAA Technical Specialist Conference*, Pasadena, CA, October 19–20, 1976.
2. Breckenridge, R.W., *Background on Rotary Reciprocating Refrigerators: 1962 to 1976*, unpublished report, Arthur D. Little, Inc., Cambridge, MA, 1977.
3. Hughes, J.L., and Herr, K.C., "Mariner Mars 1969 Infrared Spectrometer: Gas Delivery System and Joule–Thomson Cryostat," *Cryogenics*, 13(9), 513–519, 1973.
4. Nast, T.C., Bell, G.A., and Wedel, R.K., "Orbital Performance of a Solid Cryogen Cooling System for a Gamma Ray Detector," *Advances in Cryogenic Engineering*, Vol. 21, Plenum Press, New York, 1976, pp. 435–442.
5. Sherman, A., "History, Status and Future Applications of Spaceborne Cryogenic Systems," *Advances in Cryogenic Engineering*, Vol. 27, Plenum Press, New York, 1982, pp. 1007–1029.
6. Nast, T.C., "Status of Solid Cryogen Coolers," *Advances in Cryogenic Engineering*, Vol. 31, Plenum Press, New York, 1986, pp. 835–849.
7. Smithson, J.C., and Luksa, N.C., "Refurbishment of the Cryogenic Coolers for the Skylab Earth Resources Experiment Package," *Proceedings of 9th Aerospace Mechanism Symposium*, August 1975.
8. Barnett, T.L., and Juday, R.D., "Skylab S191 Visible-Infrared Spectrometer," *Applied Optics*, 16(4), 967–972, 1977.

9. Nast, T.C., Barnes, C.B., and Wedel, R.K., "Development and Orbital Operation of a Two-Stage Solid Cryogen Cooler," *Journal of Spacecraft and Rockets*, 15(2), 85–91, 1978.

10. Keller, C.W., Cunnington, G.R., and Glassford, A.P., *Final Report, Thermal Performance of Multilayer Insulations*, NASA CR-134477, Lockheed LMSC, Sunnyvale, CA, April 5, 1974.

11. Foster, W.O., Naes, L.A., and Barnes, C.B., "Thermal Conductivity Measurements of Fiberglass/Epoxy Structural Tubes from 4 K to 320 K," AIAA Paper 75-711, presented at *AIAA Thermophysics Specialist Conference*, May 1975.

12. Nast, T.C., "A Review of Multilayer Insulation Theory, Calorimeter Measurements, and Applications," *Recent Advances in Cryogenic Engineering—1993*, ASME HTD-Vol. 267, Kelley, J.P., and Goodman, J., eds., American Society of Mechanical Engineers, New York, 1993, pp. 29–43.

13. Selzer, P.M., Fairbank, W.M., and Everitt, C.W.F., "A Superfluid Plug for Space," *Advances in Cryogenic Engineering*, Vol. 16, Plenum Press, New York, 1971, pp. 277–281.

14. Leo, B., *Designers Handbook for Spaceborne Two-Stage Vuilleumier Cryogenic Refrigerators*, Technical Report AFFDL-TR-70-54, June 1970.

15. Cygnarowicz, T.A., and Sherman, A., *Design Scaling of Fractional Watt Vuilleumier Refrigeration System*," Goddard Space Flight Center Report X-163-71-446, October 1971.

16. Breckenridge, R.W., "A 3.6 K Reciprocating Refrigerator," *Advances in Cryogenic Engineering*, Vol. 14, Plenum Press, New York, 1969, p. 387.

17. Van Mal, H.H., and Maynheer, A. "Hydrogen Refrigerator for the 20 K Region with LaNi$_5$-Hydride Thermal Adsorption Compressor for Hydrogen," *4th ICEC*, IPC Science and Tech. Press, Surrey, England, 1972.

18. Naes, L.G., and Nast, T.C., "Long Life Orbital Operation of Stirling Cycle Mechanical Refrigerators," *Cryogenically Cooled Sensor Technology; Proceedings of SPIE Seminar, San Diego, CA, July 29–30, 1980*, (A81-39470 18-35) SPIE, Bellingham, WA, 1980, pp. 126–135.

19. Naes, L.G., and Nast, T.C., "Two Years Orbital Performance Summary of Stirling Cycle Mechanical Refrigerators," *SPIE Proceedings: Modern Utilization of Infrared Technology VII*, Vol. 304, Society for Photo-Optical Instrumentation Engineers, Bellingham, WA, 1981, pp. 95–100.

20. Colaprete, S.J., "Contribution to Space Shuttle Achievement," *Cryogenic Technology*, April 1981.

21. Urbach, A.R., and Mason, P.V., "IRAS Cryogenic System Flight Performance Report," *Advances in Cryogenic Engineering*, Vol. 29, Plenum Press, New York, 1984, pp. 651–659.

22. Farmer, C.B., Raper, O.F., and O'Callaghan, F.G., *Final Report on the First Flight of the ATMOS Instrument during the Spacelab 3 Mission, April 29 through May 6, 1985,* JPL Publication 87-32, Jet Propulsion Laboratory, Pasadena, CA, 1987.

23. Mason, P.V., et al., "Preliminary Results of the Spacelab 2 Superfluid Helium Experiment," *Advances in Cryogenic Engineering*, Vol. 31, Plenum Press, New York, 1986, pp. 869–879.

24. Urban, E.W., and Ladner, D.R., "Preliminary Flight Performance Report of the Infrared Telescope on Spacelab 2," *Proc. of the Workshop on Helium Transfer in Space*, National Bureau of Standards, Boulder, CO, 1986.

25. Johnson, A., "Spacecraft-Borne Long Life Cryogenic Refrigeration—Status and Trends," *Refrigeration for Cryogenic Sensors*, NASA Conf. Publication 2287, NASA Goddard Space Flight Center, Greenbelt, MD, 1983, p. 47–79.

26. Russo, S.C., "Cryogenic Technology Advances at Hughes Aircraft Company," *Proc. of the Second Interagency Meeting on Cryocoolers*, Easton, MD, September 24, 1986, pp. 107–119.

27. Breckenridge, R.W., "Current Status of Rotary Reciprocating Refrigerator Development," *Proc. of the Second Interagency Meeting on Cryocoolers*, Easton, MD, September 24, 1986, pp. 1–26.

28. Harris, R., Chenoweth, J., and White, R., "Cryocooler Development for Space Flight Applications," *SPIE Technical Symposium Paper* 280-10, Washington, DC, April 1981.

29. Mastrup, F.N., and Price, K.D., "Thermodynamic Performance Measurements of a 10K, $Ga_3Ga_5O_{12}$ Paramagnetic Stage," *Proc. of Interagency Meeting on Cryocoolers*, Monterey, CA, August 1988, pp. 149–159.

30. Barclay, J.A., et al., "Experimental Results on a Low-Temperature Magnetic Refrigerator," *Advances in Cryogenic Engineering*, Vol. 31, Plenum Press, New York, 1986, pp. 743–752.

31. Barclay, J.A., et al., "Design Limitations on Magnetic Refrigerators Imposed by Magnet Forces," *Proc. of the 4th International Cryocooler Conf.*, Easton, MD, September 25–26, 1986, pp. 89–98.

32. Stolfi, F., Goldowsky, M., Ricciardelli, J., and Shapiro, P., "A Magnetically Suspended Linearly Driven Cryogenic Refrigerator," *Refrigeration for Cryogenic Sensors*, NASA Conf. Publication 2287, NASA Goddard Space Flight Center, Greenbelt, MD, 1983, pp. 263–303.

33. Davey, G., "The Oxford Miniature Cryogenic Refrigerator," *Advances in Infrared Detectors and Systems*, Conference Pub. 204, Institution of Electrical Engineers, London, 1981.

34. Curtis, J.T. et al., "Remote Sounding of Atmospheric Temperature from Satellites V. The Pressure Modulator Radiometer for Nimbus F," *Proc. Royal Society of London, A* 337, 135–150, 1974.

35. Drummond, J.R. et al., "The Stratospheric and Mesospheric Sounder on Nimbus 7," *Phil. Trans. Royal Society of London, A* 296, 1980, pp. 219–241.

36. Taylor, F.W., et al., "Infrared Radiometer for the Pioneer Venus Orbiter, I: Instrument Description," *Applied Optics*, 18(23), 3893–3900, 1979.

37. Davey, G., and Orlowska, A., "Miniature Stirling Cycle Cooler," *Cryogenics*, 27, 148–151, 1987.

38. Werrett, S., et al., "Development of a Small Stirling Cycle Cooler for Spaceflight Applications," *Advances in Cryogenic Engineering*, Vol. 31, Plenum Press, New York, 1986, pp. 791–799.

39. Bradshaw, T.W., et al., "Performance of the Oxford Miniature Stirling Cycle Refrigerator," *Advances in Cryogenic Engineering*, Vol. 31, Plenum Press, New York, 1986, pp. 801–809.

40. Bradshaw, T.W., *Miniature Stirling Cycle Refrigerators for Space Use*, Report RAL-85-107, Rutherford Appleton Laboratory, Chilton, Didcot, UK, November 1985.

41. Chan, C.K., "Optimal Design of Gas Adsorption Refrigerators for Cryogenic Cooling," *Refrigeration for Cryogenic Sensors*, NASA Conf. Publication 2287, NASA Goddard Space Flight Center, Greenbelt, MD, 1983, pp. 323–341.

42. Jones, J., "Hydride Cryogenic Refrigerator Test Results," *Refrigeration for Cryogenic Sensors*, NASA Conf. Publication 2287, NASA Goddard Space Flight Center, Greenbelt, MD, 1983, pp. 357–374.

43. Frank, D. et al., *Advanced Long Life Cooler Development Program—1985*, Lockheed Report LMSC-D062022, Prepared for Hughes Aircraft Company, January 1986.

44. Donabedian, M., "Thermal Uncertainty Margins for Cryogenic Sensor Systems," Paper AIAA-91-1426, *AIAA 26th Thermophysics Conf.*, Honolulu, HI, June 24–26, 1991.

45. Nast, T., *Study of a Solid Hydrogen Cooler for Spacecraft Instruments and Sensors*, LMSC-D-766177, Final Report for NAS5-25792, August 1980.

46. Volz, S.M., et al., "Final Cryogenic Performance Report for the NASA Cosmic Background Explorer," *Advances in Cryogenic Engineering*, Vol. 37B, Plenum Press, New York, 1992, pp. 1183–1192.

47. Bell, G.A., Burriesci, L.G., and Naes, L.G, "CLAES Cryostat On-Orbit Performance versus Ground Test Predictions," *Proceedings of SPIE*, 1765, 217–226, 1993.

48. Naes, L.G., et al., "Design and Performance Analysis of the CLAES Ne/CO_2 Cryostat," *Cryogenic Optical Systems and Instruments III; Proc. of the SPIE, San Diego, CA, Aug. 17–19, 1988* (A90-11251 01-31) SPIE, Bellingham, WA, 1989, pp. 369–377.

49. Kawada, M., and Kudo, I., "Japanese Development of Cryocoolers for Applications in Space," *Proc. of 3rd Japanese–Sino Joint Seminar*, October 23–27, 1989, pp. 36–41.

50. Lipa, J.A., et al., "Lambda Point Experiment in Microgravity," *Cryogenics*, 34(5), 341–347, 1994.

51. Kawecki, T., "High Temperature Superconducting Space Experiment Cryogenic System Overview," *7th International Cryocooler Conference Proceedings*, Air Force Phillips Laboratory Report PL-CP–93-1001, Kirtland Air Force Base, NM, April 1993, pp. 1098–1106.

52. DiPirro, M.J., and Kittel, P., "The Superfluid Helium On-Orbit Transfer (SHOOT) Experiment,"*Advances in Cryogenic Engineering*, Vol. 33, Plenum Press, New York, 1988, pp. 893–900.

53. Priest, R.E., et al., "Ricor K506B Cryocooler Performance During the Clementine Mission and Ground Testing: A Status Report," *Cryocoolers 8*, Plenum Press, New York, 1995, pp. 883–892.

54. Glaser, R.J., Ross, R.G., Jr., and Johnson, D.L., "STRV Cryocooler Tip Motion Suppression", *Cryocoolers 8*, Plenum Press, New York, 1995, pp. 455–463.

55. Collaudin, B., and Rando, N., "Cryogenics in Space: A Review of the Missions and the Technologies," *Cryogenics* 40, 797–819, 2000.

56. Sugimura, R.S., Russo, S.C., and Gilman, D.C., "Lessons Learned during the Integration Phase of the NASA IN-STEP Cryo System Experiment," *Cryocoolers 8*, Plenum Press, New York, 1995, pp. 869–882.

57. Murakami, M., et al., "Thermal Design and Test of the IRTS Cryostat," *Advances in Cryogenic Engineering*, Vol. 35A, Plenum Press, New York, 1990, pp. 295–302.

58. Fujii, G., et al., "On-orbit Thermal Behavior of the IRTS Cryogenic System," *Cryogenics*, 36(10), 731–739, 1996.

59. Seidel, A., "ISO after Completing its Successful Mission," *Cryogenics,* 39, 135–148, 1999.

60. Thomas, P.J., "SDIO and Air Force Cryocooler Technology Developments at USAF Phillips Laboratory," *7th International Cryocooler Conference Proceedings*, Air Force Phillips Laboratory Report PL-CP–93-1001, Kirtland Air Force Base, NM, April 1993, pp. 3–13.

61. Ross, R.G., Jr., "JPL Cryocooler Development and Test Program Overview," *7th International Cryocooler Conference Proceedings*, Air Force Phillips Laboratory Report PL-CP–93-1001, Kirtland Air Force Base, NM, April 1993, pp. 14–25.

62. Castles, S., et al., "NASA/GSFC Cryocooler Development Program," *7th International Cryocooler Conference Proceedings*, Air Force Phillips Laboratory Report PL-CP–93-1001, Kirtland Air Force Base, NM, April 1993, pp. 26–39.

63. Kawada, M., and Fujisada, H., "Long-life Cryocooler Development Program for ASTER," *Cryocoolers 8*, Plenum Press, New York, 1995, pp. 35–53.

64. Chan, C.K., et al., "Stirling Space Cooler," *7th International Cryocooler Conference Proceedings*, Air Force Phillips Laboratory Report PL-CP–93-1001, Kirtland Air Force Base, NM, April 1993, pp. 50–56.

65. Stacy, D., McCormick, J., and Valenzuela, J., "Development and Demonstration of a Diaphragm Stirling 65K Standard Spacecraft Cryocooler," *7th International Cryocooler Conference Proceedings*, Air Force Phillips Laboratory Report PL-CP–93-1001, Kirtland Air Force Base, NM, April 1993, pp. 40–49.

66. Bradshaw, T.W., "First Results on a Prototype Two Stage Miniature Stirling Cycle Cooler for Space Applications," *Proc. of Fourth International Cryocooler Conference*, Easton, MD, September 1986, pp. 303–309.

67. Bradshaw, T.W., and Orlowska, A.H., "A Closed-Cycle 4K Mechanical Cooler for Space Applications," *Proc. of 9th European Symposium on Space Environmental Control Systems*, Florence, Italy, 1991.

68. Salomonovich, A.E., et al., "Space Helium Refrigerator," *Cryogenics*, 21(8), 474–478, 1981.

69. Ross, R.G., Jr., "A Study of the Use of 6K ACTDP Cryocoolers for the MIRI Instrument on JWST,"*Cryocoolers 13*, Springer Science & Business Media, New York, 2005, pp. 15–24.

70. Chan, C.K., et al., "Miniature Pulse Tube Cooler," *7th International Cryocooler Conference Proceedings*, Air Force Phillips Lab Report PL-CP–93-1001, Kirtland AFB, NM, April 1993, pp. 113–124.

71. Burt, W.W. and Chan, C.K., "Demonstration of a High Performance 35K Pulse Tube Cryocooler," *Cryocoolers 8*, Plenum Press, New York, 1995, pp. 313–319.

72. Burt, W.W., and Chan, C.K., "New Mid-Size High Efficiency Pulse Tube Coolers," *Cryocoolers 9*, Plenum Press, New York, 1997, pp. 173–182.

73. Johnson, D.L., et al., "Performance Characterization of the TRW 3503 and 6020 Pulse Tube Coolers," *Cryocoolers 9*, Plenum Press, New York, 1997, pp. 183–193.

74. Swift, W., and Sixsmith, H., "Performance of a Long Life Reverse Brayton Cryocooler," *7th International Cryocooler Conference Proceedings*, Air Force Phillips Lab Report PL-CP–93-1001, Kirtland AFB, NM, April 1993, pp. 84–97.

75. Swift, W.L., "Single-Stage Reverse Brayton Cryocooler: Performance and Engineering Model," *Cryocoolers 8*, Plenum Press, New York, 1995, pp. 499–506.

76. Swift, W.L., et al., "Initial Operation of the NICMOS Cryocooler on the Hubble Space Telescope," *Cryocoolers 12*, Kluwer Academic/Plenum Publishers, New York, 2003, pp. 563–570.

77. Bard, S., and Jones, J.A., "Development and Testing of an 80K Oxide Sorption Cryocooler," *Proceedings of the 5th International Cryocooler Conference*, Monterey, CA, August 18–19, 1988, pp. 13–23.

78. Bard, S., et al., "10K Sorption Cryocooler Flight Experiment (BETSCE)," *7th International Cryocooler Conference Proceedings*, Air Force Phillips Lab Report PL-CP–93-1001, Kirtland AFB, NM, April 1993, pp. 1107–1119.

79. Alverez, J., et al., "Design and Component Test Performance of an Efficient 4W, 130K Sorption Refrigerator," *Advances in Cryogenic Engineering*, Vol. 35B, Plenum Press, New York, 1990, pp. 1367–1374.

80. Davis, T., Reilly, J., and Tomlinson, B.J., "Air Force Research Laboratory Cryocooler Technology Development,"*Cryocoolers 10*, Kluwer Academic/Plenum Publishers, New York, 1999, pp. 21–32.

81. Tward, E., et al., "Miniature Space Pulse Tube Cryocoolers," *Cryogenics*, 39(8), 717–720, 1999.

82. Kawecki, T., "High-Temperature Superconducting Space Experiment II (HTSSE II) Overview and Preliminary Cryocooler Integration Experience," *Cryocoolers 8*, Plenum Press, New York, 1995, pp. 893–900.

83. Mand, G.S., Drummond, J.R., Henry, D., and Hackett, J., "MOPITT On-orbit Stirling Cycle Cooler Performance," *Cryocoolers 11*, Kluwer Academic/Plenum Publishers, New York, 2001, pp. 759–768.

84. Kawada, M., et al., "Performance Characteristics of the ASTER Cryocooler in Orbit," *Cryocoolers 12*, Kluwer Academic/Plenum Publishers, New York, 2003, pp. 737–746.

85. Tomlinson, B.J., et al., "Multispectral Thermal Imager (MTI) Space Cryocooler Development, Integration, and Test," *Cryocoolers 10*, Kluwer Academic/Plenum Publishers, New York, 1999, pp. 129–138.

86. Stubstad, J.M., et al., "The Space Technology Research Vehicle (STRV)-2 Program," AIAA-1999-4483, *AIAA Space Technology Conference and Exposition*, Albuquerque, NM, September 28–30, 1999.

87. Boyle, R., and Ross, R.G., Jr., "Overview of NASA Space Cryocooler Programs," *Advances in Cryogenic Engineering*, Vol 47B, American Institute of Physics, New York, 2002, pp. 1037–1044.

88. Murtagh, D., et al., "An Overview of the Odin Atmospheric Mission," *Can. J. Phys.*, 80, 309–319, 2002.

89. Boyle, R., Banks, S., Cleveland, P., and Turin, P., "Design and Performance of the HESSI Cryostat," *Cryogenics,* 39(12), 969–973, 1999.

90. Boyle, R., Banks, S., and Shirey, K., "Final Qualification and Early On-Orbit Performance of the RHESSI Cryocooler," *Cryocoolers 12*, Kluwer Academic/Plenum Publishers, New York, 2003, pp. 755–760.

91. Swift, W.L., et al., "The NICMOS Turbo-Brayton Cryocooler—Two Years in Orbit," *Cryocoolers 13*, Springer Science & Business Media, New York, 2005, pp. 633–639.

92. *"Coolers," EnviSat AATSR Product Handbook*, Issue 1.2, European Space Agency, 1 September 2004, p. 28.

93. "FPS Cooler Assembly (FCA)," *EnviSat MIPAS Product Handbook*, Issue 1.2, European Space Agency, 1 September 2004, p. 163.

94. Ross, R.G., Jr., and Green, K., "AIRS Cryocooler System Design and Development,"*Cryocoolers 9*, Plenum Press, New York, 1997, pp. 885–894.

95. Ross, R.G., Jr., Johnson, D.L., Collins, S.A., Green, K., and Wickman, H. "AIRS PFM Pulse Tube Cooler System-level Performance,"*Cryocoolers 10*, Plenum Press, New York, 1999, pp. 119–128.

96. Ross, R.G., Jr., and Rodriguez, J.I., "Performance of the AIRS Pulse Tube Coolers and Instrument—A First Year in Space," *Advances in Cryogenic Engineering*, Vol. 49B, American Institute of Physics, New York, 2004, pp. 1293–1300.

97. Briet, R., and Serene, F., "INTEGRAL Spectrometer Cryostat Design and Performance after 1.5 Years in Orbit," *Cryocoolers 13*, Springer Science & Business Media, New York, 2005, pp. 619–628.

98. Bonsignori, R., et al., *VIRTIS Visual and Infrared Imaging Spectrometer for the Rosetta Mission*, International Astronautical Federation, 1997.

99. Collins, S.A., Rodriguez, J.I., and Ross, R.G., Jr., "TES Cryocooler System Design and Development," *Advances in Cryogenic Engineering*, Vol 47B, American Institute of Physics, New York, 2002, pp. 1053–1060.

100. Rodriguez, J.I., et al., "On-Orbit Performance of the TES Pulse Tube Coolers and Instrument—A First Year in Space," *Advances in Cryogenic Engineering*, Vol. 51B, American Institute of Physics, New York, 2006, pp. 1937–1944.

101. Lock, J., et al., "HIRDLS Cooler Subsystem On-Orbit Performance," *Advances in Cryogenic Engineering*, Vol. 51B, American Institute of Physics, New York, 2006, pp. 1945–1950.

102. Raab, J., et al., "JAMI Flight Pulse Tube Cooler System," *Cryocoolers 12*, Kluwer Academic/Plenum Publishers, New York, 2003, pp. 191–197.

103. Bartschi, B.Y., Morse, D.E., and Woolston, T.L., "The Spatial Infrared Imaging Telescope III," *Johns Hopkins APL Technical Digest*, 17(2), 215–225, 1996.

104. Miller, C.D., "Development of the Long-Lifetime Solid Nitrogen Dewar for NICMOS," *Advances in Cryogenic Engineering*, Vol. 43A, Plenum Press, New York, 1998, pp. 927–333.

105. Miller, C.D., "Pre- and Post-Launch Performance of the NICMOS Dewar," *Advances in Cryogenic Engineering*, Vol. 43A, Plenum Press, New York, 1998, pp. 935-940.

106. Elliot, D., Hacking, P. and Schember, H., "Engineering Design of the Wide-Field Infrared Explorer (WIRE)," *SPIE Annual Meeting*, San Diego, CA, July 1994.

107. Finley, P.T., Schweickart, R.B., and Hopkins, R.A., "The Space Infrared Telescope Facility (SIRTF) Cryogenic Telescope Assembly (CTA) Cryogenic and Thermal System," *Cryogenics*, 44, 367–373, 2004.

108. Taber, M.A., et al., "Operational Cryogenic Experience with the Gravity Probe B Payload," *Advances in Cryogenic Engineering*, Vol. 47, American Institute of Physics, New York, 2002, pp. 1241–1248.

109. Serlemitsos, A.T., et al., "Adiabatic Demagnetization Refrigerator for Space Use," *Advances in Cryogenic Engineering*, Vol. 35B, Plenum Press, New York, 1990, pp. 1431–1437.

110. Amundsen, R.M., et al., *Development of the Materials in Devices as Superconductors (MIDAS) Experiment,* NASA/TM1998208440, Langley Research Center, Virginia, May 1998.

111. Bowman, R.C., Jr., Karlmann, P.B., and Bard, S., *Brilliant Eyes Ten-Kelvin Sorption Cryocooler Experiment—Final Report*, JPL Publication 97-14, Jet Propulsion Lab, Pasadena, CA, September 1997.

112. Fernandez, R., and Levenduski, R., "Flight Demonstration of the Ball Joule–Thomson Cryocooler," *Cryocoolers 10*, Plenum Publishing Corp., New York, 1999, pp. 449–456.

113. Luchik, T.S., "Performance Improvement of the CheX Flight Cryostat," *Advances in Cryogenic Engineering*, Vol. 41B, Plenum Press, New York, 1996, pp. 1135–1142.

114. Kenny, J.T., and Pollock, H.R., "STRV-1d QWIP Technology Validation in Space Flight," *2001 IEEE Aerospace Conference Proceedings*, March 10–17, 2001 Big Sky, MT, Vol. 1, 2001, pp. 181–186.

115. Ross, R.G., Jr., "Vibration Suppression of Advanced Space Cryocoolers—An Overview," *Proceedings of the International Society of Optical Engineering (SPIE) Conference*, San Diego, CA, March 2–6, 2003.

116. Clappier, R.R., and Kline-Schoder, R.J., "Precision Temperature Control of Stirling-cycle Cryocoolers," *SPIE Proceedings*, Vol. 2227, 1994.

117. Ross, R.G., Jr., "IMAS Pulse Tube Cryocooler Development and Testing," *Integrated Multispectral Atmospheric Sounder (IMAS) Instrument Technology Development and Demonstration, Final Report*, Internal Document, Jet Propulsion Laboratory, December 14, 1998, pp. 3-1–3-16.

118. Chan, C.K., et al., "High Capacity Two-Stage Pulse Tube Cooler," *Cryocoolers 12*, Kluwer Academic/Plenum Publishers, New York, 2003, pp. 219–224.

119. Foster, W.G., et al., "Development of a High Capacity Two-Stage Pulse Tube Cryocooler," *Cryocoolers 12*, Kluwer Academic/Plenum Publishers, New York, 2003, pp. 225–232.

120. Barr, M.C., Price, K.D., and Pruitt, G.R., "Long-life Cryocooler Performance and Production," *Cryogenics*, 44(6–8), 409–412, 2004.

121. Marquardt, E.D., et al., "Ball Aerospace Next Generation 2-Stage 35K SB235 Coolers," *Cryocoolers 13*, Springer Science & Business Media, New York, 2003, pp. 65–70.

122. Bowman, R.C., et al., "Evaluation of Hydride Compressor Elements for the Planck Sorption Cryocooler," *Cryocoolers 12*, Kluwer Academic/Plenum Publishers, New York, 2003, pp. 627–635.

123. Prina, M., et al., "Initial Test Performance of a Closed-Cycle Continuous Hydrogen Sorption Cryocooler, the Planck Sorption Breadboard Cooler," *Cryocoolers 12*, Kluwer Academic/Plenum Publishers, New York, 2003, pp. 637–642.

124. Jones, B.G., and Ramsay, D.W., "Qualification of a 4 K Mechanical Cooler for Space Application," *Cryocoolers 8*, Plenum Press, New York, 1995, pp. 525–535.

125. Scull, S.R., et al., "Design and Development of a 4 K Mechanical Cooler," *Cryocoolers 10*, Plenum Press, New York, 1999, pp. 513–528.

126. Duband, L., Collaudin, B., and Jamotton, P., "Sub-Kelvin Sorption Coolers for Space Application," *Cryocoolers 11*, Kluwer Academic/Plenum Publishers, New York, 2001, pp. 567–576.

127. Benoit, A., et al., "Development of a 0.1 K Cryocooler for Space Applications—Status," *Proc. 6th European Symposium on Space Environment Control Systems*, ESA SP-400, Vol. 2, May 1997, pp. 497–502.

128. Camus, Ph., et al., "Status of the Planck Open-Cycle Dilution Cryogenic System," *Proceedings of the European Space Cryogenics Workshop 2005*, June 14–16, 2005.

129. Shirron, P., et al., "Development of a Cryogen-Free Continuous ADR for the Constellation-X Mission," *Cryogenics*, 44(6–8), 581–588, 2004.

130. Ross, R.G., Jr., and Johnson, D.L., "NASA's Advanced Cryocooler Technology Development Program (ACTDP)," *Advances in Cryogenic Engineering*, Vol. 51A, American Institute of Physics, New York, 2006, pp. 607–614.

12

Understanding Properties and Fabrication Processes of Superconducting Nb₃Sn Wires

M. SUENAGA

Materials Science Department, Brookhaven National Laboratory, 76 Cornell Ave., Upton, NY 11973, USA

Abstract

The fabrication of multifilamentary Nb₃Sn wires was started by the discovery of the bronze process, a solid-state diffusion process, to form filamentary A15 structure compounds in 1969–1970. Through a number of improvements and modifications of the original process in the ensuing years, these wires are now indispensable components for the construction of magnets, producing very high magnetic fields for nuclear magnetic resonance spectroscopy, magnetic fusion experiments, and future high-energy particle accelerators. A comprehensive review article summarizes the state of the knowledge up to 1980 on the formation mechanisms and the superconducting properties of the A15 compounds that were fabricated by this process. Since 1980, significant advances have been made in the basic understanding of the factors controlling the growth processes, and basic superconducting properties of the bronze-processed Nb₃Sn. In particular, significant progress has been made in understanding the effects of alloying on these properties and mechanisms for flux-line pinning in the compound. Furthermore, for the practical usage of these wires, tremendous progress in the critical-current densities of multifilamentary Nb₃Sn wires has been made over the last several years. This chapter reviews these new findings about Nb₃Sn by the solid-state diffusion process and the critical-current densities of the state-of-the-art multifilamentary Nb₃Sn wires.

12.1 Introduction

Composite superconductors, which consist of fine filaments of Nb₃Sn, an A15 structure intermetallic compound, in a normal-metal matrix, have gained universal acceptance as the conductors of choice for the construction of magnets for producing very high magnetic fields. Currently, magnets made from these wires are very common for such applications as nuclear magnetic resonance (NMR), spectroscopy, International Thermonuclear Experimental Reactor-Experimental Design Activity (ITER-EDA), and future high-energy particle accelerators. Current metallurgical methods for producing the fine filamentary superconductors

with brittle intermetallic compounds such as Nb_3Sn were developed over many years following its discovery by Matthias et al. in 1954 [1]. Critical development of multifilamentary wires was started by simultaneous and independent discoveries of the so-called "bronze process" by three scientists in 1969 and 1970 [2]. The method relied on the fact that the A15 compound layers, such as Nb_3Sn and V_3Ga, could be formed at the interface of Nb(V) and Cu–Sn(Ga) without forming undesirable compounds when such composites were heated at elevated temperatures, e.g. 700 °C, after the composites were mechanically co-reduced in size. Prior to the discovery of the bronze process, Nb_3Sn conductors were made in the form of tapes. Even though high-field magnets were made with these tapes, these magnets were very difficult to use and, hence, were limited to laboratory usage.

In 1980, a comprehensive review article was written [3] covering the history of the discovery, the various modifications to the original wire process, the mechanisms of the formation and growth of the compound layers, and the physical and the superconducting properties of the compounds that were made by this process. Also, by 1980, manufacturers were producing substantial amounts of multifilamentary pure Nb_3Sn wires, and a number of high-field magnets were successfully constructed with these wires. Furthermore, by this time, a number of key factors about the process and the properties of the compounds that were made by this method were well understood in general terms, as described in the above-mentioned article. For example, the diffusion of Sn through the grain boundaries was well established as the mechanism for the growth of the compound layer [4,5]. Also, the grain boundaries were known to be the magnetic-flux-pinning centers in these compounds, and, in fact, it was shown that critical-current densities of A15 compounds were inversely proportional to the grain size [6,7]. At that time, however, the details of some of the pertinent issues about the properties of pure and alloyed Nb_3Sn, such as how flux lines were pinned by the boundaries, were not understood. Also, during the late 1970s, the effects of alloying the compounds, particularly Nb_3Sn, were actively investigated, and the additions of small amounts of Ta were found to be most effective in increasing the critical-current densities J_c of Nb_3Sn at high magnetic fields, $\gg 10$ T at 4.2 K [8,9]. However, another alloying element, Ti, which also had a lasting significance for the development of multifilamentary Nb_3Sn, was yet to be reported at the time of writing the above article. But results on the additions of Ti in Nb_3Sn were reported soon after [10,11], and it became very obvious that both of these elemental additions would make significant advances in high-field properties of multifilamentary Nb_3Sn wires. In fact, based on these findings, all of the present multifilamentary Nb_3Sn wires contained small amounts of Ti, Ta, or both of these elements.

Intrinsic superconducting properties of Nb_3Sn, which were altered by alloying additions, were also not available in detail at that time, even though the above two elementary additions became very important for high-field applications of the wires. Furthermore, questions were raised regarding the validity of Kramer's theory [12] on flux pinning in A15 compounds by the detailed analysis of the Kramer plot [3,13]. (Use of such a plot linearizes the data for critical-current density variations by applied magnetic fields by plotting $J_c^{1/2}(\mu_0 H)^{1/4}$ versus $\mu_0 H$ [14]

and is discussed below.) However, no suggestion was made to improve upon the theory at that time. Some answers to these questions were found in the early 1980s, and these findings are important in understanding properties and in improving the processing of Nb_3Sn. Furthermore, most of these new advances were made by using pure and alloyed monofilamentary Nb_3Sn wires by the bronze process, but the properties investigated would be applicable to those multifilamentary Nb_3Sn made by other modified processes, such as the internal-Sn and the powder-in-tube processes. In addition, during the period 1980–2005, tremendous improvements in high-field critical-current densities of multifilamentary Nb_3Sn wires were made, and these made possible the successful construction of very high-field magnets for NMR spectroscopy, ITER-EDA, and high-energy physics applications.

In this chapter, the effects of adding Ta and Ti on the critical-current densities $J_c(\mu_0 H)$ of Nb_3Sn in the bronze-processed monofilamentary wires are illustrated first by comparing critical-current densities of the alloyed Nb_3Sn wires with those of the pure ones. Then, the intrinsic superconducting properties of the bronze-processed pure and alloyed Nb_3Sn, as well as their compositions, are summarized. The chemical compositions of grain boundaries of pure and alloyed Nb_3Sn and a theoretical analysis of their effects on flux pinning are also summarized. The scaling law for $J_c(\mu_0 H)$ is briefly discussed. Then, at the end of this chapter, advances that were made in the critical-current densities and the processing methods of the state-of-the-art Nb_3Sn multifilamentary wires are presented.

12.2 Superconducting Properties of Alloyed Nb_3Sn

12.2.1 Critical-Current Densities

As mentioned above, from late 1970 to early 1980, the alloy additions to the bronze-processed Nb_3Sn wires were extensively studied [3]. Among the many elemental additions to Nb_3Sn that were studied, the additions of Ta and Ti by small amounts turned out to be most effective in raising J_c in high magnetic fields, and they became very important for commercial applications of Nb_3Sn multifilamentary wires for production of magnets to create very high magnetic fields. This will be clear when the state-of-the-art Nb_3Sn wires are discussed at the end of this chapter. Figure 12.1 illustrates the effects of adding these elements on critical-current densities of the wires [9,10]. The alloying was accomplished through the use of alloyed Nb filaments with the respective elements. The effects of the additions are illustrated by plotting the $J_c(\mu_0 H)$ data in a so-called Kramer plot, i.e. $J_c^{1/2}(\mu_0 H)^{1/4}$ versus $\mu_0 H$ [14]. (The validity of this relationship derived from Kramer's theory is discussed in References [3] and [13]; extension of the theory is discussed below.) As shown in Figure 12.1, the additions made the values of extrapolated upper critical fields $\mu_0 H_{c2}$ and J_c in high fields increase substantially over those for pure Nb_3Sn, even though the values of low-field J_c are significantly smaller than those for pure Nb_3Sn. Since Nb_3Sn wires were used for producing high fields, $\mu_0 H \gg 10$ T, these findings became very important, as evidenced by
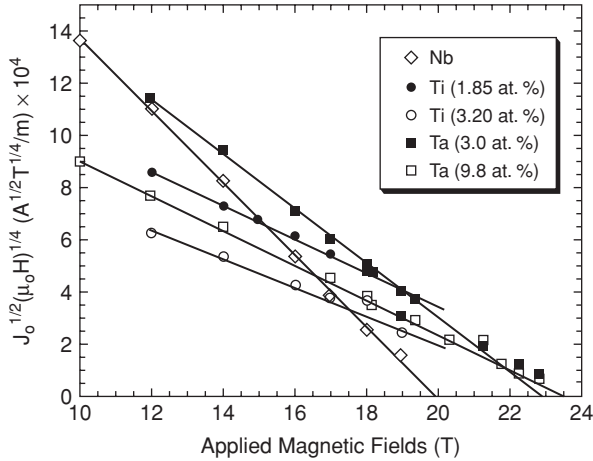
FIGURE 12.1. Variations in critical-current densities are shown as a function of applied magnetic fields for pure and alloyed Nb_3Sn monofilamentary wires. The alloy contents in parentheses are those present in Nb_3Sn.

the fact that all of the present wires contain Ta, Ti, or both of these elements. Although Ta can be added only though alloying Nb filaments, it was shown that Ti can be added through alloying the matrix in the bronze process [11] and the Sn cores in the internal-Sn process [15,16], as well as through alloying Nb filaments. The methods of adding Ti to the compound turned out to be much more diverse and provide more flexibility in fabrication of Ti-alloyed Nb_3Sn than for Ta. This can be seen in the recent development of the wires [17]. It should be noted that the wires in Figure 12.1 are monofilamentary wires with a ratio of 1:2 for the core to matrix diameters, and the chemical composition of the matrix was 13 wt% Cu. Since the superconducting properties of Nb_3Sn are strongly dependent on the ratios and the compositions, the $J_c(\mu_0 Hi)$ values shown in Figure 12.1 should be taken only for illustrating the effects of alloying Nb_3Sn. However, the differences in the slopes of the Kramer plots between those that are alloyed with Ta and those with Ti are intrinsic properties of these alloyed wires (see Section 12.4).

12.2.2 Intrinsic Superconducting Properties

As expected, alloying Nb_3Sn altered the intrinsic superconducting properties, such as critical temperature T_c and H_{c2}, through changes in its chemical composition. A thorough study of these parameters upon the alloying was performed for monofilamentary Nb_3Sn wires [18]. Here, the superconducting properties of Nb_3Sn alloyed with Ti and Ta are summarized from that article. In this study, in order to access the "intrinsic" superconducting properties of the Nb_3Sn layers, the properties were measured after the matrix was chemically removed. This was necessary because the compressive stress applied to the Nb_3Sn layers by the matrix (due to the differential
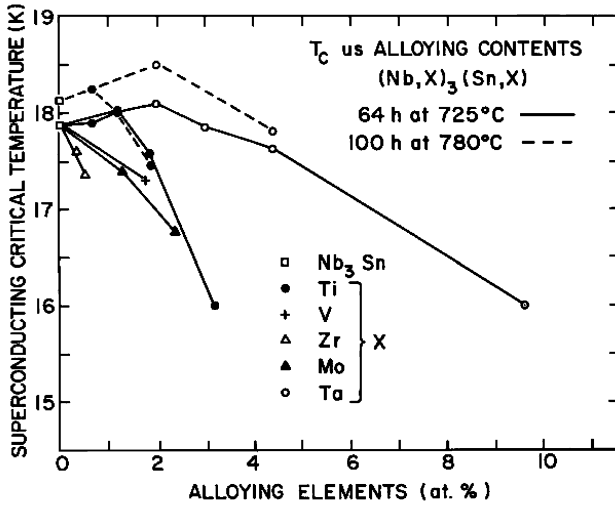
FIGURE 12.2. The effects of alloying Nb_3Sn on the critical temperatures of Nb_3Sn are shown as a function of alloying compositions. The wires were heat-treated at 725 °C for 120 h, and the bronze matrix was removed prior to the measurements [18]. Reprinted with permission from *J. Appl. Phys.* Copyright © 1986 by American Institute of Physics.

thermal contraction between the matrix and the superconducting core, Nb_3Sn and unreacted Nb) significantly lowered its superconducting properties. The degree of the reduction was dependent on the volumetric ratio of the superconducting core to the matrix [19,20].

Figure 12.2 shows the variations of T_c as a function of various alloying elements. Of particular interest are the variations with Ti and Ta additions. In both cases, small (~0.2–0.3 K) increases in T_c were observed at small alloying contents by these elements, and T_c peaked at ~1 at.% and ~3 at.% additions of Ti and Ta respectively. The additional alloying by these elements resulted in lowering the T_c. These data were taken from those wires that were heated at 725 °C for 64 h. As shown, the T_c of the wires could be made higher if the wires were heat treated at higher temperatures and longer periods, e.g. 780 °C for 100 h. This is likely due to the increased degrees of atomic ordering of the compound by higher and longer heat treatments. However, since J_c generally decreased with increasing heat-treatment temperatures, lower temperatures (such as 700 and 725 °C) were often used for heat-treating these wires. Thus, data for the wires that were heated to 725 °C are shown here. The causes for the slight increases in T_c by the additions were not understood. Figure 12.3 summarizes the variations of $\mu_0 H_{c2}$ at 4.2 K due to the alloying. As is clearly seen, the values of $\mu_0 H_{c2}$ were significantly increased by the additions of Ta and Ti and, in both cases, increased by ~4 T. As described in detail in Reference [18], these increases were caused by the increased normal-state resistivity ρ_N of Nb_3Sn, since $\mu_0 H_{c2}$ is proportional to its resistivity.
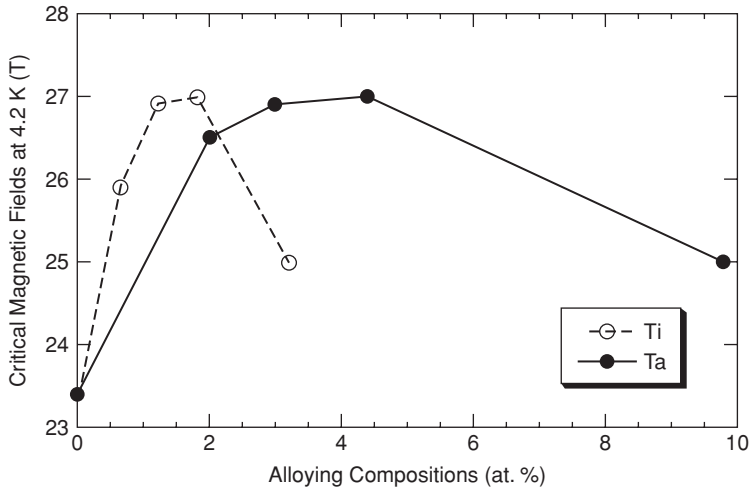
FIGURE 12.3. Critical magnetic fields dependence of Nb_3Sn alloyed with Ta and Ti on the alloying contents are shown. The values of the critical fields are for $T = 4.2$ K. The wires were heat-treated at 725 °C for 120 h, and the bronze matrix was removed prior to the measurements [18]. Reprinted with permission from *J. Appl. Phys.* Copyright © 1986 by American Institute of Physics.

In the case of Ti additions, it was found that the resistivity increased approximately linearly from ~0.1 m$\Omega \cdot$ m for pure Nb_3Sn to ~0.5 m$\Omega \cdot$ m by 3 at.% addition of Ti. This large increase was likely due to some fraction of Ti substituting in the Sn site as well as those of Nb, as discussed below.

12.3 Chemical Compositions of Alloyed Nb_3Sn

12.3.1 Bulk Compositions

To relate the effects of alloying on T_c and H_{c2}, the average compositions of alloyed Nb_3Sn layers were measured by using a wavelength-dispersive X-ray spectrometer attached to a scanning electron microscope. The results are given in Table 12.1 [18]. As shown in Table 12.1, only a fraction of Ti in the Nb core (approximately one-half) was incorporated into the Nb_3Sn layers. On the other hand, Ta was incorporated nearly totally in the core. Another notable difference in the compositions of Nb_3Sn layers, which are alloyed by Ti and Ta, was the difference in the Sn contents in the Nb_3Sn layers. As shown in Figure 12.4, the additions of Ti had a very strong effect on the Sn contents of the Nb_3Sn layers. For example, 3.2 at.% incorporation of Ti in the compound resulted in 2.7 at.% reduction in the Sn content, whereas only a small reduction in Nb (~0.5 at.%) was observed. On the other hand, 3.0 at.% Ta addition to the compound reduced the Sn content by a 0.9 at.%, whereas Nb was reduced by 2.7 at.%. These data indicate that Ta primarily replaced Nb, whereas Ti surprisingly substituted a significant amount

TABLE 12.1. Chemical composition of Nb_3Sn in the bulk and at grain boundaries

Nb core composition	Heat-treatment (°C/h)	Bulk composition[a] (at.%)				Grain boundary composition[b] (at.%)			
		Nb	X	Sn	Cu	Nb	X	Sn	Cu
Nb	775/64	74.3	–	24.2	1.5	55.5	–	27.8	16.7
Nb 2.2 at.% Ti	725/120	75	1.2	22.2	1.6	52.5	2.8	30.7	14.3
	750/64					55.2	2.4	29.5	12.8
Nb 3.3 at.% Ti	725/120	74.8	2	21.3	1.9	49.3	5.7	29.9	15.1
	750/64					51.5	5.1	30.3	13.1
Nb 6.4 at.% Ti	725/120	74.9	3.2	21.9	1.1	52.7	7.3	28.3	11.8
	750/64					50.4	7.7	29.1	12.8
Nb 8.2 at.% Ti	725/120	74	4.6	20.3	1.1	48.5	8.8	29.3	13.3
	750/64					48.8	9.7	27.5	13.4
Nb 2.2 at.% Ta	725/120	74.4	2	23.7	1.2				
Nb 4.0 at.% Ta	725/120	72.7	3	24.2	0.8				
Nb 5.6 at.% Ta	725/120	71.2	4.4	24.5	0.8	47.5	6.4	29.6	16.6
Nb 8.7 at.% Ta	750/300	68.8	6.4	23.5	1.2	59.4	8.6	24.1	7.8
Nb (Sn dip)	950/4	75.1		24.9		65.8		34.2	
						44.6		55.3	

[a]By wavelength spectrometer on a scanning electron microscope.
[b]By scanning Auger microprobe, and the corrections for the backgrounds for Nb, Sn, and Cu and for the changes in the Auger intensities due to the surface oxygen contamination at the surface are not included.
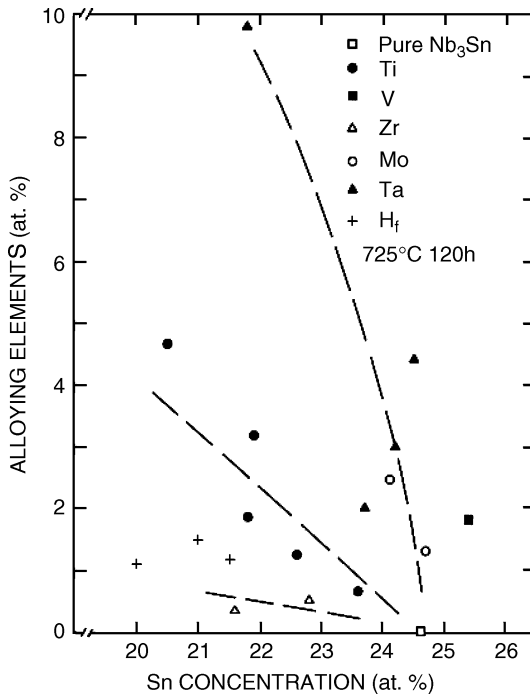
FIGURE 12.4. The relationship between the alloying and Sn contents in alloyed Nb_3Sn [18]. Reprinted with permission from *J. Appl. Phys.* Copyright © 1986 by American Institute of Physics.
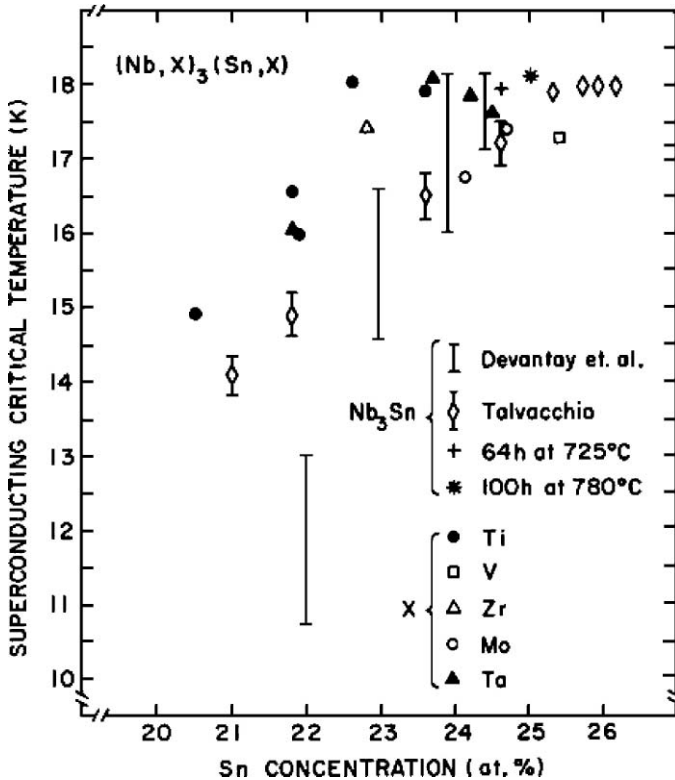
FIGURE 12.5. Superconducting critical temperatures as a function of Sn contents for pure and alloyed Nb_3Sn that were made by different processes [18]. Reprinted with permission from *J. Appl. Phys.* Copyright © 1986 by American Institute of Physics.

for the Sn site. Another interesting observation arising from these composition measurements was the fact that the effects of the reduction of the Sn content on lowering T_c of Nb_3Sn layers were much weaker in these alloyed Nb_3Sn samples than those which were found for pure nonstoichiometric Nb_3Sn made by other means. This was particularly notable for the Ti additions, as shown in Figure 12.5 [18]. As shown, T_c for the Nb_3Sn alloyed by Ta and Ti, which were made by the bronze process, hardly changed up to ~3 at.% reduction in the Sn contents. On the other hand, as also shown in Figure 12.5, T_c for pure nonstoichiometric Nb_3Sn made by electron-beam evaporation [21] and bulk-sintering [22] methods decreased by more than 2 K for the same reduction in the Sn content.

12.3.2 Grain-Boundary Compositions

As mentioned above, the grain boundaries are the diffusion path for Sn, which migrates from the Cu–Sn matrix to the Nb–Nb_3Sn interface for the growth of

the compound layer. Also, Sn is the primary diffusing species for this compound formation, as evidenced by the formation of Kirkendall voids at the Nb_3Sn–(Cu–Sn) matrix interface. However, beyond this knowledge, very little was known about the nature of the boundaries in 1980. For example, the growth rate of the compound layer was shown to depend on the Sn content in the matrix, i.e. the higher the Sn content, the faster the layer growth rates [23]. Yet, it was not clear how the grain-boundary diffusion mechanism can describe this observed phenomenon. To explain this, Welch postulated that the Sn content (or the chemical activity of Sn) in the boundary had to be higher than that in the grain interior [24]. Then, the Sn gradient in the boundaries across the layer could be varied, depending on the composition of the matrix, and, thus, the growth rate would be varied accordingly (see Reference [3]). Also, a small amount (∼1 at.%) of Cu was always detected in the average composition of the compound layers, and Cu was suspected to be in the grain boundaries rather than in the interior of the grains. In addition, it was well known that the boundaries are the flux-pinning centers in A15 compounds, as mentioned above, and the strength of the boundary pinning was expected to depend on the degrees of the crystallographic disorder and the thickness of the boundaries. Thus, to clarify these questions, it was important to determine experimentally the compositions and the thickness of the boundaries in pure and alloyed Nb_3Sn layers that are made by the bronze process.

The determination of the chemical composition of the grain boundaries of Nb_3Sn layers by Auger electron spectroscopy revealed that the composition of the boundary was very different from the stoichiomentric values: 44.1 at.%, 30.6 at.%, and 25.4 at.% for Nb, Sn, and Cu respectively for pure Nb_3Sn [25]. In addition, no Cu signal was detected in the interior of the grains. These results clearly confirmed the above two postulates about the grain boundary compositions, i.e. a higher Sn content than the stoichiometeric value and Cu being concentrated at the boundaries. These measurements were made on the in-situ-fractured Nb_3Sn tapes, which were made such that the original Nb layer was fully reacted to form Nb_3Sn. These tapes contained several abnormally grown Nb_3Sn grains of >10 μm in diameter among the smaller grains. The large grains fractured transgranularly, while the small grains fractured intergranularly. One very important aspect of having these two types of fractured surface was related to solving the usual problem of the use of an ion-sputtering technique to perform depth profiling for the compositional changes into the grain interior from the surface. Normally, it is not possible to obtain a reliable composition as a function of the depth by this method, since there are large differential sputtering rates, particularly between Nb and Sn. This problem was minimized by ascertaining the differential sputtering rate from the data taken at the transglanularly fractured surfaces. In practice, the data were obtained by taking the differences of the concentrations from each of these two regions as a function of the depth. The results of the compositional depth profiling for the Nb deficiency from the stoichiometric value are shown in Figure 12.6. This shows that the compositionally disordered region of the boundary had a significant depth (1–2 nm), and this information was important for the analysis of grain-boundary flux pinning.
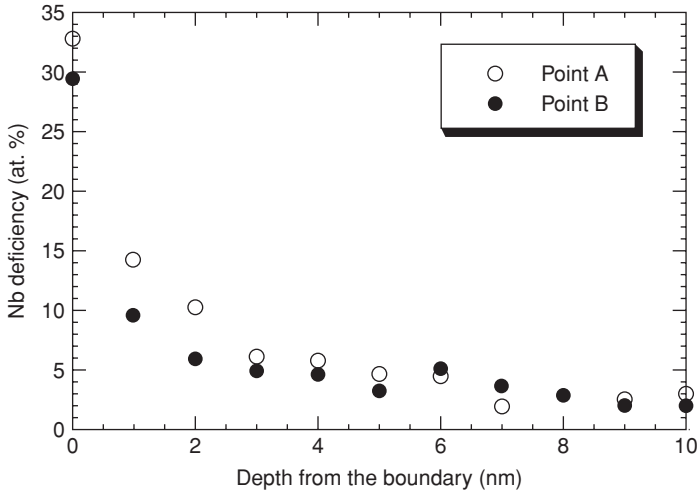
FIGURE 12.6. Deficiency in stoichiometric value at the Nb_3Sn grain boundary and its variations with depth into the interior of the grains.

Alloying Nb_3Sn is also expected to alter the compositions of the grain boundaries of the compounds. To observe the compositional changes at the boundaries from that of unalloyed Nb_3Sn, the boundary compositions were measured for primarily Ti-alloyed Nb_3Sn by the bronze process; the results are also shown in Table 12.1 [26]. One consistent trend observed in Table 12.1 is that the amounts of Ti in the boundaries are essentially twice that within the grains, as shown in Figure 12.7. This may be related to Ti having a strong affinity to Cu in forming their compounds. Other elements, Nb, Sn, and Cu in the boundaries, changed by smaller amounts with the Ti additions, and no consistent variations of their amounts were observed. On the other hand, Ta in the boundaries was substantially less than that in the grains, and the amount of Cu in the boundary was nearly one-half that in the boundary of pure and alloyed Nb_3Sn. Also, in one attempt to determine the effects of alloying Nb_3Sn on the grain-boundary thickness for alloyed Nb_3Sn, a depth profile for the compositions was performed for Nb_3Sn that was alloyed with 1.2 at.% Ti. This indicated that the boundaries were significantly thicker (~5 nm) than for pure Nb_3Sn. This may not be too surprising, since, as shown in Figure 12.7, the concentration of Ti in the boundary is substantially greater than in the grain interior. Although further measurements are needed, this has significant implications for the pinning strength of a boundary.

The other interesting data in Table 12.1 are the boundary compositions of "pure" Nb_3Sn, which was made from an Sn-coated Nb foil. These boundaries also exhibited very large deviations from the stoichiometric value. (The commercial Nb_3Sn tapes by the Sn-dipping process contained Cu for the enhancement
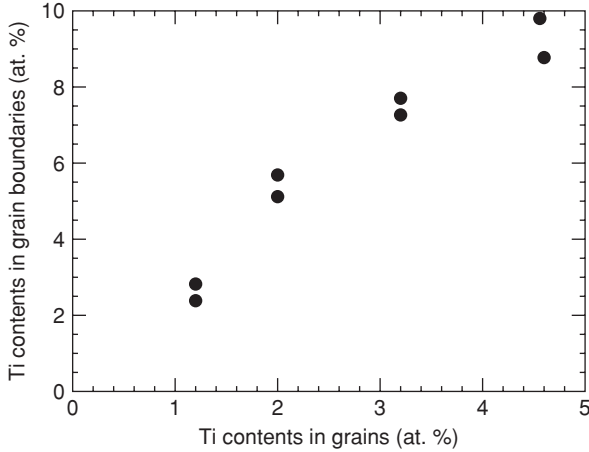
FIGURE 12.7. The Ti contents for Nb_3Sn at the grain boundaries and the interior of the grains are compared for Ti-alloyed Nb_3Sn.

of the growth rates, but the present tape was made without the Cu addition.) Two different compositions cited in Table 12.1 came from two different regions of the compound layer, and it was not clear why such a large difference was found. However, it is clear that the deviations, which were seen in the boundaries of the bronze-processed Nb_3Sn, are not special properties of the method that was used to fabricate Nb_3Sn, but are a general property of the boundary in this compound.

12.4 Effects of Alloying on Layer and Grain Growth

Alloying of the compound also affects the growth of its layers and grain sizes. The compound thicknesses and the grain sizes of Nb_3Sn with Ta and Ti additions are plotted in Figure 12.8 as a function of the alloying contents (in atomic percent) in the compounds after each wire was heat-treated for 64 h at 725 °C. It is clearly noted that the effects of the additions by Ti and Ta were quite different on the growth of the compound layers and their grain sizes. The Ti additions rapidly increased the growth of the layers, as well as the grain sizes, with increasing amounts of Ti. (A sudden drop in the layer thickness at a Ti concentration of $\sim$4 at.% in Figure 12.8 is due to the formation of a nonsuperconducting layer between Nb_3Sn and the matrix.) However, the increases in the thicknesses and grain sizes by the Ta additions were much less than those by the Ti additions, and they saturated at high alloying contents. Another interesting observation from Figure 12.8 is that the rates of the increases in the thicknesses and the grain sizes per atomic percent of the additions are very similar for each elemental addition for Ti and Ta when
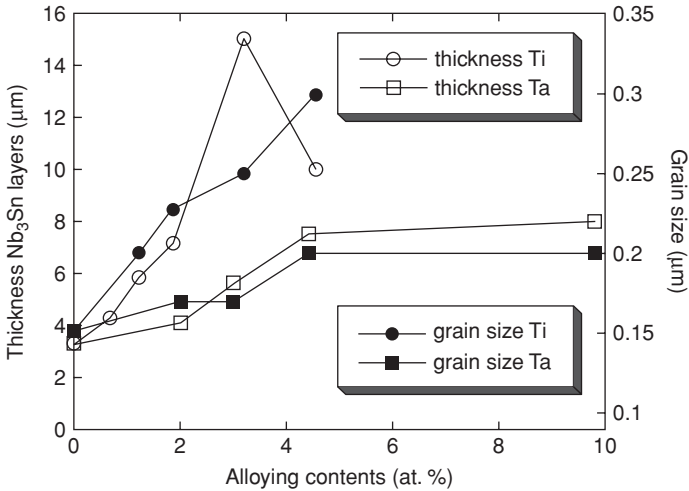
FIGURE 12.8. Effects of alloying on grain and layer growth are shown as a function of the alloying contents, Ta and Ti.

the thickness and the grain-size scales are normalized. The very significant rates of the increase in the thicknesses that were found with the Ti additions suggested that the grain-boundary diffusion rates of Sn toward the reaction front were increased by a substantial amount. However, the grains grew quite rapidly with increasing amounts of Ti in the compound, and the enlarged grains reduced the total area of the grain boundaries in the compound for the grain boundary-diffusion of Sn. Thus, the growth rate could be lowered by the additions. However, the rapidly increased growth rates suggested that the addition also increased the bulk diffusion rates of Sn and Nb. This is supported by the fact that the grain sizes also increased similarly with the layer thickness, since the increased grain growth could take place only with the increased bulk diffusion rates of Sn and Nb. As mentioned above, a good fraction of Ti substitutes for the Sn site in the compound and may be the source of the increased bulk diffusion rate. Furthermore, the difference in the rates of grain growth per atomic additions between those by Ta and Ti explains the difference in the changes in the slopes for the Kramer plots (shown in Figure 12.1) for these additions. For example, a 1.85 at.% addition of Ti resulted in a much smaller slope of the Kramer plot than that obtained by a 3.0 at.% Ta addition. As discussed below, the slopes are inversely proportional to the square root of the grain size. Thus, the larger grain sizes in the Ti-alloyed Nb_3Sn with respect to those of the Ta-alloyed Nb_3Sn resulted in lower slopes for the former than those observed for the latter. This difference in the slopes appears to be an intrinsic property of these elemental additions, since a similar difference was reported for the multifilamentary Nb_3Sn wires, which were alloyed with Ta or Ti, for ITER-EDA [27].

12.5 Flux-Line Pinning and Field Dependence of Critical Currents

12.5.1 Flux Pinning by Grain Boundaries

As mentioned earlier, critical-current densities of A15 compounds are inversely proportional to the grain size, and this is a strong indication of the boundaries being the primary flux-line pinning centers in these compounds. The pinning of flux lines by the boundaries was thought to be due mainly to the changes in the local values of the Ginzburg–Landau constant κ [$=H_{c2}/(2H_c)^{0.5} = \lambda(T)/\xi(T)$] caused by the dispersive scattering of the normal-state electrons at the boundaries. This was often referred to as $\delta\kappa$ pinning. The first theoretical attempt to estimate the pinning force per unit length of a flux line by a boundary was made by Zerweck [28]. He considered the pinning potential from altered condensation energy due to the change in the size and the shape of the flux-line core caused by the electron scattering by an infinitely thin boundary. Following Zerweck, Yetter et al. [29] treated the case where a rigid flux lattice interacts with a boundary. In both of these cases, the results were obtained numerically. Following these studies, Welch [30] obtained an expression for the interaction in a closed form that was suitable for computer simulation for the interaction of a flux line with a boundary, and it was "physically transparent in its interpretation." Moreover, his treatment was suitable for analyzing the interaction from nonideal boundaries, such as for the boundaries in the bronze-processed Nb_3Sn.

Here, we summarize Welch's work, which approximated the interaction energy ΔE of the flux line and the boundary by using the Ginzberg–Landau first-order perturbational approach and arrived at the pinning force F by the boundary as

$$\frac{F}{\mu_0 H_c^2 \xi_0} = \pi \frac{\xi}{d\xi_0} \left(\frac{\Delta\kappa}{\kappa}\right)_0 \frac{1}{1 + 2.0\,(\xi/d) + 2.32\,(\xi/d)^2}, \tag{12.1}$$

where ξ_0 and ξ are the BCS and the Ginzburg–Landau coherence lengths respectively, and d is the exponential decay length of κ away from the boundary. Both of ξ and κ depend on the electron mean free path l and are characterized by the impurity parameter α ($=0.882\xi_0/l$). Approximate expressions for these in terms of α are given as

$$(\xi/\xi_0)_{T=0} = (1.83 + 1.63\alpha)^{-1/2} \tag{12.2}$$

and

$$(\Delta\kappa/\kappa)_0 = 1.63\,(1.83 + 1.63\alpha)^{-1}. \tag{12.3}$$

Thus, it is convenient to plot the pinning force in terms of α, as shown in Figure 12.9 [30]. The result is the interaction force for a single flux line with an infinitely thin boundary (solid line) that increases and then decreases after reaching a peak value with increasing value of α. This result was similar to Zerweck's, even though Welch calculated the pinning force F from the first-order change in energy
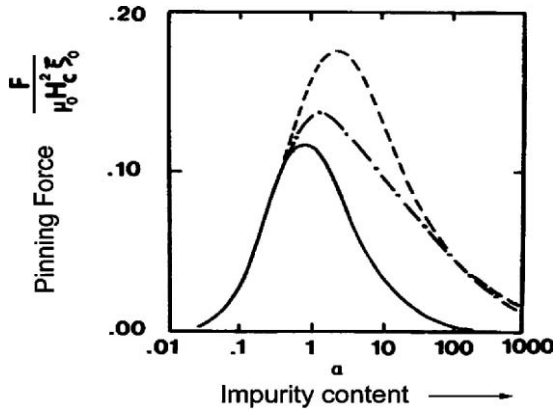
FIGURE 12.9. The normalized pinning force density as a function of impurity parameter α. The solid curve is for the ideal boundary, the dot–dash curve is for a boundary with the effective width enhanced by a constant value $\Delta d = 0.1\xi_0$, and the dashed curve is for a boundary with effective width enhanced to the optimum size of $d = 1.5\xi$ [30]. Copyright © 1984 by the Institute of Electrical and Electronic Engineering, Inc.

due to the change in κ while keeping the core size constant. The dot–dash curve is for the case in which a constant width, $\Delta d = 0.1\xi_0$, was added to the boundary width d. As shown in Figure 12.9, this caused a small increase in the peak value of the pinning force at a slightly larger value of α. Talvacchio [21] also obtained a similar result by using the method of Yetter et al., i.e. the interaction of the rigid flux-line lattice with the boundary, but he added a constant boundary width of $\Delta d = 0.5$ nm. For pure Nb_3Sn, these additions would not make a significant difference in F, since its value of α is 0.56, just below the peak in the solid line where the thickness of the boundary has very little effect on F. The dashed curve in the figure is the envelope of F for the case in which the optimum d ($\sim1.5\xi$) is added for each α, showing a possibility of increasing the pinning force by increasing the thickness of the boundary.

Since the resistivity and T_c values are available for pure and Ti-alloyed Nb_3Sn by the bronze process [18], we can calculate the values of α and examine whether the pinning strength of the bronze-processed Nb_3Sn can be improved by varying α or the thickness of the boundaries. The resistivities of pure and (3.2 at.%) Ti-alloyed Nb_3Sn by the bronze process (whose T_c is 16 K) are approximately 1 mΩ and 5.5 mΩ m respectively. These give electron mean free paths l of 9 nm and 1.6 nm respectively. The values of ξ_0 are 5.7 nm and 7.7 nm for T_c values of 18 K and 16 K for the pure and the alloyed Nb_3Sn respectively. These values were taken from those for the stoichiometric and nonstoichiometric Nb_3Sn films with the same T_c values by electron-beam evaporation [31]. Then, the impurity parameters α are 0.56 and 4.13 for the pure and the alloyed Nb_3Sn respectively. These values of α are comparable to those found by Talvacchio for stoichiometric and nonstoichiometric Nb_3Sn films by electron-beam evaporation, i.e. $\alpha \approx 0.5$–3.0

[21]. This range of α is an interesting region in Figure 12.9, since it covers the region of α where the maximum pinning force is accessible.

For pure Nb_3Sn without the boundary distortion, the pinning force for $\alpha = 0.56$ is slightly below the maximum value. Interestingly, the increase in thickness by 1 nm to 2 nm, as observed above, or those additions of $\Delta d \approx 0.5$ nm or $\Delta d = 0.1\xi_0 \approx 0.6$ nm will not enhance the pinning strength very much. This is because the value of α is in the region where the effect of the increased thickness has very little influence on F. However, owing to the increased values of α and the increased thickness of the boundary in the Ti-alloyed Nb_3Sn, there is a strong possibility for a substantial increase (by $\sim$50%) in the pinning strength of the boundary of the optimally alloyed Nb_3Sn over that for the boundary in pure Nb_3Sn. For example, T_c for Nb_3Sn with 1.2 at.% Ti is $\sim$18 K and its resistivity is $\sim$3 mΩ m. Then, $\alpha \approx$ 1.67, and the optimum thickness of the boundary is $d \approx 1.5\xi \approx 4$ nm. Also, as discussed above, a significant increase in the boundary width ($\sim$5 nm) was observed by the Ti addition. Thus, this particular composition or a slightly larger Ti addition could be near the optimum in the pinning strength F. Unfortunately, it is difficult to assess whether such increases in F are realized by the additions in the $J_c(\mu_0 H)$ data in Figure 12.1 or similar data, since the additions cause rapid grain growth (a factor of two in the same range of Ti alloying; see Figure 12.8), which reduces $J_c(\mu_0 H)$ by the same amount. Also, the above theoretical calculation is for the interaction of a single flux line with the boundary, whereas most of the $J_c(\mu_0 H)$ available data are only for high magnetic fields. These facts make a direct comparison of J_c data and the above theoretical results difficult. More detailed measurements of $J_c(\mu_0 H)$ at lower fields and grain sizes are needed to clarify the above observation.

12.5.2 Scaling Law for $J_c(\mu_0 H)$

In 1973, Kramer identified the important role of flux-line lattice shear in critical-current densities of superconducting materials displaying a global pinning force varying predominantly as $(1 - b)^2$ in high magnetic fields, where $b = B/B_{c2}$ [12]. A rearranged form of his expression for the global pinning force in high fields was extensively used for characterizing the high-field behavior of $J_c(B)$ and for approximating upper critical fields of Nb_3Sn wires. This is given by

$$J_c^{1/2} B^{1/4} = 1.18 \times 10^5 \frac{B_{c2}}{\kappa}(1 - b) \tag{12.4}$$

in the limit of $a_0 \rho^{0.5} \ll 1$, where $a_0 [=(\phi_0/B)^{1/2}]$ is the flux-line lattice spacing and ρ is the pinning site density. It was found that most of $J_c(B)$ for Nb_3Sn wires follow this expression, i.e. $J_c^{1/2} B^{1/4}$, is linear with b. (Thus, these plots are called Kramer plots.) The main success of the model is that the straight line can be fitted to the data in high fields, as shown in Figure 12.1. However, this expression is applicable for $a_0 \rho^{0.5} \ll 1$, and this means that there is no dependence of J_c on the pinning density. On the contrary, J_c of these wires depends strongly on the grain size of the compound, as noted for the data in Figure 12.1. Another difficulty was

seen in the values of κ extracted from the slopes of Kramer plots. These had little relation to known κ values of the compound and also varied quite inconsistently with varying reaction treatments for a given wire [3,13].

As pointed out by Evetts and Plummer [32], the difficulty associated with the theory did not take into account the fact that the lattice shear took place between regions that are weakly pinned and others that are strongly pinned. The size of these regions is critical in the determination of the pinning force [32]. To remedy this situation, they assumed that each grain supported independently a Lorentz force approaching that required to initiate flux shear within the grain. Then, on the basis of dimensional analysis, they suggested the maximum shear τ_{max} is given by

$$\tau_{max} = \frac{c_{66}}{\pi} = \frac{1}{2}(J_c B)\frac{D^3}{D^2}, \tag{12.5}$$

where c_{66} is the shear constant for the lattice and D is the grain size or the channel size for the regions of the lattice which are in motion. Then, an equivalent expression to Equation (12.4) is

$$(J_c B)^{1/2} = 2.7 \times 10^2 \frac{B_{c2}}{\kappa D^{1/2}}(1-b). \tag{12.6}$$

Plotting $J_c(B)$ data for Nb_3Sn following this expression shows that $(J_c B)^{1/2}$ has a significant region where it is linear with B at the highest fields. The extrapolated B_{c2} values are very slightly greater than those obtained from Equation (12.4). Also, this expression has an explicit dependence of J_c on the grain size.

A more rigorous phenomenological model was developed by Welch [33] for the flux-line lattice shear related to the pinning force. One of the important aspects of his model is the following. Analogous to the theory of plastic flow of metals [34], he suggested that the critical shear stress in the flux-line lattice should be modified as

$$\tau_{max} = \frac{c_{66}}{L}a_0, \tag{12.7}$$

where L is the characteristic length scale of the dislocation structure of the flux-line lattice with the flux-line lattice spacing a_0. Very interestingly, this modification recovers the B dependence of J_c in the form of Equation (12.4) with the effective grain size or the channel width as in Equation (12.6). Then, it appears that the use of the "Kramer plot" is qualitatively justified in characterizing the high-field behavior of Nb_3Sn wires if these modifications of Kramer's original theory are taken into consideration. However, a quantitative analysis is required to see, with these modifications, if one could examine whether the grain size is an appropriate dimension for the channel size for moving lattice regions and the appropriate values of κ are obtained. A further modification of the flux-line-shear model was discussed by Wordenweber [35]. This included the corrections for the orientations of the channels with respect to the Lorentz force and the nonuniformity of the channel sizes. In addition, the size of the flux channel D, as well as L, is likely to

be dependent on the applied field, and this may have to be taken into account to describe the high-field behavior of $J_c(\mu_0 H)$.

12.6 The State-of-the-Art Multifilamentary Nb$_3$Sn Wires

As mentioned at the beginning, tremendous progress in improvements in $J_c(\mu_0 H)$ of multifilamentary Nb$_3$Sn wires has been made over the last several years. A brief summary is given for high values of $J_c(\mu_0 H)$ being achieved in the state-of-the-art wires which are made by two main processes, i.e. the bronze process and the internal-Sn process. The so-called powder-in-tube processes are currently making a resurgence in Europe [36] and Japan [37]. This method relies on the reaction of the powders in Nb tubes in a copper matrix to form Nb$_3$Sn after the composite has been reduced in size. The powders are generally a high-Sn–(Nb-Sn) compound with some additional Cu. The first Nb$_3$Sn wire was made by this approach 44 years ago by Kunzler et al. [38], except that they used preformed Nb$_3$Sn powders. The development of multifilamentary wires by this process was started at Netherlands Energy Research Foundation in 1979, and they used NbSn$_2$ and Cu powders [39]. This was recently picked up by Shape Memory Innovation, and some of their reported critical currents for these wires are promising [36]. A similar effort started at Kobe Steel Ltd provides some encouraging results. In this case, a powder of Ta–Sn intermetallic phases with Cu was used in Ta-alloyed Nb tubes [37]. However, it appears that these processing methods require further development to establish their compatibility for large-scale fabrication in order to compete with the already well-established processes, the internal-Sn or the bronze-processed wires, in terms of cost [40] and in J_c values at very high fields [41–43]. Thus, we limit our discussion of critical-current densities in wires made by the above-mentioned two processes that have survived the test of time. Recently, detailed reviews for the development of wires in the US have been published by Scanlan et al. [40] and Gregory [44]. The former described the conductor development program for high-energy particle accelerators, and the latter summarized the development at Intermagnetics General Corp./Advanced Superconductors (IGC/AS) (now Outokumpo Advanced Superconductors) for ITER-EDA and high-energy physics applications.

12.6.1 The Bronze Process

As noted previously, this original process for fabricating multifilamentary superconducting wires with brittle intermetallic compounds was used extensively in the early years. The use of Nb$_3$Sn wires made by this process has diminished somewhat in recent years due to the limitation in achieving very high non-Cu current densities (the critical currents divided by the area excluding pure Cu for the stabilization). This limitation arises from the fact that the available Sn for the formation of Nb$_3$Sn is limited by the solid-solution phase boundary for the Cu–Sn system. (The maximum solubility of Sn in Cu is 15.8 wt% at $\sim$500 °C. But, generally, the matrix contents of Sn that were used in multifilamentary wires of Nb$_3$Sn were

limited to the order of ∼13 wt%, since it was difficult to make truly uniform large bronze billets with high-Sn contents.) However, the wires made by this process have still been playing an important role for two major high-field magnet applications. These are magnets for high-frequency NMR spectroscopy and ITER-EDA. Perhaps it is not very surprising that the wires made by this process have played, and still are expected to play, an important role in the ITER-EDA and the future ITER project. This is because its requirements for the non-Cu J_c are relatively modest, and its requirements for hysteresis losses are quite strict in comparison with those for high-energy particle accelerator applications. The hysteresis losses, which are proportional to the size of the filaments, are generally low in bronze-processed Nb_3Sn wires because the filaments are separated.

The development of wires by this method for 930 kHz NMR magnets [45,46] was surprising, since it required a high overall current density at very high magnetic fields, ∼22 T. (This is currently the highest frequency NMR system.) This was accomplished by increasing the Sn content in the bronze matrix for the wires beyond the solid-solution limit, although by a small amount, in conjunction with a small addition of Ti in the matrix. This extra Sn addition helped to grow the Nb_3Sn layers with more equiaxed grains than a lower Sn-content matrix. The equiaxed grains provided higher current densities. However, the uses of the bronze-processed wires for these applications are probably at the limit of their usefulness. For example, future magnetic fusion reactors, beyond the ITER project, would most likely require magnets that can produce magnetic fields on the order of 16 to 20 T. Similarly, magnets for higher frequency NMR systems would require fields significantly higher than 22 T, and this would be very difficult to produce for magnets employing bronze-processed wires.

12.6.2 The Internal-Sn Process

This process was the first modification to the bronze process for the fabrication of multifilamentary Nb_3Sn wires, and was reported in 1977 by Hashimoto et al. [47] to overcome the limitation in the Sn content in the bronze matrix and to avoid the extensive annealing process required for the bronze process during the reduction in size of the composite. In spite of the possible advantages over the bronze process, its development was not pursued extensively until the mid-1980s [15,16,48–50], and serious development of the wires by this process came for the ITER project in the mid to late 1990s. Interestingly, the development of this processing method for the wires started in the US by Zietlin [51], then at IGC/AS, after hearing about the process in 1980 at the first meeting for "the US–Japan collaboration on high-magnetic-field superconductors for the Magnetic Fusion Program in US and Japan." Since then, wires that were made by this process from the Japanese and the US program have contributed substantially toward the construction of the magnets for ITER-EDA. After the US terminated its ITER participation (recently, it has rejoined ITER), the US manufacturers of superconducting wires responded to the US conductor development program by the Office of High Energy Physics, US Department of Energy (DOE) in 1999. The goals of the program were (1)
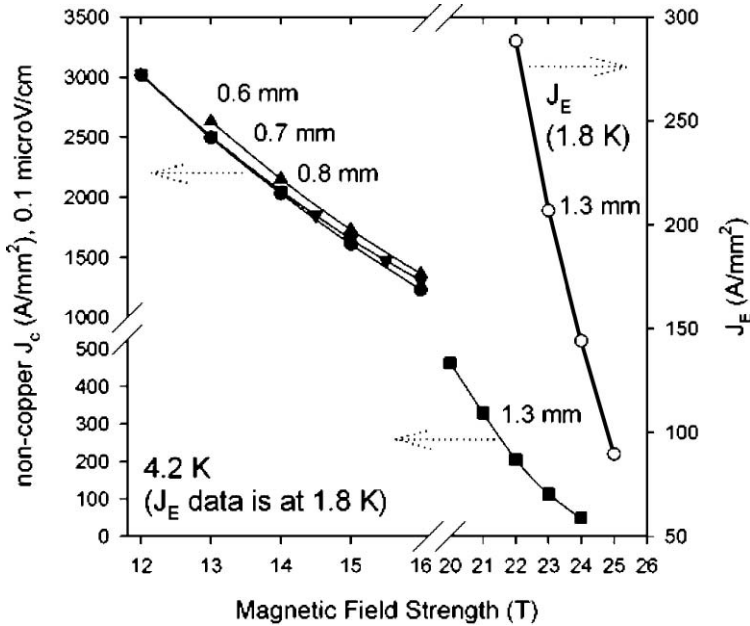
FIGURE 12.10. Critical current densities of an internal-tin-processed Nb_3Sn wire as a function of applied magnetic fields at 4.2 K and 1.8 K [43]. Copyright 2005 © by the Institute of Electrical and Electronic Engineering, Inc.

to increase J_c at 12 T and 4.2 K to a 3000 A/mm^2 level (non-Cu area), which was an increase of J_c by over 50% from the values achieved at that time, and (2) to reduce the cost for the next-generation particle accelerators for high-energy physics experiments. To achieve such high current densities in Nb_3Sn wires, it was essential to have substantially larger amounts of Sn and Nb available in the matrix than could be achieved in the bronze process. For this purpose, the internal-Sn process was very suitable. Thus, all the US manufacturers employed this approach for their wire development. The J_c values increased every year; and, as shown in Figure 12.10, for example, Oxford Instrument-Superconductor Technology produced wires with J_c values well above the US DOE goal by 2004 [41–43]. The next goal for the manufacturers was to reduce the effective filament sizes that were needed for meeting the magnetic-field quality requirements in accelerator magnets. This became necessary because the Nb_3Sn filaments are merged together to form a large single filament within the diffusion barrier (a subelement), since the amounts of Nb filaments and Sn within the barrier have to be increased so much to meet the goal for J_c in the program.

One of the important benefits in the above development of high-current-density wires was their application to very high-magnetic-field magnets for NMR spectroscopy, since the relatively large filament size was not an issue for this application. By taking advantage of these high J_c values in high fields, it is reported that these
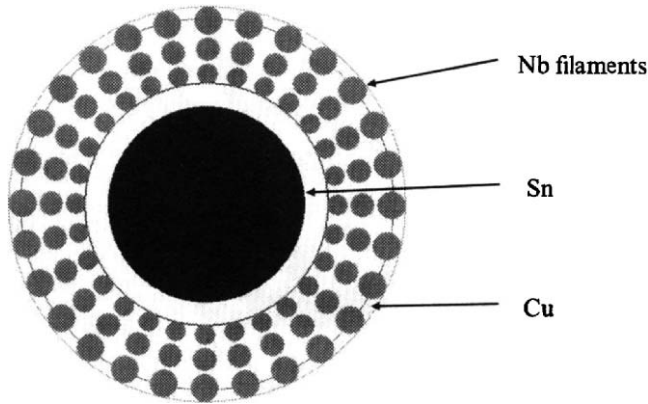
FIGURE 12.11. The arrangement of the superconducting filaments in the subelement is illustrated. This leads to lowering of the hysteresis losses in the multifilamentary Nb_3Sn wires by the internal tin process [53]. Copyright © 2004 the Cryogenic Society of Japan.

wires are currently being used to construct a 950 MHz NMR system, and the possibility of using these wires in the construction of a magnet for a 1 GHz MNR system, which requires a $\sim$25 T magnet, is also being discussed [52]. As seen by these examples, very impressive progress has been made in terms of increased critical-current densities in these wires, but very little has been discussed about how precisely the Sn from the core migrates through the interfilamentary spaces and reacts with the Nb to form Nb_3Sn. The overall Sn content for the wires is so high that the matrix area between the filaments is no longer a Cu–Sn bronze, as in the case of low-Sn-content wires. Thus, there is a distinct possibility that the Nb_3Sn is formed by the reaction between Nb and Cu_6Sn_5, or even possibly $CuSn_2$, rather than Nb and a solid-solution Cu–Sn alloy. A thorough investigation of the reaction to form Nb_3Sn will likely be beneficial for understanding the effects of different heat-treatments on the grain sizes and critical currents in these Nb_3Sn wires.

As mentioned above, this processing method will keep playing an ever-important role in producing a large amount of the wires that are required for the up-coming ITER construction. One of the interesting developments for this application is the recently reported modification of the Nb filament arrangement for the subelements to reduce AC (hysteresis) losses of the wires [53]. As a part of their wire development at Mitsubishi Electric Corporation, they placed Nb filaments radially rather than in the standard hexagonal pattern for the subelements, while the size of the filaments became larger from the inside to the outside, as shown in Figure 12.11. This type of wire retained the J_c values slightly above those (1000 A/mm^2) for the earlier similar wires for ITER, while reducing AC losses by one-fifth to $\sim$300 mJ/m^3.

Also, there are a number of ways in which Ti is incorporated in Nb_3Sn wires. One very interesting recent development is the method that was developed by the group at Oxford Instrument-Superconducting Technology: replacing a portion of
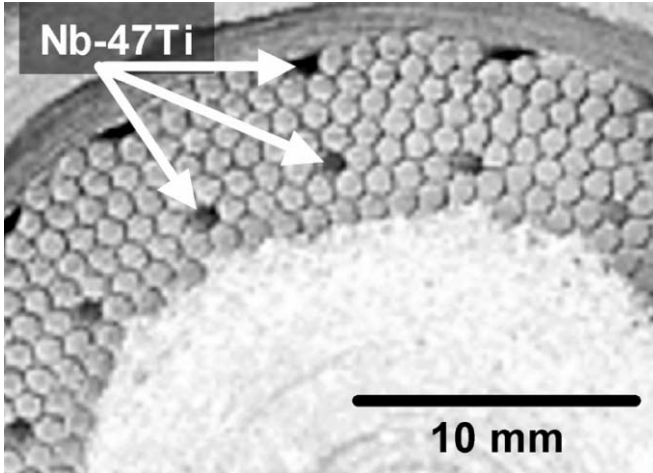
FIGURE 12.12. Cross-section of a high J_c subelement billet made with a mixture of pure Nb (lighter shade) and Nb–47 wt% Ti rods (darker shade). During heat-treatment the Nb–Ti rods dissolve, and the Ti diffuses throughout the subelement filament pack to form Ti-alloyed Nb_3Sn [43]. Copyright © 2005 by the Institute of Electrical and Electronic Engineering, Inc.

Nb rods in the initial assemblage of the composites by Nb–47% Ti alloy rods rather than using Ti-alloyed Nb rods or Sn cores to alloy Nb_3Sn [43]. Surprisingly, after reduction in size and heat-treatment, Ti in these filaments diffuses through the matrix, and alloys Nb_3Sn uniformly. Figure 12.12 shows the remains of Nb–47 wt% Ti alloy rods after the wire was fully reacted to form Nb_3Sn. (Note that Nb–47% Ti alloy is the most extensively used alloy for the commercial superconducting magnets.) On the other hand, the group at Mitsubishi Electric incorporates Ti into their wires by wrapping a pure Ti foil around each pure Nb rod [53,54]. Similarly, Gregory more recently demonstrated that Ti could also be incorporated by wrapping Nb–47 wt% Ti foil around the Nb rods [17]. The Ti in these methods is also distributed uniformly among the Nb_3Sn filaments, provided the amount of the Ti added is chosen appropriately. The properties of the Nb_3Sn wires alloyed by these methods were very similar to those alloyed by the conventional method of incorporating Ti into the compound through Ti-alloyed Nb filaments or the use of the Ti–Sn cores. The importance of these innovations is that they may reduce the cost of manufacturing the wires, since less expensive pure Nb rods rather than the more expensive alloyed Nb rods or the Sn core with Ti can be used in the assembly of the composites. These examples show that there is more room for improvement in the internal-Sn fabrication process of Nb_3Sn wires for high-magnetic-field applications. However, an interesting question, which is not addressed yet, is how Ti is incorporated into Nb_3Sn during these new ways of adding Ti into the wires. This may be related to the fact that the addition of Ti forms the compound through significant bulk diffusion of Sn and Nb, as mentioned

above. Obviously, this is an interesting problem that requires further studies to be clarified. Also, this understanding could possibly lead to further improvements in properties and processing methods for the wires.

References

1. Matthias, B.T., Geballe, T.H., Geller, S., and Corenzwit, E., *Phys. Rev.*, 95, 1435, 1954.
2. Howlett, E.W., Great Britain Pat. 52,623/69 (Filed Oct. 27, 1969). US Pat. 3,728,165 [Filed Oct. 19, 1970]. Kaufman, A.R., and Pickett, J.J., *Bull. Amer. Phys. Soc.*, 15, 833, 1970. Also, 1970 Applied Superconducting Conference, Boulder, Colorado. Tachikawa, K., *International Cryogenic Engineering Conference*, Berlin, 1970, Iliffe Sci. Tech. Pub., 1971, p. 339.
3. Suenaga, M., "Metallurgy of Continuous Filamentary A15 Superconductors," *Superconductor Materials Science: Metallurgy, Fabrication, and Applications*, Foner S., and Schwartz, B.B., eds., Plenum Press, New York, 1981. pp. 201–276.
4. Farrell, H.H., Gilmer, G.H., and Suenaga, M., *J. Appl. Phys.*, 45, 4025–4035, 1975; *Thin Solid Films*, 25, 253–264, 1975.
5. Togano, K., Asano, Y., and Tachikawa, K., *J. Less-Common Metals*, 68, 15, 1979.
6. Scanlan, R.M., Fietz, W.A., and Koch, E.F., *J. Appl. Phys.*, 46, 2244–2249, 1975.
7. Livingston, J.D., *Phys. Stat. Solidi A*, 44, 295, 1977.
8. Livingston, J.D., *IEEE Trans. Magn.*, 14, 611, 1978.
9. Suenaga, M., Aihara, K., Kaiho, K., and Luhman, T.S., "Superconducting Properties of $(Nb,Ta)_3Sn$ Wires Fabricated by the Bronze Process," *Advances in Cryogenic Engineering,* Vol. 26, Clark, A.F., and Reed, R.P., eds., Plenum Press, New York, 1980, pp. 442–450.
10. Suenaga, M., Okuda, S., Sabatini, R., Itoh, K., and Luhman, T.S., "Superconducting Properties of $(Nb,Ti)_3Sn$ Wires Fabricated by the Bronze Process," *Advances in Cryogenic Engineering,* Vol. 28, Reed, R.P., and Clark, A.F., eds., Plenum Press, New York, 1982, pp. 379–387.
11. Tachikawa, K., Asano, T., and Takeuchi, T., *Appl. Phys. Lett.*, 39, 766–768, 1981. Tachikawa, K., Takeuchi, T., Asano, T., Ikjima, Y., and Sekine, H., "Effects of the IVa Elemental Additions on Composite-Processed Nb_3Sn," *Advances in Cryogenic Engineering,* Vol. 28, Reed, R.P., and Clark, A.F., eds., Plenum Press, New York, 1982. pp. 389–398. Tachikawa, K., Sekine, H., and Iijima, Y., *J. Appl. Phys.*, 53, 5354–5356, 1983.
12. Kramer, E., *J. Appl. Phys.*, 44, 1360–1370, 1973.

13. Suenaga, M., and Welch, D.O., "Flux Pinning in Bronze Processed Nb$_3$Sn Wires," *Filamentary A15 Superconductors* , Suenaga, M., and Clark, A.F., eds., Plenum Press, New York, 1980, pp. 131–142.

14. Rupp, G., Springer, E., and Roth, S., *Cryogenics*, 17, 144, 1977.

15. Kuroda, T., Suenaga, M., Klamut, C.J., and Sabatini, R.L., "Internal Sn Processed Multifilamentary Wires Alloyed with Mg, Zn + Ni, and Ti Through the Sn Core," *Advances in Cryogenic Engineering*, Vol. 32, Reed, R.P., and Clark, A.F., eds., Plenum Press, New York, 1986, pp. 1011–1018.

16. Miyashita, S., Yoshizaki, K.., Hashimoto, Y., Itoh, K., and Tachikawa, K., "The Structure and Superconducting Properties of Multifilamentary Nb$_3$Sn Wires by Internal Sn Diffusion Process Using Sn–Ti Cores," *Advances in Cryogenic Engineering,* Vol. 32, Reed, R.P., and Clark, A.F., eds., Plenum Press, New York, 1986, pp. 995–1002.

17. Gregory, E., Tomsic, M., Suption, M.D., Peng, X., Wu, X., Collings, E.W., and Zeitlin, B.A., *IEEE Trans. Appl. Supercond.*, 15, 3478, 2005.

18. Suenaga, M., Welch, D.O., Sabatini, R.L., Kammerer, O.F., and Okuda, S., *J. Appl. Phys.*, 59, 840–853, 1986.

19. Luhman, T.S., and Suenaga, M., *Appl. Phys. Lett.*, 29, 61–63, 1976.

20. Ekin, J., "Strain Effects in Superconducting Compound," *Advances in Cryogenic Engineering,* Vol. 30, Clark, A.F., and Reed, R.P., eds., Plenum Press, New York, 1984. pp. 823–835.

21. Talvacchio, J., Thesis, Stanford University, 1982.

22. Devantay, H., Jorda, J. L., Dcroux, M., Muller, J., and Flukiger, R., *J. Mater. Sci.*, 16, 2145, 1981.

23. Suenaga, M., Horigami, O., and Luhman, T.S., *Appl. Phys. Lett.*, 25, 624–27, 1974.

24. Cited in Ref. [25].

25. Suenaga, M., and Jensen, W., *Appl. Phys. Lett.*, 43, 791–793, 1983.

26. Suenaga, M., Cordman, R.R., and Welch, D.O., "Chemical Compositions of Grain Boundaries in Pure and Alloyed Nb$_3$Sn," Preliminary report in *Proceedings of International Symposium on Flux Pinning and Electromagnetic Properties of Superconductors*, Matsushita, T., Yamafuji, K., and Irie, F., eds., 1986, pp. 142–145.

27. Bruzzone, P., ten Kate, H.H., Nishi, M., Shikov, A., Minervini, J., and Takayasu, M., *Advances in Cryogenic Engineering*, Vol. 42B, Summers, L., ed., Plenum Press, New York, 1995, pp. 1351–1358.

28. Zerweck, G., *J. Low Temp. Phys.*, 42, 1, 1981.

29. Yetter, W.E., Thomas, D.A., and Kramer, E.J., *Philos. Mag. B*, 46, 523, 1982.

30. Welch, D.O., *IEEE Trans. Magn.*, MAG-21, 827–830, 1984.

31. Orlando, T.P., McNiff, E.J., Foner, S., and Beasley, M.R., *Phys Rev. B*, 19, 4545–4561, 1979.

32. Evetts, J.E., and Plummer, C.J.G., "Flux Pinning in Polycrystalline A15 Bronze Route Filaments," *Proceedings of International Symposium on Flux Pinning and Electromagnetic Properties of Superconductors*, Matsushita, T., Yamafuji, K., and Irie, F., eds., 1986, pp. 146–151.

33. Welch, D.O., *J. Adv. Sci.*, 4, 81–85, 1992; *IEEE Trans. Appl. Supercond.*, 3, 1476–1478, 1993.

34. Cottrell, A.H., *Dislocations and Plastic Flow in Crystals*, Clarendon Press, Oxford, 1953.

35. Wordenweber, R., *Rep. Prog. Phys.*, 62, 187–236, 1999.

36. Lindenhovius, J.L.H., Hornseveld, E.M., den Ouden, A., Wessel, W.A.J., and ten Kate, H.H.J., *IEEE Trans. Appl. Supercond.*, 10, 975–978, 2000.

37. Miyazaki, T., Kato, H., Zaitsu, K., Miyatake, T., Hamada, M., and Tchikawa, K., *IEEE Trans. Appl. Supercond.*, 15, 3490, 2005.

38. Kunzler, J.E., Buchler, E., Hsu, F.S.L., and Wernick, J.H., *Phys. Rev. Lett.*, 6, 89–92, 1961.

39. van Beijenen, C.A.M., and Elen, J.D., *IEEE Trans. Magn.*, MAG-15, 87–90, 1979.

40. Scanlan, R.M., Dieterich, D.R., and Gourlay, S.A., "A New Generation Nb_3Sn Wire, and the Prospects for Its Use in Particle Accelerators," *Advances in Cryogenic Engineering,* Vol. 50B, Balachandran, U., ed., American Institute of Physics, New York, 2004, pp. 349–358.

41. Hong, S.A., Field, M., Parrell, J.A., and Zhang, Y., " Nb_3Sn Critical Current Density Improvement for Very High Field Superconducting Magnets," *Proceedings of International Workshop on Progress of Nb-Based Superconductors*, Inoue, K., Takeuchi, T., and Kikuchi, A., eds., 2004, pp. 129–134.

42. Parrell, J.A., Field, M.B., Zhang, Y., and Hong, S., " Nb_3Sn Conductor Development for Fusion and Particle Accelerator Applications," *Advances in Cryogenic Engineering,* Vol. 50B, Balachandran, U., ed., American Institute of Physics, New York, 2004, pp. 369–375.

43. Parrell, J.A., Field, M.B., Zhang, Y., and Hong, S., *IEEE Trans. Appl. Supercond.*, 15, 1200–1204, 2005.

44. Gregory, E., "Lessons Learned on the Development and Manufacture of Internal-Tin Nb_3Sn Strand from Work on ITER CSMC and Other Fusion and HEP Applications," *Advances in Cryogenic Engineering,* Vol. 50, Balachandran, U., ed., American Institute of Physics, New York, 2004, pp. 359–368.

45. Miyazaki, T., Miyatake, T., Kato, T., Zaitsu, K., Hanada, M., Murakami, Y., and Hase, T., *J. Cryog. Soc. Jpn.*, 39, 415–442, 2004 (in Japanese).

46. Yoshikawa, M., Kiyoshi, T., Matsumoto, S., Sato, A., Wada, H., Ito, S., Miki, T., Ozaki, O., Miyazaki, T., Hamada, M., Murakami, Y., Hirose, R., and Noguchi, T., *J. Cryog. Soc. Jpn.*, 39, 625–631, 2004 (in Japanese).

47. Hashimoto, Y., Yoshizaki, K., and Tanaka, M., *Proceedings of 5th International Cryogenic Conference,* Kyoto, Japan, 1974.

48. Higuchi, N., Tsuchiya, K., Klamut, C.J., and Suenaga, M., "Superconducting Properties of Nb_3Sn Multifilamentary Wires Fabricated by Internal Tin Process," *Advances in Cryogenic Engineering*, Vol. 30**,** Clark, A.F., and Reed, R.P., eds., Plenum Press, New York, 1984, pp. 738–746.

49. Imazumi, M., Wakata, M., Yoshizaki, K., Fujiwara, F., and Hashimoto, Y., "The Effects of In Addition on the Properties of Internal Tin Diffusion Processed Nb_3Sn Wires," *Advances in Cryogenic Engineering*, Vol. 30, Clark, A.F., and Reed, R.P., eds., Plenum Press, New York, 1984, pp. 779–786.

50. Hazelton, D.W., Ozeryansky, G.M., Walker, M.S., Zeitlin, B.A., Hemachalam, K., Dalder, E.N.C., and Summers, L., "Internal Sn Process Nb_3Sn Conductors for 18 T," *Advances in Cryogenic Engineering,* Vol. 32, Reed, R.P., and Clark, A.F., eds., Plenum Press, New York, 1986, pp. 1003–1009.

51. Zietlin, B.A., Supergenics, LLC, personal communication, August 2005.

52. Hong, S., Oxford Superconducting Technology, personal communication, August 2005.

53. Kubo, Y., Egawa, K., Nagai, T., Sone, T., Ikeda, B., Hasegawa, M., and Kosuge, M., *J. Cryog. Soc. Jpn.*, 40, 86, 2005 (in Japanese).

54. Kubo, Y., US Patent 6,251,529.

13

High-Temperature Superconductors: A Review of $YBa_2Cu_3O_{6+x}$ and $(Bi,Pb)_2Sr_2Ca_2Cu_3O_{10}$

H.C. FREYHARDT[a] AND E.E. HELLSTROM[b]

[a]*Institut für Materialphysik, Universität Göttingen, 37077 Göttingen, Germany*
[b]*Applied Superconductivity Center, University of Wisconsin-Madison, Madison, WI 53706, USA*

Abstract

Since high-temperature superconductors were discovered in 1986, there have been extensive research efforts to understand the nature of superconductivity in these materials and to fashion them into forms that can be used in practical applications. This chapter reviews basic aspects of superconductivity in the families of copper-oxide-based high-temperature superconductors. It discusses methods used to fabricate $YBa_2Cu_3O_{6+x}$ and $ReBa_2Cu_3O_{6+x}$ (Re = rare earth) into bulk monoliths and reviews the ongoing studies and development work to make them into coated conductors. It examines the oxide-powder-in-tube method to fabricate Ag-sheathed $(Bi,Pb)_2Sr_2Ca_2Cu_3O_{10}$ wire and current applications where these wires are used.

13.1 Introduction

Nearly a century on from Heike Kamerlingh Onnes's 1911 discovery of superconductivity in Hg [1] at 4.2 K, scientists and engineers continue to dream of finding or synthesizing materials that are superconducting at higher temperatures, even above room temperature. However, before 1986, Nb_3Ge, which is an intermetallic compound with an A-15 structure, had the highest T_c of 23.2 K. Many attempts to reach higher T_c failed, both theoretically, by exploring new or alternative electron pairing mechanisms (e.g. excitonic superconductivity [2]) and experimentally, by searching for new classes of materials (including organic conductors [3] and oxides, e.g. $LiTi_2O_4$ and $BaPb_{1-x}Bi_xO_3$ [4,5]). In 1986, 75 years after the discovery of superconductivity, Bednorz and Müller published a paper entitled "Possible High-T_c Superconductivity in the Ba–La–Cu–O System" [6], in which they demonstrated a sharp drop in the resistivity of these materials at 30 K; but it was not given much attention. It was only after October 1986, when Bednorz et al. [7] submitted their results demonstrating the diamagnetic behavior in these ceramic oxides, that the new field of high-temperature superconductivity (HTS) was born. The "gold rush" commenced at the end of 1986 and the beginning of

1987, when Tanaka and coworkers confirmed the findings of Bednorz and Müller. This occurred at the fall 1986 meeting of the Materials Research Society in Boston, when a fax message (which was also novel at that time) arrived from Japan to be presented in an overcrowded room. This launched an intensive worldwide search for new high-temperature superconductors by physicists, materials scientists, and solid-state scientists, as well as by crystallographers and chemists, leading to an enthusiasm culminating in the Woodstock of Physics at a special meeting of the American Physical Society in New York. Within weeks a new system, Y–Ba–Cu–O, was found by groups at the universities of Alabama and Houston [8] that showed superconductivity at 90 K. In Spring 1988, researchers at the National Research Institute for Metals in Tsukuba discovered the Bi–Sr–Ca–Cu–O system with T_c values up to 115 K [9] and, at the University of Alabama, Tl–Ba–Ca–Cu–O with T_c values up to 120 K [10]. Materials with even higher T_c values were discovered in the early 1990s in the Hg–Ba–Ca–Cu–O system [11]. Schilling et al. [12] found a T_c of 135 K in the so-called Hg-1223 phase, which was increased to 164 K in optimally doped material at a pressure of 31 GPa [13]. In January 2001, Akimitsu's group at the Aoyma-Gakuin University (Tokyo) found HTS in MgB_2 at around 40 K [14]. This is the only HTS material that does not contain Cu.

Although superconductivity was discovered at the beginning of the 20th century, it took almost 50 years to explain the phenomenon. Bardeen, Cooper, and Schrieffer demonstrated in their theory [15] (now called the BCS theory, for which they received the Nobel Prize in 1972) that at low temperatures a weak interaction, mediated by quantized lattice vibrations or virtual phonons, couples two electrons of opposite spin and momentum together into an electron pair, a so-called Cooper pair, with zero spin and momentum. In normal metals, electrons are scattered by lattice vibrations, impurities, or lattice defects, which causes electrical resistance. In materials where electrons are bound into Cooper pairs, no electron scattering occurs, so there is no electrical resistance, i.e. we get a conductor with infinite conductivity, which we call a superconductor. At temperatures above T_c, or by applying a sufficiently high magnetic field or large enough current, the Cooper pairs are destroyed and resistivity occurs. Predictions of the BCS theory, which was further extended, have been confirmed, and superconducting materials are used in major applications. Pb alloys and Nb are used mainly in electronics, and NbTi and Nb_3Sn are used to build magnets.

There were new difficulties explaining the properties and the experimental findings of the new high-temperature superconductors. This was partly due to the complex crystal structure of these materials. Let us explain this by considering $YBa_2Cu_3O_{6+x}$, which is slated to become one of the 'workhorse' HTS materials. Here, x determines the oxygen stoichiometry of the compound. $YBa_2Cu_3O_{6+x}$ can be visualized as a modification of the $BaTiO_3$ perovskite structure. It is composed of a stack of three perovskite units (Figure 13.1). There are two CuO_2 planes, one on either side of the Y. Note that there is no O on the Y plane. The top and bottom layers of the unit cell contain only Cu for $x = 0$, and contain CuO chains for $x = 1$. Figure 13.1 shows the CuO chains, corresponding to $x = 1$.

FIGURE 13.1. Crystal structure of the high-temperature superconductor $YBa_2Cu_3O_{6+x}$ for $x = 1$. The O atoms that form the CuO chains are circled.

Barium

Yttrium

Copper

Oxygen
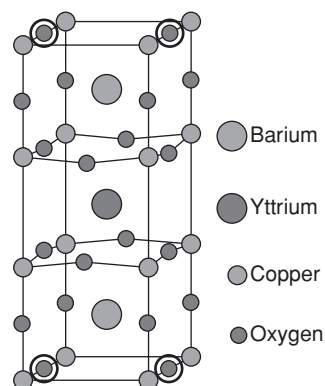
The electronic properties of $YBa_2Cu_3O_{6+x}$ are determined by a subtle balance between the various interaction forces (Coulomb repulsion, antiferromagnetic exchange interaction, electron–phonon coupling) leading to an antiferromagnetically ordered insulator for $x = 0$, with a tetragonal unit cell. Doping $YBa_2Cu_3O_{6+x}$ with oxygen creates CuO chains at the top and bottom of the unit cell, and, because of the strong electronegativity of oxygen, extracts electrons from the CuO_2 planes. The maximum T_c is 93 K for $x = 0.93$ (Figure 13.2). Early on, the existence of flux quantization demonstrated that a pairing mechanism must be involved to generate the superconducting state in HTS material. However, there is still uncertainty whether the pairing is caused by a phonon-assisted coupling of the electrons, just as in low-temperature superconductors, or is due to more complicated magnetic effects created by the HTS lattice.

$YBa_2Cu_3O_{6+x}$, here denoted as YBCO-123, belongs to a family of structurally related compounds that includes YBCO-124 (e.g. see Reference [16]) and
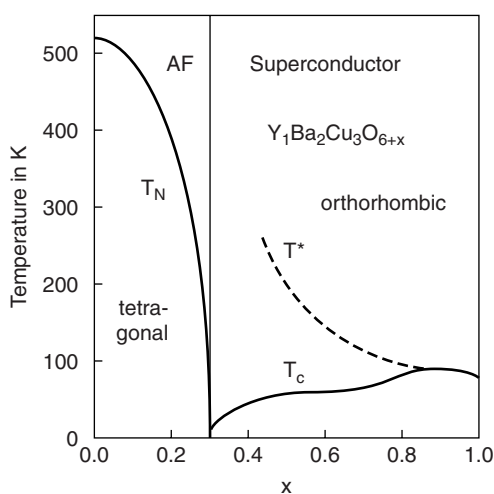
FIGURE 13.2. Schematic phase diagram of $YBa_2Cu_3O_{6+x}$. With increasing oxygen content, the tetragonal antiferromagnetic phase becomes orthorhombic and superconducting. T^* denotes the existence of a pseudogap.
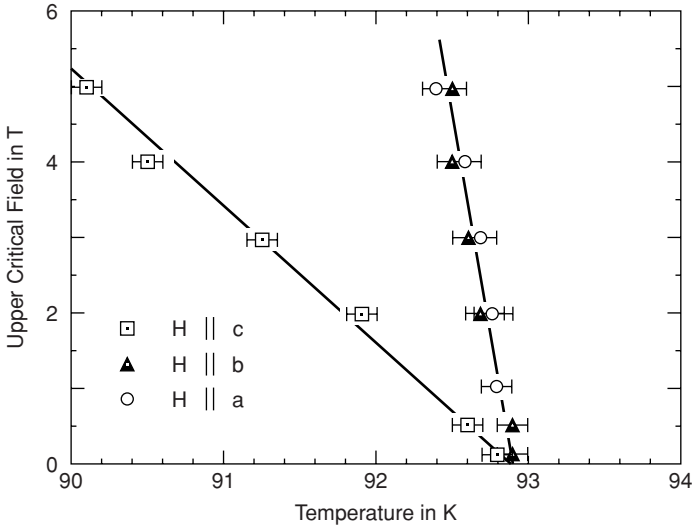
FIGURE 13.3. Upper critical field B_{c2} of $YBa_2Cu_3O_{6+x}$ parallel and perpendicular to the c-axis (after Reference [21]).

YBCO-247 (e.g. see Reference [17]). These compounds can also be visualized as stacking of layers. The superconducting CuO_2 layers are separated by insulating layers from a further kind of layer, i.e. the CuO chain layers, which can be considered as donors of the electrons, e.g. those formed from the CuO chains. This becomes even more pronounced in the three other important families of HTS materials, namely $Bi_2Sr_2Ca_{n-1}Cu_nO_{2n+4+\delta}$ ($n = 1, 2, 3$; e.g. see Reference [18]), $Tl_mBa_2Ca_{n-1}Cu_nO_{2n+m+2+\delta}$ (where $m = 1$ or 2 and $n = 1, 2, 3$ or 4; e.g. see Reference [19]) and $HgBa_2Ca_{n-1}Cu_nO_{2n+2+\delta}$ ($n = 1, 2, \ldots, 5$; e.g. see Reference [20]).

The highly conducting CuO_2 sheets are sandwiched between poorly conducting layers, so anisotropic superconducting properties are expected. This is indeed found and demonstrated by considering as an example the upper critical field B_{c2} of YBCO (Figure 13.3).

B_{c2} for H parallel to the c-axis is smaller than B_{c2} for H parallel to the a or b directions, indicating larger coherence length in the c direction. As in classical type-II superconductors, flux lines form in the material at fields greater than the lower critical field B_{c1}. Owing to the strong anisotropy and the layered structure of the HTS material, the flux lines can exhibit an anisotropic, ellipsoidal cross-section and even split into a row of 'flux pancakes' that form a pancake vortex. Once a current is flowing in the HTS material, the flux lines or flux pancakes move under the action of a Lorentz force that is perpendicular to the magnetic field and current direction. This flux motion creates losses that can be avoided by introducing defects and second-phase particles to pin the flux lines.

The development of HTS focused on (i) basic issues, including understanding the phenomenon of superconductivity in HTS materials, i.e. the underlying mechanism, as well as searching for materials with higher transition temperatures; (ii) understanding the flux structure of HTS material and its anisotropic nature; (iii) understanding, controlling, and optimizing defect structures to manipulate and tailor flux pinning and critical currents. There has been a broad, parallel effort by materials and solid-state scientists, chemists, and engineers to adjust, modify, and create processes to manufacture not only bulk HTS materials and HTS wires and tapes, but also HTS thin films for electronic applications. This is illustrated below for YBCO and $(Bi,Pb)_2Sr_2Ca_2Cu_3O_{10}$.

Much of what has been described above for YBCO is also valid for $ReBa_2Cu_3O_{6+x}$ (Re = rare earth). The majority of research and development work on coated conductors (CCs) has been done on YBCO, whereas extensive work with ReBCO has been done to make bulk monoliths. Below we refer to YBCO, even though work has also been done on ReBCO.

13.2 YBCO, the Workhorse

After the discovery of YBCO in spring 1987, there was a worldwide effort to synthesize YBCO and ReBCO by using a wide variety of physical and chemical technologies. Just like others, at Göttingen we [22] "cooked" mixtures of oxides and carbonates of Y, Ba, and Cu in air and synthesized YBCO pellets, which was astonishingly simple and successful. At the end of 1987, we [23] began growing single crystals of YBCO to characterize their physical properties better. The melt is highly aggressive, so platinum crucibles had to be used, and a furnace designed for the growth of CdTe crystals was modified for the crystal growth. As one knows from detailed studies of the phase diagrams published later, we did not get a single crystal, but the materials had a T_c of about 90 K and a critical transport current J_c of 1.5×10^5 A/cm^2 at 20 K (magnetically measured), which was lower than expected. Although we did not know it at the time, we had formed a melt-textured material, (e.g. see References [24,25]). Small single crystals were grown quite early [26], but it took several more years to grow perfect, well-defined YBCO crystals [27]. At the end of the 1980s and in the 1990s, the interrelation between oxygen stoichiometry, the tetragonal-to-orthorhombic phase transformation, and T_c was worked out together with the details of the flux structure in the intermediate state of the type-II superconducting YBCO (e.g. see Reference [28]).

To use these HTS materials, e.g. in power engineering applications, requires J_c in moderate or high magnetic fields, preferably at high temperatures, e.g. at 77 K. How can this be achieved? It requires engineering the YBCO to overcome two fundamental problems. First, the layered structure of YBCO leads to strong anisotropy, in which the supercurrent flowing along the CuO_2 planes parallel to the a–b planes is much larger than current that flows perpendicular to them, i.e. parallel to the c direction. Second, because of the small coherence lengths, grain boundaries that have moderate to large grain-boundary misorientations are detrimental for

current transfer; they are weak links, as shown by Dimos et al. [29]. Applications of HTS materials, therefore, require materials textured in three dimensions. This required developing new processing routes to make textured YBCO wires.

13.3 Melt-Processed YBCO

In contrast to bulk low-temperature superconductors, which are thermally unstable because of their small specific heat, bulk HTS materials are thermally stable because of their larger specific heat, even for large sample sizes. Bulk YBCO monoliths with high J_c at 77 K act as permanent magnets with high coercive fields and remanent magnetic moments that can be employed for magnetic levitation. If these are polycrystalline, then the presence of grain boundaries considerably reduces J_c. In principle, the best way to avoid grain boundaries is to grow single crystals. There have been various efforts to grow single crystals, from flux growth, top-seeded solution growth [30], and the traveling-solvent floating-zone methods [31], to mention only a few. An essential prerequisite is good knowledge of the respective phase diagram. In the YBCO system, Figure 13.4 shows that the desired YBCO phase (123) forms on cooling by a peritectic reaction between liquid and Y_2BaCuO_5 (Y-211) (e.g. see Reference [32, p. 19]).

The single-crystal growth techniques yield large-volume monoliths that are desirable for permanent-magnet applications, where the magnitude of the trapped
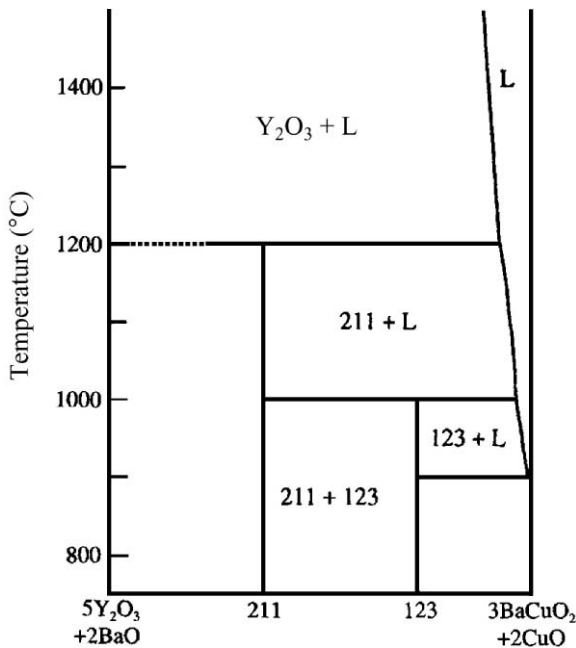
FIGURE 13.4. Pseudobinary phase diagram for the YBCO system [31].

FIGURE 13.5. Typical melt-textured, top-seeded YBCO monolith (after Reference [33]). Scale is in centimeters.
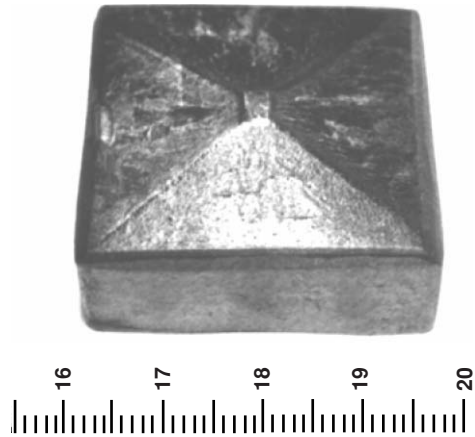
magnetic field is proportional to J_c and the volume of the monolith, but they are tedious and slow. Different methodologies have been developed to fabricate large monoliths. Melt-processing technologies have been found effective in increasing J_c through a combination of grain alignment and controlled introduction of pinning centers, such as precipitates, twins, stacking faults, or dislocations. In 1988, Jin et al. [24] developed melt-texture growth (MTG) that reduced the number of grain-boundary weak links. In this process, a sintered YBCO sample is partly melted and then cooled in a temperature gradient. Later, many variations were made (see summaries in Reference [32]) to try to avoid the disadvantages of MTG, which are the nonuniform distribution of the Y-211 phase and its growth, which lead to poor connectivity of the YBCO. One modification is the melt-powder melt-growth (MPMG) process. An important precondition was the modification of the phase distribution in the partly molten state before solidification. The microstructure of the monoliths could be tailored by starting from precursor mixtures with a surplus of Y-211 and adding Pt or CeO_2, which served to refine the Y-211 particles in the textured YBCO and thus to increase J_c. Figure 13.5 shows a typical example of a large-current-carrying YBCO monolith intended for a flywheel application [33]. This knowledge was expanded and applied to process ReBCO monoliths with a single or mixture of rare earths. The key to success was learning to design the microstructure in an optimal way, combined with improving the mechanical properties. Large-grain ReBCO can now trap magnetic fields up to 17 T at 29 K (Figure 13.6).

13.4 YBCO-Coated Conductors: Second-Generation High-Temperature Superconductors

The three-dimensional grain alignment is even more difficult to achieve in thin films of YBCO and ReBCO deposited on a tape substrate. This is the so-called

FIGURE 13.6. Large, trapped magnetic fields in ReBCO monoliths at various temperatures (after Reference [34]).
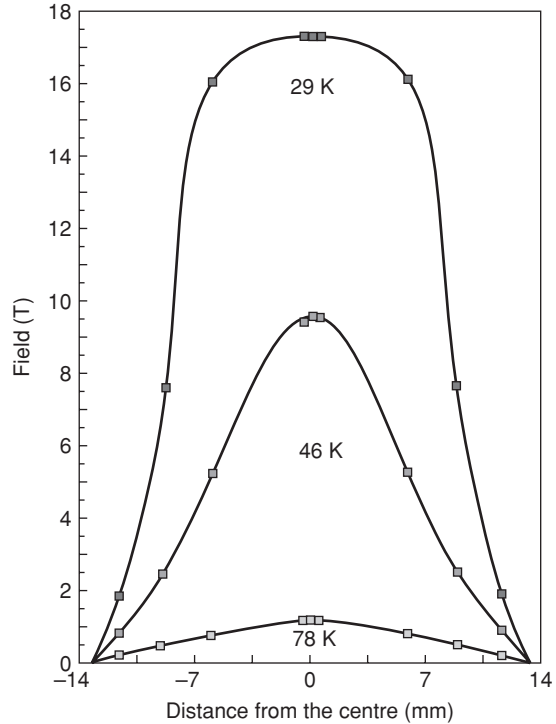
coated conductor (CC) geometry, which is also known as the second-generation conductor. Furthermore, because YBCO is brittle like the A-15 low-temperature superconductors, fabricating a YBCO-CC requires a complex, composite architecture. Two approaches are employed to create three-dimensional texturing of YBCO in long tapes (Figure 13.7).

To achieve the three-dimensional texture, YBCO films must be grown heteroepitaxially on a well-textured template. The difference between the two techniques is how the template is textured. One technique uses thermo-mechanically textured (TMT) metal substrates with an overlaying buffer architecture that acts as a diffusion barrier and transfers the texture from the substrate to the YBCO film. The other technique begins with an untextured polycrystalline Ni–Cr alloy or stainless steel substrate, onto which is deposited a highly textured buffer film that is produced by forced texturing, using ion-beam-assisted deposition (IBAD) or inclined-substrate deposition (ISD). To avoid cracking or delaminating the YBCO layer, the thermal expansion of the metallic substrate and YBCO must be matched.

13.4.1 Substrates

The TMT metal substrates must be thin (typically 50–100 μm), mechanically strong, and highly (100) or cube textured, i.e. nontextured grains must be
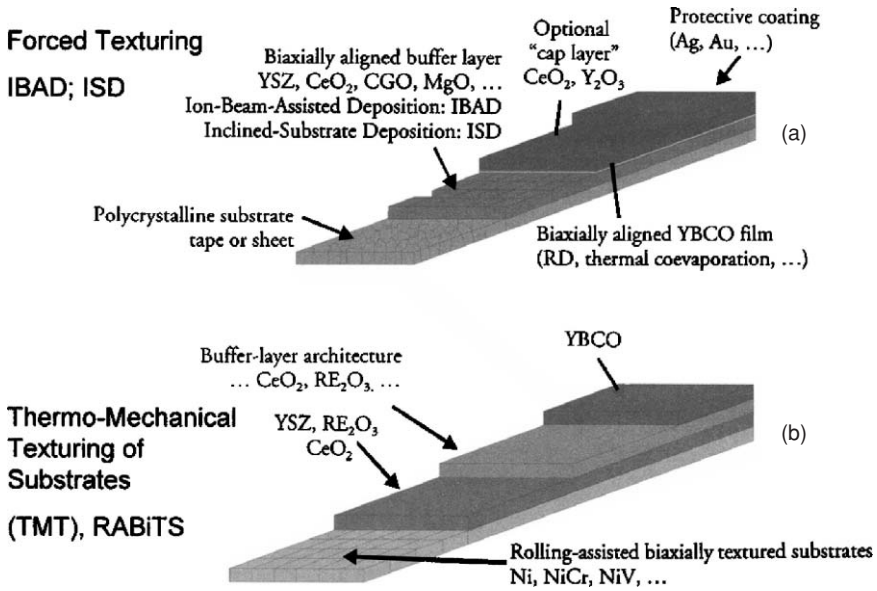
FIGURE 13.7. Architecture of CC made with (a) IBAD and ISD and (b) TMT (also known as RABiTS) substrates.

completely eliminated. At first, Ni was widely used because of its ability to form excellent cube texture after heavy cold-rolling and appropriate annealing and because of its excellent oxidation resistance [35]. This is sometimes referred to as RABiTS, for rolling-assisted biaxially textured substrates [35]. However, Ni is very soft, with a yield strength of only 40 MPa for a TMT tape, so it is difficult to tape without damaging it. In addition, the ferromagnetism of Ni is undesirable for several applications in magnetic fields. The mechanical strength can be increased by solid-solution and precipitate hardening. Ni–V, Ni–Cr, Ni–Mo and, particularly, Ni–W alloys with up to 9 at.% W have been studied [36]. Higher yield strength, up to 200 MPa, can be achieved by using thin (40, 80 μm) Ni4.5W/Ni15Cr composite TMT tapes [37]. Alloying reduces or even eliminates ferromagnetism in the substrate materials. TMT tapes that are thicker than 25 to 30 μm have excellent in-plane and out-of-plane texture (e.g. see Reference [36]). Details about the grains in the textured substrate, including the grain-size distribution and grain-boundary misorientation distribution, are determined by electron backscattering diffraction (e.g. see Reference [38]). The microstructure generally consists of equiaxed grains, or sometimes elongated grains, which are made using special processing conditions that are favorable for current percolation in the overlaying HTS material (see Reference [39]).

In contrast, the IBAD (and ISD) substrates are untextured polycrystalline Ni-Cr alloys (Hastelloy or Inconel) or Ni–Cr stainless steel tapes (of the ZFW Göttingen and EHTS GmbH & Co. KG). They are nonmagnetic, mechanically strong (yield

strength of 800 MPa), can be rolled down to thicknesses below 30 μm, and are easily polished with very little surface roughness (e.g. see References [40, 241]).

13.4.2 Buffer-Layer Architectures

It was, and still is, a challenge to select an optimum combination of suitable buffer layers that serve as the diffusion barrier and provide lattice matching and/or texture transfer. Different families of buffer-layer materials have been used, including fluorite-type (yttria-stabilized zirconia (YSZ) or CeO_2), perovskite type ($BaZrO_3$, $SrZrO_3$, $SrTiO_3$, $CaTiO_3$, $Ca_{1-x}Sr_xTiO_3$, $LaAlO_3$, $LaMnO_3$), and rock-salt type (MgO, TiN).

Of these, YSZ and MgO are considered most suitable for forced texturing. Iijima et al. [42] first successfully textured YSZ by an IBAD technology and then applied it to long Hastelloy tapes [43]. Highly textured IBAD-YSZ has been deposited on long Ni–Cr stainless steel tapes [44], with good in-plane texture (full width at half maximum (FWHM) values <10° [45]) for typical buffer-layer thicknesses of up to 1.5 μm. High-rate pulsed laser deposition (PLD) and e-beam deposition of the CeO_2 cap layer, onto which the YBCO is deposited, reduced the FWHM values to <4° [45, 46]. Higher speed IBAD texturing of buffers was made possible by switching to MgO, which is a rock-salt-type buffer. However, it requires a much more complicated multilayer buffer architecture [47]. ISD inclines the sample surface with respect to a single ion beam, whereas IBAD uses two ion beams, with the assisting beam at an angle to the substrate. ISD can force texturing of MgO, particularly when a homoepitaxial MgO film is deposited on the ISD MgO.

Interesting approaches that do not rely entirely on vacuum technologies have recently appeared as possible low-cost alternatives for fabricating CCs. One of these alternatives employs textured Ni or Ni alloy on which a NiO layer is grown by controlled surface oxidation. This is called surface oxidation epitaxy (e.g. see Reference [48]). The NiO layer is grown by a one- or two-step heat treatment. The out-of-plane and in-plane FWHM values are 2° and 4–8° respectively [48]. The template match required for the YBCO layers is achieved by subsequent deposition of $BaZrO_3$, $SrZrO_3$, or $Ca_{1-x}Sr_xTiO_3$ buffers. Chemical techniques, including MOCVD (metal–organic chemical vapor deposition), MOD (metal–organic deposition), and sol–gel techniques are being developed and used to deposit single and multiple buffer-layer stacks on TMT and IBAD substrates. With careful selection of layer structure and chemistry (e.g. see References [49,50]), it is possible to fulfill the requirements needed for a suitable buffer for the CC, i.e. small lattice mismatch between the superconductor film and the metal substrate, high texture quality, low chemical reactivity, and low oxygen, as well as cation diffusion to protect the substrate from oxidation and the YBCO film from contamination.

13.4.3 YBCO Deposition

Substantial progress understanding YBCO materials, as well as in developing applications, became possible with improved thin-film deposition techniques. Several

FIGURE 13.8. Coated conductor tapes produced by high-rate PLD on YSZ-buffered SS tapes (40 m, 235 A/cm-width) from EHTS (right [52]) and by multiplume PLD (212 m, 245 A/cm-width, Hastelloy/IBAD-$Gd_2Zr_2O_7$/PLD-CeO_2/multiplume PLD-YBCO) from SRL/ISTEC (left [54]).

important developments are highlighted, in particular the physical deposition methods of PLD, reactive thermal coevaporation (TCE) and liquid-phase epitaxy (see review in Reference [51]), as well as chemical methods, including MOCVD, MOD, and sol–gel.

From the very beginning of work on YBCO CCs, PLD has been one of the most reliable and reproducible techniques for processing high-performance YBCO. The community has learned to control the vaporization of YBCO by the nanosecond laser pulse and the deposition of YBCO on suitably heated substrates. High-rate PLD of YBCO (EHTS and ZFW gGmbH, Germany) increased the integrated (volume) deposition rate to technologically attractive values, while maintaining a good overall in-plane texture of the YBCO. Up to 40 m of IBAD-YSZ CC on stainless steel substrates can be routinely processed now [52] (Figures 13.8 and 13.9) with I_c values of 235 A/cm-width and a champion value of 494 A/cm-width for short tape at 77 K. The tapes exhibit low AC losses and are very strain tolerant. Recently, Yamada et al. [54] at ISTEC-SRL, Nagoya, achieved 245 A/cm-width in a record 212 m long CC consisting of Hastelloy/IBAD-$Gd_2Zr_2O_7$/PLD-CeO_2/multiplume PLD-YBCO.
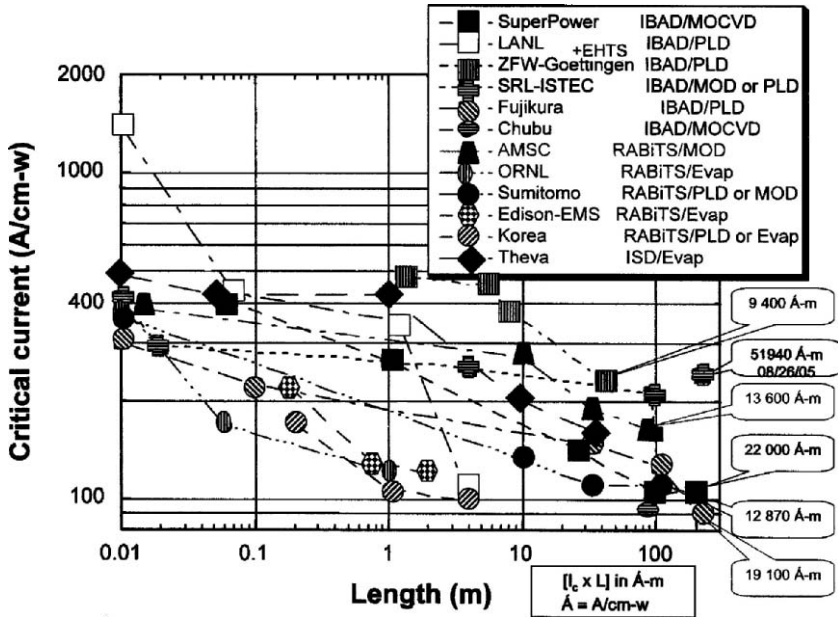
FIGURE 13.9. I_c as a function of length for CC tapes manufactured by using various processing technologies (after Reference [53]).

I_c values greater than 1000 A/cm-width were achieved at Los Alamos National Laboratory in multilayer YBCO films deposited on IBAD substrates [53]. CC tapes 10 m in length have been made with TCE, which is an alternative vacuum deposition method. The conductor architecture was Hastelloy/ISD-MgO/homo-MgO/TCE-YBCO and the YBCO had an in-plane texture of 8–9° and I_c of 200 A/cm-width (end to end). Short-sample J_c was 2.5 MA/cm^2 [53,55]. Liquid-phase epitaxy is different from other film formation methods because the YBCO is deposited from a high-temperature Y–Ba–Cu–O solution, similar to single crystal growth using top-seeded solution growth [56]. High growth rates, up to 10 μm/min, can be achieved, leading to thick films exceeding 10 μm. However, there are several problems. The high temperature used to grow the film leads to films with few defects that have low J_c. In addition, the buffer layer can dissolve in the solution, which can contaminate the YBCO and reduce its T_c. Some of these disadvantages can be circumvented by a hybrid liquid-phase epitaxy method, in which a high-rate "liquid-assisted" growth of the epitaxial film occurs by diffusive transport of Y, which can be supplied by a variety of methods, through a thin, liquid-flux layer [57].

Chemical deposition of YBCO and ReBCO has only recently appeared as a lower cost alternative for depositing YBCO. They are well established for producing high-performance ceramics. They typically involve three processing steps: deposition, pyrolysis and growth of YBCO, and oxygenation (e.g. see Reference

[50]). In the first step, metal–organic precursor solutions, e.g. Y, Ba, and Cu tri-fluoroacetates (TFAs), are deposited by spin coating, dip coating or slot-die coating on well-textured, suitably buffered substrates. The second step is pyrolysis then growth of YBCO. This can be done in several stages. In the first stage of the heat treatment, often called calcination, a homogeneous, nanocrystalline film of oxides and fluorides (for the TFA process) is generated. In the second stage, the calcined film is heated to 700 to 800 °C in a well-controlled atmosphere, and the YBCO layer grows heteroexpitaxially on the buffer layer. In the third step, the YBCO film is oxygenated to achieve the correct oxygen stoichiometry. This TFA manufacturing technology is used by the American Superconductor Corporation [58], where I_c values of 160 to 175 A/cm-width are achieved in long Ni–W-RABiTS/Y_2O_3/YSZ/CeO_2/TFA-MOD-YBCO neutral-axis tapes (see Figure 13.9). The Institut de Ciència de Materials de Barcelona [52] also focuses its efforts on chemical deposition of YBCO, in particular TFA-YBCO, on chemically deposited buffer systems on TMT and IBAD substrates. A $J_c \geq 1$ MA/cm^2 has been demonstrated on CCs with chemically deposited buffer and YBCO layers.

13.4.4 Conclusions and Prospects for Coated Conductors

Initially, CC production was based entirely on vacuum techniques, such as PLD and thermal evaporation. Several groups worldwide have significantly enhanced the international state of the art in this field (EHTS, ZFW gGmbH, LANL/MST-STC, SRL/ISTEC, and Theva). Continuously and reproducibly producing cost-effective, long CCs with the specifications required for specific applications remains the central challenge. In recent years, the use of nonvacuum chemical deposition technologies (MOCVD, MOD, sol–gel) have appeared as promising alternatives for low-cost and easily scalable production. This, however, requires a synergistic approach across many disciplines. One of the objectives is to achieve an all-chemical production of CC tape.

13.5 Applications of $(Bi,Pb)_2Sr_2Ca_2Cu_3O_{10}$ (2223) Wire

Ag-sheathed $(Bi,Pb)_2Sr_2Ca_2Cu_3O_{10}$ (2223) wire, known as the first-generation conductor, is more mature than CCs. It is commercially available in long lengths from American Superconductor Corp. (AMSC), Sumitomo Electric Industries (SEI), Innova Superconductor Technology, Inc., and European Advanced Superconductors (EAS). The vast majority of wire is manufactured by AMSC and SEI. The standard size of wire is about 4 mm wide, 225 μm thick, and up to 1.5 km in length. The critical current I_c in long wires is as high as $\sim$150 A. AMSC plans for their CC to be a "form fit" replacement for 2223 wire in HTS applications.

2223 wire is used in many applications. AMSC sells current leads made from 2223 wire that reduce the heat leak along the current leads, lowering the cryogenic operating expenses [59]. They have developed a dynamic synchronous condenser, called a SuperVAR (for superconducting volt-ampere-reactive), to provide peak

and dynamic reactive compensation to an electric power system [60]. The first system is being tested by a utility company. AMSC has built a 5 MW ship propulsion motor as a demonstration project for the US Navy [61], and Siemens made 2223 wire from EAS into a 4 MW generator for marine applications [62]. These latter three rotating machines use 2223 wire in their rotor field winding.

There are several transmission-line projects built with 2223 wire that has been made into cable. 2223 wire made by Innova is being used in a 30 m transmission line installed in the Puji Substation in the China Southern Power Grid. SEI is supplying 2223 wire made using their overpressure process, discussed below, for the cable in a 350 m transmission line that is being installed between two Niagara Mohawk substations in Albany, New York [63]. The plan calls for replacing a 30 m section of the 2223 cable with YBCO CC cable made with SuperPower CC tape in late 2006.

An advantage that CCs has over 2223 at 77 K is its better in-field J_c performance. This can be further improved in CCs by creating pinning centers in the YBCO grains with chemical additives [64]. In contrast, no effective pinning centers have yet been created in 2223 with chemical additives [65]. Another advantage is that CCs are potentially less expensive than 2223. The cost metric for commercial superconducting wire is $/(kA m) (/(kA m) in Europe). 2223 is expensive because it has a lot of Ag in the sheath, whereas CC tape contains very little intrinsically expensive material. As the performance of 2223 wire increases, i.e. as I_c increases, its cost will continue to decrease.

13.6 The First High-Temperature Superconductivity Wires

Heine et al. [66] were the first to fabricate an HTS wire. They made the Ag-sheathed wire with $Bi_2Sr_2CaCu_2O_8$ (2212) by using the oxide-powder-in-tube (OPIT) method, which is described below. Their first wire was 35 cm long. Its self-field J_c was 1.2×10^3 A/cm^2 at 77 K and 5.5×10^4 A/cm^2 at 4.2 K. It had J_c of 1.4×10^4 A/cm^2 at 4.2 K in 26 T, which was the highest J_c at 26 T reported at the time. This showed that 2212 could be used in very high fields because of its high B_{c2} [67], a characteristic it shares with 2223 [68]. Ag-sheathed 2223 wire was made shortly afterwards using the same basic OPIT processes, but with a different heat treatment [69]. Today, Ag-sheathed 2212 and 2223 wires are still made with the OPIT method. The process has become more refined over the years, and 2223 wires up to 1.5 km long have been made [70], but the basic processes to make the wires are the same today as they were in the beginning.

The overall goal of OPIT processing is to form a wire in which the 2223 grains are well aligned and connected together so that supercurrent can run from end to end in the wire. The 2223 does not need the high degree of three-dimensional alignment required for YBCO CCs. However, the 2223 grains should be aligned so that the superconducting CuO_2 planes, which are parallel to the a–b planes, are as parallel as possible to the flat face of the tape. There are several models

showing that this configuration maximizes *a–b* plane connectivity between grains and minimizes *c*-axis current transport increases J_c [71–73].

The following portion of the chapter is written for those who are interested in learning about the current technology for processing high-J_c 2223 wire. It does not discuss 2212 wire, which is only useful below $\sim$20 K and is used to build very high-field magnets. It is arranged following the steps in the OPIT process, beginning by examining the powder and Ag that are used to make the green wire. It investigates processing parameters used to convert the oxide powder to the superconducting 2223 phase in situ in the wire and then explores how the microstructure and phase assemblage develop during the heat treatment and mechanical deformation steps as the precursor oxides are converted into the fully reacted high-J_c 2223 wire. Throughout, it mentions the processing choices that have been made to achieve high J_c. It concludes by identifying areas where we believe additional study will improve J_c even further.

13.7 The Oxide-Powder-in-Tube Process

In concept, making a 2223 wire is quite simple: one forms grains of the super-conducting 2223 phase and connects them together so supercurrent can flow from one end of the wire to the other. In practice, however, much more is involved in the actual process. The superconducting phase $(Bi,Pb)_2Sr_2Ca_2Cu_3O_x$, which has six chemical species, is difficult to synthesize, and so far no one has prepared phase-pure 2223. This means that all 2223 wires contain a mixture of 2223 and other phases. The OPIT technique, shown schematically in Figure 13.10, is the
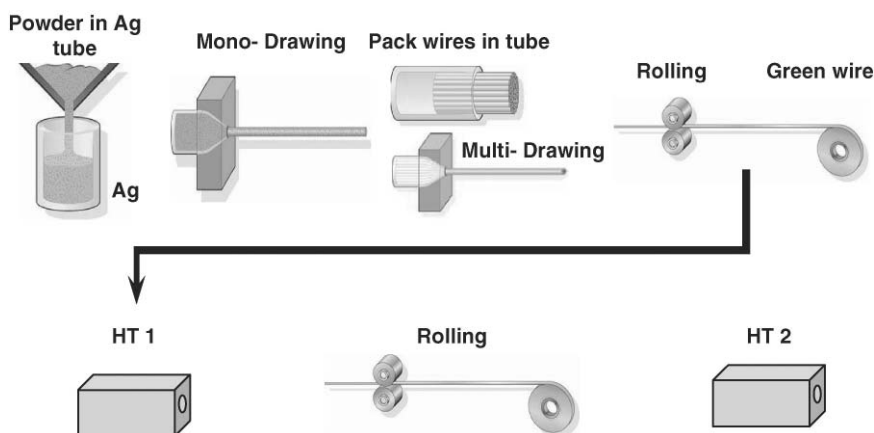
FIGURE 13.10. Schematic diagram showing the steps used to make a Ag-sheathed OPIT wire. The OPIT steps are (1) fill Ag tube with precursor powder, (2) mechanically fabricate the green wire, (3) heat-treat 1 (HT1), (4) roll wire, and (5) heat-treat 2 (HT2). Adapted from AMSC website.

standard way to make Ag-sheathed 2223 wire. The OPIT steps are: (1) fill a tube with precursor powder, (2) fabricate the green wire mechanically, (3) heat-treat 1 (HT1), (4) roll wire, and (5) heat-treat 2 (HT2). We begin by examining the precursor powders that are used to form the green wire and the Ag sheath material.

13.7.1 Powder

As mentioned above, synthesizing the 2223 phase is challenging, particularly when it is done in situ in the wire. In the late 1980s and 1990s, 2223 was made by about every technique used to make ceramics. Some of these methods that can be used to make large quantities of powder are solid-state reaction [74], decomposition of dried aqueous solutions [75], freeze-drying [76], and aerosol-spray pyrolysis [77]. A common characteristic of each of these synthesis techniques is that the amount of 2223 phase can be controlled by changing the temperature T, time t, and oxygen partial pressure pO_2 used in the reaction. The precursor powder made by these different techniques can be reacted so that its 2223 content can vary from almost entirely 2223 with a small amount of other phases, to having little or no 2223 in the oxide powders. It has been found that the highest J_c wires are made using precursor powder that contains essentially no 2223.

The overall composition used for 2223 does not have the "ideal" 2:2:2:3 stoichiometry and includes Pb that replaces part of the Bi [78]. Pb is used because it was observed that it increases the amount of liquid that forms in the system, which speeds up the formation of 2223 and does not affect its superconducting properties [78]. Pb-free 2223 can be synthesized, but without the Pb the kinetics are much slower [79].

Pb can be present in different phases in the precursor powder. This affects the formation of 2223, as shown by Luo et al. [80]. They fixed the total amount of Pb and used precursor mixtures with different amounts of Pb-doped 2212 and Ca_2PbO_4. They found the best formation of 2223 and highest J_c when most of the Pb was in the 2212 and only a small amount was in Ca_2PbO_4. Later work by Jeremie et al. [81] showed that it is possible to change the Pb content reversibly in Pb-doped 2212 by varying the temperature. This also changed the symmetry of the 2212 phase from tetragonal with low Pb content to orthorhombic with high Pb content. They also showed that having most of the Pb in the Pb-doped 2212 yielded 2223, which reacted fastest and was the most phase pure.

The predominant phase in the precursor powder is typically 2212. The other phases depend on the overall "2223" stoichiometry and the T and pO_2 used in the reaction. Other phases that can be present with 2212 include CuO, $(Sr,Ca)_2CuO_2$ (2:1 alkaline earth cuprate (AEC)), $(Sr,Ca)_{14}Cu_{24}O_x$ (14:24 AEC), Ca_2PbO_4, and $(Bi,Pb)_3Sr_2Ca_2CuO_x$ (3221) [82].

13.7.2 Ag Sheath

The precursor powder is packed into an Ag tube, which has been the sheath material for all Bi-based wires beginning with Heine et al.'s first 2212 wire [66]. It is not

likely to be replaced by another material, because it has several properties that make it the ideal sheath material. Ag does not oxidize and it is permeable to oxygen, allowing oxygen to move into and out of the oxide core during the heat treatment. During the heat treatments, the Ag sheath is the "crucible" in which 2223 forms. Although Ag lowers the temperature at which 2223 begins to melt [83], it is not incorporated into the 2223 structure and does not affect its T_c [84]. 2223 forms preferentially at the Ag–oxide interface at lower temperatures than in the middle of the oxide core, and these 2223 grains align parallel to the smooth Ag–oxide interface [85]. When the Ag-sheathed wire is used in superconducting applications, the Ag sheath is a normal conductor that can carry the current if the 2223 goes normal.

In fully processed Ag-sheathed 2223 wire, a pure Ag sheath is very soft, and the fully processed wire cannot withstand much stress before I_c degrades (<85–100 MPa at room temperature, depending on the Ag fill factor [71]). Pure Ag also has high electrical and thermal conductivity. To increase its strength, and to reduce its conductivity, Ag has been alloyed with a variety of materials. The majority of studies have been done with Au, Cu, Mg, Mn, and Pd [86]. Typically, the Ag alloy begins as a solid solution, and the green wire is made with the alloy. Solid-solution hardening gives a small increase in hardness. The main increase in hardness occurs during the heat treatments, when oxygen diffuses into the Ag sheath and reacts with the alloying element (Cu, Mg, and Mn) to form small oxide particles that dispersion-harden the Ag. The Vickers hardness of Ag was reported to increase from 33 kg/mm^2 in pure Ag to 260 kg/mm^2 in Ag with 5 at.% Mg that had been heat-treated in O$_2$ [86]. Au and Pd, which remain in solid solution in the Ag because they do not oxidize, increase the electrical and thermal conductivity. For instance, adding 11–15 at.% Au reduces the thermal conductivity at 77 K from ~6 W/(cm K) for pure Ag to 0.6 W/(cm K) for the alloy [87]. This lower thermal conductivity makes Ag(Au) sheath useful for current leads [88].

During the heat treatment, Cu from the 2223 core can diffuse into the Ag to form an Ag–Cu solid solution that depletes the Cu content in the oxide core [89]. In addition, Cu from the 2223 core can diffuse through the Ag sheath and react with oxides that the wire touches during thermal processing, or Cu from the 2223 core may react with the oxide particles that dispersion-harden the Ag, e.g. forming (Mg,Cu)O in an Ag(Mg) sheath [90].

13.7.3 Mechanical Deformation to Form the Green Wire

The oxide-packed Ag tube is drawn as a round wire and then it is drawn into a hexagonal shape. The hexagonal shape maximizes the packing density when filaments are stacked in another Ag tube to form a multifilament billet. This is drawn as a round wire and rolled to the final dimensions. The dimensions for commercially available, fully processed 2223 wire are ~4–4.5 mm wide and 200–240 μm thick. The superconducting fraction in the wire ranges from ~33–40% of the cross-sectional area. The powder particle size, particularly the hard AECs, must be small to maintain a smooth Ag–oxide interface when drawing and rolling

the green wire. The drawing and rolling schedules have been developed to avoid sausaging.

13.7.4 Heat Treatment 1 (HT1)

Varying T, t, pO_2 during HT1 has an enormous effect on the reaction kinetics and phase assemblage that forms during HT1. MacManus-Driscoll et al. [83] determined the pO_2–T stability range, subsolidus relations, and regions where liquid forms for the 2223 phase in the presence of Ag. Work on reaction kinetics as a function of pO_2 showed that 2223 formed fastest when using 1/13 atm O_2 [91], leading to the use of 0.075 or 0.08 atm O_2. 2223 is also synthesized in air. Luo et al. [82] investigated how pO_2 affects the phase assemblage as 2223 forms from the precursor powder. They found that CuO and 2:1 AEC are present using 0.075 atm O_2, whereas 2:1 AEC and 14:24 AEC are present using 0.21 atm O_2. Baurceanu et al. [92] developed a method based on varying T and pO_2 during HT1 to break up the nonsuperconducting phases that form during HT1.

As described below, a small amount of liquid is vital for fast 2223 reaction kinetics. Changing the pO_2 used to synthesize 2223 changes the temperature at which liquid forms in the system: increasing pO_2 decreases the temperatures at which liquid forms [93]. Holesinger et al. [94] used transmission electron microscopy (TEM)–energy-dispersive X-ray spectrometry to determine the liquid composition present when 2223 was forming. They reported that the composition of the liquid did not vary much between 100 and 300 min at 827 °C. What happens to the liquid as the wire is cooled from the reaction temperature is discussed in Section 13.7.6.

The temperature at which the reaction occurs determines the 2223 formation mechanism and reaction rate. There is no liquid present at low temperature, so 2223 forms by solid-state reaction, which has very slow kinetics [95]. If very high temperatures are used, then 2223 melts incongruently [96]; one could try to make 2223 wires using melt processing, similar to how 2212 wires are made [97]. Yamada et al. [98] investigated melt processing of 2223. They were able to form some aligned 2223 from the melt in Ag-sheathed flat wire by adjusting the temperature at which they began slow cooling and controlling the pO_2. They did not report J_c in their melt-processed wire. Melt processing of 2223 has not been pursued. We see that solid-state reaction and melt processing are not optimum methods to form 2223 wire.

The favored method is to use an intermediate temperature where only a small amount of liquid forms in the system. The 2223 forms by a liquid-assisted reaction. The presence of a small amount of liquid speeds up the kinetics [99]. Liquid-assisted processing has been found to be the optimum method to make 2223: the kinetics are faster than the solid-state reaction, and most of the precursor powder can be converted into 2223. Having a small amount of liquid also helps form grains that are connected together so they carry supercurrent. Commercial 2223 wire is made using liquid-assisted processing. Aota et al. [93] found that 2223 formed rapidly at ~820 to 835 °C in 0.075 atm O_2. The low side of this temperature range was set by having enough liquid that the kinetics are fast, and the maximum

temperature was set by not being so high that the nonsuperconducting phases rapidly grew to large size. Liquid is needed in both HT1 and HT2, so the same temperature range is used for both heat treatments.

The powder-melting characteristics are sensitive to the overall "2223" composition, the phase assemblage in the powder, the homogeneity of the mixture, and pO_2. We believe one of the key reasons for AMSC and SEI's success with 2223 wire is that each company begins with a very reproducible precursor powder.

It was mentioned above that early work showed J_c was lower when starting with fully converted 2223 precursor powder [99]. In a green wire made with fully converted 2223, HT1 needs to connect the 2223 grains together. However, the 2223 grains do not sinter together well without a small amount of liquid in the system. Starting with fully reacted 2223, very little liquid is present until the 2223 phase begins to melt, which requires higher temperatures than normally used to form the 2223 and, in the worst case, can result in forming large grains of nonsuperconducting phases. Even if the 2223 grains could be connected, the 2223 grains in the green wire are not aligned, and there is no mechanism that can align the preexisting 2223 grains during the heat treatment.

As discussed below, liquid is also needed in HT2, so the precursor powder cannot be fully converted to 2223 in HT1. Jiang et al. [100] found that ∼85% conversion in HT1 gave the maximum J_c.

To understand what changes occur during the heat treatments and intermediate rolling, Jiang et al. [100] investigated the microstructural, phase, and electromagnetic properties of 2223 wire at various stages during the OPIT process. Figure 13.11 shows what samples were studied and lists the density, J_c, and irreversibility field H^* for the samples. For high J_c, the 2223 should be aligned with its a–b plane parallel to the face of the flat wire. As 2223 forms during the heat treatment, the 2223 that forms next to the Ag–oxide interface has the highest degree of alignment, and the alignment decreases going into the center of the filament away from the interface. The density decreases because pores form in the center of the filaments as the randomly oriented 2223 grains grow. This decrease in density is called retrograde densification [101].

Figure 13.11 shows that J_c is low after HT1. Unreacted precursor powder prevents the 2223 grains from being fully connected together, and the porosity that
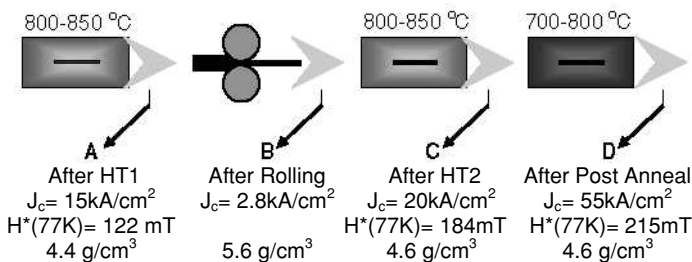
FIGURE 13.11. Physical and superconducting properties of 2223 wire at different points in the heat-treatment cycle [101]. The density of the green wire before HT1 was 5.6 g/cm^3.

causes the decrease in density also limits the 2223 connectivity. Increasing J_c requires densifying the wire and finishing the conversion to 2223.

13.7.5 Rolling

It was recognized from the beginning that a series of heat treatments with a mechanical deformation between each heat treatment was needed to make a high-J_c 2223 wire [69]. The first work was done with short lengths of wire that were uniaxially pressed between each heat treatment. Pressing is not a viable manufacturing process for long 2223 wire, so it was replaced by rolling. However, it was observed that J_c of rolled wire was lower than that of pressed wire that was processed identically. Using magneto-optical imaging, Parrell et al. [102] showed that the major difference between rolling and pressing was the direction of the cracks in the deformed wire. Pressing creates cracks that run parallel to the long axis of the wire. They do not block the current as much as the cracks in rolled wire that run perpendicular to the long axis of the wire. They are very effective at blocking current. Using TEM, Holesinger et al. [103] have observed breaks and c-axis cracks in 2223 grains after rolling. Figure 13.11 shows that rolling decreased J_c by more than 80% owing to breaking of the 2223 grains [100]. The magneto-optical study also showed that the deformation cracks did not fully heal in subsequent heat treatments [102].

The deformation step has positive attributes that outweigh the negative aspect of breaking the 2223 grains. At the macroscopic level, deformation densifies the core, and at the microscopic level it breaks up and mixes grains in the oxide core (see below). It was initially thought that rolling improved the 2223 alignment; however, through-sample X-ray diffraction experiments showed that intermediate rolling actually decreases the 2223 alignment texture [104], which is explained below.

When one synthesizes a complex oxide by using a solid-state reaction (or a liquid-assisted reaction), the mixture of starting materials is ground together, pressed into a pellet, and fired, with these three steps being repeated until the reaction goes to completion. In the OPIT process, rolling breaks up grains, exposing new, unreacted surfaces, mixes the unreacted grains together, and brings the powders in closer contact: rolling provides the in situ grinding, mixing, and pressing needed for a successful solid-state (or liquid-assisted) reaction. This allows more 2223 to form in HT2 and some, but not all, of the rolling cracks to heal [105]. Holesinger et al. [103] have observed broken grains of 2212 and 2223 in TEM images of samples after rolling.

Rolling is thus a balancing act between the beneficial effects that enhance the formation of 2223 in HT2 and breaking the 2223 grains. Rolling can have another negative effect. It can deform the smooth Ag–oxide interface, which decreases the 2223 alignment. This occurs because the AEC phases are smaller and harder than in the 2212 and 2223 and, during rolling, penetrate further into the Ag than in the 2212 or 2223. This creates hillocks on the formerly smooth Ag–oxide interface that misalign the 2223 at the Ag–oxide interface [103]. In the porous center of the

filament, the randomly oriented, plate-like 2223 grains break into small pieces that remain randomly oriented.

13.7.6 Heat Treatment 2 (HT2)

The main purposes of HT2 are to form additional 2223, heal rolling cracks and to give 2223 the best superconducting properties possible. As mentioned above, liquid is vital to form 2223 and heal cracks, so the maximum temperature in HT2 is the same or slightly higher than in HT1. However, at the end of HT2, not all of the 2212 is converted to 2223, and fully processed wire contains remnant nonsuperconducting phases. As mentioned above, magneto-optical imaging shows that HT2 does not heal all the cracks. Figure 13.11 shows that the density decreases during HT2. This is a repeat of what happens in HT1, in which new, randomly oriented 2223 grains form, creating pores that decrease the density [100]. Early studies used many deformation and heating steps to form as much 2223 and increase J_c as high as possible. Today, commercial 2223 wire manufacturers use two heat treatments and one intermediate rolling step to maximize J_c while minimizing processing costs.

Liquid that forms at the highest temperatures in HT2 is present in the wire as it begins to cool. A through-sample neutron diffraction study showed that, during cooling, the amount of 2223 remains constant whereas the amount of 2212 increases, presumably due to 2212 forming from liquid during cooling [106].

Jiang et al. [107] studied changes in J_c due to adding a postannealing step after HT2. A broad definition of postannealing is any additional thermal processing after the end of the main heat treatment in HT2. For a three-step HT2 consisting of heating at 828 °C/36 h, then 822 °C/48 h, then 805 °C/24 h and cooling to room temperature at 1.5 °C/min, Jiang et al. found that J_c (77 K self-field) was 25.4 kA/cm^2 (note: the rest of the J_c data in Section 13.7 are for 77 K self-field). When the sample was reheated for 24 h at 783 °C, which is below the temperature at which 2223 rapidly forms, and cooled at 1.5 °C/min, J_c increased by ~20% to 30.0 kA/cm^2. Scanning electron microscopy (SEM) and X-ray diffraction showed the 3221 phase had formed in the 783 °C sample. When the 783 °C sample was reheated for 48 h at 822 °C (where 2223 could form), then cooled at 1.5 °C/min, J_c decreased to 16.2 kA/cm^2 and 3221 was gone. Studies by Yuan et al. [108] indicate that the 3221 phase forms from the liquid that is present at 820–835 °C, where 2223 is formed. We believe that the increase in J_c at 783 °C is due to removing liquid from the grain boundaries by forming 3221 and other crystalline phases, which increases the 2223 connectivity. On reheating the 783 °C sample to 822 °C, liquid forms from 3221 and other phases. After cooling at 1.5 °C/min from 822 °C, J_c decreased by ~50% because the liquid did not have time to form 3221 at this fast cooling rate, so the liquid wets and blocks the grain boundaries. However, with slower cooling (1 °C/h), 3221 was present after cooling from 820 °C to 780 °C and J_c increased compared with that after 1.5 °C/min cooling [109]. These studies show that the liquid that forms at the highest temperature in HT2 is present as the

sample is cooled, and slow cooling can help convert the liquid to crystalline phases and increase J_c.

In addition to forming 3221, 2212 also forms from the liquid. This was seen in a through-sample neutron diffraction study [106] and was recently shown in quenching studies by Nakao-Kametani and Osamura [110]. They determined the amount of 2212 and other crystalline and amorphous phases from Rietveld refinement of X-ray patterns of air-quenched samples. They cooled samples from 822 °C to 800 °C, 790 °C, and 780 °C at cooling rates of 0.18 °C/min, 0.27 °C/min, and 0.35 °C/min respectively and then held for 46 h. At each final temperature they found that the amount of 2212 had increased and liquid had decreased. Their study showed that all the liquid was consumed after cooling and then holding at 780 °C. This sample contained the most 2212 and 3221, and J_c had increased during cooling to and holding at 780 °C. On cooling and holding at 790 and 800 °C, 2212 formed, but some of the liquid was still present. 2212 is considered in more detail in Section 13.8.

After HT2, fully reacted, high-J_c wire still contains rolling cracks and porosity, in addition to remnant oxides that have not converted to 2223. All these are current-limiting mechanisms that reduce J_c. Rikel et al. [111] developed overpressure (OP) processing, which is a variation of hot isostatic pressing, to eliminate pores and cracks during HT2. This process is now used commercially by SEI and has processed wire up to 1.5 km in length [70]. OP processing uses a flowing mixture of inert gas and O_2 to apply a high pressure (up to 300 atm in SEI's system [70]) to the 2223 wire during HT2. The inert gas is insoluble in Ag, so it applies the compressive stress that causes the pores to shrink and cracks to heal during the heat treatment. O_2 diffuses rapidly through the Ag, so the pO_2 sets the thermodynamic conditions needed to form 2223. By using OP processing, Yuan et al. [112] achieved $J_c = 30.8$ kA/cm^2 (77 K, 0.1 T), which was the highest 0.1 T J_c reported at that time and an increase of 30% over a sample processed identically at 1 atm. They used a total pressure of ∼150 atm with $pO_2 = 0.075$ atm, which is the same pO_2 used in their 1 atm studies. Hellstrom et al. have reviewed OP processing [113].

Yuan et al. [114] measured the density of monocore filaments that had undergone OP processing during and after HT2. It had increased from ∼80% to >95% of the theoretical density. This densification significantly improves the properties of the 2223 wire. Figure 13.12 shows the microstructure of 1 atm and 150 atm OP-processed 2223 wire. There is a striking improvement in microstructure of the OP sample: it does not have the large pores and cracks that are present in the 1 atm sample. Magneto-optical images showed that OP processing healed cracks from the intermediate rolling [115]. In addition, their magneto-optical images showed that the current flow was uniformly distributed across the entire filament cross-section, rather than flowing only near the Ag interface, as it does in the 1 atm samples. Further, local J_c calculated from magneto-optical current reconstruction (MOCR) showed small, local regions with J_c as high as ∼300 kA/cm^2 in the OP samples compared with small, local regions with J_c as high as ∼200 kA/cm^2 in 1 atm samples. The improved microstructure also increases the mechanical properties of OP-processed wire. SEI reported that OP processing increased the tensile strength
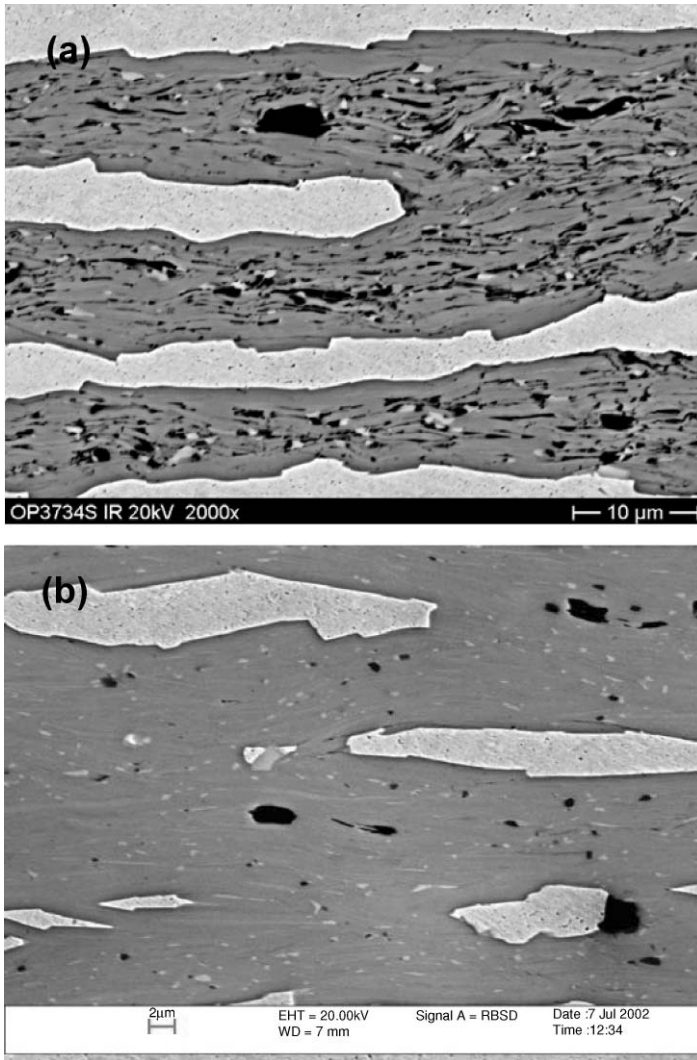
FIGURE 13.12. SEM micrograph of filaments in 2223 wire that was heat-treated (a) entirely in 1 atm total pressure and (b) with OP processing using 148 atm total pressure in the final heating step.

from 85–100 MPa for 1 atm samples to 155–205 MPa for OP samples (measured at room temperature) [70]. The high and low values are for wires with two different Ag fill factors. Figure 13.13 shows J_c in OP- and 1-atm-processed wires.

The microstructure of the OP sample in Figure 13.12b appears to be more homogeneous and better aligned and to have fewer second phases than the 1 atm sample (Figure 13.12a). With this significant improvement in microstructure, one wonders why J_c increased by only ~30%. We believe that higher magnification

FIGURE 13.13. J_c as a function of magnetic field at 77 K for 1 atm and OP-processed (148 atm) wire [116].
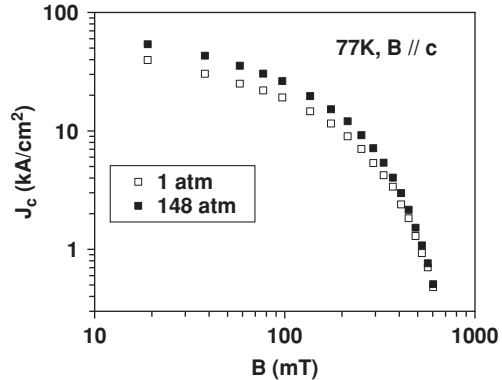
SEM images show part of the answer: the OP samples still contain cracks, pores, and nonsuperconducting phases; they are just much smaller than in the 1 atm sample. Figure 13.12b shows light gray streaks that run parallel to the 2223 grains in the OP microstructure. These are 2212 grains that can limit the supercurrent. We believe that all these defects need to be eliminated, or at least reduced, to increase the overall J_c in the wire to the locally high J_c values ($\sim$300 kA/cm^2) determined from MOCR.

13.8 Future Work

We believe there are two broad areas where further research will improve J_c. These are related to improvements in the microstructure and improving flux pinning. We focus on improvements in microstructure first. Fully processed 2223 wire contains phases other than 2212 because of incomplete conversion to 2223 and lack of knowledge of the exact composition of the one-phase region for 2223. It may never be possible to eliminate all the extraneous phases in 2223 wire, so the best strategy is to concentrate on reducing those that are most harmful to current flow. We believe the most harmful are 2212 and remnant liquid. We will begin with 2212. It has a variable T_c that can range from $\sim$90 K to below 70 K, and it can be present in three distinct forms in the wires: as half-cell intergrowths within the 2223 grains, as discrete 2212 grains in 2223 colonies, and as discrete grains outside the 2223 colonies [94]. We believe that the 2212 grains within the colonies are most detrimental to J_c. These 2212 grains are sandwiched between two 2223 grains, and the c-axes of all three grains are aligned in the same direction. At 77 K, supercurrent that flows in the c direction in 2223 colonies is hindered by these 2212 grains, which have lower T_c and lower J_c than the surrounding 2223 [71–73,117]. The 2212 half-cell intergrowths in the 2223 grains can also block current flow in the c direction. However, the half-cells are thin and may be less of an impediment to supercurrent because the system can proximity couple across

the half cell. The discrete 2212 grains outside the 2223 colonies have the smallest effect on the current because they, like the other crystalline phases, block only a small fraction of the cross-section.

It may be possible to reduce the 2212 by changing the thermo-mechanical processing of existing 2223 wires. However, much work has been done optimizing the thermo-mechanical processing of these commercial wires, so it is unlikely that new processing schemes will be developed that will simultaneously decrease the 2212 content and increase J_c. However, 2212 SQUID index measurements [112], which measure the relative amount of 2212 in a sample, show that OP processing decreases the 2212 content relative to samples with identical 1 atm processing. This has also been reported by SEI [70]. We do not know how OP reduces the amount of 2212.

Changing the overall 2223 composition used for the wire may reduce the amount of 2212 in fully processed wire. This will most probably also require changes in the thermal processing. Finding a new composition and developing a processing schedule that increase J_c will probably require a major research effort.

Additional OP processing studies are needed to understand how to further reduce or eliminate the remaining pores and cracks. This will increase the 2223 connectivity and should increase J_c. This can be done with existing 2223 wire, and it may be the most productive way to increase J_c.

Further study is needed to understand the liquid that is present when 2223 forms, from what phases it forms, and to what it converts on cooling. The goal is to have liquid present to form 2223 and to remove all the liquid on cooling. We believe that we want the liquid to convert to a phase assemblage on cooling that does not include 2212.

Adding flux-pinning centers is markedly different in 2223 and YBCO. Pinning centers can be introduced by chemical means in YBCO [64]; no chemical additions or substitutions have created effective pinning centers in 2223 [65]. The only truly effective pinning centers in 2223 are damage tracks from ion irradiation or nuclear decay (e.g. see Reference [65] and references cited therein), which are not practical for commercial 2223 wire. New doping studies on 2223 that focus on measuring the irreversibility field in addition to J_c and T_c are needed to see whether there are any overlooked chemical dopants or additives that may increase flux pinning in 2223.

Recent work by Yuan [116] using through-process, oil-quenched samples showed that J_c increased by more than a factor of two during the last few hours of HT2 as the sample was cooled to room temperature. It is surprising that, after ~100 h of thermal processing, the last few hours of the heat treatment while the sample is cooling have such a profound effect on J_c. SEM studies show that the microstructure does not change significantly during cooling, other than the grains of 3221 that form during the postannealing. MOCR indicates a small increase in J_c due to increasing connectivity as the liquid is converted to 3221. However, MOCR shows a larger increase in J_c due to increasing flux pinning during cooling [118]. We believe this flux pinning is due to the 2223 and 2212 picking up oxygen as the wire cools. This increases T_c of the 2223 and decreases T_c of the 2212 while

simultaneously increasing the Kramer irreversibility field [116]. Understanding the relevant pinning mechanism and pinning centers, along with details of how the oxygen stoichiometry and associated 2223 defect chemistry change during cooling, is a fertile research area that will further increase J_c.

13.9 Summary

The development of YBCO-CCs that carry high current is advancing rapidly. This requires the YBCO material to be deposited with three-dimensional alignment, so the supercurrent can flow from one grain to the next along the length of the wire. New processing advances and advanced understanding of the materials science of YBCO-CCs promise to improve their performance and decrease their cost.

Ag-sheathed 2223 wire is currently the most developed HTS conductor. Although it is chemically more complicated than YBCO, it is easier to process. In this chapter we outlined research areas we believe will lead to increases in the current-carrying capacity of 2223 wire and will decrease its cost.

In the long run, we expect that Ag-sheathed 2223 and YBCO-CCs will coexist in the market.

References

1. Onnes, H.K., *Akad. van Wetenschappen (Amsterdam)*, 14, 113, 818, 1911; "The Superconductivity of Mercury." *Comm. Phys. Lab. Univ. Leiden*, Nos. 122 and 124, 1911.
2. Little, W.A., *Phys. Rev.* 134, A1416, 1964.
3. Jerome, D., Mazaud, A., Ribault M., and Bechgaard, K., *J. Phys. (Paris)*, 41, L95, 1980.
4. Johnston, D.C., *J. Low Temp. Phys.*, 25, 145, 1976.
5. Sleight, A.W., Gillson, J.L., and Bierstedt, P.E., *Solid State Commun.*, 17, 27, 1975.
6. Bednorz, J.G., and Müller, K.A., *Z. Phys. B*, 64, 189, 1986.
7. Bednorz, J.G., Takashige, M., and Müller, K.A., *Europhysics Lett.*, 3, 379, 1987.
8. Wu, M.K., Asburn, R., Tong, J., Hor, P.H., Meng, L., Huang, J., Wang, Y.Q., and Chu, C.W., *Phys. Rev. Lett.*, 58, 908, 1987.
9. Maeda, H., Tanaka, Y., Fukutomi, M., and Asano, T., *Jpn. J. Appl. Phys.*, 27, L209, 1988.
10. Sheng, Z.Z., and Hermann, A.M., *Nature*, 332, 138, 1988.
11. Putilin, S.N., Antipov, E.V., Chmaissem, O., and Marezio, M., *Nature*, 362, 226, 1993,
12. Schilling, A., Cantoni, M., Guo, J.D., and Ott, H.R., *Nature*, 363, 56, 1993.

13. Gao, L., Xue, Y.Y., Chen, F., Xiong, Q., Meng, R.L., Ramirez, D., and Chu, C.W., *Phys. Rev. B*, 50, 4260, 1994.

14. Akimitsu, J., first report on January 10, 2001, at a symposium on "Transition Metal Oxides" in Sendai, Japan. Nagamatsu, J., Nakagawa, N., Muranaka, T., Zenitani, Y., and Akimitsu, J., *Nature*, 410, 63, 2002.

15. Bardeen, J., Cooper, L.N., and Schrieffer, J.R., *Phys. Rev.*, 108, 1175, 1957.

16. Karpinski, J., Kaldis, E., Jilek, E., Rusiecki, S., and Bucher, B., *Nature*, 336, 660, 1988.

17. Bordet, P., Chaillout, C., Chenavas, J., Hodeau, J.L., Marezio, M., Karpinski, J., and Kaldis, E., *Nature*, 334, 596, 1988.

18. Mikheenko, P.N., Uprety, K.K., and Dou, S.X., "BSCCO," *Handbook of Superconducting Materials*, Cardwell, D.A., and Ginsley, D.S., eds., IoP, Bristol 2003, p. 947.

19. Bellingeri, E., and Flükiger, R., "TlSCCO," *Handbook of Superconducting Materials,* Cardwell, D.A., and Ginsley, D.S., eds., IoP, Bristol 2003, p. 993.

20. Schwartz, J., and Sastry, P.V.P.S.S., "HgSCCO," *Handbook of Superconducting Materials*, Cardwell, D.A., and Ginsley, D.S., eds., IoP, Bristol 2003, p. 1029.

21. Welp, U., Grimsditch, M., You, H., Kwok, W.K., Fang, M.M., Crabtree, G.W., and Liu, J.Z.,*Physica C*, 161, 1–5, 1989.

22. Freyhardt, H.C., and Winzer, K., Universität Göttingen, 1987, unpublished.

23. Freyhardt, H.C., and Gelsdorf, F., Universtiät Göttingen, 1987, unpublished.

24. Jin, S., Tiefel, T.H., Sherwood, R.C., Davis, M.E., van Dover, R.B., Kammlott, G.W., Fastnacht,R.A., and Keith, H.D., *Appl. Phys. Lett.*, 52, 2074, 1988.

25. Salama, K., Selvamanickam V., Gao, L., and Sum, K., *Appl. Phys. Lett.*, 54, 2352, 1989.

26. Schneemeyer, L.F., Gregory, E.M., and Waszczak, J.V., *Phys. Rev. B*, 36, 8804, 1987.

27. Erb, A., Walker, E., and Flükiger, R., *Physica C*, 258, 9, 1996.

28. Blatter, G., Feigelman, M.V., Geshkenbein, V.B., Larkin, A.I., and Vinokur, V.M., *Rev. Mod. Phys.*, 66, 1125, 1994.

29. Dimos, D., Chaudhari, P., and Mannhart, J., *Phys. Rev. B*, 41, 4038, 1990.

30. Rao, S.M., Loo, B.H., Wang, N.P., and Kelly, R.J., *J. Cryst. Growth*, 110, 989, 1991.

31. Ota, K., and Ito, T., *Physica C*, 227, 77, 1994.

32. Murakami, M., ed., *Melt Processed High-Temperature Superconductors*, World Scientific, 1992. Murakami, M., *Supercond. Sci. Technol.*, 5, 185, 1992.

33. Leenders, A., Walter, H., and Freyhardt, H.C., personal communication, German DYNASTORe project, 2004.

34. Tomita M., and Murakami, M, *Nature*, 421, 517, 2003.

35. Goyal, A., Norton, D.P., Budai, J.D., Paranthaman, M., Specht, E.D., Kroeger, D.M., Christen, D.K., He, Q., Saffian, B., List, F.A., Lee, D.F., Martin, P.M., Klabunde, C.E., Hattfield, E., and Sikka, V.K., *Appl. Phys. Lett.*, 69, 1795, 1996.

36. Goyal, A., "RABiTS: Status and Issues," *HTS Wire Development Workshop*, St Petersburg, USA, January 2003. *DOE Peer Review on Superconductivity for Electric Systems*, Washington, August 2005.

37. Sarma, V.S., Eickemeyer, J., Singh, A., Schultz, L., and Holzapfel, B., *Acta Mater.*, 51, 4919, 2003.

38. Hänisch, J., Sarma, V.S., Zeimetz, B., Schindler, F., Eickemeyer, J., Schultz, L., and Holzapfel, B., *Supercond. Sci. Technol.*, 17, 1003, 2004.

39. Hammerl, G., Herrnberger, A., Schmehl, A., Weber, A., Wiedemann, K., Schneider, C.W., and Mannhart, J., *Appl. Phys. Lett.*, 81, 3209, 2002. Also Holzapfel, B. et al.,

"Improving the Critical Current Density of Coated Conductors in the Presence of Magnetic Fields," *EUCAS 2005*, Vienna, September 12, 2005.

40. Freyhardt, H.C., Hoffmann, J., Wiesmann, J., Dzick, J., Heinemann, K., Issaev, A., Usoskin, A., and Garcia-Moreno, F., *Applied Superconductivity*, 4, 435, 1998.

41. Usoskin, U., Freyhardt, H.C., and Issaev, A., "YBCO Coated Conductors Manufactured via High-Rate Pulsed Laser Deposition," *Frontiers in Superconducting Materials—New Materials and Application Symposium*, December 1–4, 2003, Boston, p. 5.

42. Iijima, Y., Tanabe, N., Kohno, O., and Ikeno, Y., *Physica C*, 185, 1961, 1991. Iijima, Y., Onabe, K, Futaki, N., Tanabe, N., Sadaka, N, Kohno, O, and Ikeno, Y, *J. Appl. Phys.*, 74, 1905, 1993.

43. Iijima, Y., Kakimoto, K., Sutoh, Y., Ajimura, S., and Saitoh, T., *Supercond. Sci. Technol.*, 17, S264, 2004.

44. Usoskin, A., Rutt, A., Knoke, J., and Krauth, H., "Long-Length YBCO Coated Stainless Steel Tapes with High Critical Currents,"*Proc. CEC–ICMC*, Keystone, Colorado, September 2005.

45. Issaev, A., Usoskin, A., Knoke, J., and Freyhardt, H.C., "Superconducting Properties of Long Coated Tapes. Optimization of Buffer/Shunt Layer Architecture," *Proc. International Workshop on Coated Conductors for Applications CCA2003*, Orta S. Giulio, September 2003.

46. Muroga, T., Watanabe, T., Miyata, S., Iwai, H., Yamada, Y., and Shiohara, Y., "Enhancement of Grain Alignment and Deposition Rate of CeO_2 Cap Layer on IBAD Tape for YBCO Coated Conductor," *Proc. International Workshop on Coated Conductors for Applications CCA2003*, Orta S. Giulio, September 2003

47. Arendt, P., and Foltyn, S., "Development of Coated Conductors Based on IBAD-MgO," *Superconductivity for Electric Systems Annual Peer Review*, Washington, July 2004

48. Evetts, J.E., Kursumovic, A., Tomov, R.I., Rutter, N.R., Driscoll, J.L., Glowacki, B.A., Sandiumenge, F., Cavallaro, A., Pomar, A., Puig, T, Obradors, X., Hühne, R., Holzapfel, B., Qi, X., and Lockmann, Z., "Development of 'Robust' Buffer Layer Architecture for Non-Vacuum Coated Conductor Processing," *Proc. International Workshop on Coated Conductors for Applications CCA2003*, Orta S. Giulio, September 2003.

49. Clem, P.G., Voigt, J.A., Siegal, M.P., Venturini, E.L., Rupich, M., Kodenkandath, T., Li, X., Schoop, U., Paranthaman, M., List, F.A., Holesinger, T.A., Gibbson, and B., Matias, V., "Solution Deposition for YBCO Coated Conductors," *Superconductivity for Electric Systems Annual Peer Review*, Washington, July 2004.

50. Obradors, X., Puig, T., Pomar, A., Sandiumenge, F., Pinol, S., Mestres, N., Castano, O., Coll, M., Cavallaro, A., Palau, A., Gasquez, J., Gonzalez, J.C., Guiterrez, J., Roma, N., Ricart, S., Moreto, J.M., Rossel, M.D., and van Tendeloo, G., *Supercond. Sci. Technol.*, 17, 1055, 2004.

51. Freyhardt, H.C., Wördenweber, R., Utz, B., Usoskin, A., and Yamada, Y., "Physical Vapour Thin Film Deposition Techniques," *Handbook of Superconducting Materials*, Cardwell, D.A., and Ginsley, D.S., eds., IoP, Bristol 2003, p. 741.

52. Usoskin, A., Rutt, A., Knoke, J., and Dietrich, R., *Proc. CEC–ICMC Conf.*, Keystone, Colorado, USA, August 2005.

53. Arendt, P, Los Alamos Nat. Lab., personal communication, September 2005; with additions of H.C. Freyhardt.

54. Yamada, Y., Ibi, A., Fukushima, H., Kuriki, R., Takahashi, K., Kobayshi, H., Konishi, M., Miyata, S., Shiohara, Y., Kato, T., and Hirayama, T., *Proc. CEC–ICMC Conf.*, Keystone, Colorado, USA, August 28–September 1, 2005.

55. Prusseit, W., *Methods of HTS Deposition: Thermal Evaporation*, Theva Dünnschicht GmbH, 2000. Prusseit, W., Sigl, G., Nemetschek, R., Hoffmann, C., Handke, J., Lümkemann, A., and Kinder, H., *IEEE Trans. Appl. Superconductivity*, 15, 2608, 2005.

56. Yamada, Y., and Shiohara, Y., *Physica C*, 217, 182, 1993.

57. Kursumovic, A., Tomov, R.I., Hühne, R., MacManus-Discoll, J.L., Glowacki, B.A., and Evetts, J.E., *Supercond. Sci. Technol.*, 17, 1215, 2004.

58. Malozemoff, A.P., *Second-Generation HTS Wire: An Assessment*, American Superconductor Corporation, March 2004.

59. Kovalsky, L., Xing Yuan, Tekletsadik, K., Keri, A., Bock, J., and Breuer, F., *IEEE Trans. Appl. Supercond.*, 15, 2130–2133, 2005.

60. Kalsi, S.S., Madura, D., and Ingram, M., *IEEE Trans. Appl. Supercond.*, 15, 2146–2149, 2005.

61. Snitchler, G., Gamble, B., and Kalsi, S.S., *IEEE Trans. Appl. Supercond.*, 15, 2206–2209, 2005.

62. European Advanced Superconductors, http://www.advancedsupercon.com/pdf/press_release_EAS_HTS_generator.pdf, 2006.

63. SuperPower, I., http://www.igc.com/superpower/products/hts_components/12_5kv.htm#acp, 2006.

64. Haugan, T., Barnes, P.N., Wheeler, R., Meisenkothen, F., and Sumption, M., *Nature*, 430, 867–870, 2004.

65. Dou, S.X., Wang, X.L., Guo, Y.C., Hu, Q.Y., Mikheenko, P., Horvat, J., Ionescu, M., and Liu, H.K., *Supercond. Sci. Technol.*, 10, 52–67, 1997.

66. Heine, K., Tenbrink, J. and Thoner, M., *Appl. Phys. Lett.*, 55, 2441–2443, 1989.

67. Alexandrov, A.S., Zavaritsky, V.N., Liang, W.Y., and Nevsky, P.L., *Phys. Rev. Lett.*, 76, 983–986, 1996.

68. Babic, E., Kusevic, I., Zadro, K., Ivkov, J., Marohnic, Z., Drobac, D., Prester, M., Hua Kun Liu, Shi Xue Dou, Todorovic-Marinic, D., and Kursumovic, A., *Fizika A*, 4, 549–560, 1995.

69. Maeda, H., Asano, T., Kumakura, H., Sekine, H., Yanagisawa, E., Numata, K., Togano, K., and Tanaka, Y., *High Temperature Superconducting Compounds: Processing and Related Properties. Proceedings of the 1989 Symposium*, 1989, pp. 439–449.

70. Kobayashi, S., Kato, T., Yamazaki, K., Ohkura, K., Fujino, K., Fujikami, J., Ueno, E., Ayai, N., Kikuchi, M., Hayashi, K., Sato, K., and Hata, R., *IEEE Trans. Appl. Supercond.*, 15, 2534–2537, 2005.

71. Bulaevskii, L.N., Daemen, L.L., Maley, M.P., and Coulter, J.Y., *Phys. Rev. B*, 48, 13,798–13,816, 1993.

72. Hensel, B., Grasso, G., and Flukiger, R., *Physical Review B*, 51, 15,456–15,473, 1995.

73. Riley, G.N., Jr., Malozemoff, A.P., Li, Q., Fleshler, S., and Holesinger, T.G., *J. Met.*, 49, 24–27, 1997.

74. Maeda, H., Tanaka, Y., Fukutomi, M., and Asano, T., *Jpn. J. Appl Phys.*, 27, 209–210, 1988.

75. Liu, H.K., Dou, S.X., Savvides, N., Zhou, J.P., Tan, T.X., Bourdillon, A.J., Kviz, M., and Sorrell, C.C., *Physica C*, 157, 93–98, 1989.

76. Kang-Ho Song, Hua-Kun Liu, Shi-Xue Dou, and Sorrell, C.C., *J. Amer. Ceram. Soc.*, 73, 1771–1773, 1990.

77. Ward, T.L., Lyons, S.W., Kodas, T., Brynestad, J., Kroeger, D.M., and Hsu, H.,*Physica C*, 200, 31, 1992.
78. Hatano, T., Aota, K., Ikeda, S., Nakamura, K., and Ogawa, K.,*Jpn. J. Appl. Phys.*, 27, L2055–L2058, 1988.
79. Sastry, P.V.P.S.S., and West, A.R.,*Physica C*, 250, 87–92, 1995.
80. Luo, J.S., Dorris, S.E., Fischer, A.K., LeBoy, J.S., Maroni, V.A., Feng, Y., and Larbalestier, D.C.,*Supercond. Sci. Technol.*, 9, 412–421, 1996.
81. Jeremie, A., Alami-Yadri, K., Grivel, J., and Flukiger, R.,*Supercond. Sci. Technol.*, 6, 730–735, 1993.
82. Luo, J.S., Merchant, N., Escorcia-Aparicio, E.J., Maroni, V.A., Tani, B.S., Carter, W.L., and Riley, G.N., Jr.,*J. Mater. Res.*, 9, 3059–3067, 1994.
83. MacManus-Driscoll, J.L., Bravman, J.C., Savoy, R.J., Gorman, G., and Beyers, R.B.,*J. Amer. Ceram. Soc.*, 77, 2305–2313, 1994.
84. Dou, S.X., Song, K., Liu, H.K., Sorrell, C.C., Apperley, M.H., and Savvides, N.,*Appl. Phys. Lett.*, 56, 493–494, 1990.
85. High, Y.E., Feng, Y., Sung, Y.S., Hellstrom, E.E., and Larbalestier, D.C.,*Physica C*, 220, 81–92, 1994.
86. Navarro, R.,*Supercond. Sci. Technol.*, 13, 147–170, 2000.
87. Fujishiro, H., Ikebe, R., Noto, I., Matsukawa, M., Sasaoka, T., Nomura, K., Sato, J., and Kuma, S.,*IEEE Trans. Magn.*, 30, 1645–1650, 1994.
88. Sasaoka, T., Sato, J., Fukushima, K., Okada, M., Endo, M., Yaegashi, Y., and Nagano, M.,*Cryogenics*, 37, 409–415, 1997.
89. Majewski, P., Aubele, A., Fahr, T., and Aldinger, F.,*Physica C*, 351, 62–66, 2001.
90. Wesolowski, D.E., Rikel, M.O., Jiang, J., Arsac, S., and Hellstrom, E.E.,*Superconductor Science and Technology*, 18, 934–943, 2005.
91. Endo, U., Koyama, S., and Kawai, T.,*Jpn. J. Appl. Phys.*, 27, 1476–1479, 1988.
92. Baurceanu, R.M., Maroni, V.A., Merchant, N.M., Fischer, A.K., McNallan, M.J., and Parrella, R.D.,*Supercond. Sci. Technol.*, 15, 1167–1175, 2002.
93. Aota, K., Hattori, H., Hatano, T., Nakamura, K., and Ogawa, K.,*Jpn. J. Appl. Phys.*, 28, L2196–L2199, 1989.
94. Holesinger, T.G., Ayala, A., Baurceanu, R.M., and Maroni, V.A.,*IEEE Trans. Appl. Supercond.*, 11, 2991–2994, 2001.
95. Luo, J.S., Merchant, N., Escorcia-Aparicio, E., Maroni, V.A., Gruen, D.M., Tani, B.S., Riley, G.N., Jr., and Carter, W.L.,*IEEE Trans. Appl. Supercond.*, 3, 972–975, 1993.
96. Hatano, T., Aota, K., Hattori, H., Ikeda, S., Nakamura, K., and Ogawa, K.,*Cryogenics*, 30, 611–613, 1990.
97. Matsumoto, A., Kitaguchi, H., Kumakura, H., Nishioka, J., and Hasegawa, T.,*Supercond. Sci. Technol.*, 17, 989–992, 2004.
98. Yamada, Y., Graf, T., Seibt, E., and Flukiger, R.,*IEEE Trans. Magn.*, 27, 1495–1498, 1991.
99. Yamada, Y., Obst, B., and Flukiger, R.,*Supercond. Sci. Technol.*, 4, 165–171, 1991.
100. Jiang, J., Cai, X.Y., Polyanskii, A.A., Schwartzkopf, L.A., Larbalestier, D.C., Parrella, R.D., Li, Q., Rupich, M.W., and Riley, G.N., Jr.,*Supercond. Sci. Technol.*, 14, 548–556, 2001.
101. Johnson, D.W., Jr., and Rhodes, W.W.,*J. Amer. Ceram. Soc.*, 72, 2346–24350, 1989.
102. Parrell, J.A., Polyanskii, A.A., Pashitski, A.E., and Larbalestier, D.C.,*Supercond. Sci. Technol.*, 9, 393–398, 1996.
103. Holesinger, T.G., Bingert, J.F., Parrella, R.D., and Riley, G.N., Jr.,*AIP Conf. Proc. B*, 614, 724–731, 2002.

104. Thurston, T.R., Wildgruber, U., Jisrawi, N., Haldar, P., Suenaga, M., and Wang, Y.L.,*J. Appl. Phys.*, 79, 3122–3132, 1996.
105. Larbalestier, D.C., Babcock, S.E., Cai, X.Y., Dorris, S.E., Edelman, H.S., Gurevich, A., Parrell, J.A., Pashitski, A., Polyanskii, A., I-Fei Tsu, and Wang J.-L., *Applied Superconductivity 1995. Proceedings of EUCAS 1995, Second European Conference on Applied Superconductivity*, Vol. 1, 1995, pp. 29–34.
106. Giannini, E., Bellingeri, E., Passerini, R., and Flukiger, R.,*Physica C*, 315, 185–197, 1999.
107. Jiang, J., Cai, X.Y., Chandler, J.G., Patnaik, S., Polyanskii, A.A., Yuan, Y., Hellstrom, E.E., and Larbalestier, D.C.,*IEEE Trans. Appl. Supercond.*, 13, 3018–3021, 2003.
108. Yuan, Y., Cai, X.Y., Jiang, J., Huang, Y., Larbalestier, D.C., and Hellstrom, E.E.,*IEEE Trans. Appl. Supercond.*, 15, 2530–2533, 2005.
109. Jiang, J., University of Wisconsin–Madison, unpublished, 2005.
110. Nakao-Kametani, F., and Osamura, K.,*Supercond. Sci. Technol.*, 18, 290–296, 2005.
111. Rikel, M.O., Williams, R.K., Cai, X.Y., Polyanskii, A.A., Jiang, J., Wesolowski, D., Hellstrom, E.E., Larbalestier, D.C., DeMoranville, K., Riley, G.N., Jr.,*IEEE Trans. Appl. Supercond.*, 11, 3026, 2001.
112. Yuan, Y., Jiang, J., Cai, X.Y., Larbalestier, D.C., Hellstrom, E.E., Huang, Y., and Parrella, R.,*Appl. Phys. Lett.*, 84, 2127–2129, 2004.
113. Hellstrom, E.E., Yuan, Y., Jiang, J., Cai, X.Y., Larbalestier, D.C., and Huang, Y.,*Supercond. Sci. Technol.*, 18, S325–S331, 2005.
114. Yuan, Y., Williams, R.K., Jiang, J., Larbalestier, D.C., Cai, X.Y., Rikel, M.O., DeMoranville, K.L., Huang, Y., Li, Q., Thompson, E., Riley, G.N., Jr., Hellstrom, E.E.,*Physica C*, 372–376, 883–886, 2002.
115. Patnaik, S., Feldmann, D.M., Polyanskii, A.A., Yuan, Y., Jiang, J., Cai, X.Y., Hellstrom, E.E., Larbalestier, D.C., and Huang, Y.,*IEEE Trans. Appl. Supercond.*, 13, 2930–2933, 2003.
116. Yuan, Y., Ph.D. thesis, University of Wisconsin–Madison, 2004.
117. Umezawa, A.; Feng, Y.; Edelman, H.S.; High, Y.E.; Larbalestier, D.C.; Sung, Y.S.; Hellstrom, E.E.; and Fleshler, S., *Physica C*, 198, 261, 1992.
118. Liao, S.-Y., Ph.D. thesis, University of Wisconsin–Madison, 2004.

14
A Paradigm Shift in Cryopreservation: Molecular-Based Advances to Improve Outcome

J.M. BAUST[a] AND J.G. BAUST[b]

[a]*Bioengineering and Biology Department, The State University of New York at Binghamton, Binghamton, NY 13902, USA*
[b]*Biological Sciences and Bioengineering Department, The State University of New York at Binghamton, Binghamton, NY 13902, USA*

Abstract

First-generation strategies of cryopreservation developed in the mid 1950s focused on the maintenance of structural integrity of cells through inclusion of penetrating cryoprotectants and management of ice and chemo-osmotic perturbations. There is now an increasing body of evidence suggesting that elevated levels of cryoprotective agents impact and alter the cellular proteome, genome, and fragmentome. Accordingly, second-generation cryopreservation strategies consider a combination of first-generation principles with new concepts in preservation solution design that reduce the effects of preservation-induced oxidative stresses. This chapter provides the background for this change in strategies.

14.1 Introduction

The field of biopreservation has and continues to experience rapid expansion, due in part to the growing interest and successes in the areas of personalized medicine, drug discovery, and biosensors development [1]. Even after a half century of research focused on improving cryopreservation, preservation problems exist. Lane [2], while discussing the future of cryopreservation, noted that "Few scientific problems have proved as intractable as cryopreservation" and that, "... cryobiology has been straitjacketed by its need to conform to the intractable laws of biophysics. For all its successes, cryobiology has been stuck in a rut." Further, Mazur [3] concluded that "The problem today is that applying basic principles of biophysics simply cannot solve many of the remaining challenges in cryobiology." Others have commented similarly [4–6]. The story of cryopreservation and future successes must now add a focus on cellular stress response.

With expanded applications, new demands are being placed on the preservation sciences to provide methodologies that facilitate retention of high degrees of cell viability and function in specialized cell systems, including stem cells, umbilical cord blood cells, engineered cells and tissues. These emerging demands have

pushed traditional approaches and guiding parameters in the preservation sciences to a limit [2]. As a result, cryopreservation research focus has now shifted into the areas of cell and molecular biology to drive scientific, technological, and methodological development [7]. These efforts have led to a series of discoveries over the last 5 years focused on the molecular responses of cells to low temperature and has resulted in a paradigm shift aimed at developing improved preservation processes.

The underlying discovery guiding this change of focus has been the discovery of the activation of apoptosis during and following preservation [8]. In 1998, Baust et al. [9] first reported on the involvement of apoptosis as a mechanism of cell death contributing to cryopreservation failure. Subsequent to that report, a number of publications have appeared focusing on the phenomena of cryopreservation-induced apoptosis and molecular-based cell death following cryopreservation [10–21].

This chapter is focused on these new approaches to biopreservation with an emphasis on molecular-based modes of cryopreservation failure. In addition, discussion on how controlling these factors has and will continue to lead to improved cryopreservation, as well as hypothermic storage outcome, is provided.

14.1.1 Biopreservation

Efforts to improve the effectiveness of long-tried and often unsuccessful preservation methods for biological materials which rely on low temperatures have led to the development of a new scientific specialty: biopreservation. Most efforts to sustain living biologics in a dormant state yielding "real time on demand" reanimation rely primarily on either hypothermic (refrigerated) storage or frozen preservation [22].

Hypothermic storage utilizes temperatures in the range of 0 to ∼32 °C, but more typically 0 to 10 °C. Scientific advances within the hypothermic storage field have centered primarily on improving tissue and organ preservation in support of transplantation. The detail of dependent mechanistic factors typically relate to ion balance, buffering capacity, free-radical scavenging, oncotic support, and the provision of nutrients [23–25]. The scientific investigation aimed at improving cryopreservation, defined as the maintenance of biologics at temperatures below –80 °C and typically below –140 °C, has primarily focused on the control of osmotic fluxes and ice formation to improve outcome [26]. This focus contributed to the development of the "two-factor hypothesis" and associated methods relating survival of cells in solution to a dependence on the rate of cooling of the system. Suboptimal cooling rates (too slow) cause cells to be exposed to prolonged toxic conditions, especially in the presence of molar concentrations of cryoprotective agents, such as dimethyl sulfoxide (DMSO) or glycerol. The "solution effects" that result are considered lethal, a widely accepted supposition that originated from Lovelock's classic demonstration of the relationship between red blood cell (RBC) death and sodium chloride concentration [27]. On the other hand, cooling at supra-optimal rates (too fast) does not allow for adequate cellular dehydration

(reduced intracellular levels of freezable water), thereby increasing the probability of lethal intracellular ice formation [26, 27].

The relative isolation of the cryopreservation sciences (processes) from the cellular-based fundamentals garnered from organ-based hypothermic storage research is notable. Specifically, there has been an isolation of analysis between physical parameters associated with the water-to-ice phase change (i.e. freezing events) during the preservation process [27] from an understanding of a chill–freeze continuum that exists. This isolation has contributed to a failure to recognize that the hypothermic continuum impacts survival [1]. Today, many of the limitations faced in efforts to recover higher percentages of normally functioning cells upon removal from cryogenic storage can be linked to this disciplinary disconnect. An underlying premise of the hypothermic continuum is that it is essential to recognize that, despite the presence of extracellular ice, cells that are structurally preserved (avoid intracellular ice formation) remain in a state of deepening hypothermia until vitrification (T_g) of both the preservation solution and intracellular milieu. It is also important to recognize that as cooling progresses below the nucleation temperature, solute levels continue to rise due to freeze concentration [3]. Finally, cell function, even though suppressed, will not cease until the intracellular glass transition T_g temperature is reached [28].

The isolation of thought and approach within low-temperature research has created a series of intellectual subdisciplinary cul-de-sacs [2]. Modern concepts in biopreservation incorporate relevant interdisciplinary foci, including engineering and cellular and molecular biology (i.e. cell signaling, genomics, proteomics, and metabolomics) in combination with the fundamental principles of cryobiology. Importantly, biopreservation requires the simultaneous management of numerous lethal stressors to obtain normal recovery of cellular systems throughout the diversity of fields including cell-based therapies, reproduction (animal and human), cell and tissue banking (clinical and environmental), drug discovery, organ preservation, etc. [29].

14.1.2 The Hypothermic Continuum

Nearly all biopreservation procedures in mammalian systems begin with reducing the temperature to, most commonly, 10 to 0 °C. The flow of heat from the sample (cooling) institutes a change in energy state causing a reduction in chemical reactions resulting in the uncoupling and shunting of biochemical reactions. This reduction in available kinetic energy and disruption of metabolism results in the depletion of adenylates due to the cessation of aerobic production of ATP, which further leads to an interference with membrane-dependent transport [30], especially calcium [31, 32], potassium, and sodium [32, 33].

With cooling, the cell and organelle membrane lipid domains undergo a series of phase changes. These phase changes reflect the fluidity changes in the membrane, the transition from the liquid-crystalline state to the gel state [34, 35], indicated by discontinuities in Arrhenius plots [34–37]. These changes result in a "leaky" membrane, thereby contributing to ionic imbalances, leakage of activated lysosomal and

lipoprotein hydrolases [38, 39], activation of calcium-dependent phospholipases [40–42], and the release of free fatty acids [43]. These membrane-related events can cause changes at the mitochondrial domain such that, when coupled with an alteration in the bcl-2:bax (anti- and pro-apoptotic) proteins, cytochrome c release and activation of the apoptotic cascade may result [7, 44–47]. Concomitantly, there is also the disruption of the cellular cytoskelatal matrix, including changes in actin and tubulin arrangements [48–50].

The detrimental events associated with the hypothermic continuum occur with minor changes in the kinetic energy levels of the cell. Q_{10}, a measure representing an average of the total change in metabolism, approximates a 50% change in oxygen consumption (metabolism) in mammalian systems for each 10 °C change in temperature [35, 51, 52]. For example, the oxygen consumption of a cell at 5 °C is reduced to ∼10% versus 100% at 37 °C [53–55]. Q_{10} does not reflect the response of individual reactions, but an average of enzymatic processes; therefore, it is indicative of shifts in metabolic pathways [34–37, 56]. The impact of hypothermia is global at the cellular level [57]. The nature of the oxidative stressors experienced at the cellular level in the cold, including the generation of free radicals, results in the activation of multiple routes of cell death.

14.2 Cryopreservation

Cryopreservation protocols extend through the hypothermic continuum, reaching equilibrium in the glassy (vitrified) state. The addition of cryoprotective compounds often includes a diversity of penetrating and nonpenetrating agents contained within an isotonic cell culture or buffered electrolyte media [19].

Following the addition of and incubation in the cryoprotective cocktail, cooling is extended at a given rate (1 °C/min is typical for many mammalian cells). A seeding step is included in the –2 to –6 °C range to prevent excessive undercooling (supercooling) of the cell and the cryopreservation cocktail. Seeding supports the gradual growth of extracellular ice, allowing for the efflux of water from the cell, which results in cell shrinkage and the maintenance of the freeze concentration equilibrium of solutes across the cell membrane [58]. This freeze concentration reduces the availability of freezable water in a cell while moving the intracellular viscosity toward T_g. When cooling rates are too rapid, cells remain too hydrated, resulting in the increased probability of lethal intracellular ice formation. When cooling is supra-optimal (too fast), intracellular ice may form, causing cells to rupture upon thawing or to have an increased probability of undergoing early stage (within a few hours) cellular necrosis [12, 18, 59]. With too slow cooling, it has been hypothesized that the extended exposure to the multimolar freeze-concentrated solutes results in toxic solution effects [26, 60, 61]. Mazur [3] has provided elegant descriptions of the breadth of physicochemical changes that occur during cryopreservation.

As temperature passes below the equilibrium freezing (melting) point of the preservation medium, controlled, slow cooling rates are typically utilized to

lower the sample temperature to –40 to –80 °C followed by transfer to ultra low-temperature storage (i.e. liquid nitrogen immersion, liquid nitrogen vapor phase, or <–135 °C mechanical storage). This temperature range is ideal, because it falls below the reported glass transition temperatures T_g of pure water [62]. Further, the T_g for cryoprotective mixtures varies substantially and has been reported to be in the –115 to –90 °C range. Below T_g, system viscosity increases exponentially, so that there is a cessation of all measurable molecular translational motion. Accordingly, the moment of diffusion (diffusion distance equivalent to one molecular diameter) increases from less than a microsecond to decades, hence the presumption that molecular interactions (i.e. metabolism) are impossible during the sub-T_g storage interval [63]. With the cell's transition through T_g, the hypothermic continuum effectively halts. Prior to reaching T_g, chemical reactivity continues at reduced rates, yielding the potential for sustained free-radical and other types of damage. It is for this reason that long-term storage at -80 °C ($\geq$6–12 months) is ill advised, even for biological material such as serum, macromolecules, etc.

Thawing of a cryopreserved sample is typically accomplished in a rapid manner by placing the sample (cryovial) in a 37–40 °C bath, agitating the vial until sample ice melts, and then diluting the cryoprotectant cocktail with cell culture media in a single step or a multiple stepwise dilution process.

14.2.1 Current Status: Traditional Approaches to Cryopreservation

Glycerol was first reported to have cryoprotective function in avian spermatozoa [64] and human erythrocytes (RBCs) [65], leading to the birth of mammalian cryopreservation in the late 1940s. Within the next decade, the discovery that the addition of DMSO to the cryopreservation cocktail yielded enhanced survival resulted in noticeable growth of cryopreservation applications [66]. With initial cryopreservation efforts focused on two highly differentiated cellular products (RBCs and spermatozoa) with fixed post-differentiation life spans, the full spectrum of the impacts of preservation stress on the complex biology of typical cells was obscured. Given their fully differentiated terminal state, these systems do not serve as adequate cellular models for the spectrum of molecular-based events associated with post-thaw, cryopreservation-induced delayed-onset cell death, thereby masking the full extent of cryopreservation-induced lethal effects. When one considers a listing of stress factors associated with cryopreservation, a relatively clear picture of the critical involvement played by the cell's biology in responding to a cryopreservation regime emerges. This emergent scenario necessitates a second-generation preservation paradigm focused on improved preservation outcomes.

14.3 Understanding Cell Death

14.3.1 Molecular-Based Cellular Response to Preservation

As described previously, the field of biopreservation is experiencing rapid expansion [1] due to new fields of interest and the successes in the areas of personalized

medicine and drug discovery. With expanded applications, new demands have pushed the preservation sciences to a limit [2]. As a result, several preservation groups have adopted an alternate approach that combines the disciplines of cell and molecular biology with cryobiology in search of continued scientific, technological, and methodological improvements [7]. This shift has resulted in recent discoveries related to the molecular response of cells during and following the preservation processes. Accordingly, a scientific paradigm shift, leading to new approaches designed to improve preservation, has occurred. This paradigm shift began in 1998 when Baust et al. [9] identified apoptosis, in addition to necrosis and ice rupture, as a distinct mechanism of cell death contributing to cryopreservation failure. Since that time, studies have shown that cryopreservation-induced apoptosis and molecular-based cell responses play a significant role in cell death following cryopreservation outcomes [10–21].

14.3.2 Modes of Cell Death

Multiple modes of cell death which occur many hours to days post-thaw [7, 19] are now recognized in association with cryopreservation failure. We have previously discussed the preservation process emphasizing the importance of the effect of a cell's response to the cold [7, 8]... The control of a cell's response to low temperature requires reducing the level of stress experienced during the cooling process. In general, an increase in cellular stress results in the activation of apoptotic and necrotic cascades leading to increased cell death. Management of this stress response, and, therefore, the multiple paths of cell death (ice rupture, necrosis, and apoptosis), is now believed to play a critical role in preservation efficacy.

14.3.3 Physical Events Leading to Cell Death

Ice-related cell destruction is the most commonly noted form of cell death associated with suboptimal cryopreservation. Scientists have dedicated careers to an understanding of the control and prevention of ice-related cell rupture since the late 1940s, when Polge et al. [64] published on the use of glycerol as a cryoprotective agent. Following this lead, numerous studies have been devoted to preventing intracellular ice formation to improve cryopreservation outcome [12, 66–72]. Studies on compounds that influence ice formation/growth by reducing levels of freezable water within a cell have extended our understanding of the cryopreservation process. Now, with the use of agents such as glycerol, DMSO, propanediol, etc., the effective control and prevention of intracellular ice formation is commonplace [66, 73–80]. It is this focus that has played a critical role in the advancement of cryopreservation over the last 50 years. Ironically, it is also this focus which has led to "cryobiology ... (being)... stuck in a rut" [2].

14.3.4 Necrosis: Pathological Cell Death

While ice-related rupture has been the primary focus of most cryobiologists, necrotic cell death has also been observed in numerous cases of cryopreservation

failure [8, 81, 82]. Necrosis is an energy-independent form of cell death characterized by the swelling of a cell and its constituent organelles, loss of membrane integrity, lysosomal rupture, random DNA fragmentation by endonucleases and ultimately cell lysis [83–86]. As a result of cell rupture and the associated release of cytokines, there is typically an activation of an immune and inflammatory responses in vivo [83, 84, 86]. The progression of necrosis often occurs rapidly in a matter of minutes to hours. Induction is typically seen in a response to severe cellular stress and results in the activation of detrimental intracellular signaling cascades. Necrotic cell death has been reported to be activated by stressors such as ischemia, osmotic shock, severe thermal stress, ionic disregulation, toxic agents, etc. Interestingly, many of these necrotic activating stressors are also involved in or associated with hypothermic storage and cryopreservation.

14.3.5 Apoptosis: Gene-Regulated Cell Death

Programmed cell death, or apoptosis, is integrally involved in the homeostatic maintenance of cell number [87]. Developmental apoptosis plays a role in neuronal innervation of muscles and the deletion of excess cells (tissue sculpting), such as the webbing between a human's fingers and toes, etc. [87–89]. Kerr [85] coined the term 'apoptosis' when referring to cells undergoing a natural form of cell death that he described as 'shrinking necrosis'. Kerr's work quickly led to a distinct field of investigation dedicated to unraveling apoptosis and the associated processes (genes, proteins, cascades, time course, and related morphological characteristics) [87, 89–95].

These studies revealed that apoptosis is a highly conserved (evolutionary) set of cellular processes among complex multicellular organisms [96–98]. Apoptosis is energy dependent, characterized by the activation of specific intracellular proteases, cellular shrinking, maintenance of cell membrane integrity, phospholipid inversion, nonrandom DNA cleavage into 180 kDa fragments, and the formation of membrane blebs (apoptotic bodies). Apoptosis is typically an in vivo inflammation-free process that does not activate an immediate immune response, in contrast to necrosis.

Three specific stages of progression can be used to define apoptosis: initiation, execution, and termination. Each stage is represented by a complex series of events ultimately leading to cell death. ATP is required throughout the process. If ATP is unavailable, then the apoptotic progression ends and has been reported to shunt to a necrotic cell death pathway [99], often termed secondary necrosis [19, 29].

14.3.6 Induction of Apoptosis

Apoptosis can be initiated by any number of stresses (i.e. radiation, cytotoxic agents, nutrient deprivation, anoxia, growth factor withdrawal, temperature, excess or diminished gene product, etc.) [8, 12, 15, 94, 100–104]. Following induction at the organelle level (i.e. membrane, mitochondria, nucleus), the apoptotic cascade proceeds and may include, but is not limited to, caspase activation, mitochondrial

release of cytochrome c, cell cycle arrest, lipid translocation (externalization of phosphotidyl serine), alterations in gene expression, etc. [87, 93, 105–108]. This full sequence of events leads the cell through the execution stage into the termination stage, where DNA is cleaved by endonucleases into ordered fragments followed by the formation of membrane blebs, apoptotic bodies, and the complete systematic disassembly of the cell. Initiation of apoptotic cascades typically occurs at one of three primary locations within a cell: the cell membrane, mitochondria, or nucleus [9, 15, 97, 106, 109]. Despite the often distinct initiating organelle, a series of feedback, amplification, and biochemical cross-talk signaling loops are typically activated, resulting in the potentiation of the apoptotic signal through multiple pathways [103, 110]. This complex process is believed to have evolved as a form of biochemical redundancy to assure ordered cell death. It is this feature that makes apoptotic control in cryopreservation difficult, as will be discussed in Section 14.5.1 [19].

14.3.7 Transitional Cell Death

Molecular-based cell death is typically thought to proceed through either an apoptotic or necrotic pathway. Apoptosis has been viewed as a "true organized molecular response," with necrosis considered "to involve random molecular events" at the intracellular signaling level. While traditionally accurate, the scientific view of the cell death landscape has evolved substantially over the past few years to suggest that classical apoptosis and necrosis represent more extremes on a continuum of molecular-based cell death, rather than two discontinuous processes. Apoptosis is now considered to be a mode of cell death that can present itself in many forms. Bras et al. [111] suggest that there are three types of apoptosis: (a) Type I, the conventional view of apoptosis, not involving lysosomes, but relying on caspase activation (presently, over a dozen caspases are recognized, many of which are linked in the apoptotic cascade [112, 113]); (b) Type II, by contrast, is characterized by lysosomal-linked autophagocytosis,; (c) Type III, lysosomal-independent, necrosis-like apoptosis, characterized by swelling of intracellular organelles. It is now thought in many cases of cell death that a cell's commitment to death causes an apoptotic response to be activated and proceed to the point of cellular execution (Type I classical apoptosis) or to a point where the stress becomes too great or energy reserves (ATP levels) too low for continuation. Once either extreme is reached, the cell has committed to death and shunts from apoptosis to necrosis for the completion of the death process (secondary necrosis) [29, 99, 114, 115]. Leist et al. [99] first reported on the ability of cells to switch from apoptotic to necrotic cell death and back again. In that study, cellular apoptosis was initiated, energy was depleted, and cell death shifted to necrosis. When energy substrates were added back to the system, cell death characteristics reverted back to apoptotic, but only to a point following which this reversal was no longer possible.

Transitional cell death has been demonstrated in a number of subsequent studies, including some in cryopreservation, and has provided a basis for the cell death continuum concept emphasized here. Common stressors, such as nutrient

deprivation, DNA damage, cytokine exposure, cytotoxic agents, oxygen depriva-
tion, ionic imbalance, etc., have been shown to result in the activation of both
apoptosis and necrosis in a multiplicity of cell systems. The determination of
apoptotic or necrotic activation is believed to be based on the relative degree of the
stress experienced by the cell. The transitional nature of the cell death pathways in
response to similar stressors creates a difficult environment to characterize. This
is especially true as it applies to situations where multiple stressors are involved,
such as cryopreservation and hypothermic preservation.

14.4 Molecular-Based Cryopreservation-Induced Cell Death

Upon review of the stresses associated with cryopreservation, it seems intuitive that
apoptotic processes would be involved. For example, Jurisicova et al. [116] reported
on observations of programmed cell death (PCD; apoptosis) of pre-implanted hu-
man embryos following cryopreservation. In that study, it was stated that "the PCD
was due to either natural incidence of lethal chromosomes in the human population
or the in vitro fertilization and culture conditions." Borderie and Laroche [117]
next reported on the observation of discrepancy in human keratinocyte survival
(20–54%) evident by differences obtained through trypan blue and flow cytometry
analysis following –80°C storage. It was further noted that there was a popula-
tion of apoptotic cells at 24 h post-thaw. In 1998, a first report directly linking
apoptosis to cryopreservation failure was put forth [9]. Analysis of the DNA frag-
mentation patterns (180–200 bp DNA fragment bands) demonstrated that apoptosis
occurred post-thaw. The electrophoretic-based DNA characteristics of apoptotic
(DNA banding or ladder) and necrotic (DNA smear) cell death were not completely
detectable until many hours to days post-thaw. This evidence further suggested a
significant temporal component to cell death following cryopreservation. Since
that report, there have been many studies focused on apoptotic involvement in
cryopreservation failure [8, 11, 12, 14, 18, 21, 118–125].

14.4.1 Apoptosis in Cryopreservation

Apoptosis following cryopreservation has been documented in a wide variety of
cellular systems, including cord blood cells, fibroblasts, hepatocytes, peripheral
blood, mononuclear cells, oocytes, ovarian tissue, renal cells, spermatozoa, vas-
cular tissue, etc. [10, 12, 16, 19, 21, 121, 124, 126]. Fowke et al. [81] and Baust
et al. [8] separately reported in 2000 on apoptosis following cryopreservation in
peripheral blood mononuclear cells (PBMCs) and renal cells respectively. In 2001,
Fu et al. [10] and Yagi et al. [11] reported on the involvement of apoptosis in hep-
atocytes following cryopreservation. Schuurhuis et al. [126], Lund et al. [127] and
Baust et al. [124] have further documented apoptosis in PBMCs following thawing.
Reports such as these continue to solidify the foundation of molecular-based cell
death following cryopreservation as a universal phenomenon influencing outcome.

14.4.2 Cryopreservation-Induced Delayed-Onset Cell Death

A review of the literature on cell death associated with cryopreservation allows one to conclude that molecular-based cell death (apoptosis) plays a critical role in the outcome of most cellular systems. Two critical points underlying this statement (and interpretation of the literature base) are (1) the temporal component of cell death and (2) the assay system used for evaluation [128]. To these points, evaluation of cell populations within a few hours post-thaw does not allow for the identification of the full extent of apoptosis or necrosis. Owing to the time course of the cell death machinery, this holds true regardless of the assay system utilized. Reports have shown that it takes many hours to days for the molecular-based cell death associated with cryopreservation to manifest following thawing. It is all too common that many investigators fail to recognize this temporal component when seeking to identify, characterize, and understand molecular cell death following preservation. In 2001, a report in the journal *Cell Transplantation* first documented timing of cell death following cryopreservation, terming the phenomenon cryopreservation-induced delayed-onset cell death [12]. That study found that necrosis peaked 6 h post-thaw and apoptosis 12 h post-thaw. Determination of apoptotic and necrotic populations in that study was based on early stage indicators, thereby identifying cells indistinguishable from living populations based upon typical viability indicators (i.e. trypan blue). Owing to the ordered, temporal progression of the cell death cascades, a nadir in cell survival was not observed in this study until 24 h post-thaw. One of the most significant practical findings of this study was that the timing of assessment of cryopreservation outcome was critical in order to facilitate accurate survival measures.

The identification of the temporal component of cryopreservation failure led to a series of investigations designed to gain insight into the progression of molecular cell death. In 2002, Baust et al. [18] reported on a genomic response of cells following cryopreservation contributing to the temporal component. In that study, following thawing, there was a transcriptional upregulation of activity of key apoptotic proteins 12–18 h post-thaw, along with caspase-3 proteolytic activity having an extended plateau of activity (21–36 h) post-thaw. Concurrently, Vogel et al. [129] reported on the time course of proteolytic activation of caspase-3 over 36 h following cryopreservation in a renal model. Schmidt-Mende et al. [118] further substantiated the observation of post-thaw protease activation in a bone marrow cell model. In their study, a high level of intrinsic proteolytic activity was found following preservation leading to the cleavage of various apoptotic-signaling proteins. Their data further illustrated that protease activity could be blocked by the inclusion of a protease inhibitor in the freeze medium. These findings on the benefits of apoptotic inhibitors were in agreement with several other previously published reports, and further demonstrated that improved cryopreservation outcome was possible through addressing cell stress levels during and following cryopreservation. More recently, Paasch et al. [120] have reported on caspase involvement in human spermatozoa, in addition to Yagi et al. [11] in a porcine hepatocyte model. Expanding on these reports of specific proteolytic alterations, Vogel et al. [130] reported on

numerous alterations in the overall cellular proteome following cryopreservation in a human fibroblast model.

Despite substantial numbers of reports detailing the effects of post-cryopreservation apoptosis, there are, nonetheless, a few reports challenging this concept in selected systems. In 2002, Riccio et al. [123] reported that cryopreservation of PBMCs did not result in increased levels of apoptosis when observed 24 h post-thaw. However, in 2005, Baust et al. [124] found that, following cryopreservation, PBMC necrosis and apoptosis peaked at 4 h and 8 h post-thaw respectively, with negligible levels of either noted at 24 h. The discrepancy between these two studies serves as an example of the influence that the temporal component and cell type specificity can have on data collection and, ultimately, on the interpretation of results due to the complexity of a cell's molecular response to cryopreservation.

14.4.3 Initiation of Cryopreservation-Induced Molecular Death

It is now clear that much of the cell death following cryopreservation is linked to the execution of molecular-based cell death cascades. However, to date, few detailed investigations into the initiating stresses have been reported. As described previously, the preservation process exposes cells to stressors, many of which can initiate a molecular death response [1, 7, 19, 131]. These factors include metabolic uncoupling, production of free radicals, alterations in cell membrane structure and fluidity, disregulation of cellular ionic balances, release of calcium from intracellular stores, osmotic fluxes, and cryoprotective agent toxicity. This listing of stresses associated with cryopreservation is by no means complete, but serves as a guide to the complexity of the stress response and multiplicity of potential cellular initiation sites. In an effort to provide insight into the effect of the various stressors associated with cryopreservation, studies have begun to focus on potential initiation sites of apoptosis within a cell. These studies remain in the early stages; nonetheless, they have begun to shed light on the role of various pathways of molecular cell death, including the cell membrane, nucleus, and mitochondria associated with low-temperature exposure.

14.4.4 Effects of Cryopreservation on Cell Function

Recent studies have shown that the delayed molecular effects following thawing extend beyond that of all survival or death, impacting function as well. Overall function of cellular systems following cryopreservation has been an issue often overlooked in the past due to the focused immediate challenges presented by working to improve survival. The literature contains numerous reports citing high post-thaw cell viability and function. Further examination of these studies however, reveals that in many cases there are significant compromises in function of many cellular systems post-thaw (i.e. hepatocytes [132, 133], pancreatic islets [134], cardiac cells [135], blood cells [136], and stem cells [137]). Abrahamsen et al.

[14] used flow cytometry to assess sample quality levels (apoptosis and necrosis) following cryopreservation as a means of establishing dosing parameters for cancer patients. This application was necessary and beneficial because they found that the cryopreservation process significantly affected the level of $CD34^+$-expressing cells in PBMC samples. In 2002, de Boer et al. [13] confirmed the findings of cryopreservation-based impairment of function in $CD34^+$ cells which resulted in a reduction in their effectiveness for use in stem cell graft procedures. Reports detailing similar reduction/losses in post-thaw functionality in gametes have also been described [138, 139]. Studies on the cryopreservation of spermatozoa have now linked molecular-based stress responses and the loss of acrosomal and motility functions. Other studies have now associated negative effects of cryopreservation on the impairment of biochemical functionality in hepatocytes [17, 140] and cardiomyocytes [135]. These studies have helped to further our understanding and increase our recognition of the downstream effects that cryopreservation may have on cellular function.

14.4.5 Control of Cryopreservation-Induced Molecular Response

With the growing understanding of molecular events associated with cryopreservation, investigations have begun to focus on their control in an effort to improve preservation outcome. Targeted apoptotic control (TAC) [19] is now a central theme in studies designed to improve post-thaw outcome. Among these efforts, modifications in preservation solution design have proven most effective.

The new challenge facing the preservation sciences is the development of a molecular-based logic in the design of preservation solution(s) necessary to support a cell's round-trip excursion through the hypothermic continuum, while maintaining the basis of avoiding intracellular ice formation. The basic listing of cellular stress factors presented earlier can serve as a template to guide the design of improved preservation methods, assuming adequate structural preservation. Understanding and addressing these stress responses is critical because there are well-noted differences in the sensitivity of various cell types to preservation processes. Van Buskirk et al. [29] and Mathew et al. [141] reported on these variations in several cell models, with the data suggesting a possible need for cell-matched preservation solutions. The basis for differing cellular response to preservation was linked to the role that caspase-3, an apoptotic executioner enzyme, played in the post-cold response and the effect of its inhibition. These and other studies have provided a basis for the now emerging multi-solution hypothesis, which suggests that distinct cell types manage stress response through differing molecular pathways.

14.4.6 Preservation Solution Design

The early attempts at intelligent design of a preservation medium were made by the Belzer and Southard team [23, 24]. in the development of ViaSpan® (the University

of Wisconsin solution) to support the transport of organs (pancreas, kidney, and liver) in anticipation of transplantation. ViaSpan®, formulated for short-term hypothermic storage, was the first solution designed to manage selected putative stress factors and became the first intracellular-like preservation medium. In the decade that followed, additional organ preservation solutions were commercially developed (i.e. Celsior, HTK-Custodiol, HypoThermosol, and others).

14.4.7 Extracellular Preservation Media

The most significant shift in the approach to improving cryopreservation outcome in recent years has been that of carrier media design. Most traditional cryopreservation media formulations consist of a basal cell culture medium with serum protein and DMSO. While providing for physical protection, DMSO, and proteins components, the basal solutions fail to support the molecular response of cells to the various stresses during preservation. These traditional solutions fall short for reasons that include, but are not limited to (a) failure to buffer changes in pH appropriately, (b) failure to prevent or minimize cellular generation of free-radical products, (c) energy deprivation, etc. Also, all culture-media-based solutions do not provide a suitable ionic environment necessary for effective cell maintenance during preservation (i.e. low Na, high K) [25, 142]. Accordingly, the compositions of these traditional preservation media do not provide for adequate protection at a cellular or molecular level and offer little benefit to post-thaw survival [19].

While these classic solutions provide physical preservation, they are often severely limited in supporting cellular function. These limitations are seen when assessing post-thaw survival and specific cell functions. Generally speaking, little cell death is noted within 1 h post-thaw; however, over the next 24 h in culture, a significant portion of the cell population succumbs to cryopreservation-induced delayed-onset cell death (floating cells) that is unrelated to immediate physical trauma (ice rupture). With a traditionally based optimized protocol, greater than 90% of the cells avoided ice-related damage, but delayed molecular events can result in continued increased death (≥50% more) over time (Table 14.1) [12]. Cryopreservation in extracellular-like media not only reduces survival, but also compromises cellular function, compromising both the genome and proteome. For example, primary hepatocytes preserved in 10% DMSO contained in culture medium effectively lose the ability to maintain normal proteomic function. In studies by Sosef et al. [140] and Sugimachi et al. [143] it was demonstrated that surviving hepatocytes failed to recover complete protein synthetic capabilities even with 14 days post-thaw.

14.4.8 Intracellular Preservation Media

The examples above reveal the dichotomy that exists in interpreting survival post-thaw [144]. The cause of these response differentials is not related to cryoprotectant concentration per se, but rather the carrier medium composition. In contrast to traditional carrier media, today's cryopreservation solutions are designed as

TABLE 14.1. Comparison of 24-h post-thaw viabilities of selected cell systems following cryopreservation in either extracellular or intracellular-like media with varying levels of DMSO

| Tissue system | Cell type | Viability (%) | | | |
| | | 5% DMSO | | 10% DMSO | |
		Media	CryoStor	Media	CryoStor
Kidney	MDCK	28	71	43	70
	RPTEC	20	55	35	50
Skin	Human adult fibroblasts	29	68	20	25
	Human neonate fibroblasts	47	88	59	81
	Keratinocytes	50	70	40	55
	A431	40	72	50	48
	EpiDerm	N/A	N/A	28	55
Liver	Rat hepatocytes	N/A	N/A	60	80
	Human adult hepatocytes	12	40	22	23
	Human neonate hepatocytes	6	52	17	52
	HepG2/C3A	15	72	55	78
Prostate	LNCaP	36	68	51	65
Eye	BCE	30	63	15	18
Blood	PBMC	24	44	N/A	N/A
Blood vessels	HUVEC	25	48	44	48
	CASMC	N/A	N/A	42	61
	CAEC	44	69	N/A	N/A
	Rat aorta	5	22	14	49
Muscle	Skeletal muscle	31	56	28	54
	CASMC	N/A	N/A	42	61
Reproductive	CHO	52	90	75	90
Stem cells	Dermal progenitor	48	75	N/A	N/A
	Myoblasts	31	56	28	54

intracellular-type carrier media (low Na^+, high K^+) [8, 25, 142]. These solutions contain buffers with an extended dynamic range of thermal activity, supplemental free-radical scavengers, energy substrates, etc. [19]. These cryopreservation solution formulations have depended on much of the knowledge gained in the field of hypothermic storage solutions and provide more effective cryopreservation.

14.4.9 Ionic Composition

Ion disregulation is a critical negative cellular event occurring during preservation and is responsible for triggering a host of cell stress responses. This is an important aspect of solution design, as cellular ion pumps shut down during low-temperature storage. Accordingly, many of today's preservation solutions have shifted from high Na^+/low K^+ (traditional culture media) to that of low to moderate Na^+/high K^+ [142]. These solutions have been termed intracellular-type preservation solutions, based upon ionic composition being more similar to that of the intracellular environment [25, 142, 145]. Another important feature is that the concentrations

are not merely designed to reflect the intracellular ionic concentrations under normothermic conditions, but also to provide the appropriate concentrations necessary to maintain the proper ionic balance at low temperature.

14.4.10 pH Buffering

Another critical aspect of preservation solution design is the maintenance of proper physiological pH levels during the preservation process. Traditional cell culture media rely on phosphate and bicarbonate buffers to regulate pH. While very effective at normothermic temperatures, these systems lose their buffering capacity at hypothermic temperatures. New approaches and the resultant solutions incorporate organic buffers, such as HEPES, to provide for effective buffering throughout an extended range of hypothermic temperatures [146].

14.4.11 Osmotic Control

With the disregulation of ionic gradients, control of osmotic swelling of cells during preservation becomes increasingly important. Accordingly, today's more effective hypothermic and cryopreservation solutions incorporate several osmotic buffering components. Such agents include lactobionate, sucrose, mannitol, and dextran. These components serve several functions independently, but act, as a group, to control the extent of cellular swelling during the preservation process.

14.4.12 Energy Substrates

While the goal of preserving a biologic is to reduce cellular activity and thereby extend biological time, the maintenance of available cellular energy levels during and following storage remains important. Accordingly, modern preservation solutions have also incorporated various energy substrates, such as adenosine and glucose, to help maintain this reserve. The presence of these compounds during preservation serves an important role as a readily available energy source upon return of the cells to normothermic conditions. This provides the necessary energy for a cell to utilize for the activation of cellular repair processes and the regulation of stress responses following preservation. Without this component, cells emerging from preservation often do not have adequate energy reserves to recover and, therefore, activate cell death pathways either through apoptosis or secondary necrosis.

14.4.13 Free-Radical Scavengers

Recent studies have detailed the role that free radicals play in inducing cell damage during and following the preservation process. It has been long appreciated in the area of organ preservation that the inclusion of the free-radical scavenger glutathione in the solution during preservation significantly improves outcome [23–25, 142]. While glutathione remains a mainstay, it is now recognized that it alone

does not provide adequate protection against multiple categories of free-radical damage. Newer preservation solutions now incorporate more potent scavengers, such as vitamin E analogs, to reduce further the damaging effects of free radicals and prevent the subsequent activation of apoptosis [145].

14.5 Effects of New Solution Design on Cryopreservation Outcome

With the alteration in preservation solution design coupled with the control of the molecular response of cells to low temperatures, successful improvements in cell survival and function have now been reported in cellular systems, including hepatocytes [140], cord blood [147], stem cells, PBMCs [124], fibroblasts [12], keratinocytes [18], blood vessels [148], engineered tissue [59], etc. In the majority of these studies, evaluation of the intracellular-like cryopreservation medium CryoStor[TM]has been conducted, with reports of significant improvement in cell survival, function, and growth. In many cases, a doubling of cell number has been shown at the low point in cell survival when compared with DMSO plus cell culture medium. Interestingly, in most of those studies, the improvement in viability and sample quality was not noted immediately post-thaw, but hours later, once the molecular-based events had fully manifested. For example, Figure 14.1 illustrates
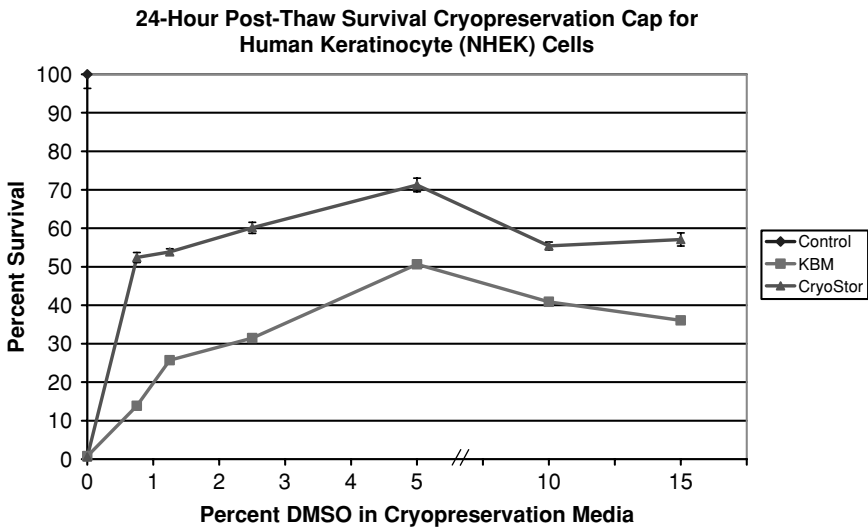
FIGURE 14.1. Post-thaw survival cap of normal human keratinocytes following cryopreservation in keratinocytes cell culture media (KBM) of CryoStor supplemented with different levels of DMSO. Cells were cryopreserved using a standard stepwise process to –196 °C, thawed rapidly, and assayed 24 h subsequent to return to nomothermic temperatures for cell survival using the metabolic probe, alamarBlue (adapted from Baust et al. [149]).

the 24-h post-preservation survival of human dermal keratinocytes preserved in KGM (keratinocytes growth medium), an extracellular-like solution, and DMSO-free CryoStor™, an intracellular-like solution [19]. To each basal solution, DMSO was added to final concentrations ranging from 0 to 15%. Upon thawing, similar viability levels were obtained in most of the conditions; but, following 24 h of post-storage culture, a much different picture emerged. In this example, a day following thawing, the classic cryopreservation cap was apparent, as survival increased with DMSO concentrations to an optimum level, followed by a decline in survival at higher DMSO concentrations [149]. Studies such as this one allow several observations to be drawn: first, in the extracellular-like medium, optimal survival is demonstrated using KBM™+ 5% DMSO; second, a change in the carrier medium from the extracellular-like medium formulation to the intracellular-like CryoStor™, with an equivalent level of DMSO, results in a significant increase in survival; third, by utilizing an intracellular-like solution, keratinocyte cell survival could be maintained at an elevated level even when DMSO concentrations are decreased manifold. Additionally, studies have now shown that the improvement in cell survival (such as in the above example) and function is due to a reduction in the levels of both apoptosis and necrosis during post-thaw recovery [12, 18]. This patterned response has now been observed in many cell systems analyzed and has begun to expose a limitation of the two-factor hypothesis, a point recently acknowledged by Mazur and coworkers [3, 26, 60].

Today, the principal difference in the approaches to cryopreservation and the resultant outcomes presented are dependent on carrier solution composition. Essentially, through the integration of an intracellular-type solution with an acknowledgment and understanding of the molecular response of a cell to low temperature, one is able to improve cryopreservation outcome significantly [7, 124]. Critical to fully understanding this success is the need for an in-depth knowledge of the cell death pathways activated as a result of cryopreservation- induced oxidative stress. As discussed, the processes and pathways associated with the induction of apoptosis and necrosis are complex, and our current state of knowledge with regard to the extent and activation sites of these molecular-based events continues to grow. While a detailed understanding of these processes remains in its infancy, the literature base describing this paradigm shift has expanded rapidly over the last 5 years. These studies show that this shift towards the use of new-generation cryopreservation solutions is significantly changing cryopreservation outcomes.

14.5.1 Application of Targeted Apoptotic Control

New solution design has provided for an improvement in cryopreservation outcome. A logical next step in improving preservation outcome is TAC [19]. Involvement of apoptosis in cryopreservation failure provides an avenue for investigating the feasibility of TAC. In 2000, we reported on the attempt to control the activation of apoptosis following cryopreservation through direct caspase inhibition [8]. TAC, in combination with intracellular-like preservation solutions, markedly improved cell survival. In a later study it was shown that TAC resulted in the

reduction of both post-thaw apoptosis and necrosis [12]. The data from that study also provided a basis for the hypothesis describing transitional cell death contributing to cryopreservation failure. More recent reports have detailed the benefit of TAC in improving hepatocyte cryopreservation [11], as well as other cell systems. Robilotto et al. [150] have recently expanded this concept in a report describing the benefits of calpain inhibitors during cryopreservation to improve cell survival, adding yet another potential strategy for TAC.

14.6 Summary

Many applications in cell-based therapy, regenerative and reparative medicine, biobanking, tissue engineering, drug discovery, biosensor packaging, and biodefense require normal, predictable, and timely return to functions of cellular systems following preservation. This is often not the outcome when traditional preservation technologies are applied. Further, there exists a growing body of evidence suggesting that elevated levels of cryoprotective agents impact and alter the cellular proteome, genome, and fragmentome.

Without a doubt, molecular-based study has again propelled cryopreservation to the forefront of scientific discovery. As our knowledge expands, advancements will continue to overcome the present-day limits of successful preservation. Today, the union between the optimized structural preservation strategies and the cell-molecular-based approaches to preservation will ultimately yield true improvements in post-preservation outcome. The first generation of cryopreservation developments focused on the maintenance of structural integrity of cells through the inclusion of penetrating cryoprotectants and the resultant management of ice and chemo-osmotic perturbations. Second-generation strategies integrate with and improved upon preservation outcome through a combination of first-generation principles with new concepts in preservation solution design that mitigate the detrimental effects of preservation-induced oxidative stresses. This approach directly modulates the post-thaw launch of apoptotic and necrotic cell death cascades (delayed-onset cell death) [7, 131].

As such, given the current direction of cryopreservation science, it appears that the future lies in the combination of next-generation solutions and specific strategies, such as TAC or genetically activated survival programs [131] to improve post-thaw survival and function for application in a diversity of settings, including complex cell, tissue, organ, and even organismal cryopreservation.

References

1. Baust, J.G., "Concepts in Biopreservation," Baust, J.G., and Baust, J.M., eds, *Advances in Biopreservation*, T&F Informa, Boca Raton, Florida, 2006, in press.
2. Lane, N., "The Future of Cryobiology," Fuller, B.J., Lane, N., and Benson, E.E., eds, *Life in the Frozen State*, CRC Press, Boca Raton, FL, 2004, pp. 645–657.

3. Mazur, P., "Principles of Cryobiology," Fuller, B.J., Lane, N., and Benson, E.E., eds, *Life in the Frozen State*, CRC Press, Boca Raton, FL, 2004, pp. 3–65.

4. Fahy, G.M., "The Relevance of Cryoprotectant 'Toxicity' to Cryobiology," *Cryobiology*, 23(1), 1–13, 1986.

5. Fuller, B.J., "Cryoprotectants: The Essential Antifreezes to Protect Life in the Frozen State," *Cryo Letters*, 25(6), 375–388, 2004.

6. Parks, J.E., "Hypothermia and Mammalian Gametes," Karow, A.M., and Critser, J.K., eds, *Reproductive Tissue Banking: Scientific Principles*, Academic Press, San Diego, 1997, pp. 229–262.

7. Baust, J.M., "Molecular Mechanisms of Cellular Demise Associated with Cryopreservation Failure," *Cell Preservation Technology*, 1(1), 17–32, 2002.

8. Baust, J.M., Van Buskirk, R., and Baust, J.G., "Cell Viability Improves Following Inhibition of Cryopreservation-Induced Apoptosis," *In Vitro Cell Dev. Biol. Anim.*, 36(4), 262–270, 2000.

9. Baust, J.M., Van Buskirk, R., and Baust, J.G., "Cryopreservation Outcome is Enhanced by Intracellular-Type Medium and Inhibition of Apoptosis," *Cryobiology*, 37(4), 410–411, 1998.

10. Fu, T., Guo, D., and Huang, X., et al., "Apoptosis Occurs in Isolated and Banked Primary Mouse Hepatocytes," *Cell Transplant*, 10(1), 59–66, 2001.

11. Yagi, T., Hardin, J.A., Valenzuela, Y.M., Miyoshi, H., Gores, G.J., and Nyberg, SL., "Caspase Inhibition Reduces Apoptotic Death of Cryopreserved Porcine Hepatocytes," *Hepatology*, 33(6), 1432–1440, 2001.

12. Baust, J.M., Vogel, M.J., Van Buskirk, R., and Baust, J.G., "A Molecular Basis of Cryopreservation Failure and Its Modulation to Improve Cell Survival," *Cell Transplant*, 10(7), 561–571, 2001.

13. de Boer, F., Drager A.M., Pinedo H.M., et al., "Extensive Early Apoptosis in Frozen–Thawed CD34-Positive Stem Cells Decreases Threshold Doses for Haematological Recovery After Autologous Peripheral Blood Progenitor Cell Transplantation," *Bone Marrow Transplant*, 29(3), 249–255, 2002.

14. Abrahamsen, J.F., Bakken, A.M., Bruserud, O., and Gjertsen, B.T., "Flow Cytometric Measurement of Apoptosis and Necrosis in Cryopreserved PBPC Concentrates from Patients with Malignant Diseases," *Bone Marrow Transplant*, 29(2), 165–171, 2002.

15. Peter, M.E., Heufelder, A.E., and Hengartner, M.O., "Advances in Apoptosis Research," *Proc. Natl. Acad. Sci. U. S. A.*, 94(24), 12,736–12737, 1997.

16. Xiao, M., and Dooley, D.C., "Assessment of Cell Viability and Apoptosis in Human Umbilical Cord Blood Following Storage," *J. Hematother. Stem Cell Res.*, 12(1), 115–122, 2003.

17. Matsushita, T., Yagi, T., Hardin, J.A., et al., "Apoptotic Cell Death and Function of Cryopreserved Porcine Hepatocytes in a Bioartificial Liver," *Cell Transplant*, 12(2), 109–121, 2003.

18. Baust, J.M., Van Buskirk, R., and Baust, J.G., "Gene Activation of the Apoptotic Caspase Cascade Following Cryogenic Storage," *Cell Preservation Technology*, 1(1), 63–80, 2002.

19. Baust, J.M., "Advances in Media for Cryopreservation and Storage," *Bioprocess International,* 3(Suppl 3), 46–56, 2005.

20. Martin, G., Sabido, O., Durand, P., and Levy, R., "Cryopreservation Induces an Apoptosis-Like Mechanism in Bull Sperm," *Biol. Reprod.*, 71(1), 28–37, 2004.

21. Paasch, U., Grunewald, S., Agarwal, A., and Glandera, H.J., "Activation Pattern of Caspases in Human Spermatozoa," *Fertil. Steril.*, 81(Suppl. 1), 802–809, 2004.

22. Gao, D., Mazur, P., and Critser, K.K., "Fundamentals of Mammalian Spermatozoa," Karow, A.M., and Critser, J.K., eds, *Reproductive Tissue Banking: Scientific Principles*, Academic Press, San Diego, 1997, pp. 263–328.

23. Southard, J.H., van Gulik, T.M., Ametani, M.S., et al., "Important Components of the UW Solution," *Transplantation*, 49(2), 251–257, 1990.

24. Southard, J.H., and Belzer. F.O., "Organ Preservation," *Annu. Rev. Med.*, 46, 235–247, 1995.

25. Taylor, M.J., Elrifai, A.M., and Bailes, J.E., "Hypothermia in Relation to the Acceptable Limits of Ischemia for Bloodless Surgery," *Advances in Low-Temperature Biology*, 3(1), 1–64, 1996.

26. Mazur, P., "The Role of Intracellular Freezing in the Death of Cells Cooled at Supraoptimal Rates," *Cryobiology*, 14(3), 251–272, 1977.

27. Lovelock, J.E., "The Haemolysis of Human Red Blood-Cells by Freezing and Thawing," *Biochim. Biophys. Acta*, 10(3), 414–426, 1953.

28. Taylor, M.J., Song, Y.C., and Brockbank, K.G.M., "Vitrification in Tissue Preservation," Fuller, B.J., and Benson, L.N., eds, *Life in the Frozen State*, CRC Press, Boca Raton, FL, 2004, pp. 603–692.

29. Van Buskirk, R.G., Baust, J.M., Snyder, K.K., Mathew, A.J., and Baust, J.G., "Hypothermic Storage and Cryopreservation—Successful Short- and Long-Term Preservation of Cells and Tissues," *Bioprocess International*, 2(10), 42–49, 2004.

30. Huang, J.S., Downes, G.L., Childress, G.L., Felts, J.M, and Belzer, F.O., "Oxidation of 14C-Labeled Substrates by Dog Kidney Cortex at 10 and 38 Degrees C," *Cryobiology*, 11(5), 387–394, 1974.

31. Tani, M., and Neely, J.R., "Role of Intracellular Na^+ in Ca^{2+} Overload and Depressed Recovery of Ventricular Function of Reperfused Ischemic Rat Hearts: Possible Involvement of H^+–Na^+ and Na^+–Ca^{2+} Exchange," *Circ. Res.*, 65(4), 1045–1056, 1989.

32. Renlund, D.G., Gerstenblith, G., Lakatta, E.G., Jacobus, W.E., Kallman, C.H., and Weisfeldt. M.L., "Perfusate Sodium During Ischemia Modifies Post-Ischemic Functional and Metabolic Recovery in the Rabbit Heart," *J. Mol. Cell. Cardiol.*, 16(9), 795–801, 1984.

33. Neely, J.R., and Grotyohann, L.W., "Role of Glycolytic Products in Damage to Ischemic Myocardium. Dissociation of Adenosine Triphosphate Levels and Recovery of Function of Reperfused Ischemic Hearts," *Circ. Res.*, 55(6), 816–824, 1984.

34. Lyons, J.M., and Raison, J.K., "A Temperature-Induced Transition in Mitochondrial Oxidation: Contrast Between Cold and Warm Blooded Animals," *Comp. Biochem. Physiol.*, 37, 405–411, 1970.

35. Raison, J.K., "The Influence of Temperature-Induced Phase Changes on the Kinetics of Respiratory and Other Membrane-Associated Enzyme Systems," *J. Bioenerg.*, 4(1), 285–309, 1973.

36. Southard, J.H., Van der Laan, N.C., Lutz, M., Pavlock, G.S., Belzer, J.P., and Belzer, F.O., "Comparison of the Effect of Temperature on Kidney Cortex Mitochondria from Rabbit, Dog, Pig, and Human: Arrhenius Plots of ADP-Stimulated Respiration," *Cryobiology*, 20(4), 395–400, 1983.

37. Wilson, J.M., and McMurdo, A.C., "Chilling Injury in Plants," Morris, G.J., and Clarke, A., eds, *Effects of Low Temperature on Biological Membranes,* Academic Press, London, 1987, pp. 146–172.

38. Ricciutti, M.A., "Lysosomes and Myocardial Cellular Injury," *Am. J. Cardiol.*, 30(5), 498–502, 1972.

39. Weglicki, W.B., Owens, K., Ruth, R.C., and Sonnenblick, E.H., "Activity of Endogenous Myocardial Lipases During Incubation at Acid pH," *Cardiovasc. Res.*, 8(2), 237–342, 1974.

40. Liu., X., Engelman, R.M., Rousou, J.A., and Das, D.K., "Myocardial Reperfusion Injury During Adult Cardiac Surgery," Das, D.K., ed., *Pathophysiology of Reperfusion Injury,* CRC Press, Boca Raton, FL, 1993, pp. 263–293.

41. de Jong, J.W., "Cardioplegia and Calcium Antagonists: A Review," *Ann. Thorac. Surg.*, 42(5), 593–598, 1986.

42. Schwertz, D.W., Halverson, J., Isaacson, T., Feinberg, H., and Palmer, J.W., "Alterations in Phospholipid Metabolism in the Globally Ischemic Rat Heart: Emphasis on Phosphoinositide Specific Phospholipase C Activity," *J. Mol. Cell. Cardiol.*, 19(7), 685–697, 1987.

43. White, B.C., Wiegenstein. J,G., and Winegar, C.D., "Brain Ischemic Anoxia: Mechanisms of Injury." *JAMA*, 251(12), 1586–1590, 1984.

44. Jennings, R.B., and Ganote, C.E., "Mitochondrial Structure and Function in Acute Myocardial Ischemic Injury," *Circ. Res.*, 38(5 Suppl. 1), 180–191, 1976.

45. Jennings, R.B., and Ganote, C.E., "Structural Changes in Myocardium During Acute Ischemia*," Circ. Res.*, 35(Suppl 3), 156–172, 1974.

46. Clarke, D.M., Baust, J.M., Van Buskirk, R.G., and Baust, J.G., "Addition of Anticancer Agents Enhances Freezing-Induced Prostate Cancer Cell Death: Implications of Mitochondrial Involvement," *Cryobiology*, 49(1), 45–61, 2004.

47. Baust, J.G., and Gage, A.A., "The Molecular Basis of Cryosurgery," *BJU Int.*, 95(9), 1187–1191, 2005.

48. Russotti, G., Brieva, T.A., Toner, M., and Yarmush, M.L., "Induction of Tolerance to Hypothermia By Previous Heat Shock Using Human Fibroblasts in Culture," *Cryobiology*, 33(5), 567–580, 1996.

49. Brinkley, B.R., and Cartwright, J., Jr., "Cold-Labile and Cold-Stable Microtubules in the Mitotic Spindle of Mammalian Cells," *Ann. N. Y. Acad. Sci.*, 253, 428–439, 1975.

50. Stefanovich, P., Ezzell, R.M., Sheehan, S.J., Tompkins, R.G., Yarmush, M.L., and Toner, M., "Effects of Hypothermia on the Function, Membrane Integrity, and Cytoskeletal Structure of Hepatocytes," *Cryobiology*, 32(4), 389–403, 1995.

51. Fuhram, G.J., and Fuhram, F.A., "Oxygen Consumption of Animals and Tissues as a Function of Temperature," *J. Gen. Physiol.*, 42, 215, 1959.

52. van't Hoff, A., *Etudes sur la Dynamique Chimique*, Muller, Amsterdam, 1884.

53. Lanir, A., Clouse, M.E., and Lee, R.G., "Liver Preservation for Transplant. Evaluation of Hepatic Energy Metabolism by ^{31}P NMR," *Transplantation*, 43(6), 786–790, 1987.

54. Fuller, B.J., Gower, J.D., and Green, C.J., "Free Radical Damage and Organ Preservation: Fact or Fiction? A Review of the Interrelationship Between Oxidative Stress and Physiological Ion Disbalance," *Cryobiology*, 25(5), 377–393, 1988.

55. Stubenitsky, B.M., Ametani, M., Danielewicz, R., Southard, J.H., and Belzer, F.O., "Regeneration of ATP in Kidney Slices After Warm Ischemia and Hypothermic Preservation," *Transpl. Int.*, 8(4), 293–297, 1995.

56. Scholander, P.P., Flaff, W., Waters, V., and Irving, L., "Climatic Adaptations in Arctic and Tropical Poikilotherma," *Physiol. Zool.*, 26, 67–92, 1953.

57. Storey, K.B., and Storey, J.M., "Metabolic Rate Depression and Biochemical Adaptation in Anaerobiosis, Hibernation and Estivation," *Q. Rev. Biol.*, 65(2), 145–174, 1990.

58. Mazur, P., and Cole, K.W., "Influence of Cell Concentration on the Contribution of Unfrozen Fraction and Salt Concentration to the Survival of Slowly Frozen Human Erythrocytes," *Cryobiology*, 22(6), 509–536, 1985.

59. Baust, J.M., Van Buskirk, R., and Baust, J.G., "Cryopreservation of an Engineered Skin Equivalent: the Apoptosis Paradigm," *Advances in Heat and Mass Transfer in Biotechnology*, Vol. 363, BED, HTD, ASME, New York, 1999, pp. 71–76.

60. Mazur, P., Leibo, S.P., and Chu, E.H., "A Two-Factor Hypothesis of Freezing Injury. Evidence from Chinese Hamster Tissue-Culture Cells," *Exp Cell Res*, 71(2), 345–355, 1972.

61. Rhoads, L.S., Zlobinsky, Y., Van Buskirk, R.G., Baust, J.G., "Patterns of Latent Heat Liberation During Controlled Rate Cooling: Absence of Effects on the Survival of Cryopreserved Cells," *Cryo-Letters*, 12, 329–338, 1991.

62. Franks, F., "The Properties of Aqueous Solutions at Sub-Zero Temperature," Franks, F., and Mathias, S., eds, *Biophysics of Water*, John Wiley, New York, 1982, pp. 279–294.

63. Rall, W.F., Mazur, P., and McGrath, J.J., "Depression of the Ice-Nucleation Temperature of Rapidly Cooled Mouse Embryos by Glycerol and Dimethyl Sulfoxide," *Biophys. J.*, 41(1), 1–12, 1983.

64. Polge, C., Smith, A.U., and Parkes, A.S., "Retrieval of Spermatozoa After Vitrification and Dehydration at Low Temperature," *Nature*, 164, 666–667, 1949.

65. Smith, A.U., "Prevention of Haemolysis During Freezing and Thawing of Red Blood-Cells," *Lancet*, 2(27), 910–911, 1950.

66. Lovelock, J.E., and Bishop, M.W., "Prevention of Freezing Damage to Living Cells by Dimethyl Sulphoxide," *Nature*, 183(4672), 1394–1395, 1959.

67. Borderie, V.M., Lopez, M., Lombet, A., Carvajal-Gonzalez, S., Cywiner, C., and Laroche, L., "Cryopreservation and Culture of Human Corneal Keratocytes," *Invest. Ophthalmol. Vis. Sci.*, 39(8), 1511–1519, 1998.

68. Donaldson, C., Armitage, W.J., Denning-Kendall, P.A., Nicol, A.J., Bradley, B.A., and Hows, J.M., "Optimal Cryopreservation of Human Umbilical Cord Blood," *Bone Marrow Transplant*, 18(4), 725–731, 1996.

69. Frim, J., Snyder, R.A., McGann, L.E., and Kruuv, J., "Growth Kinetics of Cells Following Freezing in Liquid Nitrogen," *Cryobiology*, 15(5), 502–516, 1978.

70. Zambelli, A., Poggi, G., Da Prada, G., et al., "Clinical Toxicity of Cryopreserved Circulating Progenitor Cells Infusion," *Anticancer Res.*, 18(6B), 4705–4708, 1998.

71. Williams, R.J., "The Mechanisms of Cryoprotection in the Intertidal Mollusk," *Cryobiology*, 4, 250–255, 1969.

72. De Loecker, P., Fuller, B.J., Koptelov, V.A., Grischenko, V.I., and De Loecker, W., "Cryopreservation of Isolated Rat Hepatocytes: Effects of Iron-mediated Oxidative Stress of Metabolic Activity," *Cryobiology*, 34(2), 150–156, 1997.

73. Mazur, P., "Freezing of Living Cells: Mechanisms and Implications," *Am. J. Physiol.*, 247(3 Pt 1), C125–C142, 1984.

74. Meryman, H.T., "The Exceeding of a Minimum Tolerable Cell Volume in Hypertonic Suspension as a Cause of Freezing Injury," *The Frozen Cell*, Wolstenholme G.E.W., and O'Connor, M., eds, Ciba Foundation Symposium, Churchill, 1970, pp. 51–64.

75. Pegg, D.E., and Diaper, M.P., "On the Mechanism of Injury to Slowly Frozen Erythrocytes," *Biophys. J.*, 54(3), 471–488, 1988.

76. Paynter, S.J., Fuller, B.L., McGrath, J.J., and Shaw, R.W., "The Effects of Cryoprotectant Permeability on Mouse Oocytes," *Cryo-Letters*, 16, 321–324, 1995.

77. Coger, R., and Toner, M., "Preservation Techniques for Biomaterials," Brunzion, J.D., ed., *The Biomedical Engineering Handbook*, CRC Press, Boca Raton, FL, 1995, pp. 1567–1579.

78. Morris, C.B., "Cryopreservation of Animal and Human Cell Lines," *Methods Mol. Biol.*, 38, 179–187, 1995.

79. Eroglu, A., Russo, M.J., Bieganski, R., et al., "Intracellular Trehalose Improves the Survival of Cryopreserved Mammalian Cells," *Nat. Biotechnol.*,18(2), 163–167, 2000.

80. Loretz, L.J., Li, A.P., Flye, M.W., and Wilson, A.G., "Optimization of Cryopreservation Procedures for Rat and Human Hepatocytes," *Xenobiotica*, 19(5), 489–498, 1989.

81. Fowke, K.R., Behnke, J., Hanson, C., Shea, K., and Cosentino, L.M., "Apoptosis: A Method for Evaluating the Cryopreservation of Whole Blood and Peripheral Blood Mononuclear Cells," *J. Immunol. Methods*, 244(1–2), 139–144, 2000.

82. Martin, H., Bournique, B., Sarsat, .P., Albaladejo, V., and Lerche-Langrand, C., "Cryopreserved Rat Liver Slices: A Critical Evaluation of Cell Viability, Histological Integrity, and Drug-Metabolizing Enzymes," *Cryobiology*, 41(2), 135–144, 2000.

83. Searle, J., Kerr, J.F., and Bishop, C.J., "Necrosis and Apoptosis: Distinct modes of Cell Death With Fundamentally Different Significance," *Pathol. Annu.*, 17(Pt 2), 229–259, 1982.

84. Walker, N.I., Harmon, B.V., Gobe, G.C., and Kerr, J.F., "Patterns of Cell Death," *Methods Achiev. Exp. Pathol.*, 13, 18–54, 1988.

85. Kerr, J.F., "Shrinkage Necrosis of Adrenal Cortical Cells," *J. Pathol.*, 107(3), 217–219, 1972.

86. Columbano, A., "Cell Death: Current Difficulties in Discriminating Apoptosis From Necrosis in the Context of Pathological Processes in vivo," *J. Cell Biochem.*, 58(2), 181–190, 1995.

87. Habibovic, S., Hrgovic, Z., Bukvic, I., and Hrgovic, I., "Molecular Mechanisms in Apoptosis," *Med. Arh.*, 54(1), 33–40, 2000.

88. Peters, G., and Wirth, C.J., "The Current State of Meniscal Allograft Transplantation and Replacement,"*Knee*, 10(1), 19–31, 2003.

89. Wyllie, A.H., Kerr, J.F., and Currie, A.R., "Cell Death: The Significance of Apoptosis," *Int. Rev. Cytol.*, 68, 251–306, 1980.

90. Alnemri, E.S., "Mammalian Cell Death Proteases: A Family of Highly Conserved Aspartate Specific Cysteine Proteases," *J. Cell Biochem.*, 64(1), 33–42, 1997.

91. Cohen, G.M., "Caspases: The Executioners of Apoptosis," *Biochem. J.*, 326(Pt 1), 1–16, 1997.

92. Kanzler, S., and Galle, P.R. "Apoptosis and the Liver," *Semin Cancer Biol*, 10(3), 173–184, 2000.

93. Sheikh, M.S., and Fornace, A.J., Jr., "Death and Decoy Receptors and p53-Mediated Apoptosis," *Leukemia*, 14(8), 1509–1513, 2000.

94. Gewirtz, D.A., "Growth Arrest and Cell Death in the Breast Tumor Cell in Response to Ionizing Radiation and Chemotherapeutic Agents Which Induce DNA Damage," *Breast Cancer Res. Treat.*, 62(3), 223–235, 2000.

95. Nicotera, P., Leist, M., Fava, E., Berliocchi, L., and Volbracht, C., "Energy Requirement for Caspase Activation and Neuronal Cell Death," *Brain Pathol.*, 10(2), 276–282, 2000.

96. Xue, D., Shaham, S., and Horvitz, H.R., "The *Caenorhabditis elegans* Cell-Death Protein CED-3 is a Cysteine Protease With Substrate Specificities Similar to Those of the Human CPP32 Protease," *Genes Dev.*, 10(9), 1073–1083, 1996.

97. Yin, X.M., "Signal Transduction Mediated by Bid, a Pro-Death Bcl-2 Family Proteins, Connects the Death Receptor and Mitochondria Apoptosis Pathways," *Cell Res.*, 10(3), 161–167, 2000.

98. Hengartner, M.O., and Horvitz, H.R., "*C. elegans* Cell Survival Gene *ced-9* Encodes a Functional Homolog of the Mammalian Proto-Oncogene *bcl-2*" *Cell*, 76(4), 665–676, 1994.

99. Leist, M., Single, B., Castoldi, A.F., Kuhnle, S., and Nicotera, P., "Intracellular Adenosine Triphosphate (ATP) Concentration: A Switch in the Decision Between Apoptosis and Necrosis," *J. Exp. Med.*, 185(8), 1481–1486, 1997.

100. Fink, K.B., Andrews, L.J., Butler, W.E., et al., "Reduction of Post-Traumatic Brain Injury and Free Radical Production by Inhibition of the Caspase-1 Cascade," *Neuroscience*, 94(4), 1213–1218, 1999.

101. Emery, E., Aldana, P., Bunge, M.B., et al., "Apoptosis After Traumatic Human Spinal Cord Injury," *J. Neurosurg.*, 89(6), 911–920, 1998.

102. Elsasser, A., Suzuki, K., and Schaper, J., "Unresolved Issues Regarding the Role of Apoptosis in the Pathogenesis of Ischemic Injury and Heart Failure," *J. Mol. Cell Cardiol.*, 32(5), 711–724, 2000.

103. Brune, B., von Knethen, A., and Sandau, K.B., "Nitric Oxide and Its Role in Apoptosis," *Eur. J. Pharmacol.*, 351(3), 261–272, 1998.

104. Saikumar, P., Dong, Z., Weinberg, J.M., and Venkatachalam, M.A., "Mechanisms of Cell Death in Hypoxia/Reoxygenation Injury," *Oncogene*, 17(25), 3341–3349, 1998.

105. Reutelingsperger, C.P., and van Heerde, W.L., "Annexin V, The Regulator of Phosphatidylserine-Catalyzed Inflammation and Coagulation During Apoptosis," *Cell Mol. Life Sci.*, 53(6), 527–532, 1997.

106. Condo, I., and Testi, R., "Intracellular Mediators of Programmed Cell Death initiated at the Cell Surface Receptor," *Fas. Transpl. Int*, 13(Suppl 1), S3–S6, 2000.

107. Blankenberg, F.G., Katsikis, P.D., and Tait, J.F., et al., "In vivo Detection and Imaging of Phosphatidylserine Expression During Programmed Cell Death," *Proc Natl Acad Sci U S A*, 95(11), 6349–6354, 1998.

108. Li, P., Nijhawan, D., Budihardjo, I., et al., "Cytochrome c and dATP-Dependent Formation of Apaf-1/caspase-9 Complex Initiates an Apoptotic Protease Cascade," *Cell*, 91(4), 479–489, 1997.

109. Kroemer, G., Dallaporta, B., and Resche-Rigon, M., "The Mitochondrial Death/Life Regulator in Apoptosis and Necrosis," *Annu. Rev. Physiol.*, 60, 619–642, 1998.

110. Bratton, S.B., and Cohen, G.M., "Caspase Cascades in Chemically-Induced Apoptosis," *Adv. Exp. Med. Biol.*, 500, 407–420, 2001.

111. Bras, M., Queenan, B., and Susin, S.A., "Programmed Cell Death via Mitochondria: Different Modes of Dying," *Biochemistry (Mosc.)*, 70(2), 231–239, 2005.

112. Zimmermann, K.C., and Green, D.R., "How Cells Die: Apoptosis Pathways," *J. Allergy Clin. Immunol.*, 108(4 Suppl.), S99–S103, 2001.

113. Thornberry, N.A., and Lazebnik, Y., "Caspases: Enemies Within," *Science* 281(5381), 1312–1316, 1998.

114. Liu, C.Y., Liu, Y.H., Lin, S.M., et al., "Apoptotic Neutrophils Undergoing Secondary Necrosis Induce Human Lung Epithelial Cell Detachment," *J. Biomed. Sci.*, 10(6 Pt 2), 746–756, 2003.

115. Jaeschke, H., and Lemasters, J.J., "Apoptosis Versus Oncotic Necrosis in Hepatic Ischemia/Reperfusion Injury," *Gastroenterology*, 125(4), 1246–1257, 2003.

116. Jurisicova, A., Varmuza, S., and Casper, R.F., "Involvement of Programmed Cell Death in Preimplantation Embryo Demise," *Hum. Reprod. Update*, 1(6), 558–566, 1995.

117. Borderie, V.M., and Laroche, L., "Ultrastructure of Cultured and Cryopreserved Human Corneal Keratocytes," *Cornea*, 18(5), 589–594, 1999.

118. Schmidt-Mende, J., Hellstrom-Lindberg, E., Joseph, B., and Zhivotovsky, B., "Freezing Induces Artificial Cleavage of Apoptosis-Related Proteins in Human Bone Marrow Cells," *J. Immunol. Methods*, 245(1–2), 91–94, 2000.

119. Villalba, R., Pena, J., Luque, E., Villalba, J.M., and Gomez-Villagran, J.L., "Keratocyte Injury in Human Corneas Cryopreserved Under Standard Conditions," *Cell Tissue Bank*, 5(4), 201–204, 2004.

120. Paasch, U., Sharma, R.K., Gupta, A.K., et al., "Cryopreservation and Thawing is Associated With Varying Extent of Activation of Apoptotic Machinery in Subsets of Ejaculated Human Spermatozoa," *Biol. Reprod.*, 71(6), 1828–1837, 2004.

121. Men, H., Monson, R.L., Parrish, J.J., and Rutledge, J.J., "Degeneration of Cryopreserved Bovine Oocytes via Apoptosis During subsequent Culture," *Cryobiology*, 47(1), 73–81, 2003.

122. Sarkar, S. Kalia, V., and Montelaro, R.C., "Caspase-Mediated Apoptosis and Cell Death of Rhesus Macaque CD4+ T-Cells Due to Cryopreservation of Peripheral Blood Mononuclear Cells Can Be Rescued by Cytokine Treatment After Thawing," *Cryobiology*, 47(1), 44–58, 2003.

123. Riccio, E.K., Neves, I., Banic, D.M., et al., "Cryopreservation of Peripheral Blood Mononuclear Cells Does Not Significantly Affect the Levels of Spontaneous Apoptosis After 24-h Culture," *Cryobiology*, 45(2), 127–134, 2002.

124. Baust, J.M., Cosentino, M., Meeks, E., Baer, J., Van Buskirk, R.G., and Baust, J.G., "Apoptotic Cell Ceath Contributes Significantly to Peripheral Blood Mononuclear Cells Cryopreservation Failure," *Cryobiology,* 51(3), 354–355, 2005.

125. Duru, N.K., Morshedi, M.S., Schuffner, A., and Oehninger, S., "Cryopreservation-Thawing of Fractionated Human Spermatozoa is Associated with Membrane Phosphatidylserine Externalization and Not DNA Fragmentation," *J. Androl.*, 22(4), 646–651, 2001.

126. Schuurhuis, G.J., Muijen, M.M., Oberink, J.W., de Boer, F., Ossenkoppele, G.J., and Broxterman, H.J., "Large Populations of Non-Clonogenic Early Apoptotic CD34-Positive Cells Are Present in Frozen-Thawed Peripheral Blood Stem Cell Transplants," *Bone Marrow Transplant*, 27(5), 487–498, 2001.

127. Lund, P.K., Westvik, A.B., Joo, G.B., Ovstebo, R., Haug, K.B., and Kierulf, P., "Flow Cytometric Evaluation of Apoptosis, Necrosis and Recovery When Culturing Monocytes," *J. Immunol. Method,* 252(1–2), 45–55, 2001.

128. Van Buskirk, R.G. "Viability and Functional Assays Used to Assess Preservation Efficacy: The Multiple Endpoint/Tier Approach," *Biopreservation*, Baust, J.G., and Baust, J.M., eds, T&F Informa, Boca Raton, FL, 2006, in press.

129. Vogel, M.J., Baust, J.M., Van Buskirk, R.G., and Baust, J.G., "Apoptotic Cascades Are Activated Following Cryopreservation," *Cryobiology*, 41(4), 390, 2000.

130. Vogel, M.J., Baust, J.M., Van Buskirk, R.G., and Baust, J.G., "Proteomic Profiling Following Cryopreservation: Evidence of a Complex Set of Biomolecular Events Influencing Survival," *Cryobiology*, 47(3), 259, 2003.

131. Baust, J.M., "Properties of Cells & Tissues Influencing Preservation Outcome: Molecular Basis of Preservation Induced Cell Death," *Advances in Biopreservation*, Baust, J.G., and Baust, J.M., eds. T&F Informa, Boca Raton, FL, 2006, in press.

132. Li, A.P., Gorycki, P.D., Hengstler, J.G., et al., "Present Status of the Application of Cryopreserved Hepatocytes in the Evaluation of Xenobiotics: Consensus of an International Expert Panel," *Chem. Biol. Interact.*, 121(1), 117–123, 1999.

133. Guillouzo, A., Rialland, L., Fautrel, A., and Guyomard, C., "Survival and Function of Isolated Hepatocytes After Cryopreservation," *Chem. Biol. Interact.*, 121(1), 7–16, 1999.

134. Rajotte, R.V., "Cryopreservation of Pancreatic Islets," *Transplant Proc.*, 26(2), 395–396, 1994.

135. Yokomuro, H., Mickle, D.A., Weisel, R.D., and Li, R.K., "Optimal Conditions for Heart Cell Cryopreservation for Transplantation," *Mol. Cell. Biochem.*, 242(1–2), 109–114, 2003.

136. Dannie, E. "Peripheral Blood Stem Cell Transplantation, Part 1," *Nurs. Stand.*, 11(10), 43–45, 1996.

137. Hubel, A., "Parameters of Cell Freezing: Implications for the Cryopreservation of Stem Cells," *Transfus. Med. Rev.*, 11(3), 224–233, 1997.

138. Anzar, M., He, L., Buhr, M.M., Kroetsch, T.G., and Pauls, K.P., "Sperm Apoptosis in Fresh and Cryopreserved Bull Semen Detected by Flow Cytometry and Its Relationship With Fertility," *Biol. Reprod.*, 66(2), 354–360, 2002.

139. Duru, N.K., Morshedi, M., Schuffner, A., and Oehninger, S., "Semen Treatment with Progesterone and/or Acetyl-L-Carnitine Does Not Improve Sperm Motility or Membrane Damage After Cryopreservation-Thawing," *Fertil. Steril.*, 74(4), 715–720, 2000.

140. Sosef, M.N., Baust, J.M., Sugimachi, K., Fowler, A., Tompkins, R.G., and Toner, M., "Cryopreservation of Isolated Primary Rat Hepatocytes: Enhanced Survival and Long-Term Hepatospecific Function," *Ann. Surg.*, 241(1), 125–133, 2005.

141. Mathew, A.J., Baust, J.M., Van Buskirk, R.G., and Baust, J.G., "Cell Preservation in Reparative and Regenerative Medicine: Evolution of Individualized Solution Composition," *Tissue Eng.*, 10(11–12), 1662–1671, 2004.

142. Taylor, M.J., Bailes, J.E., Elrifai, A.M., et al., "A New Solution For Life Without Blood. Asanguineous Low-Flow Perfusion of a Whole-Body Perfusate During 3 Hours of Cardiac Arrest and Profound Hypothermia," *Circulation*, 91(2), 431–444, 1995.

143. Sugimachi, K., Sosef, M.N., Baust, J.M., Fowler, A., Tompkins, R.G., and Toner, M., "Long-Term Function of Cryopreserved Rat Hepatocytes in a Coculture System," *Cell Transplant*, 13(2), 187–195, 2004.

144. Van Buskirk. R.G., Snyder, K.K., Baust, J.G., Mathew, A.J., and Baust, J.M., "Cryopreservation: It's Not Just About Cell Yield," *Bioprocess International*, 3(4), 64–74, 2005.

145. Mathew, A., Van Buskirk, R.G., and Baust, J.G., "Improved Hypothermic Preservation of Human Renal Cells Through Suppression of Both Apoptosis and Necrosis," *Cell Preservation Technology*, 1(4), 239–253, 2003.

146. Baicu, S.C., and Taylor, M.J., "Acid–Base Buffering in Organ Preservation Solutions as a Function of Temperature: New Parameters for Comparing Buffer Capacity and Efficiency," *Cryobiology*, 45(1), 33–48, 2002.

147. Stylianou, J., Vowels, M., and Hadfield, K., "CryoStor Significantly Improves Cryopreservation of Haematopoetic Stem Cells," *HSC*, 7, 117, 2005.

148. Snyder, K.K., Baust, J.M., Van Buskirk, R.G., and Baust, J.G., "Improved Cryopreservation of Vascular Tissue," *Cryobiology*, 51(3), 357–358, 2005.

149. Baust, J.M., Van Buskirk, R., and Baust, J.G., "Modulation of the Cryopreservation Cap: Elevated Survival With Reduced Dimethyl Sulfoxide Concentration," *Cryobiology*, 45(2), 97–108, 2002.

150. Robilotto, A.T., Baust, J.M., Van Buskirk, R., and Baust, J.G., "Calpain Activation Influences Cryopreservation Outcome," *Cell Preservation Technology*, 2006, in press.

Index